UNIVERSITY OF CALIFORNIA, SAN DIEGO

Quantum Dynamics and Magneto-Structural Correlations in Molecule Based Magnets

A dissertation submitted in partial satisfaction of the requirements for the degree Doctor of Philosophy in Chemistry

by

Christopher Craig Beedle

Committee in charge:

Professor David N. Hendrickson, Chair
Professor M. Brian Maple
Professor Arnold L. Rheingold
Professor Yitzhak Tor
Professor William C. Trogler

2010

The dissertation of Christopher Craig Beedle is approved, and it is acceptable in quality and form for publication on microfilm and electronically:

Chair

University of California, San Diego

2010

DEDICATION

to Mom and Richard

EPIGRAPH

I wish I had an answer to that because
I'm tired of answering that question.

And if you ask me anything I don't
know, I'm not going to answer.

-Yogi Berra

TABLE OF CONTENTS

LIST OF FIGURES

Chapter 1

Chapter 5

Chapter 6

Chapter 7

Chapter 8

LIST OF SCHEMES

Chapter 7

LIST OF TABLES

Chapter 7

Chapter 8

ACKNOWLEDGEMENTS

I would like to thank my advisor, Professor David N. Hendrickson. It has been an honor and a privilege to work with him and to be his last doctoral student. I will forever be grateful for the opportunities he has provided for me. I would also like to thank past and recent graduate students and undergraduate students that I have had the privilege to work with, namely: Dr. Evan Rumberger, Dr. En-che Yang, Dr. Katie Heroux, Dr. Patrick Feng, James Ma, Casey Stephenson, Pauline Han, Jordan Li and others, too many to name. I'm very appreciative of grad students at UCSD that I have been fortunate enough to know including, Paul Martinez, John Goeltz, Jon Smeija and Eric Benson. They have been a constant source of support and inspiration. Thanks also to Professor Arnie Rheingold, Professor M. Brian Maple, Dr. Pei-Chun Ho, and Dr. Todd Sayles for their collaborations and meaningful discussions.

From the University of Florida, physics, I would like to thank Changhyun Koo, Dr. Jon Lawrence, Saiti Datta and Dr. Junjie Liu, for their knowledge, time and expertise. And especially, Professor Steve Hill for always wanting, and expecting my opinion. At the University of Central Florida, I wish to thank Professor Enrique del Barco, Jon Henderson and Dr. Hajrah Quddusi.

Others that I wish to thank for their time, collaboration and discussions include, Dr. Motohiro Nakano, Dr. Wolfgang Wernsdorfer, Dr. Ming-Liang Tong, Professor Jonathan Friedman and Professor Andrew Kent.

Last, but not least, I want to thank my family. 2010 has not been a kind year to my family. I hope that this dissertation and the work that went into it are a bright spot in an otherwise trying year. Without friends and family we are nothing, and I am so thankful that friends and family have always been there for me!

Chapter 2, in full, has been submitted for publication to Inorganic Chemistry, 2010. Beedle, C. C., Wang, W. G., Zhou, A. J., Wornsdorfer, W., Koo, C., Hill, S., Nakano, M., Zhang, W. X.; Tong, M. L., Chen, X. M., Hendrickson, D. N., Geometric Frustration Leading to Magnetic Metastability in a High-Spin $Cu_{17}Mn_{28}$ Complex with T_d Symmetry. The dissertation Author is the primary investigator and author of this material.

Chapter 3, in part, is a reprint: Beedle, C. C., Ho, P-C., Sayles, T., Hamilton, J. J., del Barco, E., Nakano, M., O'Brien, J., Heroux, K. J., Maple, M. B., Hendrickson, D. N., Ferromagnetic Ordering and Simultaneous Fast Magnetization Tunneling in a Ni_4 Single Molecule Magnet, *Inorganic Chemistry*, **2010**, *49* (13), 5780–5782. The dissertation author is the primary investigator and author of this material.

Chapter 4, in part, is a reprint of a published communication: Beedle, C. C., Stephenson, C. J.; Heroux, K. J., Wernsdorfer, W., Hendrickson, D. N., Photoluminescent Mn-4 Single-Molecule Magnet. *Inorganic Chemistry* **2008,** 47, (23), 10798-10800. Other material in the chapter are for a paper in preparation: Beedle, C.C., Liu, J., Quddusi, H. Heroux, K. J., Stephenson, C. J., Han, P., Li, J., del Barco, E., Hill,

S., Hendrickson, D. N., Single-Crystal magnetization, HF-EPR and Structural Determination of Two Families of Mn_4 Photoluminescent Single-Molecule Magnets. The dissertation author is the primary investigator and author on this material.

Chapter 6, in part, is a reprint: Beedle, C. C., Heroux, K. J., Nakano, M.; DiPasquale, A. G., Rheingold, A. L., Hendrickson, D. N., Antiferromagnetic Tetranuclear Manganese Complex: Wheel or Dicubane? *Polyhedron* **2007,** 26, (9-11), 2200-2206. The dissertation author is the primary investigator and author of this material.

Chapter 7, figures are a reprint: Rumberger, E. M., Shah, S. J., Beedle, C. C.; Zakharov, L. N., Rheingold, A. L., Hendrickson, D. N., Wheel-shaped [Mn-12] Single-Molecule Magnets. *Inorganic Chemistry* **2005,** 44, (8), 2742-2752. The author of the dissertation was a highly contributing investigator of the material.

Chapter 8, figures and captions are reprints from: Lawrence, J., Beedle, C. C.; Yang, E. C., Ma, J.; Hill, S., Hendrickson, D. N., High Frequency Electron Paramagnetic Resonance (HF-EPR) Study of a High Spin Co(II) Complex. *Polyhedron* **2007,** 26, (9-11), 2299-2303, and, Liu, J.; Datta, S.; Bolin, E.; Lawrence, J.; Beedle, C. C.; Yang, E.-C.; Goy, P.; Hendrickson, D. N.; Hill, S., Anisotropic Exchange in a Tetranuclear Co^{II} Complex. *Polyhedron* **2009**, 28, (9) 1922-1926. The dissertation author was a highly contributing investigator on the material.

VITA

Education:

B.S., Chemistry, 2005, University of California, San Diego

Ph.D., Chemistry, 2010, University of California, San Diego

Publications:

1. Beedle, **C. C**., Wang, W. G., Zhou, A. J., Wornsdorfer, W., Koo, C., Hill, S., Nakano, M., Zhang, W. X.; Tong, M. L., Chen, X. M., Hendrickson, D. N., **Geometric Frustration Leading to Magnetic Metastability in a High-Spin $Cu_{17}Mn_{28}$ Complex with T_d Symmetry**. (Submitted).

2. del Barco, E.; Hill, S.; Beedle, C. C.; Hendrickson, D. N.; Tupitsyn, I. S.; Stamp, P. C. E., Tunneling and inversion symmetry in single-molecule magnets: **The case of the Mn_[12] wheel molecule.** *Physical Review B* **2010,** 82, (10), 104426.

3. Beedle, C. C.; Henderson, J. J.; Ho, P. C.; Sayles, T.; Nakano, M.; O'Brien, J. R.; Heroux, K. J.; del Barco, E.; Maple, M. B.; Hendrickson, D. N., **Ferromagnetic Ordering and Simultaneous Fast Magnetization Tunneling in a Ni-4 Single-Molecule Magnet.** *Inorganic Chemistry* **2010,** 49, (13), 5780-5782.

4. Takahashi, S.; van Tol, J.; Beedle, C. C.; Hendrickson, D. N.; Brunel, L. C.; Sherwin, M. S., **Coherent Manipulation and Decoherence of S=10 Single-Molecule Magnets**. *Physical Review Letters* **2009,** 102, (8).

5. Liu, J. J.; Datta, S.; Bolin, E.; Lawrence, J.; Beedle, C. C.; Yang, E. C.; Goy, P.; Hendrickson, D. N.; Hill, S., **Anisotropic exchange in a tetranuclear Co-II complex**. *Polyhedron* **2009,** 28, (9-10), 1922-1926.

6. Ramsey, C. M.; Del Barco, E.; Hill, S.; Shah, S. J.; Beedle, C. C.; Hendrickson, D. N., **Quantum interference of tunnel trajectories between states of different spin length in a dimeric molecular nanomagnet.** *Nature Physics* **2008,** 4, (4), 277-281.

7. Feng, P. L.; Beedle, C. C.; Koo, C.; Wernsdorfer, W.; Nakano, M.; Hill, S.; Hendrickson, D. N., **Heterometallic integer-spin analogues of S=9/2 Mn-4 cubane single-molecule magnets.** *Inorganic Chemistry* **2008,** 47, (8), 3188-3204.
8. Feng, P. L.; Beedle, C. C.; Koo, C.; Lawrence, J.; Hill, S.; Hendrickson, D. N., **Origin of magnetization tunneling in single-molecule magnets as determined by single-crystal high-frequency EPR**. *Inorganica Chimica Acta* **2008,** 361, (12-13), 3465-3480.

9. de Loubens, G.; Kent, A. D.; Krymov, V.; Gerfen, G. J.; Beedle, C. C.; Hendrickson, D. N., **High frequency EPR on dilute solutions of the single molecule magnet Ni-4.** *Journal of Applied Physics* **2008,** 103, (7).

10. de Loubens, G.; Garanin, D. A.; Beedle, C. C.; Hendrickson, D. N.; Kent, A. D., **Magnetization relaxation in the single-molecule magnet Ni-4 under continuous microwave irradiation.** *Euro-Physics Letters* **2008,** 83, (3).

11. Beedle, C. C.; Stephenson, C. J.; Heroux, K. J.; Wernsdorfer, W.; Hendrickson, D. N., **Photoluminescent Mn-4 Single-Molecule Magnet.** *Inorganic Chemistry* **2008,** 47, (23), 10798-10800.

12. Bal, M.; Friedman, J. R.; Chen, W.; Tuominen, M. T.; Beedle, C. C.; Rumberger, E. M.; Hendrickson, D. N., **Radiation- and phonon-bottleneck-induced tunneling in the Fe-8 single-molecule magnet.** *Euro-Physics Letters* **2008,** 82, (1).

13. Zhou, A. J.; Qin, L. J.; Beedle, C. C.; Ding, S.; Nakano, M.; Leng, J. D.; Tong, M. L.; Hendrickson, D. N., **New Mn-12 clusters with tunable oxidation states via the use of N,N,N ',N '-tetrakis(2-hydroxyethyl)ethylenediamine.** *Inorganic Chemistry* **2007,** 46, (20), 8111-8113.

14. Wang, W. G.; Zhou, A. J.; Zhang, W. X.; Tong, M. L.; Chen, X. M.; Nakano, M.; Beedle, C. C.; Hendrickson, D. N., **Giant heterometallic Cu17Mn28 cluster with T-d symmetry and high-spin ground state**. *Journal of the American Chemical Society* **2007,** 129, (5), 1014-1015.

15. Lawrence, J.; Beedle, C. C.; Yang, E. C.; Ma, J.; Hill, S.; Hendrickson, D. N., **High frequency electron paramagnetic resonance (HFEPR) study of a high spin Co(II) complex**. *Polyhedron* **2007,** 26, (9-11), 2299-2303.

16. Feng, P. L.; Beedle, C. C.; Wernsdorfer, W.; Koo, C.; Nakano, M.; Hill, S.; Hendrickson, D. N., **Heterometallic cubane single-molecule magnets.** *Inorganic Chemistry* **2007,** 46, (20), 8126-8128.

17. de Loubens, G.; Chaves-O'Flynn, G. D.; Kent, A. D.; Ramsey, C.; del Barco, E.; Beedle, C.; Hendrickson, D. N., **Magnetization and EPR studies of the single molecule magnet Ni-4 with integrated sensors.** *Journal of Applied Physics* **2007,** 101, (9).

18. Beedle, C. C.; Heroux, K. J.; Nakano, M.; DiPasquale, A. G.; Rheingold, A. L.; Hendrickson, D. N., **Antiferromagnetic tetranuclear manganese complex: Wheel or dicubane?** *Polyhedron* **2007,** 26, (9-11), 2200-2206.

19. Rumberger, E. M.; Shah, S. J.; Beedle, C. C.; Zakharov, L. N.; Rheingold, A. L.; Hendrickson, D. N., **Wheel-shaped [Mn-12] single-molecule magnets.** *Inorganic Chemistry* **2005,** 44, (8), 2742-2752.

ABSTRACT OF THE DISSERTATION

Quantum Dynamics and Magneto-Structural

Correlations in Molecule Based Magnets

by

Christopher Craig Beedle

Doctor of Philosophy in Chemistry

University of California, San Diego 2010

Professor David N. Hendrickson, Chair

The synthesis and study of magnetic nanostructures is of both intense scientific and technological interest. A single-molecule magnet (SMM) is a molecular nanomagnet that can be magnetized as a result of having a large spin ground state that experiences appreciable magnetoanisotropy, which leads to a thermodynamic barrier between “spin-up” and “spin-down” orientations. The monodisperse nature (same size, shape and anisotropy) of SMMs permits detailed studies of the magnetization and quantum dynamics of nanomagnets. The discovery of SMMs permitted, for the first time, detailed study of quantum effects associated with nanomagnets. The magnetic and quantum properties of these complexes is heavily dictated by molecular and crystal symmetry, and paramount to employing these systems as devices is a need to

thoroughly understand and control environmental factors that govern their magnetization and quantum dynamics. To some extent this can be achieved by changing or eliminating co-crystallized solvate molecules and interchanging coordinated peripheral ligands.

Magnetic and thermodynamic studies were carried out on a high symmetry system that exhibits a large spin ground state (S =51/2), a preferred orientation in an applied magnetic field, and slow magnetization relaxation dynamics. Strong competing magnetic exchange coupling between paramagnetic copper and manganese ions, in conjunction with high symmetry, gives rise to appreciable spin-frustration and geometric-frustration. These correlated effects lead to slow magnetization relaxation behavior.

Detailed magnetization and thermodynamic studies were performed on a series of tetranuclear nickel complexes that exhibit fast magnetization tunneling and magnetic ordering. Magnetic ordering is a collective process that should drastically suppress or terminate quantum tunneling processes. It is revealed that even in an ordered state, the molecules within the crystal lattice act as single domains, thus, molecules quickly switch between magnetic ordering and single-domain quantum tunneling.

A series/family of multifunctional tetranuclear manganese SMMs (magnetic and photoluminescent) were synthesized that systematically differ in co-crystallized solvate molecules and peripheral organic ligands to study magneto-structural correlation effects and quantum tunneling of magnetization. The goal is to couple emissive excited states to the magnetic moment of the SMM, which may allow, for the first time, detailed study of quantum dynamics on a 10^{-9}-10^{-12}s time scale.

Chapter 1

Introduction to Single-Molecule Magnets

1.1 Introduction

Single molecule magnets (SMMs) are single-domain polynuclear transition metal complexes that can be individually magnetized as a result of a large spin ground state (*S*) and appreciable negative axial anisotropy (*D*).[1-4] The combination of *S* and *D* give rise to a thermodynamic barrier ($D\hat{S}_z^2$) between the "spin-up" and "spin-down" states of the magnetic moment of the individual molecules.[4-6] The magnitude of the overall spin (*S*) is governed by the number of unpaired electrons in a system and how those electrons collectively correlate, and the axial zero-field splitting parameter (*D*) naturally arises due to appreciable spin-orbit interactions and crystal-field effects.[7-11] Mn^{III} ions have been employed extensively in synthesizing SMMs as they impart appreciable anisotropy due to Jahn-Teller distortions. Recent work on Mn_3^{III} oxo-centered triangles has shown that magnetoanisotropy can be maximized by employing ligands that promote alignment of the single-ion anisotropy tensors.[12-14]

The first, and most well studied, SMM was reported in 1993[1,15] and contains the general formula: $[Mn_{12}O_{12}(O_2CMe)_{16}(H_2O)_4] \cdot 2HOOCMe \cdot 4H_2O$, commonly referred to as Mn12-Ac or Mn12-Acetate (Figure 1.1). Magnetization versus field hysteresis measurements revealed regularly spaced vertical steps in exhibited hysteresis loops (Figure 1.2) that are attributed to quantum tunneling of the magnetization (QTM) between energy states of opposite spin projection.[15] This is an incredibly important discovery, because quantum effects had only been theorized for molecular systems prior to its discovery.[10,16] Furthermore, these nanoscale molecules exhibit both "classical" and "quantum" physical behavior. This has led to extensive fundamental research which has uncovered new and interesting quantum phenomena in these nano-magnetic

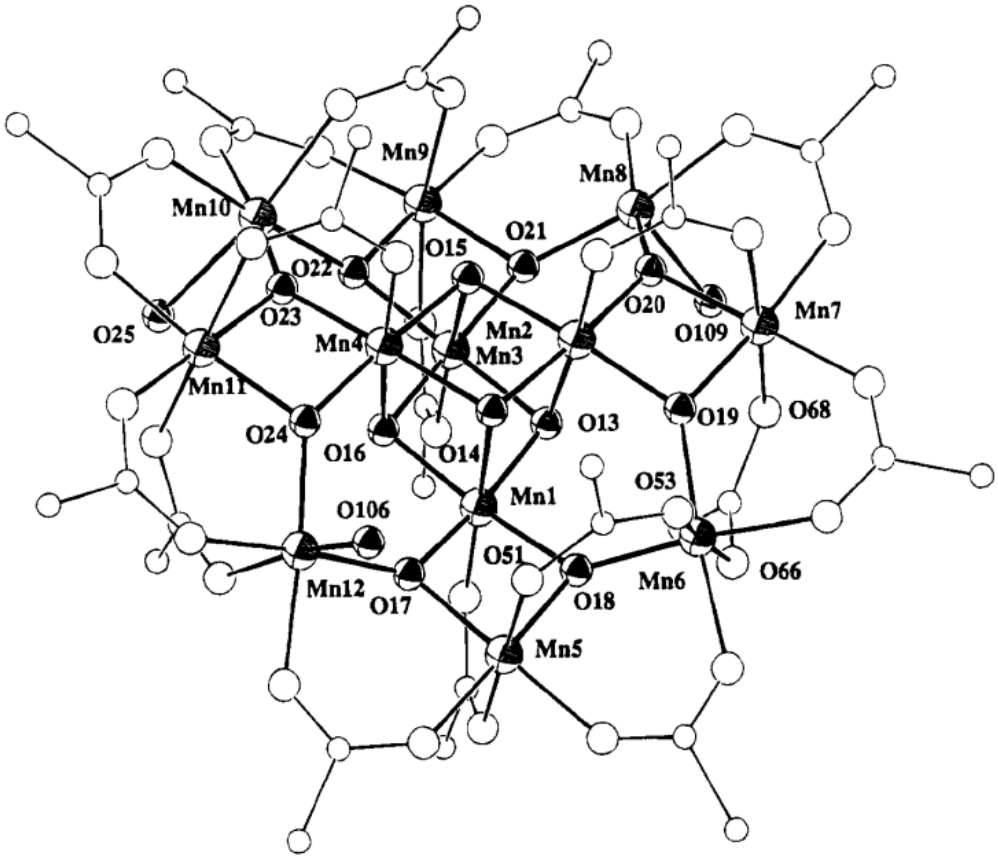

Figure 1.1. Ortep of the molecular structure of $[Mn_{12}O_{12}(O_2CMe)_{16}(H_2O)_4] \cdot 2HOOCMe \cdot 4H_2O$.[1]

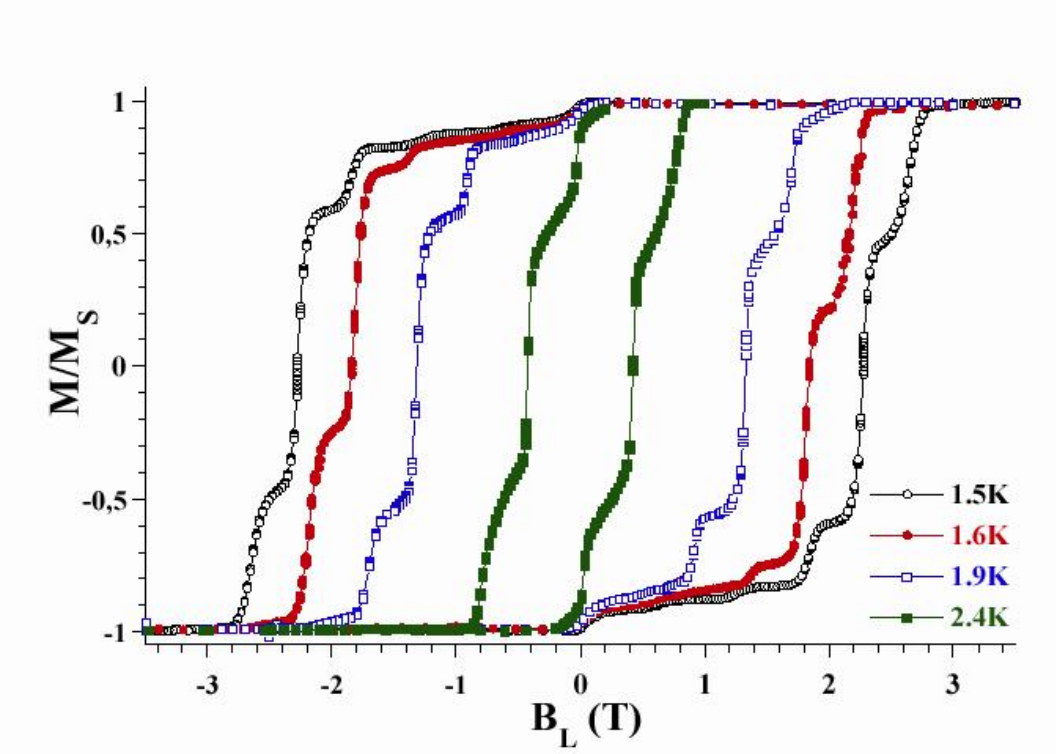

Figure 1.2. Magnetization hysteresis loops for **$[Mn_{12}O_{12}(O_2CMe)_{16}(H_2O)_4] \cdot 2HOOCMe \cdot 4H_2O$**.

materials including: spin-spin cross relaxation,[17] exchange-biased quantum tunneling,[18-21] spin-parity effects,[22,23] thermally activated and pure quantum tunneling,[24-27] and quantum phase interference (Berry-Phase).[28-31] It has been theorized that SMMs could be used in high-density magnetic storage devices and in quantum computation.

SMMs are uniquely suited for studying fundamental quantum phenomena due to their monodisperse nature, *i.e.* each molecule in the crystal has the same size, shape, anisotropy etc.[4,32-34] Employing a "bottom-up" approach, chemists have great synthetic control. For the most part, the peripheral ligands are easily exchanged, metal ions can be exchanged, and solvate molecules can be modulated or completely eliminated. This allows for the synthesis of series or families of related molecules to study how systematic changes in the crystal environment affect the physical properties of the individual molecules. Diversity in synthetic strategies has led to a variety of molecular topologies including: rods,[35] wheels,[36-44] cubanes,[18,45-51] dicubanes,[52-58] 1-D chains, as well as, 2-D and 3-D magnetic materials. [59-71]

1.2 Magnetic Exchange Interactions

The electronic structure of SMMs is dominated by the magnetic exchange ($-2J\hat{S}_i \bullet \hat{S}_j$) between adjacent paramagnetic centers bridged by another non-paramagnetic atom, usually oxygen or nitrogen. The unpaired spin on adjacent metal centers can be antiferromagnetic, where the spins are aligned antiparallel to each other, or ferromagnetic, where adjacent spins are aligned parallel to one another. In the former, antiferromagnetic coupling leads to minimization of the overall spin, while the later maximizes the overall spin. The nature of the magnetic exchange is strongly

dictated by the overlap and symmetry of the orbital wavefunctions of the metal centers and the bridging hetero-atom, and the angle (α) between them. The "magic" angle depends totally on the symmetry of the wave functions and wave function mixing; however, in many complexes this lies approximately between 97 and 115 degrees. If the angle (α) between metal centers is 180 degrees (Figure 1.3) the unpaired spins interact directly through the same p-orbital of the bridging ion. This leads to an antiferromagnetic correlation. However, when α is close to 90 degrees, the unpaired spins interact through p-orbitals that are orthogonal, and thus, depending on the nature of the metal ions, ferromagnetic interactions result.

In many SMMs the spin ground state results from a combination of ferro- and antiferromagnetic pairwise magnetic exchange interactions. An example of this is the $Mn_{12}Ac$ complex. In this complex the four $S = 3/2$ Mn^{IV} ions that make up the cubane core ferromagnetically couple ($S = (4 \times 3/2) = 6$), and the eight peripheral $S = 2$ Mn^{III} ions ferromagnetically couple ($S = (8 \times 2) = 16$). However, these two components antiferromagnetically couple to each other, yielding an overall ground state of $S = 10$.

As we will see in later chapters, one cannot always discern the nature of all of the pairwise exchange interactions. This is particularly true of large molecules (many paramagnetic centers). Furthermore, in many systems a simple model can not be established to estimate intermediate spin ground states obtained through magnetometry. In some cases this is due to competing exchange interactions that result in a spin-frustrated system. If we take the case of an equilateral triangle (Figure 1.4), where a single spin is positioned at each of the triangle vertices ($J_1 = J_2 = J_3$), if ferromagnetic exchange interactions dominate, then the spins align parallel giving a $S = 3/2$ ground

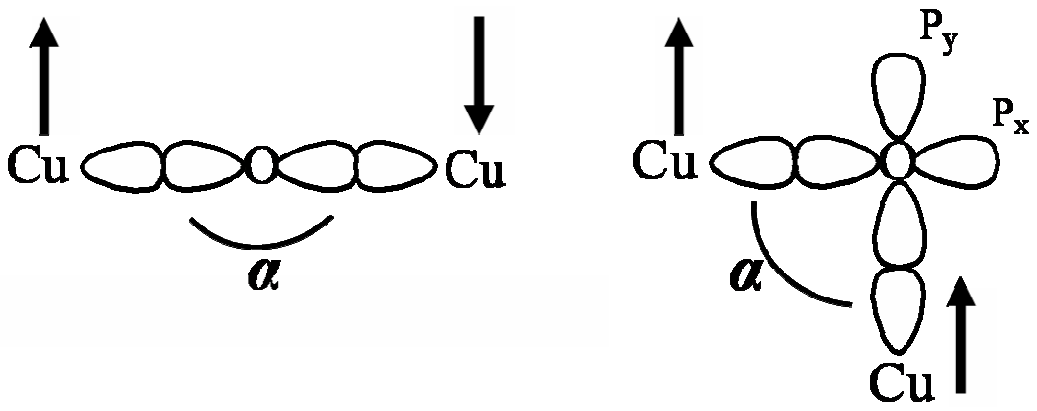

Figure 1.3. Depiction of magnetic exchange coupling between two Cu^{II} ions: Antiferromagnetic exchange (left) and ferromagnetic exchange (right).

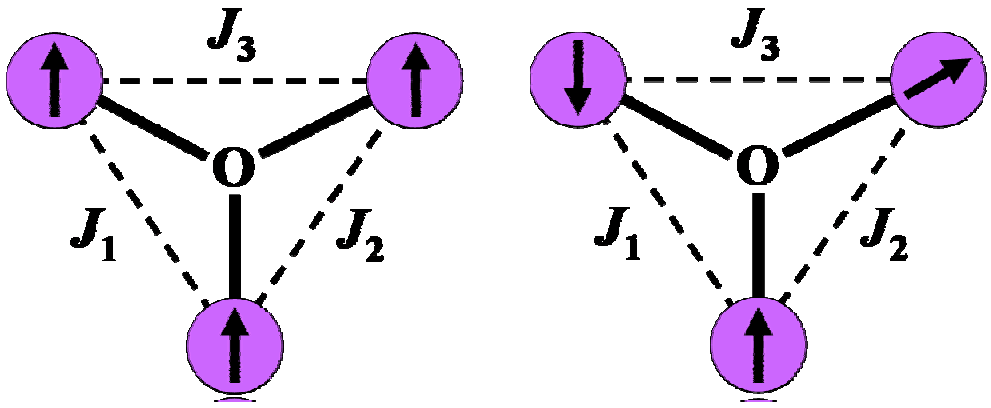

Figure 1.4. Depiction of an exchange coupled three spin model, showing ferromagnetic coupling (left) and antiferromagnetic coupling (right), leading to spin frustration.

state. However, if antiferromagnetic interactions dominate, two of the spins can antiferromagnetically couple, but the third spin is unable to simultaneously antiferromagnetically couple to the other spins, thus, the system is frustrated. Interestingly, this does not typically lead to a $S = ½$ ground state, but rather, frustration leads to tilting of the vectors of the spin projections yielding an intermediate spin ground state that is not readily obvious. There are other factors that are important in determining the nature of the exchange interactions. For instance, if we take the case of an isosceles triangle, where $J_1 = J_2 \neq J_3$, which is prevalent in mixed valent Fe and Mn based oxo-centered $[M_2^{III}M^{II}O]^{6+}$ triangles,[72-74] ferrimagnetic exchange and antisymmetric exchange play important roles in determining the electronic ground state. Antisymmetric exchange has been found to be very important in understanding the electronic structure of cubane cobalt complexes.[75,76] One must also take into account the projections of local anisotropies at individual metal centers and how they project onto the overall anisotropy (easy-axis) of the complex. Recently published work on Ni_4^{II} cubane complexes has established that when the magnitude of the local-ion anisotropy (d_i) is of the same magnitude as the local exchange coupling (J_{ij}), where i and j are discrete, nearest neighbor paramagnetic centers, symmetry dictated energy state mixing can occur.[77,78] Clearly, the electronic structure of these complexes is highly complex, making them difficult to thoroughly characterize, and in some cases, impossible to sufficiently characterize.

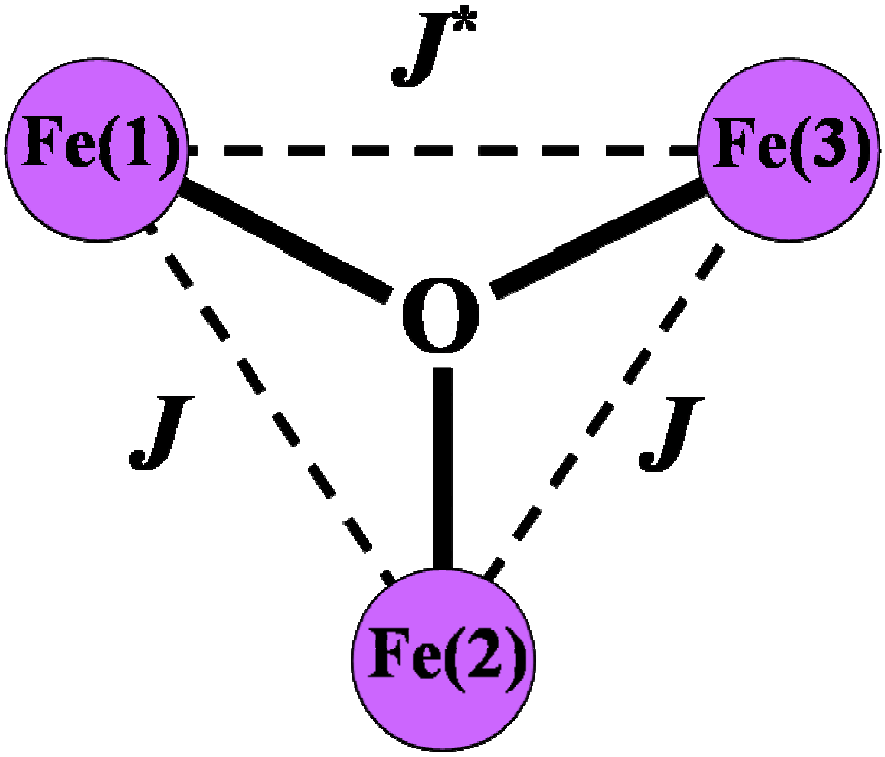

Figure 1.5. Exchange coupled model of a trinuclear iron complex, where $J = J \neq J^*$.

1.3 DC Magnetic Susceptibility

The temperature dependence of a diamagnetic or paramagnetic system can be analyzed by plotting the molar susceptibility product plotted versus the absolute temperature ($\chi_m T$ vs. T). These measurements can be performed on powder samples or with oriented single crystals. The value of the $\chi_m T$ product with decreasing temperature provides a gauge of Shottky distributions of energy states, and the nature of the magnetic exchange interactions (ferromagnetic, antiferromagnetic and diamagnetic). The Kambe equivalent operator method[79] is often used to determine the spin ground state (S), distribution of eigen-states, and evaluate magnetic exchange parameters (J) in simple systems where magnetic exchange interactions can be easily deduced, or simplified, through symmetry considerations. Figure 1.5 shows a theoretical oxo-

$$\hat{H} = -2J\sum_{ij}^{n} \hat{S}_i \hat{S}_j \qquad \textbf{(1.1)}$$

$$\hat{H} = -2J(\hat{S}_1 \cdot \hat{S}_2 + \hat{S}_2 \cdot \hat{S}_3) - 2J^*(\hat{S}_1 \cdot \hat{S}_3) \qquad \textbf{(1.2)}$$

$$\hat{S}_A = \hat{S}_1 + \hat{S}_3 \qquad\qquad \hat{S}_T = \hat{S}_A + \hat{S}_2 \qquad \textbf{(1.3)}$$

$$\hat{H} = -J(\hat{S}_T^2 - \hat{S}_A^2) - J^*(\hat{S}_A^2) \qquad \textbf{(1.4)}$$

$$E(S_T) = -J[S_T(S_T+1) - S_A(S_A+1)] - J^*[S_A(S_A+1)] \qquad \textbf{(1.5)}$$

$$\chi_M = \left(\frac{Ng^2\mu_B^2}{3kT}\right)\frac{\sum[S_T(S_T+1)(2S_T+1)e^{\frac{-E(S_T)}{k_BT}}}{\sum(2S_T+1)e^{\frac{-E(S_T)}{k_BT}}} \qquad \textbf{(1.6)}$$

centered trinuclear Fe^{III} system, where the exchange interactions Fe(1)-Fe(2) and Fe(2)-Fe(3) are equivalent and equal J, and the exchange parameter Fe(1)-Fe(3) equals J^*, where $J \neq J^*$. $\chi_m T$ vs. T data can be evaluated employing Equation 1.1, where only the isotropic exchange between nearest neighbor metal centers is evaluated, and Zeeman and axial zero-field interactions are ignored. Equations 1.2 through 1.4 are applied to find equivalent operators which satisfy the eigen-value equation (Equation 1.5). The data can then be least-squares fit employing the Heisenberg-Dirac-Van Vleck equation (Equation 1.6), where where g is the Landé g-tensor, N is Avogadro's number, μ_B is the Bohr magneton, and k_B is the Boltzmann constant. The best fit of the experimental molar susceptibility data to the theoretical model provides estimates of the sign and magnitude of the magnetic exchange parameters (J and J^*) and the eigen-energies of all of the possible spin states. It should be noted that the Kambe method is not applicable in certain topological applications such as single-stranded wheel or loop structures, as accounting for pair-wise magnetic exchange interactions between paramagnetic centers leads to double-counting, resulting in a redundant set of functions describing the electronic structure of the molecules. In these cases, a full-matrix diagonalization approach in the full Hilbert space is required to assess parameters of the applied spin Hamiltonian. Though, in the case of molecules with very large spin ground states, this approach is limited as well by available computation capabilities, *e.g.* The Hamiltonian matrix for a $S = 51/2$ system is of the dimensions $(4 \times 10^{32}) \times (4 \times 10^{32})$.

Alternatively, magnetic susceptibility data plotted as M vs. H/T (reduced magnetization) can be evaluated to discern the ground state spin (S) and the magnitude of the zero-field splitting parameter (D), where M is the net magnetization and H/T is

the applied magnetic field times the absolute inverse temperature. A plot of *M* vs. *H/T* collected at various fields in the low temperature region (1.8-5K) reveals field dependence in a sample. At sufficiently high temperatures, SMMs exhibit little net or no magnetization in zero applied fields, and individual magnetic moments freely flip between "spin-up" and Spin-down" orientations. However, in the presence of strong magnetic fields, and at sufficiently low temperatures, Boltzman distributions of energy states are systematically thermally depopulated and the magnetic moments of individual molecules align themselves in the direction of the applied field and reach a finite magnetization, or magnetization saturation. In systems void of zero-field interactions the plot of *M* vs. *H/T* reveals that the individual magnetization curves superimpose, and

$$\hat{H} = D\hat{S}_z^{\,2} + E(\hat{S}_x^{\,2} - \hat{S}_y^{\,2}) + B_4^{\,0}\hat{O}_4^{\,0} + B_4^{\,4}\hat{O}_4^{\,4} + g\mu_B\hat{\vec{S}}\cdot\hat{\vec{H}} + \hat{H}_1 \qquad \textbf{(1.7)}$$

$$M = \frac{\sum_{i=-s}^{s} (\partial E_i / \partial H)\exp(-E_i / kT)}{\sum_{i=-s}^{s} \exp(-E / kT)} \qquad \textbf{(1.8)}$$

the magnetization value will be equal to 2*S*. However, in the presence of appreciable zero-field interactions, the degeneracy of the 2*S* states is lifted and split into 2*S* +1 states and the individual magnetization curves do not superimpose. *M* vs. *H/T* data can then be evaluated employing a spin Hamiltonian (Equation 1.7), where *D* is the 2nd-order zero-field splitting parameter, $\hat{S}$ is the spin operator, $E(\hat{S}_x^{\,2} - \hat{S}_y^{\,2})$ is the rhombic

transverse second-order zero-field splitting term, $B_4^0\hat{O}_4^0$ and $B_4^4\hat{O}_4^4$ are 4th-order zero-field splitting terms, $g\mu_B\hat{\vec{S}}\cdot\hat{\vec{H}}$ is the Zeeman term and $\hat{H}_1$ represents higher order zero-field splitting terms (terms included in the spin Hamiltonian are based on symmetry considerations). Evaluation of the Hamiltonian by full-matrix diagonalization yields optimized fit parameters and eigen-energies E_i. The calculated eigen-states are employed to calculate the magnetization employing Equation 1.8. It should be noted that diagonalization of the Hamiltonian matrix is limited in that it is assumed the complex exhibits a well isolated spin ground state, *i.e.* there is no excited state mixing, S and M_s are good quantum numbers, and there are no appreciable intermolecular interactions. If the energy separations within the complex are fairly well defined, this method, in conjunction with fits of variable temperature data, is a very good gauge of the parameters: g, S, D, and J (though the absolute sign of D is ambiguous and will be discussed *vida supra*).

Zero-field cooled field-cooled (FC-ZFC) studies can also be a powerful tool for studying magnetization behavior in SMMs. The process entails cooling a sample in zero applied field to a temperature minimum ($T_{\min}$). A fixed external field is then applied, and the magnetization is monitored at regular temperature intervals to a temperature where individual magnetic moments will randomize. With the applied field on the temperature is then lowered back to $T_{\min}$. Deviation from superimposibility between the temperature up-sweep and down-sweep can reveal important information such as the crossover temperature, where the molecule transitions from a paramagnet to a SMM, *i.e.* the blocking temperature. The deviation arises because the molecules have

a memory toward their direction of magnetization. When approaching from the high-temperature side, in an applied magnetic field (FC), the magnetic moments in SMMs will spontaneously align at a critical temperature (T_B) as the magnetic moments go from a equilibrium state where moments are randomly flipping between "spin-up" and "spin-down" states to a blocked state where the single domains align (the blocking temperature will significantly vary with changing applied magnetic field strength). When approaching T_B from the low temperature side, the individual magnetic moments are strongly correlated, thus, a higher temperature must be obtained in order to randomize the individual magnetic moments (ZFC). FC-ZFC data can also be used to study magnetic phase transitions that arise due to magnetic ordering, as well as other phenomena. If data are collected in a series of applied dc fields one can deduce the correlation energy. At an applied field F_c the Zeeman energy will be of a greater magnitude than the ordering energy and the ordering will be shifted to lower temperatures or completely resolved.

1.4 AC Magnetic Susceptibility

Though the theoretical thermodynamic barrier for reversal of magnetization can be calculated by $D\hat{S}_z^2$, the kinetic energy barrier for magnetization reversal and subsequent magnetization relaxation is frequently calculated employing ac magnetic susceptibility experiments. The intrinsic barrier toward the reversal of magnetization leads to slow relaxation processes (Figure 1.8). The sample is subjected to an

$$M_{ac} = M_0 \cos\phi \sin(\omega t) = \chi' H_0 \cos(\omega t) + \chi'' H_0 \sin(\omega t) \quad \textbf{(1.9)}$$

oscillating ac field (~3Oe) in zero applied dc field. The magnetization response to the sweeping ac-field is given in Equation 1.9, where ω is the applied frequency, χ' is the real portion of the susceptibility, and χ'' is the imaginary portion of the susceptibility that arises due to energy changes as a result of absorption of the oscillating ac-field (Figure 1.6). An appreciable barrier toward magnetization reversal manifests itself as temperature and frequency dependent in-phase (χ′) and out-of-phase signals (χ′′). This is a direct result of the inability of the flipping magnetic moment of the molecules to stay in phase with the oscillating ac field. This process is both thermally and frequency controlled. Thus, as the temperature is lowered there is less thermal energy and the flipping magnetic moment is affected to a greater extent by higher frequencies. As the barrier toward magnetization reversal increases, the higher the temperature at which an out-of phase component in the ac susceptibility occurs. It is important to note that some classical systems exhibit both temperature and frequency dependent in-phase and out-of-phase components in their ac susceptibility. Therefore, though out-of-phase signals due to slow relaxation processes are a hallmark of SMMs, it can not solely be used quantitatively to identify a SMM.

The in-phase component of the ac susceptibility can be employed as a third method for establishing the spin ground state of a system. One can plot the lowest frequency (usually 10Hz) data as $\chi_m T$ vs. T and extrapolate to 0K. The value of the molar susceptibility at the y-intercept can then be compared to referenced spin states using the "spin-only" formula, which gauges the molar susceptibility based on the total

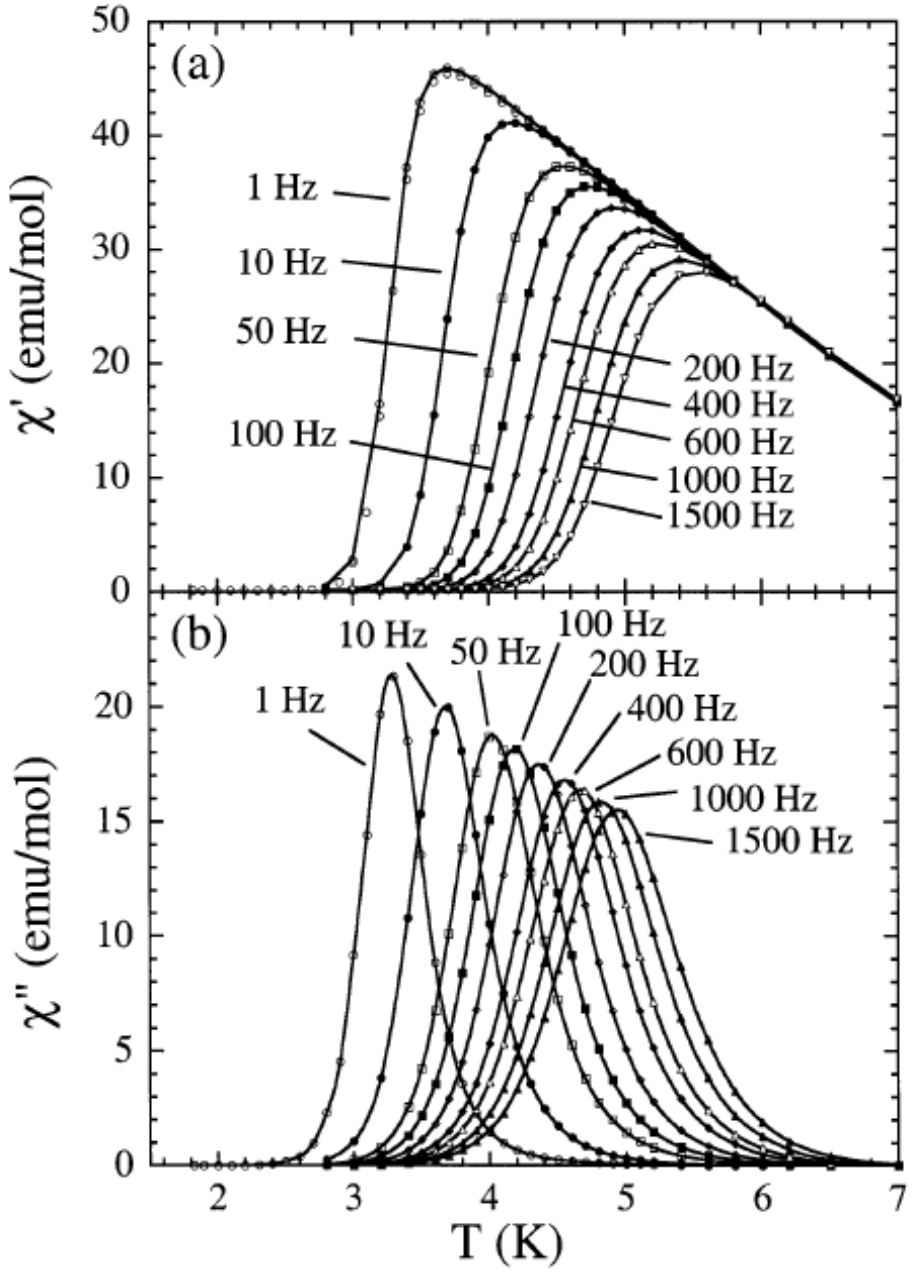

Figure 1.6. Plots of in-phase (top) and out-of-phase (bottom) ac magnetic susceptibility for $[Mn_2(saltmen)_2Ni(pao)_2(py)_2](ClO_4)_2$.[80]

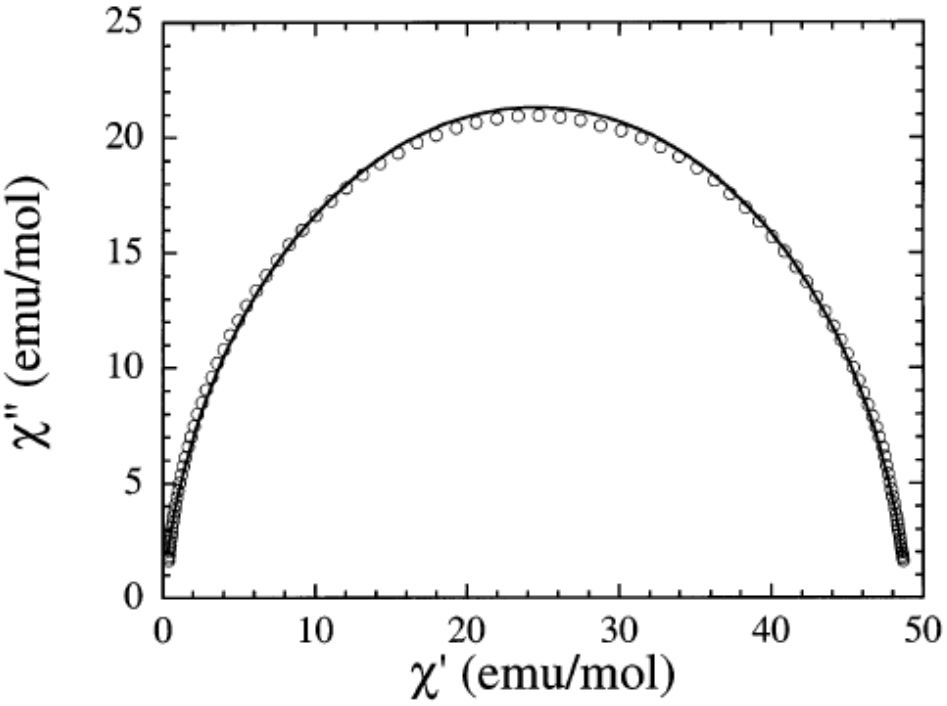

Figure 1.7. Cole-Cole plot showing semi-circle representative of magnetization relaxation behavior resulting from a single relaxation process for $[Mn_2(saltmen)_2Ni(pao)_2(py)_2](ClO_4)_2$.[80]

number of paramagnetic nuclei, the spin of those nuclei in a non-interacting environment, *i.e.* no magnetic exchange interactions. This method is particularly telling because the susceptibility response is acquired in zero applied dc field. As a result, the mixing of excited states and population of low lying states due to Zeeman interactions are minimized.

If the out-of-phase signal occurs at a high enough temperature, where the maxima and low temperature tails of the iso-fields are observed, the individual iso-fields are fit to a Gaussian function to determine the exact peak position. The resulting data can be plotted as lnτ vs. 1/T, where $\tau = 1/(2\pi\nu)$, and ν is the frequency. The data are then least-squares fit, and the slope of the best fit line is equal to U_{eff}, the activation energy, or kinetic barrier to the reversal of magnetization. In SMMs this calculated value is usually significantly lower than the theoretical barrier calculated from $D\hat{S}_z^2$. This is a strong suggestion that the effective barrier U_{eff} is lower due to quantum tunneling processes.

$$\chi(\omega) = \chi_s + \frac{\chi_0 - \chi_s}{1 + (i\omega\tau_c)^{1-\alpha}} \qquad \textbf{(1.10)}$$

$$\chi''(\chi') = -\frac{\chi_0 - \chi_s}{2\tan[(1-\alpha)\pi/2]} + \sqrt{(\chi' - \chi_s)(\chi_0 - \chi') + \frac{(\chi_0 - \chi_s)^2}{4\tan^2[(1-\alpha)\pi/2]}} \qquad \textbf{(1.11)}$$

To qualitatively look at relaxation processes in SMMS, χ′′ vs. χ′ can be plotted (Cole-Cole plot, Figure 1.7). If the resulting graph is a semi-circle (each plot point on

the graph being single-valued) then there is only one governing relaxation process. The ac magnetic susceptibility can be analyzed employing the Cole-Cole equation (Equation 1.10), where χ_0 is the adiabatic susceptibility and χ_s is the isothermal susceptibility, τ_c is the relaxation time, ω is the frequency, and α is the distribution of relaxation times. Employing Equation 1.10, the χ' and χ'' components can be disseminated and χ'' can be expressed as a function of χ' (Equation 1.11). Experimental data can then be least squares fit yielding both the relaxation time (τ_c) and distribution of relaxation rates (α). However, in most SMMs the magnetization relaxation processes can be quite complicated and are derived from any number of mechanisms including: spin-spin cross relaxation (SSCR),[17] spin-phonon interactions,[81,82] dipolar interactions,[83-87] nuclear hyperfine interactions[88,89] and mixing of low-lying excited states.[13] Thus, it is not always possible to apply simple Cole-Cole analysis.

1.5 Magnetization Versus Field Hysteresis Loops and Quantum Tunneling

The intrinsic negative axial magnetoanisotropy (D) of SMMs is conjunction with a relatively large spin ground state (S) gives rise to a thermodynamic barrier ($U = D\hat{S}_z^2$) for magnetization reversal between spin projections of opposite sign ("spin-up" and "spin-down" states). Figure 1.8 (Top) illustrates the double well potential diagram for the Mn12-Ac complex, where the m_s = 10 and m_s = -10 states are degenerate and lie at lowest energy in the absence of an applied magnetic field. For the magnetic moment to reverse its spin orientation it must either acquire enough thermal energy to climb the barrier ($kT > D\hat{S}_z^2$), or it can circumvent the barrier by quantum mechanically tunneling

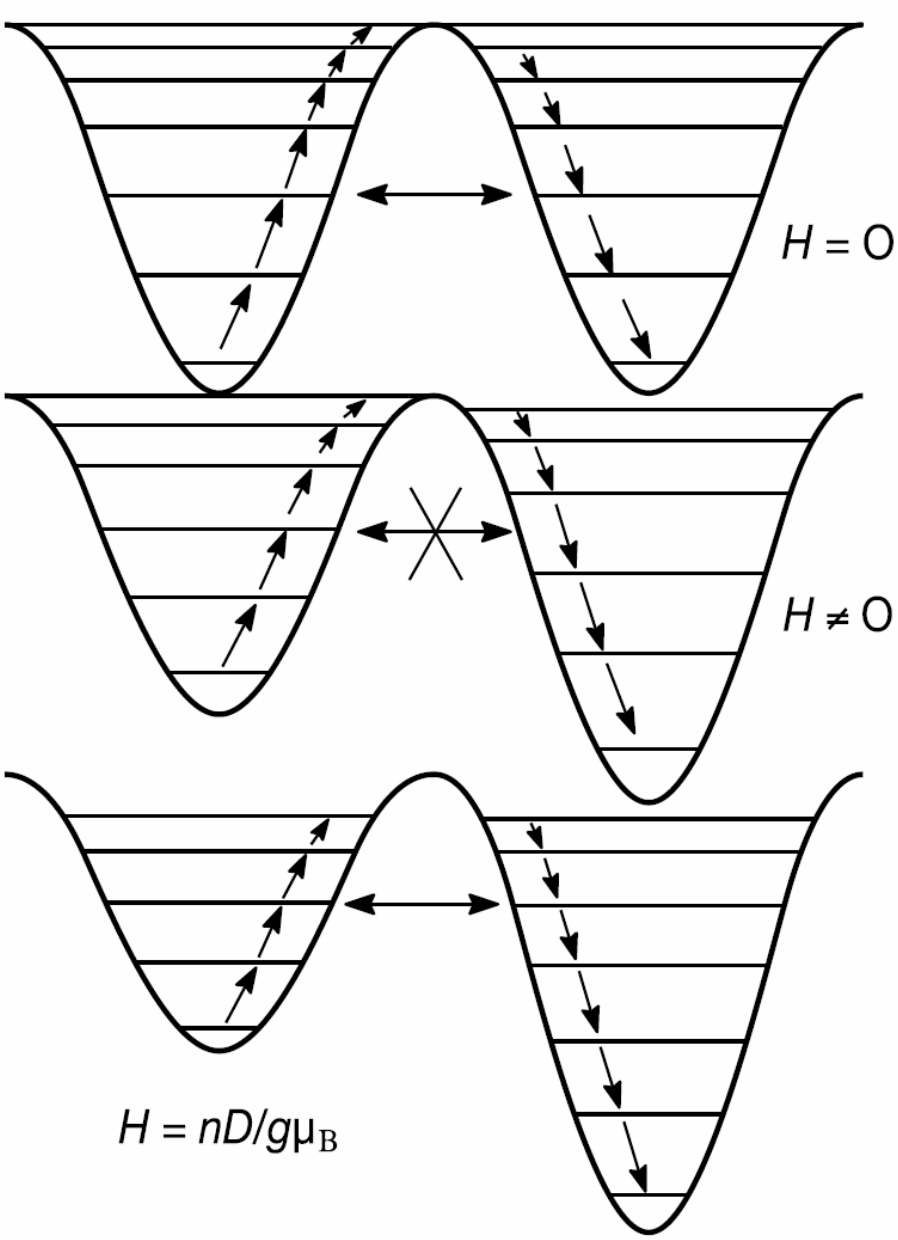

Figure 1.8. Theoretical double well potential energy barrier for a spin system with a negative zero-field splitting parameter (D). In zero applied field $H = 0$ (top), m_s states of opposite spin projection are degenerate. With application of an applied magnetic field the "sin-up" and "spin-down" states are no longer degenerate and population of m_s states favors alignment with the external field. In the quantum tunneling regime the system can be "on-resonance"(bottom) or "off-resonance"(top).[4]

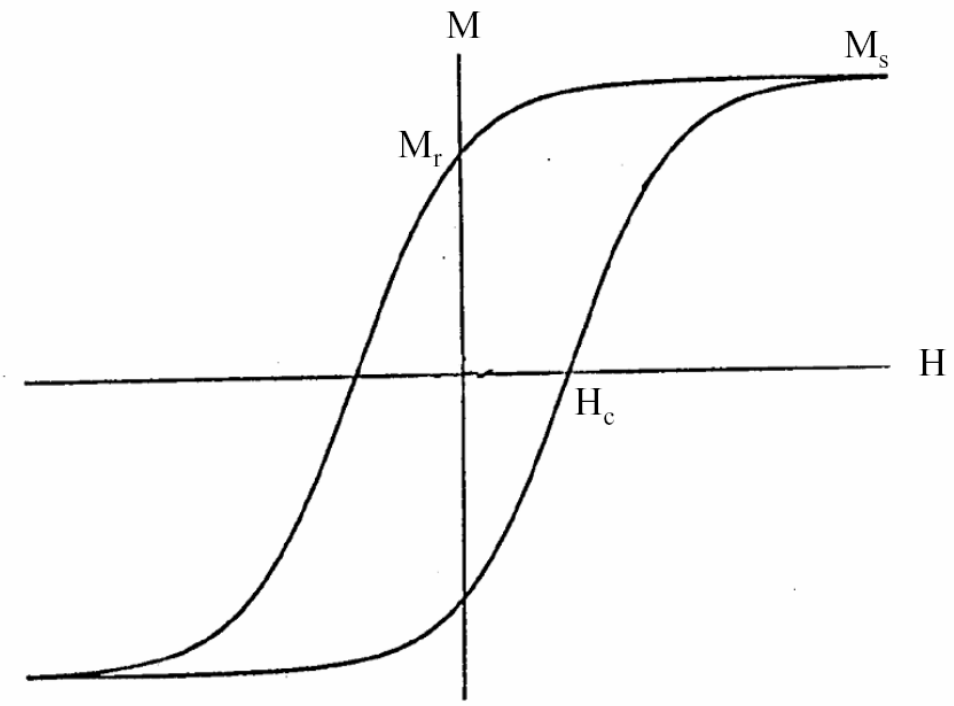

Figure 1.9. magnetization hysteresis loop for a classical magnet. M = magnetization, H = applied magnetic field strength, M_s = magnetization saturation, M_r = remnant magnetization and H_c = coercive magnetic field strength.

through the barrier. With application of an externally applied magnetic field ($H > 0$), the degeneracy of the m_s states are lifted and the Boltzman population favors the well that is in the direction of the applied magnetic field (Figure 1.8, middle).

Magnetization versus field hysteresis experiments are integral tools for studying magnetic phenomena and quantum effects. A magnetization versus field hysteresis loop for a classical magnet is presented in Figure 1.9. As the applied magnetic field is swept from $H = 0$ to $H > 0$, the magnetic moments align with the field until magnetic saturation occurs (the field at which saturation occurs is sample dependent). When the direction of the field is reversed, and if the temperature is maintained at a relatively high value, the trace of the magnetization response will superimpose and no coercivity will be exhibited. However, below the blocking temperature (T_B), following saturation of the magnetization, when the field direction is reversed the two traces will not superimpose giving rise to a symmetric loop. The coercivity is both temperature and sweep rate dependent. If the magnetic field is turned off upon reaching saturation the magnetization value will not tend to zero below T_B, but will stay essentially constant until there is enough thermal energy for the magnetization to relax or until the magnetic field strength is sufficient enough to reverse the magnetic moment. This is referred to as the coercive-field (H_c). Therefore, the magnetic moment below T_B has a "memory" toward its direction of magnetization and the magnetization value is not a linear function of the applied magnetic field. In classical magnets coercivity is the response to the destruction and reformation of multi-moment domain walls as they interact with the applied magnetic field. However, the hysteretic response in SMMs differ because the

system is made up of single molecule domains. As a result, these molecular nanoscale systems were the first systems to exhibit quantum effects.

Temperature dependent magnetization hysteresis loops for Mn12-ac are given in Figure 1.2, with the applied field directed along the easy-axis of the molecules.[1] As apposed to classical systems, the hysteresis loops for many SMMs exhibit features or "steps" in their magnetization loops as a result of quantum tunneling. The change in magnetization at each step is directly related to the magnitude of the tunnel splitting and the number of molecules that lie within the narrow energy band of the tunneling window. The greater the number of molecules in the tunneling window, the greater the change in total magnetization. This process is governed by the magnitude of the tunnel splitting. The observed resonances occur at regular intervals of the zero-field splitting parameter (D) and can be directly correlated to the magnitude of the applied magnetic field. The regular occurrence of steps can be qualitatively explained employing the three diagrams in Figure 1.8. With the application of a magnetic field the spin distribution between "spin-up" and "spin-down" states favors the direction that is aligned with the magnetic field (Figure 1.8, top). As the applied field strength is increased the system can be on-resonance or off-resonance. If the system is on-resonance, the magnetic moment can tunnel between metastable m_s states of opposite spin projection if there is appreciable overlap between wave functions. The cycling of on- and off-resonance (Figure 1.8, middle and bottom) will continue until the magnetization reaches saturation. At which time, the magnetic moments of the molecules will be predominately at lowest energy ($m_s = \pm 10$ for the Mn12-ac with $S = 10$ spin ground state). The step at $H = 0$ in Figure 1.2 is attributed to ground state

tunneling between m_s = -10 and m_s 10 states and is referred to as the k = 0 resonance. The other resonances represent transitions between the ground state and successive Δm_s values, *i.e.* k = 1 (Δm_s |-10 to +9|), k = 2 (Δm_s |-10 to +8|)…

For SMMs that exhibit steps in their magnetization versus field hysteresis loops, the k-resonances appear sequentially: k = 0, 1, 2, 3… However, only resonances dictated by the symmetry of the molecule should be observed. For instance, a molecule with two-fold symmetry should only exhibit resonances that differ by $k = \pm 2$ (k = 0, 2, 4, 6…).

In 2009 *Henderson et al.*[12] introduced the first SMM to ever experimentally follow selection rules for quantum tunneling resonances. This SMM has the general formula: $[Net_4][Mn_3Zn_2(salox)_3O(N_3)_6X_2]$, where X = Cl or Br (abbreviated as Mn_3-salox). The system is based on the well characterized $[Mn_3^{III}O]^{7+}$ oxo-centered triangle. Contrary to previously reported μ_3-oxo-centered triangles that are dominated by antiferromagnetic exchange interactions, appreciable intermolecular interactions, small spin ground states, and low crystal symmetry, the system reported by *Feng et al.*[14,90] exhibits ferromagnetic interactions and possesses a S = 6 spin ground state with C_3 molecular site symmetry. The ferromagnetic interactions are mediated by the torsion angle created by the chelating salox ligands which force the central μ_3-oxo into the same plane as the Mn^{III} ions. Furthermore, the bulky $[Net_4]^+$ counter-ions act as insulation between molecules and minimizes intermolecular interactions leading to a well-isolated spin ground state.

The three-fold symmetric rotation axis dictates that only resonances that differ by $|\Delta m_s| = 3n$ should be observed. Figure 1.10 shows the sweep rate (left) and

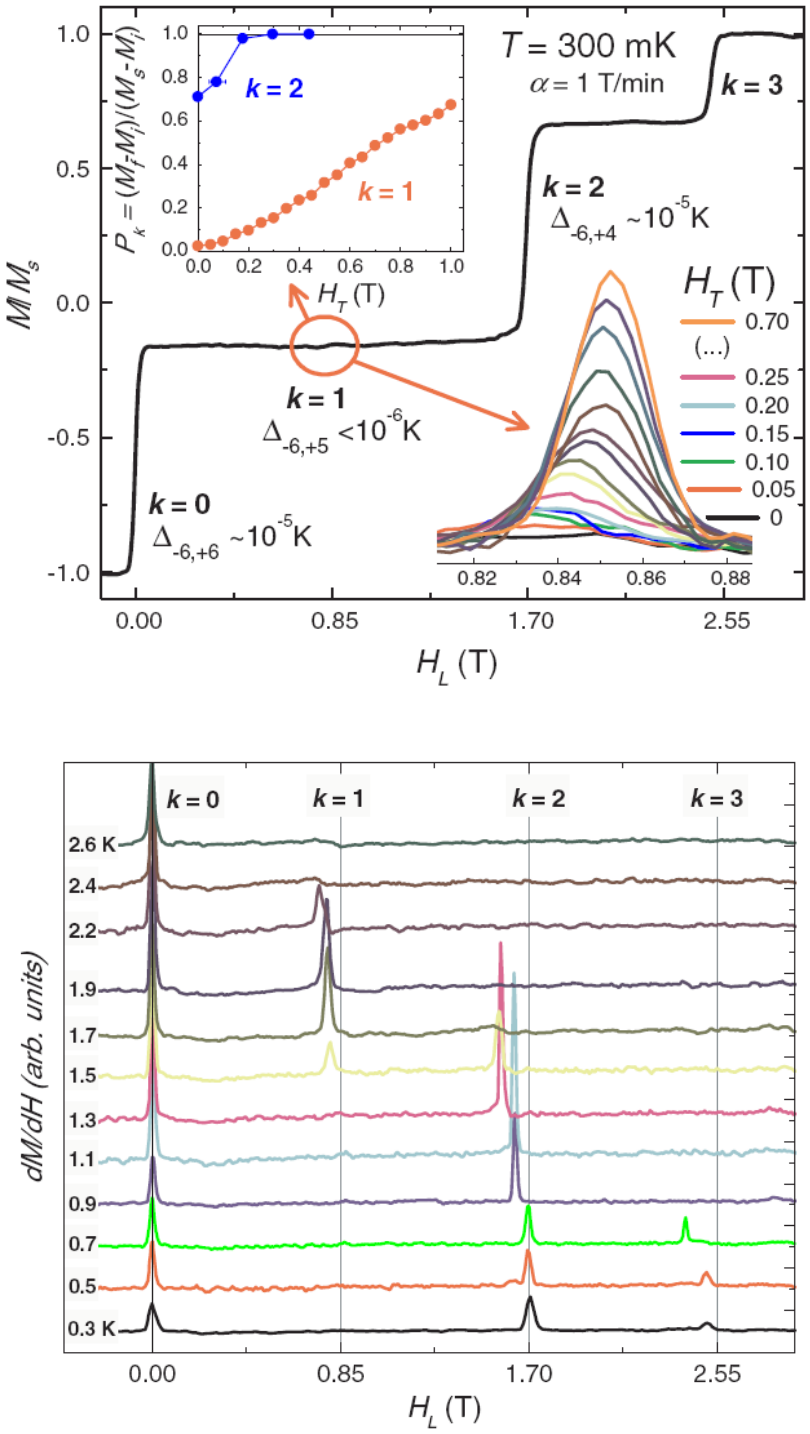

Figure 1.10. (top) Magnetization hysteresis loop for $[Net_4][Mn_3Zn_2(salox)_3O(N_3)_6Cl_2]$ sowing absence of $k = 1$ resonance, and sweep-rate dependence of the $k = 1$ resonance. (bottom) First derivative plot of magnetization vs. hysteresis loops for $[Net_4][Mn_3Zn_2(salox)_3O(N_3)_6Cl_2]$ showing temperature dependence of the k resonances.

temperature dependent (right) magnetization hysteresis loops and first derivative, respectively, for the Mn_3-salox complex. At low temperatures (T < 1.5K), and with slow sweep rates (< 0.15 Ts^{-1}) the k = 1 resonance is not exhibited, and the allowed k = 3 resonance manifests itself below 0.9K. The Jahn-Teller elongation axes of the three Mn^{III} ions were found to tilt by 8 degrees from the molecular easy axis of the individual molecules. And as a result, perturbations to transverse components are introduced that mix excited states giving rise to the k = 2 resonance. One might be able to use this insight to enhance the quantum dynamics exhibited by SMMs.

Other important benchmarks discovered in studying SMMs include spin-parity effects[22] and exchange biased quantum tunneling of the magnetization (QTM).[20] Spin-parity is a fundamental phenomenon that was first observed in the cubane S = 9/2 $[Mn_3^{III}Mn^{IV}O_3Cl_4(OAc)_4(py)_3]$ complex. The spin ground state arises as a result of ferromagnetic exchange between S = 2 Mn^{III} ions that antiferromagnetically couple to the S = 3/2 Mn^{IV} ion. In half-integer spin systems the 2S spin levels form Kramers degenerate pairs that should theoretically suppress QTM that is allowed in integer spin systems. However, *Wernsdorfer et al*.[22] showed that the Kramers degeneracy could be lifted by the application of a small transverse magnetic field, and that the sweep rate of the applied transverse field could significantly modify the tunnel spitting of QTM resonances.

Exchange biased QTM was first observed in a related complex. If the $[Mn_3^{III}Mn^{IV}O_3Cl_4(OAc)_4(py)_3]$ complex is crystallized from a different solvent the system exhibits drastically different magnetization behavior. The resulting complex forms a molecular dimer where two $[Mn_3^{III}Mn^{IV}O_3Cl_4(OAc)_4(py)_3]$ complexes are in a

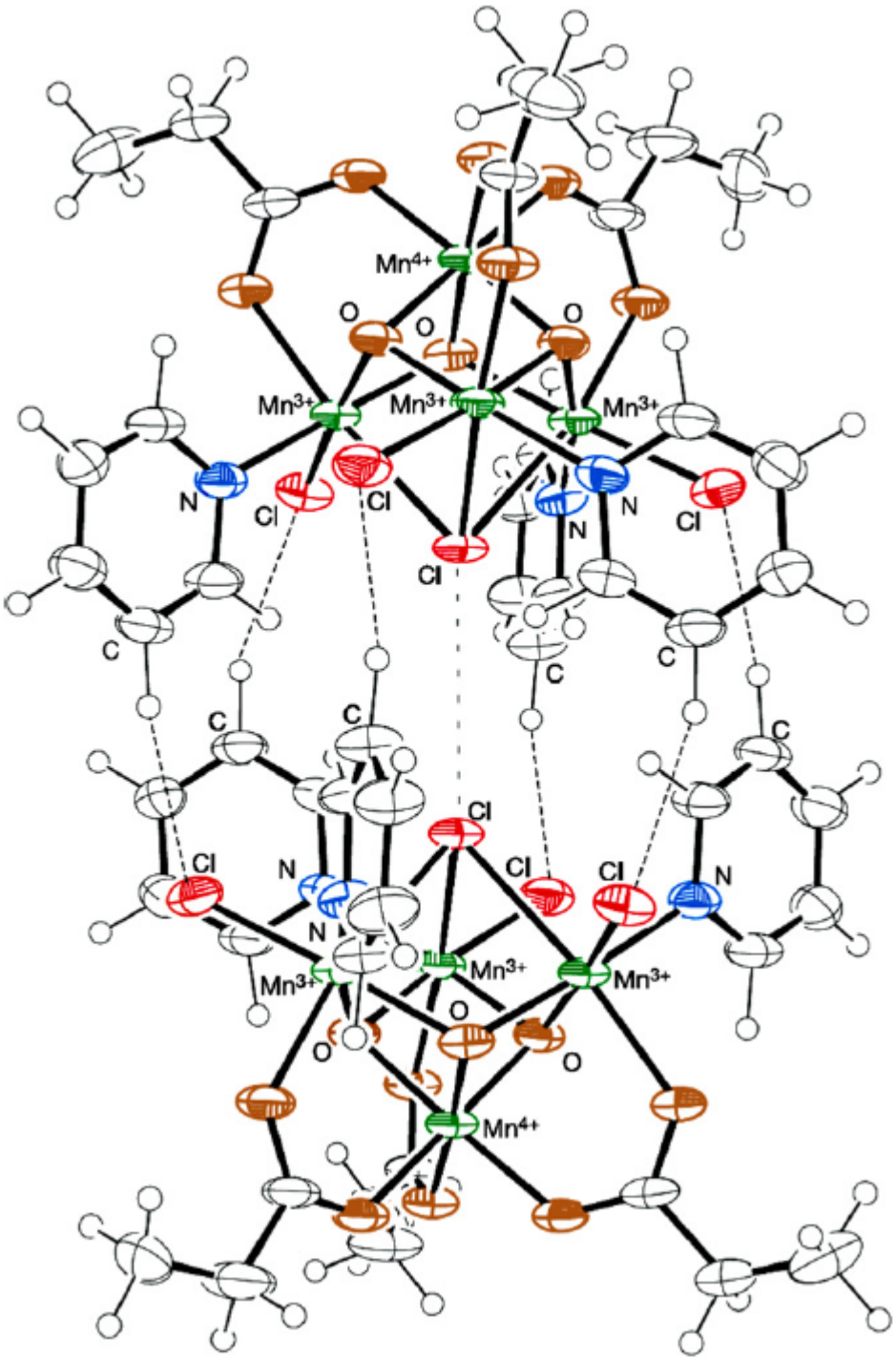

Figure 1.11. Ortep drawing of $[Mn_3^{III}Mn^{IV}O_3Cl_4(OAc)_4(py)_3]_2$ dimer with hydrogen bonding network.

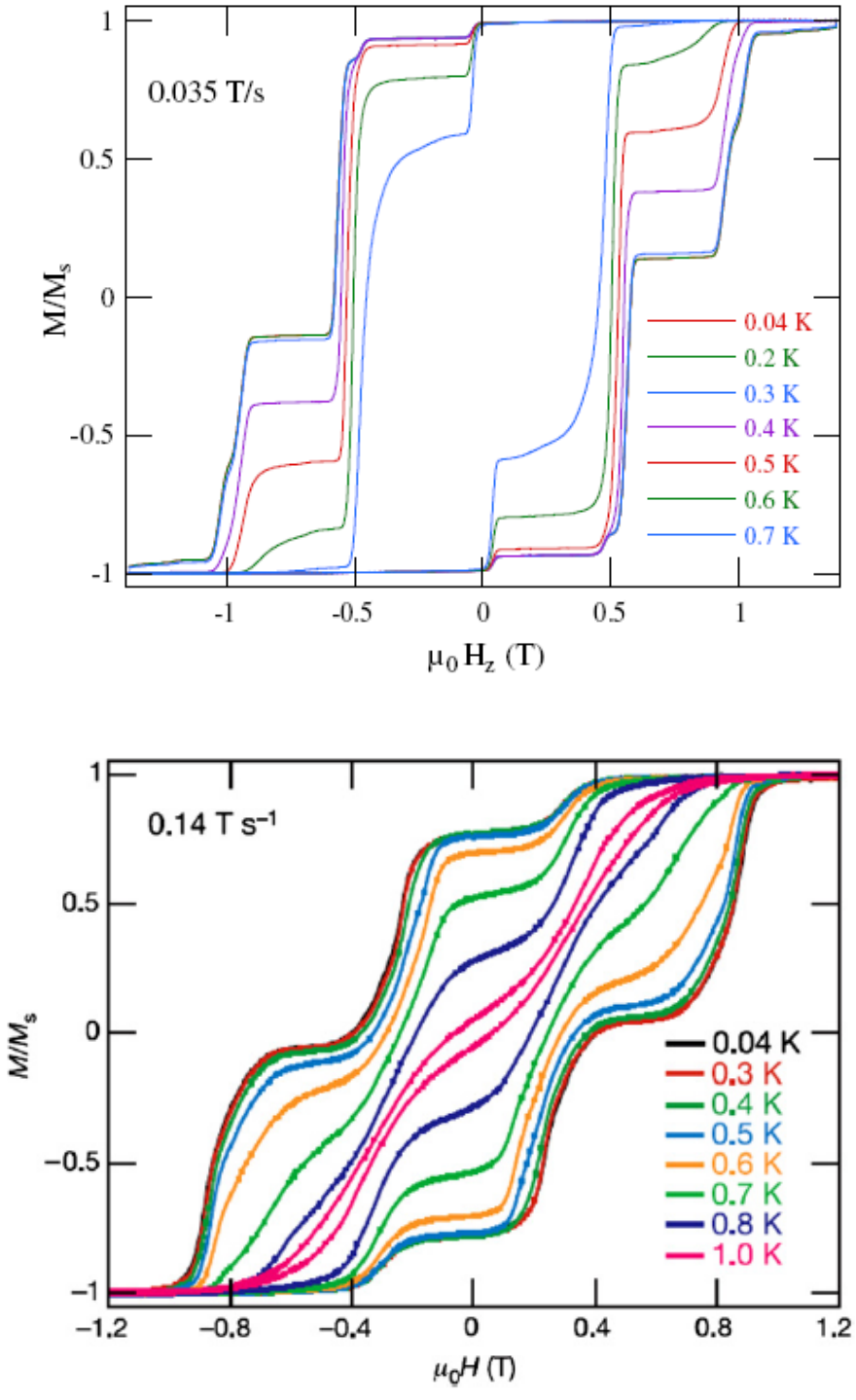

Figure 1.12. Magnetization vs. field hysteresis loops for $[Mn_3^{III}Mn^{IV}O_3Cl_4(OAc)_4(py)_3]$ (top) and $[Mn_3^{III}Mn^{IV}O_3Cl_4(OAc)_4(py)_3]_2$ dimer (bottom), denoting exchange-bias shift of the $k = 0$ tunneling resonance.

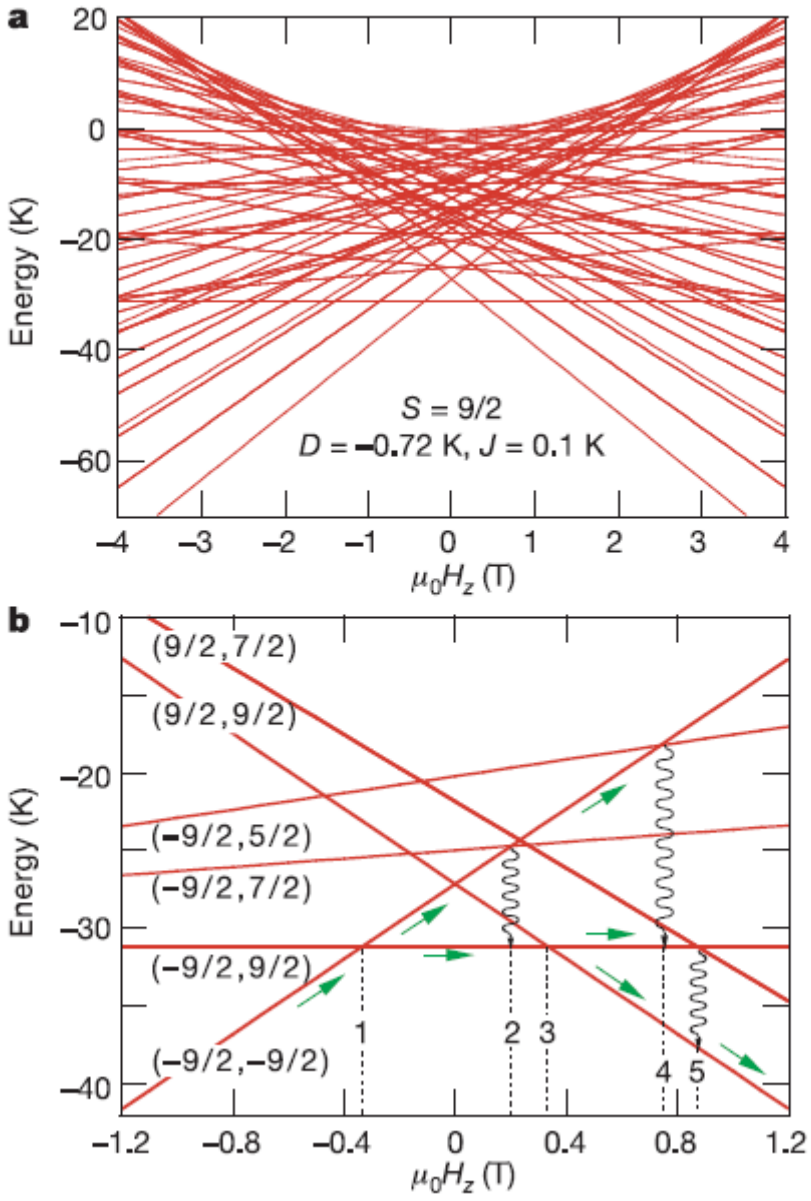

Figure 1.13. Plot of energy vs. applied magnetic field depicting energy crossings for the $[Mn_3^{III}Mn^{IV}O_3Cl_4(OAc)_4(py)_3]_2$ dimer (top). (bottom) Expanded view depicting probable crossings and anticrossings of tunneling resonances.

"head to head" configuration (Figure 1.11) with their C_3 rotational axes pointed along the crystal easy-axis, but are rotated 60 degrees relative to each other yielding S_6 molecular site symmetry for the dimers. The two $[Mn_3^{III}Mn^{IV}O_3Cl_4(OAc)_4(py)_3]$ units are interconnected via H---Cl and Cl---Cl van der Waals contacts that lead to weak antiferromagnetic intermolecular exchange between the two $S = 9/2$ halves resulting in QTM resonances that are shifted when compared to the hysteresis loops of the isolated $[Mn_3^{III}Mn^{IV}O_3Cl_4(OAc)_4(py)_3]$ complex. The temperature dependent hysteresis loops for the $[Mn_3^{III}Mn^{IV}O_3Cl_4(OAc)_4(py)_3]$ complex and the $[Mn_3^{III}Mn^{IV}O_3Cl_4(OAc)_4(py)_3]_2$ dimer are presented in Figure 1.12 top and bottom, respectively. The hysteresis loops for individual $[Mn_3^{III}Mn^{IV}O_3Cl_4(OAc)_4(py)_3]$ complexes shows a $k = 0$ resonance for ground state tunneling between the $m_s = \pm 9$ states occurs at $H = 0$ as expected. On the other hand, the $k = 0$ resonance for the dimer is shifted significantly from zero-field. The exchange bias can be reconciled by observing the spin state energy crossings plotted as total energy as a function of the applied magnetic field (Figure 1.13). For the system to show a resonance at $H = 0$ both molecules would be required to ground state tunnel from $m_s = -9/2$ to $m_s = 9/2$ simultaneously. The tunneling probability for this transition is extremely low, and thus, this tunneling resonance is not observed. The exchange biased resonance at ~ -0.37T is representative of tunneling of the two halves of the dimer from m_s (-9/2, -9/2) to m_s (9/2, -9/2). The result of antiferromagnetic interactions between $S = 9/2$ units leads each molecule to exhibit an exchange bias on the other half of the dimer, leading to considerable deviations in QTM behavior from previously reported SMMs.

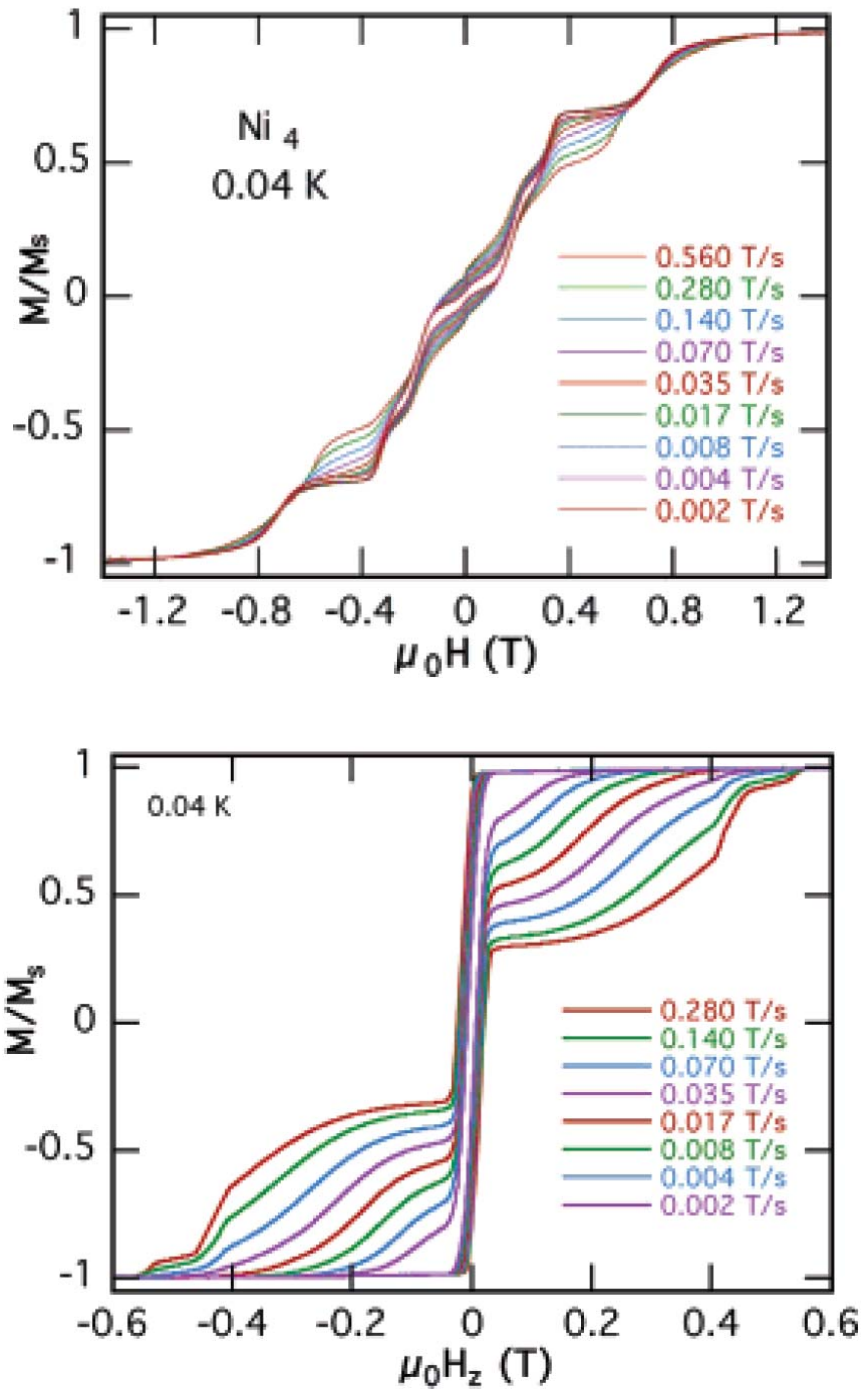

Figure 1.14. Sweep-rate dependent magnetization vs. field hysteresis loops for $[Ni(MeOH)(hmp)Cl]_4$ (top) and $[Ni(dmb)(hmp)Cl]_4$ (bottom).

Exchange bias has also been detected in $S = 4$ Ni_4^{II} SMMs[18] with S_4 site symmetry. A series of these complexes has been reported with the general formula $[Ni(ROH)(hmp)Cl]_4$, where R = methyl, ethyl and 3,3'-dimethyl-1-butanol, where hmp is the anion of 2-hydroxymethylpyridine (for simplicity these complexes will be referred to as: Ni_4-MeOH, Ni_4-EtOH and Ni_4-dmb, respectively). Detailed structural analysis shows the separation or insulation between molecules is increased by increasing the steric bulk

of the coordinated peripheral alcohol ligands. The Ni_4-MeOH and Ni_4-EtOH complexes cocrystallize with solvate molecules that form a network of intermolecular hydrogen bonds. The magnetization hysteresis loops for the Ni_4-MeOH complex (Figure 1.14, top) show an exchange bias for the $k = 0$ resonance of 0.33T.[19] Conversely, the crystal lattice of the Ni_4-dmb complex is free of solvate molecules and the exchange bias is virtually suppressed (Figure 1.14, bottom). It should be noted that the Ni_4-dmb complex exhibits a very small positive exchange bias. Chapter 3 will be devoted to discussion of the role magnetic ordering plays in exchange bias and relaxation behavior in these Ni_4 SMMs.

1.6 High-Frequency Electron Paramagnetic Resonance

The Ni_4 series of molecules is, and will continue to be, a benchmark system for studying quantum phenomena in SMMs. In particular, oriented single-crystal high-frequency electron paramagnetic resonance experiments (HF-EPR)[91-94] have provided detailed information regarding limitations of the giant spin approximation (GSA, this

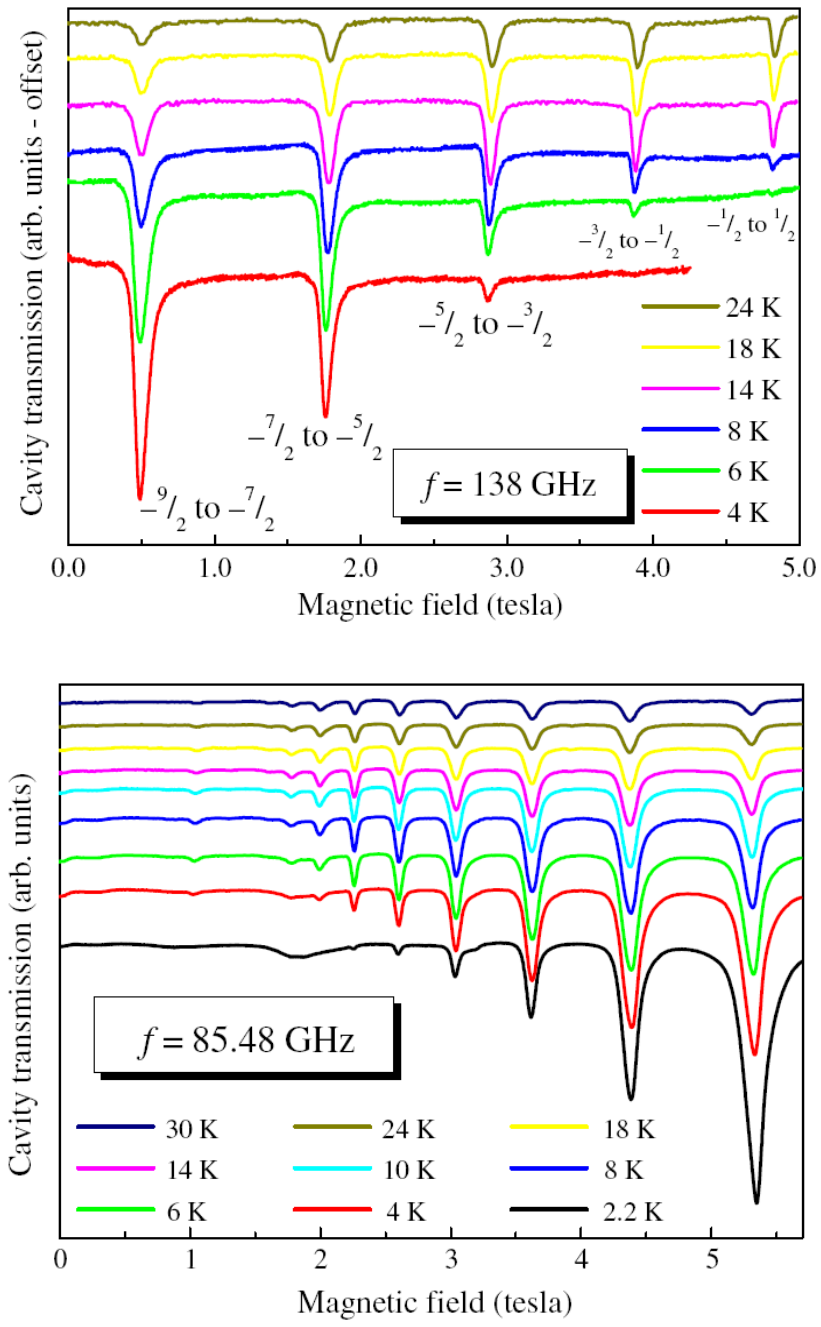

Figure 1.15. temperature dependent EPR spectra for $[Mn_3^{III}Mn^{IV}O_3(OSiMe_3)(OAc)_3(dbm)_3]$ collected with the applied field parallel (top) to the molecular easy-axis and parallel (bottom) to the hard-axis, top and bottom, respectively.

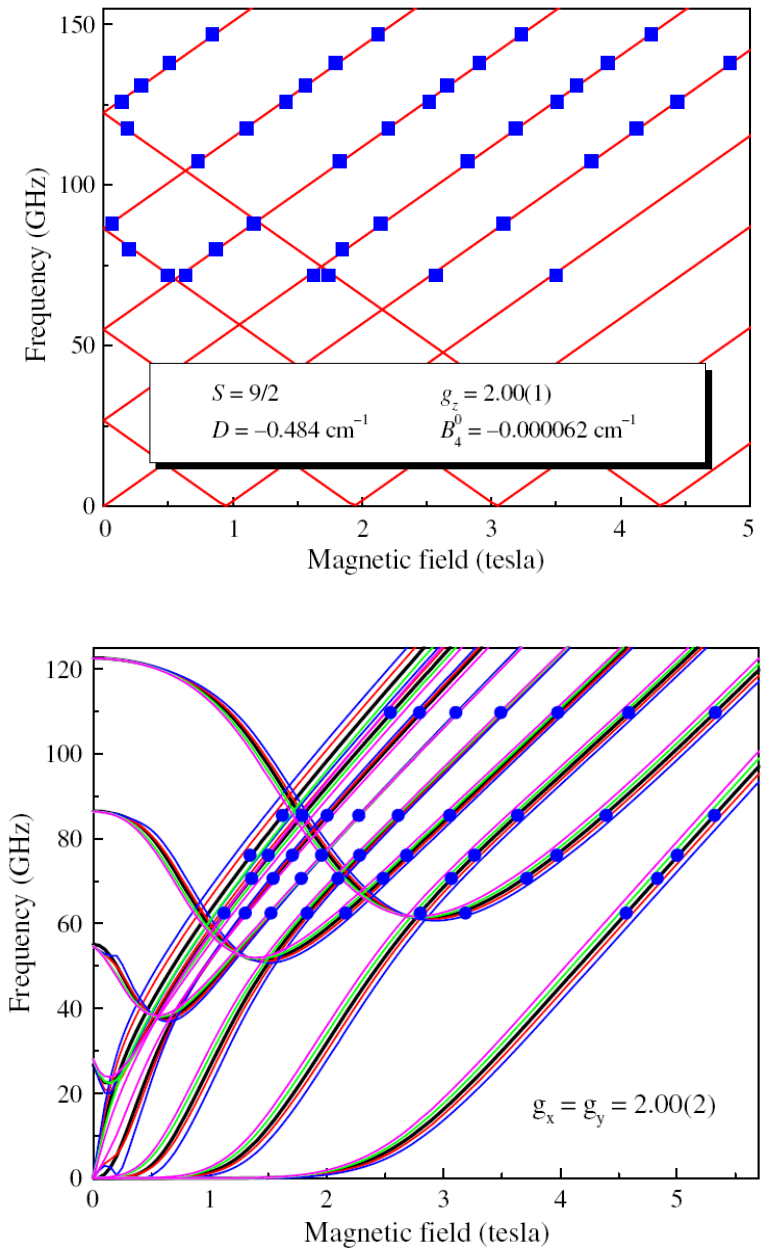

Figure 1.16. Simulations of easy-axis (top) and hard-plane (bottom) frequency dependent HFEPR data for $[Mn_3^{III}Mn^{IV}O_3(OSiMe_3)(OAc)_3(dbm)_3]$.

will be described below) and provided the first spectroscopic evidence of fourth-order and behavior in magnetic systems.

EPR spectra for many systems are generally performed on polycrystalline powder samples that are pressed into a pellet, or with frozen solutions. Because individual moments are randomized in terms of spatial orientation, the spectra are dominated by the easy-axis signal with portions of the transverse signal mixed in. From the resulting spectra approximations of Hamiltonian parameters such as *g*, *D* and *S* can be extracted. However, to study quantum phenomena one must be able to resolve the axial transverse components of the EPR signal in order to gauge transverse Hamiltonian terms, $E(\hat{S}_x^{\,2} - \hat{S}_y^{\,2}), B_4^{\,4}\hat{O}_4^{\,4}$, responsible for magnetization tunneling, and therefore, high quality oriented single-crystals need to be employed. Correct orientation of the crystal in the applied magnetic field is critical in order to minimize interference do to mixing of transverse components. If the crystal can be rotated in two mutually orthogonal planes, exact temperature dependent and frequency dependent spectra can be collected and used to unambiguously determine Hamiltonian parameters. Though not completely necessary, it is advantageous to measure samples free of lattice solvate molecules, and that have only one molecular orientation. Solvate disorder distributions of molecular orientations and *g*- and *D*-strain can introduce line-broadening and asymmetry that can complicate detailed analysis of EPR data.[85,95-98]

The large spin ground state and appreciable axial magnetoanisotropy of SMMs requires applications of large applied magnetic fields and high frequencies in order to resolve discrete EPR transitions between m_s states. In the absence of zero-field

interactions all of the energy states are degenerate and only a single broad peak will be observed in EPR spectra. Conversely, if the system exhibits appreciable anisotropy, application of a magnetic field can often resolve the $m_s = \pm 1$ states as discrete peaks in the EPR spectra.

Figure 1.15[99] shows temperature dependent EPR spectra for a single crystal of $[Mn_3^{III}Mn^{IV}O_3(OSiMe_3)(OAc)_3(dbm)_3]$ collected with the applied field parallel to the molecular easy-axis and parallel to the hard-axis, top and bottom, respectively. At 24K thermal considerations lead to approximately equal distributions of populated energy states. As the temperature is lowered, and in the presence of an applied field, depopulation of Boltzman distributions results in predominant population of the $S = -9/2$ ground state. As the magnitude of the applied magnetic field increases successive $m_s = \pm 1$ transitions are observed. When the experiment is repeated with the applied field parallel to the hard-plane the ground state transition is shifted to high field. The temperature dependent shift reveals that the sign of the axial zero-field splitting parameter is negative and is approximately equal to the spacing between m_s transitions.

Hamiltonian parameters can be extracted by simulation of iso-thermal easy-axis and hard-plane frequency dependent EPR spectra. The solid lines in Figure 1.16[99] represent simulations of frequency dependent data through exact diagonalization of the spin Hamiltonian. Easy-axis and hard-plane data are fit independently to yield a single set of fitting parameters.

The GSA is commonly used to approximate the distribution of eigen-states and gauge the magnitude and sign of zero-field splitting parameters of the spin Hamiltonian:

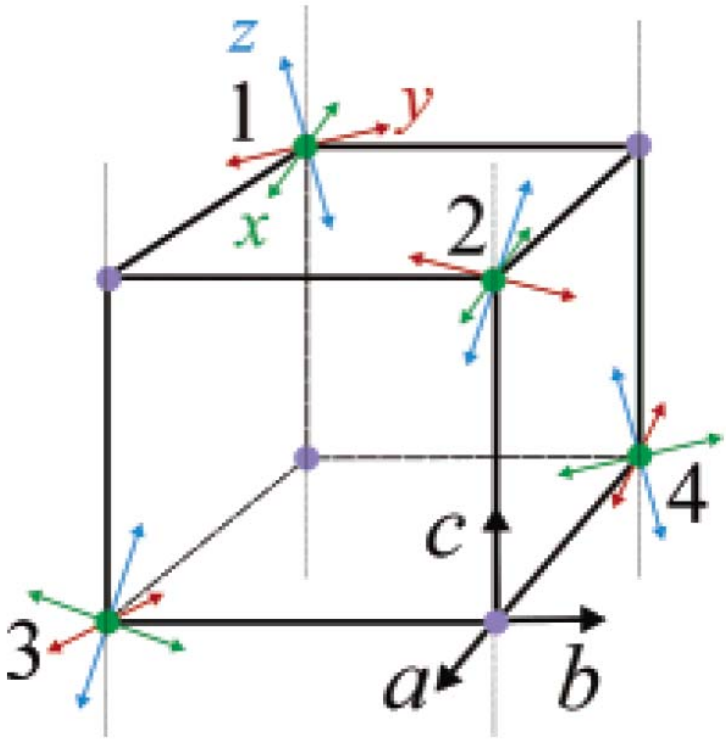

Figure 1.17. Depiction of orientations of the single-ion zero-field splitting tensorial projections for individual Ni^{II} ions in $[Ni(dmb)(hmp)Cl]_4$ relative to the easy-axis, *C* axis of the molecule.

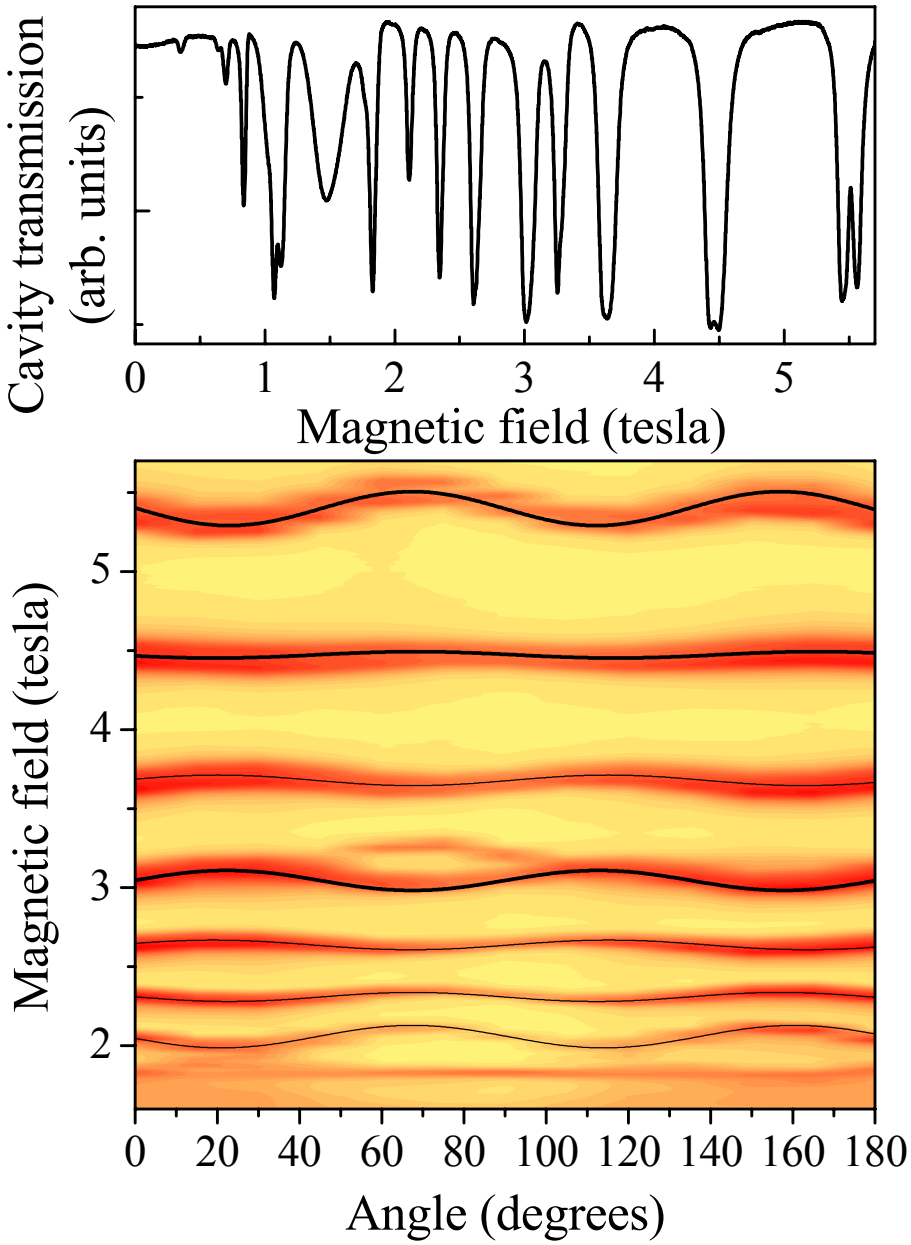

Figure 1.18. HFEPR hard plane spectra of showing four-fold behavior consistent with crystal and site symmetry of $[Ni(dmb)(hmp)Cl]_4$.

$$\hat{H} = D\hat{S}_z^{\,2} + E(\hat{S}_x^{\,2} - \hat{S}_y^{\,2}) + B_4^{\,0}\hat{O}_4^{\,0} + B_4^{\,4}\hat{O}_4^{\,4} + \hat{H}_1 \qquad \textbf{(1.12)}$$

The GSA assumes that S and M_s of the lowest energy spin state are good magnetic quantum numbers and the spin-manifolds of the system are sufficiently isolated at low temperatures. Furthermore, the GSA does not account for internal magnetic degrees of freedom, *i.e.* the tensorial projections of $g_{x,y,z}$, d_i and anisotropy in magnetic exchange.

For quantum tunneling to occur, transverse anisotropy must be present in the form of intrinsic zero-field splitting terms such as $E(\hat{S}_x^{\,2} - \hat{S}_y^{\,2}), B_4^{\,4}\hat{O}_4^{\,4}$ or higher order terms that generate an internal magnetic transverse anisotropy, or by application of an externally applied transverse magnetic field. The tetragonal crystal symmetry and S_4 molecular site symmetry of the Ni_4 system prohibits inclusion of a rhombic E-term, and evaluation of the $2S + 1$ matrix of individual $S_i = 1$ Ni^{II} ions ($2S + 1 = 3$, or a 3 x 3 matrix) reveals that there is also no intrinsic 4th-order, or higher, transverse anisotropy term present. However, the Ni_4 systems exhibit regular steps in magnetization hysteresis experiments, and exhibits very fast quantum tunneling rates. Initial simulations of magnetic susceptibility data and HF-EPR required inclusion of a transverse $B_4^{\,4}\hat{O}_4^{\,4}$ term in the spin Hamiltonian in order to achieve an acceptable fit of the experimental data, and to account for QTM. Thus the model included a transverse Hamiltonian term that has no physical relevance. It should be noted that spin-mixing can have a profound effect on quantum tunneling rates; however, it can not be solely responsible for QTM because state mixing is purely isotropic in nature. Furthermore there exists a ~32K barrier between the ground state and the first excited state in the

Ni_4-dmb complex. So the question becomes, what gives rise to QTM and fast relaxation in this interesting system?

$$\hat{H} = \sum_i \sum_{j>i} J_{ij}\hat{s}_i\hat{s}_j + \sum_i \left[d_i\hat{s}_{zi}^2 + e(s_{xi}^2 - s_{yi}^2) + \mu_B \vec{B}\cdot\vec{g}_i\cdot\hat{s}_i \right] \qquad \textbf{(1.13)}$$

HF-EPR experiments were initiated that employed a diamagnetic Zn_4-dmb analogue of the Ni_4-dmb complex that was systematically doped with very small amounts of Ni^{II} ions. The dmb complex was chosen because the crystal lattice contains no solvate molecules, so intermolecular interactions and disorder are minimized, and the dmb complexes crystallize with one molecular orientation. Detailed oriented single-crystal HF-EPR data revealed the zero-field splitting (zfs) tensorial projections of the individual Ni^{II} ions are tilted 15 degrees relative to the principal S_4 rotation axis of the molecule (Figure 1.17).[94] Simulations of frequency dependent HF-EPR data employing Equation 1.13, yielded fitting parameters of gz = 2.30, gx = gy = 2.20, E_i = 1.20 cm^{-1} and d_i = -5.30 cm^{-1}. The 81 x 81 [$(2S_i + 1)^4$] matrix was then exactly diagonalized employing the single-ion parameters extracted through HF-EPR yielding a molecular zfs parameter of D = -0.69 cm^{-1}, and coupling constant J_{ij} of 5.21 cm^{-1}. In contrast to Equation 1.12, which treats the system as a ridged spin system with equivalent g and anisotropy tensors in terms of orientation and magnitude, Equation 1.13 allows treatment of the individual ions, and how the single-ion tensorial values project on to the ground state. When the magnitude of the local zsf tensor (d_i) is of the same magnitude as the local magnetic exchange parameter (J_{ij}), the interplay leads to

symmetry dictated state mixing (tetragonal crystal symmetry and four-fold molecular symmetry). This results in correlation between m_s states differing by ±4 which naturally give rise to fourth-order zfs terms such as $B_4^4\hat{O}_4^4$ and physical relevance for its inclusion in the spin Hamiltonian. Thus, the transverse $B_4^4\hat{O}_4^4$ term is the dominant term leading to QTM. Furthermore, angle dependent oriented single-crystal HF-EPR on the Ni_4-dmb complex yielded, for the first time, spectroscopic evidence of the four-fold symmetry of a SMM (Figure 1.18). The angle dependent data were collected via multiple rotations exactly in the hard plane (xy) of the molecules, and clearly exhibits significant four-fold behavior. The black lines are simulations of the experimental data.

A fundamental requirement for quantum computing and quantum information storage is establishment of coherent quantum tunneling between metastable states that exhibit an appreciably long decoherence time. An inherent issue with using SMMs for these devices is that many of these complexes exhibit significant intermolecular interactions, dipolar interactions, spin-phonon interactions and nuclear hyperfine interactions that lead to extremely fast decoherence times. Recently however, *Takahashi et al.*[100] reported a benchmark study on S = 10 Fe_8 SMMs (Figure 1.19) where the spin-spin decoherence time (T_2) was measured, for the first time employing pulsed-EPR techniques. SMMs are extremely sensitive to their environment. Small perturbations due to dipolar interactions and nuclear hyperfine interactions can have a major impact on decoherence rates. It is believed that nuclear hyperfine interactions are the dominant decoherence pathway for Mn based SMMs (I = 5/2). Spin-phonon relaxation times (T_1) have been previously reported employing continuous wave HF-

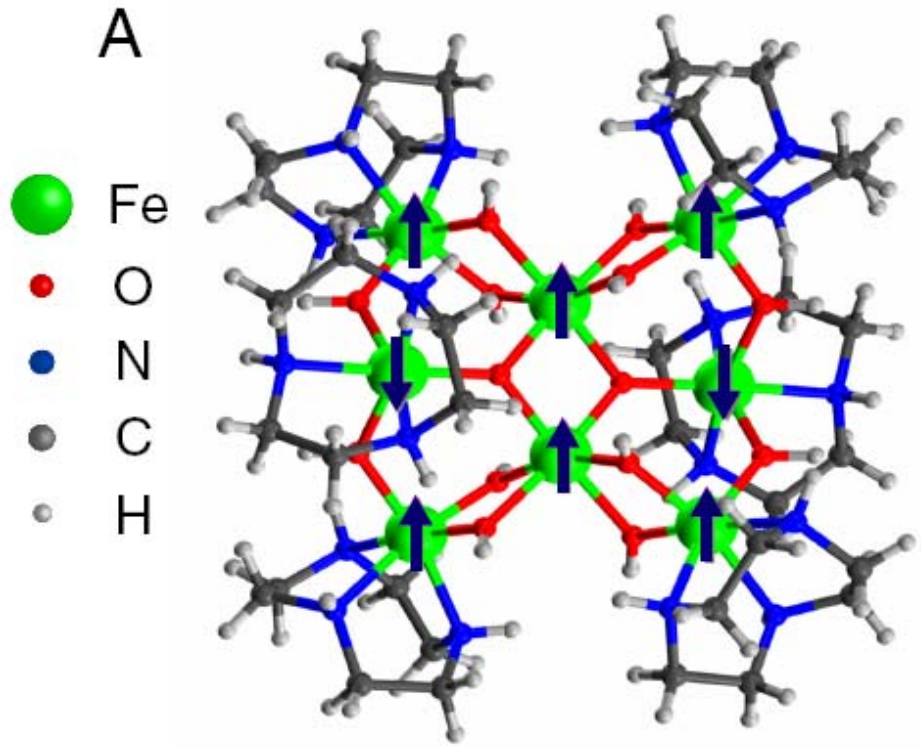

Figure 1.19. Ortep drawing with spin coupling diagram of $[Fe_8O_2(OH)_{12}(C_6H_{15}N_3)_6]Br8{\cdot}9H_2O$ (Fe_8) single-molecule magnet.

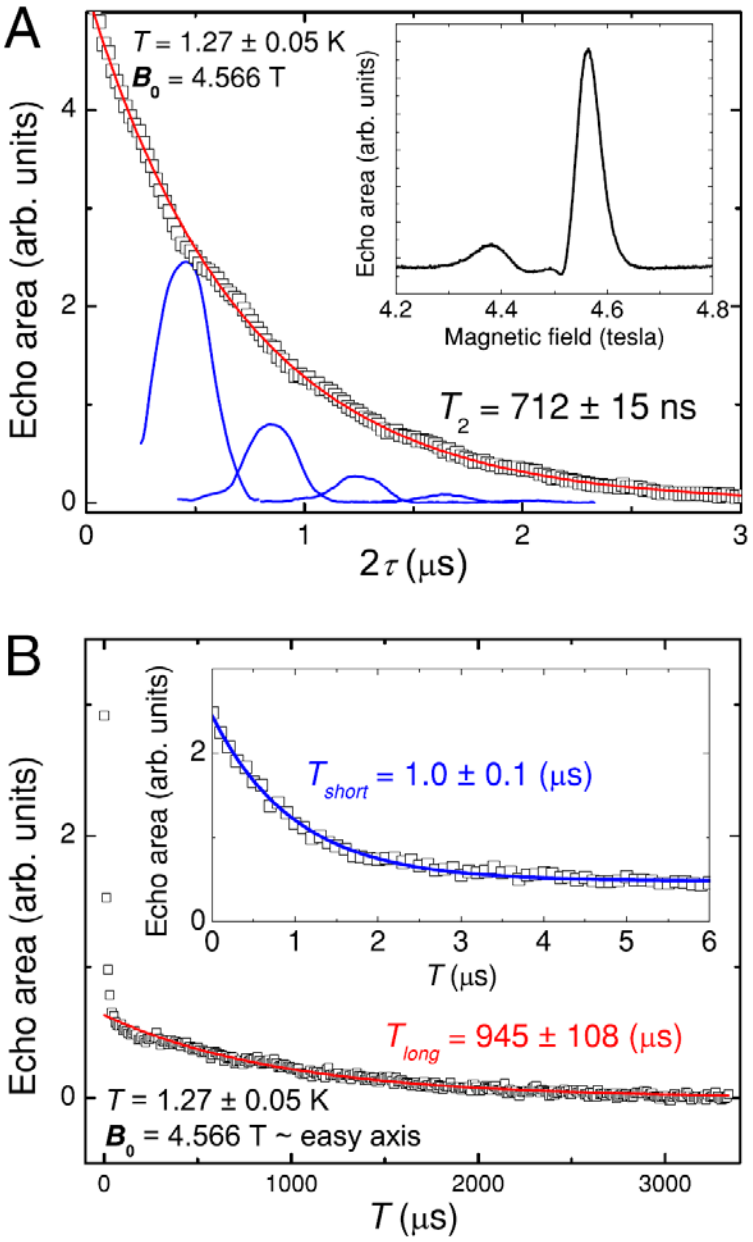

Figure 1.20. Spin-echo pulsed HFEPR for $[Fe_8O_2(OH)_{12}(C_6H_{15}N_3)_6]Br8{\cdot}9H_2O$ (Fe_8). (top) simulation of relaxation rate yielding a spin-spin relaxation time (T_2) of 712ns, and (bottom) simulation of spin-phonon relaxation times (T_1) employing different delay times in the spin-echo sequence.

EPR, but spin-spin relaxation (T_2) has never been observed. Under continuous wave experiments non-linear heating of the spin-bath can occur within a crystal that enhances spin-phonon and spin-spin decoherence rates. Also, SMMs frequently experience thermally controlled phonon- bottlenecks at low temperatures that can significantly mask mechanisms of spin relaxation processes.

The energy gap between the S = -10 and S = -9 first excited state is 11.2K in the Fe_8 SMM, thus at the resonance peak (inset Figure 1.20A) at ~4.6T the spin-bath is polarized and nearly all the spins are in the S = -10 ground state at temperatures below 1.93K and only the ground state first excited state transition is observed. A Hahn echo sequence was employed ($\pi/2 - \tau - \pi - \tau -$ echo), where τ is the time delay between microwave pulses of 240GHz. Echo's were observed at 1.27K (Figure 1.20A) with varying delay times. A value of T_2 = 712ns was measured by fitting the decay rate of the echo area to a single exponential function. The sequence was repeated with the dc magnetic field applied along the hard-plane with nearly identical results. T_1 (spin-phonon relaxation rate) was also measured for the Fe_8 complex using a modified echo sequence and two temperature dependent echo's were observed (Figure 1.20B). The calculated spin-phonon relaxation rate was found to be two orders of magnitude longer than previously reported systems. A future goal is to synthesize molecular systems that optimize properties that will yield tunable spin-spin and spin-phonon decoherence rates.

1.7 Thermodynamics of Single-Molecule Magnets

Calorimetric studies can provide valuable information in regards to the physical environment of magnetic materials,[58,73,101-108] and has been extensively utilized in

studying magnetic systems. Macroscopic crystals are made up of single domain magnetic molecules, so bulk specific heat data reflects the numerous molecular degrees of freedom and microscopic environments of SMMs. Calorimetry is extremely sensitive to even subtle changes in the crystal environment, including: order-disorder, as well as crystallographic and magnetic phase transitions. Specific heat measurements are normally carried out adiabatically at constant pressure and are plotted as C_p (J / mol K) vs. T, where T is the absolute temperature. In the absence of a phase transition in the plot of C_p vs T a broad non-linear feature, consistent with crystal symmetry, is observed that decreases in molar heat capacity until a minimum is reached that becomes virtually temperature independent. This occurs when normal lattice modes are quenched and thermal depopulation of excited states leaves only the ground state of the molecule populated. If however, a crystallographic or magnetic phase transition is present, at the crossover temperature T_c, a sharp, or broad, peak in the molar heat capacity will be observed. First-order phase transitions, transitions which occur iso-thermally with exhibited latent heat, are rare in magnetic materials. Most phase transitions exhibited by SMMs are 2nd order or higher and the sharp peak exhibits asymmetric tails above and below the critical temperature. The tail above the critical temperature can be attributed to short range intermolecular interactions within the crystal lattice.

The total heat capacity can be divided in to three components for magnetic molecules: 1) the lattice contribution (C_{Lattice}); 2) the temperature dependence of the populated m_s energy levels of the spin multiplet, or Schottky distribution (C_{Schottky}); and 3) the magnetic portion (C_{magnetic}), which describes the contribution due to dipolar coupling, nuclear hyperfine and other intermolecular interactions. In the low

temperature limit, the lattice contribution to the heat capacity can be estimated by employing the Debye model:

$$\frac{C}{kN} \sim \frac{12\pi^4}{5}\left(\frac{T}{T_D}\right)^3 \qquad \textbf{(1.14)}$$

where C, is the heat capacity, T is the absolute temperature, and T_D is the Debye temperature. At low temperatures (where C_p exhibits T^3 temperature dependence) this function correctly correlates the phonon contribution to the specific heat capacity and its relationship to the absolute temperature. If there is no phase transition in the temperature range at low temperatures, T_B indicates the highest temperature normal mode of the crystal lattice. If a gauge of the lattice contribution over a wide temperature range is needed, two methods have been found useful. The most precise method is to employ a diamagnetic analogue of the molecule being studied. This approach eliminates contributions from Schottky and magnetic portions of the heat capacity, which allows direct subtraction of the lattice energy from the overall heat capacity. However, in most cases this method is not possible. The other approach involves collecting heat capacity data in the presence of large magnetic fields (>9T). In such high fields one can assume that the Schottky contribution is quenched and that only the ground state of the molecule is populated. The zero-field and high-field heat capacity data can then be compared to asses the lattice contribution.

$$C_{Schottky(H,P)} = \frac{dU}{dT} \quad \textbf{(1.15)}$$

$$\hat{H} = \sum_i \sum_{j>i} J_{ij}\hat{s}_i\hat{s}_j + \sum_i \left[d_i\hat{s}_{zi}^2 + e(s_{xi}^2 - s_{yi}^2) + \mu_B\vec{B}\cdot\vec{g}_i\cdot\hat{s}_i \right] \quad \textbf{(1.16)}$$

$$U = \frac{\sum E(S_T) * e^{-(E(S_T)/k_BT)}}{\sum e^{-(E(S_T)/k_BT)}} \quad \textbf{(1.17)}$$

$$S = \int C_p d\ln T \quad \textbf{(1.18)}$$

The Schottky contribution (C_{Schottky})(Equation 1.15), where U is the internal energy of the system, and T is the absolute temperature, can be calculated through full-matrix diagonalization of dc magnetic susceptibility data to calculate all possible eigen-energies in the system, using Equation 1.16. The internal energy U is then evaluated employing Equation 1.17, where $E(S_T)$ represents the energies of discrete eigen-states, -$E(S_T)/k_BT$ is the Boltzman factor and $\sum e^{-E(S_T)/kT}$ is the canonical partition function. The magnetic portion of the heat capacity can then be simply determined by subtraction of the other components (C_{p} - C_{Lattice} - C_{Schottky} = C_{magnetic}). If a phase transition is present the excess entropy ΔS can be evaluated by integrating C_{p} with respect to ln$T$ (Equation 1.18). If the phase transition is purely magnetic in nature ΔS will equal Rln(2S + 1), where R is the gas constant, and 2S = 1 is the spin degeneracy of the system.

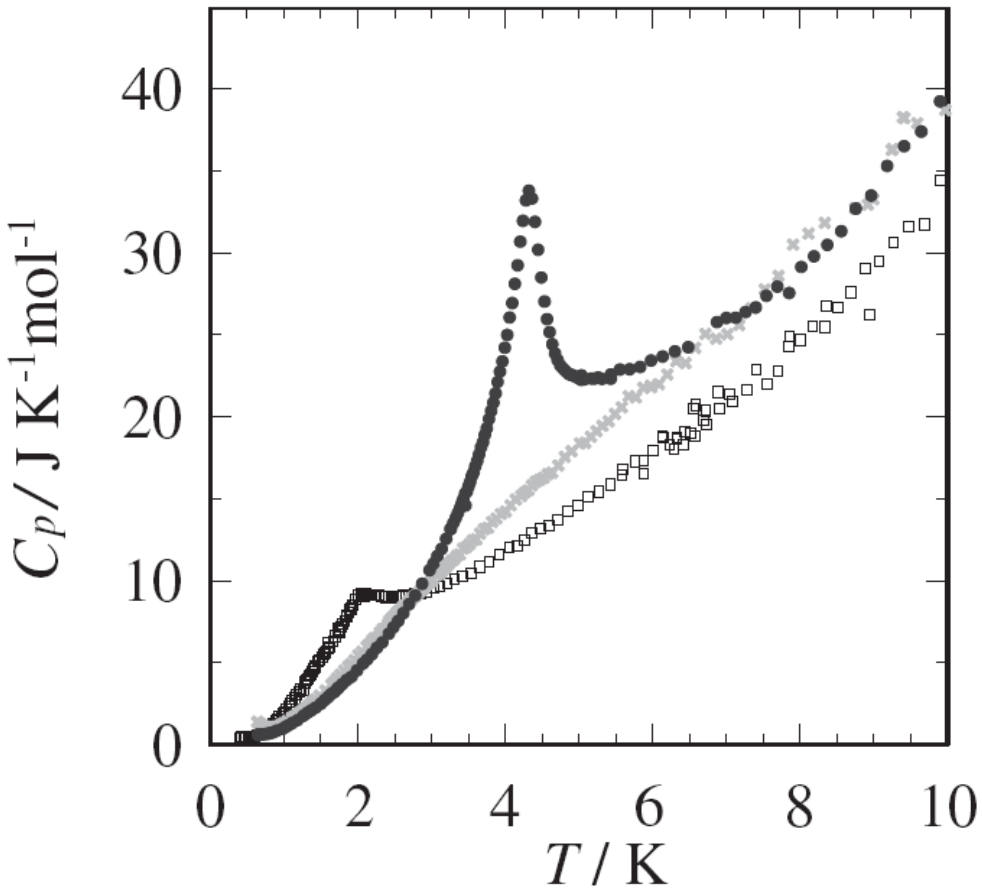

Figure 1.21. Temperature dependences of the heat capacities of $[Mn_4(hmp)_6(N(CN)_2)_2](ClO_4)_2$ ($Mn4–hmp_6$) (denoted by filled circles), $[Mn_4(hmp)_4Br_2(OMe)_2(N(CN)_2)_2]\cdot 2THF\cdot 0.5H_2O$ ($Mn_4–hmp_4Br_2$) (denoted by squares), and $[Mn_4(hmp)_4(pdm)_2(N(CN)_2)_2](ClO_4)2\cdot H_2O\cdot 2MeCN$ ($Mn_4–hmp_4pdm_2$) (denoted by crosses).[105]

Figure 1.21 shows the molar heat capacity as a function of temperature for a series of tetranuclear manganese complexes.[105] The three complexes have identical exchange coupled magnetic cores, but differ in their coordinated peripheral ligands. All three complexes, Mn_4–hmp_6, Mn_4–hmp_4Br_2 and Mn_4–hmp_4pdm_2 form two-dimensional sheets in their crystal lattices as a result of coupling through dicyanamide anions. This series of molecules is a perfect example of the sensitivity of calorimetry. Though all of these complexes form 2-D sheets in their crystal lattice, only the Mn_4–hmp_6 and Mn_4-hmp_4Br_2 complexes exhibit anomalies in their molar heat capacity. It was determined that the heat capacity peaks for Mn_4–hmp_6 and Mn_4–hmp_4Br_2 are a result of temperature dependent 3-D antiferromagnetic ordering, and that the ordering temperature differential, 4.3K for Mn_4–hmp_6 and 2.10K for Mn_4–hmp_4Br_2 is directly related to intermolecular coupling J between Mn_4 units which is mediated by the dicyanamide bridging ligands, J = -0.016K and -0.007K, respectively. It was determined that inter-cluster exchange interactions for the Mn_4–hmp_4pdm_2 were negligible which is consistent with the plot of molar heat capacity for this complex.

In chapter 3 we will examine the origin and nature of magnetic ordering in Ni_4^{II} SMMs. In addition to providing important information regarding magnetic and crystallographic phase transitions, molar heat capacity data can be effectively employed to rule out phase transitions as a possible origin for anomalous behavior in magnetization and HF-EPR experiments. This will be discussed in chapters 2, 4 and 5.

1.8 Outline of the Dissertation

Chapter 2 presents crystal, magnetization and HF-EPR data on a high-spin high symmetry molecule with the metal content $Cu_{17}Mn_{28}$ that exhibits significant magnetization relaxation rates as a result of a strongly spin-frustrated and geometrically-frustrated magnetic core. The high T_d molecular site symmetry should exhibit no preference to alignment in an applied magnetic field; however, frustration leads to polarization of uncompensated spin that exhibits magnetization hysteresis loops and slow magnetization relaxation below 1.1K. Thus, the origin of the magnetization relaxation in the complex is of a different origin than previously reported SMMs.

Chapter 3 presents detailed magnetization and specific heat measurements on a series of Ni_4^{II} SMMs. Ac and dc magnetic studies have revealed a significant drop in magnetization at low temperatures, and appreciable negative exchange-bias is present in two molecules, while a third exhibits a 0.012T positive exchange-bias in magnetization versus field hysteresis loops. Specific heat data in conjunction with FC-ZFC magnetization measurements reveal that magnetic ordering occurs in these molecules that leaves magnetization tunneling rates nearly unaffected.

Chapters 4, 5 and 6 present detailed crystallographic, magnetic susceptibility, magnetization hysteresis and HF-EPR data on four series of related tetranuclear Mn molecules. Chapter 4 focuses on structural, magnetic properties, and photoluminescent properties of two series of Mn_4 SMMs. Though not reported in this dissertation, the future goal is to employ time-resolved fluorescence and simultaneous magnetization hysteresis measurements to probe quantum dynamics on a fluorescence time scale. Chapter 5 presents detailed oriented single-crystal magnetization hysteresis and HF-

EPR data on two of the complexes introduced in Chapter 4. Chapter 6 presents 2 series of tetranuclear Mn complexes, where the spin of the ground state can be tuned yielding dominant antiferromagnetic exchange interactions and $S = 1$ ground states. The core topology is identical to the $S = 9$ SMMs in Chapter 4 and 5, however, the use of a strong chelating ligand reverses the positions of Mn^{II} and Mn^{III} ions in the exchange coupled core.

Chapter 7 presents detailed structural and magnetic properties of a series on single stranded molecular wheels. These interesting Mn based SMMs have a $S = 7$ spin ground state and significant magnetoanisotropy.

Chapter 8 documents HF-EPR studies on a pair of related cobalt and Zn/cobalt cubane molecules to determine if they are SMMs and to study the effects of anisotropy in magnetic exchange interactions.

1.9 References

(1) Sessoli, R.; Tsai, H. L.; Schake, A. R.; Wang, S. Y.; Vincent, J. B.; Folting, K.; Gatteschi, D.; Christou, G.; Hendrickson, D. N. *Journal of the American Chemical Society* **1993**, *115*, 1804-1816.

(2) Eppley, H. J.; Tsai, H. L.; Devries, N.; Folting, K.; Christou, G.; Hendrickson, D. N. *Journal of the American Chemical Society* **1995**, *117*, 301-317.

(3) Tsai, H. L.; Eppley, H. J.; DeVries, N.; Folting, K.; Christou, G.; Hendrickson, D. N. *Molecular Crystals and Liquid Crystals Science and Technology Section a-Molecular Crystals and Liquid Crystals* **1995**, *273*, A167-A173.

(4) Christou, G.; Gatteschi, D.; Hendrickson, D. N.; Sessoli, R. *Mrs Bulletin* **2000**, *25*, 66-71.

(5) Gatteschi, D.; Sessoli, R. *Journal of Magnetism and Magnetic Materials* **2004**, *272-276*, 1030-1036.

(6) Gatteschi, D.; Sessoli, R.; Villian, J. *Molecular Nanomagnets*; Oxford University Press: Oxford, 2006.

(7) Aubin, S. M. J.; Sun, Z. M.; Eppley, H. J.; Rumberger, E. M.; Guzei, I. A.; Folting, K.; Gantzel, P. K.; Rheingold, A. L.; Christou, G.; Hendrickson, D. N. *Inorganic Chemistry* **2001**, *40*, 2127-2146.

(8) Aubin, S. M. J.; Wemple, M. W.; Adams, D. M.; Tsai, H. L.; Christou, G.; Hendrickson, D. N. *Journal of the American Chemical Society* **1996**, *118*, 7746-7754.

(9) Abbati, G. L.; Cornia, A.; Fabretti, A. C.; Caneschi, A.; Gatteschi, D. *Inorganic Chemistry* **1998**, *37*, 3759-3766.

(10) Kahn, O. *Molecular magnetism*; VCH: New York, NY, 1993.

(11) Kahn, O. *Philosophical Transactions of the Royal Society of London Series a-Mathematical Physical and Engineering Sciences* **1999**, *357*, 3005-3023.

(12) Henderson, J. J.; Koo, C.; Feng, P. L.; del Barco, E.; Hill, S.; Tupitsyn, I. S.; Stamp, P. C. E.; Hendrickson, D. N. *Physical Review Letters* **2009**, *103*, 4.

(13) Hill, S.; Datta, S.; Liu, J.; Inglis, R.; Milios, C. J.; Feng, P. L.; Henderson, J. J.; del Barco, E.; Brechin, E. K.; Hendrickson, D. N. *Dalton Transactions*, *39*, 4693-4707.

(14) Feng, P. L.; Koo, C.; Henderson, J. J.; Manning, P.; Nakano, M.; del Barco, E.; Hill, S.; Hendrickson, D. N. *Inorganic Chemistry* **2009**, *48*, 3480-3492.

(15) Sessoli, R.; Gatteschi, D.; Caneschi, A.; Novak, M. A. *Nature* **1993**, *365*, 141-143.

(16) Wernsdorfer, W. *Advances in Chemical Physics, Vol 118* **2001**, *118*, 99-190.

(17) Wernsdorfer, W.; Bhaduri, S.; Tiron, R.; Hendrickson, D. N.; Christou, G. *Physical Review Letters* **2002**, *89*, 197201.

(18) Yang, E. C.; Wernsdorfer, W.; Hill, S.; Edwards, R. S.; Nakano, M.; Maccagnano, S.; Zakharov, L. N.; Rheingold, A. L.; Christou, G.; Hendrickson, D. N. *Polyhedron* **2003**, *22*, 1727-1733.

(19) Yang, E. C.; Wernsdorfer, W.; Zakharov, L. N.; Karaki, Y.; Yamaguchi, A.; Isidro, R. M.; Lu, G. D.; Wilson, S. A.; Rheingold, A. L.; Ishimoto, H.; Hendrickson, D. N. *Inorganic Chemistry* **2006**, *45*, 529-546.

(20) Wernsdorfer, W.; Allaga-Alcalde, N.; Hendrickson, D. N.; Christou, G. *Nature* **2002**, *416*, 406-409.

(21) Wernsdorfer, W.; Aliaga-Alcalde, N.; Tiron, R.; Hendrickson, D. N.; Christou, G. *Journal of Magnetism and Magnetic Materials* **2004**, *272-76*, 1037-1041.

(22) Wernsdorfer, W.; Bhaduri, S.; Boskovic, C.; Christou, G.; Hendrickson, D. N. *Physical Review B* **2002**, *65*, 180403.

(23) Gomes, A. M.; Novak, M. A.; Wernsdorfer, W.; Sessoli, R.; Sorace, L.; Gatteschi, D. *Journal of Applied Physics* **2000**, *87*, 6004-6006.

(24) Gatteschi, D.; Sessoli, R. *Angewandte Chemie-International Edition* **2003**, *42*, 268-297.

(25) Aubin, S. M. J.; Spagna, S.; Eppley, H. J.; Sager, R. E.; Folting, K.; Christou, G.; Hendrickson, D. N. *Molecular Crystals & Liquid Crystals Science & Technology Section A-Molecular Crystals & Liquid Crystals* **1997**, *305*, 181-192.

(26) Chudnovsky, E. M. *Journal of Applied Physics* **1993**, *73*, 6697-6702.

(27) Loss, D.; Divincenzo, D. P.; Grinstein, G.; Awschalom, D. D.; Smyth, J. F. *Physica B* **1993**, *189*, 189-203.

(28) Wernsdorfer, W.; Chiorescu, I.; Sessoli, R.; Gatteschi, D.; Mailly, D. *Physica B* **2000**, *284*, 1231-1232.

(29) Loss, D.; Schoeller, H.; Goldbart, P. *Physica B* **1994**, *194*, 1145-1146.

(30) Wernsdorfer, W.; Sessoli, R.; Caneschi, A.; Gatteschi, D.; Cornia, A. *Journal of the Physical Society of Japan* **2000**, *69*, 375-382.

(31) Ramsey, C. M.; Del Barco, E.; Hill, S.; Shah, S. J.; Beedle, C. C.; Hendrickson, D. N. *Nature Physics* **2008**, *4*, 277-281.

(32) Prokofev, N. V.; Stamp, P. C. E. *Journal of Low Temperature Physics* **1996**, *104*, 143-209.

(33) Prokofev, N. V.; Stamp, P. C. E. *Journal of Low Temperature Physics* **1998**, *113*, 1147-1152.

(34) Gatteschi, D.; Caneschi, A.; Pardi, L.; Sessoli, R. *Science* **1994**, *265*, 1054-1058.

(35) Brechin, E. K.; Soler, M.; Christou, G.; Helliwell, M.; Teat, S. J.; Wernsdorfer, W. *Chemical Communications* **2003**, 1276-1277.

(36) Affronte, M.; Guidi, T.; Caciuffo, R.; Carretta, S.; Amoretti, G.; Hinderer, J.; Sheikin, I.; Jansen, A. G. M.; Smith, A. A.; Winpenny, R. E. P.; van Slageren, J.; Gatteschi, D. *Physical Review B* **2003**, *68*.

(37) Honecker, A.; Meier, F.; Loss, D.; Normand, B. *European Physical Journal B* **2002**, *27*, 487-495.

(38) Manoli, M.; Prescimone, A.; Bagai, R.; Mishra, A.; Murugesu, M.; Parsons, S.; Wernsdorfer, W.; Christou, G.; Brechin, E. K. *Inorganic Chemistry* **2007**, *46*, 6968-6979.

(39) Shah, S. J.; Ramsey, C. M.; Heroux, K. J.; DiPasquale, A. G.; Dalal, N. S.; Rheingold, A. L.; del Barco, E.; Hendrickson, D. N. *Inorganic Chemistry* **2008**, *47*, 9569-9582.

(40) Rumberger, E. M.; Shah, S. J.; Beedle, C. C.; Zakharov, L. N.; Rheingold, A. L.; Hendrickson, D. N. *Inorganic Chemistry* **2005**, *44*, 2742-2752.

(41) Shah, S. J.; Ramsey, C. M.; Heroux, K. J.; O'Brien, J. R.; DiPasquale, A. G.; Rheingold, A. L.; del Barco, E.; Hendrickson, D. N. *Inorganic Chemistry* **2008**, *47*, 6245-6253.

(42) Rumberger, E. M.; Hill, S.; Edwards, R. S.; Wernsdorfer, W.; Zakharov, L. N.; Rheingold, A. L.; Christou, G.; Hendrickson, D. N. *Polyhedron* **2003**, *22*, 1865-1870.

(43) Rumberger, E. M.; Zakharov, L. N.; Rheingold, A. L.; Hendrickson, D. N. *Inorganic Chemistry* **2004**, *43*, 6531-6533.

(44) McInnes, E. J. L.; Piligkos, S.; Timco, G. A.; Winpenny, R. E. P. *Coordination Chemistry Reviews* **2005**, *249*, 2577-2590.

(45) Aubin, S. M. J.; Dilley, N. R.; Pardi, L.; Krzystek, J.; Wemple, M. W.; Brunel, L. C.; Maple, M. B.; Christou, G.; Hendrickson, D. N. *Journal of the American Chemical Society* **1998**, *120*, 4991-5004.

(46) Feng, P. L.; Beedle, C. C.; Koo, C.; Wernsdorfer, W.; Nakano, M.; Hill, S.; Hendrickson, D. N. *Inorganic Chemistry* **2008**, *47*, 3188-3204.

(47) Feng, P. L.; Beedle, C. C.; Wernsdorfer, W.; Koo, C.; Nakano, M.; Hill, S.; Hendrickson, D. N. *Inorganic Chemistry* **2007**, *46*, 8126-8128.

(48) Nakano, M.; Matsubayashi, G. E.; Muramatsu, T.; Kobayashi, T. C.; Amaya, K.; Yoo, J.; Christou, G.; Hendrickson, D. N. *Molecular Crystals and Liquid Crystals* **2002**, *376*, 405-410.

(49) Nihei, M.; Hoshino, N.; Ito, T.; Oshio, H. *Polyhedron* **2003**, *22*, 2359-2362.

(50) Wemple, M.; Christou, G.; Hendrickson, D. N.; Folting, K. *Abstracts of Papers of the American Chemical Society* **1992**, *204*, 104-Inor.

(51) Winpenny, R. E. P. *Comments on Inorganic Chemistry* **1999**, *20*, 233-262.

(52) Yang, C. I.; Lee, G. H.; Wur, C. S.; Lin, J. G.; Tsai, H. L. *Polyhedron* **2005**, *24*, 2215-2221.

(53) Beedle, C. C.; Heroux, K. J.; Nakano, M.; DiPasquale, A. G.; Rheingold, A. L.; Hendrickson, D. N. *Polyhedron* **2007**, *26*, 2200-2206.

(54) Heroux, K., J. ; Rheingold, A., L.; Hendrickson, D., N. *European Journal of Inorganic Chemistry* **2009**, *2009*, 3541-3544.

(55) Ako, A. M.; Mereacre, V.; Hewitt, I. J.; Clerac, R.; Lecren, L.; Anson, C. E.; Powell, A. K. *Journal of Materials Chemistry* **2006**, *16*, 2579-2586.

(56) Wemple, M. W.; Tsai, H. L.; Wang, S. Y.; Claude, J. P.; Streib, W. E.; Huffman, J. C.; Hendrickson, D. N.; Christou, G. *Inorganic Chemistry* **1996**, *35*, 6437-6449.

(57) Wittick, L. M.; Murray, K. S.; Moubaraki, B.; Batten, S. R.; Spiccia, L.; Berry, K. J. *Dalton Transactions* **2004**, 1003-1011.

(58) Yamaguchi, A.; Kusumi, N.; Ishimoto, H.; Mitamura, H.; Goto, T.; Mori, N.; Nakano, M.; Awaga, K.; Yoo, J.; Hendrickson, D. N.; Christou, G. *Journal of the Physical Society of Japan* **2002**, *71*, 414-417.

(59) Coulon, C.; Miyasaka, H.; Clerac, R. In *Single-Molecule Magnets and Related Phenomena* 2006; Vol. 122, p 163-206.

(60) Feng, P. L.; Hendrickson, D. N. *Inorganic Chemistry*, *49*, 6393-6395.

(61) Gatteschi, D.; Guillou, O.; Zanchini, C.; Sessoli, R.; Kahn, O.; Verdaguer, M.; Pei, Y. *Inorganic Chemistry* **1989**, *28*, 287-290.

(62) Miyasaka, H.; Madanbashi, T.; Sugimoto, K.; Nakazawa, Y.; Wernsdorfer, W.; Sugiura, K.; Yamashita, M.; Coulon, C.; Clerac, R. *Chemistry-a European Journal* **2006**, *12*, 7029-7040.

(63) Miyasaka, H.; Nezu, T.; Sugimoto, K.; Sugiura, K.; Yamashita, M.; Clerac, R. *Chemistry-a European Journal* **2005**, *11*, 1592-1602.

(64) Oshio, H.; Nagashima, U. *Inorganic Chemistry* **1992**, *31*, 3295-3301.

(65) Oshio, H.; Okamoto, H.; Kikuchi, T.; Ito, T. *Inorganic Chemistry* **1997**, *36*, 3201-3203.

(66) Wang, S.; Ferbinteanu, M.; Yamashita, M. *Inorganic Chemistry* **2007**, *46*, 610-612.

(67) Wernsdorfer, W.; Clerac, R.; Coulon, C.; Lecren, L.; Miyasaka, H. *Physical Review Letters* **2005**, *95*.

(68) Yoo, J.; Wernsdorfer, W.; Yang, E. C.; Nakano, M.; Rheingold, A. L.; Hendrickson, D. N. *Inorganic Chemistry* **2005**, *44*, 3377-3379.

(69) Braun, H. B.; Loss, D. *International Journal of Modern Physics B* **1996**, *10*, 219-234.

(70) Galan-Mascaros, J. R.; Dunbar, K. R. *Angewandte Chemie-International Edition* **2003**, *42*, 2289-2293.

(71) Oshio, H.; Kikuchi, K.; Ito, T. *Chemistry Letters* **2000**, 1138-1139.

(72) Eppley, H. J.; deVries, N.; Wang, S. Y.; Aubin, S. M.; Tsai, H. L.; Folting, K.; Hendrickson, D. N.; Christou, G. *Inorganica Chimica Acta* **1997**, *263*, 323-340.

(73) Nakano, M.; Sorai, M.; Vincent, J. B.; Christou, G.; Ho, G. J.; Hendrickson, D. N. *Inorganic Chemistry* **1989**, *28*, 4608-4614.

(74) Vincent, J. B.; Chang, H. R.; Folting, K.; Huffman, J. C.; Christou, G.; Hendrickson, D. N. *Journal of the American Chemical Society* **1987**, *109*, 5703-5711.

(75) Lawrence, J.; Beedle, C. C.; Yang, E. C.; Ma, J.; Hill, S.; Hendrickson, D. N. *Polyhedron* **2007**, *26*, 2299-2303.

(76) Liu, J.; Datta, S.; Bolin, E.; Lawrence, J.; Beedle, C. C.; Yang, E.-C.; Goy, P.; Hendrickson, D. N.; Hill, S. *Polyhedron* **2009**, *28*, 1922-1926.

(77) Wilson, A.; Lawrence, J.; Yang, E. C.; Nakano, M.; Hendrickson, D. N.; Hill, S. *Physical Review B (Condensed Matter and Materials Physics)* **2006**, *74*, 140403.

(78) Wilson, A.; Yang, E. C.; Hendrickson, D. N.; Hill, S. *Polyhedron* **2007**, *26*, 2065-2068.

(79) Kambe, K. *Journal of the Physical Society of Japan* **1950**, *5*, 48.

(80) Clerac, R.; Miyasaka, H.; Yamashita, M.; Coulon, C. *Journal of the American Chemical Society* **2002**, *124*, 12837-12844.

(81) del Barco, E.; Hernandez, J. M.; Sales, M.; Tejada, J.; Rakoto, H.; Broto, J. M.; Chudnovsky, E. M. *Physical Review B* **1999**, *60*, 11898-11901.

(82) Leuenberger, M. N.; Loss, D. *Physical Review B* **2000**, *61*, 1286-1302.

(83) Barbara, B.; Thomas, L.; Lionti, F.; Chiorescu, I.; Sulpice, A. *Journal of Magnetism and Magnetic Materials* **1999**, *200*, 167-181.

(84) del Barco, E.; Kent, A. D.; Rumberger, E. M.; Hendrickson, D. N.; Christou, G. *Europhysics Letters* **2002**, *60*, 768-774.

(85) Hill, S.; Maccagnano, S.; Achey, R.; Dalal, N.; Park, K. *International Journal of Modern Physics B* **2002**, *16*, 3326-3329.

(86) Park, K.; Novotny, M. A.; Dalal, N. S.; Hill, S.; Rikvold, P. A. *Physical Review B* **2002**, *66*, -.

(87) Waldmann, O.; Ako, A. M.; GuÌˆdel, H. U.; Powell, A. K. *Inorganic Chemistry* **2008**, *47*, 3486-3488.

(88) Wernsdorfer, W.; Caneschi, A.; Sessoli, R.; Gatteschi, D.; Cornia, A.; Villar, V.; Paulsen, C. *Physical Review Letters* **2000**, *84*, 2965-2968.

(89) Wernsdorfer, W.; Ohm, T.; Sangregorio, C.; Sessoli, R.; Gatteschi, D.; Paulsen, C. *Physica B* **2000**, *284*, 1229-1230.

(90) Feng, P. L.; Koo, C.; Henderson, J. J.; Nakano, M.; Hill, S.; del Barco, E.; Hendrickson, D. N. *Inorganic Chemistry* **2008**, *47*, 8610-8612.

(91) Edwards, R. S.; Maccagnano, S.; Yang, E. C.; Hill, S.; Wernsdorfer, W.; Hendrickson, D.; Christou, G. *Journal of Applied Physics* **2003**, *93*, 7807-7809.

(92) Kirman, C.; Lawrence, J.; Hill, S.; Yang, E. C.; Hendrickson, D. N. *Journal of Applied Physics* **2005**, *97*.

(93) Lawrence, J.; Yang, E.-C.; Edwards, R.; Olmstead, M. M.; Ramsey, C.; Dalal, N. S.; Gantzel, P. K.; Hill, S.; Hendrickson, D. N. *Inorganic Chemistry* **2008**, *47*, 1965-1974.

(94) Yang, E. C.; Kirman, C.; Lawrence, J.; Zakharov, L. N.; Rheingoid, A. L.; Hill, S.; Hendrickson, D. N. *Inorganic Chemistry* **2005**, *44*, 3827-3836.

(95) Hill, S.; Edwards, R. S.; North, J. M.; Park, K.; Dalal, N. S. *Polyhedron* **2003**, *22*, 1889-1896.

(96) Hill, S.; Maccagnano, S.; Park, K.; Achey, R. M.; North, J. M.; Dalal, N. S. *Physical Review B* **2002**, *65*, 224410.

(97) Park, K.; Dalal, N. S.; Rikvold, P. A. *Journal of Chemical Physics* **2002**, *117*, 11292-11300.

(98) Park, K.; Novotny, M. A.; Dalal, N. S.; Hill, S.; Rikvold, P. A. *Physical Review B* **2002**, *65*, 014426.

(99) Feng, P. L.; Beedle, C. C.; Koo, C.; Lawrence, J.; Hill, S.; Hendrickson, D. N. *Inorganica Chimica Acta* **2008**, *361*, 3465-3480.

(100) Takahashi, S.; van Tol, J.; Beedle, C. C.; Hendrickson, D. N.; Brunel, L.-C.; Sherwin, M. S. *Physical Review Letters* **2009**, *102*, 087603.

(101) Affronte, M.; Cornia, A.; Lascialfari, A.; Borsa, F.; Gatteschi, D.; Hinderer, J.; Horvatic, M.; Jansen, A. G. M.; Julien, M. H. *Physical Review Letters* **2002**, *88*, -.

(102) Asano, K.; Inoue, K.; Nakano, M.; Miyazaki, Y.; Sorai, M.; Nakatani, K.; Kahn, O. *Bulletin of the Chemical Society of Japan* **1999**, *72*, 1749-1757.

(103) Bhattacharjee, A.; Miyazaki, Y.; Nakano, M.; Yoo, J.; Christou, G.; Hendrickson, D. N.; Sorai, M. *Polyhedron* **2001**, *20*, 1607-1613.

(104) Fominaya, F.; Gandit, P.; Gaudin, G.; Chaussy, J.; Sessoli, R.; Sangregorio, C. *Journal of Magnetism and Magnetic Materials* **1999**, *195*, L253-L255.

(105) Fujisaki, T.; Nakazawa, Y.; Oguni, M.; Nakata, M.; Yamashita, M.; Lecren, L.; Miyasaka, H. *Journal of the Physical Society of Japan* **2007**, *76*, 104602.

(106) Miyazaki, Y.; Bhattacharjee, A.; Nakano, M.; Saito, K.; Aubin, S. M. J.; Eppley, H. J.; Christou, G.; Hendrickson, D. N.; Sorai, M. *Inorganic Chemistry* **2001**, *40*, 6632-6636.

(107) Sorai, M.; Maeda, Y.; Oshio, H. *Journal of Physics and Chemistry of Solids* **1990**, *51*, 941-951.

(108) Sorai, M.; Nakano, M.; Miyazaki, Y. *Chemical Reviews* **2006**, *106*, 976-1031.

Chapter 2

Geometric Frustration Leading to Magnetic Metastability in a High-Spin $Cu_{17}Mn_{28}$ Cluster with T_d Symmetry

2.1 Introduction

The synthesis and study of magnetic nanostructures is of both intense scientific and technological interest. A single-molecule magnet (SMM) is a molecular nanomagnet that can be magnetized as a result of having a large spin ground state that experiences appreciable magnetoanisotropy.[1,2] The magnitude of the energy barrier between the "spin-up" and the "spin down" states of a SMM with a half-integer ground state is $|D|(S^2-{}^1/_4)$, where S is the spin of the ground state and D gauges the magnitude of the axial zero-field splitting ($D\hat{S}_z^2$). There are two major areas of interest in SMMs. First, the monodisperse nature (same size, shape and anisotropy) of SMMs permits detailed studies of the magnetization dynamics of nanomagnets.[3-7] Second, SMMs have been suggested [8,9] as good media for quantum computing. In the case of the first area of interest, it should be noted that it has been a long standing goal to determine whether quantum effects are important in the smallest size nanomagnets. The discovery of SMMs permitted, for the first time, detailed study of quantum relaxation associated with nanomagnets. The quantum effects that have been studied for SMMs include: (1) ground-state tunneling of the direction of magnetization;[10-12] (2) thermally activated magnetization tunneling in excited M_s states;[13-16] (3) quantum phase interference;[17] (4) spin parity effects;[18,19] (5) magnetic exchange biasing of quantum tunneling;[20-22] (6) spin-spin cross relaxation effects on tunneling;[23] and quantum coherence/decoherence.[24-28]

Chemistry initiated this new area of molecular nanomagnets and chemistry will predominantly control the progress made in understanding the magnetization dynamics in SMMs and employing SMMs in devices. Although polynuclear Mn complexes are

the most prevalent of SMMs, molecular nanomagnets comprised of Fe^{III},[29-32] Ni^{II},[21,33-36] V^{III},[37] Fe^{II},[38] or Co^{II} [39] ions have also been reported.

In the last few years there has been an increased effort to prepare and characterize new heterometallic SMMs. Transition metal ions have been combined with rare earth ions, because some of the latter ions exhibit considerable anisotropy and may help to increase the blocking temperatures of SMMs.[40] The anisotropy of 4f ions such as Dy^{III} is a zero-field interaction due mainly to crystal fields. While several 3d-4f complexes have been found to function as SMMs,[41-47] very recent papers by Hamamatsu *et al*.[48] and by Pointillart *et al*.[49] have shown that considerable additional research is needed in order to understand the magnetization relaxation effects in 3d-4f SMMs and mononuclear 4f ions.

In a second strategy to prepare polynuclear heterometallic complexes that are SMMs, cyanometalate complexes have been used as building blocks for high-spin cluster complexes. In many cases CN^- ligands on kinetically inert metal ions combined with blocking ligands such as 1,4,7-triazacyclononane (tacn) on another metal ion have given several SMMs.[50-60] The use of cyanometalate building blocks allows for controlled systematic approaches to building up polynuclear complexes due to the kinetic inertness of the cyanometalate units.

There are very few examples of heterometallic SMMs that contain two first row transition metals. Feng *et al.* recently reported integer spin system analogs of the well studied $S = 9/2$ $Mn^{IV}Mn_3^{III}$ cubane complexes.[61,62] These distorted heterometallic cubane complexes consist of three ferromagnetically coupled trivalent manganese ions that lie in a plane and a apical divalent nickel or zinc ion that yield well isolated $S = 5$ or

S = 6 spin ground states, respectively. In the nickel case, antiferromagnetic coupling between the divalent nickel ion and the trivalent manganese ions leads to a S = 5 spin ground state; whereas, the diamagnetic zinc ion produces no perturbation to the ferromagnetic exchange between S = 2 Mn^{III} ions, and affords a S = 6 spin ground state. This family of tetranuclear SMMs exhibits notable variations in tunneling rates depending on the nature of the divalent apical ion, solvate molecules and the nature of the peripheral carboxylate ligands which leads to discernible changes in the molecular site symmetry.

Oshio *et al*.[63] communicated the preparation and properties of a heterometallic $Mn^{III}_2Ni^{II}_2$ complex with a "dicubane" type of structure. Magnetic susceptibility and high-field EPR data indicate that this complex has an S = 6 ground state, while the observation of hysteresis in the plot of magnetization versus magnetic field at 0.55 K confirms that this tetranuclear complex is a SMM. Oshio *et al*.[64] also reported a dinuclear $Mn^{III}Cu^{II}$ complex that is a SMM. The ferromagnetic exchange interaction in this complex results in a S = 5/2 ground state with an axial zero-field interaction ($D\hat{S}_z^2$) where D = -1.81 cm^{-1}. Confirmation that this complex is a SMM came from frequency-dependent out-of-phase AC signals observed below 1.5 K, however, even at temperatures as low as 0.2 K little coercive field was detected in the magnetization versus magnetic field plot.

Finally, we communicated [65] the preparation and properties of a heterometallic $Cu_{17}Mn_{28}$ complex that also exhibits frequency-dependent out-of-phase AC signals, as well as, temperature and sweep rate dependent magnetization hysteresis. This complex is interesting for several reasons: (1) there are five different metal oxidation states,

$Cu^{I}_{4}Cu^{II}_{13}Mn^{II}_{4}Mn^{III}_{12}Mn^{IV}_{12}$; (2) the complex has a relatively large $S \simeq 51/2$ ground state; (3); there are low-energy excited spin states, perhaps one with $S \simeq 63/2$; and (4) the complex has a T_d symmetry in the crystal that precludes second-order axial type magnetoanisotropy.

The origin of magnetization relaxation and anisotropy often times is difficult to deduce, especially in large molecules containing many exchange coupled paramagnetic ions. There are a number of published reports of molecules that exhibit magnetization hysteresis and magnetic susceptibility normally attributed to SMMs, in the absence of axial type anisotropy. In 2006, Ako *et al*. [66]communicated a Mn_{19} complex with a S = 83/2 spin ground state that exhibits slow magnetization relaxation dynamics and M verses H/T behavior normally attributed to SMMs. However, it was later revealed through EPR measurements that the sign of the zero-field splitting parameter D is of the easy-plane not easy axis type, and that the exhibited SMM behavior is due to strong intermolecular dipolar coupling.[67] Also, Shaw *et al.*[68] reported a high symmetry Ni_{10} complex that exhibits slow magnetization relaxation dynamics up to 17K, not due to magnetic interactions or axial anisotropy, but rather as a consequence of resonant phonon-trapping.[69] In both cases, there are symmetry allowed zero-field splitting Hamiltonian terms that can naturally give rise to anisotropy. In this paper we show considerably more data, including single-crystal magnetization versus magnetic field hysteresis data, high-frequency paramagnetic resonance and heat capacity data in an effort to determine the origin of metastability and relaxation behavior in the high symmetry $Cu_{17}Mn_{28}$ complex.

2.2 Experimental Section

2.2.1 Compound Preparation

All Reactions were performed under aerobic conditions and all chemicals were obtained from commercial sources and used without further purification.

$[Cu_{17}Mn_{28}O_{40}(tea)_{12}(HCO_2)_6(H_2O)_4]\cdot 36H_2O$ (2A). Copper powder (0.32 g, 5 mmol) and $Mn(O_2CCH_3)_2\cdot 4H_2O$ (2.45 g, 10 mmol) were dissolved in DMF (30 mL) containing triethanolamine (0.56 g, 3.77 mmol). The resulting black slurry was heated with stirring at 85°C in air for 8 hours. A black precipitant formed that was allowed to settle and then removed by gravity filtration. The resulting dark-green solution was left undisturbed for several months yielding dark green-black cube-shaped crystals suitable for x-ray crystallographic studies. The crystals were filtered and washed with dry diethylether and dried using silicon gel at room temperature. Mass collected 0.91 g (Yield 52% by copper). Elemental analysis Calcd (%) for **2A** (6003.24): C, 15.61; H, 3.86; N, 2.80. Found: C, 16.07; H, 3.81; N, 2.73. FTIR (cm^{-1}): 3420 (br), 2924 (m), 2863 (m), 2363 (w), 1576 (s), 1357 (s), 1066 (s), 910 (w), 660 (m), 544 (w).

2.2.2 X-Ray Crystallography

Diffraction intensities of complex **2A** were collected on a Bruker Apex CCD area-detector diffractometer (Mo K□, □ = 0.71073 Å) at 123(2) K. The raw data frames were integrated with SAINT$^+$. Absorption corrections were applied by using the multiscan program SADABS (G. M. Sheldrick, SADABS, program for empirical absorption correction of area detector data; University of Göttingen, Göttingen, Germany, 1996). The structure was solved using direct methods, and all non-hydrogen

atoms were refined anisotropically by least-squares on F^2 using the SHELXTL program. Hydrogen atoms on organic ligands were generated by the riding mode (C-H = 0.96 Å) (G. M. Sheldrick, SHELXTL97, program for crystal structure refinement, University of Göttingen, Germany, 1997).

2.2.3 Physical Measurements

IR spectra were recorded from KBr pellets in the range 4000–400 cm^{-1} with a Bruker-tensor 27 spectrometer. DC magnetic susceptibility measurements were performed on finely ground polycrystalline samples, restrained in parafilm to prevent torquing of the micro-crystallites in an applied magnetic field, using Quantum Design MPMS XL-7 SQUID and Quantum Design MPMS 5 magnetometers equipped with 7T and 5T magnets, respectively. Magnetic susceptibility measurements were performed in the 1.8-300 K temperature range with applied fields of 0.1-70 kG. Ac magnetic susceptibilities measurements were obtained with 3 G AC fields at frequencies in the range of 1-997 Hz with zero applied DC magnetic field. Data were corrected for magnetic contributions from the parafilm and sample holder, and a correction for diamagnetism was estimated from Pascal's constants yielding the overall paramagnetic contribution to the molar magnetic susceptibility. Single crystal hysteresis and magnetic relaxation measurements done below 1.8 K were performed using a micro-SQUID array.[70] High-frequency (40 – 160 GHz) electron paramagnetic resonance (HFEPR) measurements were carried out on a single crystal of $Cu_{17}Mn_{28}$ using a millimeter-wave vector network analyzer (MVNA) and a sensitive cavity technique.[71] The split-pair magnet with a 7 T horizontal field was used to apply a DC magnetic field

to the sample which was aligned in a cylindrical cavity. The angle dependence of EPR data was investigated rotating the sample relative to the DC magnetic field to change the angle between the orientation of the crystal and magnetic field by a room temperature stepper motor. The temperature was stabilized relative to a calibrated Cernox^{TM} thermometer using a combination of heaters and cold helium gas flow in the range of 3 – 20 K.

2.3 Results and Discussion

2.3.1 Synthesis

The rational synthesis of high nuclearity homometallic and heterometallic clusters remains a considerable challenge. A number of synthetic strategies have been used to self-assemble high nuclearity first row transition metal complexes. One approach that has been instituted is the use of building blocks as starting materials such as homo-valent and mixed-valent "triangle" [M_3O], "butterfly" and "dicubane" [M_4O_2] and "cubane" [M_4O_4] clusters of first row transition metals. Another synthetic approach commonly employed involves starting with simple divalent and trivalent transition metal salts of halides, carboxylates, and perchlorates in the presence of oxidizing agents such as dichromate salts and permanganate salts.

$$M^0 + NH_4^+ + 0.5\ O_2 \rightarrow M^{2+} + H_2O + NH_3 \quad \textbf{(2.1)}$$

$$M^0 + M'X_2 + NR'(ROH)_2 + 0.5\ O_2 \rightarrow MM'X_2NR'(RO)_2 + H_2O \quad \textbf{(2.2)}$$

Recently, a number of homometallic and heterometallic complexes have been synthesized using aminoalcohols as chelating and bridging ligands such as derivatives of 2-hydroxymethylpyridine (Hhmp), diethanolamines (H_2Rdea, R = alkyl substituent) and triethanolamine (H_3tea).[72-81] Polydentate aminoalcohols are proving to be very versatile ligands due to their ability to coordinate in various binding modes, act as coordination site caps, and impart structural flexibility. In many cases, the need for strong oxidizing agents is removed because the aminoalcohols in the presence of molecular oxygen promote metal center oxidation. Furthermore, aminoalcohols have been shown to play a crucial role in the formation of mixed-metal complexes involving zero-valent copper as a starting material. The reaction of zero-valent copper powder with divalent transition metal salts, such as $Co^{II}/Zn^{II}/Cd^{II}/Pd^{II}$, in the presence of molecular oxygen and ammonium salts or aminoalcohols, such as triethanolamine (H_3tea), has produced a number of topologically and magnetically interesting mixed-metal complexes.[82,83] The oxygen-splitting two-electron redox process producing mono-valent or di-valent copper is driven by the presence of an available proton source (Equation 2.1). Following deprotonation of the aminoalcohol, the alkoxy arms can then operate as coordination site caps on single metal centers or as heteroatom bridges between multiple metal centers leading to the assembly of extended structures (Equation 2.2). The application of zero-valent copper metal as a vehicle to assemble homo and heterometallic polyoxometallate frameworks has been exploited in this current work to synthesize a high nuclearity heterometallic mixed-metal cluster.

Table 2.1. Crystal data and structure refinement for complex **2A**.

Empirical formula	$C_{78}\ H_{230}\ Cu_{17}\ Mn_{28}\ N_{12}\ O_{128}$	
Formula weight	6003.24	
Temperature	123(2) K	
Wavelength	0.71073 Å	
Crystal system	Cubic	
Space group	I-43m	
Unit cell dimensions	a = 20.3441(9) Å	α= 90°.
	b = 20.3441(9) Å	β= 90°.
	c = 20.3441(9) Å	γ= 90°.
Volume	8420.1(6) $Å^3$	
Z	2	
Density (calculated)	2.368 g/cm^3	
Absorption coefficient	4.229 mm^{-1}	
F(000)	5998	
Crystal size	0.13 x 0.12 x 0.11 mm^3	
Theta range for data collection	2.00 to 27.91°.	
Index ranges	-26<=h<=26, -26<=k<=26, -26<=l<=26	
Reflections collected	46387	
Independent reflections	1837 [R(int) = 0.0535]	
Completeness to theta = 27.91°	98.3 %	
Absorption correction	Semi-empirical from equivalents	
Max. and min. transmission	0.6511 and 0.6157	
Refinement method	Full-matrix least-squares on F^2	
Data / restraints / parameters	1837 / 33 / 126	
Goodness-of-fit on F^2	1.087	
Final R indices [I>2sigma(I)]	R1 = 0.0456, wR2 = 0.1178	
R indices (all data)	R1 = 0.0481, wR2 = 0.1195	
Absolute structure parameter	0.04(5)	
Largest diff. peak and hole	1.077 and -1.366 e.$Å^{-3}$	

$R = \Sigma||F_o| - |F_c||/\Sigma|F_o|$. [b] $R(\omega F^2) = \{\Sigma[\omega(F_o^2 - F_c^2)^2]/\Sigma[\omega(F_o^2)^2]\}^{1/2}$; $\omega = 1/[\sigma^2(F_o^2) + (aP)^2 + bP]$, $P = [2F_c^2 + \max(F_o, 0)]/3$.

Table 2.2. Selected bond distances and angles for complex **2A**. Bond distances are given in Å and bond angles in degrees.

Parameter		**Parameter**	
Cu(1)-O(1)	1.975(11)	Mn(2)-O(7)	2.143(8)
Cu(2)-O(1w)	1.984(15)	Mn(2)-O(2)	2.221(6)
Cu(2)-O(2)	1.993(7)	Mn(2)-O(6*k*)	1.923(6)
Cu(3)-O(4)	1.918(7)	Mn(2)-O(3)	1.962(4)
Cu(3)-O(5)	1.932(9)	Mn(3)-O(4)	2.333(6)
Cu(3)-N(1)	1.989(7)	Mn(3)-O(5)	2.046(9)
Cu(3)-O(6)	2.148(6)	Mn(1)···Mn(1*g*)	2.847(3)
Mn(1)-O(1)	1.936(5)	Mn(1)···Mn(1*i*)	2.914(2)
Mn(1)-O(2)	1.894(4)	Mn(2)···Mn(2*g*)	2.894(3)
Mn(1)-O(3)	1.894(7)	Mn(1)···Mn(2)	3.008(2)
Mn(1)-O(4)	1.903(4)	Mn(1)···Mn(3)	3.235(2)
O(1)-Cu(1)-O(1*a*)	109.5	O(6*k*)-Mn(2)-O(3)	169.7(3)
O(1w)-Cu(2)-O(2)	116.2(2)	O(3*g*)-Mn(2)-O(3)	81.7(3)
O(2*d*)-Cu(2)-O(2*e*)	102.0(2)	O(6*f*)-Mn(2)-O(7)	95.1(3)
O(4)-Cu(3)-O(5)	85.7(3)	O(3)-Mn(2)-O(7)	92.9(3)
O(4)-Cu(3)-N(1)	172.6(3)	O(6*f*)-Mn(2)-O(2)	94.5(2)
O(5)-Cu(3)-N(1)	86.9(4)	O(5)-Mn(3)-O(5*h*)	104.2(3)
O(4)-Cu(3)-O(6)	100.1(2)	O(5)-Mn(3)-O(4)	73.1(3)
O(5)-Cu(3)-O(6)	127.6(2)	O(5*h*)-Mn(3)-O(4)	127.6(2)
N(1)-Cu(3)-O(6*f*)	84.5(2)	O(3)-Mn(2)-O(2)	76.5(2)
O(6)-Cu(3)-O(6*f*)	102.9(3)	O(7)-Mn(2)-O(2)	165.9(3)
N(1)-Cu(3)-O(6)	84.5(2)	O(5*h*)-Mn(3)-O(4*h*)	73.1(3)
O(4)-Cu(3)-O(6*f*)	100.1(2)	O(4)-Mn(3)-O(4*h*)	69.5(3)
O(2)-Mn(1)-O(1)	94.4(3)	Mn(1)-O(1)-Cu(1)	119.6(3)
O(3)-Mn(1)-O(1)	178.6(4)	Mn(1)-O(2)-Cu(2)	125.3(2)
O(4)-Mn(1)-O(1)	81.0(3)	Mn(1)-O(4)-Cu(3)	127.2(2)
O(2*g*)-Mn(1)-O(2)	82.5(3)	Mn(1*g*)-O(2)-Mn(1)	97.5(3)
O(2)-Mn(1)-O(3)	86.6(2)	Mn(1)-O(1)-Mn(1*i*)	97.6(4)
O(2*g*)-Mn(1)-O(4*h*)	94.2(3)	Mn(1*i*)-O(4)-Mn(1)	99.9(3)
O(2)-Mn(1)-O(4*h*)	174.2(2)	Mn(1)-O(3)-Mn(2)	102.5(2)
O(3)-Mn(1)-O(4*h*)	98.0(2)	Mn(2*g*)-O(3)-Mn(2)	95.0(3)
O(2*g*)-Mn(1)-O(4)	174.2(2)	Mn(1)-O(2)-Mn(2)	93.6(2)
O(2)-Mn(1)-O(4)	94.2(3)	Mn(1)-O(4)-Mn(3)	99.1(2)
O(3)-Mn(1)-O(4)	98.0(2)	Cu(3)-O(4)-Mn(3)	95.8(3)
O(4*h*)-Mn(1)-O(4)	88.7(4)	Cu(3)-O(5)-Mn(3)	105.4(4)
O(6*f*)-Mn(2)-O(3*g*)	169.7(3)	Mn(2*e*)-O(6)-Cu(3)	126.2(3)
O(6*f*)-Mn(2)-O(3)	91.4(2)	Cu(2)-O(2)-Mn(2)	113.5(3)

Symmetry codes: *a*) -y, x, -z; *b*) y, -x, -z; *c*) -x, -y, z; *d*) -y, -x, z; *e*) -z, -x, y; *f*) x, z, y; *g*) -x, y, -z; *h*) y, z, x; *i*) z, x, y; *j*) y, x, z; *k*) -y, z, -x.

2.3.2 Description of Crystal Structure

Complex **2A** crystallizes in the cubic *I*-43*m* space group, with the crystal faces collinear with the crystallographic cell faces. Crystallographic data and selected bond distances and angles are given for complex **2A** in Table 2.1 and Table 2.2, respectively. An ORTEP illustration of complex **2A** is given in Figure 2.1. Complex **2A** has T_d molecular site symmetry with the four principal C_3 axes located through the body diagonals of the unit cell. Complex **2A** contains three different manganese oxidation states (+2, +3 and +4, that is rare in manganese chemistry)[84] and two copper oxidation states (+1 and +2). The presence of five metal oxidation states is unprecedented in mixed-metal chemistry.

The giant $[Cu_{17}Mn_{28}O_{40}]^{42+}$ core contains four Cu^{I} ions, thirteen Cu^{II} ions, four Mn^{II} ions, twelve Mn^{III} ions, twelve Mn^{IV} ions, twenty-eight μ_4-O^{2-}, and twelve μ_3-O^{2-} ions. The $[Cu_{17}Mn_{28}O_{40}]^{42+}$ core is capped by twelve aminoalcohol ligands (tea^{3-}), six formate (HCO_2^-) ligands, and four water ligands to complete the sphere of the neutral complex. Coordination environments of the metals are illustrated in Figure 2.2 where peripheral aminoalcohol and formate carbon atoms, Hydrogen atoms, and water solvate molecules have been omitted for clarity.

The valencies of the metal centers was established by charge consideration, bond lengths, bond valence sum (BVS) calculations,[85] and the presence of Jahn-Teller (*JT*) tetragonal elongation axes located on the Mn^{III} (Mn2) metal centers. The six pairs of *JT* axes are perpendicular to the six crystal faces, and are collinear with the crystallographic *a*, *b* and *c* axes and are found along O2-Mn2-O7 bonds that point

directly at the O7 atoms of the carbonyl group of each of the six apical formate ligands (Figure 2.3).

The main structural core of complex **2A** consists of six $[Mn^{IV}_2Mn^{III}_2O_4]^{6+}$ oxo-bridged distorted cubane units (Figure 2.4, bottom left) and four $[Mn^{IV}_3Mn^{II}O_4]^{6+}$ distorted cubane units (Figure 2.4, bottom right) interconnected forming symmetric tetrahedral cage (Figure 2.4, top). Each $[Mn^{IV}_3Mn^{II}O_4]^{6+}$ cubane unit is joined to three $[Mn^{IV}_2Mn^{III}_2O_4]^{6+}$ units via corner-sharing through each of its three Mn^{IV} (Mn1) ions (Figure 2.3, bottom right). The six $[Mn^{IV}_2Mn^{III}_2O_4]^{6+}$ cubane units lie on the mid-points of the six edges that make up the tetrahedral geometry of the cluster. All of the twenty-eight Mn ions, twenty-eight μ_4-O^{2-}, and twelve μ_3-O^2 oxide ions are contained within the core cage structure. Mn^{IV} (Mn1) centers are present in near idealized octahedral coordination environments with Mn-O distances of 1.894-1.936 Å and O-Mn-O bond angles of 93.6(2)-102.5(2)^o. The twelve Mn^{III} (Mn2) ions occupy tetragonally elongated octahedral geometries with axial bond lengths for Mn2-O2 and Mn2-O7 equal to 2.221(6) and 2.143(8) Å, respectively, and meridial bond lengths of Mn2-O6 = 1.923(6) Å and Mn2-O3 = 1.962(4) Å. Associated bond angles for O-Mn-O moieties range between 81.7(3)° and 95.1(3)° and the axial O6-Mn2-O3 angle of 169.7(3)° is less than the 180° expected for an idealized system. The four Mn^{II} (Mn3) ions that form the apex of each of the $[Mn^{IV}_3Mn^{II}O_4]^{6+}$ cubane units (Figure 2.4, bottom right) are in distorted trigonal-prismatic coordination geometries in which they are bonded to three μ_4-O^{2-} (O4) ions in a $[Mn^{IV}_3Mn^{II}O_4]^{6+}$ cubane unit and complete their coordination spheres with bonds to three μ_2-O^{2-}(O6) atoms from single alkoxide arms of three neighboring tea^{3-} ligands.

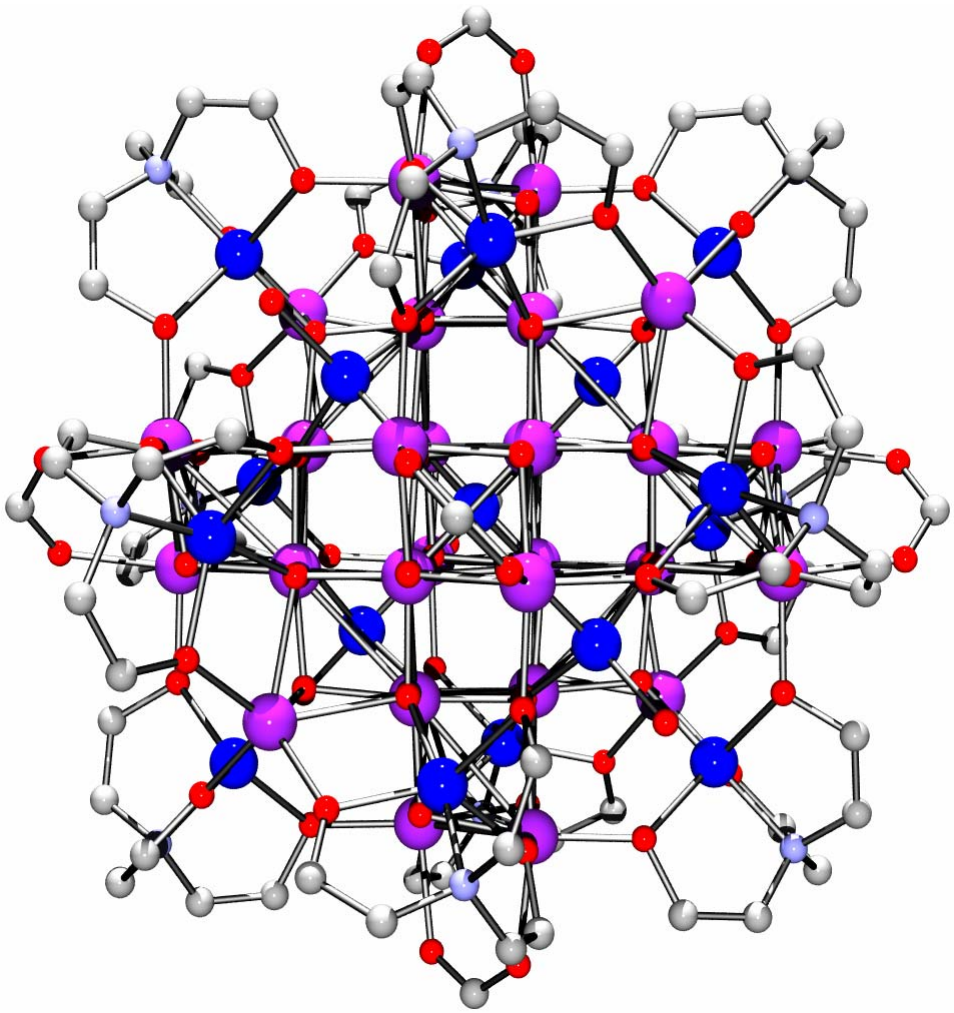

Figure 2.1. ORTEP drawing rendered in PovRay of complex **2A**. Hydrogens and water solvate molecules have been omitted for clarity.

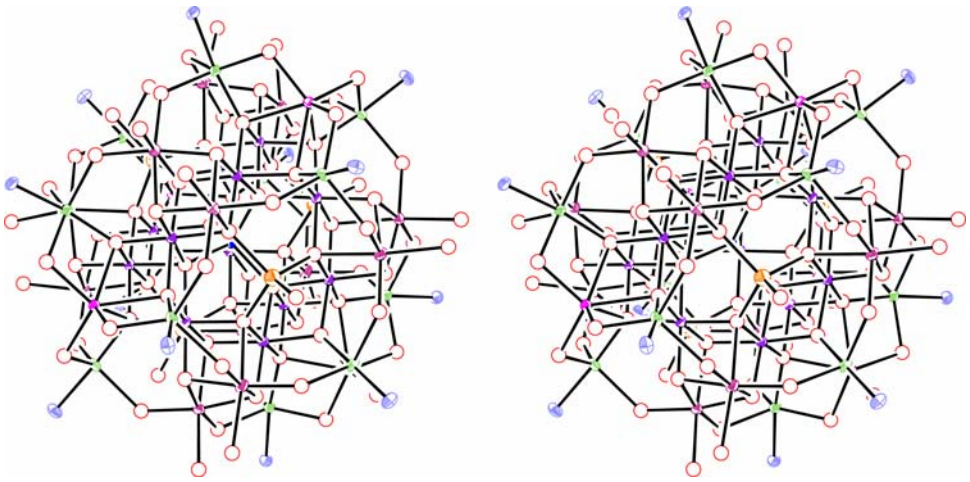

Figure 2.2. Stereo pair ORTEP illustration of the $[Cu_{17}Mn_{28}O_{40}]$ cluster illustrating the coordination environments associated with the three crystallographically independent manganese sites and the three crystallographically independent copper centers. Formate and triethanolamine carbons and hydrogens have been omitted for clarity. All atoms are shown with thermal ellipsoid probabilities of 50% except Oxygens (red) which are presented as idealized spheres for viewing clarity. Atom color code: Mn^{IV} (Mn1,■); Mn^{III} (Mn2,■); Mn^{II} (Mn3, ■); Cu^{II} (Cu1, ■); Cu^{I} (Cu2,■); Cu^{II} (Cu3,■); N (■); O (■).

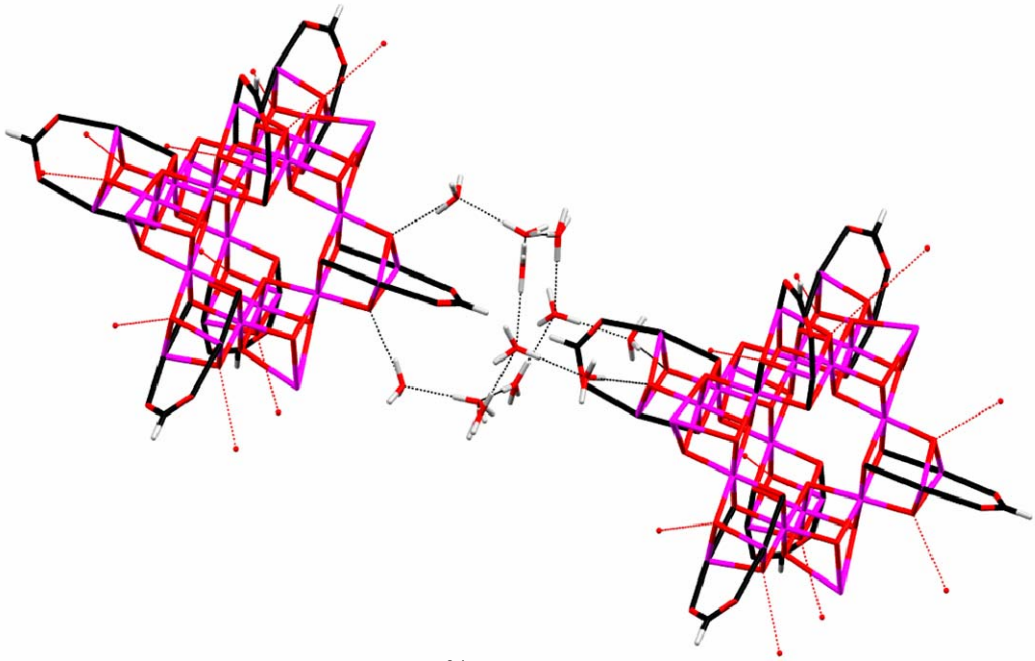

Figure 2.3. Illustration of $[Mn_{28}O_{36}]^{24+}$ cage of complex **2A** showing Jahn-Teller axes in black. Also illustrated is the hydrogen bonding network between neighboring molecules with peripheral tea^{3-} ligands, copper ions and coordinated water molecules are omitted for clarity.

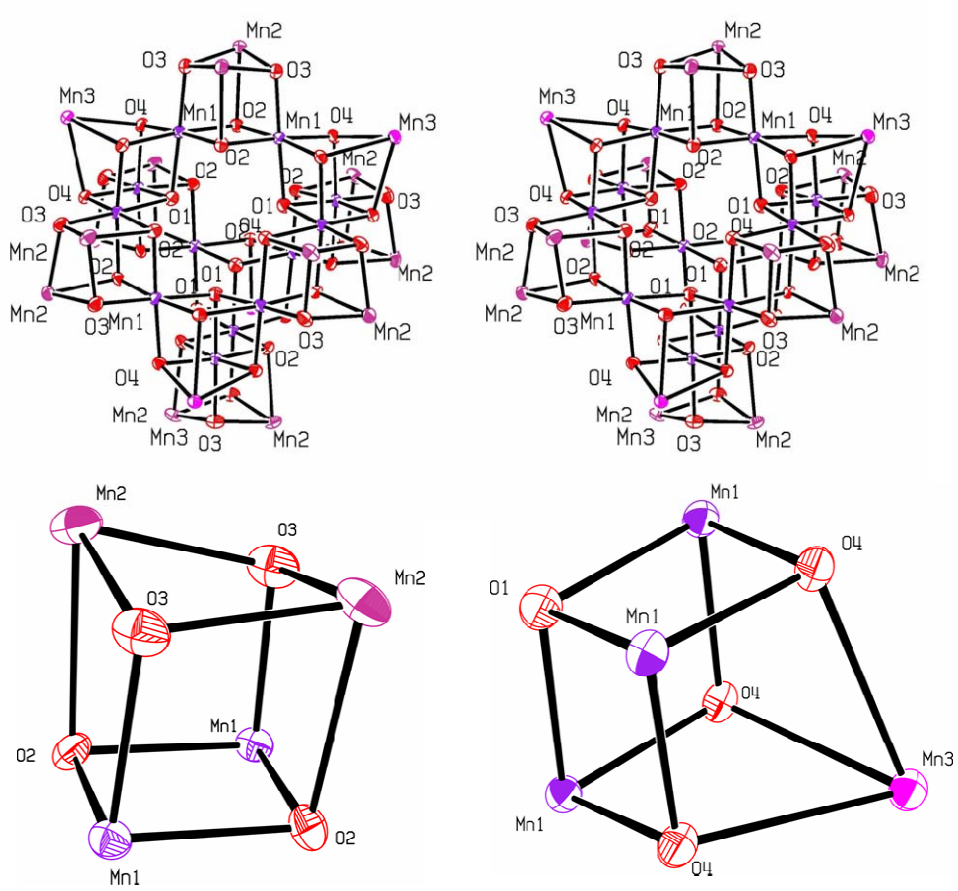

Figure 2.4. Top: Stereo pair ORTEP drawing illustrating the core Mn_{28} cluster containing six $[Mn^{IV}_2Mn^{III}_2O_4]$ cubanes (bottom left) and four $[Mn^{IV}_3Mn^{II}O_4]$ cubanes (bottom right). Atom color code: Mn^{IV} (Mn1,■); Mn^{III} (Mn2,■); Mn^{II} (Mn3, ■); Oxygens are red. Thermal ellipsoids are shown at 50% probability.

The Cu^{II} ions in complex **2A** occupy two different coordination environments. At the center of the manganese cage is a Cu^{II} (Cu1) metal center that is bonded in perfect tetrahedral geometry to the four μ_4-O^{2-} (O1) ions (Figure 2.2) located at a vertex of each of the four $[Mn^{IV}_3Mn^{II}O_4]$ cubane units (Cu1-O1 = 1.975(11) Å, O1-Cu1-O1 bond angle = 109.5°). The remaining twelve Cu^{II} (Cu3) ions are all symmetry-related and are coordinated in a distorted trigonal bipyramidal environment capped by a terminal tea^{3-} ligand in a μ_4:η^1:η^2:η^2 coordination mode, where axial positions are occupied by N(1) of the tea^{3-} aminoalcohol and a μ_4-O^{2-} (O4) oxide atom from a $[Mn^{IV}_3Mn^{II}O_4]^{6+}$ cubane unit, and meridial coordination sites are occupied by the three alkoxide arms of the tea^{3-} ligand (O-Cu3-O = 102.9(3)-127.58(17)^o and N1-Cu3-O4 = 172.6(3)^o).

Each of the four Cu^{I} (Cu2) ions are tetrahedrally coordinated and each Cu2 ion connects three $[Mn^{IV}_2Mn^{III}_2O_4]^{6+}$ cubane units together via their μ_4-O^{2-} (O2) oxide ions (Figure 2.2). A terminal water ligand completes the Cu^{I} (Cu2) tetrahedral coordination sphere (Cu-O2 = 1.975(11) Å)(O1W-Cu2-O2 = 116.2(2)° and O2-Cu2-O2 = 102.0(2)°).

Each $[Cu_{17}Mn_{28}]$ molecule in the unit cell is hydrogen bonded to six other $[Cu_{17}Mn_{28}]$ molecules via an intricate network of disordered water molecules (Figure 2.3). Centered between neighboring $[Cu_{17}Mn_{28}]$ complexes is a non-planar ring of eight disordered water molecules. The ring is composed of four symmetry related $O(3W)H_2$ molecules and four $O(4W)H_2$ molecules (O(3W)···H(4W) = 1.89 Å). The centroid of the ring is parallel to the crystallographic cell axes and is orthogonal to the formate ligands on neighboring $[Cu_{17}Mn_{28}]$ complexes as viewed in Figure 2.3. Two symmetry related water molecules ($O(2W)H_2$) lie between the ring and the $[Cu_{17}Mn_{28}]$ complex

are H-bonded to it via the μ_3-O(3) atoms that are located at vertices of $[Mn^{IV}_2Mn^{III}_2O_4]$ cubane units (Figure 2.4, bottom left)(O(2W)···H(3W) = 1.88 Å and H(2W)···μ_3-O(3) = 1.95 Å).

2.3.3 DC Magnetic Susceptibility

Figure 2.5 illustrates the variable temperature DC magnetization data for complex **2A** collected on microcrystalline powder samples measured in the temperature range of 300 K to 1.8 K with applied external magnetic fields of 0.01, 0.1, 1, 3 and 5 Tesla. The plot of $\chi_m T$ versus T shows a steady rise in molar magnetic susceptibility as the temperature is lowered from 300 K, and reaches a maximum molar susceptibility of ~ 336.6 $cm^3 \cdot K \cdot mol^{-1}$ at 3.5 K with an applied magnetic field of 0.01 Tesla. The maximum value of $\chi_m T$ suggests that complex **2A** possess a large spin in its ground state (S = 51/2 for $\chi_m T$ = 338 $cm^3 \cdot mol^{-1} \cdot K$ with g = 2). As the temperature is lowered below 3.5 K there is a rapid decline in molar susceptibility with a minimum at the lowest temperature measured (1.8 K) of ~324.2 $cm^3 \cdot mol^{-1} \cdot K$. The $\chi_m T$ value of ~72.3 $cm^3 \cdot mol^{-1} \cdot K$ at 300 K is less than the expected theoretical spin-only value of 80.9 $cm^3 \cdot K \cdot mol^{-1}$ for $4Cu^{I}$, $13Cu^{II}$, $4Mn^{II}$, $12Mn^{III}$ and $12Mn^{IV}$ non-interacting metal centers. The deviation of $\chi_m T$ is due to competing ferromagnetic and antiferromagnetic magnetic exchange interactions within the exchange coupled core of complex **2A**. As illustrated in Figure 2.5, complex **2A** exhibits a high degree of field dependence in its molar magnetic susceptibility. As the external magnetic field is increased from 0.01 T up to 5 T there is a marked shift in both the maximum value of the $\chi_m T$ product and the temperature at which the maximum occurs. For 0.1, 1, 3 and 5 Tesla the maximum $\chi_m T$

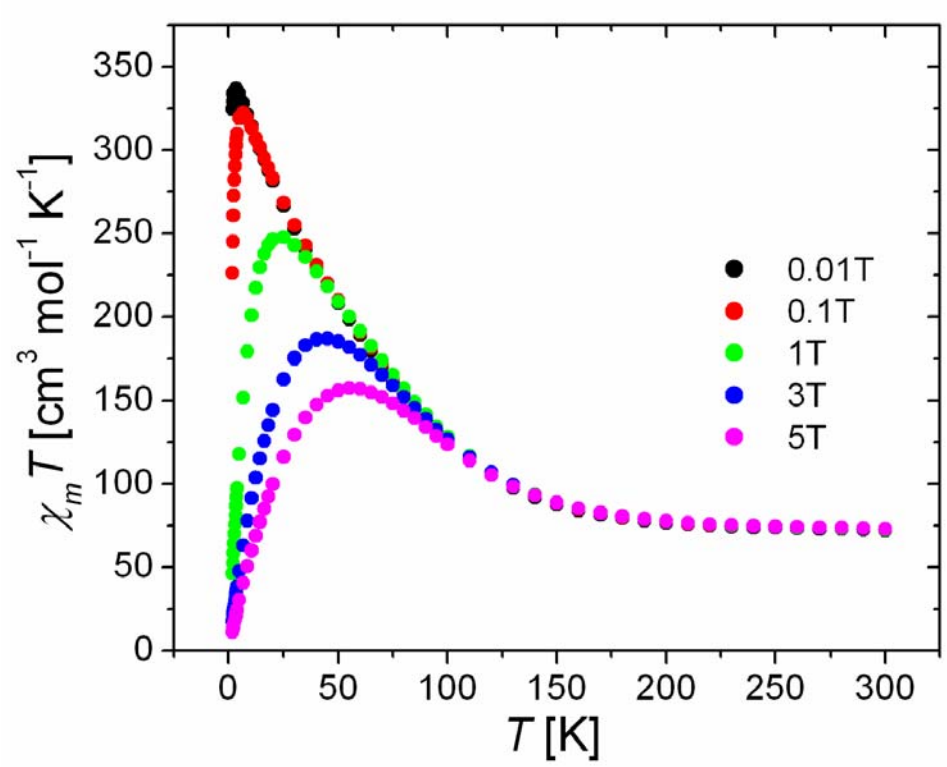

Figure 2.5. Plot of dc magnetic susceptibility for complex **2A** taken from 300K to 1.8K with applied fields as shown in figure.

value and the temperatures at which they occur are 322.2 $cm^3 \cdot mol^{-1} \cdot K$ at 6.9 K, 246.4 $cm^3 \cdot mol^{-1} \cdot K$ at 25 K and 186.7 $cm^3 \cdot mol^{-1} \cdot K$ at 45 K and 157.4 $cm^3 \cdot mol^{-1} \cdot K$ at 55 K respectively. The observed field dependence in DC susceptibility is a consequence of Zeeman induced changes in spin state populations.

Efforts were initiated to fit the variable temperature magnetic susceptibility data employing the Kambe [86] equivalent operator method; however, no simple coupling scheme could be developed that could reasonably describe the electronic structure of complex **2A**, and a full-matrix diagonalization approach was not possible due to the sheer size of the Hamiltonian matrix (4×10^{32}) x (4×10^{32}) needed to extract spin Hamiltonian parameters and the resulting eigenstates of complex **2A**.

2.3.4 AC Magnetic Susceptibility

AC magnetic susceptibility measurements were carried out on a microcrystalline powder sample of complex **2A** in the 1.8-5 K range with a 3 G applied AC field at frequencies between 100 and 10KHz. The in-phase molar susceptibility (χ') and out-of-phase molar susceptibilities (χ'') are plotted in Figure 2.6. As the temperature is lowered from 5 to 1.8 K there is a steady rise in χ' (Figure 2.6, top) which is consistent with the dc susceptibility measurements. The onset of frequency dependence (~2.5K) in the out-of-phase portion of the AC susceptibility is presented in Figure 2.6 (bottom). Because only the onset of frequency dependence is seen and no peak is observed for any of the measured frequencies, information regarding magnetization relaxation dynamics cannot be extracted from the AC susceptibility measurements and this topic will be addressed *vide infra*. At the lowest temperature measured (1.8 K), the out-of-phase portion of the

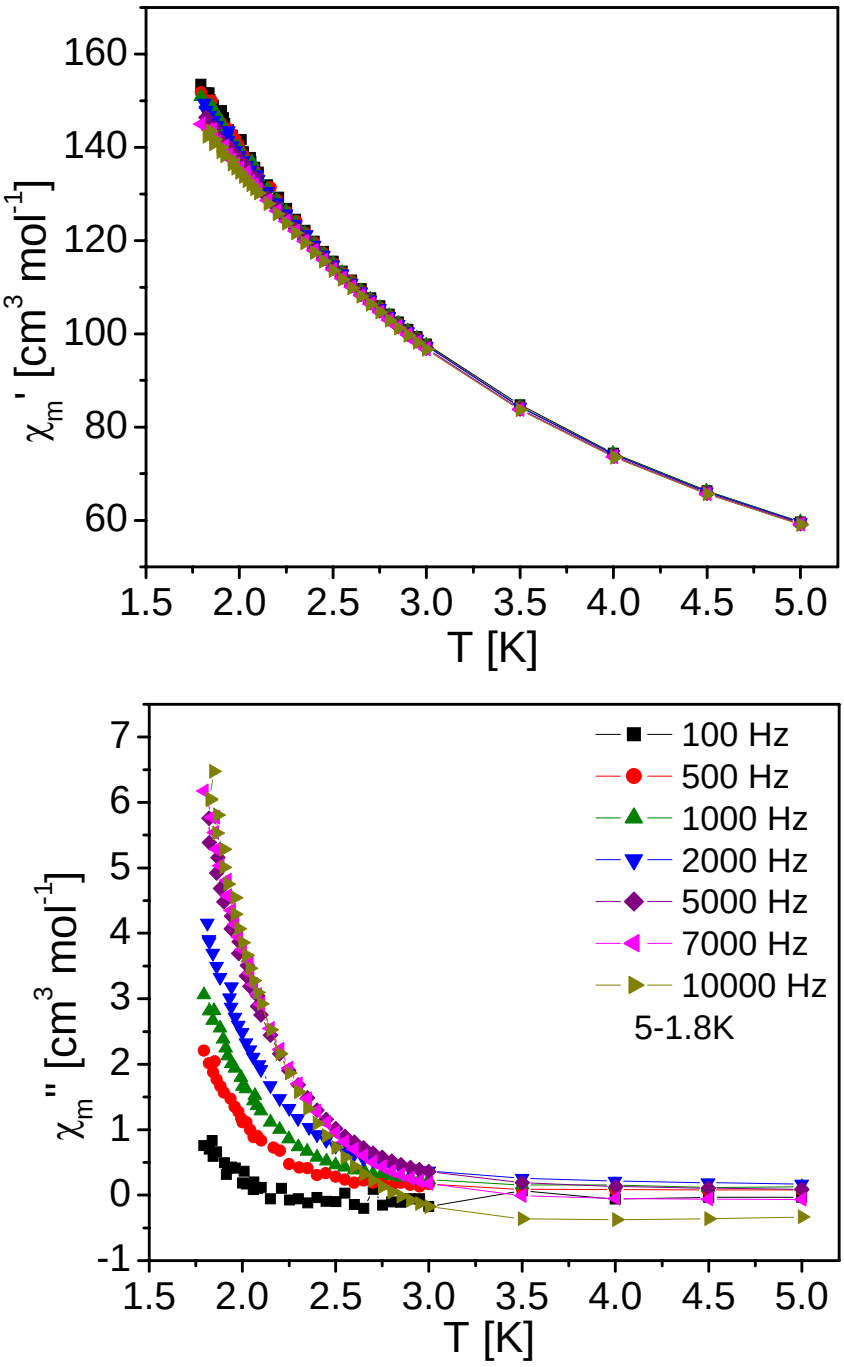

Figure 2.6. Ac susceptibility measurements for a polycrystalline sample of complex **2A** measured in the 1.8-5 K range. The in-phase signals (χ') are shown in the top plot, and the out-of-phase signals (χ'') are presented in the bottom plot.

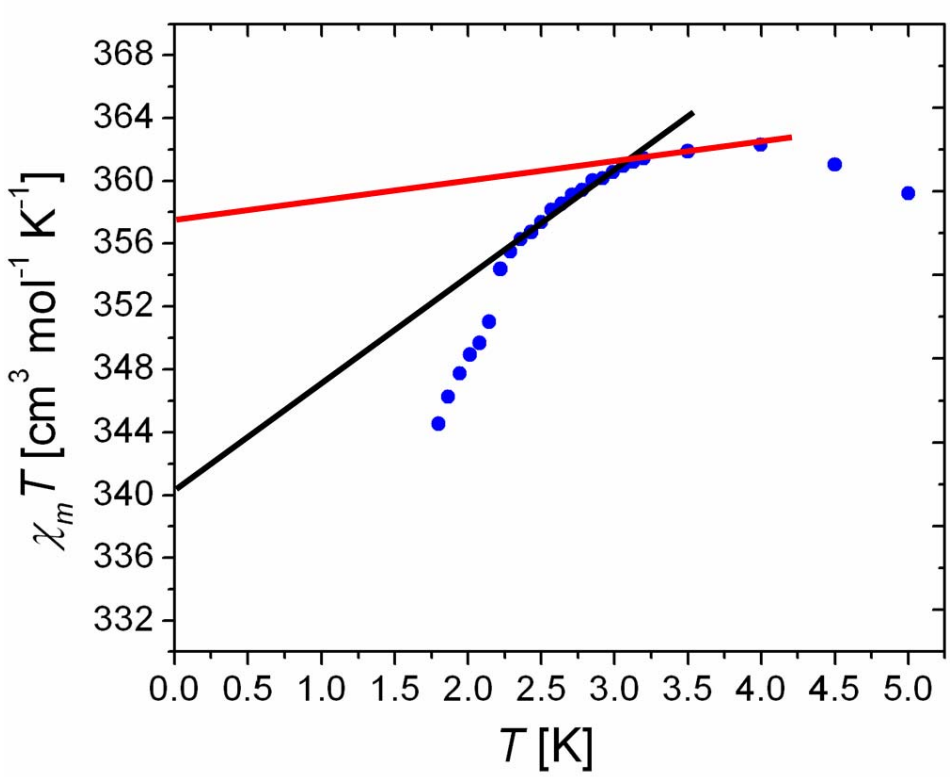

Figure 2.7. Extrapolation of ac 1Hz data in a 3 G ac field and zero dc field to 0 K with upper and lower bound shown in black and red lines.

ac susceptibility is less than two percent of χ' which is very small in comparison to many known SMMs.[21,29-37] Extrapolation to zero Kelvin of the 1 Hz in-phase molar susceptibility data (not shown) with zero applied dc field (Figure 2.7), plotted as $\chi_m T$, reveals an upper and lower bound when portions of the data near the $\chi_m T$ maximum are fit using least-squares fitting methods. The upper bound (red line) yields a $\chi_m T$ value of ~358 $cm^3 \cdot mol^{-1} \cdot K$ and the lower bound (black line) yields a $\chi_m T$ value of ~340 $cm^3 \cdot mol^{-1} \cdot K$. The $\chi_m T$ value expected for spin ground states of $S = 49/2$, $S = 51/2$ and $S = 53/2$ ground states is 312 $cm^3 \cdot mol^{-1} \cdot K$, 337 $cm^3 \cdot mol^{-1} \cdot K$ and 364 $cm^3 \cdot mol^{-1} \cdot K$, respectively. Extrapolation of the 1 Hz AC data to 0 K is in good agreement with the assignment of a spin ground state of $S = 51/2$ made using DC susceptibility data collected at 0.01 Tesla

2.3.5 Magnetization Hysteresis

In order to study magnetization relaxation dynamics, and to ascertain whether complex **2A** is a SMM, magnetization hysteresis data were collected employing a micro-SQUID array in the temperature range of 0.040-1.1 K at scan rates of 0.001-0.280 T/s. Measurements were performed using the transverse field method.[86] Below ~1K, at a constant scan rate of 0.28 T/s, complex **2A** exhibits hysteresis loops that exhibit increasing coercivity with decreasing temperature (Figure 2.8). Figures 2.9 and 2.10 illustrate hysteresis loops collected at fixed temperatures of 0.5 K and 0.04 K, respectively, while varying the scan rate of the applied DC magnetic field. In the case of the 0.5 K measurements (Figure 2.9), there is increased coercivity as the scan rate is increased. Conversely, when measured at 0.04 K (Figure 2.10) the coercivity of the

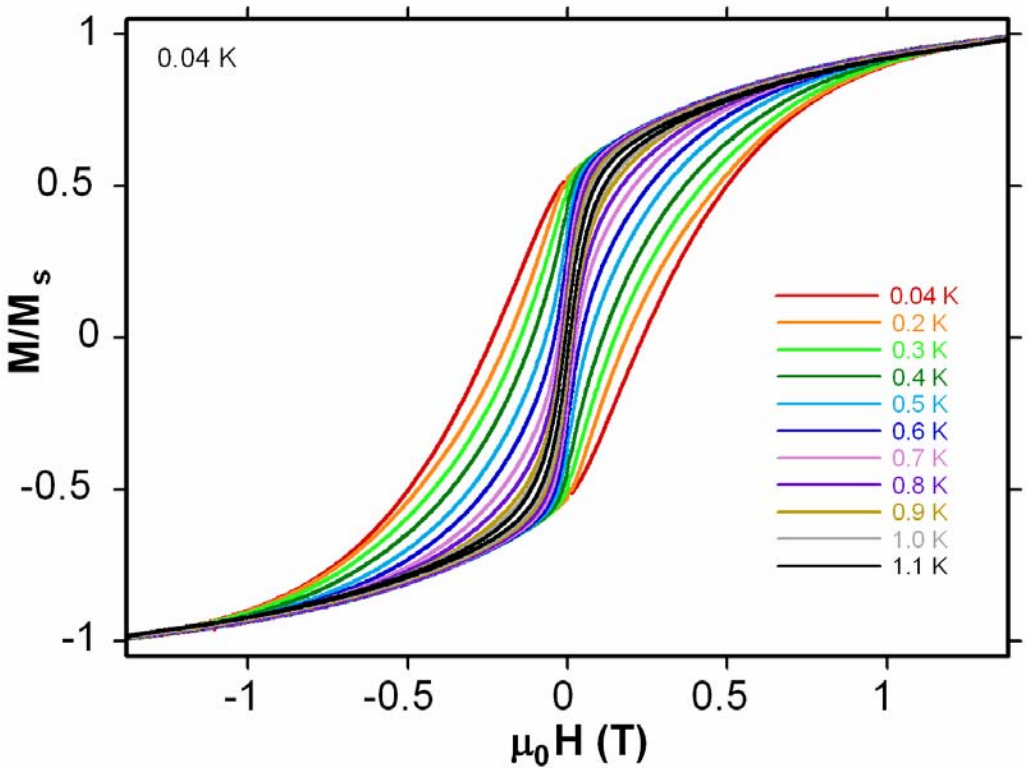

Figure 2.8. Magnetization hysteresis loops of a single crystal of complex **2A** measured in the temperature range of 0.04-1.1 K with the external magnetic field oriented parallel to the easy axis of the crystal.

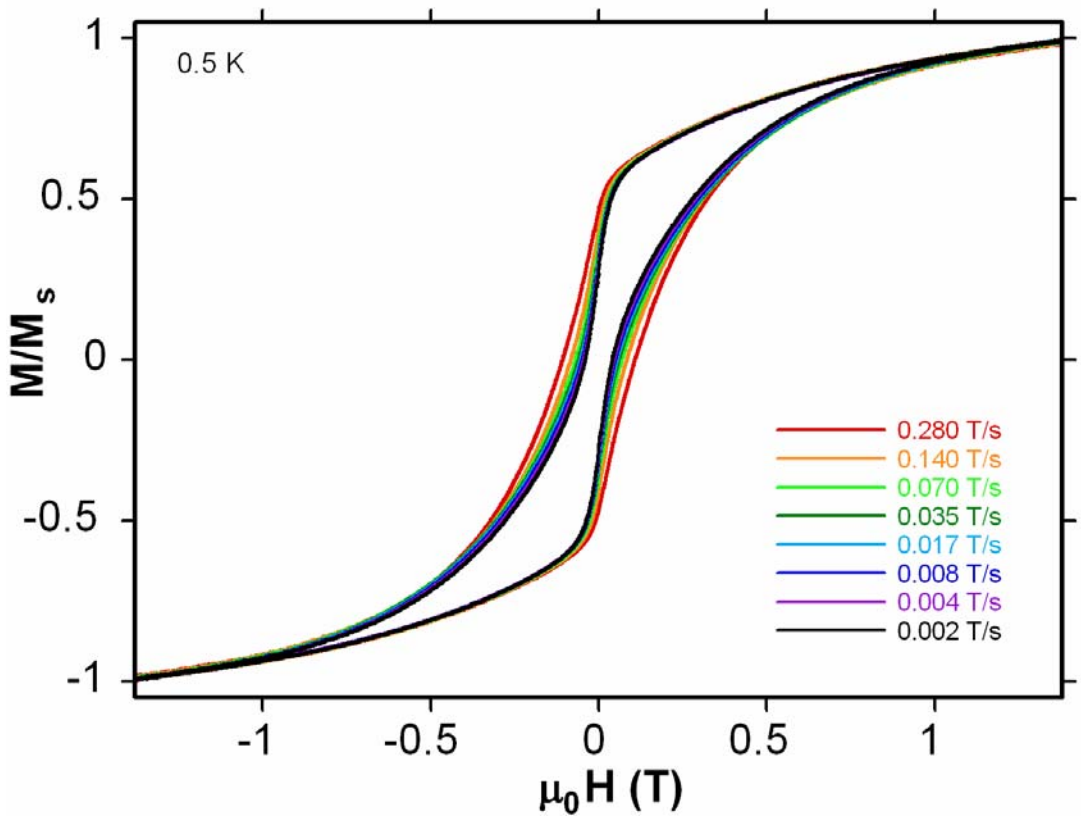

Figure 2.9. Magnetization hysteresis loops of a single crystal of complex **2A** at 0.5 K at various scan rates from 0.002 to 0.280 T/s. The magnetic field is parallel to the easy axis. The magnetization is plotted as a fraction of the maximum value of *M*s, the saturation magnetization.

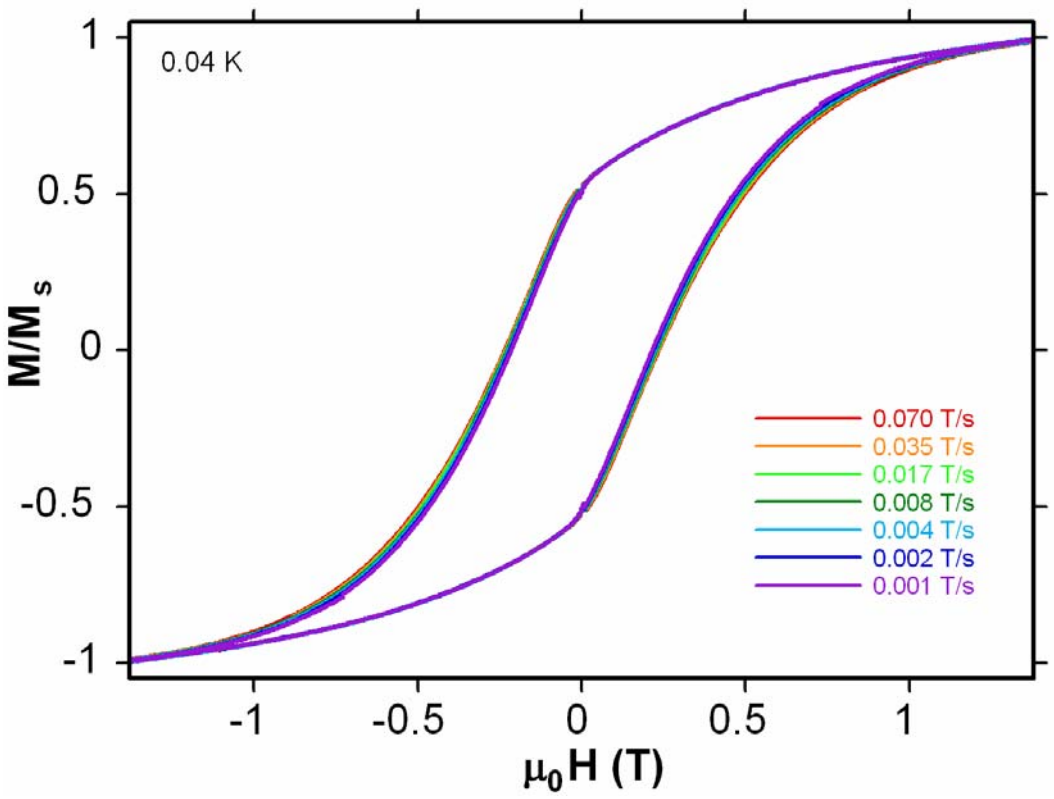

Figure 2.10. Magnetization hysteresis loops of a single crystal of complex **2A** at 0.04 K at various scan rates from 0.001 to 0.070 T/s. The magnetic field is parallel to the easy axis. The magnetization is plotted as a fraction of the maximum value of *M*s, the saturation magnetization.

hysteresis loops is essentially independent of the applied scan rate. The combination of temperature and scan rate dependence (increased coercivity) in the magnetization versus magnetic field hysteresis plots indicates clearly that complex **2A** exhibits significant relaxation behavior. As evident in Figures 2.8-10, there are no steps seen in the hysteresis plots for complex **2A**. Lack of steps in magnetization hysteresis measurements is well documented for a number of systems that exhibit large spin ground states, [66,87-93] and has been attributed to various factors including: large distributions of magnetization relaxation rates, *S*-mixing of low-lying spin states into the ground state spin manifold, micro-environments within the crystal lattice due to ligand and solvate disorder, and intermolecular interactions.[94-98]

2.3.6 Magnetization Relaxation

To further probe SMM behavior, DC magnetization decay experiments were carried out on a single crystal of complex **2A** in the temperature range of 0.04-1.1 K. The data are plotted in Figure 2.11 as magnetization, in units of magnetic saturation (M / M_s), versus the magnetization relaxation time (τ, in seconds). A DC magnetic field was applied along the easy axis of a single crystal and when magnetization saturation was achieved the external field was removed and the magnetization decay time (τ) was measured as the fraction of magnetization remaining when M / M_s reached 10% of its saturated value. The 90% relaxation value was selected so that measurements could be made over a larger temperature range. An Arrhenius plot is given in Figure 2.12 as the natural logarithm of the relaxation time (τ) verses the inverse absolute temperature, and was derived from the data in Figures 2.8 and 2.11. The dashed line indicates the

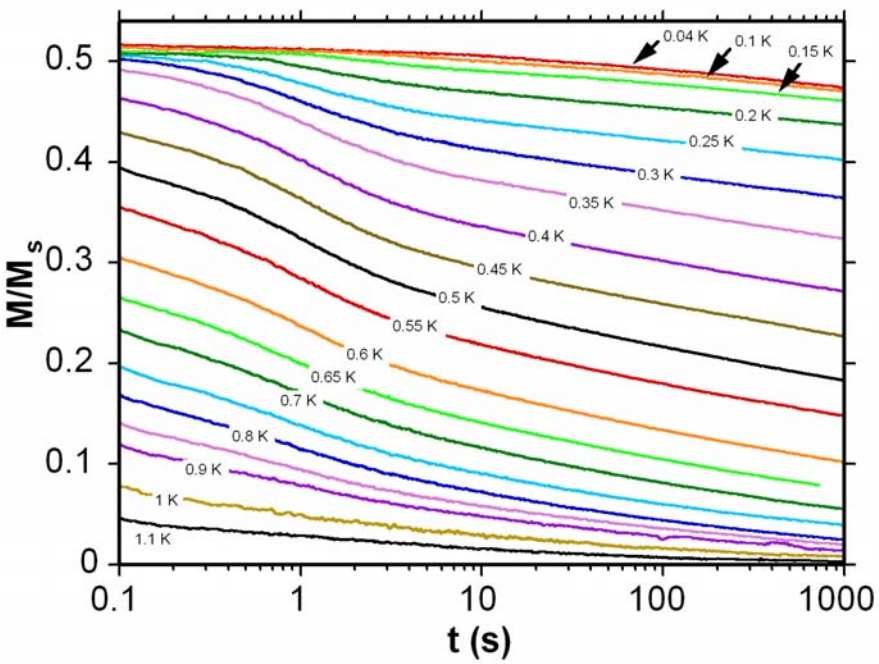

Figure 2.11. Magnetization relaxation versus time for a single crystal of complex **2A** in the temperature range 0.04-1.1 K at zero dc field. Relaxation times were taken as the time it took for the magnetization to decay to 0.1*M*s (where *M*s represents the saturation magnetization).

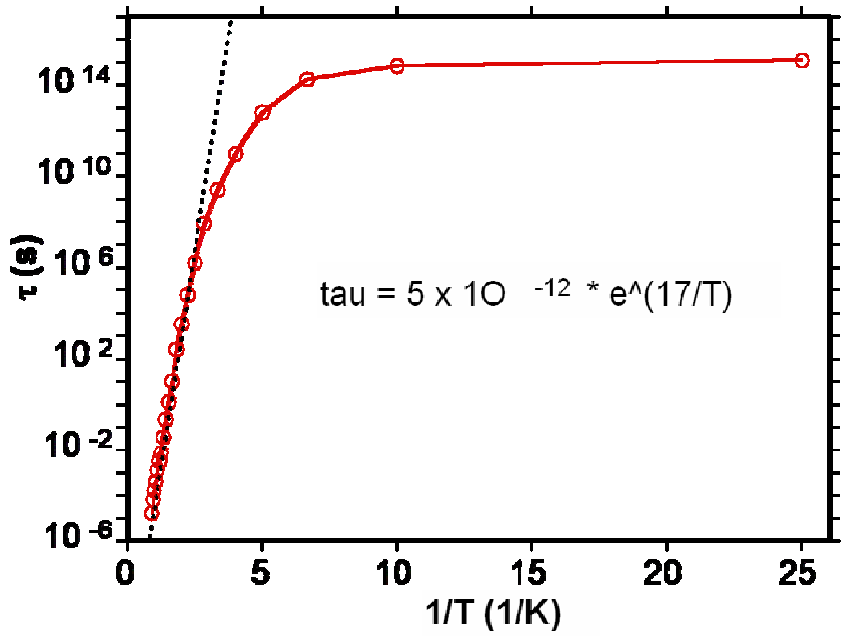

Figure 2.12. Temperature dependence of the logarithm of the magnetization relaxation time versus the inverse absolute temperature for a single crystal of complex **2A** based on the data shown in Figures 2.8 and 2.11.

relaxation rate-temperature correlation in the high temperature limit. Below the high temperature limit, between ~0.5 K and ~0.1 K, the magnetization relaxation rate decreases dramatically. And below ~0.1 K, the relaxation rate is essentially independent of temperature which is indicative of ground state QTM.

Evaluation of the relaxation data in Figure 2.12 employing the Arrhenius equation ($\tau = \tau_0 \exp(U_{eff} / kT)$, where τ_0 is the pre-exponential factor, U_{eff} is the effective barrier toward the reversal of magnetization, k is Boltzman's constant and T is the absolute temperature in Kelvin, yields an effective barrier (U_{eff}) of 17K (11.8 cm^{-1}) and $\tau_0 = 5 \times 10^{-12}$ s. This calculated value of τ_0 is orders of magnitude smaller than τ_0 for known SMMs.[1-3]

2.3.7 Reduced Magnetization

In order to obtain information related to the spin ground state and other Hamiltonian parameters, theoretical fits of magnetization versus field data (reduced magnetization) were carried out in the temperature range of 1.8-4 K with external DC fields of 0.5-7 T. Non-superimposable isofields in a reduced magnetization plot, $M/N\beta$ versus H/T, where M is the magnetization, N is Avogadro's number, β is the Bohr magneton, and H/T is ratio of the magnetic field to the absolute temperature, is usually associated with axial zero-field splitting (Figures 12 and 13).

$$H = \vec{g}\mu_B \hat{S} \cdot \vec{B} + D\hat{S}_z^2 + E(\hat{S}_x^2 - \hat{S}_y^2) + B_4^0 \hat{O}_4^0 + B_4^4 \hat{O}_4^4 + H^1 + H^2 \qquad \textbf{(2.3)}$$

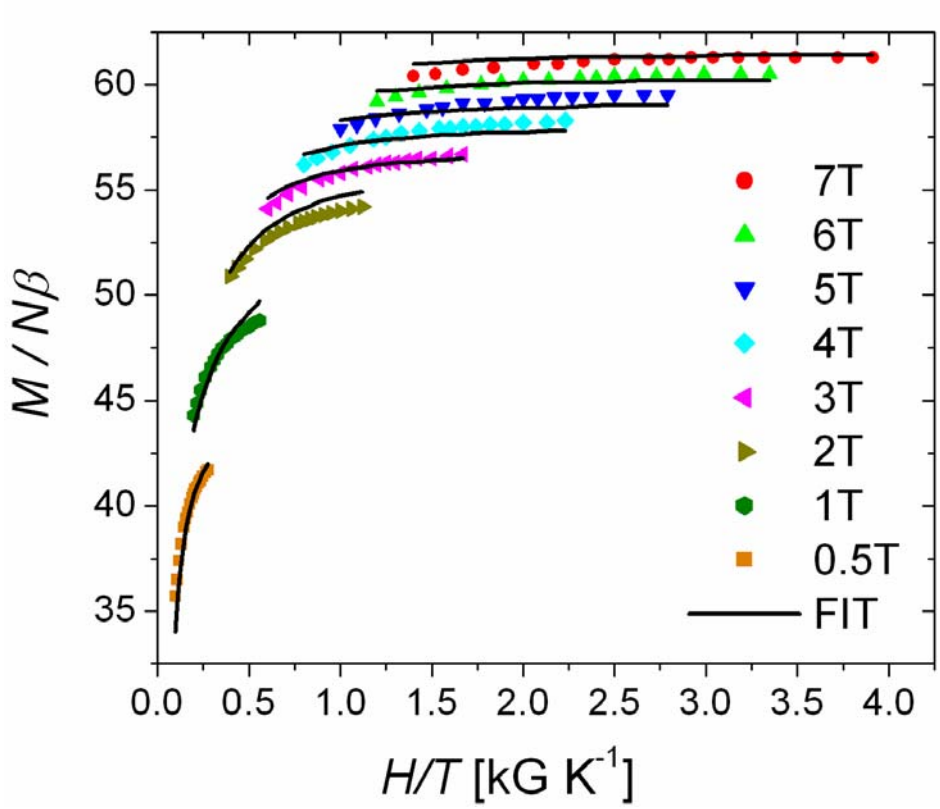

Figure 2.13. Reduced magnetization of a polycrystalline sample of complex **2A** measured with a dc magnetic field of 0.5-7 T in the temperature range of 1.8-4 K.

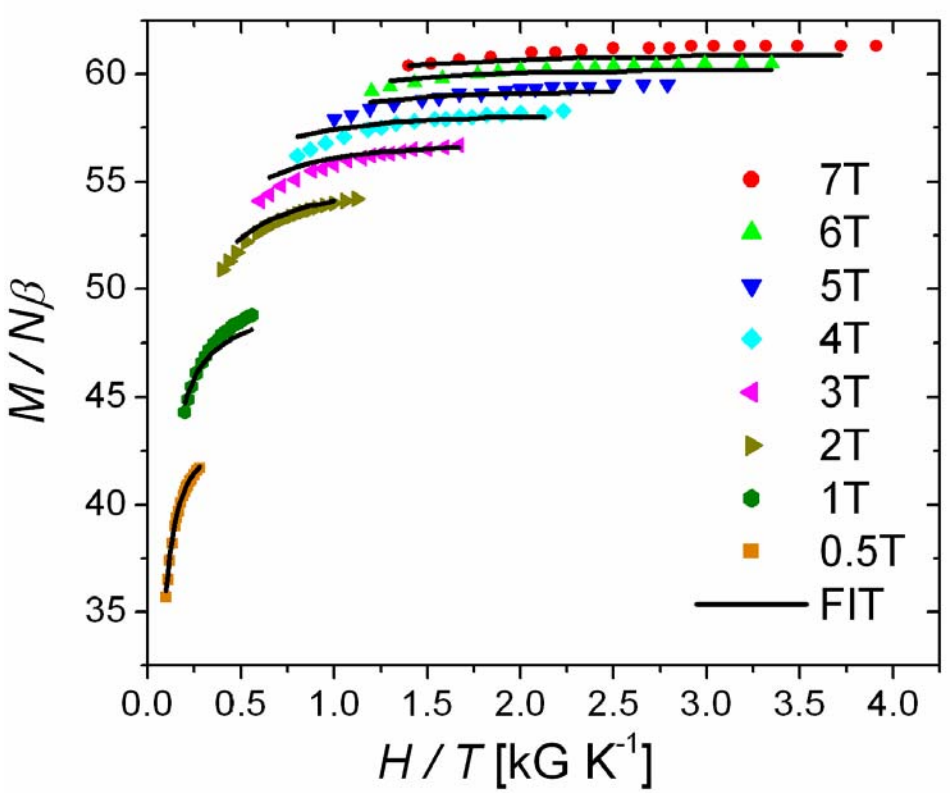

Figure 2.14. Reduced magnetization of a polycrystalline sample of complex **2A** measured with a dc magnetic field of 0.5-7 T in the temperature range of 1.8-4 K.

Equation 2.3 represents a general energy Hamiltonian, where $\vec{g}\mu_B\hat{S}\cdot\vec{B}$ is the Zeeman energy term (μ = Boltzman constant, g = Landé g-tensor, B = external magnetic field and S = spin operator). $D\hat{S}_z^2$ and $E(\hat{S}_x^2-\hat{S}_y^2)$ are the quadratic axial and rhombic zero field splitting terms, respectively. The fourth and fifth terms represent fourth-order axial and transverse ($B_4^0\hat{O}_4^0$ and $B_4^4\hat{O}_4^4$) zero-field interactions, respectively. And the last terms H^1 and H^2 represent higher order zero-field terms (4^{th}, 6^{th}….etc.) and other solid state effects such as dipolar coupling, interactions with solvate molecules, respectively. It is important to reiterate that if T_d molecular site symmetry is strictly preserved none of the second-order zero-field splitting terms in Equation 2.3 are symmetric to all operations in the irreducible representation and thus are forbidden. This raises an important question

as to the origin of non-superimposability of the iso-fields in the $M/N\beta$ versus H/T plot (Figures 2.13 and 2.14) which will be discussed in detail *vide infra*.

$$H=\frac{\Delta}{2}\bullet\sum_{S_Z}|63/2,S_Z\rangle\langle 63/2,S_Z|-\frac{\Delta}{2}\bullet\sum_{S_Z}|51/2,S_Z\rangle\langle 51/2,S_Z|-\mu_B\mu_0H_Z\sum_{S,S_Z}g_SS_Z \qquad \textbf{(2.4)}$$

It was initially reported in our communication of complex **2A** [65] (Figure 2.13) that the magnetization data collected between 0.5 and 7 T could not be fit to a single, well isolated single spin ground state (*i.e.* S and M_s are not good quantum numbers). However, it was found that a good fit of the three lowest fields could be obtained employing a S = 51/2 spin ground state, and that magnetization data from the three

highest fields could be fit to a $S = 61/2$ spin ground state. Since axial and rhombic zero-field splitting terms are not allowed in T_d symmetry, the Hamiltonian in Equation 2.4, where $|S,S_Z\rangle$ ($S = 51/2$ or $63/2$; $S_Z = -S, \ldots, +S$) is the vector basis set, Δ is the energy separation between spin states, μ_B is the Bohr magneton, μ_0 is the vacuum permeability constant, and H_z is the applied magnetic field, was used to fit the $M/N\beta$ versus H/T data (Figure 2.13). This Hamiltonian assumes that only the two spin states ($S = 51/2$ and $S = 61/2$) are populated and that they are separated by an energy gap Δ of 5K. As evident in Figure 2.13, the theoretical fit (solid black lines) of M versus H/T to the experimental data is very good; however, it is also apparent from detailed magnetization versus field hysteresis and high-frequency EPR experiments (see next section) that complex **2A** exhibits some degree of anisotropy leading to a barrier toward the reversal of magnetization, suggesting the possibility that T_d symmetry may not be strictly preserved, or that other factors are governing exhibited magnetic properties.

The intermediate spin ground state of complex **2A** could arise as a consequence of strongly competing magnetic exchange interactions yielding a spin frustrated magnetic core.[99-101] Figure 2.15 depicts a section of the central core of complex **2A** showing the interconnectivity and exchange pathways of one $[Mn^{IV}_2Mn^{III}_2O_4]^{6+}$ cubane, one $[Mn^{IV}_3Mn^{II}O_4]^{6+}$ cubane unit and bridging Cu^{II} ions. It is well documented that Mn^{IV}-Mn^{IV}, Mn^{IV}-Mn^{III}, and Mn^{IV}-Mn^{II} interactions tend to be strongly aniferromagnetic,[102] and depending on the bridging M-O-M bond angle α, Mn^{III}-O-Mn^{III} exchange interactions can range from antiferromagnetic for large values of α to ferromagnetic for values of α approaching 90°. The $Mn^{III}(2)$-O(3)-$Mn^{III}(2)$ bond angle $\alpha = 95.0(3)°$, in the present case, is expected to be moderately ferromagnetic (all Mn^X-

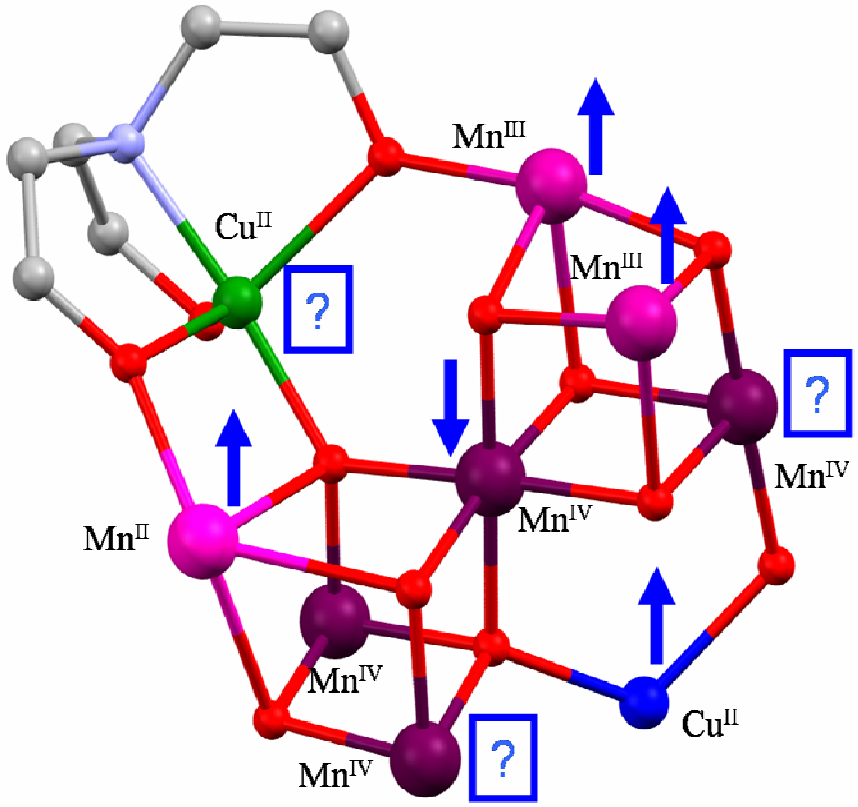

Figure 2.15. Super-exchange pathways and interconnectivity of $[Mn^{IV}_2Mn^{III}_2O_4]^{6+}$ and $[Mn^{IV}_3Mn^{II}O_4]^{6+}$ cubanes and Cu^{II} ions in the structural core of complex **2A**. Blue arrows indicate spin-orientation, and blue question marks indicate spin-frustrated exchange pathways.

O-Cu exchange interactions are expected to be antiferromagnetic with $\alpha > 105°$). It is evident in Figure 2.15 that within a $[Mn^{IV}_2Mn^{III}_2O_4]^{6+}$ cubane unit that ferromagnetic coupling between Mn^{III} ions (spin-up, blue arrows) will allow one of the Mn^{IV} ions to antiferromagnetically couple (spin-down, blue arrow), but the other Mn^{IV} ion is unable to simultaneously antiferromagnetically couple with both a neighboring Mn^{III} and Mn^{IV} ion. This is also clearly evident in the $[Mn^{IV}_3Mn^{II}O_4]^{6+}$ cubane units, where antiferromagnetic exchange is frustrated between the three Mn^{IV} ions and the Mn^{II} ion. A spin-frustrated magnetic core can lead to mixing of low-lying energy states which can give rise to magnetic metastability.

2.3.8 High-Frequency Electron Paramagnetic Resonance (HF-EPR)

HF-EPR has become a powerful tool for studying SMM systems with high spin ground states and significant magnetoanisotropy. While bulk susceptibility measurements provide estimations of Hamiltonian parameters due to a Boltzman distribution of spin states, HF-EPR directly extracts Hamiltonian parameters such as *g*, the sign and magnitude of the quadratic axial and rhombic terms (*D* and *E*), and as well, unambiguous determinations of higher order Hamiltonian parameters (*i.e.* 4^{th}, 6^{th} … etc.).[61,62] In complexes where the product of $\left|DS_z^2\right|$ is appreciable, discrete M_s transitions (*i.e.* $M_s = 5$ to $M_s = 4$, $M_s = 4$ to $M_s = 3$ etc.) separately appear on the EPR spectra due to Zeeman effects. However, in systems where there is appreciable disorder or when *D* is small or negligible, discrete transitions show as an over-lay single peak evident in Figure 2.16 for complex **2A**. Moreover, line broadening effects, due primarily to *D*- and *g*-strain [103-106] and distributions of molecular environments [107,108]

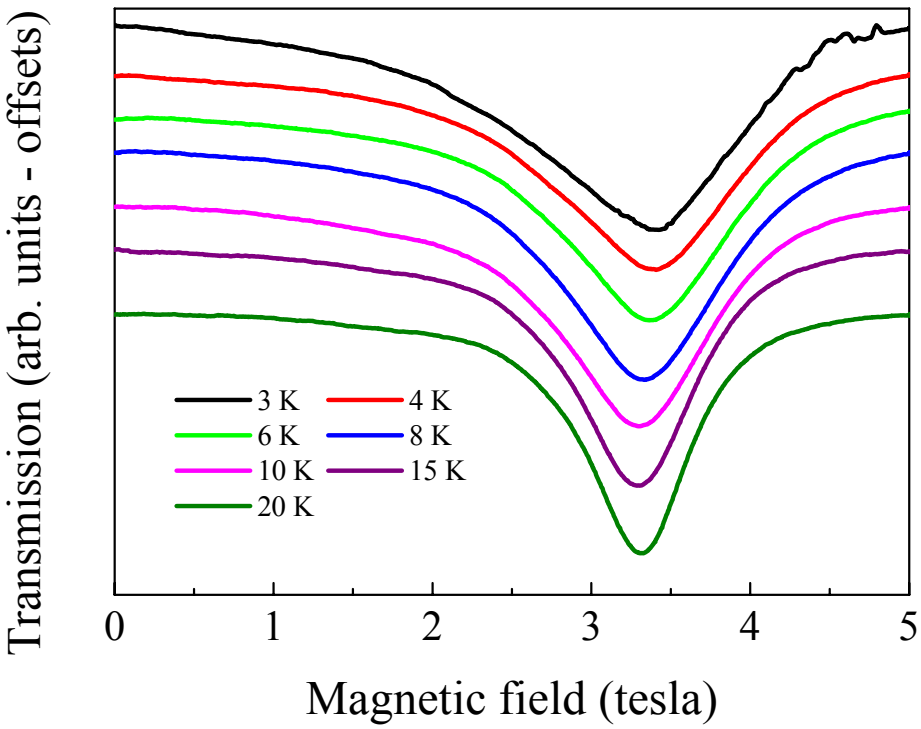

Figure 2.16. Temperature dependence at 91.4 GHz for complex **2A**.

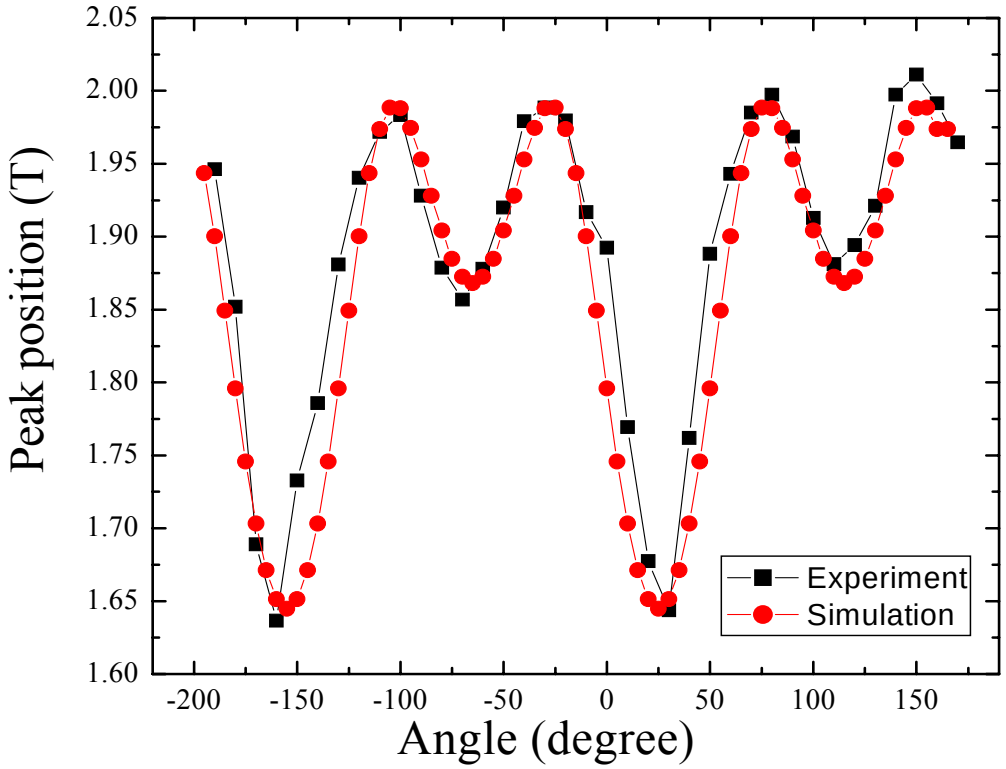

Figure 2.17. Plot of peak position versus angle. Black squares (red circles) indicate experimental (simulation) data. Experiment was performed with 60.0 GHz at 2 K. Following is the parameters for simulation; $S = 51/2$, $g = 2.30$, $B_4^0 = -6.0*10^{-6}$ GHz, $B_4^4 = -3.0*10^{-5}$ GHz, $\alpha = 45^o$, $\beta = 33^o$, $f = 60$ GHz.

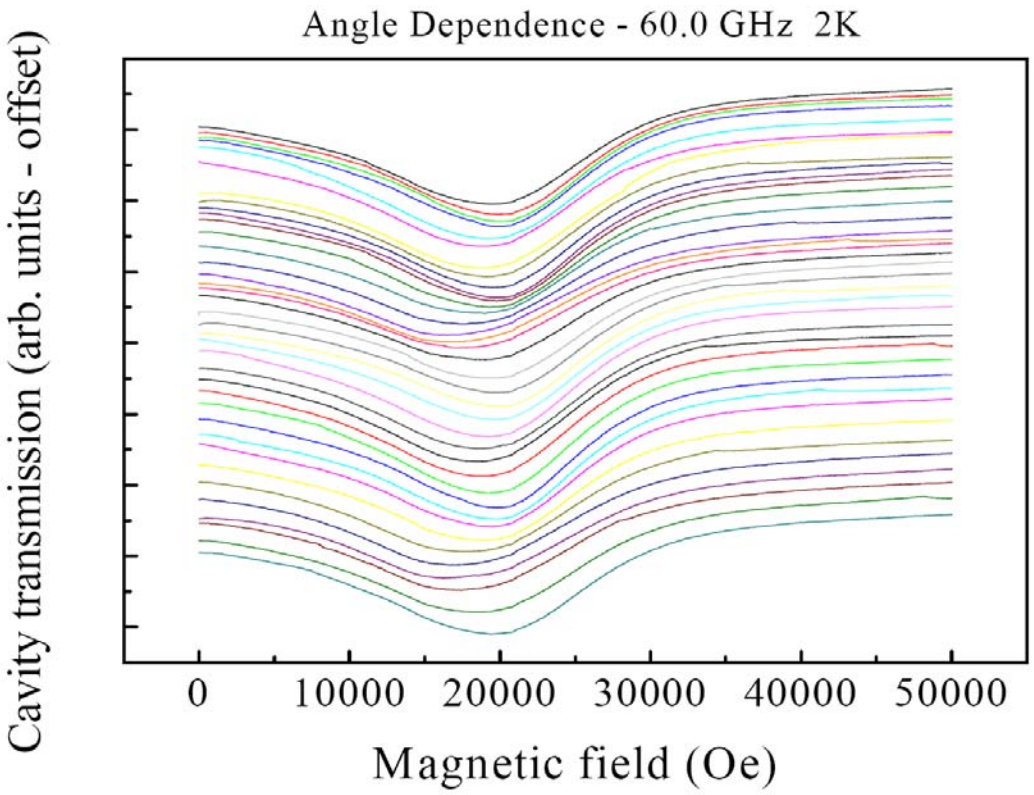

Figure 2.18. Relative angle dependent peak position at 2 K and 60.0 GHz. EPR spectra were gathered in 360˚ angle range by 10˚ steps for complex **2A**.

can lead to poor resolution of transitions. HF-EPR is, however, still useful to observe the trace of negligible magnetoanisotropy of complex **2A** from the asymmetric broad line width at low temperature and clear angle dependence of the single peak.

Temperature dependence data (Figure 2.16) collected on an oriented single crystal between 3-20 K at 91.4 GHz show a single symmetric peak at 20 K that shifts to higher field and becomes increasingly asymmetric as the temperature is lowered from 20-3 K.The temperature dependent line shift shows again the exchange interactions in complex **2A.** Since the line shift by the dipole field at low temperature shows reverse behavior, i.e. the line shift at low field as temperature decreases might be hidden by the effect of exchange interactions. The temperature dependent shift in peak position shows that complex **2A** exhibits some measure of axial anisotropy; furthermore, the evolution of temperature dependent asymmetry is most likely due to Boltzman depopulation effects and anisotropy. However, the small magnitude of the anisotropy that is present does not allow for resolution of discrete Zeeman induced M_s to $M_s \pm 1$ transitions. The fact that no discrete M_s transitions are seen in the HF-EPR spectra makes assignment of the exact magnitude of the anisotropy in the system impossible to unambiguously determine.

Angle dependent EPR spectra observed at 2 K and 60.0 GHz further confirms the presence of magnetoanisotropy of single crystal of complex **2A**. EPR spectra were gathered in a 360˚ angle by 10˚ steps. Figure 2.17 and 2.18 illustrates peak position data extracted from angle dependent EPR spectra, plotted as magnetic field (Tesla) versus angle (degrees) between the DC magnetic field direction and an assigned orientation of the sample. Green dotted lines are for the indication of 90˚ intervals. It is apparent from

analysis of Figure 2.17 that complex **2A** exhibits appreciable angle dependent periodicity. There is clearly both two-fold and weak four-fold periodicity present. These two modes of periodicity are superimposed on each other with well matched intervals. Application of a magnetic field in conjunction with field misalignment could lift T_d symmetry and explain the two-fold periodicity. The origin of the four fold symmetry in Figure 2.17 could arise from the fourth-order $S_x^4 + S_y^4 + S_z^4$ term that is symmetry allowed in tetrahedral (T_d) site symmetry. If T_d site symmetry is strictly preserved, the leading Hamiltonian zfs term would be the symmetry allowed fourth-order term given in Equation 2.6, where S is the total spin, S_x, S_y and S_z are the x, y and z coordinate spin components, and S_+ and S_- are raising and lowering operators.

$$S_x^4 + S_y^4 + S_z^4 - (3/5)S^4 = (3/2)S_z^4 - S^2S_z^2 - (1/10)S^4 + (1/8)[S_+^2 + S_-^2]^2 \qquad \textbf{(2.6)}$$

The $S_x^4 + S_y^4 + S_z^4$ fourth-order operator could give rise to bistability and QTM if individual spins first tunnel from the z_+ (spin up) orientation to orthogonal $x_\pm$ or $y_\pm$ orientations, and then tunnel from one of these orientations to z_- (spin down). Furthermore, simulation of the experimental data can be modeled quite well (Figure 2.17) employing fourth-order anisotropy terms and alignment of the field at an angle that falls between Jahn-Teller elongated principal axes.

2.3.9 Origin of Relaxation in $Cu_{17}Mn_{28}$

The core of complex **2A** (Figure 2.4) is composed of an octahedron of $[Mn^{IV}_2Mn^{III}_2O_4]^{6+}$ cubane units, interpenetrated and interconnected by the four tetrahedrally arranged $[Mn^{IV}_3Mn^{II}O_4]^{6+}$ cubane units. The symmetry of the core (T_d) dictates that the collective single-ion anisotropies will project out no net 2nd order anisotropy ($D = E = 0$), evident by the projections of the Jahn-Teller axes shown in Figure 2.3, where the twelve Mn^{III} *JT* axes form mutually orthogonal pairs, and all Mn^{II}, Cu^{II} and Mn^{IV} paramagnetic ions have inversion symmetry equivalents. However, single-crystal HF-EPR, single-crystal magnetization hysteresis, ac magnetic susceptibility and reduced magnetization measurements all suggest that there is a significant degree of magnetization relaxation behavior this system. The exhibited metastability cannot be explained via magnetic ordering or a crystallographic phase transition, as each would manifest itself as a sharp peak in heat capacity measurements. It is clear that no such peak is evident in heat capacity data (Figure 2.19) at the temperature (~1K) where coercivity is seen in magnetization hysteresis plots for complex **2A**. Furthermore, there seems to be no compelling evidence to support symmetry lowering due to crystallographic disorder, or significant intermolecular interactions as anisotropy sources. For such a large molecule the calculated R = 4.81% is very good, and though there exists an intricate three dimensional hydrogen bonded network of water molecules that interconnect neighboring $Cu_{17}Mn_{28}$ molecules, the exchange pathway is through multiple water molecules (Figure 2.3) and would therefore be expected to be extremely weak.

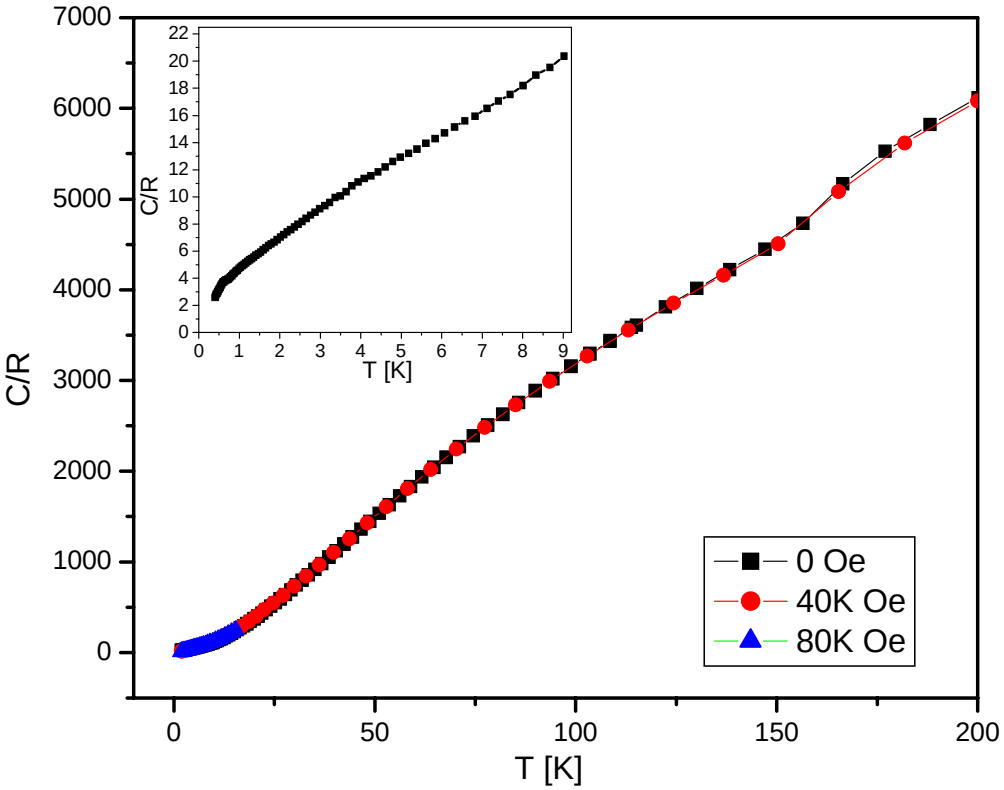

Figure 2.19. Specific Heat of complex **2A** in the temperature range of 0.4-200K.

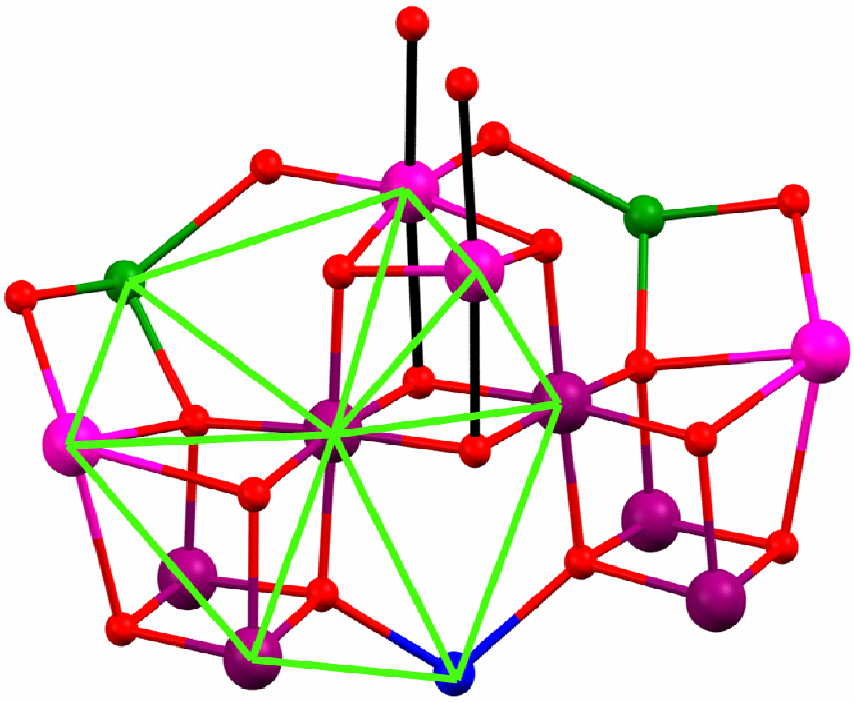

Figure 2.20. Representative section of the structural core of complex **2A** showing the extensive symmetric network of edge and vertice sharing triangles leading to geometric frustration.

Heterovalent and homovalent oxo-centered triangles of Fe Cr and Mn have been well studied and characterized. Exchange coupling in heterovalent Mn triangles generally leads to a $S = 3/2$ or $S = 1/2$ spin ground state. The $S = 3/2$ ground state can be justified by simply assuming ferromagnetic coupling between trivalent Mn^{III} ion with antiferromagnetic coupling of the divalent Mn^{II} ion ($S = 2_{Mn}{}^{III} + 2_{Mn}{}^{III} - 5/2_{Mn}{}^{II} = 3/2$), and the $S = 1/2$ case arises from spin frustration due to competing exchange parameters leading to a spin vector projection that is not readily obvious.[100] The $Cu_{17}Mn_{28}$ complex experiences similarly frustrated exchange pathways. However, anisotropy in the Mn_3 triangles arises due to symmetry dictated Hamiltonian energy terms (D, E etc.), where as, the relaxation behavior in complex **2A** does not arise from intrinsic second-order anisotropy terms due to its high T_d site symmetry.

Recent experimental and theoretical studies on zero-dimensional systems such as Keplerate $\{Mo_{72}Fe_{30}\}$[109], and purely theoretical studies on the Heisenberg icosahedron,[110] and the Kagome lattice,[111] as well as larger quantum and classical spin lattices[112] have revealed that extremely interesting magnetic behavior can arise in high symmetry systems due to geometric frustration. Geometric frustration occurs in highly symmetric spin arrays where competing spins on the vertices of edge-sharing triangles, or other geometric shapes such as cubes and tetrahedrons, result in high concentrations of degenerate energy states. The outcome of strongly competing magnetic exchange interactions can give rise to metastability, *i.e.* slow relaxation and hysteresis behavior, in complexes that are not SMMs. [110]

Though solvate and molecular disorder can collectively contribute to the exhibited magnetoanisotropy of complex **2A**, the relaxation dynamics are governed by

geometric frustration. Figure 2.20, depicts a representative section of the $Cu_{17}Mn_{28}$ core. It is evident that the $Cu_{17}Mn_{28}$ core can be viewed as a highly symmetric series of edge-sharing and corner-sharing triangles. When mapped onto the whole of the molecule, the interconnected triangles form a perfectly symmetric spin lattice, as is documented for the Keplerates and the icosa- and icosadodecahedrons. The observed hysteretic behavior thus arises due to competition between the magnitude of the Heisenberg exchange coupling (J_{ij}) between geometrically frustrated spins, and the susceptibility of those spins to align in an external magnetic field. This leads to temperature and sweep-rate dependant magnetization relaxation (hysteresis and ac out-of-phase signals) between metastable states in the absence of second-order axial or easy-plane anisotropy. The density of states arising from geometric frustration is also consistent with non-superimposibility of the isofields in reduced magnetization data.

Previous studies of geometric frustration have all been conducted on systems dominated by strong antiferromagnetic Heisenberg exchange interactions, where it is assumed that the Heisenberg exchange J is much larger than intermolecular interactions, leading to a small spin ground state. The $Cu_{17}Mn_{28}$ complex represents a very unusual high-spin case of magnetic metastability due to geometric frustration. It would be interesting to synthesize small highly symmetric, high-spin, magnetic molecules in order to study the interplay between local anisotropies (d) and the local magnetic exchange interaction (J_{ij}), where i and j are nearest neighbor paramagnetic ions, in order to study how the interaction affects the magnitude of the geometric frustration, and subsequent magnetization hysteresis and relaxation behavior.

2.4 Conclusion

For the first time, the use of zero-valent copper metal in conjunction with polydentate aminoalcohol ligands has been used to assemble an oxo-bridged, high symmetry, heterometallic complex with a large S = 51/2 spin ground state. The core contains an unprecedented five metal oxidation states: CuI, CuII, MnII, MnIII and MnIV. It is clear from HFEPR, AC susceptibility and magnetization versus field hysteresis measurements that the Cu17Mn28 complex exhibits magnetic bistability and SMM like behavior due to geometric frustration. Fits of reduced magnetization data clearly indicate that only two energy states need to be evaluated, and that inclusion of zero-field splitting is not strictly required in the fitting model. To our knowledge, the Cu17Mn28 complex is the only high spin magnetic molecule to exhibit geometric frustration, and efforts are underway to synthesize simple, low-nuclearity, high symmetry systems in order to perform fundamental studies on the effects of geometric frustration in high-spin polyoxometallates.

Chapter 2, in full, has been submitted for publication to Inorganic Chemistry, 2010. Beedle, C. C., Wang, W. G., Zhou, A. J., Wornsdorfer, W., Koo, C., Hill, S., Nakano, M., Zhang, W. X.; Tong, M. L., Chen, X. M., Hendrickson, D. N., Geometric Frustration Leading to Magnetic Metastability in a High-Spin Cu17Mn28 Complex with Td Symmetry. The dissertation Author is the primary investigator and author of this material.

2.5 References

(1) Sessoli, R.; Gatteschi, D.; Caneschi, A.; Novak, M. A. *Nature* **1993**, *365*, 141-143.

(2) Sessoli, R.; Tsai, H. L.; Schake, A. R.; Wang, S. Y.; Vincent, J. B.; Folting, K.; Gatteschi, D.; Christou, G.; Hendrickson, D. N. *Journal of the American Chemical Society* **1993**, *115*, 1804-1816.

(3) Christou, G.; Gatteschi, D.; Hendrickson, D. N.; Sessoli, R. *Mrs Bulletin* **2000**, *25*, 66-71.

(4) Gatteschi, D.; Sessoli, R. *Angewandte Chemie-International Edition* **2003**, *42*, 268-297.

(5) Chudnovsky, E. M.; Tejada, J. *Macroscopic Quantum Tunneling of the Magnetic Moment*; Cambridge Univesity Press: Cambridge, 1998.

(6) Gatteschi, D.; Sessoli, R.; Villian, J. *Molecular Nanomagnets*; Oxford University Press: Oxford, 2006.

(7) Stamp, P. C. E. *Nature* **1996**, *383*, 125.

(8) Leuenberger, M. N.; Loss, D. *Nature* **2001**, *410*, 789-793.

(9) Tejada, J.; Chudnovsky, E. M.; del Barco, E.; Hernandez, J. M.; Spiller, T. P. *Nanotechnology* **2001**, *12*, 181-186.

(10) Aubin, S. M. J.; Dilley, N. R.; Pardi, L.; Krzystek, J.; Wemple, M. W.; Brunel, L. C.; Maple, M. B.; Christou, G.; Hendrickson, D. N. *Journal of the American Chemical Society* **1998**, *120*, 4991-5004.

(11) Hendrickson, D. N.; Christou, G.; Ishimoto, H.; Yoo, J.; Brechin, E. K.; Yamaguchi, A.; Rumberger, E. M.; Aubin, S. M. J.; Sun, Z. M.; Aromi, G. *Polyhedron* **2001**, *20*, 1479-1488.

(12) Sangregorio, C.; Ohm, T.; Paulsen, C.; Sessoli, R.; Gatteschi, D. *Physical Review Letters* **1997**, *78*, 4645-4648.

(13) del Barco, E.; Kent, A. D.; Hill, S.; North, J. M.; Dalal, N. S.; Rumberger, E. M.; Hendrickson, D. N.; Chakov, N.; Christou, G. *Journal of Low Temperature Physics* **2005**, *140*, 119-174.

(14) Friedman, J. R.; Sarachik, M. P.; Tejada, J.; Ziolo, R. *Physical Review Letters* **1996**, *76*, 3830-3833.

(15) Sorace, L.; Wernsdorfer, W.; Thirion, C.; Barra, A. L.; Pacchioni, M.; Mailly, D.; Barbara, B. *Physical Review B* **2003**, *68*, 220407.

(16) Thomas, L.; Lionti, F.; Ballou, R.; Gatteschi, D.; Sessoli, R.; Barbara, B. *Nature* **1996**, *383*, 145-147.

(17) Wernsdorfer, W.; Sessoli, R. *Science* **1999**, *284*, 133-135.

(18) Hendrickson, D. N.; Christou, G.; Wernsdorfer, W.; Hill, S. O.; Aliaga-Alcade, N.; Bhaduri, S.; Edward, R. S.; Aubin, S. M. J.; Sun, Z. *Mat. Res. Soc. Symp. Proc.* **2003**, *746*, Q1.1.1.

(19) Wernsdorfer, W.; Bhaduri, S.; Boskovic, C.; Christou, G.; Hendrickson, D. N. *Physical Review B* **2002**, *65*, 180403.

(20) Wernsdorfer, W.; Allaga-Alcalde, N.; Hendrickson, D. N.; Christou, G. *Nature* **2002**, *416*, 406-409.

(21) Yang, E. C.; Wernsdorfer, W.; Zakharov, L. N.; Karaki, Y.; Yamaguchi, A.; Isidro, R. M.; Lu, G. D.; Wilson, S. A.; Rheingold, A. L.; Ishimoto, H.; Hendrickson, D. N. *Inorganic Chemistry* **2006**, *45*, 529-546.

(22) Aromi, G.; Batsanov, A. S.; Christian, P.; Helliwell, M.; Parkin, A.; Parsons, S.; Smith, A. A.; Timco, G. A.; Winpenny, R. E. P. *Chemistry-a European Journal* **2003**, *9*, 5142-5161.

(23) Wernsdorfer, W.; Bhaduri, S.; Tiron, R.; Hendrickson, D. N.; Christou, G. *Physical Review Letters* **2002**, *89*, 197201.

(24) Hill, S.; Edwards, R. S.; Aliaga-Alcalde, N.; Christou, G. *Science* **2003**, *302*, 1015-1018.

(25) Takahashi, S.; van Tol, J.; Beedle, C. C.; Hendrickson, D. N.; Brunel, L.-C.; Sherwin, M. S. *Physical Review Letters* **2009**, *102*, 087603.

(26) Chudnovsky, E. M.; Martinez-Hidalgo, X. *Physical Review B* **2002**, *66*, -.

(27) del Barco, E.; Vernier, N.; Hernandez, J. M.; Tejada, J.; Chudnovsky, E. M.; Molins, E.; Bellessa, G. *Europhysics Letters* **1999**, *47*, 722-728.

(28) Tejada, J. *Polyhedron* **2001**, *20*, 1751-1756.

(29) Barra, A. L.; Caneschi, A.; Cornia, A.; de Biani, F. F.; Gatteschi, D.; Sangregorio, C.; Sessoli, R.; Sorace, L. *Journal of the American Chemical Society* **1999**, *121*, 5302-5310.

(30) Gatteschi, D.; Sessoli, R.; Cornia, A. *Chemical Communications* **2000**, 725-732.

(31) Goodwin, J. C.; Sessoli, R.; Gatteschi, D.; Wernsdorfer, W.; Powell, A. K.; Heath, S. L. *Journal of the Chemical Society-Dalton Transactions* **2000**, 1835-1840.

(32) Wernsdorfer, W.; Caneschi, A.; Sessoli, R.; Gatteschi, D.; Cornia, A.; Villar, V.; Paulsen, C. *Physical Review Letters* **2000**, *84*, 2965-2968.

(33) Andres, H.; Basler, R.; Blake, A. J.; Cadiou, C.; Chaboussant, G.; Grant, C. M.; Gudel, H. U.; Murrie, M.; Parsons, S.; Paulsen, C.; Semadini, F.; Villar, V.; Wernsdorfer, W.; Winpenny, R. E. P. *Chemistry-a European Journal* **2002**, *8*, 4867-4876

(34) Cadiou, C.; Murrie, M.; Paulsen, C.; Villar, V.; Wernsdorfer, W.; Winpenny, R. E. P. *Chemical Communications* **2001**, 2666-2667.

(35) Kirman, C.; Lawrence, J.; Hill, S.; Yang, E. C.; Hendrickson, D. N. *Journal of Applied Physics* **2005**, *97*.

(36) Ochsenbein, S. T.; Murrie, M.; Rusanov, E.; Stoeckli-Evans, H.; Sekine, C.; Gudel, H. U. *Inorganic Chemistry* **2002**, *41*, 5133-5140.

(37) Castro, S. L.; Sun, Z. M.; Grant, C. M.; Bollinger, J. C.; Hendrickson, D. N.; Christou, G. *Journal of the American Chemical Society* **1998**, *120*, 2365-2375.

(38) Oshio, H.; Hoshino, N.; Ito, T.; Nakano, M. *J. Am. Chem. Soc.* **2004**, *126*, 8805-8812.

(39) Yang, E. C.; Hendrickson, D. N.; Wernsdorfer, W.; Nakano, M.; Zakharov, L. N.; Sommer, R. D.; Rheingold, A. L.; Ledezma-Gairaud, M.; Christou, G. *Journal of Applied Physics* **2002**, *91*, 7382-7384.

(40) Boudreaux, E. A.; Mulay, L. N. *Theory and Applications of Molecular Paramagnetism*; John Wiley & Sons: New York, 1976; Vol. Chapters 5 and 6.

(41) Osa, S.; Kido, T.; Matsumoto, N.; Re, N.; Pochaba, A.; Mrozinski, J. *Journal of the American Chemical Society* **2004**, *126*, 420-421.

(42) Aronica, C.; Pilet, G.; Chastanet, G.; Wernsdorfer, W.; Jacquot, J. F.; Luneau, D. *Angewandte Chemie (International Edition in English)* **2006**, 4659.

(43) Zaleski, C. M.; Depperman, E. C.; Kampf, J. W.; Kirk, M. L.; Pecoraro, V. L. *Angewandte Chemie International Edition* **2004**, *43*, 3912-3914.

(44) Costes, J. P.; Dahan, F.; Wernsdorfer, W. *Inorganic Chemistry* **2006**, *45*, 5-7.

(45) Zaleski, C. M.; Kampf, J. W.; Mallah, T.; Kirk, M. L.; Pecoraro, V. L. *Inorganic Chemistry* **2007**, *46*, 1954-1956.

(46) Ferbinteanu, M.; Kajiwara, T.; Choi, K. Y.; Nojiri, H.; Nakamoto, A.; Kojima, N.; Cimpoesu, F.; Fujimura, Y.; Takaishi, S.; Yamashita, M. *J. Am. Chem. Soc.* **2006**, *128*, 9008-9009.

(47) He, F.; Tong, M. L.; Chen, X. M. *Inorganic Chemistry* **2005**, *44*, 8285-8292.

(48) Hamamatsu, T.; Yabe, K.; Towatari, M.; Osa, S.; Matsumoto, N.; Re, N.; Pochaba, A.; Mrozinski, J.; Gallani, J. L.; Barla, A.; Imperia, P.; Paulsen, C.; Kappler, J. P. *Inorganic Chemistry* **2007**, *46*, 4458-4468.

(49) Pointillart, F.; Bernot, K.; Sessoli, R.; Gatteschi, D. *Chemistry-a European Journal* **2007**, *13*, 1602-1609.

(50) Wang, S.; Zuo, J.-L.; Zhou, H.-C.; Choi, H. J.; Ke, Y.; Long, J. R.; You, X.-Z. *Angewandte Chemie International Edition* **2004**, *43*, 5940-5943.

(51) Zhao, H.; Lopez, N.; Prosvirin, A. V.; Chifotides, H. T.; Dunbar, K. R. *Dalton Transactions* **2007**, 878.

(52) Sokol, J. J.; Hee, A. G.; Long, J. R. *Journal of the American Chemical Society* **2002**, *124*, 7656-7657.

(53) Choi, H. J.; Sokol, J. J.; Long, J. R. *Inorganic Chemistry* **2004**, *43*, 1606-1608.

(54) Berlinguette, C. P.; Vaughn, D.; Canada-Vilalta, C.; Galan-Mascaros, J. R.; Dunbar, K. R. *Angewandte Chemie-International Edition* **2003**, *42*, 1523-1526.

(55) Palii, A. V.; Ostrovsky, S. M.; Klokishner, S. I.; Tsukerblat, B. S.; Berlinguette, C. P.; Dunbar, K. R.; Galan-Mascaros, J. R. *J. Am. Chem. Soc.* **2004**, *126*, 16860-16867.

(56) Schelter, E. J.; Prosvirin, A. V.; Dunbar, K. R. *J. Am. Chem. Soc.* **2004**, *126*, 15004-15005.

(57) Dunbar, K. R.; Schelter, E. J.; Palii, A. V.; Ostrovsky, S. M.; Mirovitskii, V. Y.; Hudson, J. M.; Omary, M. A.; Klokishner, S. I.; Tsukerblat, B. S. *Journal of Physical Chemistry A* **2003**, *107*, 11102-11111.

(58) Schelter, E. J.; Prosvirin, A. V.; Reiff, W. M.; Dunbar, K. R. *Angewandte Chemie International Edition* **2004**, *43*, 4912-4915.

(59) Karadas, F.; Schelter, E. J.; Prosvirin, A. V.; Bacsa, J.; Dunbar, K. R. *Chemical Communications* **2005**, 1414-1416.

(60) Li, D.; Parkin, S.; Wang, G.; Yee, G. T.; Prosvirin, A. V.; Holmes, S. M. *Inorganic Chemistry* **2005**, *44*, 4903-4905.

(61) Feng, P. L.; Beedle, C. C.; Koo, C.; Wernsdorfer, W.; Nakano, M.; Hill, S.; Hendrickson, D. N. *Inorganic Chemistry* **2008**, *47*, 3188-3204.

(62) Feng, P. L.; Beedle, C. C.; Wernsdorfer, W.; Koo, C.; Nakano, M.; Hill, S.; Hendrickson, D. N. *Inorganic Chemistry* **2007**, *46*, 8126-8128.

(63) Oshio, H.; Nihei, M.; Koizumi, S.; Shiga, T.; Nojiri, H.; Nakano, M.; Shirakawa, N.; Akatsu, M. *Journal of the American Chemical Society* **2005**, *127*, 4568-4569.

(64) Oshio, H.; Nihei, M.; Yoshida, A.; Nojiri, H.; Nakano, M.; Yamaguchi, A.; Karaki, Y.; Ishimoto, H. *Chemistry-a European Journal* **2005**, *11*, 843-848.

(65) Wang, W. G.; Zhou, A. J.; Zhang, W. X.; Tong, M. L.; Chen, X. M.; Nakano, M.; Beedle, C. C.; Hendrickson, D. N. *Journal of the American Chemical Society* **2007**, *129*, 1014-1015.

(66) Ako, A. M.; Hewitt, I. J.; Mereacre, V.; Clérac, R.; Wernsdorfer, W.; Anson, C. E.; Powell, A. K. *Angewandte Chemie International Edition* **2006**, *45*, 4926-4929.

(67) Waldmann, O.; Ako, A. M.; Gu; x; del, H. U.; Powell, A. K. *Inorganic Chemistry* **2008**, *47*, 3486-3488.

(68) Shaw, R.; Tidmarsh, I. S.; Laye, R. H.; Breeze, B.; Helliwell, M.; Brechin, E. K.; Heath, S. L.; Murrie, M.; Ochsenbein, S.; Gudel, H.-U.; McInnes, E. J. L. *Chemical Communications* **2004**, 1418-1419.

(69) Carretta, S.; Santini, P.; Amoretti, G.; Affronte, M.; Candini, A.; Ghirri, A.; Tidmarsh, I. S.; Laye, R. H.; Shaw, R.; McInnes, E. J. L. *Physical Review Letters* **2006**, *97*, 207201.

(70) Wernsdorfer, W. *Advances in Chemical Physics, Vol 118* **2001**, *118*, 99-190.

(71) Monty, M.; Stephen, H.; Philippe, G.; Michel, G. *Review of Scientific Instruments* **2000**, *71*, 186-200.

(72) Rumberger, E. M.; Shah, S. J.; Beedle, C. C.; Zakharov, L. N.; Rheingold, A. L.; Hendrickson, D. N. *Inorganic Chemistry* **2005**, *44*, 2742-2752.

(73) Murugesu, M.; Wernsdorfer, W.; Abboud, K. A.; Christou, G. *Angewandte Chemie International Edition* **2005**, *44*, 892-896.

(74) Murugesu, M.; Raftery, J.; Wernsdorfer, W.; Christou, G.; Brechin, E. *Inorganic Chemistry* **2004**, *43*, 4203-4209.

(75) Beedle, C. C.; Heroux, K. J.; Nakano, M.; DiPasquale, A. G.; Rheingold, A. L.; Hendrickson, D. N. *Polyhedron* **2007**, *26*, 2200-2206.

(76) Khan, M. I.; Tabussum, S.; Doedens, R. J. *Chemical Communications* **2003**, 532-533.

(77) Wittick, L. M.; Murray, K. S.; Moubaraki, B.; Batten, S. R.; Spiccia, L.; Berry, K. J. *Dalton Transactions* **2004**, 1003-1011.

(78) Wittick, L. M.; Jones, L. F.; Jensen, P.; Moubaraki, B.; Spiccia, L.; Berry, K. J.; Murray, K. S. *Dalton Transactions* **2006**, 1534-1543.

(79) Beedle, C. C.; Stephenson, C. J.; Heroux, K. J.; Wernsdorfer, W.; Hendrickson, D. N. *Inorganic Chemistry* **2008**, *47*, 10798-10800.

(80) Roubeau, O.; Clérac, R. *European Journal of Inorganic Chemistry* **2008**, *2008*, 4325-4342.

(81) Heroux, K., J. ; Rheingold, A., L.; Hendrickson, D., N. *European Journal of Inorganic Chemistry* **2009**, *2009*, 3541-3544.

(82) Makhankova, V. G.; Vassilyeva, O. Y.; Kokozay, V. N.; Skelton, B. W.; Reedijk, J.; Van Albada, G. A.; Sorace, L.; Gatteschi, D. *New Journal of Chemistry* **2001**, *25*, 685-689.

(83) Makhankova, V. G.; Vassilyeva, O. Y.; Kokozay, V. N.; Skelton, B. W.; Sorace, L.; Gatteschi, D. *Journal of the Chemical Society-Dalton Transactions* **2002**, 4253-4259.

(84) Sun, Z.; Gantzel, P. K.; Hendrickson, D. N. *Inorganic Chemistry* **1996**, *35*, 6640-6641.

(85) Liu, W.; Thorp, H. H. *Inorganic Chemistry* **1993**, *32*, 4102-4105.

(86) Wernsdorfer, W.; Chakov, N. E.; Christou, G. *Physical Review B* **2004**, *70*, 132413.

(87) Brechin, E. K.; Boskovic, C.; Wernsdorfer, W.; Yoo, J.; Yamaguchi, A.; Sanudo, E. C.; Concolino, T. R.; Rheingold, A. L.; Ishimoto, H.; Hendrickson, D. N.; Christou, G. *Journal of the American Chemical Society* **2002**, *124*, 9710-9711.

(88) Brechin, E. K.; Sanudo, E. C.; Wernsdorfer, W.; Boskovic, C.; Yoo, J.; Hendrickson, D. N.; Yamaguchi, A.; Ishimoto, H.; Concolino, T. E.; Rheingold, A. L.; Christou, G. *Inorganic Chemistry* **2005**, *44*, 502-511.

(89) Sanudo, E. C.; Wernsdorfer, W.; Abboud, K. A.; Christou, G. *Inorganic Chemistry* **2004**, *43*, 4137-4144.

(90) Soler, M.; Wernsdorfer, W.; Folting, K.; Pink, M.; Christou, G. *Journal of the American Chemical Society* **2004**, *126*, 2156-2165.

(91) Tasiopoulos, A. J.; Vinslava, A.; Wernsdorfer, W.; Abboud, K. A.; Christou, G. *Angewandte Chemie-International Edition* **2004**, *43*, 2117-2121.

(92) Murugesu, M.; Wernsdorfer, W.; Abboud, K. A.; Christou, G. *Polyhedron* **2005**, *24*, 2894-2899.

(93) Murugesu, M.; Takahashi, S.; Wilson, A.; Abboud, K. A.; Wernsdorfer, W.; Hill, S.; Christou, G. *Inorganic Chemistry* **2008**, *47*, 9459-9470.

(94) Cornia, A.; Fabretti, A. C.; Sessoli, R.; Sorace, L.; Gatteschi, D.; Barra, A. L.; Daiguebonne, C.; Roisnel, T. *Acta Crystallographica Section C-Crystal Structure Communications* **2002**, *58*, m371-m373.

(95) del Barco, E.; Kent, A. D.; Hill, S.; North, J. M.; Dalal, N.; Rumberger, E. M.; Hendrickson, D. N.; Chakov, N. E.; Christou, G. *Condensed Matter* **2004**, *cond-mat/0404390*.

(96) Hill, S.; Anderson, N.; Wilson, A.; Takahashi, S.; Petukhov, K.; Chakov, N. E.; Murugesu, M.; North, J. M.; Barco, E. d.; Kent, A. D.; Dalal, N. S.; Christou, G. *Polyhedron* **2005**, *24*, 2284-2292.

(97) Hill, S.; Edwards, R. S.; North, J. M.; Park, K.; Dalal, N. S. *Polyhedron* **2003**, *22*, 1889-1896.

(98) Parks, B.; Loomis, J.; Rumberger, E.; Yang, E. C.; Hendrickson, D. N.; Christou, G. *Journal of Applied Physics* **2002**, *91*, 7170-7172.

(99) Cador, O.; Gatteschi, D.; Sessoli, R.; Barra, A.-L.; Timco, G. A.; Winpenny, R. E. P. *Journal of Magnetism and Magnetic Materials* **2005**, *290-291*, 55-60.

(100) Mccusker, J. K.; Jang, H. G.; Wang, S.; Christou, G.; Hendrickson, D. N. *Inorganic Chemistry* **1992**, *31*, 1874-1880.

(101) Mccusker, J. K.; Vincent, J. B.; Schmitt, E. A.; Mino, M. L.; Shin, K.; Coggin, D. K.; Hagen, P. M.; Huffman, J. C.; Christou, G.; Hendrickson, D. N. *Journal of the American Chemical Society* **1991**, *113*, 3012-3021.

(102) Kahn, O. *Molecular magnetism*; VCH: New York, NY, 1993.

(103) Amigo, R.; del Barco, E.; Casas, L.; Molins, E.; Tejada, J.; Rutel, I. B.; Mommouton, B.; Dalal, N.; Brooks, J. *Physical Review B* **2002**, *65*, 172403.

(104) Maccagnano, S.; Achey, R.; Negusse, E.; Lussier, A.; Mola, M. M.; Hill, S.; Dalal, N. S. *Polyhedron* **2001**, *20*, 1441-1445.

(105) Park, K.; Novotny, M. A.; Dalal, N. S.; Hill, S.; Rikvold, P. A. *Physical Review B* **2002**, *65*, 014426.

(106) Parks, B.; Loomis, J.; Rumberger, E.; Hendrickson, D. N.; Christou, G. *Physical Review B* **2001**, *64*, 184426.

(107) Hill, S.; Maccagnano, S.; Park, K.; Achey, R. M.; North, J. M.; Dalal, N. S. *Physical Review B* **2002**, *65*, 224410.

(108) Takahashi, S.; Edwards, R. S.; North, J. M.; Hill, S.; Dalal, N. S. *Physical Review B* **2004**, *70*, 094429.

(109) Schröder, C.; Nojiri, H.; Schnack, J.; Hage, P.; Luban, M.; Kögerler, P. *Physical Review Letters* **2005**, *94*, 017205.

(110) Schröder, C.; Schmidt, H.-J.; Schnack, J.; Luban, M. *Physical Review Letters* **2005**, *94*, 207203.

(111) Zhitomirsky, M. E. *Physical Review Letters* **2002**, *88*, 057204.

(112) Schulenburg, J.; Honecker, A.; Schnack, J.; Richter, J.; Schmidt, H. J. *Physical Review Letters* **2002**, *88*, 167207.

Chapter 3

Heat Capacity and Magnetization Studies of Magnetic Ordering in Ni_4^{II} Single-Molecule Magnets

3.1 Introduction

The discovery of single-molecule magnets (SMMs) has allowed for the detailed study of quantum effects such as ground-state tunneling of the direction of magnetization;[1-3], exchange bias, [4,5] and spin-spin cross relaxation effects[6] associated with nanomagnetic materials. This is due to the fact that SMMs are monodisperse in nature (i.e. they have the same size, shape and anisotropy).[7,8] A SMM can be magnetized as a result of having a large spin ground state (*S*) that experiences considerable Ising-type axial magnetoanisotropy (*D*). The combination of a large *S* and *D*, give rise to a potential energy barrier ($|D|S_z^2$) between the "spin-up" and "spin-down" states.[7-10]

SMMs have been proposed as potential candidates for quantum computation.[11-16] However, one of the major challenges in implementing these molecular systems is the ability to control tunneling decoherence below the blocking temperature (T_B) of an SMM. Spin decoherence arises from a number of sources including: nuclear hyperfine interactions, intermolecular dipolar interactions, spin-lattice relaxation (T_1), spin-spin relaxation (T_2) and long and short- range magnetic ordering. Magnetic ordering has been observed in a number of molecular nanomagnets[17-19] and has been shown to strongly affect tunneling rates and observed magnetic behavior.

The $[Ni(hmp)(ROH)Cl]_4$ series of complexes, where hmp^- is the anion of 2-hydroxymethylpyridine, R = the aliphatic groups MeOH, EtOH and 3,3'-dimethyl-1-butanol (dmb), are a benchmark study in SMM research. It has been shown [5] the introduction of bulky aliphatic groups significantly modulates intermolecular interactions and subsequent magnetization dynamics. The $[Ni(hmp)(dmb)Cl]_4$ (Ni_4^{dmb})

complex, for the first time, provided spectroscopic evidence of fourth-order Hamiltonian terms,[20] and oriented single-crystal high-frequency electron paramagnetic resonance studies (HFEPR) demonstrated profound limitations to the simple theoretical models often employed by physicists and chemists to analyze the complex electronic structure of SMMs.[21,22]

Magnetization versus field hysteresis loops for single crystals of $[Ni(hmp)(MeOH)Cl]_4$ (Ni_4^{MeOH}) and $[Ni(hmp)(EtOH)Cl]_4$ (Ni_4^{EtOH}), and a first derivative plot (*dM/dH* vs. *H*) for $[Ni(hmp)(dmb)Cl]_4$ (Ni_4^{dmb}) are presented in Figure 3.1, top left, top right and bottom center, respectively.[5,23] The first step, or ground state tunneling transition, is exchange-biased and is shifted from zero-field. The exchange-bias for the Ni_4^{MeOH} and Ni_4^{EtOH} complexes are shifted to negative fields (-0.33T and -0.28T, respectively) which is attributed significant antiferromagnetic intermolecular exchange interactions between Ni_4 complexes as propagated by solvate water molecules, and non-classical hydrogen bonding between protons on hmp^- ligands on one Ni_4 molecule weakly interacting with chloride ions of neighboring Ni_4 molecules.[5] The magnitude of the shift from zero-field can be directly attributed to the shielding ability of the aliphatic substituent of coordinated alcohol ligands.[5] Contrary to the Ni_4^{MeOH} and Ni_4^{EtOH} complexes, the Ni_4^{dmb} experiences the greatest shielding due to its large aliphatic 3,3'-dimethylbutyl groups. Also the crystal lattice of the Ni_4^{dmb} complex contains no solvate molecules. Interestingly though, rather than shifting the first step to zero-field, the step becomes positively exchange-biased (0.012T)(Figure 3.1, bottom center). This has been suggested as being due to ferromagnetic interactions between the Ni_4 complexes.

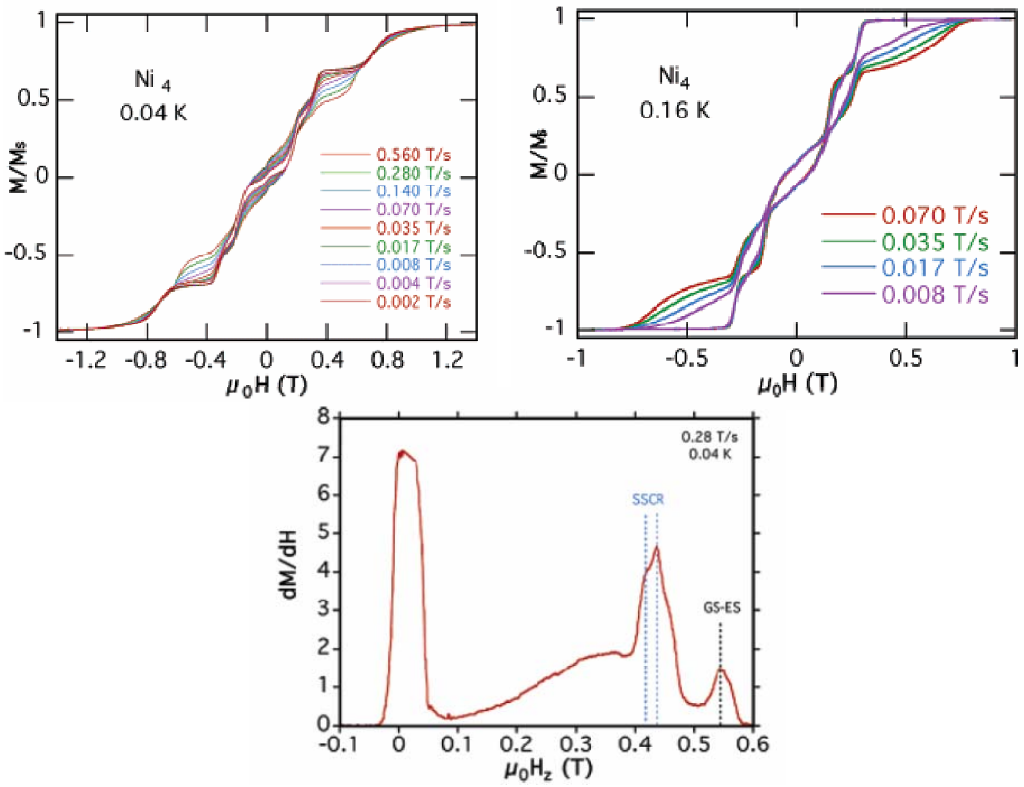

Figure 3.1. Plots of magnetization versus field hysteresis loops for **[Ni(hmp)(MeOH)Cl]$_4$** (Ni_4^{MeOH}) and **[Ni(hmp)(EtOH)Cl]$_4$** (Ni_4^{EtOH}), top left and top right, respectively, and first derivative plot (*dM/dH* vs. *H*) for **[Ni(hmp)(dmb)Cl]$_4$** (Ni_4^{dmb}). Each complex exhibits exchange-bias in the ground state tunneling transition (first step in the hysteresis loops) of: -0.33T, -0.28T and +0.012T, respectively.

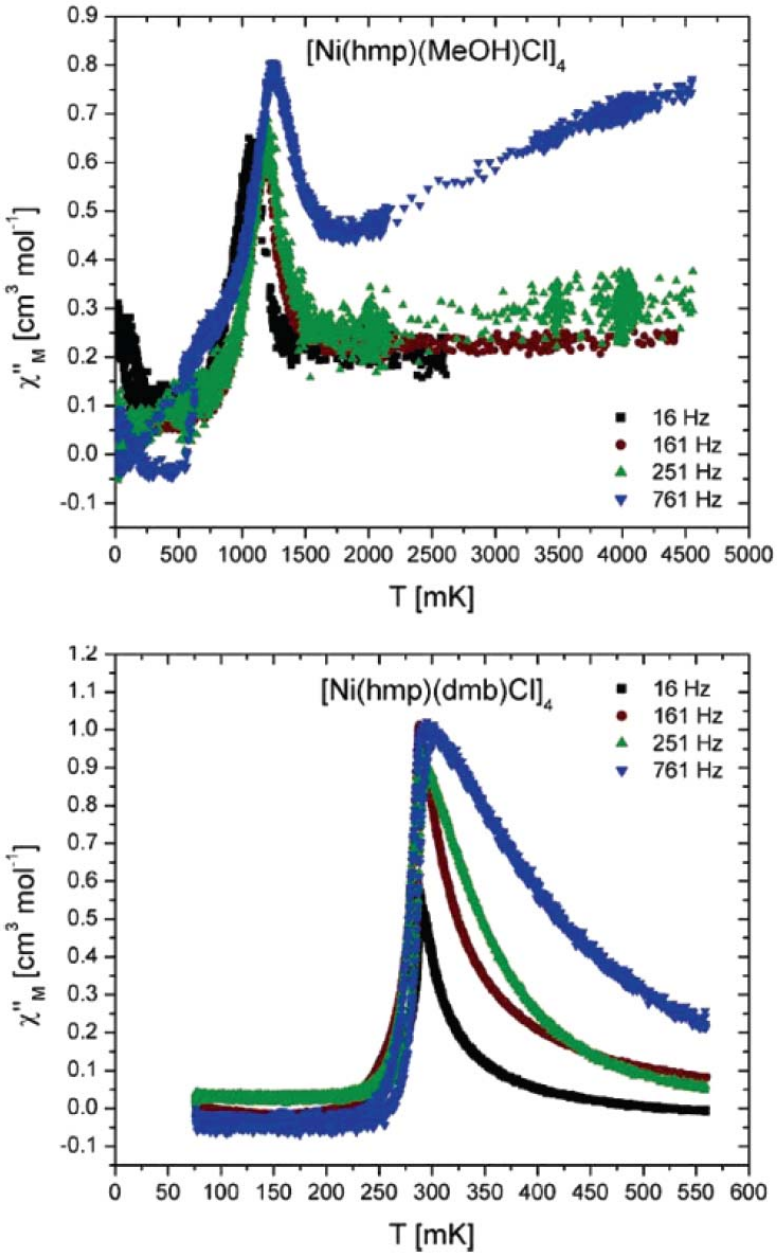

Figure 3.2. Plots of the out-of-phase components of ac magnetic susceptibility for **[Ni(hmp)(MeOH)Cl]$_4$** (Ni$_4^{MeOH}$)(top) and **[Ni(hmp)(dmb)Cl]$_4$** (Ni$_4^{dmb}$)(bottom), showing ordering transitions at 1100mK and 290mK, respectively.

To further probe the magnetization dynamics of the Ni_4 complexes low-temperature ac magnetic susceptibility experiments were performed for the Ni_4^{MeOH} and Ni_4^{dmb} complexes (Figure 3.2, top and bottom, respectively).[5] Frequency and temperature dependence are exhibited for both complexes, though quite weak for Ni_4^{MeOH}, where the out-of-phase component of the magnetization increases with decreasing temperature as a result of the inability of magnetic moments to stay in-phase with the oscillating magnetic field. However, at a critical temperature, 1200mK for Ni_4^{MeOH} and 290mK for Ni_4^{dmb}, there is an abrupt decrease in the observed susceptibility that has been attributed to short- and long-range magnetic ordering processes.[24] Of note, one would expect quantum tunneling rates to be severely impacted my magnetic ordering because the probability of all of the molecules in the ordered domain to tunnel simultaneously is very low; however, the tunneling rates for these three Ni_4 complexes is relatively unaffected. The Ni_4 series of molecules exhibit extremely fast magnetization tunneling rates in comparison to other SMMs (Table 3.1). The relaxation rate was calculated by fitting temperature dependent relaxation data, and fit employing arrhenius analysis (Figure 3.3 top and bottom, respectively.[5]

Ni_4^{dmb}, in particular, is an attractive system for several reasons. First, the Ni_4^{dbm} molecule crystallizes in the high symmetry $I4_1$/a tetragonal space group with only one crystallographically independent molecule in the unit cell with high S_4 site symmetry. Second, the large aliphatic substituent on the dmb alcohol ligand provides substantial electronic insulation between neighboring Ni_4^{dbm} molecules. And third, there are no solvate molecules in the crystal. Solvate disorder has been shown to give rise to wide

distributions in microenvironments within the crystal lattice that can detrimentally impact the ability to precisely interpret experimental data.[25-30]

Specific heat measurements are an invaluable tool for studying the physical properties of crystalline materials. Heat-capacity is extremely sensitive to crystallographic and magnetic phase transitions and can lead to great insight regarding long and short-range ordering and the nature of the ordering.[17,31-36] One difficulty in employing heat-capacity to study SMMs is that these complicated molecules (many atoms) make it difficult to separate the magnetic portion of the heat-capacity from the lattice contribution. Even at low temperatures (< 1 K) lattice and Schottky contributions can be considerable.

Presented in this chapter are heat capacity and oriented single-crystal magnetization hysteresis data for $[Ni(hmp)(dmb)Cl]_4$ (Ni_4^{dmb})[5,23] and preliminary heat capacity and magnetization data for $[Ni(hmp)(MeOH)Cl]_4$ (Ni_4^{MeOH})[5,23] and $[Ni(hmp)(EtOH)Cl]_4$ (Ni_4^{EtOH})[5,23] complexes. The goal was to uncover the origin of any magnetic ordering and simultaneous fast magnetization tunneling.

3.2 Experimental Section

3.2.1 Compound Preparation

$[Ni(hmp)(MeOH)Cl]_4$, $[Ni(hmp)(EtOH)Cl]_4$, and $[Ni(hmp)(dmb)Cl]_4$, complexes **3A-C,** were prepared as previously described in literature.[5,23]

$[Zn(hmp)(MeOH)Cl]_4$ (complex **3D).** A mixture of $ZnCl_2 \cdot 4H_2O$ (4.80 g, 20 mmol), 2-hydroxymethylpyridine (hmpH) (2.18 g, 20 mmol), and NaOMe (sodium methoxide, 1.08 g, 20 mmol) in 100 mL of methanol (MeOH) was refluxed for 30 min.

The resulting milky-white solution was gravity filtered while it was still hot. Opaque/white crystals suitable for X-ray analysis were collected after the solution cooled (approximately 3 days). The yield was 38% based on Zn.

[Zn(hmp)(dmb)Cl]$_4$ (complex **3E).** 4.0 g of complex **3D** was dissolved in a solution of 50 g of 3,3'-dimethyl-1-butanol (dmb) and 50 mL of dichloromethane. The solution was stirred for 30 minutes and then allowed to slowly evaporate undisturbed. Opaque/white X-ray diffraction quality crystals were collected after 2 weeks. Yield was 86% by Zn.

3.2.2 X-ray Crystallography

Crystal data and refinement data for **[Zn(hmp)(MeOH)Cl]$_4$ (**Zn_4^{MeOH} (**3D**)**)** and **[Zn(hmp)(dmb)Cl]$_4$ (**Zn_4^{dmb} (**3E**)**)** presented in Tables 3.2-3, respectively. Selected bond distances and bond angles for **[Zn(hmp)(MeOH)Cl]$_4$ (**Zn_4^{MeOH} (**3D**)**)** and **[Zn(hmp)(dmb)Cl]$_4$ (**Zn_4^{dmb} (**3E**)**)** are presented in Tables 3.4-7.

[Zn(hmp)(MeOH)Cl]$_4$ (Zn_4^{MeOH} (**3D**)**)** and **[Zn(hmp)(dmb)Cl]$_4$ (**Zn_4^{dmb} (**3E**)**)** A colorless block, of dimensions: 0.10 x 0.10 x 0.10 mm for Zn_4^{MeOH} (**3D**) and 0.10 x 0.15 x 0.15 mm for Zn_4^{dmb} (**3E**), was mounted on a Cryoloop with Paratone oil. Data were collected in a nitrogen gas stream at 293(2) K using phi scans. Crystal-to-detector distance was 60 mm and exposure time was 10 and 5 seconds per frame using a scan width of 0.3° for complexes Zn_4^{MeOH} (**3D**) and Zn_4^{dmb} (**3E**), respectively. Data collection was 98.2% and 100.0% complete to 25.00° in θ for complexes Zn_4^{MeOH} (**3D**) and Zn_4^{dmb} (**3E**), respectively. A total of 13541 reflections were collected covering the indices, -21<=*h*<=6, -14<=*k*<=20, -31<=*l*<=36. 4260 reflections were found to be

symmetry independent, with an R_{int} of 0.0348. Indexing and unit cell refinement indicated a I-centered, tetragonal lattice. The space group was found to be I-42d for complex Zn_4^{MeOH} (**3D**). A total of 24972 reflections were collected covering the indices, -16<=h<=16, -16<=k<=16, -46<=l<=46. 3508 reflections were found to be symmetry independent, with an R_{int} of 0.0266. Indexing and unit cell refinement indicated a I-centered, tetragonal lattice. The space group was found to be I-41/a for Zn_4^{dmb} (**3E**). The data were integrated using the Bruker SAINT software program and scaled using the SADABS software program. Solution by direct methods (SIR-2004) produced a complete heavy-atom phasing model consistent with the proposed structure. All non-hydrogen atoms were refined anisotropically by full-matrix least-squares (SHELXL-97 (Sheldrick, 1997)). All hydrogen atoms were placed using a riding model. Their positions were constrained relative to their parent atom using the appropriate HFIX command in SHELXL-97. Disordered solvent (methanol) was removed by the Squeeze routine which is detailed in the cif file for complex Zn_4^{MeOH} (**3D**).

Table 3.1. Quantum tunneling rates for a number of SMMs, as reported in reference 5, including ground state spin, zero-field splitting parameter and theoretical barrier to magnetization reversal.
a[1], *b*[37], *c*[3], *d*[38], *e*[39], *f*[40] and *g*[41]

complex	QTM rate (s^{-1})	S	D (cm^{-1})	$\lvert D\rvert S^2$ (cm^{-1})
complex 3	2×10^{-1}	4	−0.6	9.6
Mn_4 cubane[a]	3.2×10^{-2}	$^9/_2$	−0.53	10.6
Mn_{12}−Ac[b]	$<10^{-8}$	10	−0.46	46
Fe_8[c]	4.5×10^{-5}	10	−0.19	19
Mn_4 dicubane[d]	10^{-4}	8	−0.25	16
Mn_{30}[e]	10^{-6}	5	−0.51	12.8
Mn_{18}[f]	1.3×10^{-8}	13	−0.13	22
Mn_2[g]	5×10^{3}	4	−2.3	36.7

[a] $[Mn_4O_3Cl(O_2CCH_3)_3(dbm)]$. [b] $[Mn_{12}O_{12}(O_2CCH_3)_{16}(H_2O)_4]$. [c] $[(tacn)_6Fe_8O_2(OH)_{12}]^{8+}$. [d] $[Mn_4(OAc)_2(pdmH)_6(H_2O)_4](ClO_4)_2$. [e] $[Mn_{30}O_{24}(OH)_8(O_2CCH_2Bu^t)_{32}(H_2O)_2(MeNO_2)_4]$; [f] $[Mn_{18}O_{14}(O_2CMe)_{18}(hep)_4(hepH)_2(H_2O)_2](ClO_4)_2$. [g] $[Mn_2(Saltmen)_2(ReO_4)_2]$.

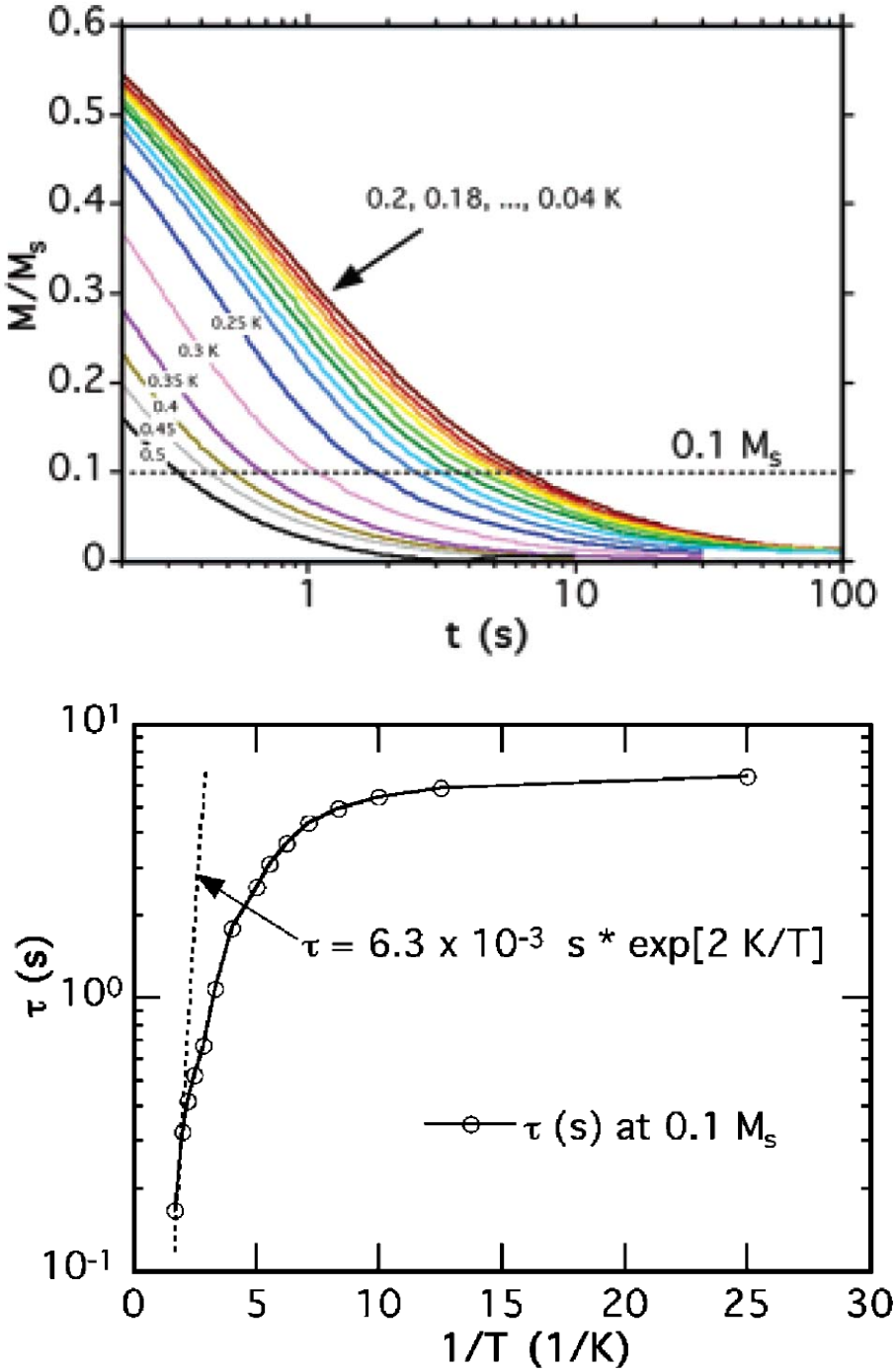

Figure 3.3. Magnetization relaxation data (0.004 to 0.6K, top) for **[Ni(hmp)(dmb)Cl]$_4$ (3C),** where the relaxation at 90% decay of M_s (magnetization saturation) is fit to arrhenius behavior yielding relaxation rate and τ the pre-exponential function.

Table 3.2. Crystal data and structure refinement **[Zn(hmp)(MeOH)Cl]$_4$ (**Complex **3D).**

Empirical formula	C29 H44 Cl4 N4 O9 Zn4	
Formula weight	995.96	
Temperature	293(2) K	
Wavelength	0.71073 Å	
Crystal system	Tetragonal	
Space group	I-42d	
Unit cell dimensions	a = 16.0970(11) Å	α= 90°.
	b = 16.097 Å	β= 90°.
	c = 29.597(2) Å	γ = 90°.
Volume	7669.0(8) Å^3	
Z	8	
Density (calculated)	1.725 Mg/m^3	
Absorption coefficient	2.804 mm^{-1}	
F(000)	4048	
Crystal size	0.10 x 0.10 x 0.10 mm^3	
Crystal color/habit	colorless block	
Theta range for data collection	1.44 to 28.27°.	
Index ranges	-21<=h<=6, -14<=k<=20, -31<=l<=36	
Reflections collected	13541	
Independent reflections	4260 [R(int) = 0.0348]	
Completeness to theta = 25.00°	98.2 %	
Absorption correction	Semi-empirical from equivalents	
Max. and min. transmission	0.7668 and 0.7668	
Refinement method	Full-matrix least-squares on F^2	
Data / restraints / parameters	4260 / 0 / 221	
Goodness-of-fit on F^2	1.022	
Final R indices [I>2sigma(I)]	R1 = 0.0236, wR2 = 0.0595	
R indices (all data)	R1 = 0.0246, wR2 = 0.0598	
Absolute structure parameter	0.021(9)	
Largest diff. peak and hole	0.408 and -0.420 e.Å^{-3}	

[a] $R = \Sigma||F_o| - |F_c||/\Sigma|F_o|$. [b] $R(\omega F^2) = \{\Sigma[\omega(F_o^2 - F_c^2)^2]/\Sigma[\omega(F_o^2)^2]\}^{1/2}$;
$\omega = 1/[\sigma^2(F_o^2) + (aP)^2 + bP]$, $P = [2F_c^2 + \max(F_o, 0)]/3$.

Table 3.3. Crystal data and structure refinement for **[Zn(hmp)(dmb)Cl]$_4$(**complex**3E).**

Empirical formula	C48 H80 Cl4 N4 O8 Zn4	
Formula weight	1244.44	
Temperature	100(2) K	
Wavelength	0.71073 Å	
Crystal system	Tetragonal	
Space group	I41/a	
Unit cell dimensions	a = 12.9319(10) Å	α= 90°.
	b = 12.9319(10) Å	β= 90°.
	c = 35.068(6) Å	γ = 90°.
Volume	5864.6(11) Å^3	
Z	4	
Density (calculated)	1.409 Mg/m^3	
Absorption coefficient	1.848 mm^{-1}	
F(000)	2592	
Crystal size	0.10 x 0.10 x 0.01 mm^3	
Theta range for data collection	1.68 to 28.27°.	
Index ranges	-16<=h<=16, -16<=k<=16, -46<=l<=46	
Reflections collected	24972	
Independent reflections	3508 [R(int) = 0.0381]	
Completeness to theta = 25.00°	100.0 %	
Absorption correction	Semi-empirical from equivalents	
Max. and min. transmission	0.9818 and 0.8368	
Refinement method	Full-matrix least-squares on F^2	
Data / restraints / parameters	3508 / 0 / 158	
Goodness-of-fit on F^2	1.046	
Final R indices [I>2sigma(I)]	R1 = 0.0266, wR2 = 0.0651	
R indices (all data)	R1 = 0.0322, wR2 = 0.0673	
Largest diff. peak and hole	0.840 and -0.239 e.Å^{-3}	

[a] $R = \Sigma||F_o| - |F_c||/\Sigma|F_o|$. [b] $R(\omega F^2) = \{\Sigma[\omega(F_o^2 - F_c^2)^2]/\Sigma[\omega(F_o^2)^2]\}^{1/2}$;
$\omega = 1/[\sigma^2(F_o^2) + (aP)^2 + bP]$, $P = [2F_c^2 + \max(F_o, 0)]/3$.

Table 3.4. Bond distances for **[Zn(hmp)(MeOH)Cl]$_4$ (**complex **3D).**

O(4)-C(14)	1.423(3)	Zn(1)-O(1)#1	2.0698(17)
N(2)-C(7)	1.336(3)	Zn(1)-N(1)	2.114(2)
N(2)-C(11)	1.345(3)	Zn(1)-O(1)#2	2.1462(16)
C(7)-C(8)	1.384(4)	Zn(1)-O(1)	2.1437(16)
C(1)-C(2)	1.372(4)	Zn(1)-Cl(1)	2.3506(7)
C(11)-C(10)	1.389(4)	Zn(2)-O(2)	2.0516(17)
C(11)-C(12)#4	1.516(3)	Zn(2)-N(2)	2.102(2)
C(5)-C(4)	1.375(3)	Zn(2)-O(2)#3	2.1150(16)
C(5)-C(6)#2	1.517(3)	Zn(2)-O(2)#4	2.1698(15)
C(2)-C(3)	1.379(4)	Zn(2)-Cl(2)	2.3518(6)
C(12)-C(11)#3	1.516(3)	O(1)-C(6)	1.421(3)
C(6)-C(5)#2	1.517(3)	O(1)-Zn(1)#5	2.0698(17)
C(10)-C(9)	1.386(4)	O(1)-Zn(1)#2	2.1462(16)
C(8)-C(9)	1.378(4)	O(2)-C(12)	1.398(3)
C(3)-C(4)	1.378(4)	O(2)-Zn(2)#4	2.1150(16)
N(1)-C(1)	1.339(3)	O(2)-Zn(2)#3	2.1697(15)
N(1)-C(5)	1.348(3)	O(3)-C(13)	1.421(3)

Symmetry transformations used to generate equivalent atoms:
#1 y+1/2,-x+5/2,-z+3/2 #2 -x+3,-y+2,z #3 -y+3,x,-z+2 #4 y,-x+3,-z+2 #5 -y+5/2,x-1/2,-z+3/2

Table 3.5. Bond angles for **[Zn(hmp)(MeOH)Cl]$_4$ (**complex **3D).**

O(1)#1-Zn(1)-N(1)	157.34(7)	O(2)-Zn(2)-Cl(2)	101.83(5)
O(1)#1-Zn(1)-O(1)#2	80.60(7)	N(2)-Zn(2)-Cl(2)	101.51(6)
N(1)-Zn(1)-O(1)#2	77.89(7)	O(2)#3-Zn(2)-Cl(2)	97.03(4)
O(1)#1-Zn(1)-O(1)	80.66(7)	O(2)#4-Zn(2)-Cl(2)	176.63(5)
N(1)-Zn(1)-O(1)	102.01(7)	C(6)-O(1)-Zn(1)#5	127.46(14)
O(1)#2-Zn(1)-O(1)	79.01(7)	C(6)-O(1)-Zn(1)#2	110.34(13)
O(1)#1-Zn(1)-Cl(1)	101.76(5)	Zn(1)#5-O(1)-Zn(1)#2	98.26(7)
N(1)-Zn(1)-Cl(1)	100.26(6)	C(6)-O(1)-Zn(1)	117.41(14)
O(1)#2-Zn(1)-Cl(1)	174.81(5)	Zn(1)#5-O(1)-Zn(1)	98.34(7)
O(1)-Zn(1)-Cl(1)	96.75(5)	Zn(1)#2-O(1)-Zn(1)	100.61(7)
O(2)-Zn(2)-N(2)	155.56(8)	C(12)-O(2)-Zn(2)	125.95(14)
O(2)-Zn(2)-O(2)#3	81.37(7)	C(12)-O(2)-Zn(2)#4	120.26(14)
N(2)-Zn(2)-O(2)#3	102.83(7)	Zn(2)-O(2)-Zn(2)#4	99.37(7)
O(2)-Zn(2)-O(2)#4	80.06(7)	C(12)-O(2)-Zn(2)#3	109.52(14)
N(2)-Zn(2)-O(2)#4	77.00(7)	Zn(2)-O(2)-Zn(2)#3	97.61(7)
O(2)#3-Zn(2)-O(2)#4	80.44(6)	Zn(2)#4-O(2)-Zn(2)#3	98.98(6)
C(1)-N(1)-C(5)	118.6(2)	N(1)-C(5)-C(4)	121.4(2)
C(1)-N(1)-Zn(1)	126.77(16)	N(1)-C(5)-C(6)#2	116.4(2)
C(5)-N(1)-Zn(1)	114.60(17)	C(4)-C(5)-C(6)#2	122.2(2)
C(7)-N(2)-C(11)	119.0(2)	C(1)-C(2)-C(3)	119.0(3)
C(7)-N(2)-Zn(2)	126.19(16)	O(2)-C(12)-C(11)#3	111.25(19)
C(11)-N(2)-Zn(2)	114.70(18)	O(1)-C(6)-C(5)#2	110.8(2)
N(2)-C(7)-C(8)	122.4(2)	C(9)-C(10)-C(11)	119.0(2)
N(1)-C(1)-C(2)	122.5(2)	C(9)-C(8)-C(7)	119.0(2)
N(2)-C(11)-C(10)	121.6(2)	C(4)-C(3)-C(2)	118.7(3)
N(2)-C(11)-C(12)#4	116.2(2)	C(10)-C(9)-C(8)	119.0(3)
C(10)-C(11)-C(12)#4	122.2(2)	C(3)-C(4)-C(5)	119.8(2)

Table 3.6. Bond distances for **[Zn(hmp)(dmb)Cl]$_4$ (**complex **3E).**

C(1)-N(1)	1.343(2)	C(8)-C(9)	1.542(2)
C(1)-C(2)	1.382(2)	C(9)-C(11)	1.523(3)
C(2)-C(3)	1.390(3)	C(9)-C(12)	1.527(2)
C(3)-C(4)	1.384(2)	C(9)-C(10)	1.532(3)
C(4)-C(5)	1.391(2)	N(1)-Zn(1)	2.1297(14)
C(5)-N(1)	1.342(2)	O(1)-Zn(1)#2	2.0728(11)
C(5)-C(6)#1	1.515(2)	O(1)-Zn(1)	2.1281(11)
C(6)-O(1)	1.4071(18)	O(1)-Zn(1)#1	2.1378(11)
C(6)-C(5)#1	1.515(2)	Cl(1)-Zn(1)	2.3397(4)
C(7)-O(2)	1.4294(19)	Zn(1)-O(1)#3	2.0728(11)
C(7)-C(8)	1.518(2)	Zn(1)-O(1)#1	2.1378(11)

Symmetry transformations used to generate equivalent atoms:

#1 -x+3,-y+3/2,z+0 #2 -y+9/4,x-3/4,-z+1/4 #3 y+3/4,-x+9/4,-z+1/4

Table 3.7. Bond angles for **[Zn(hmp)(dmb)Cl]$_4$ (**complex **3E).**

N(1)-C(1)-C(2)	122.91(16)	C(1)-N(1)-Zn(1)	126.92(11)
C(1)-C(2)-C(3)	118.16(16)	C(6)-O(1)-Zn(1)#2	125.28(9)
C(4)-C(3)-C(2)	119.24(16)	C(6)-O(1)-Zn(1)	119.97(9)
C(3)-C(4)-C(5)	119.31(16)	Zn(1)#2-O(1)-Zn(1)	98.39(4)
N(1)-C(5)-C(4)	121.42(15)	C(6)-O(1)-Zn(1)#1	110.79(9)
N(1)-C(5)-C(6)#1	116.44(13)	Zn(1)#2-O(1)-Zn(1)#1	98.08(4)
C(4)-C(5)-C(6)#1	122.13(14)	Zn(1)-O(1)-Zn(1)#1	99.63(4)
O(1)-C(6)-C(5)#1	111.03(12)	O(1)#3-Zn(1)-O(1)	80.99(4)
O(2)-C(7)-C(8)	111.24(14)	O(1)#3-Zn(1)-N(1)	156.21(5)
C(7)-C(8)-C(9)	115.32(14)	O(1)-Zn(1)-N(1)	103.50(4)
C(11)-C(9)-C(12)	108.82(17)	O(1)#3-Zn(1)-O(1)#1	80.77(4)
C(11)-C(9)-C(10)	111.14(18)	O(1)-Zn(1)-O(1)#1	79.91(4)
C(12)-C(9)-C(10)	108.18(16)	N(1)-Zn(1)-O(1)#1	77.15(4)
C(11)-C(9)-C(8)	110.38(15)	O(1)#3-Zn(1)-Cl(1)	103.74(3)
C(12)-C(9)-C(8)	108.33(15)	O(1)-Zn(1)-Cl(1)	97.80(3)
C(10)-C(9)-C(8)	109.91(16)	N(1)-Zn(1)-Cl(1)	98.81(4)
C(5)-N(1)-C(1)	118.95(14)	O(1)#1-Zn(1)-Cl(1)	174.64(3)
C(5)-N(1)-Zn(1)	114.10(10)		

3.2.3 Physical Measurements

Magnetic measurements were carried out on a ~100^3 μm^3 pyramidal-shaped single crystal of Ni_4^{dmb} (**3C**) placed on top of a high-sensitivity micro-Hall effect magnetometer.[42] The sample magnetization was recorded at different temperatures down to 20 mK in an Oxford Instruments $^3He/^4He$ dilution cryostat. Zero-field cooled (ZFC) and field-cooled (FC) magnetization curves recorded at different magnetic fields (15-2070 Oe) applied along the easy magnetic axis of the molecules. In these measurements the sample is cooled from 1 K down to 20 mK in the absence of magnetic fields (ZFC). Then, a magnetic field is applied along the easy magnetic axis of the molecules and the temperature is raised up to 1 K again at a rate of ~3 K/min. Maintaining the same applied magnetic field, the temperature is lowered down to 20 mK at a rate of ~3 K/min (FC), while the magnetization is being monitored.

The low temperature heat capacity measurements for Ni_4^{dmb} (**3C**) and Zn_4^{dmb} (**3E**) were performed in a dilution refrigerator by using a relaxation calorimeter, which is composed of a silver sample platform, a thermometer, and a heating chip. Depending on the amount of the heat capacity and the internal thermal equilibrium time, either 1-tau or 2-tau fit was used to analyze the temperature response with respect to the heat pulse input to the calorimeter. [33,43] 2.10 mg Apiezo N grease was used to attach four pieces of single crystals of Ni_4^{dmb} (**3E**) of mass 58.89 mg onto the calorimeter.

3.3 Results and Discussion

3.3.1 Synthesis

Synthesis of complex Zn_4^{MeOH} (**3D**) requires continuous heating at reflux without achieving a full boil. If a boil is reached the crystallized product is a mixture of mononuclear $Zn(hmp)_2$ and the desired Zn_4^{MeOH} (**3D**) product. Reflux is needed due to the low solubility of Na(OMe) in anhydrous methanol. Furthermore, if cooling is allowed to happen to rapidly, poor quality, twinned or micro-crystalline products result. Slow cooling is aided by wrapping the crystallization flask in aluminum foil. In contrast to the synthesis of Ni_4^{MeOH} (**3D**), [5] the Zn_4^{MeOH} (**3D**) complex will crystallize with various ratios of MeOH and H_2O as coordinated ligands if the reaction takes place in standard commercial methanol. However, anhydrous methanol can be used under aerobic conditions to yield the fully substituted Zn_4^{MeOH} (**3D**) complex. No special conditions are required for crystallization of the Zn_4^{dmb} (**3E**) complex. Even in the presence of anhydrous ethanol a fully substituted Zn_4^{EtOH} complex was not obtainable. Rather, Zn_4 complexes with various ratios of ethanol and water ligands were obtained in high yield.

3.3.2 Description of Crystallographic Structure

$[Zn(hmp)(MeOH)Cl]_4$ (Zn_4^{MeOH} (3D)) crystallizes in the tetragonal space group *I*42*d* with two symmetry independent molecules in the unit cell, one in a general position, and the other on an inversion center. An Ortep representation for Zn_4^{MeOH} (**3D**) is given in Figure 3.4. The asymmetric unit contains one quarter of each molecule (Figure 3.5), with the rest of the atoms generated by the symmetry transformations: #1

y+1/2,-x+5/2,-z+3/2, #2 -x+3,-y+2,z, #3 -y+3,x,-z+2, #4 y,-x+3,-z+2, #5 -y+5/2,x-1/2,-z+3/2. Each molecule is a distorted cubane with Zn^{II} ions occupying alternating vertices. The other four vertices are occupied by oxo-atoms from the hmp^- ligands. The rest of the octahedrally coordinated Zn sites are occupied by a chloride ion, a nitrogen from the pyridine ring of a hmp^- ligand and the oxo-atom from a methanol ligand. Each independent molecule has S_4 molecular site symmetry.

The Zn_4^{MeOH} (**3D**) complex exhibits interamolecular hydrogen bonding between coordinated chloride ions and the alcohol proton of a methanol ligand (Figure 3.6). The O-H---Cl distances for the two symmetry dependent molecules are 2.229Å and 2.267Å which is in excellent agreement with distances found in the analogous Ni_4^{MeOH} (**3A**) complex of 2.20Å and 2.22Å.[5,23] The Ni_4^{MeOH} (**3A**) exhibits hydrogen bonding between Ni_4 molecules and water solvate molecules. Unfortunately this comparison could not be made with the Zn_4^{MeOH} (**3D**) complex, as extreme positional disorder of lattice water molecules precluded modeling and they were squeezed out during crystal refinement. Figures 3.7-8 show packing diagrams for Zn_4^{MeOH} (**3D**) showing the head to tail packing arrangement and a view along the crystallographic *c*-axis which shows the rotation of molecules along the 4_2 screw-axis. A unit cell comparison between Zn_4^{MeOH} (**3D**) and Ni_4^{MeOH} (**3A**) reveals that they are nearly identical as expected: α = 16.0970(11) Å, β = 16.097 Å and γ = 29.597(2) Å for Zn_4^{MeOH} (**3D**), and α = 16.1421 Å, β = 16.1421 Å and γ = 29.4689 for Ni_4^{MeOH} (**3A**),[5] with unit cell volumes of 7669.0Å^3 and 7678.6 Å^3, respectively, indicating that the two structures are identical.

$[Zn(hmp)(dmb)Cl]_4$ (Zn_4^{dmb} (3E)) crystallizes in the tetragonal space group $I4_1/a$, with only one symmetry independent molecule in the unit cell. An Ortep drawing

for Zn_4^{dmb} (**3E**) is presented in Figure 3.9. The asymmetric unit (Figure 3.10) contains one quarter of the molecule with the symmetry equivalent atoms generated by the symmetry transformations: #1 -x+3,-y+3/2,z+0, #2 -y+9/4,x-3/4,-z+1/4, #3 y+3/4,-x+9/4,-z+1/4. The oxo-bridged distorted cubane core is identical to the Zn_4^{MeOH} (**3D**) construction with the coordinated methanol ligands being replaced by 3,3'-dimethyl-1-butanol ligands. Complex Zn_4^{dmb} (**3E**) crystallizes with no lattice solvate molecules. A packing diagram is given in Figure 3.11 shown looking down the crystallographic *a*-axis. Figure 3.12 shows a single molecule as viewed down the crystallographic *c*-axis, and clearly shows the S_4 molecular site symmetry of the molecules in the unit cell.

Intramolecular hydrogen bonds between O-H---Cl in Zn_4^{dmb} (**3E**) and Ni_4^{dmb} (**3C**) are 2.299Å and 2.300Å, respectively. Also nearest neighbor Cl---Cl contacts are also identical, 5.904Å and 6.036Å for Zn_4^{dmb} (**3E**) and Ni_4^{dmb} (**3C**), respectively. Unit cell comparisons for Zn_4^{dmb} (**3E**) and Ni_4^{dmb} (**3C**) also agree that the two complexes are nearly identical: α = 12.9319(10) Å, β = 12.9319(10) Å and γ = 35.068(6) Å for Zn_4^{dmb} (**3E**) and α = 12.8389(3) Å, β = 12.8389(3) Å and γ = 35.047(2) Å for Ni_4^{dmb} (**3C**).

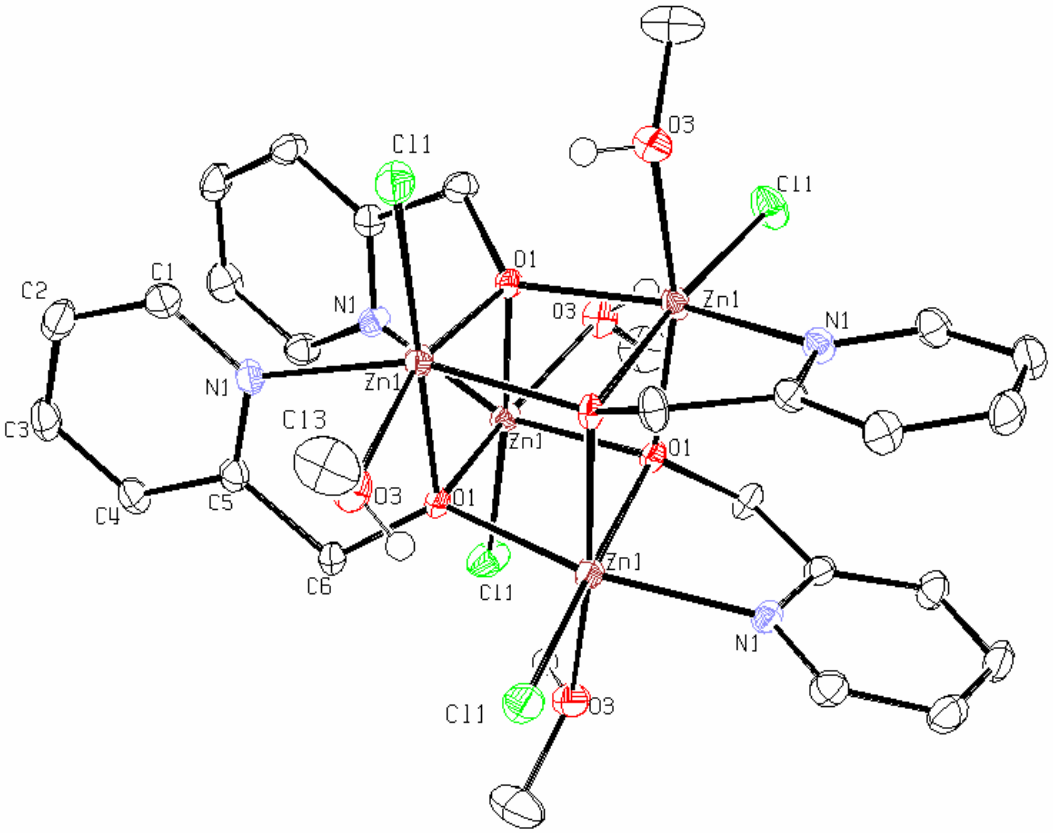

Figure 3.4. Ortep rendering of **[Zn(hmp)(MeOH)Cl]$_4$** with thermal ellipsoids at 50%. Hydrogens have been removed for clarity.

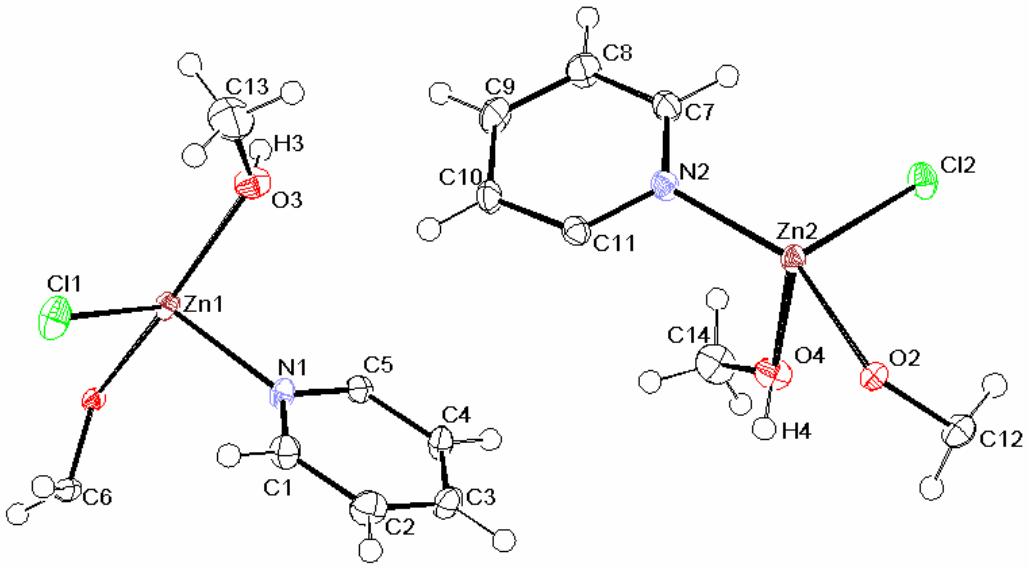

Figure 3.5. Ortep rendering of the two independent asymmetric units of **[Zn(hmp)(MeOH)Cl]$_4$** with thermal ellipsoids at 50%.

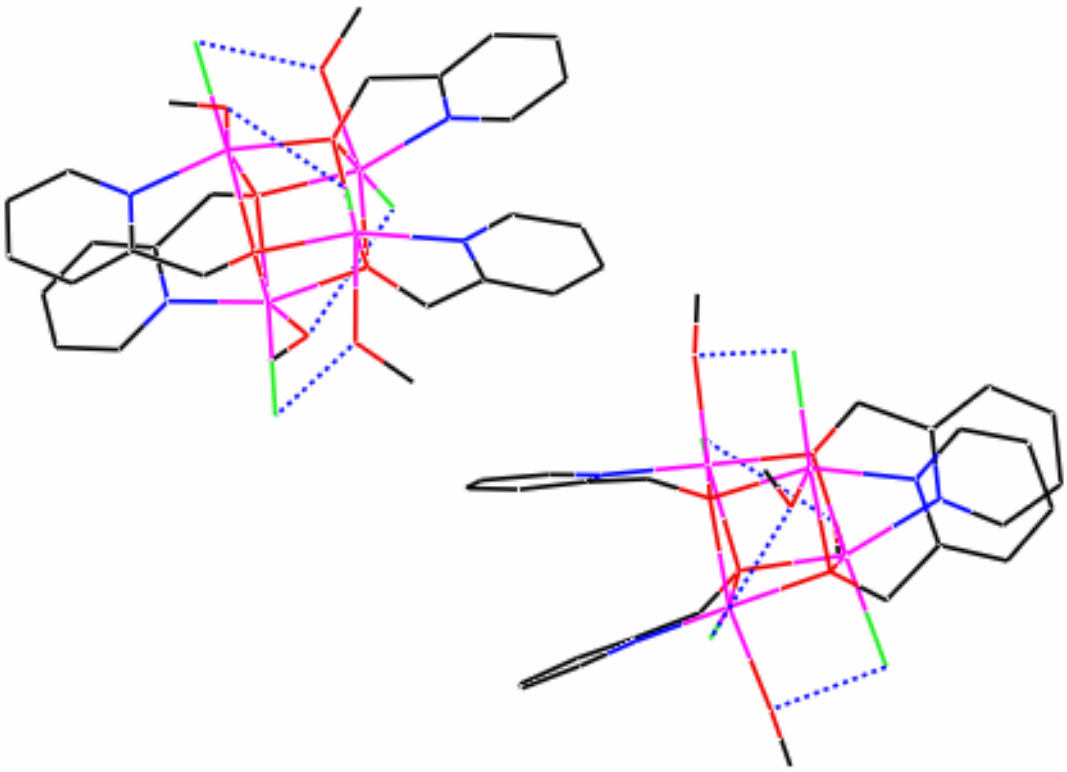

Figure 3.6. Intramolecular hydrogen-bonding in **[Zn(hmp)(MeOH)Cl]$_4$.**

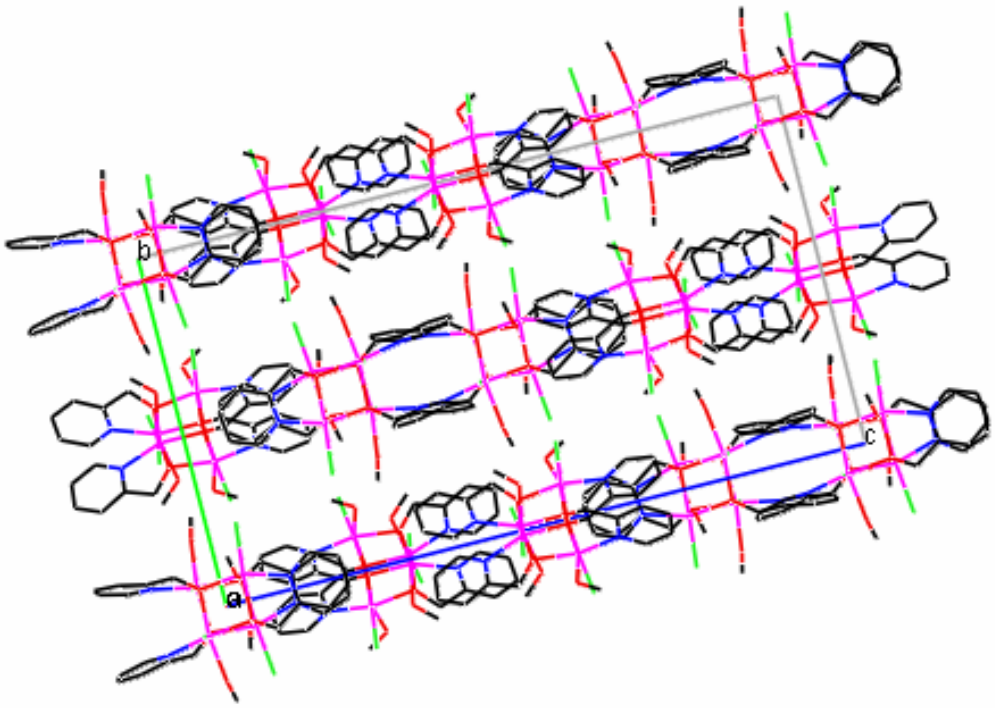

Figure 3.7. Crystal packing diagram of **$[Zn(hmp)(MeOH)Cl]_4$.**

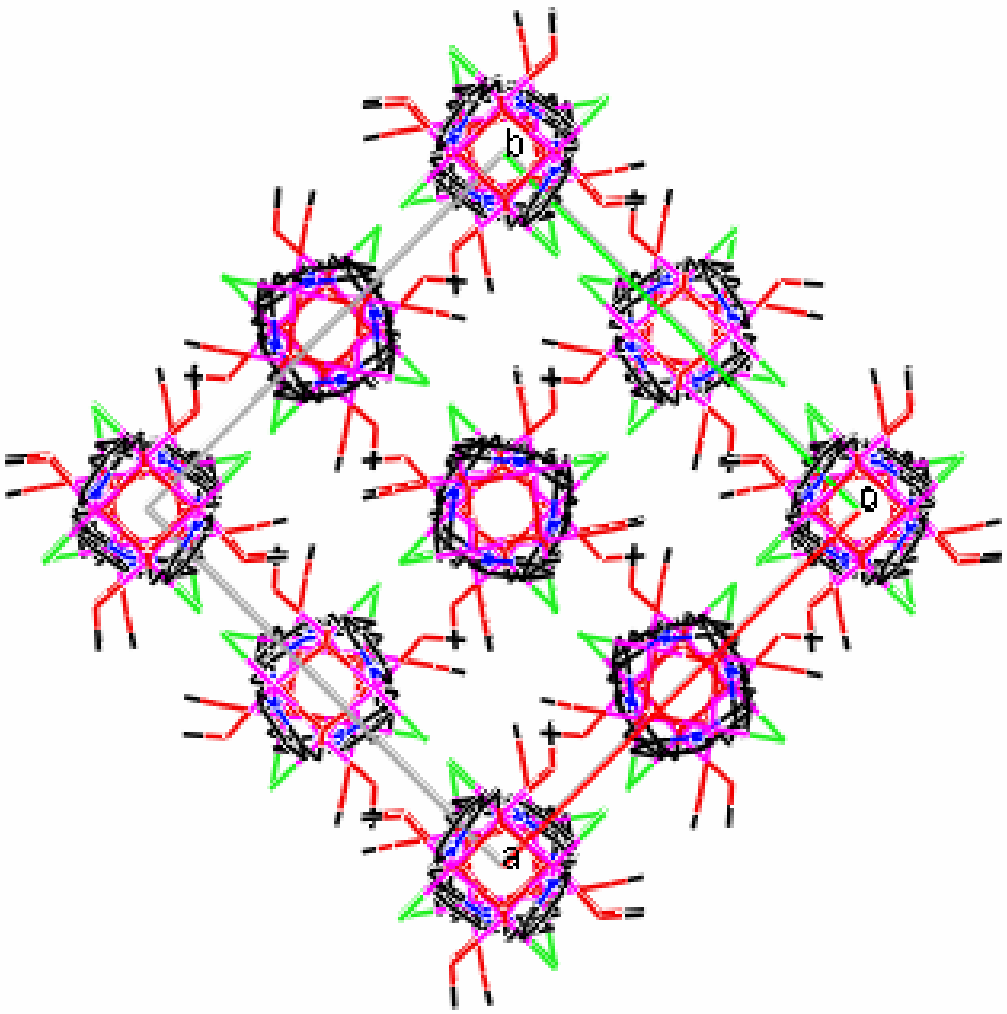

Figure 3.8. Crystal packing diagram of **[Zn(hmp)(MeOH)Cl]$_4$** oriented along the *c*-axis of the unit cell.

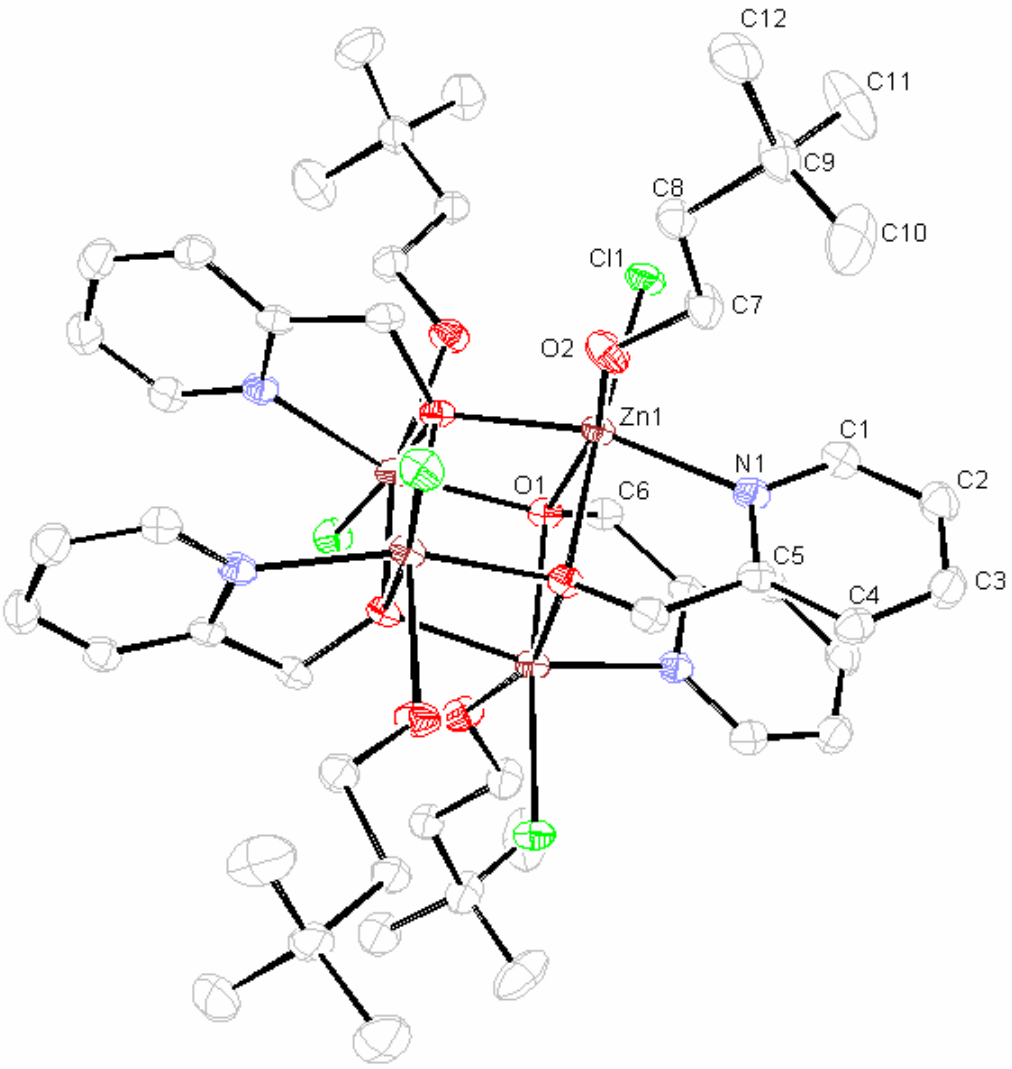

Figure 3.9. Ortep rendering of **[Zn(hmp)(dmb)Cl]$_4$** with thermal ellipsoids at 50%. Hydrogens have been removed for clarity.

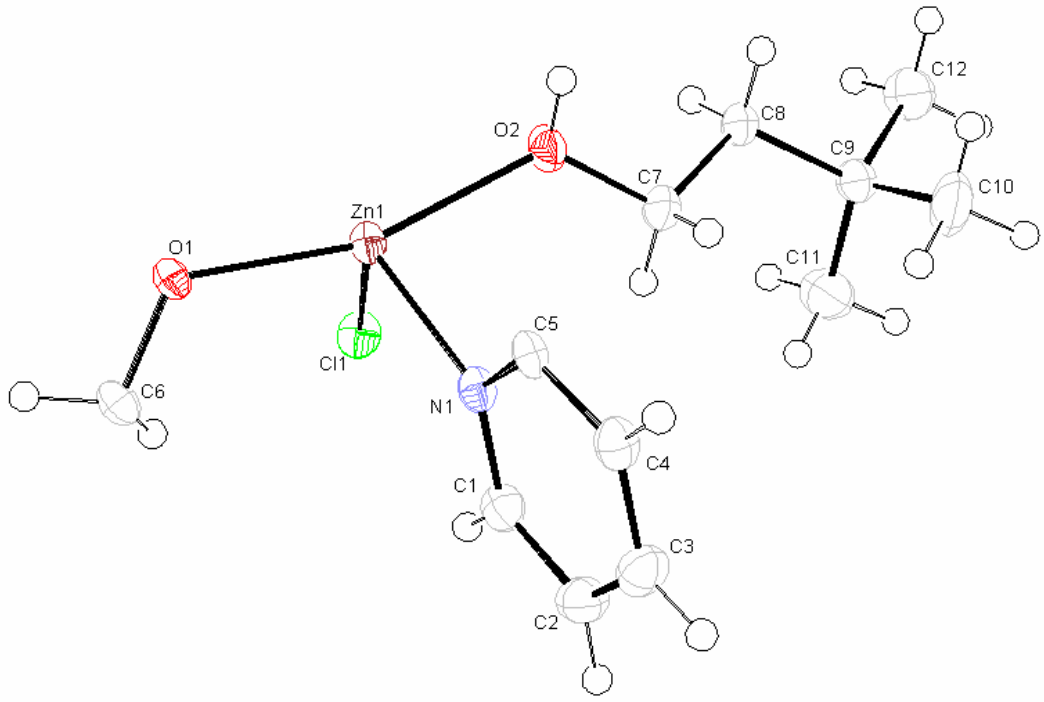

Figure 3.10. Ortep rendering of the asymmetric unit of **[Zn(hmp)(dmb)Cl]$_4$** with thermal ellipsoids at 50%.

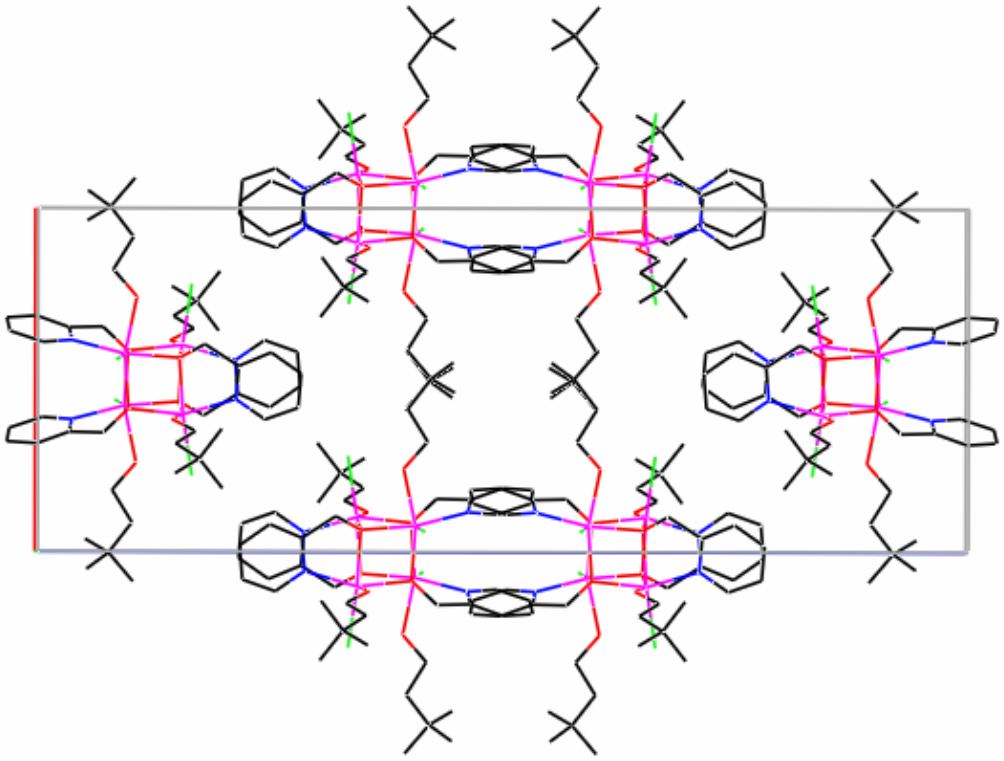

Figure 3.11. Crystal packing diagram of **[Zn(hmp)(dmb)Cl]$_4$** looking along the crystallographic *a*-axis.

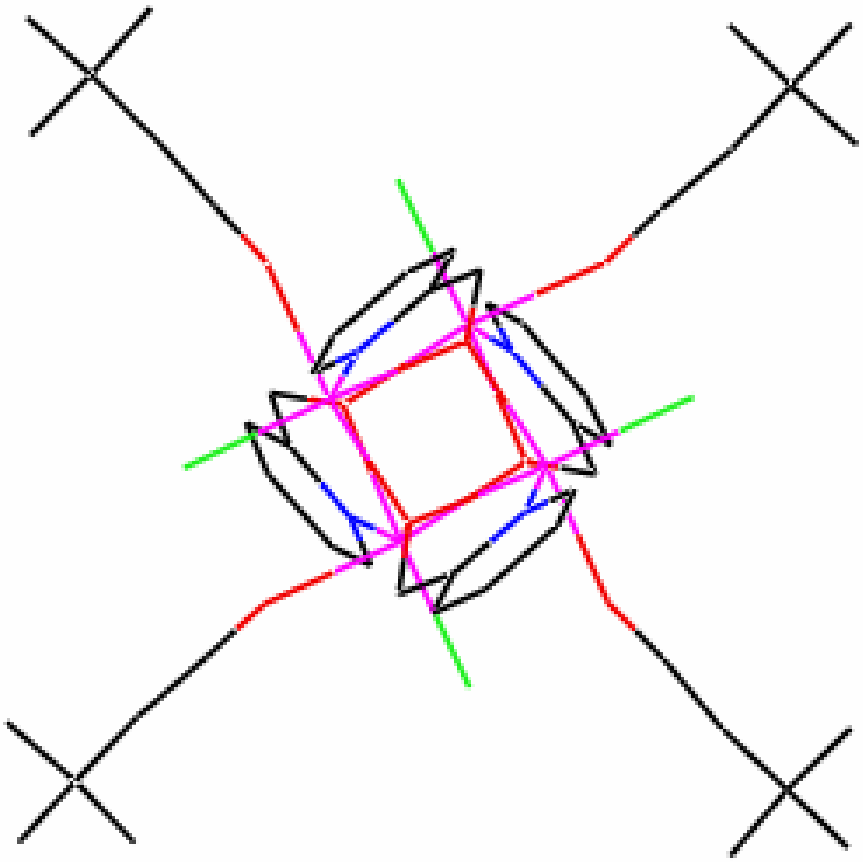

Figure 3.12. Looking along the crystallographic *c*-axis of **[Zn(hmp)(dmb)Cl]$_4$** displaying the S_4 site symmetry.

3.3.3 Heat Capacity of Ni_4 and Zn_4 Complexes

Figure 3.13 displays polycrystalline heat capacity (C_P(T)) data for Ni_4^{dmb} (**3C**), plotted linear scale bottom and log scale top, with applied magnetic fields (H) of 0T, 0.25T and 0.47T in the temperature range 0.04-4.5K (depiction of the data collection platform and mounted crystals are given in Figure 3.14). A very sharp λ-peak is clearly evident in the H = 0 T trace at ~300 mK (Figure 3.13, black trace). The observed excess heat capacity cannot be explained by dipolar ordering (dipolar ordering in the Ni_4^{dmb} (**3C**) lattice was previously calculated to be 90 mK)[5], and temperature considerations (300 mK) preclude a crystallographic phase transition. The total heat capacity consists of three parts: 1) the Shottky contribution, which arises due to thermal distributions of energy states, 2) the lattice contribution, and 3) the magnetic contribution. The Schottky contribution to the heat capacity (Figure 3.15) strongly suggests that only the ground state (M_s = ±4) is populated in the temperature range of the phase transition, and thus contributes minimally, at low temperatures, to the magnitude of the observed peak in the heat capacity.

The Schottky contribution and internal energy (U) were obtained by full-matrix diagonalization of magnetic susceptibility data employing the Hamiltonian in Equation 3.1, where the parameters g = 2.2, D = -7.6 K and J = 5.08 K were obtained through oriented single-crystal high-frequency electron paramagnetic resonance single-ion studies, where diamagnetic Zn_4^{dmb} crystals were doped with very small amounts of Ni^{II} ions.[44] The resulting eigen values were evaluated employing Equation 3.2, where $E(S_T)$ are the eigen energies of the system, k_B is the Boltzman factor, and T is the absolute temperature.

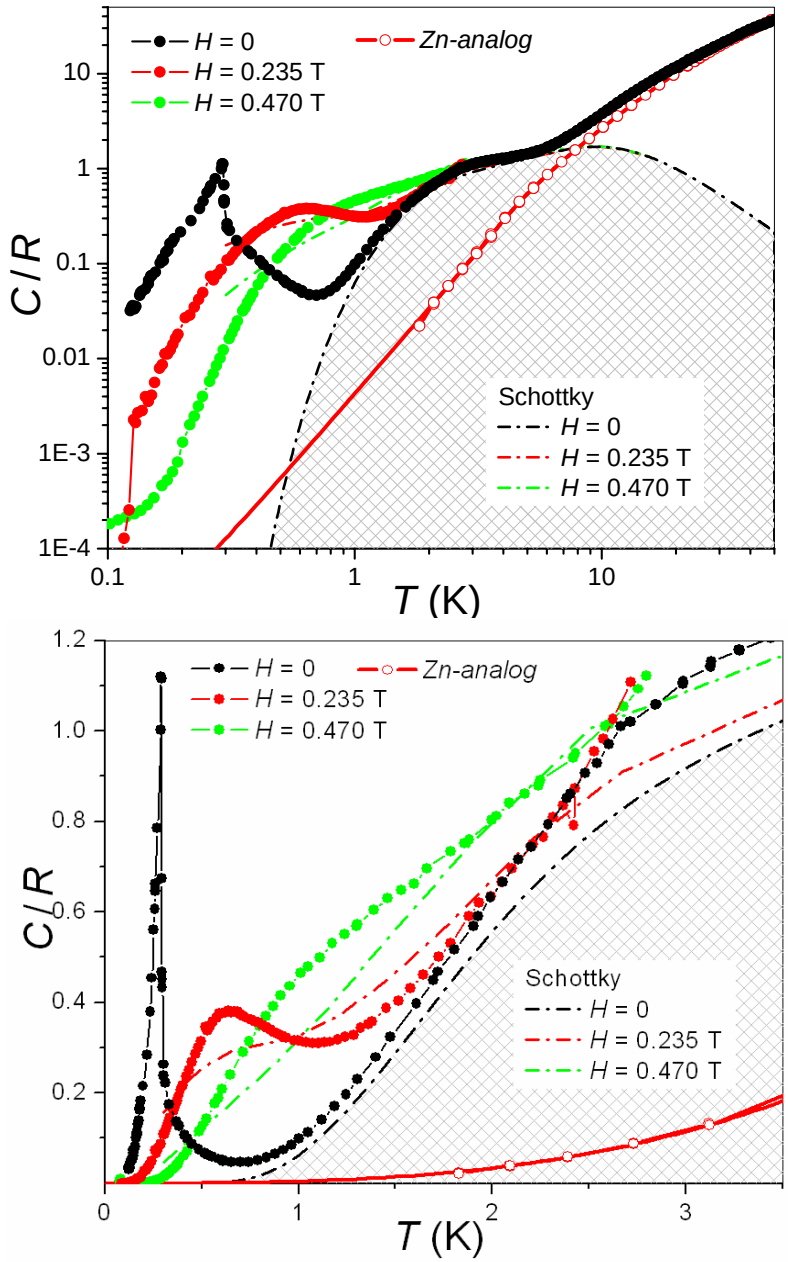

Figure 3.13. Logarithmic scale top and linear scale bottom: 1)Heat capacity for a crystalline sample of **[Ni(hmp)(dmb)Cl]$_4$** (Ni_4^{dmb}) collected down to millikelvin temperatures with applied fields of 0T, 0.235T and 0.470 T. 2) Heat capacity for a crystalline sample of **[Zn(hmp)(dmb)Cl]$_4$** (Zn_4^{dmb}) collected down to millikelvin temperatures with an applied field of 0T (red circles). 3) Calculated Schottky contribution from full-matrix diagonalization of the single-ion Hamiltonian. Dashed lines correspond to theoretical simulations based on Hamiltonian parameters.

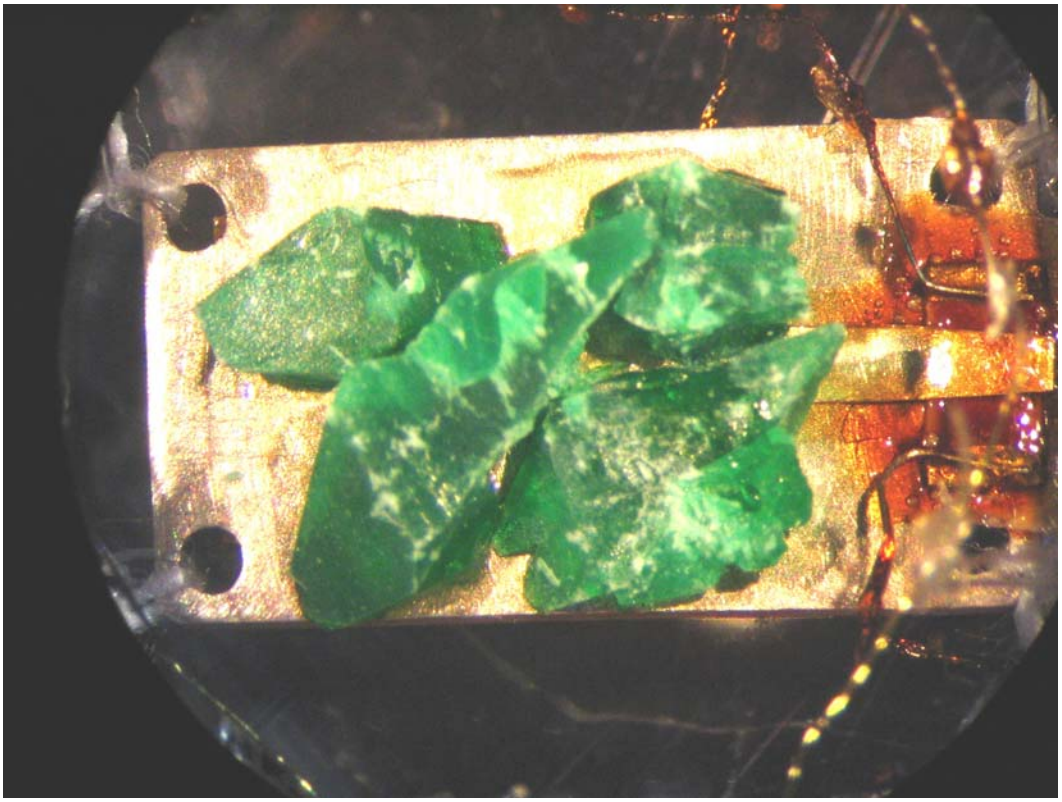

Figure 3.14. Crystals of complex **3C** on the platform used for low-temperature heat capacity measurements.

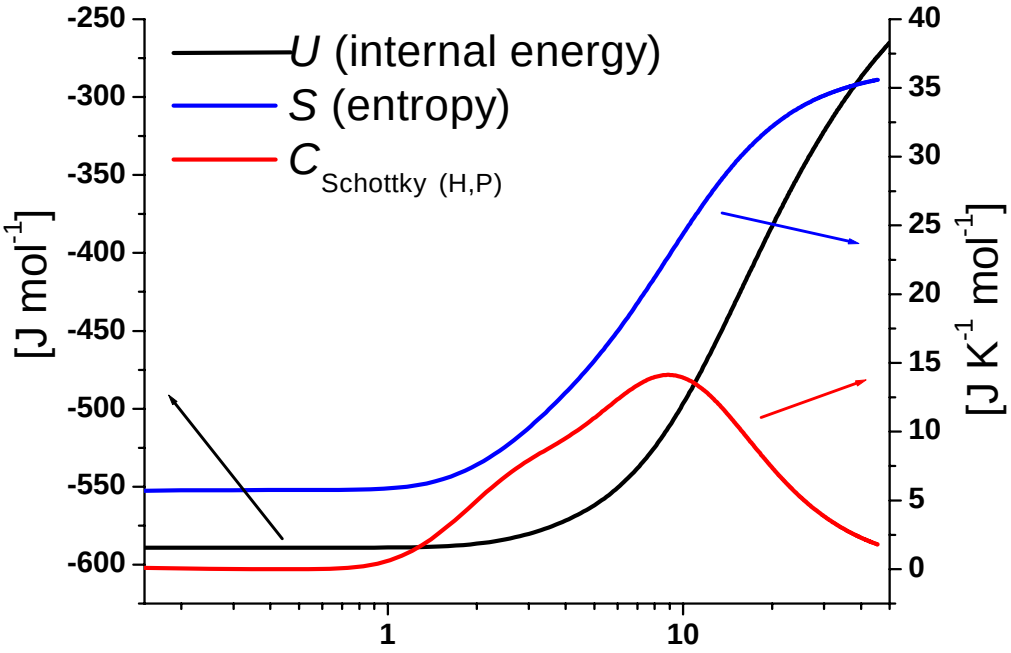

Figure 3.15. Internal energy (U), Entropy (S) and Schottky contributions calculated from full-matrix diagonalization of the single-ion Hamiltonian.

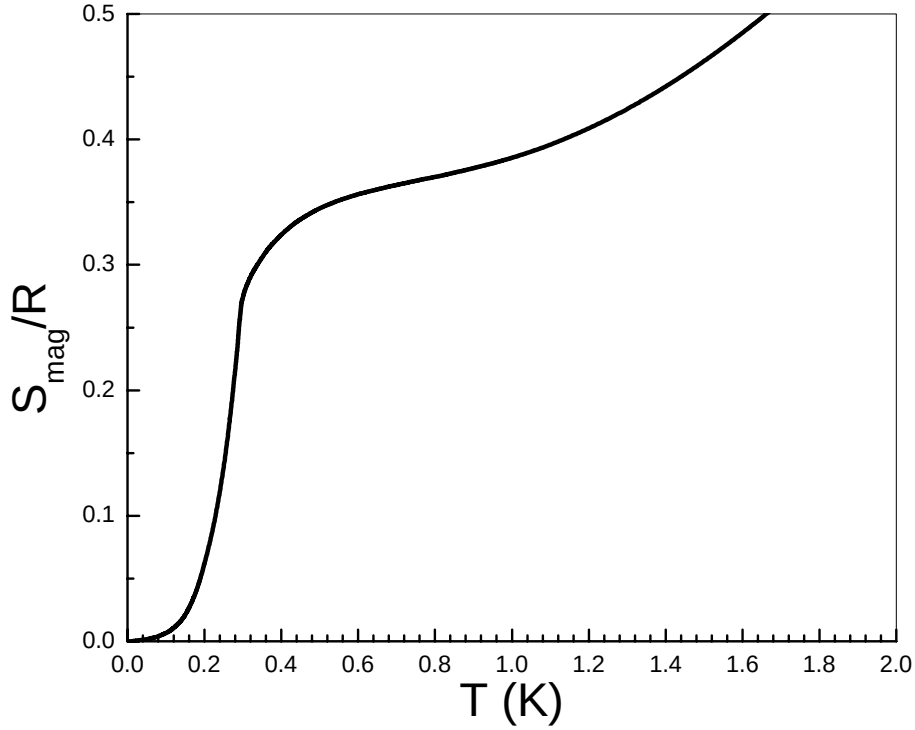

Figure 3.16. Magnetic entropy gain for **Ni(hmp)(dmb)Cl]$_4$** (Ni_4^{dmb}) was evaluated by integrating $H = 0$ C_P data with respect to ln T.

The lattice contribution to the heat capacity was calculated by subtraction of heat capacity data collected on the analogous diamagnetic Zn_4^{dmb} (**3E**) (Figures 3.9 and 3.13). The number of available phonon modes is significantly quenched, and thus, the lattice contribution to the overall heat capacity is negligible at very low temperatures.

$$\hat{H} = \sum_i \sum_{j>i} J_{ij}\hat{s}_i\hat{s}_j + \sum_i \left[d_i\hat{s}_{zi}^2 + e(s_{xi}^2 - s_{yi}^2) + \mu_B\vec{B}\cdot\vec{\vec{g}}_i\cdot\hat{s}_i \right] \quad \textbf{(3.1)}$$

$$C_{(H,P)} = \frac{\partial U}{\partial T}, \qquad U = \frac{\sum E(S_T) * e^{-(E(S_T)/k_BT)}}{\sum e^{-(E(S_T)/k_BT)}} \quad \textbf{(3.2)}$$

With an applied field of H = 0.25 T (Figure 3.13, red trace) the heat capacity peak shifts to higher temperature (0.1 K-1.3 K) and becomes broader, indicating that the applied field is of a larger magnitude than the ordering energy. The broad peak is not a shift of the ordering temperature of the peak, but is due to field-modulated short-range magnetic ordering. When the applied field reaches H = 0.5T, the phase transition in the heat capacity wholly disappears and only contributions from short-range ordering are present (Figure 3.13, green trace)

The magnetic entropy gain was evaluated by integrating H = 0 C_P data with respect to ln T below T_c (0 to 1.7 K)(Figure 3.16). The resulting calculation yielded a value of ~0.38R which is less than the expected value of R ln (2S + 1) = 0.69R for an S = 4 spin system in its M_s = ±4 ground state (R = gas constant). The small value of ΔS = 0.38R arises due to the low coordination number (z = 4) of the crystal diamond

structure, and spin frustration characteristic of dipolar Ising systems, which in conjunction, prevent easy attainment of ferromagnetic 3D long-range ordering.

Preliminary low-temperature heat capacity for Ni_4^{MeOH} (**3A**) and Ni_4^{EtOH} (**3B**) are presented in Figures 3.17 and 3.18, plotted as molar heat capacity versus absolute temperature. The data for Ni_4^{MeOH} (**3A**) shows a sharp λ-peak at ~1200mK which is in general agreement with ac magnetic susceptibility experiments previously reported.[5] With the application of a 0.1T magnetic field, the peak shifts slightly to lower temperature. With an applied field of 1T the transition is totally suppressed as is seen in the Ni_4^{dmb} (**3C**) complex. Plotted in conjunction with the molar heat capacity for the Ni_4^{MeOH} (**3A**) complex are the Zn_4^{MeOH} (**3D**) heat capacity data. In the temperature range measured, the lattice contribution to the overall heat capacity is essentially zero (blue trace in Figure 3.17 and purple trace Figure 3.18). A sharp peak is also evident in the plot of molar heat capacity for the Ni_4^{EtOH} (**3B**) complex at ~900mK. Though the heats of formation are slightly different for the MeOH and EtOH complexes, the molar heat capacity for Zn_4^{MeOH} (**3D**) is included to show the approximate lattice contribution to the overall heat capacity. As noted in the the synthesis section, synthesis of the Zn_4 analogue was achieved. However, the Ni_4^{MeOH} (**3A**) and Ni_4^{EtOH} (**3B**) complexes crystallize in the same tetragonal I42d space group with two symmetry independent molecules in the unit cell. Furthermore, the basic lattice structure in terms of solvate molecules is very similar. Thus, it is reasonable to assume that the lattice heat capacity of the two Zn_4 complexes would be similar. The Ni_4^{EtOH} (**3B**) shows little field dependence with applied fields <0.3T, but application of a 1T field exhibits an increase

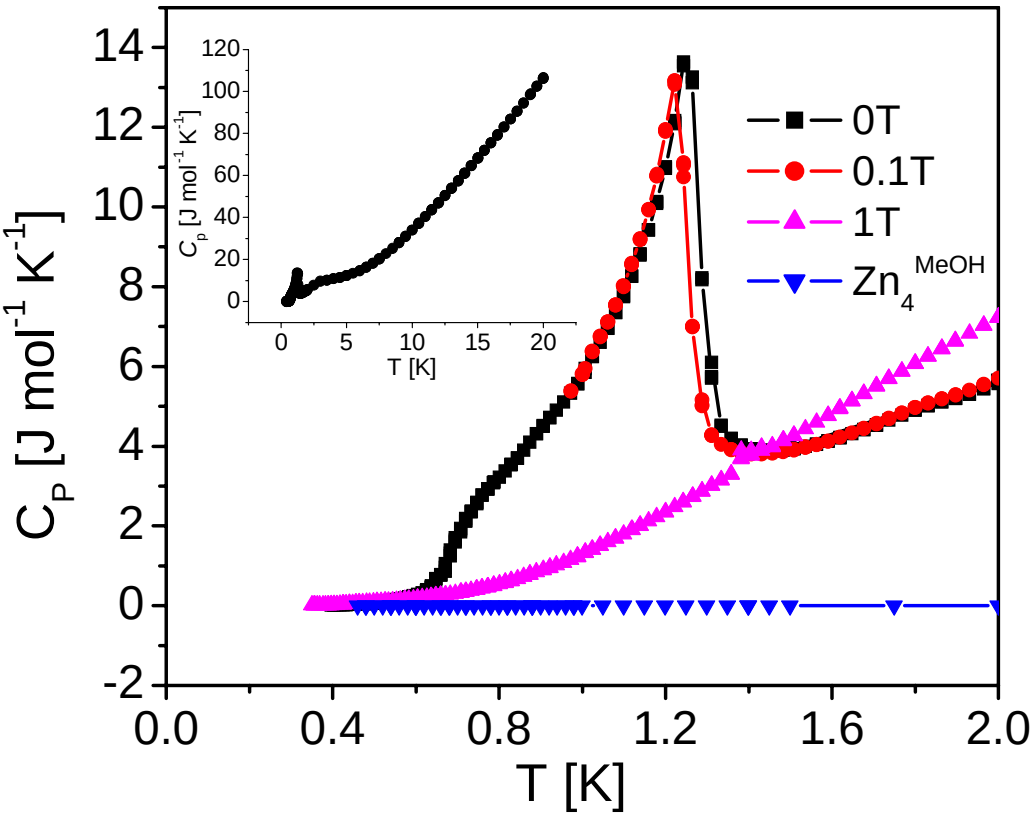

Figure 3.17. Heat capacity data for **[Ni(hmp)(MeOH)Cl]$_4$** (Ni_4^{MeOH} (**3A**)) collected between 0.4-2.0K, with applied fields of 0, 0.1 and 1T. Inset shows Ni_4^{MeOH} (**3A**) Cp data from 20-0.4K in zero applied field.

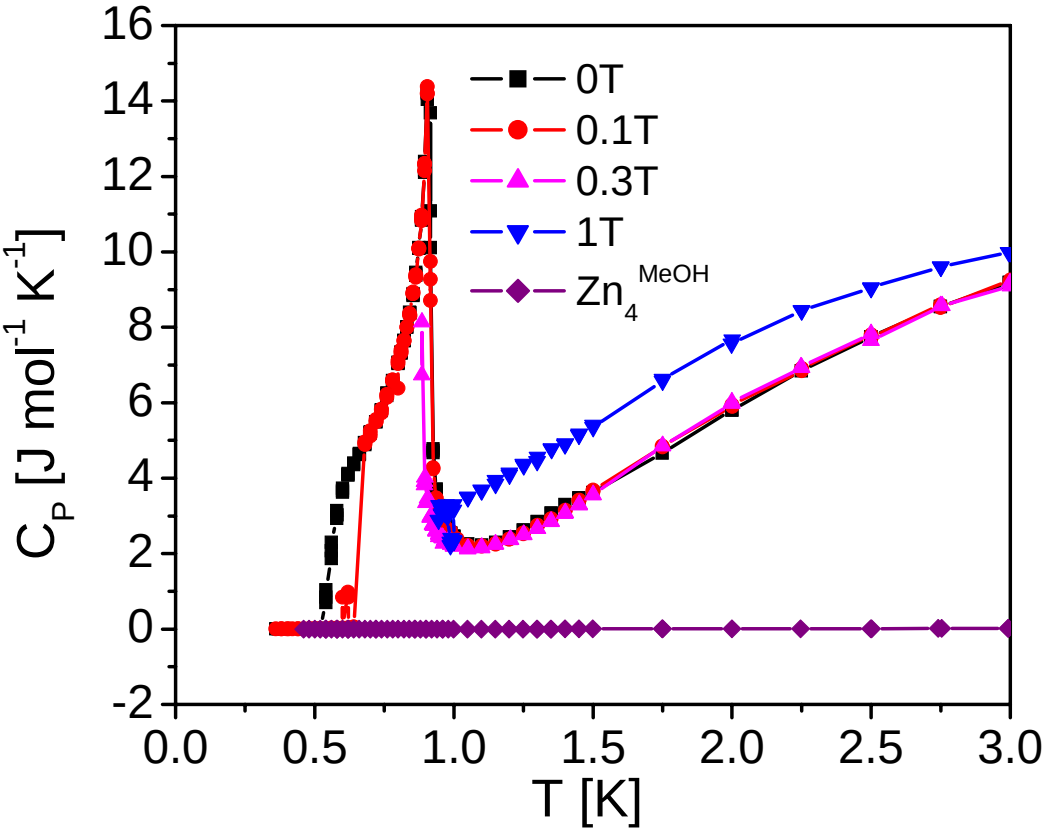

Figure 3.18. Heat capacity data for **[Ni(hmp)(EtOH)Cl]$_4$** (**Ni_4^{EtOH}** (**3B**)) collected between 0.4-3.0K, with applied fields of 0, 0.01, 0.3 and 1T.

in *C*p above the critical temperature (T_c = ~900mK) that is most likely attributable to short-range ordering.

3.3.4 Single-Crystal Field-Cooled, Zero-Field Magnetization

In order to study more closely the field effects on the ferromagnetic ordering in Ni_4^{dmb} (**3C**), oriented single-crystal magnetization measurements were performed. Zero-field cooled (ZFC) and field-cooled (FC) magnetization curves collected with applied magnetic fields of 15-2000Oe Oe along the easy magnetic axis are presented in Figure 3.19. The sample was cooled from 1K down to 20mK in the absence of various applied fields (ZFC). The temperature is then raised back up to 1K again at a rate of ~3 K/min (continuous lines in Figure 3.19). Maintaining the same applied field, the temperature is then cycled back down to 20mK (FC), while the magnetization is monitored (dashed lines in Figure 3.19). In the measurement obtained with an applied magnetic field of H = 15 Oe (black curves in Figure 3.19), the results reveal that immediately after the application of the applied field, the sample reaches a finite magnetization value that remains constant until the temperature reaches a critical value of T_c ~300 mK. At higher temperatures the magnetization decreases inversely proportional to the temperature, $M = f(1/T)$ (superparamagnetic regime). This behavior is indicative of ferromagnetic ordering, and the transition temperature of ~300 mK is in very good agreement with the specific heat measurements and previous AC and DC magnetization measurements.[5,23,44] We associate the observed hysteretic behavior between the ZFC and FC measurements to different distributions of dipolar fields felt by the molecules during the two processes. The distribution is broader in the FC process due to

temperature mediated disorder within the system. As a consequence, fewer molecules lie within the tunneling window, and thus, the tunneling-mediated ordering process is lengthened. Conversely, in the ZFC case, the individual magnetic moments are fully polarized as the system approaches the transition temperature. The ferromagnetic ordering transition is broadened and shifted to lower temperatures by the application of successively larger longitudinal magnetic fields, and is completely eliminated in fields greater than ~170Oe, when the Zeeman interaction energy becomes greater than the intermolecular coupling energy. This is clearly observed in Figure 3.20, where the temperature derivatives of the ZFC and FC magnetization curves are presented. The inset shows the behavior of the transition temperature as a function of the applied field. The plateau below ~170Oe represents the critical temperature of the ferromagnetic transition (~300 mK). Interestingly, the ferromagnetic ordering in this regime is promoted by the fast quantum tunneling relaxation rate exhibited by Ni_4^{dmb} (**3C**).[5] Note that in an ordered system, coupled molecules are expected to tunnel simultaneously. The statistical probability of this occurring is much less than for a single-molecule tunneling due to greater *inertia*, and thus, should drastically reduce tunneling relaxation rates. However, the tunneling rates[5] in this system seem relatively unaffected by the ferromagnetic ordering event.

Figure 3.21 shows the universal scaling of the data from Figure 3.19, plotted as a function of *H/T*. The data collapses into a single curve when the ordering is suppressed by both temperature (T>300mK) and field (H>150Oe) considerations. Furthermore, Figure 3.22 shows that curves over 150Oe do not collapse at the top, because the magnetization curve at low-temperatures is dominated by phonon-

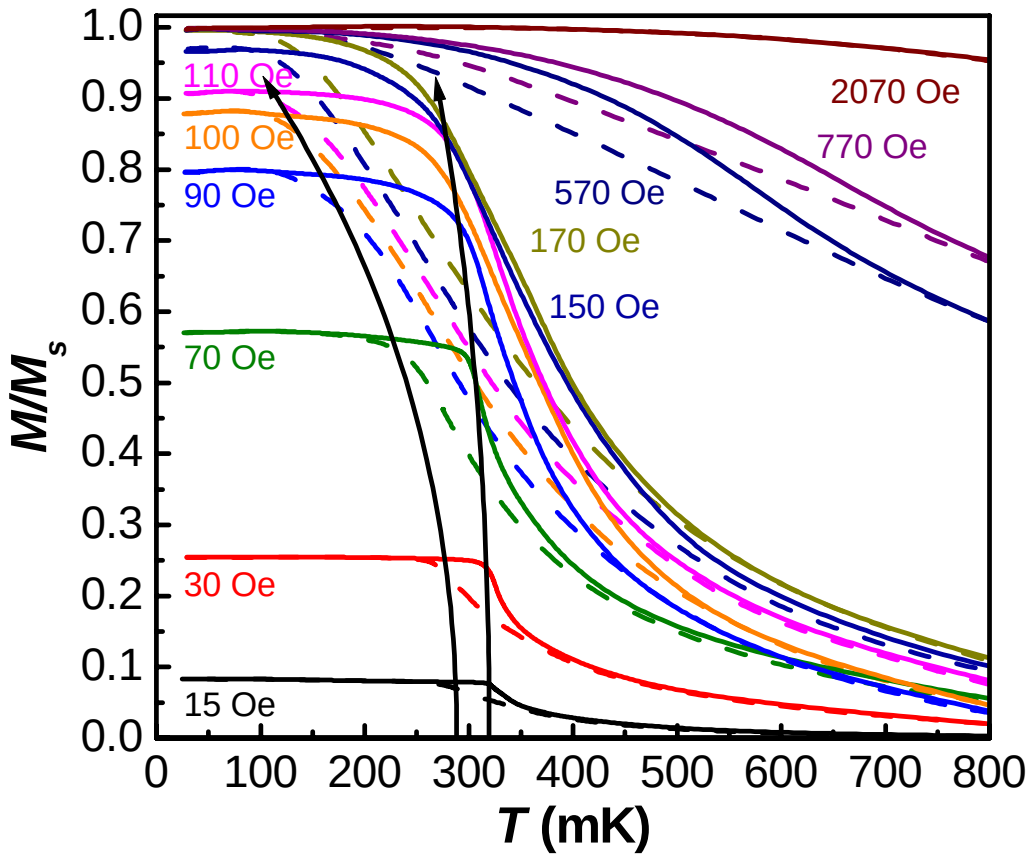

Figure 3.19. Zero-field cooled (continuous lines) and FC (dashed lines) magnetization curves for different magnetic field values (from 15 Oe to 2070 Oe) in the temperature range 20-800 mK. The sharp transition at ~300 mK corresponds to ferromagnetic coupling due to intermolecular exchange interactions.

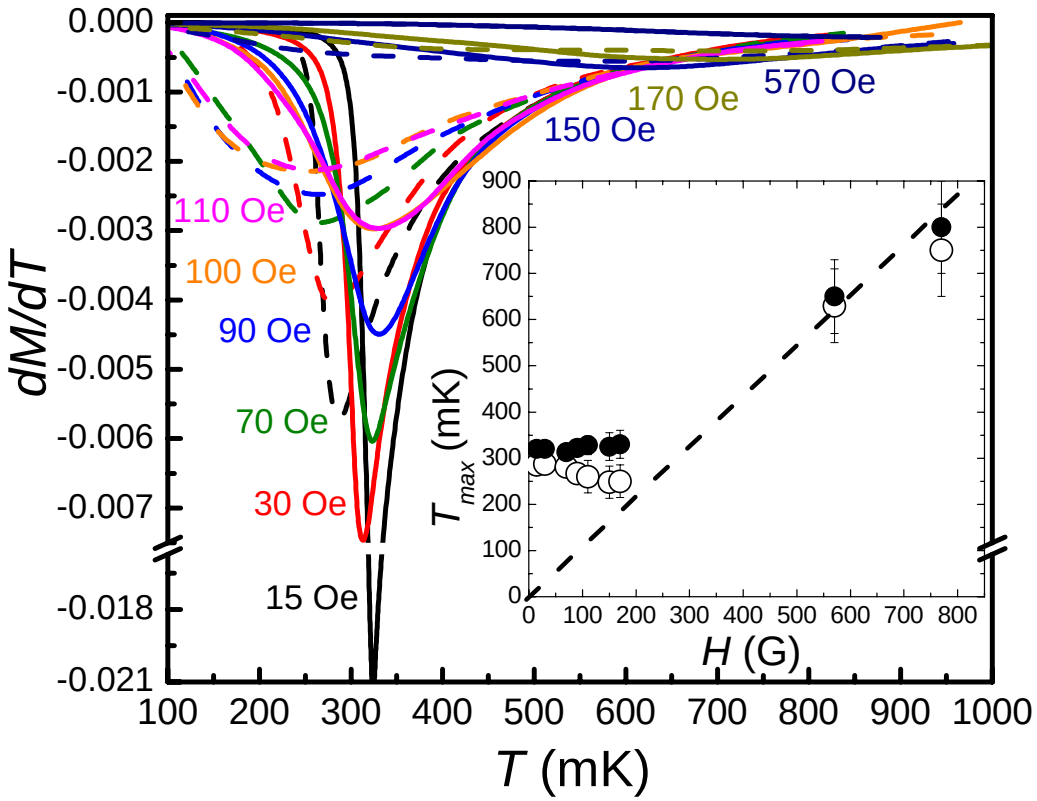

Figure 3.20. Derivatives of the ZFC (continues lines) and FC (dashed lines) magnetization curves presented in Figure 3.17 for Ni_4^{dmb}. The inset shows the behavior of the temperature of the peak as a function of the applied field. The plateau below 170 Oe is associated with a ferromagnetic ordering of the molecular spins within the sample below ~300 mK.

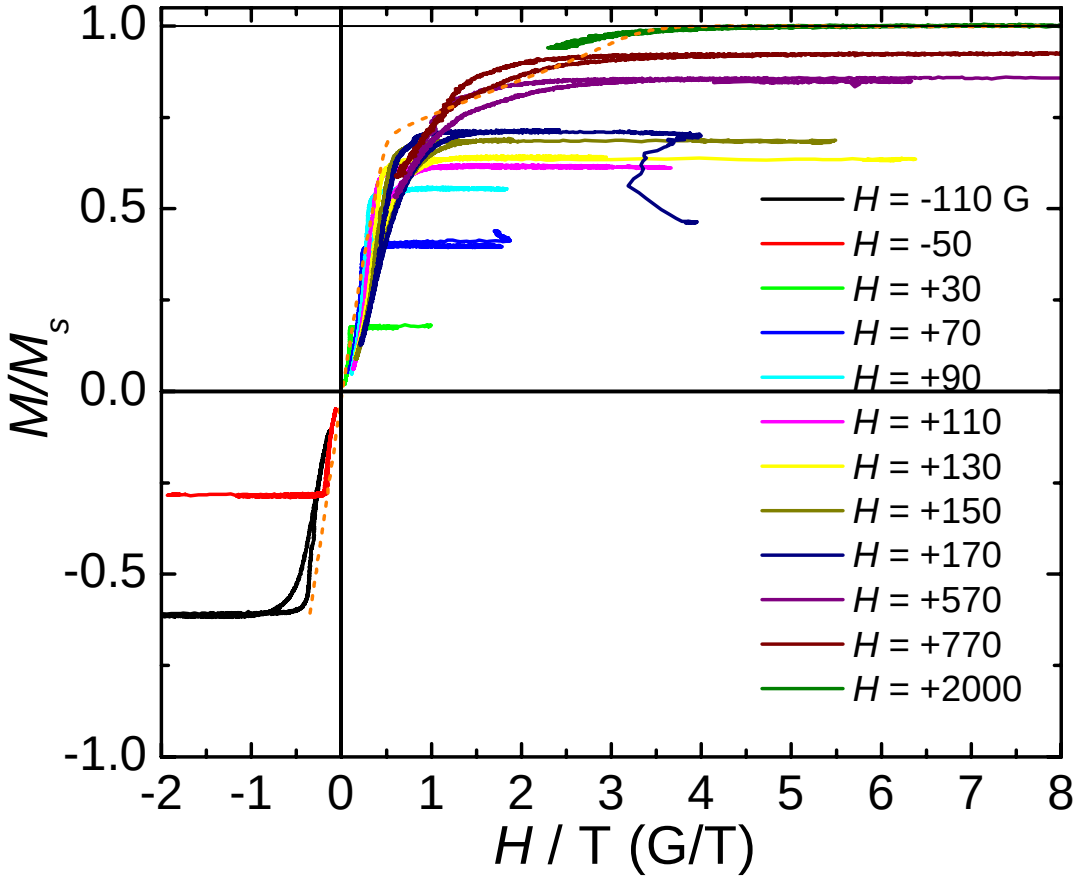

Figure 3.21. Representation of the data presented in Figure 3.18 plotted as magnetization versus *H/T*.

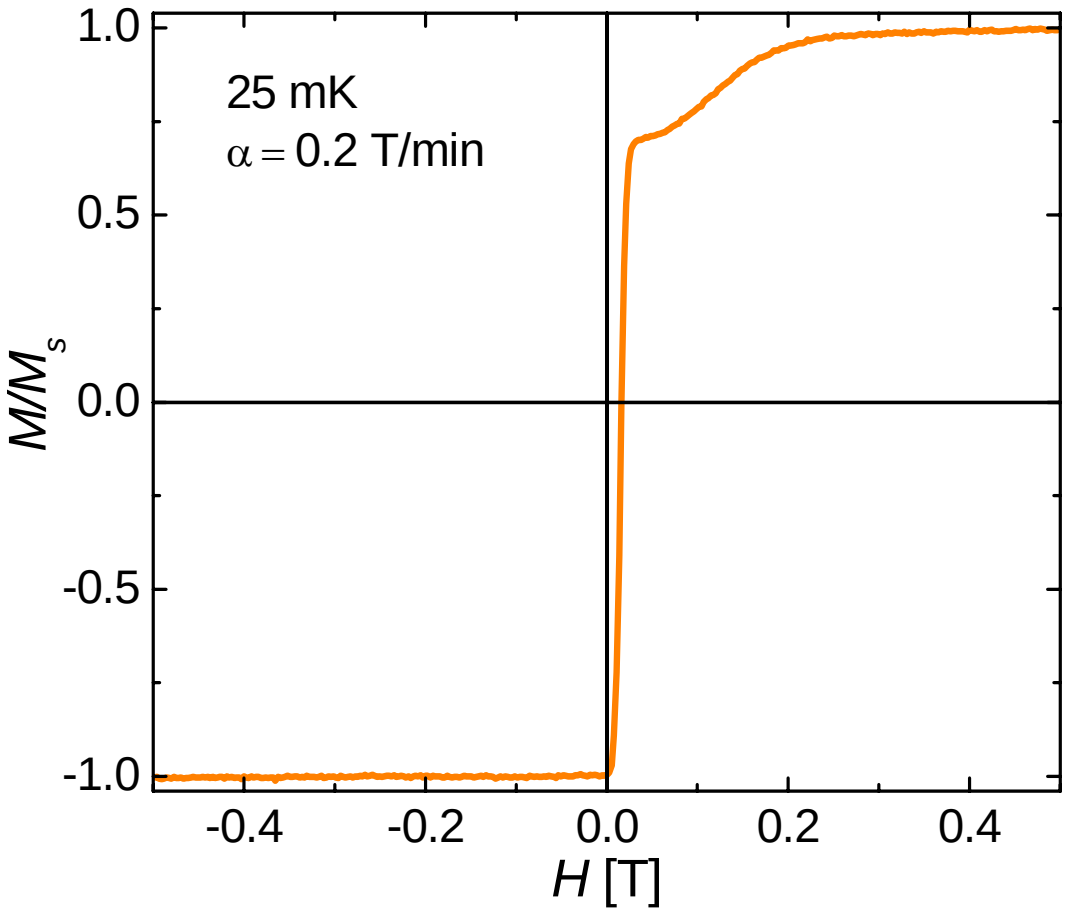

Figure 3.22. Magnetization versus field curve collected at 25mK with an applied sweep rate of 0.2T/minute. The anomaly is due to phonon-bottle neck processes at low temperatures.

bottleneck (see orange lines in Figures 3.21 and 3.22). The anomalies at low temperatures in Figure 3.21 are a result of experimental thermal fluctuations below 25mK and are generated by the experimental apparatus not the sample.

The single-molecule tunneling window is principally governed by the magnitude of the tunnel splitting associated with the quantum superposition between opposite spin projections ("spin-up" and "spin-down"), and can be modulated by application of a magnetic field. The energy associated with tunneling windows for individual molecules can be significantly affected by intermolecular interactions, thus, decreasing the number of molecules available for tunneling. This should lead to a significant reduction of relaxation rates. However, phonon-mediated tunneling transitions between the ground spin states of the molecules could account for the elevated tunneling rates observed in this ordered system. This could occur even if molecules are out of the tunneling window due to exchange-bias effects. *Direct* phonon-mediated transitions between the $M_s = \pm 4$ states will have a high probability in the Ni_4 system due to its low spin ($S = 4$) and intrinsic fourth-order transverse anisotropy (i.e. $S_+^4 + S_-^4$), which is imposed by tetragonal crystal symmetry, and facilitates phonon transitions between M_s states differing by multiples of ±4. In addition, when the wavelength of the generated phonons is larger than the separation between molecules, molecules can simultaneously relax accompanied by a coherent emission of phonons.[45] This may explain the high relaxation rates observed in this system. Note, the observation of an *increase* in relaxation rates due to *collective* photon-mediated processes has been previously suggested.[46,47]

Figure 3.23 presents magnetization versus field hysteresis loops for Ni_4^{dmb} (**3C**) collected at 190mK with applied transverse magnetic fields between 0 and 3T. The

coercive field, which is directly related to magnitude of the exchange in the long-range ferromagnetic ordering process, decreases systematically with the application of larger transverse applied magnetic field strength. At low temperatures, with a field applied along the easy-axis or *z*-axis, a coercive field of ~150 Gauss is sufficient to suppress the magnetic ordering in the system. However, with application of a transverse field, a field strength of >1.25T is required to overcome the magnetic ordering.

Figure 3.24 depicts the behavior of the coercive field as a function of the transverse field for temperatures between 30 and 1000mK. The inset shows the coercive field at zero transverse field as a function of temperature (note the transition at 300mK). For applied transverse magnetic fields greater than 1.25-1.5T, there is no ordering evident even at the lowest temperature measured (30mK). Therefore, it is concluded that a transverse field of 1.5 T, which modulates the magnitude of the tunnel splitting, is essentially equivalent to an applied longitudinal field of 150Gauss. The transverse field increases the tunnel splitting potentially allowing a greater number of molecules to be within the energy gap of the tunneling window, thus, a decrease in the coercive field strength is needed to induce tunneling.

In contrast to the FC-ZFC data for Ni_4^{dmb} (**3C**), the data for Ni_4^{MeOH} (**3A**) are quite different (preliminary data, Figure 3.25). In the Ni_4^{dmb} (**3C**) case the FC and ZFC magnetization curves superimpose below the ordering temperature. However, it is clearly evident that the magnetization maximum for the FC data is significantly greater than for the ZFC data. The ordering process for the Ni_4^{dmb} (**3C**) complex reaches a field and temperature dependent saturation below T_c (magnetization becomes constant).

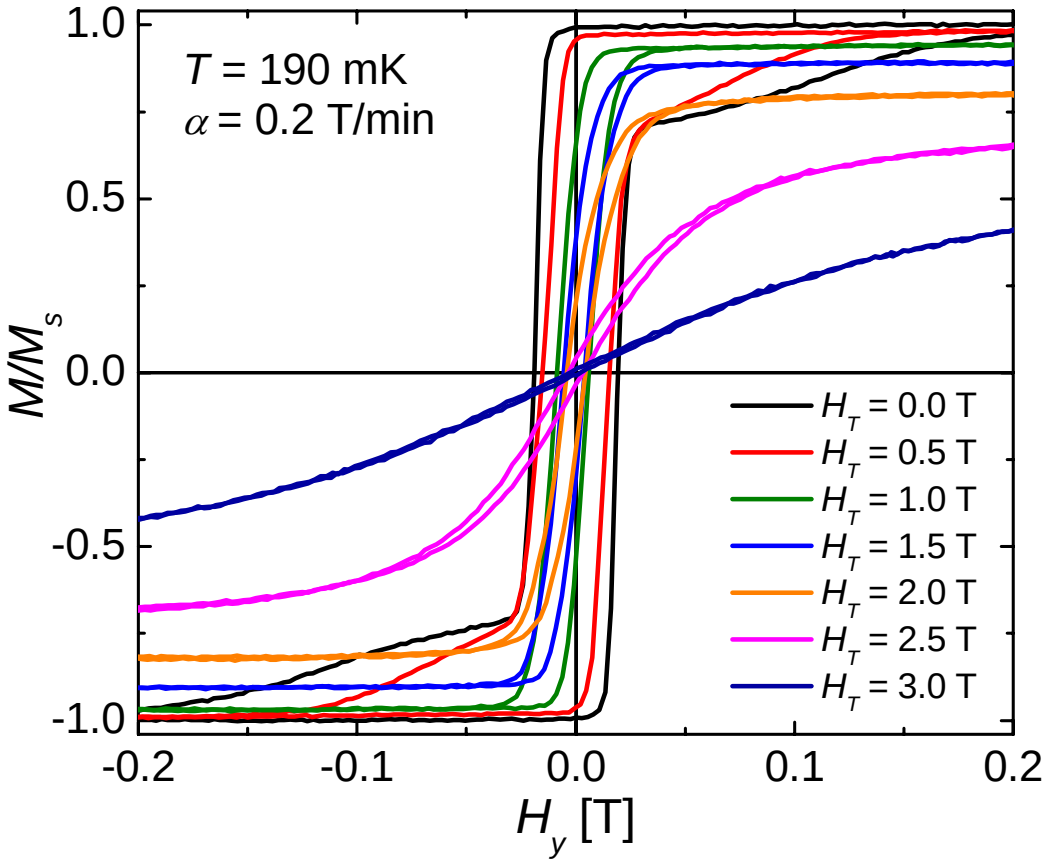

Figure 3.23. Magnetization versus field hysteresis loops for **Ni(hmp)(dmb)Cl]$_4$** (Ni_4^{dmb}) collected at 190mK, with applied transverse fields of 0T to 3T. The applied sweep rate is 0.2T per minute.

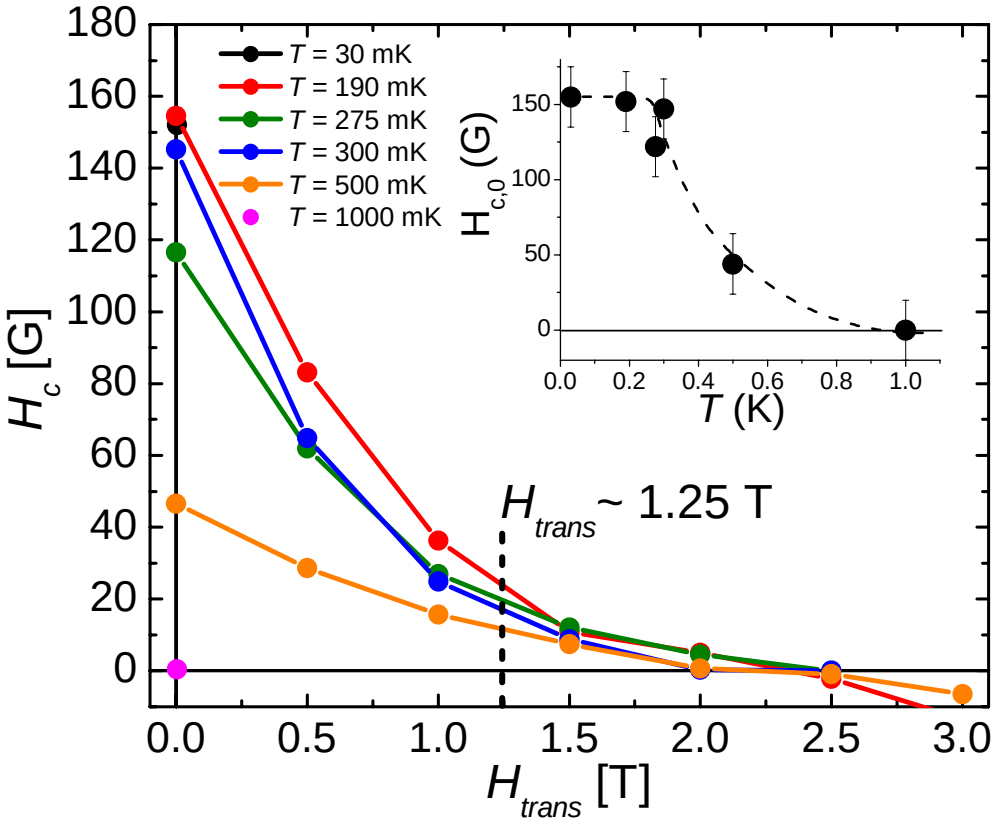

Figure 3.24. Plot shows the behavior of the coercive field as a function of the transverse applied magnetic field for temperatures between 30 and 1000mK. The inset shows the coercive field at zero applied transverse field as a function of temperature.

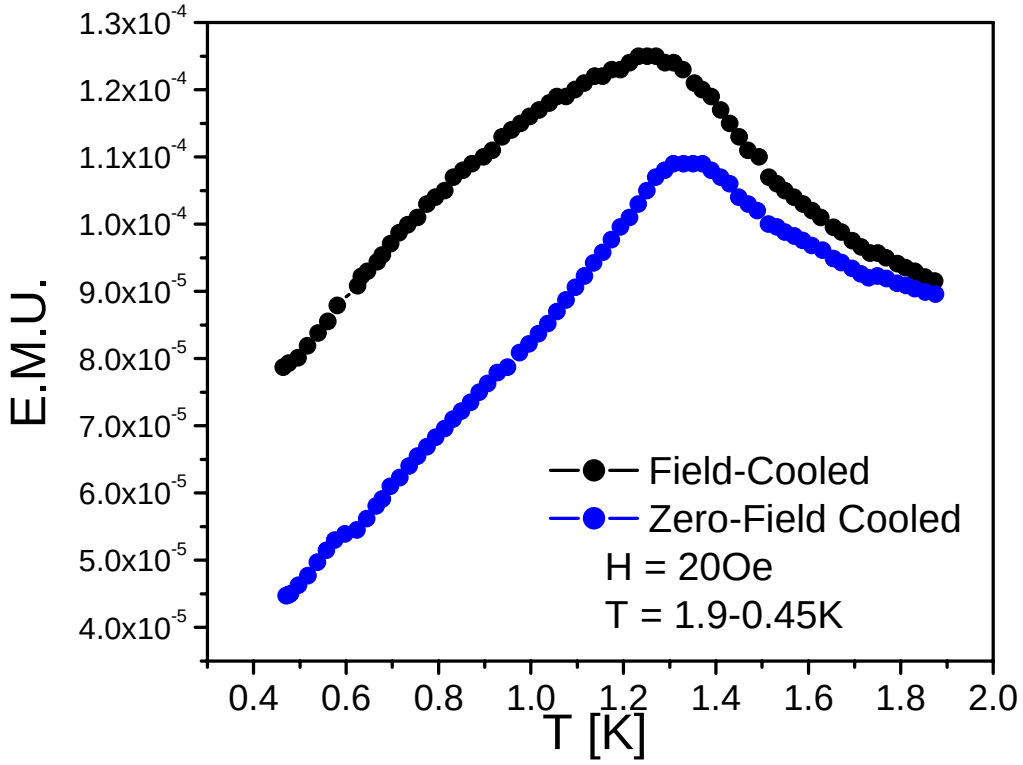

Figure 3.25. Field-cooled zero-field cooled (FC-ZFC) data for **[Zn(hmp)(MeOH)Cl]$_4$** (**Zn_4^{MeOH}** (**3D**)).

Conversely, both the FC and ZFC traces in Figure 3.25 exhibit a significant drop in magnetization below T_c which is likely due to the onset on antiferromagnetic ordering. The assumption that antiferromagnetic interactions are present is further substantiated by magnetization hysteresis data. The hysteresis loops for Ni_4^{MeOH} (**3A**) and Ni_4^{EtOH} (**3B**) both exhibit a significant negative exchange-bias (-0.33T and -0.28T, respectively), whereas the Ni_4^{dmb} (**3C**) complex exhibits a small positive exchange-bias (+0.012T). In a ferromagnetic ordering event one would expect that a relatively steady value for the susceptibility will persist below the ordering temperature, and if antiferromagnetic interactions are dominant below the ordering temperature, the magnetization should show an overall decrease. Field dependent studies and detailed heat capacity data are currently being collected on the Ni_4^{MeOH} (**3A)** Ni_4^{EtOH} (**3B)** complexes to conclude the nature of the low temperature behavior of these interesting complexes, and will be published at a later date.

3.4 Conclusion

The Ni_4^{dmb} (**3C**) complex has proven be a benchmark system, and has been paramount to the study of SMMs due to its unique physical properties. To our knowledge there are no other SMMs that undergo long-range ferromagnetic ordering at low temperatures while experiencing fast quantum tunneling. Furthermore, the long-range ordering appears to have little effect on tunneling rates in this system. As stated above, magnetic ordering in conjunction with fast magnetization tunneling is anti-intuitive as tunneling probability is very low for the simultaneous tunneling of molecules within the crystal lattice. An explanation is that the molecules behave as

single domain particles within the crystal lattice, and that the thickness of domain walls is shorter than the distance between Ni_4 molecules. In this manner, a dynamic domain structure can exist where correlation between single domains can take place (ferromagnetically or antiferromagnetically) but molecules that lie along the domain walls continue to tunnel. In an attempt to explain the observed physical properties of this system, we have initialized more in depth single-crystal magnetization studies, of the Ni_4 series of molecules to probe the field and temperature dependence of the magnetic ordering and magnetization tunneling rates. It has been shown that changing peripheral ligands in the Ni_4 series of molecules modulates ordering temperatures and the nature of the ordering (antiferromagnetic or ferromagnetic), and has a significant effect on tunneling rates. It is our hope that in studying this interesting series of Ni_4 SMMs, we may shed new light on the study of SMMs and the quantum behavior exhibited by these interesting systems.

Chapter 3, in part, is a reprint: Beedle, C. C., Ho, P-C., Sayles, T., Hamilton, J. J., del Barco, E., Nakano, M., O'Brien, J., Heroux, K. J., Maple, M. B., Hendrickson, D. N., Ferromagnetic Ordering and Simultaneous Fast Magnetization Tunneling in a Ni_4 Single Molecule Magnet, *Inorganic Chemistry*, **2010**, *49* (13), 5780–5782. The dissertation author is the primary investigator and author of this material.

3.5 References

(1) Aubin, S. M. J.; Dilley, N. R.; Pardi, L.; Krzystek, J.; Wemple, M. W.; Brunel, L. C.; Maple, M. B.; Christou, G.; Hendrickson, D. N. *Journal of the American Chemical Society* **1998**, *120*, 4991-5004.

(2) Hendrickson, D. N.; Christou, G.; Ishimoto, H.; Yoo, J.; Brechin, E. K.; Yamaguchi, A.; Rumberger, E. M.; Aubin, S. M. J.; Sun, Z. M.; Aromi, G. *Polyhedron* **2001**, *20*, 1479-1488.

(3) Sangregorio, C.; Ohm, T.; Paulsen, C.; Sessoli, R.; Gatteschi, D. *Physical Review Letters* **1997**, *78*, 4645-4648.

(4) Wernsdorfer, W.; Allaga-Alcalde, N.; Hendrickson, D. N.; Christou, G. *Nature* **2002**, *416*, 406-409.

(5) Yang, E. C.; Wernsdorfer, W.; Zakharov, L. N.; Karaki, Y.; Yamaguchi, A.; Isidro, R. M.; Lu, G. D.; Wilson, S. A.; Rheingold, A. L.; Ishimoto, H.; Hendrickson, D. N. *Inorganic Chemistry* **2006**, *45*, 529-546.

(6) Wernsdorfer, W.; Bhaduri, S.; Tiron, R.; Hendrickson, D. N.; Christou, G. *Physical Review Letters* **2002**, *89*, 197201.

(7) Sessoli, R.; Gatteschi, D.; Caneschi, A.; Novak, M. A. *Nature* **1993**, *365*, 141-143.

(8) Sessoli, R.; Tsai, H. L.; Schake, A. R.; Wang, S. Y.; Vincent, J. B.; Folting, K.; Gatteschi, D.; Christou, G.; Hendrickson, D. N. *Journal of the American Chemical Society* **1993**, *115*, 1804-1816.

(9) Gatteschi, D.; Sessoli, R. *Angewandte Chemie-International Edition* **2003**, *42*, 268-297.

(10) Christou, G.; Gatteschi, D.; Hendrickson, D. N.; Sessoli, R. *Mrs Bulletin* **2000**, *25*, 66-71.

(11) Leuenberger, M. N.; Loss, D. *Physica E* **2001**, *10*, 452-457.

(12) Meier, F.; Levy, J.; Loss, D. *Physical Review B* **2003**, *68*, (13).

(13) Meier, F.; Levy, J.; Loss, D. *Physical Review Letters* **2003**, *90*.

(14) Schliemann, J.; Khaetskii, A.; Loss, D. *Journal of Physics-Condensed Matter* **2003**, *15*, R1809-R1833.

(15) Tejada, J.; Chudnovsky, E. M.; del Barco, E.; Hernandez, J. M.; Spiller, T. P. *Nanotechnology* **2001**, *12*, 181-186.

(16) Rocha, A. R.; GarcÃ-a-SuÃ¡rez, V. c. M.; Bailey, S. W.; Lambert, C. J.; Ferrer, J.; Sanvito, S. *Nature Materials* **2005**, *4*, 335-339.

(17) Yamaguchi, A.; Kusumi, N.; Ishimoto, H.; Mitamura, H.; Goto, T.; Mori, N.; Nakano, M.; Awaga, K.; Yoo, J.; Hendrickson, D. N.; Christou, G. *Journal of the Physical Society of Japan* **2002**, *71*, 414-417.

(18) Affronte, M.; Lasjaunias, J. C.; Wernsdorfer, W.; Sessoli, R.; Gatteschi, D.; Heath, S. L.; Fort, A.; Rettori, A. *Physical Review B* **2002**, *66*.

(19) Affronte, M.; Sessoli, R.; Gatteschi, D.; Wernsdorfer, W.; Lasjaunias, J. C.; Heath, S. L.; Powell, A. K.; Fort, A.; Rettori, A. *Journal of Physics and Chemistry of Solids* **2004**, *65*, 745-748.

(20) Feng, P. L.; Beedle, C. C.; Koo, C.; Lawrence, J.; Hill, S.; Hendrickson, D. N. *Inorganica Chimica Acta* **2008**, *361*, 3465-3480.

(21) Wilson, A.; Lawrence, J.; Yang, E. C.; Nakano, M.; Hendrickson, D. N.; Hill, S. *Physical Review B (Condensed Matter and Materials Physics)* **2006**, *74*, 140403.

(22) Wilson, A.; Yang, E. C.; Hendrickson, D. N.; Hill, S. *Polyhedron* **2007**, *26*, 2065-2068.

(23) Yang, E. C.; Wernsdorfer, W.; Hill, S.; Edwards, R. S.; Nakano, M.; Maccagnano, S.; Zakharov, L. N.; Rheingold, A. L.; Christou, G.; Hendrickson, D. N. *Polyhedron* **2003**, *22*, 1727-1733.

(24) Beedle, C. C.; Henderson, J. J.; Ho, P.-C.; Sayles, T.; Nakano, M.; O'Brien, J. R.; Heroux, K. J.; del Barco, E.; Maple, M. B.; Hendrickson, D. N. *Inorganic Chemistry* **2010**, *49*, 5780-5782.

(25) del Barco, E.; Kent, A. D.; Hill, S.; North, J. M.; Dalal, N.; Rumberger, E. M.; Hendrickson, D. N.; Chakov, N. E.; Christou, G. *Condensed Matter* **2004**, *cond-mat/0404390*.

(26) del Barco, E.; Kent, A. D.; Rumberger, E. M.; Hendrickson, D. N.; Christou, G. *Europhysics Letters* **2002**, *60*, 768-774.

(27) Hill, S.; Anderson, N.; Wilson, A.; Takahashi, S.; Petukhov, K.; Chakov, N. E.; Murugesu, M.; North, J. M.; Barco, E. d.; Kent, A. D.; Dalal, N. S.; Christou, G. *Polyhedron* **2005**, *24*, 2284-2292.

(28) Hill, S.; Edwards, R. S.; North, J. M.; Park, K.; Dalal, N. S. *Polyhedron* **2003**, *22*, 1889-1896.

(29) Lawrence, J.; Yang, E.-C.; Edwards, R.; Olmstead, M. M.; Ramsey, C.; Dalal, N. S.; Gantzel, P. K.; Hill, S.; Hendrickson, D. N. *Inorganic Chemistry* **2008**, *47*, 1965-1974.

(30) Parks, B.; Loomis, J.; Rumberger, E.; Yang, E. C.; Hendrickson, D. N.; Christou, G. *Journal of Applied Physics* **2002**, *91*, 7170-7172.

(31) Bhattacharjee, A.; Miyazaki, Y.; Nakano, M.; Yoo, J.; Christou, G.; Hendrickson, D. N.; Sorai, M. *Polyhedron* **2001**, *20*, 1607-1613.

(32) Fominaya, F.; Gandit, P.; Gaudin, G.; Chaussy, J.; Sessoli, R.; Sangregorio, C. *Journal of Magnetism and Magnetic Materials* **1999**, *195*, L253-L255.

(33) Hwang, J. S.; Lin, K. J.; Tien, C. *Review of Scientific Instruments* **1997**, *68*, 94-101.

(34) Miyazaki, Y.; Bhattacharjee, A.; Nakano, M.; Saito, K.; Aubin, S. M. J.; Eppley, H. J.; Christou, G.; Hendrickson, D. N.; Sorai, M. *Inorganic Chemistry* **2001**, *40*, 6632-6636.

(35) Nakano, M.; Sorai, M.; Vincent, J. B.; Christou, G.; Ho, G. J.; Hendrickson, D. N. *Inorganic Chemistry* **1989**, *28*, 4608-4614.

(36) Sorai, M.; Nakano, M.; Miyazaki, Y. *Chemical Reviews* **2006**, *106*, 976-1031.

(37) Aubin, S. M. J.; Spagna, S.; Eppley, H. J.; Sager, R. E.; Folting, K.; Christou, G.; Hendrickson, D. N. *Molecular Crystals & Liquid Crystals Science & Technology Section A-Molecular Crystals & Liquid Crystals* **1997**, *305*, 181-192.

(38) Yoo, J.; Yamaguchi, A.; Nakano, M.; Krzystek, J.; Streib, W. E.; Brunel, L. C.; Ishimoto, H.; Christou, G.; Hendrickson, D. N. *Inorganic Chemistry* **2001**, *40*, 4604-4616.

(39) Soler, M.; Wernsdorfer, W.; Folting, K.; Pink, M.; Christou, G. *Journal of the American Chemical Society* **2004**, *126*, 2156-2165.

(40) Brechin, E. K.; Sanudo, E. C.; Wernsdorfer, W.; Boskovic, C.; Yoo, J.; Hendrickson, D. N.; Yamaguchi, A.; Ishimoto, H.; Concolino, T. E.; Rheingold, A. L.; Christou, G. *Inorganic Chemistry* **2005**, *44*, 502-511.

(41) Miyasaka, H.; Nakata, K.; Sugiura, K.; Yamashita, M.; Clerac, R. *Angewandte Chemie-International Edition* **2004**, *43*, 707-711.

(42) Kent, A. D.; von Molnar, S.; Gider, S.; Awschalom, D. D. *Journal of Applied Physics* **1994**, *76*, 6656-6660.

(43) Willekers, R. W.; Meijer, H. C.; Mathu, F.; Postma, H. *Cryogenics* **1991**, *31*, 168-173.

(44) Yang, E. C.; Kirman, C.; Lawrence, J.; Zakharov, L. N.; Rheingoid, A. L.; Hill, S.; Hendrickson, D. N. *Inorganic Chemistry* **2005**, *44*, 3827-3836.

(45) Chudnovsky, E. M.; Garanin, D. A. *Physical Review Letters* **2004**, *93*, 257205.

(46) del Barco, E.; Kent, A. D.; Yang, E. C.; Hendrickson, D. N. *Physical Review Letters* **2004**, *93*, 157202.

(47) del Barco, E.; Kent, A. D.; Yang, E. C.; Hendrickson, D. N. *Polyhedron* **2005**, *24*, 2695-2700.

Chapter 4

Magnetic, Structural and Photoluminescent Properties of Two Families of Mn_4 Single-Molecule Magnets

4.1 Introduction

There is currently much interest in polynuclear transition metal complexes that function as SMMs.[1] The regular arrangement of exchange-coupled paramagnetic ions can give rise to a large spin ground state (S) that in conjunction with appreciable negative magnetoanisotropy (D) gives rise to a barrier to the reversal of magnetization ($|D|S_z^2$) and slow magnetization relaxation dynamics below a critical blocking temperature (T_c). Most notably, these complexes have been shown to exhibit interesting physical phenomena such as quantum tunneling of magnetization (QTM), spin-parity effects, spin-spin cross-relaxation, and coherence/decoherence effects.[2-7] It has been suggested that SMMs could be good candidates for quantum information storage and quantum computation.[8-14] A formidable hurdle for application in this area requires coherent manipulation of quantum tunneling between two energetically degenerate M_s states, which can be profoundly impacted by spin-lattice interactions, intermolecular interactions and nuclear spins. However, SMMs appear to be perfectly suited to studying coherence/decoherence effects because they are mono-disperse (same size, shape etc.) and they can be systematically modified through replacement of peripheral coordinated ligands and solvate molecules to minimize factors that lead to tunneling decoherence.

SMMs have been synthesized from a wide variety of third-row transition metals including: $Mn^{II, III, IV}$, [5,15,16] Fe^{III},[17-20] Ni^{II},[21-25] V^{III},[26] Fe^{II},[27] or Co^{II} [28]. And, though the origin of magnetic anisotropy in lanthanides arises due to crystal field effects rather than spin-orbit interactions, several complexes based on 4f orbital configurations have been found to exhibit slow magnetization relaxation dynamics.[29-35] Of the transition

metals that have been used to synthesize SMM's, manganese has yielded the most diverse collection in terms of variation in topologies, spin and anisotropy, leading to a number of bench-mark molecular systems.[3,36] Manganese is particularly well-suited for synthesizing SMMs due to a number of important factors; 1) the availability of multiple oxidation states (Mn^{II}, Mn^{III}, Mn^{IV} etc.), and their inherent redox activity, lends flexibility and versatility in creating structures of similar construction with dramatically different magnetic properties. Recently Feng *et al.* [37,38] synthesized integer spin analogs of the well studied S = 9/2 Mn_4O_3R series of SMM's; 2) manganese ions can exist in a number of stable coordination geometries which has produced a wide range of interesting topologies such as rods, cubanes, dicubanes and wheels, to name but a few.[39-63] By changing coordination geometries one can, to some extent, dictate the magnitude and sign of magnetic exchange pathways, profoundly impacting the ground state spin, anisotropy and exhibited quantum phenomena; 3) Jahn-Teller tetragonally elongated Mn^{III} centers offer an excellent, and well understood, source of magnetoanisotropy; and, 4) the lability of coordination sites of manganese ions can be manipulated to yield a wide variety of interesting zero- and multi-dimensional SMMs.[64-72]

The tetranuclear manganese dicubane family of single-molecule magnets is particularly interesting in that the 0-dimensional Mn_4 dicubane SMMs have been used as a building block for 2-dimensional and 3-dimensional systems. Furthermore, in the presence of ligands that can act as bridges between molecules such as dicyanamide, azide and halides, 1-dimensional coordination polymers and single-chain magnets (SCMs) have been synthesized.

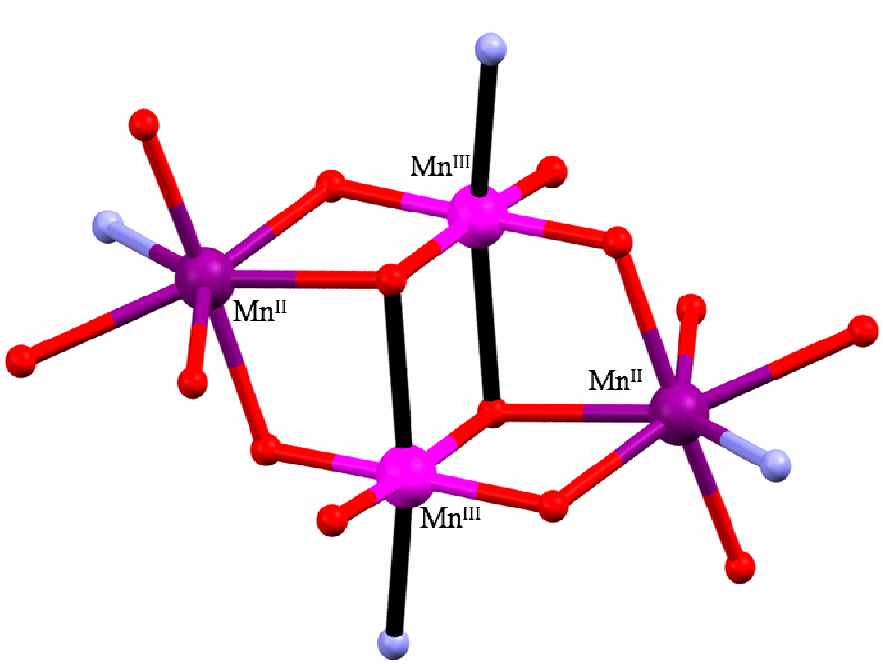

Scheme 4.1. Exchange coupled $[Mn_4O_6]$ dicubane core with Jahn-Teller axes shown in black. The Mn^{III} atoms occupy the inside "body" positions and the Mn^{II} atoms are on the outside "wing" positions.

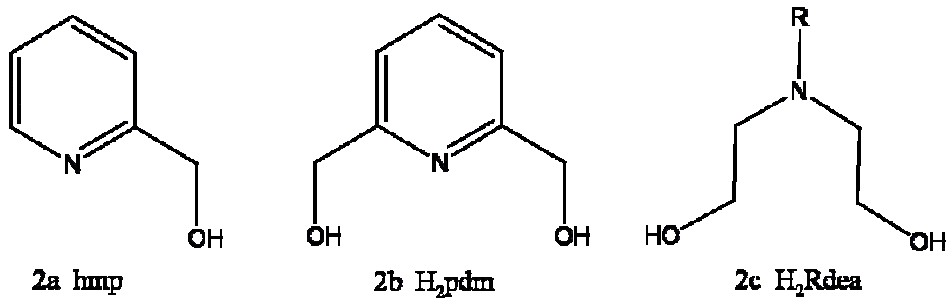

Scheme 4.2. Ligands used for synthesis of Mn_4 complexes with dicubane topology. 2a: 2-hydroxymethylpyridine (hmp); 2b: 2,6-dihydroxymethylpyridine (H_2pdm); 2c: diethanolamines, where R = methyl, ethyl, butyl, ethoxy (H_2Rdea).

The $[Mn_4O_6]$ core of the manganese dicubanes, shown in Scheme 4.1, consists of two Mn^{III} ions (body) and two Mn^{II} ions (wings) that are bridged by oxo-atoms from coordinated aninoalcohols, carboxylates and pyridylalcohols. The oxo bridges act as the Mn-O-Mn superexchange pathways, J_{wb} (Mn^{III}-O-Mn^{II} wing-body interaction) and J_{bb} (Mn^{III}-O-Mn^{III} body-body interaction) within the $[Mn_4O_6]$ core. By far the most prevalent, are Mn_4 dicubanes synthesized employing 2-hydroxymethylpyridine (Hhmp) and 2-6-dihydroxymethylpyridine (H_2pdm) (Scheme 4.2a and **4.2b**). Most of the derivatized pyridine based complexes are cationic species that are fairly well insulated from each other due to the presence of large anions and solvate molecules within the crystal lattice, reducing intermolecular exchange and dipolar interactions. Nearly all of these complexes have a spin ground state of $S = 9$ with positive values of J_{wb} and J_{bb},[63] indicating ferromagnetic exchange pathways, with Mn^{III}-Mn^{III} distances of 3.25-3.38 Å, Mn^{II}-Mn^{III} distances of 3.24-3.31 Å, Mn^{III}-O-Mn^{III} bond angles of 99-101 degrees and Mn^{II}-O-Mn^{III} bond angles of 92-96 degrees and 107-114 degrees.

Recently, a number of tetranuclear manganese dicubane single-molecule magnets have been synthesized employing triethanolamine (H_3tea) and R-diethanolamines, where R = methyl, and n-butyl (Scheme 4.2c).[63,73,74] These versatile ligands have also been used to synthesize a number of interesting topologies including wheels, rods, and extended clusters.[58,59,63,75-78]

Interestingly, in chapter 6[58] of this dissertation and the work of Murray *et al.*,[79,80] the presence of chelating ligands such as dibenzoylmethane (dbm) and diacetylacetone (acac) with R-diethanolamines leads to low-spin $S = 1$ complexes, where the geometry of the exchange-coupled core is structurally identical to the $S = 9$ $[Mn_4]$ single-molecule

magnets. The chelating diketone leads to a reversal of the placement of the Mn^{II} and MnIII ions within the core (Scheme 4.1), where in these complexes the Mn^{II} ions are found in the body positions, and the Mn^{III} ions are found in the wing positions. The di-ketone occupies two coordination sites in the meridial plane of the Mn^{III} ions and the Jahn-Teller axis is perpendicular to the plane of the di-ketone. The small spin state results because the dominant Mn^{III}-O-Mn^{III} exchange interactions normally found in the body positions have been replaced by strong antiferromagnetic coupling between Mn^{II} ions.

In recent years, progress[36,81] has been made in understanding SMMs employing techniques such as oriented single-crystal high-frequency electron paramagnetic resonance (HFEPR), and the micro-SQUID magnetometer.[82] These techniques are paramount to the study of SMMs at the single-crystal level, *i.e.* how molecules within the crystal lattice interact with each other and their environment; however, there is intense interest in studying the dynamics of isolated single molecules. Though application to the study of SMMs has not been realized, single-molecule spectroscopy[83-85] has yielded a great deal of insight into the electronic and vibronic structure of photoluminescent organics isolated in a solid matrix. Recently, efforts have been made to study SMMs at the single molecule level by placing them on surfaces to examine their conductive properties as it relates to molecular electronics.[83,86-88] However, it is difficult to determine the exact position or dispersion of species deposited on surfaces (*e.g.* 1, 2, or more molecules or clusters of molecules may be present). By employing SMMs with photoluminescent properties, it may be possible to precisely ascertain the positions and concentration of molecules on surfaces. Furthermore, if the photo-excited

states of photoluminescent ligands are coupled directly to the magnetic moment of a SMM (below their blocking temperature, T_B) it may provide a new tool for studying fundamental quantum behavior exhibited by SMMs on a 10^{-9}-10^{-12} s time scale. The structural, bulk-magnetic and photoluminescent properties of two related series of tetranuclear manganese mixed-valent single-molecule magnets are presented in this chapter.

4.2 Experimental Section

4.2.1 Compound Preparation

All reactions were performed under aerobic conditions. The ligands 9-Anthracenecarboxylic acid (Hanca), *β*-naphthoic acid, triethylamine (Et_3N), *N*-methyldiethanolamine (H_2mdea), *N*-ethyldiethanolamine (H_2edea), *N*-butyldiethanolamine (H_2n-bdea), *N*-benzyldiethanolamine (H_2bzdea) and dibenzoylmethane (Hdbm) were purchased from Sigma Aldrich and used without further purification. All solvents were used as purchased without further purification.

$[Mn_4(anca)_4(mdea)_2(Hmdea)_2]\cdot 2CHCl_3$ (Complex **4A**). $MnCl_2\cdot 4H_2O$ (200 mg, 1.01 mmol) and 9-anthracenecarboxylic acid (222 mg, 1.00 mmol) were dissolved in 20 mL of a 2:1 solution of $CHCl_3$ and MeOH affording a pale yellow solution. To this was added *N*-methyldiethanolamine (241 mg, 2.02 mmol). The solution was stirred for 30 minutes during which time the solution turned dark brown. The resulting solution was gravity filtered and layered with acetonitrile. Dark brown plates formed after one week. Anal. Calc (Found) for C81 H83 Mn4 N4 O16 Cl3: C, 56.70 (56.99); H, 4.89 (5.03); N,

3.31 (5.10). Selected IR data (cm^{-1}): 3422.6 (br), 3049.8 (m), 2857.7 (m), 1577.6 (s), 1444.6 (m), 1319.2 (s), 1072.44 (s), 885.1 (w), 734.5 (s), 649.8 (m), 560.7 (w).

$[Mn_4(anca)_4(Hedea)_2(edea)_2]\cdot 2CHCl_3,2EtOH$ (Complex **4B**). $MnCl_2\bullet 4H_2O$ (204 mg, 1.03 mmol) and 9-anthracenecarboxylic acid (233 mg, 1.05 mmol) were dissolved in 10 mL of a 1:1 solution of $CHCl_3$ and EtOH and were stirred for 15 minutes affording a pale yellow/brown solution. To this was added *N*-ethyldiethanolamine (304 mg, 2.28 mmol). The solution was stirred for 45 minutes during which time, the solution turned dark red/brown. The resulting solution was gravity filtered and layered with hexanes. Dark brown plates suitable for x-ray diffraction were collected after 3 weeks. Anal. Calc (Found) for C90 H104 Cl6 Mn4 N4 O18: C, 58.00 (58.52); H, 5.63 (6.42); N, 3.04 (3.61). Selected IR data (cm^{-1}): 3428.9 (br), 3050.2 (m), 2968.9 (s), 2847.1 (s), 1623.5 (s), 1607.4 (s), 1485.3 (w), 1444.2 (m), 1384.5 (s), 1303.5 (s), 1269.6 (m), 1156.5 (w), 1093.5 (s), 1071.2 (s), 1006.1 (w), 911.0 (m), 855.7 (w), 864.7 (w), 796.2 (w), 733.4 (s), 662.7 (m), 637.5 (m), 599.6 (w), 560.8 (m), 512.1 (m), 426.2 (w).

$[Mn_4(anca)_4(Hn\text{-}bdea)_2(n\text{-}bdea)_2]\bullet 1MeCN,0.5CHCl_3$ (Complex **4C**). $MnCl_2\bullet 4H_2O$ (220 mg, 1.11 mmol) and 9-anthracenecarboxylic acid (229 mg, 1.03 mmol) were dissolved in 10 mL of a 1:1 solution of $CHCl_3$ and MeOH and were stirred for 20 minutes affording a light-brown solution. To this was added *N*-butyldiethanolamine (312 mg, 1.93 mmol). The resulting solution was stirred for 30 minutes during which time, the solution turned dark red/brown. The solution was gravity filtered and layered with Hexanes and MeCN. Dark brown plates suitable for x-ray diffraction were collected after 6 weeks. Anal. Calc (Found) for C92 H106 Mn4 N4

O16: C, 63.38 (62.16); H, 6.13 (6.83); N, 3.21 (3.26). Selected IR data (cm^{-1}): 3429.7 (br), 3049.3 (m), 2955.0 (s), 2859.5 (s), 1579.4 (s), 1485.1 (w), 1444.2 (m), 1384.71 (s), 1319.3 (s), 1304.9 (s), 1271.1 (s), 1077.7 (s), 1012.6 (w), 910.9 (w), 883.5 (w), 864.6 (w), 844.6 (w), 733.4 (s), 663.3 (m), 637.6 (m), 600.25 (w), 560.6 (m), 510.7 (w), 439.0 (w).

$[Mn_4(anca)_4(Hbzdea)_2(bzdea)_2]\cdot MeCN$ (Complex **4D**). $MnCl_2\bullet 4H_2O$ (209 mg, 1.06 mmol) and 9-anthracenecarboxylic acid (237 mg, 1.07 mmol) were dissolved in 10 mL of CH_2Cl_2 and stirred for one hour yielding a light-brown/yellow solution. To this was added *N*-benzyldiethanolamine (357 mg, 1.82 mmol). The resulting solution was stirred for one hour during which time the solution turned dark red/brown. The solution was gravity filtered and layered with MeCN. Dark brown plates suitable for x-ray diffraction were collected after 4 weeks. Anal. Calc (Found) for C116 H116 Mn4 N10 O16: C, 66.28 (65.41); H, 5.30 (5.40); N, 3.65 (3.57). Selected IR data (cm^{-1}): 3430 (br), 3054.7 (m), 3050.8 (m), 2859.1 (m), 1619.0 (s), 1610.1 (s), 1555.6 (s), 1453.0 (m), 1444.2 (m), 1386.1 (m), 1343.4 (m), 1319.0 (s), 1305.3 (s), 1268.2 (m), 1122.8 (s), 1062.5 (m), 1047.2 (m), 906.8 (w), 879.8 (w), 730.2 (s), 759.7 (m), 702.5 (m), 665.3 (w), 649.8 (m), 619.9 (w), 561.1 (w), 539.2 (w), 511.8 (w), 436.4 (w).

$[Mn_4(\beta\text{-naphth})_4(Hmdea)_2(mdea)_2]\cdot Et_2O$ (Complex **4E**). $MnCl_2\bullet 4H_2O$ (231 mg, 1.16 mmol) and *β*-Naphthoic acid (177 mg, 1.03 mmol) were dissolved in 10 mL of CH_3OH and stirred for 10 minutes, yielding a light-brown/yellow solution, to which, *N*-methyldiethanolamine (416 mg, 3.49 mmol) was added dropwise. The resulting solution was stirred for 1.5 hours during which time the solution turned dark red/brown. The solution was gravity filtered and layered with Et_2O. Dark brown plates suitable for

x-ray diffraction were collected after 4 weeks. Anal. Calc (Found) for C70 H88 Mn4 N4 O17: C, 55.74 (53.73); H, 5.70 (5.78); N, 4.06 (3.94). Selected IR data (cm^{-1}): 3429.9 (br), 2856.2 (s), 1632.8 (m), 1608.3 (m), 1584.9 (m), 1553.0 (m), 1504.0 (w), 1463.8 (m), 1395.8 (s), 1330.3 (s), 1264.6 (w), 1237.3 (w), 1203.6 (w), 1134.4 (w), 1093.1 (m), 1030.3 (w), 921.2 (w), 871.6 (w), 791.9 (s), 763.6 (m), 636.8 (w), 593.4 (m), 539.8 (w), 509.9 (w), 473.5 (w).

$[Mn_4(\beta\text{-naphth})_4(Hedea)_2(edea)_2]\cdot MeCN,EtOH$ (Complex **4F**). $MnCl_2 \bullet 4H_2O$ (220 mg, 1.11 mmol) and *β*-Naphthoic acid (177 mg, 1.03 mmol) were dissolved in a solution containing 5mL of EtOH and 8mL of CH_3CN, and was stirred for 30 minutes, yielding a light-brown/yellow solution. To this solution, *N*-ethyldiethanolamine (304 mg, 2.28 mmol) and 0.2mL of triethylamine was added dropwise. The resulting solution was stirred for 30 hours during which time the solution turned dark red/brown. The solution was gravity filtered and layered with hexanes. Dark brown plates suitable for x-ray diffraction were collected after 3 weeks. Anal. Calc. (Found) C72 H95 Mn4 N5 O17: C, 56.81 (54.59); H, 6.29 (6.30); N, 4.60 (3.93). Selected IR data (cm^{-1}): 3428.4 (br), 3056.0 (w), 2932.0 (w), 2846.7 (m), 1624.5 (s), 1616.2 (m), 1600.9 (m), 1589.5 (m), 1555.8 (s), 1463.8 (m), 1434.5 (w), 1394.6 (s), 1381.9 (s), 1360.8 (m), 1333.5 (s), 1236.4 (w), 1203.3 (w), 1093.9 (s), 1045.72 (m), 913.9 (w), 789.9 (s), 764.9 (m), 637.8 (m), 596.3 (w), 560.1 (w), 510.5 (w), 471.4 (w).

$[Mn_4(\beta\text{-naphth})_4(Hn\text{-}bdea)_2(n\text{-}bdea)_2]\cdot 2CH_2Cl_2$ (Complex **4G**). $MnCl_2 \bullet 4H_2O$ (196 mg, 0.990 mmol) and *β*-Naphthoic acid (179 mg, 1.04 mmol) were dissolved in 10mL of CH_2Cl_2 , and was stirred for one hour, yielding a light-brown/yellow solution. To this solution, *N*-butyldiethanolamine (322 mg, 2.00 mmol) was added dropwise.

The resulting solution was stirred for 30 hours during which time the solution turned dark red/brown. The solution was gravity filtered and layered with hexanes. Dark brown plates suitable for x-ray diffraction were collected after 2 weeks. Anal. Calc. (Found) C78 H102 Cl4 Mn4 N4 O16: C; 56.66 (57.38); H, 6.42 (6.84); N, 3.43 (3.60). Selected IR data (cm^{-1}): 3430.4 (br), 2955.4 (s), 2860.1 (s), 1617.9 (s), 1584.9 (m), 1556.4 (m), 1465.38 (m), 1392.3 (s), 1377.7 (s), 1353.2 (s), 1334.1 (s), 1236.8 (m), 1202.8 (w), 1132.4 (w), 1090.8 (m), 908.9 (w), 792.0 (s), 765.0 (m), 637.8 (w), 596.6 (w), 544.8 (w), 516.1 (w), 473.5 (w).

4.2.2 X-ray Crystallography

Crystallographic data for complexes **4A-4G** is presented in Tables 4.2-4.4. Selected bond angles and bond distances for complexes **4A-4G** are listed in Tables 4.5 and 4.6, respectively.

$[Mn_4(anca)_4(mdea)_2(Hmdea)_2]\cdot 2CHCl_3$ (4A). A brown plate, 0.30 x 0.10 x 0.02 mm in size, was mounted on a Cryoloop with Paratone oil. Data were collected in a nitrogen gas stream at 100(2) K using phi and omega scans. Crystal-to-detector distance was 60 mm and exposure time was 20 seconds per frame using a scan width of 0.3°. Data collection was 99.2% complete to 25.00° in 2. A total of 57966 reflections were collected covering the indices, -20<=*h*<=21, -22<=*k*<=22, -28<=*l*<=28. 27777 reflections were found to be symmetry independent, with an R_{int} of 0.0561. Indexing and unit cell refinement indicated a primitive, triclinic lattice. The space group was found to be P-1 (No. 2). The data were integrated using the Bruker SAINT software program and scaled using the SADABS software program. Solution by Patterson

methods (DIRDIF-99) produced a complete heavy-atom phasing model consistent with the proposed structure. All non-hydrogen atoms were refined anisotropically by full-matrix least-squares (SHELXL-97). All hydrogen atoms were placed using a riding model. Their positions were constrained relative to their parent atom using the appropriate HFIX command in SHELXL-97. Disordered solvate molecules (4 $CHCl_3$ molecules per unit cell, ~220 electrons) were treated by the Squeeze method, the details of which can be found in the cif file. Carbon atoms of anthracene rings are positionally disordered leading to larger than normal thermal ellipsoids or isotropic refinement. Three disordered amine ligands were modeled using free variables and were refined to the following occupancies (Table 4.1)

$[Mn_4(anca)_4(Hedea)_2(edea)_2]\cdot 2CHCl_3$,EtOH (4B). A brown prism 0.20 x 0.20 x 0.05 mm in size was mounted on a Cryoloop with Paratone oil. Data were collected in a nitrogen gas stream at 100(2) K using phi and omega scans. Crystal-to-detector distance was 60 mm and exposure time was 10 seconds per frame using a scan width of 0.5°. Data collection was 62.4% complete to 25.00° in θ. A total of 9002 reflections were collected covering the indices, -8<=*h*<=16, -17<=*k*<=16, -21<=*l*<=22. 6560 reflections were found to be symmetry independent, with an R_{int} of 0.0152. Indexing and unit cell refinement indicated a primitive, triclinic lattice. The space group was found to be P-1 (No. 2). The data were integrated using the Bruker SAINT software program and scaled using the SADABS software program. Solution by direct methods (SHELXS-97) produced a complete heavy-atom phasing model consistent with the proposed structure. All non-hydrogen atoms were refined anisotropically by full-matrix least-squares (SHELXL-97). All hydrogen atoms were placed using a riding model.

Their positions were constrained relative to their parent atom using the appropriate HFIX command in SHELXL-97. One $CHCl_3$ and one EtOH solvent molecules were refined anisotropically while a disordered $CHCl_3$ and EtOH were treated by the Squeeze method, the details of which can be found in the cif.

$[Mn_4(anca)_4(Hn\text{-}bdea)_2(n\text{-}bdea)_2]\cdot 1MeCN,0.5CHCl_3$ (4C). A brown plate 0.15 x 0.10 x 0.05 mm in size was mounted on a Cryoloop with Paratone oil. Data were collected in a nitrogen gas stream at 100(2) K using phi and omega scans. Crystal-to-detector distance was 60 mm and exposure time was 20 seconds per frame using a scan width of 0.5°. Data collection was 90.7% complete to 25.00° in θ. A total of 36005 reflections were collected covering the indices, -18<=*h*<=18, -21<=*k*<=21, -23<=*l*<=23. 15327 reflections were found to be symmetry independent, with an R_{int} of 0.0618. Indexing and unit cell refinement indicated a primitive, triclinic lattice. The space group was found to be P-1 (No. 2). The data were integrated using the Bruker SAINT software program and scaled using the SADABS software program. Solution by direct methods (SHELXS-97) produced a complete heavy-atom phasing model consistent with the proposed structure. All non-hydrogen atoms were refined anisotropically by full-matrix least-squares (SHELXL-97). All hydrogen atoms were placed using a riding model. Their positions were constrained relative to their parent atom using the appropriate HFIX command in SHELXL-97.

$[Mn_4(anca)_4(Hbzdea)_2(bzdea)_2]\cdot MeCN$ (4D). A brown plate 0.15 x 0.10 x 0.05 mm in size was mounted on a Cryoloop with Paratone oil. Data were collected in a nitrogen gas stream at 100(2) K using phi and omega scans. Crystal-to-detector distance was 60 mm and exposure time was 60 seconds per frame using a scan width of

1.0°. Data collection was 91.0% complete to 62.79° in θ. A total of 32751 reflections were collected covering the indices, -13<=*h*<=10, -21<=*k*<=20, -20<=*l*<=25. 14450 reflections were found to be symmetry independent, with an R_{int} of 0.0846. Indexing and unit cell refinement indicated a primitive, triclinic lattice. The space group was found to be P-1 (No. 2). The data were integrated using the Bruker SAINT software program and scaled using the SADABS software program. Solution by direct methods (SHELXS-97 (Sheldrick, 2008)) produced a complete heavy-atom phasing model consistent with the proposed structure. All non-hydrogen atoms were refined anisotropically by full-matrix least-squares (SHELXL-97 (Sheldrick, 1997)). All hydrogen atoms were placed using a riding model. Their positions were constrained relative to their parent atom using the appropriate HFIX command in SHELXL-97. Disordered solvent (acetonitrile) was treated by the squeeze method, the details of which can be found in the cif file.

$[Mn_4(\beta\text{-naphth})_4(Hmdea)_2(mdea)_2]\cdot Et_2O$ (4E). A brown plate 0.40 x 0.10 x 0.07 mm in size was mounted on a Cryoloop with Paratone oil. Data were collected in a nitrogen gas stream at 100(2) K using phi and omega scans. Crystal-to-detector distance was 60 mm and exposure time was 30 seconds per frame using a scan width of 0.5°. Data collection was 95.6% complete to 25.00° in θ. A total of 20664 reflections were collected covering the indices, -12<=*h*<=12, -14<=*k*<=12, -16<=*l*<=15. 5731 reflections were found to be symmetry independent, with an R_{int} of 0.0637. Indexing and unit cell refinement indicated a primitive, triclinic lattice. The space group was found to be P-1 (No. 2). The data were integrated using the Bruker SAINT software program and scaled using the SADABS software program. Solution by direct methods

(SHELXL-97) produced a complete heavy-atom phasing model consistent with the proposed structure. All non-hydrogen atoms were refined anisotropically by full-matrix least-squares (SHELXL-97). All hydrogen atoms were placed using a riding model. Their positions were constrained relative to their parent atom using the appropriate HFIX command in SHELXL-97. The disordered methyldiethanolamine ligand was modeled with a Part instruction (Part 1 = C13, C15, C16; Part 2 = C13A, C15A, C16A) and was refined to 52% occupancy of Part 1 vs. Part 2. Disordered solvent (isopropyl ether) was treated by the squeeze method, the details of which can be found in the cif file.

$[Mn_4(\beta\text{-naphth})_4(Hedea)_2(edea)_2]\cdot MeCN,EtOH$ (4F). A brown block 0.20 x 0.15 x 0.07 mm in size was mounted on a Cryoloop with Paratone oil. Data were collected in a nitrogen gas stream at 100(2) K using phi and omega scans. Crystal-to-detector distance was 60 mm and exposure time was 10 seconds per frame using a scan width of 0.5°. Data collection was 99.6% complete to 25.00° in θ. A total of 30357 reflections were collected covering the indices, -14<=*h*<=14, -24<=*k*<=24, -22<=*l*<=22. 8243 reflections were found to be symmetry independent, with an R_{int} of 0.0526. Indexing and unit cell refinement indicated a primitive, monoclinic lattice. The space group was found to be P2(1)/c (No. 14). The data were integrated using the Bruker SAINT software program and scaled using the SADABS software program. Solution by direct methods (SIR-2004) produced a complete heavy-atom phasing model consistent with the proposed structure. All non-hydrogen atoms were refined anisotropically by full-matrix least-squares (SHELXL-97). All hydrogen atoms were placed using a riding model. Their positions were constrained relative to their parent

atom using the appropriate HFIX command in SHELXL-97. Disordered solvent (MeCN, EtOH) was treated by the Squeeze method, the details of which can be found in the cif file.

$[Mn_4(\beta\text{-naphth})_4(Hn\text{-bdea})_2(n\text{-bdea})_2]\cdot 2CH_2Cl_2$ (4G). A brown needle 0.3 x 0.10 x 0.07 mm in size was mounted on a Cryoloop with Paratone oil. Data were collected in a nitrogen gas stream at 100(2) K using phi and omega scans. Crystal-to-detector distance was 60 mm and exposure time was 30 seconds per frame using a scan width of 0.5°. Data collection was 77.2% complete to 25.00° in θ. A total of 17239 reflections were collected covering the indices, -6<=*h*<=10, -29<=*k*<=28, -25<=*l*<=16. 6553 reflections were found to be symmetry independent, with an R_{int} of 0.0417. Indexing and unit cell refinement indicated a primitive, monoclinic lattice. The space group was found to be P2(1)/n (No. 14). The data were integrated using the Bruker SAINT software program and scaled using the SADABS software program. Solution by direct methods (SIR-2004) produced a complete heavy-atom phasing model consistent with the proposed structure. All non-hydrogen atoms were refined anisotropically by full-matrix least-squares (SHELXL-97). All hydrogen atoms were placed using a riding model. Their positions were constrained relative to their parent atom using the appropriate HFIX command in SHELXL-97.

Table 4.1. Refinement of occupancies for complex **4A**

Part 1	**Part 2**	**Occupancy**
C32, C33, C34	C32A, C33A, C34A	0.83405
C112, C114, C115	C12A, C14A, C15A	0.82936
C152, C153, C154	C52A, C53A, C54A	0.68710

Table 4.2. Crystallographic data for complexes **4A** and **4B.**

	4A	**4B**
formula	C80 H82 Mn4 N4 O16	C93 H109 Cl9 Mn4 N4 O19
formula weight	7255.97	2125.65
temp [K]	100(2)	100(2)
wavelength [Å]	0.71073	0.71073
crystal system	triclinic	Triclinic
space group	P-1	P-1
a [Å]	17.980(3)	13.131(7)
b [Å]	19.068(3)	13.186(7)
c [Å]	24.091(4)	16.885(9)
α [deg]	78.123(3)	102.220(7)
β [deg]	78.922(3)	101.604(8)
γ [deg]	85.405(3)	113.529(6)
V [Å^3]	7925(2)	2483(2)
Z, Z′	4, 0.5	1, 0.5
cryst color, habit	brown plate	brown prism
D_{calc} (mg m^{-3})	1.520	1.422
abs. coefficient	0.895	0.806
F(000)	3736	1090
theta range	2.18 to 25.03°.	1.78 to 28.44°.
reflns measured	57966	9002
reflns independent	27777 [R(int) = 0.0561]	6560 [R(int) = 0.0152]
comp. to theta [25.00°]	99.2 %	92.4 %
abs. correction	Semi-empirical from equivalents	
Refinement method	Full-matrix least-squares on F^2	
Data / restraints / param.	27777 / 0 / 1855	6560 / 0 / 534
Goodness-of-fit on F2	1.075	1.029
$R(F)$,[a] $R(\omega F^2)$[b]	R1 = 0.0920	R1 = 0.0679
($I > 2\sigma(I)$)	R1 = 0.1293	R1 = 0.0755
Largest diff. peak / hole	1.422 and -0.587 e.Å^{-3}	0.863 and -1.422 e.Å^{-3}

[a] $R = \Sigma||F_o| - |F_c||/\Sigma|F_o|$. [b] $R(\omega F^2) = \{\Sigma[\omega(F_o^2 - F_c^2)^2]/\Sigma[\omega(F_o^2)^2]\}^{1/2}$;
$\omega = 1/[\sigma^2(F_o^2) + (aP)^2 + bP]$, $P = [2F_c^2 + \max(F_o, 0)]/3$.

Table 4.3. Crystallographic data for complexes **4C-4E.**

	4C	**4D**	**4E**
formula	C194 H224 Cl5 Mn8 N12 O32	C116 H116 Mn4 N10 O16	C70 H88 Mn4 N4 O17
formula weight	3852.62	2125.95	1477.20
temp [K]	100(2)	100(2)	100(2)
wavelength [Å]	0.71073	0.71073	0.71073
crystal system	triclinic	triclinic	triclinic
space group	P-1	P-1	P-1
a [Å]	15.313(8)	12.2213(8)	10.4980(8)
b [Å]	18.235(9)	18.9667(11)	12.3232(9)
c [Å]	19.546(10)	21.7404(12)	13.6474(10)
α [deg]	98.218(7)	90.624(4)	76.9080(10)
β [deg]	99.952(7)	93.168(5)	82.8700(10)
γ [deg]	113.728(7)	100.731(4)	81.8670(10)
V [Å^3]	4783(4)	4942.5(5)	1694.6(2)
Z, Z′	1, 0.5	2, 1	1, 0.5
cryst color, habit	brown, plate	brown plate	brown plate
D_{calc} (mg m^{-3})	1.338	1.429	1.448
abs. coefficient	0.737 [mm^{-1}]	4.674	0.801
F(000)	2013	2220	772
theta range	2.07 to 25.03°.	2.37 to 62.79°.	2.04 to 25.03°.
reflns measured	36005	32751	20664
reflns independent	15327 [R(int) = 0.0618]	14450 [R(int) = 0.0846]	5731 [R(int) = 0.0637]
comp. to theta [25.00°]	90.7 %	91.0 %	95.6 %
abs. correction	Semi-empirical from equivalents		
Refinement method	Full-matrix least-squares on F^2		
Data / restraints / param.	15327 / 72 / 1153	14450 / 228 / 1131	5731 / 0 / 429
Goodness-of-fit on F2	1.030	0.986	1.023
$R(F)$,[a] $R(\omega F^2)$[b]	R1 = 0.0621	R1 = 0.0743	R1 = 0.0532
($I > 2\sigma(I)$)	R1 = 0.1334	R1 = 0.1398	R1 = 0.0800
Largest diff. peak / hole	0.417 and -0.503 e.Å^{-3}	0.567 and -0.516 e.Å^{-3}	0.480 and -0.414 e.Å^{-3}

[a] $R = \Sigma||F_o| - |F_c||/\Sigma|F_o|$. [b] $R(\omega F^2) = \{\Sigma[\omega(F_o^2 - F_c^2)^2]/\Sigma[\omega(F_o^2)^2]\}^{1/2}$;
$\omega = 1/[\sigma^2(F_o^2) + (aP)^2 + bP]$, $P = [2F_c^2 + \max(F_o, 0)]/3$.

Table 4.4. Crystallographic data for complexes **4F-4G.**

	4F	**4G**
formula	C72 H91 Mn4 N5 O17	C78 H102 Cl4 Mn4 N4 O16
formula weight	1518.26	1713.20
temp [K]	100(2)	100(2)
wavelength [Å]	0.71073	0.71073
crystal system	monoclinic	monoclinic
space group	P 21/c	P2(1)/n
a [Å]	10.861(7)	8.5950(18)
b [Å]	18.985(13)	22.928(5)
c [Å]	17.020(11)	20.461(5)
α [deg]	90	90
β [deg]	92.100(9)	95.160(3)
γ [deg]	90	90
V [Å^3]	3507	4015.8(15)
Z, Z′	2, 0.5	2, 0.5
cryst color, habit	brown block	brown needle
D_{calc} (mg m^{-3})	1.438	1.417
abs. coefficient [mm^{-1}]	0.776	0.814
F(000)	1588	1788
theta range	1.61 to 28.45°.	1.34 to 28.05°.
reflns measured	30357	17239
reflns independent	8243 [R(int) = 0.0526]	6553 [R(int) = 0.0417]
comp. to theta [25.00°]	99.6 %	77.2 %
abs. correction	Semi-empirical from equivalents	
Refinement method	Full-matrix least-squares on F^2	
Data / restraints / param.	8243 / 0 / 419	6553 / 0 / 484
Goodness-of-fit on F2	1.135	1.080
$R(F)$,[a] $R(\omega F^2)$[b]	R1 = 0.0425	R1 = 0.0644
($I > 2\sigma(I)$)	R1 = 0.0553	R1 = 0.0903
Largest diff. peak / hole	0.594 and -0.755 e.Å^{-3}	1.027 and -0.566 e.Å^{-3}

[a] $R = \Sigma||F_o| - |F_c||/\Sigma|F_o|$. [b] $R(\omega F^2) = \{\Sigma[\omega(F_o^2 - F_c^2)^2]/\Sigma[\omega(F_o^2)^2]\}^{1/2}$;
$\Omega = 1/[\sigma^2(F_o^2) + (aP)^2 + bP]$, $P = [2F_c^2 + \max(F_o, 0)]/3$.

Table 4.5. Selected bond angles for complex **4A-4G.**

Complex 4A	**[°]**		**[°]**
Mn(1)-O(4)-Mn(2)	106.51	**Mn(2)-O(8)-Mn(2a)**	**98.42**
Mn(1)-O(8)-Mn(2)	103.62	Mn(3)-O(12)-Mn(4)	91.82
Mn(1)-O(7)-Mn(2)	107.78	Mn(3)-O(12)-Mn(4a)	103.05
Mn(1)-O(8)-Mn(2a)	90.85	Mn(3)-O(15)-Mn(4a)	108.37
Mn(2)-O(8)-Mn(2a)	**98.19**	Mn(3)-O(6)-Mn(4)	107.81
Mn(3)-O(12)-Mn(4)	91.84	**Mn(4)-O(12)-Mn(4a)**	**98.66**
Mn(3)-O(13)-Mn(4)	106.73	**Complex 4D**	
Mn(3)-O(16)-Mn(4)	107.70	Mn(1)-O(8)-Mn(2)	89.98
Mn(3)-O(12)-Mn(4a)	102.68	Mn(1)-O(8)-Mn(2a)	102.28
Mn(4)-O(12)-Mn(4a)	**99.92**	Mn(1)-O(7)-Mn(2a)	108.57
Mn(5)-O(20)-Mn(6)	91.12	Mn(1)-O(4)-Mn(2)	107.85
Mn(5)-O(21)-Mn(6)	107.21	**Mn(2)-O(8)-Mn(2a)**	**97.61**
Mn(5)-O(20)-Mn(6a)	102.47	**Complex 4E**	
Mn(5)-O(18)-Mn(6a)	107.91	Mn(1)-O(5)-Mn(2)	89.95
Mn(6)-O(20)-Mn(6a)	**98.66**	Mn(1)-O(5)-Mn(2a)	102.12
Mn(7)-O(31)-Mn(8)	89.77	Mn(1)-O(3)-Mn(2a)	108.50
Mn(7)-O(31)-Mn(8a)	103.07	Mn(1)-O(8)-Mn(2)	106.71
Mn(7)-O(28)-Mn(8)	105.66	**Mn(2)-O(5)-Mn(2a)**	**98.44**
Mn(7)-O(32)-Mn(8)	108.29	**Complex 4F**	
Mn(8)-O(31)-Mn(8a)	**98.63**	Mn(1)-O(6)-Mn(2)	91.25
Complex 4B		Mn(1)-O(6)-Mn(2a)	103.36
Mn(1)-O(5)-Mn(2)	90.47	Mn(1)-O(2)-Mn(2a)	107.50
Mn(1)-O(5)-Mn(2a)	103.14	Mn(1)-O(5)-Mn(2)	106.48
Mn(1)-O(2)-Mn(2a)	107.24	**Mn(2)-O(6)-Mn(2a)**	**98.21**
Mn(1)-O(7)-Mn(2)	106.34	**Complex 4G**	
Mn(2)-O(5)-Mn(2a)	**97.88**	Mn(1)-O(7)-Mn(2)	90.05
Complex 4C		Mn(1)-O(7)-Mn(2a)	102.56
Mn(1)-O(8)-Mn(2)	91.06	Mn(1)-O(2)-Mn(2a)	107.93
Mn(1)-O(8)-Mn(2a)	103.12	Mn(1)-O(8)-Mn(2)	107.53
Mn(1)-O(7)-Mn(2a)	107.63	**Mn(2)-O(7)-Mn(2a)**	**97.70**
Mn(1)-O(4)-Mn(2)	106.52		

Table 4.6. Selected bond distances for complex **4A-4G**

Complex 4A	**Å**		**Å**		**Å**
Mn(1)-O(4)	2.117(4)	Mn(3)-O(11)	2.486(5)	Mn(6)-O(20c)	1.961(4)
Mn(1)-O(1)	2.125(4)	Mn(3)-Mn(4)	3.2270(15)	Mn(6)-O(20)	2.218(4)
Mn(1)-O(7)	2.259(5)	Mn(4)-O(16b)	1.866(5)	Mn(6)-N(6)	2.246(5)
Mn(1)-O(8)	2.289(4)	Mn(4)-O(13)	1.902(5)	Mn(6)-Mn(6c)	3.1749(19)
Mn(1)-N(1)	2.345(6)	Mn(4)-O(15)	1.969(4)	Mn(7)-O(25)	2.101(4)
Mn(1)-O(3)	2.375(5)	Mn(4)-O(12b)	1.981(4)	Mn(7)-O(28)	2.113(4)
Mn(1)-Mn(2)	3.2324(15)	Mn(4)-O(12)	2.212(4)	Mn(7)-O(32)	2.242(4)
Mn(2)-O(7a)	1.867(5)	Mn(4)-N(4)	2.264(5)	Mn(7)-O(31)	2.312(4)
Mn(2)-O(4)	1.914(5)	Mn(4)-Mn(4b)	3.197(2)	Mn(7)-N(7)	2.339(5)
Mn(2)-O(8a)	1.953(5)	Mn(5)-O(21)	2.102(4)	Mn(7)-O(27)	2.369(5)
Mn(2)-O(6)	1.955(5)	Mn(5)-O(17)	2.113(5)	Mn(7)-Mn(8)	3.2064(14)
Mn(2)-O(8)	2.214(4)	Mn(5)-O(18)	2.242(4)	Mn(8)-O(32d)	1.870(4)
Mn(2)-N(2)	2.262(6)	Mn(5)-O(20)	2.300(4)	Mn(8)-O(28)	1.909(4)
Mn(2)-Mn(2a)	3.155(2)	Mn(5)-N(5)	2.358(5)	Mn(8)-O(31d)	1.944(4)
Mn(3)-O(9)	2.088(4)	Mn(5)-O(22)	2.441(4)	Mn(8)-O(30)	1.954(4)
Mn(3)-O(13)	2.117(4)	Mn(5)-Mn(6)	3.2261(14)	Mn(8)-O(31)	2.231(4)
Mn(3)-O(16)	2.251(4)	Mn(6)-O(18c)	1.867(4)	Mn(8)-N(8)	2.271(5)
Mn(3)-O(12)	2.280(4)	Mn(6)-O(21)	1.902(4)	Mn(8)-Mn(8d)	3.172(2)
Mn(3)-N(3)	2.367(6)	Mn(6)-O(24)	1.958(4)		
Complex 4B	**Å**		**Å**		**Å**
N(1)-Mn(1)	2.377(4)	O(5)-Mn(2a)	1.945(3)	O(8)-Mn(2)	1.935(3)
N(2)-Mn(2)	2.290(5)	O(5)-Mn(2)	2.233(4)	Mn(1)-Mn(2)	3.2225(17)
O(1)-Mn(1)	2.291(3)	O(5)-Mn(1)	2.304(3)	Mn(2)-O(2a)	1.864(3)
O(2)-Mn(2a)	1.864(3)	O(6)-Mn(1)	2.435(3)	Mn(2)-O(5a)	1.945(3)
O(2)-Mn(1)	2.258(3)	O(7)-Mn(2)	1.905(3)	Mn(2)-Mn(2a)	3.1570(16)
O(3)-Mn(1)	2.096(4)	O(7)-Mn(1)	2.118(4)		

Table 4.6. Continued.

Complex 4C	**Å**		**Å**		**Å**
N(1)-Mn(1)	2.403(4)	O(7)-Mn(1)	2.256(3)	O(15)-Mn(3)	2.250(3)
N(2)-Mn(2)	2.294(4)	O(8)-Mn(2a)	1.974(3)	O(16)-Mn(4)	1.918(3)
N(3)-Mn(3)	2.377(4)	O(8)-Mn(2)	2.244(3)	O(16)-Mn(3)	2.123(3)
N(4)-Mn(4)	2.297(4)	O(8)-Mn(1)	2.286(3)	Mn(1)-Mn(2)	3.2326(16)
O(1)-Mn(1)	2.124(3)	O(9)-Mn(3)	2.117(4)	Mn(2)-O(7a)	1.876(3)
O(3)-Mn(1)	2.490(3)	O(12)-Mn(4a)	1.972(3)	Mn(2)-O(8a)	1.974(3)
O(4)-Mn(2)	1.905(3)	O(12)-Mn(4)	2.241(3)	Mn(2)-Mn(2a)	3.1982(18)
O(4)-Mn(1)	2.126(3)	O(12)-Mn(3)	2.308(3)	Mn(4)-O(15a)	1.882(3)
O(6)-Mn(2)	1.965(3)	O(14)-Mn(4)	1.953(4)	Mn(4)-O(12a)	1.972(3)
O(7)-Mn(2a)	1.876(3)	O(15)-Mn(4a)	1.882(3)	Mn(4)-Mn(4a)	3.2008(19)
Complex 4D	**Å**		**Å**		**Å**
N(1)-Mn(1)	2.389(6)	O(7)-Mn(4)	1.868(5)	O(10)-Mn(3)	2.298(4)
N(2)-Mn(2)	2.258(6)	O(7)-Mn(1)	2.217(4)	O(11)-Mn(3)	2.121(4)
N(3)-Mn(3)	2.425(6)	O(8)-Mn(4)	1.936(4)	O(14)-Mn(3)	2.437(4)
N(4)-Mn(4)	2.265(5)	O(8)-Mn(2)	2.231(4)	O(15)-Mn(4)	1.911(5)
O(1)-Mn(1)	2.119(5)	O(8)-Mn(1)	2.319(4)	O(15)-Mn(3)	2.092(4)
O(3)-Mn(1)	2.411(4)	O(9)-Mn(2)	1.859(5)	O(16)-Mn(4)	1.940(4)
O(4)-Mn(2)	1.891(5)	O(9)-Mn(3)	2.241(4)	Mn(1)-Mn(2)	3.2173(15)
O(4)-Mn(1)	2.087(4)	O(10)-Mn(2)	1.939(4)	Mn(2)-Mn(4)	3.1414(14)
O(6)-Mn(2)	1.927(4)	O(10)-Mn(4)	2.252(4)	Mn(3)-Mn(4)	3.2352(15)
Complex 4E	**Å**		**Å**		**Å**
N(1)-Mn(1)	2.426(3)	O(5)-Mn(2a)	1.956(2)	O(8)-Mn(1)	2.110(3)
N(2)-Mn(2)	2.286(3)	O(5)-Mn(2)	2.234(2)	Mn(1)-Mn(2)	3.2289(9)
O(1)-Mn(1)	2.121(3)	O(5)-Mn(1)	2.333(3)	Mn(2)-O(3a)	1.872(3)
O(3)-Mn(2a)	1.872(3)	O(7)-Mn(2)	1.941(2)	Mn(2)-O(5a)	1.956(2)
O(3)-Mn(1)	2.240(2)	O(8)-Mn(2)	1.912(3)	Mn(2)-Mn(2a)	3.1776(11)
O(4)-Mn(1)	2.380(3)				

Table 4.6. Continued.

Complex 4F	**Å**		**Å**		**Å**
N(1)-Mn(1)	2.390(2)	O(5)-Mn(1)	2.1254(18)	O(8)-Mn(2)	1.9376(16)
N(2)-Mn(2)	2.279(2)	O(6)-Mn(2a)	1.9510(16)	Mn(1)-Mn(2)	3.2359(18)
O(2)-Mn(2a)	1.8727(17)	O(6)-Mn(2)	2.2227(17)	Mn(2)-O(2a)	1.8727(17)
O(2)-Mn(1)	2.2657(16)	O(6)-Mn(1)	2.3039(17)	Mn(2)-O(6a)	1.9510(16)
O(3)-Mn(1)	2.149(2)	O(7)-Mn(1)	2.357(2)	Mn(2)-Mn(2a)	3.1600(16)
O(5)-Mn(2)	1.9105(17)				
Complex 4G	**Å**		**Å**		**Å**
N(1)-Mn(1)	2.421(4)	O(5)-Mn(1)	2.350(3)	O(8)-Mn(2)	1.907(3)
N(2)-Mn(2)	2.373(4)	O(6)-Mn(2)	1.937(3)	O(8)-Mn(1)	2.122(3)
O(2)-Mn(2a)	1.882(3)	O(7)-Mn(2a)	1.947(3)	Mn(2)-O(2a)	1.882(3)
O(2)-Mn(1)	2.259(3)	O(7)-Mn(2)	2.255(3)	Mn(2)-O(7a)	1.947(3)
O(3)-Mn(1)	2.108(3)	O(7)-Mn(1)	2.342(3)	Mn(2)-Mn(2a)	3.1711(13)

4.2.3 Physical methods

FT-IR spectra were collected using a Thermo-Nicolet Avatar series spectrophotometer. Elemental analyses were performed by NuMega Resonance Labs (San Diego, CA) for Complexes **4A-4G.** The AC and DC magnetic susceptibility data were collected on Quantum Design MPMS SQUID magnetometers equipped with 1 Tesla and 5.5 Tesla magnets. Microcrystalline samples were restrained with eicosane to prevent torquing. Diamagnetic corrections of magnetic susceptibility data were made employing Pascal's constants. All NMR spectra were recorded at room temperature (20 °C) in d_2-dichloromethane solutions on Varian spectrometers operating at 300 MHz (^{1}H NMR) and referenced to residual solvent peaks unless otherwise noted. UV-Vis and Fluorescence measurements were collected on Perkin-Elmer spectrophotometers.

4.3 Results and Discussion

4.3.1 Synthesis

The use of amine based poly-dentate poly-alcohols has yielded a wonderfully diverse family or families of molecules with varying nuclearity and topology, such as butterflies,[58] dicubanes,[58,73,79,89] extended structures,[90] and heteronuclear complexes.[77] The amine based poly-alcohols are quite versatile and are found as bridging ligands between two metal centers or as bridging ligands between three metal centers, where the alkoxy oxygen of a ethoxy arm is in a μ_3 or μ_4 coordination mode. It can also be found as a capping ligand in both small and extended structures.

In most cases no deprotonating agent is required during synthesis, whether one begins from simple halide or carboxylate salts of Mn^{II} or Mn^{III}. Often, the addition of

R-diethanolamine or triethanol amine quickly promotes oxidation of Mn^{II} salts yielding dark brown to brown/red solutions without the presence of an oxidizing agent such as oxygen, ozone, tetrabutylammonium permanganate or potassium permanganate, though the exact mechanism is not clearly understood. Interestingly, the length of the R group does not seem to be the limiting factor when it pertains to the formation of wheel or dicubane topologies, which seem to be the topological molecular sinks in these types of reactions, as noted from the variety of starting materials that can be employed to synthesize these complexes. Rather, it appears that it is the nature of the R group on the carboxylates that seems to govern whether synthesis leads to a wheel or dicubane. This is evident in the work published by Foguet-Albiol *et al.*[73] where the product of the reaction between *N*-methyldiethanolamine and $Mn(O_2CPh)_2$ or $Mn(O_2CCH_3)_2$ leads to the formation of a dicubane and a wheel, respectively. This idea is further supported by complexes reported in this dissertation in chapters 4, 5, where large bulky carboxylate lead to the formation of dicubanes.

4.3.2 Description of Structures

$[Mn_4(anca)_4(mdea)_2(Hmdea)_2]\cdot 2CHCl_3$ (4A). An ORTEP of complex **4A** is given in Figure 4.1. Complex **4A** crystallizes in the triclinic space group P-1 with four symmetry independent halves of the molecule and four chloroform solvate molecules in the asymmetric unit. Each molecule consists of an oxo-bridged $[Mn_2^{II}Mn_2^{III}O_6]^{+4}$ core resembling two face-sharing cubanes missing opposite vertices (the shared face consists of Mn(2)-O(8) and their inversion symmetry equivalents). The divalent Mn(1) ions are arranged in a distorted pentagonal bipyramidal geometry, where three of the

coordination positions in the pentagonal-plane are occupied by an $Hmdea^-$ ligand. The apical positions are occupied by a carboxylate O(1) atom of a pendant monodentate $anca^-$ ligand and an alkoxy O(4) atom that also serves as a $Mn^{II}(1)$-O(4)-$Mn^{III}(2)$ bridge. A tridentate $Hmdea^-$ ligand bridges between $Mn^{II}(1)$ and $Mn^{III}(2)$ atoms. The final two coordination positions are occupied by a $anca^-$ oxo and a $Mn^{II}(1)$-O- $Mn^{III}(2)$ bridging O(8) alkoxy arm from one of the two dianionic $mdea^{2-}$ ligands. The trivalent Mn(2) ions are arranged in a tetragonally distorted octahedral environment capped by a tridentate $mdea^{2-}$ ligand. Oxidation states in complexes **4A-4G** were determined by the presence of Jahn-Teller (*JT*) elongations, charge considerations, and bond valence sum (BVS) calculations. The single-ion tetragonally elongated Jahn-Teller (*JT*) axes for the two Mn^{III} ions of each molecule are collinear and lie along N(2)-Mn(2)-O(8) bonds. However, the *JT* projections of all the molecules within the unit cell are not mutually collinear due to the presence of four symmetry independent species.

$[Mn_4(anca)_4(Hedea)_2(edea)_2]\cdot 2CHCl_3$,2EtOH (4B). Complex **4B** (ORTEP shown in Figure 4.2) also crystallizes in the triclinic P-1 space group but only has one symmetry-independent half of the molecule in the asymmetric unit with the other half related by an inversion center. The molecular core of **4B** is isostructural, however, to that of **4B** in that it consists of an oxo-bridged $[Mn_2^{II}Mn_2^{III}O_6]^{+4}$ pseudo-dicubane unit with the Mn^{II} ions, Mn(1), occupying the wing positions and the Mn^{III} ions, Mn(2), occupying the body positions. Both the divalent and trivalent Mn ions exhibit the same geometries and coordination spheres as seen in complex **4B**.

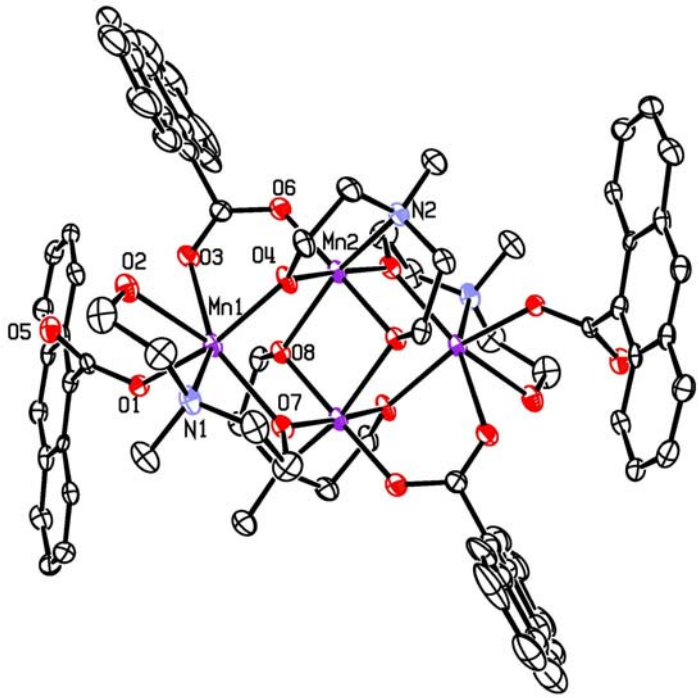

Figure 4.1. ORTEP of The **$[Mn_4(anca)_4(mdea)_2(Hmdea)_2]\cdot 2CHCl_3$ (4A)** with thermal ellipsoids at 50%. Hydrogen atoms and solvate molecules have been removed for clarity.

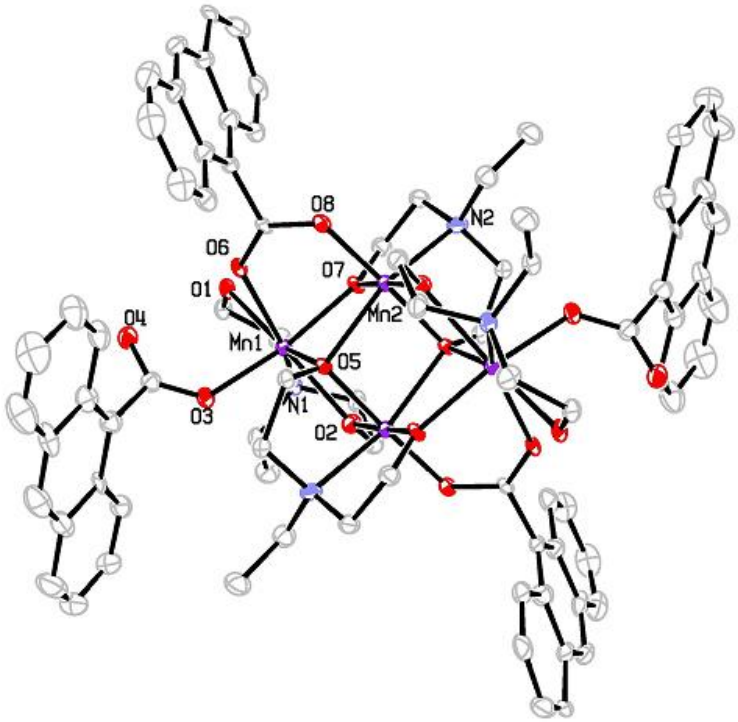

Figure 4.2. ORTEP of The **$[Mn_4(anca)_4(Hedea)_2(edea)_2]\cdot 2CHCl_3$,EtOH (4B)** with thermal ellipsoids at 50%. Hydrogen atoms and solvate molecules have been removed for clarity.

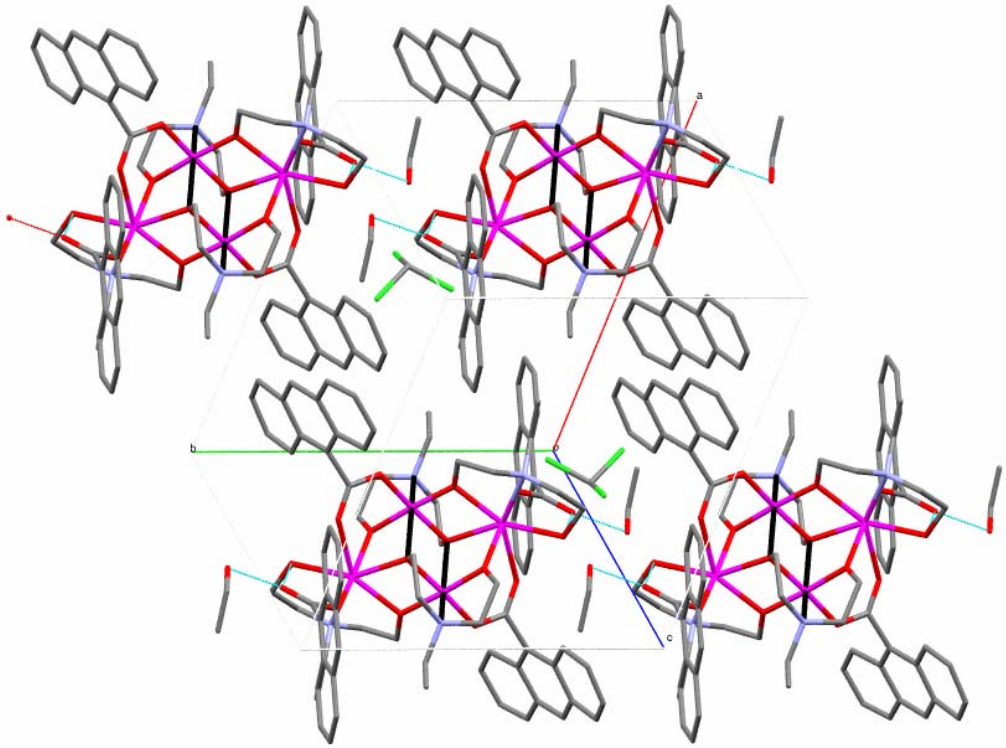

Figure 4.3. Crystal packing of **[Mn_4(anca)$_4$(Hedea)$_2$(edea)$_2$]·2$CHCl_3$,EtOH (4B)** showing hydrogen bonding between (**4B**) and ethanol solvate molecules. Colinear Jahn-Teller axes are shown in black.

The structure of complex **4B** differs from **4A** only in the exchange of the methyl group of the *N*-alkylated diethanolamine ligand to an ethyl group (H_2edea). Also, **4A** co-crystallizes with both chloroform and ethanol solvate molecules (two of each in the unit cell). While the chloroform molecules do not seem to interact with the Mn_4 units, there is an intermolecular hydrogen-bonding network between the EtOH solvate molecules (Figure 4.3), the unbound anca$^-$ ligand, and the protonated arm of the Hedea^{1-} ligand which propagates along the b-axis of the unit cell. Another noteworthy difference in complex **4B** is the orientation of the *JT* axes. As in complex **4A**, the *JT* axes of the Mn^{III} ions in **4B** are collinear (due to inversion symmetry), however, the *JT* projections of all the molecules within the unit cell are also mutually collinear in this case because of the single orientation of the molecule in the crystal lattice. Furthermore, from the crystal packing diagram of **4B**, the JT axes are found to be nearly collinear with the a-axis of the unit cell (Figure 4.3).

$[Mn_4(anca)_4(Hn\text{-}bdea)_2(n\text{-}bdea)_2]\cdot 1MeCN,0.5CHCl_3$ (4C). Complex **4C** (ORTEP shown in Figure 4.4) crystallizes in the triclinic *P*-1 space group with 2 symmetry-independent halves of the molecule in the asymmetric unit. Once again, this complex is isostructural to **4A** and **4B** with the exception of the N-alkyl group of the diethanolamine ligand being a n-butyl group (H_2bdea). The *JT* projections of the two symmetry-independent orientations of the molecules within the unit cell are nearly orthogonal to one another. The *JT* axes of one orientation align closely with the a-axis of the unit cell while the *JT* axes of the other orientation are nearly collinear with the b-axis. Despite co-crystallization of acetonitrile and chloroform solvate molecules in **4C**, there are no significant intermolecular interactions in the crystal packing.

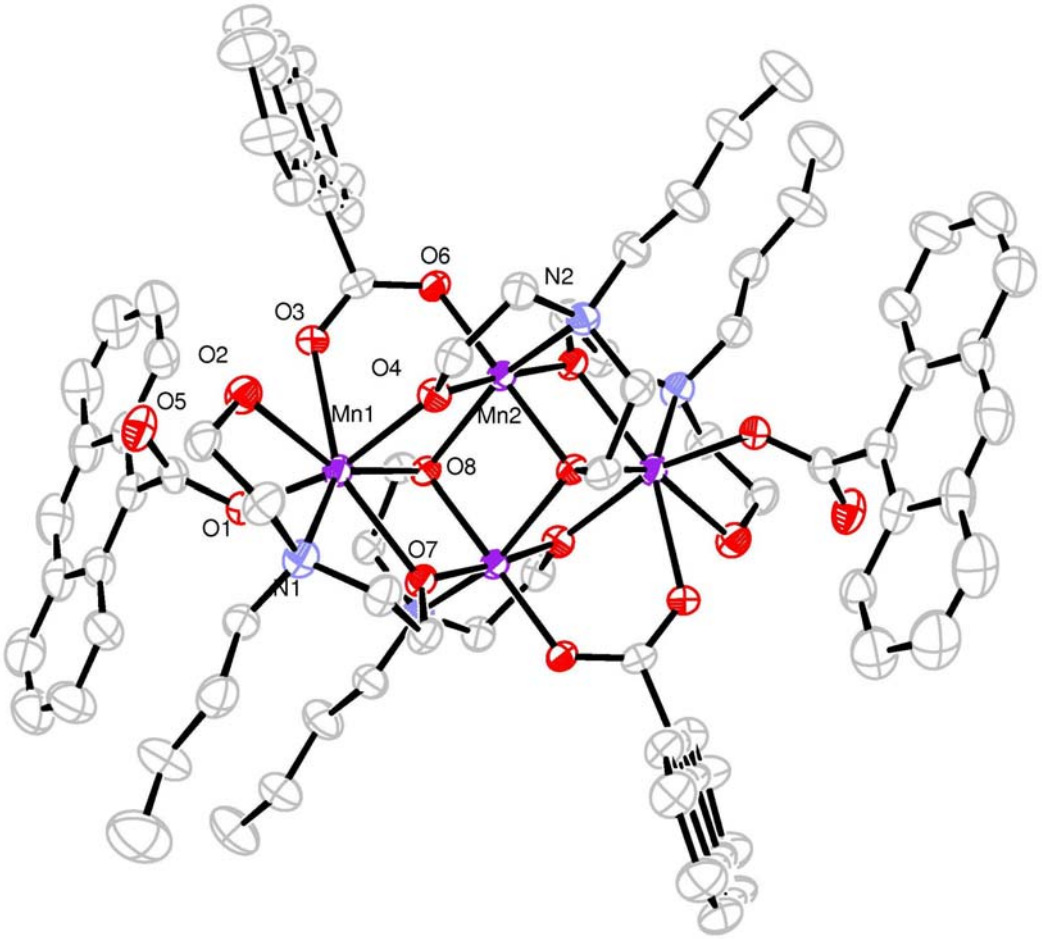

Figure 4.4. ORTEP of The **$Mn_4(anca)_4(Hn\text{-}bdea)_2(n\text{-}bdea)_2]\cdot 1MeCN,0.5CHCl_3$ (4C)** with thermal ellipsoids at 50%. Hydrogen atoms and solvate molecules have been removed for clarity.

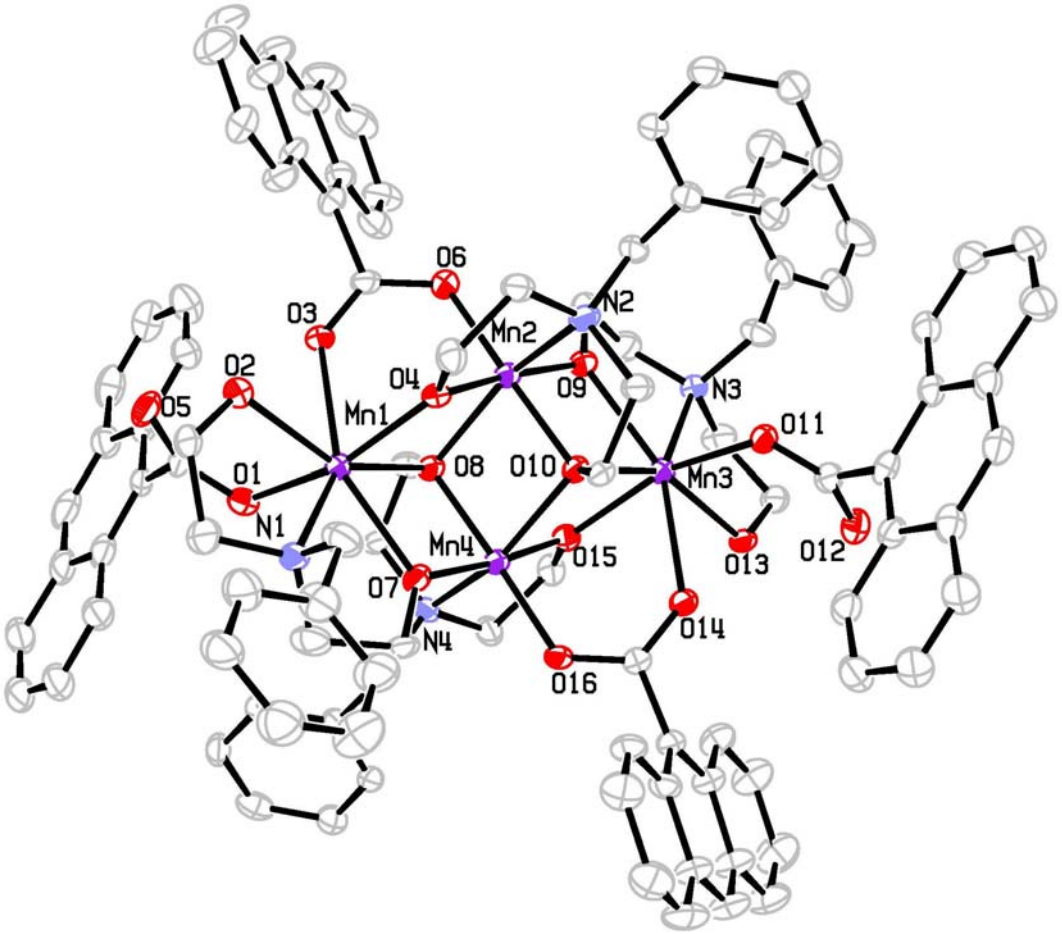

Figure 4.5. ORTEP of The **[$Mn_4(anca)_4(Hbzdea)_2(bzdea)_2$]·MeCN (4D)** with thermal ellipsoids at 50%. Hydrogen atoms and solvate molecules have been removed for clarity.

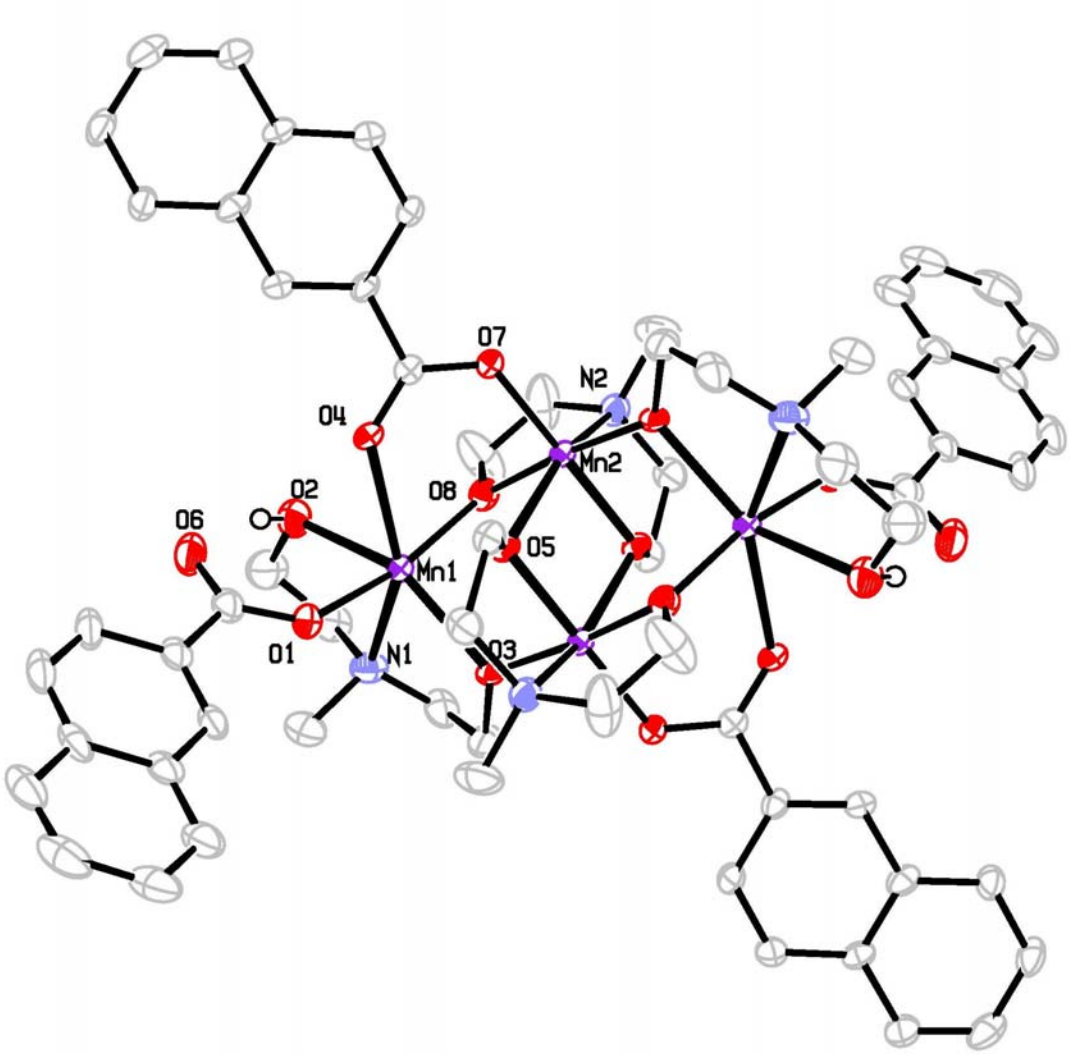

Figure 4.6. ORTEP of The **$[Mn_4(\beta\text{-naphth})_4(Hmdea)_2(mdea)_2]\cdot Et_2O$ (4E)** with thermal ellipsoids at 50%. Hydrogen atoms and solvate molecules have been removed for clarity.

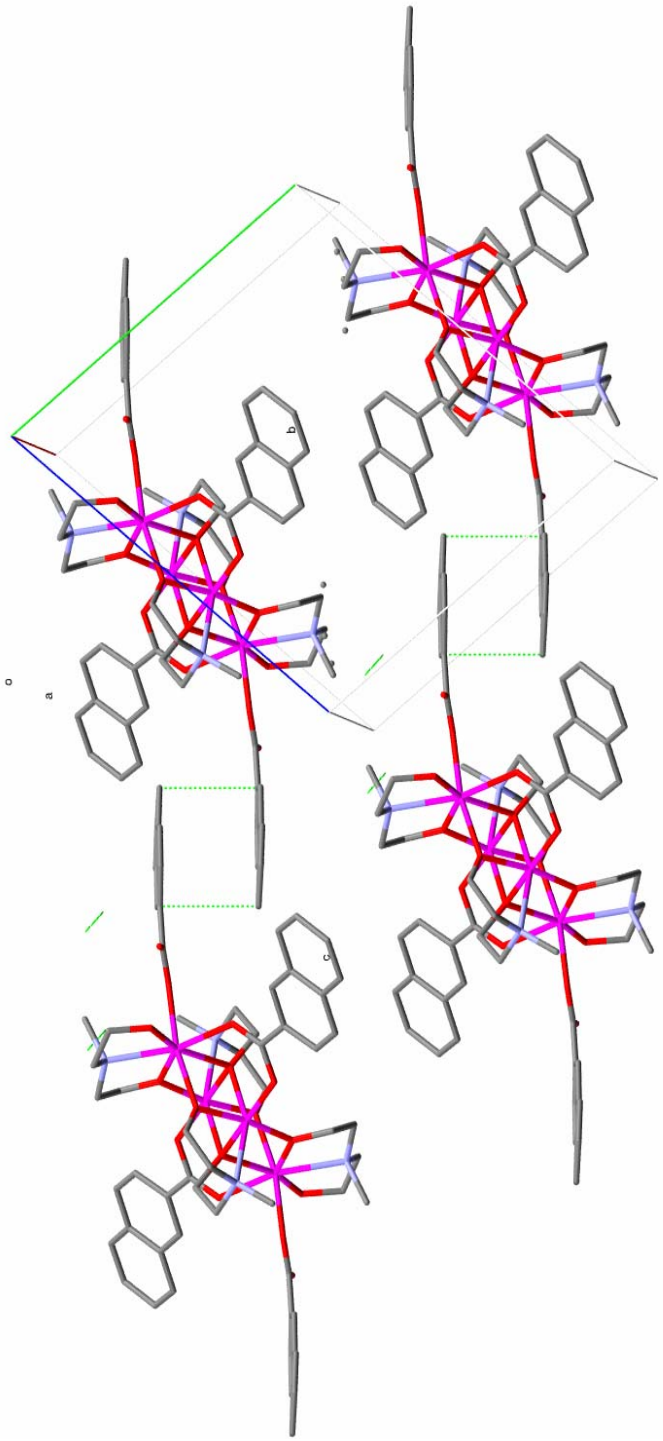

Figure 4.7. Crystal packing diagram for **$[Mn_4(\beta\text{-naphth})_4(Hmdea)_2(mdea)_2]\cdot Et_2O$ (4E)** with intermolecular π-π stacking (dotted green lines 3.331 Å).

$[Mn_4(anca)_4(Hbzdea)_2(bzdea)_2]\cdot MeCN$ (4D). Complex **4E** (ORTEP shown in Figure 4.5) crystallizes in the triclinic P-1 space group with one symmetry-independent molecule in the asymmetric unit, giving two molecules per unit cell related by inversion symmetry. This complex is also isostructural with complexes **4A-4C** where, in this case, the N-alkylated group of the diethanolmine ligand is a benzyl group (H_2bzdea). Despite the presence of two Mn_4 molecules per unit cell, the inversion symmetry allows for the *JT* projections of all the molecules to remain collinear with one another. Furthermore, the *JT* axes are aligned roughly along the a-axis of the unit cell, similar to complex **4D**. This complex co-crystallizes with acetonitrile solvate molecules which were disordered, thus preventing a full assessment of possible intermolecular interactions.

$[Mn_4(\beta\text{-naphth})_4(Hmdea)_2(mdea)_2]\cdot Et_2O$ (4E). Complex **4E** (ORTEP shown in Figure 4.6) crystallizes in the triclinic P-1 space group with one symmetry-independent half of the molecule in the asymmetric unit with the other half related by a center of inversion. As seen in the previous Mn_4 complexes with the anthracene carboxylate ligand (**4A-4D**), complexes **4E-4G** also consists of an oxo-bridged $[Mn_2^{II}Mn_2^{III}O_6]^{+4}$ pseudo-dicubane unit with the Mn^{II} ions, Mn(1), occupying the wing positions and the Mn^{III} ions, Mn(2), occupying the body positions. Both the divalent and trivalent Mn ions also exhibit the same geometries and coordination spheres as in **4A-4D**. The structural differences in **4E-4G** as compared to **4A-4D** come from the use of β-naphthoic acid (β-naphth) in place of the anthracene carboxylic acid. The β-naphth$^-$ ligand, however, adopts the same binding modes as anca$^-$ in these complexes.

The *JT* axes in complex **4E** are also parallel to one another and the *JT* projections for all the molecules in the unit cell are collinear since only one orientation

of the molecule is present. This complex co-crystallizes with disordered diethyl ether solvate molecules which are not likely involved in any significant intermolecular interactions. However, there is evidence of some π–π stacking of the naphthalene rings of neighboring dicubane units (Figure 4.7, dotted green lines).

$[Mn_4(\beta\text{-naphth})_4(Hedea)_2(edea)_2]\cdot MeCN,EtOH$ (4F). Complex **4F** (ORTEP shown in Figure 4.8) crystallizes in the monoclinic $P2_1/c$ space group with one symmetry-independent half of the molecule in the asymmetric unit with the other half generated by inversion symmetry. This complex is isostructural with complex **4E** except that H_2edea is used instead of H_2mdea. Though there is only one structurally-independent molecule in the unit cell, the crystal packing results in two different orientations of the molecule. Thus, the *JT* projections of the two orientations of the molecules are aligned perpendicular to one another in alternating sheets within the crystal lattice. This complex also co-crystallizes with disordered acetonitrile and ethanol solvate molecules and exhibits some intermolecular π–π stacking of neighboring naphthalene rings (Figure 4.9).

$[Mn_4(\beta\text{-naphth})_4(Hn\text{-bdea})_2(n\text{-bdea})_2]\cdot 2CH_2Cl_2$ (4G). Complex **4G** (ORTEP shown in Figure 4.10) crystallizes in the monoclinic $P2_1/n$ space group with one symmetry-independent half of the molecule in the asymmetric unit with the other half related by a center of inversion. Once again, this complex is isostructural with complexes **4E** and **4F** but with H_2n-bdea as the chelating ligand. Similarly to complex **4F**, complex **4G** has two different orientations of the molecule in the crystal lattice. Thus, the *JT* projections of the two orientations of the molecules are also aligned perpendicular to one another as an artifact of the symmetry generated by the monoclinic

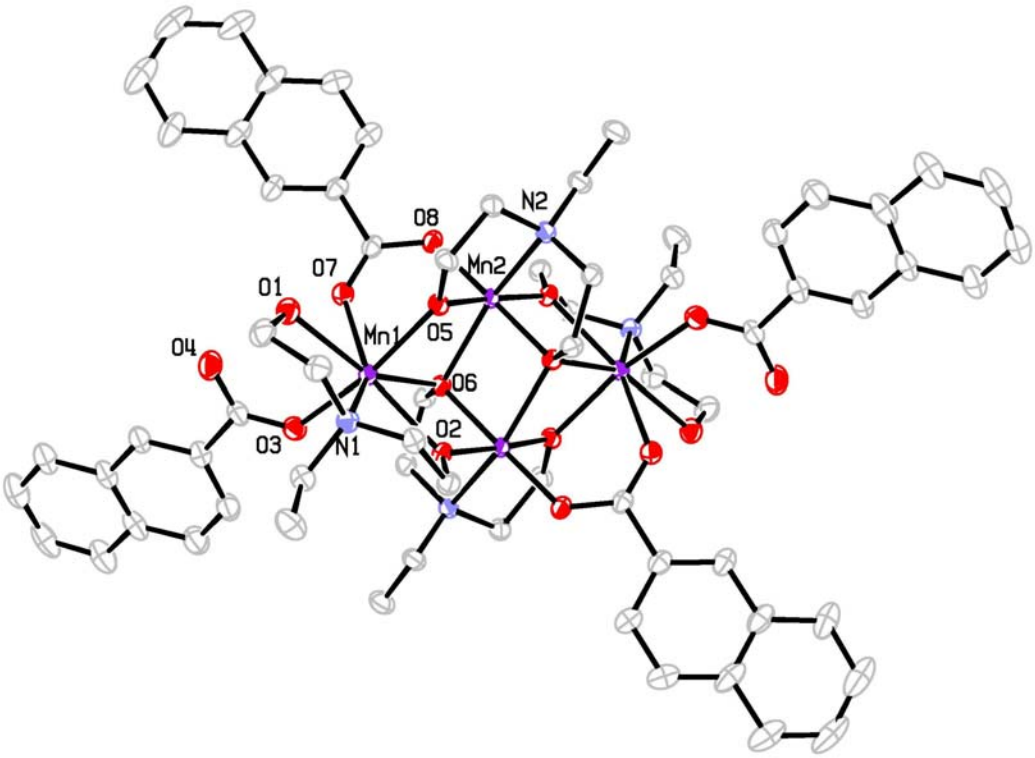

Figure 4.8. ORTEP of The **[Mn_4(β-naphth)$_4$(Hedea)$_2$(edea)$_2$]·MeCN,EtOH (4F)** with thermal ellipsoids at 50%. Hydrogen atoms and solvate molecules have been removed for clarity.

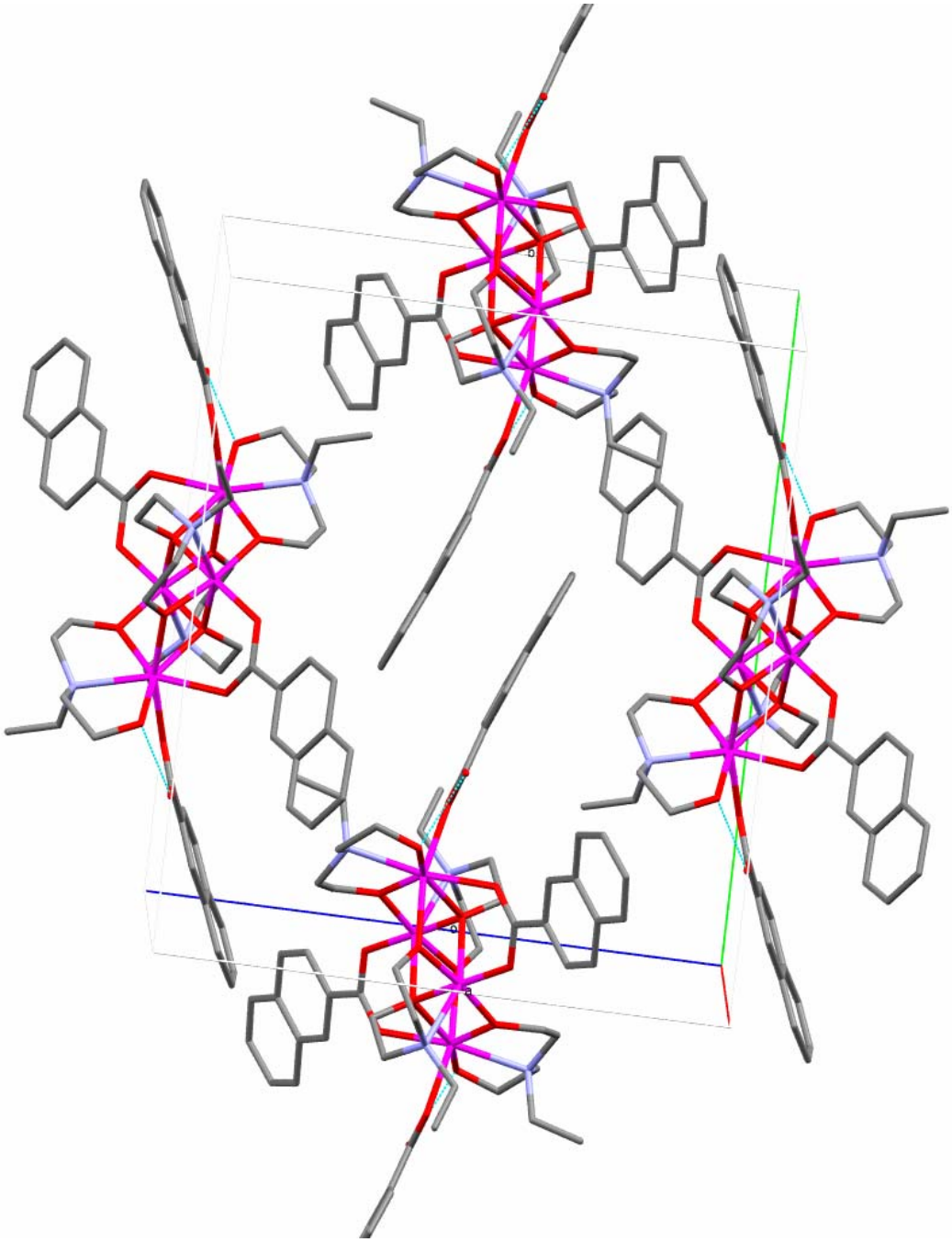

Figure 4.9. $[Mn_4(\beta\text{-naphth})_4(Hedea)_2(edea)_2]\cdot MeCN,EtOH$ (4F) crystal packing diagram, showing the two molecular orientations and π-overlap of adjacent β-naphthoic acid rings.

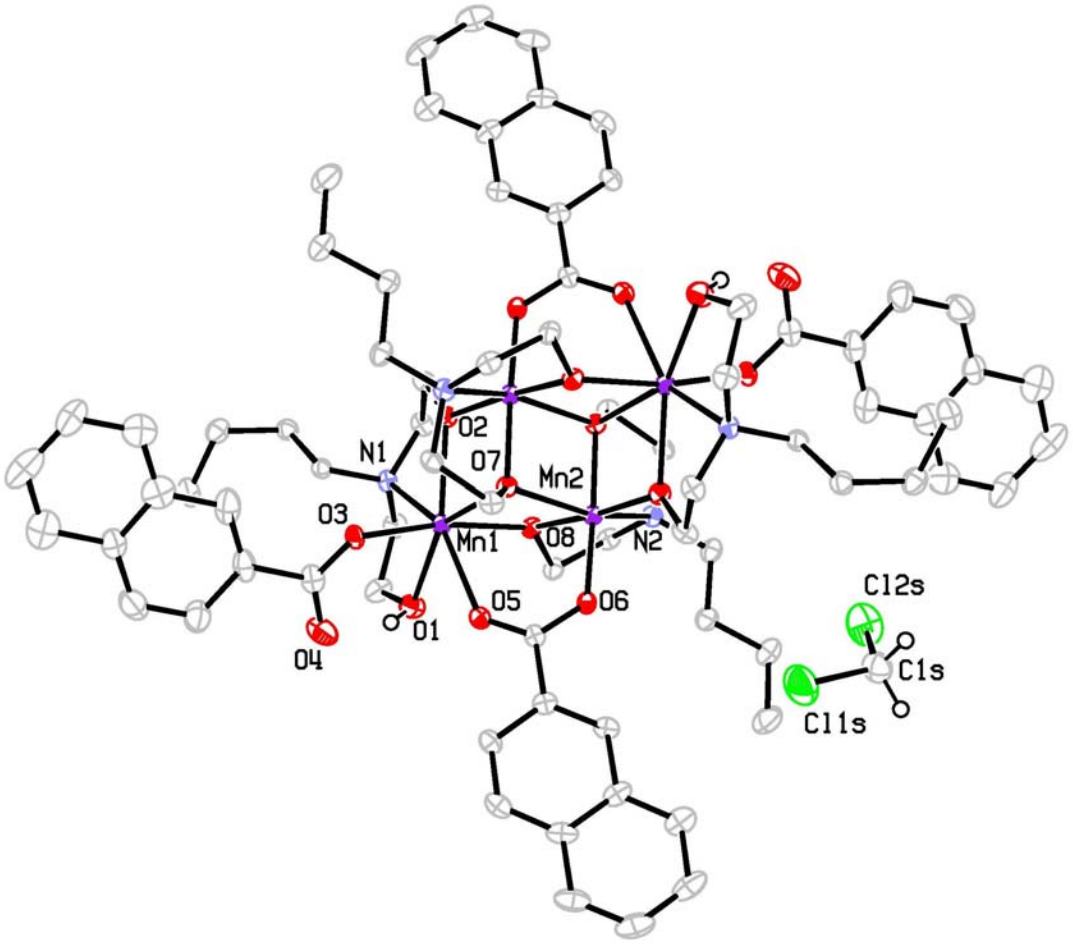

Figure 4.10. ORTEP of The **$[Mn_4(\beta\text{-naphth})_4(Hn\text{-bdea})_2(n\text{-bdea})_2]\cdot 2CH_2Cl_2$ (4G)** with thermal ellipsoids at 50%. Hydrogen atoms and solvate molecules have been removed for clarity.

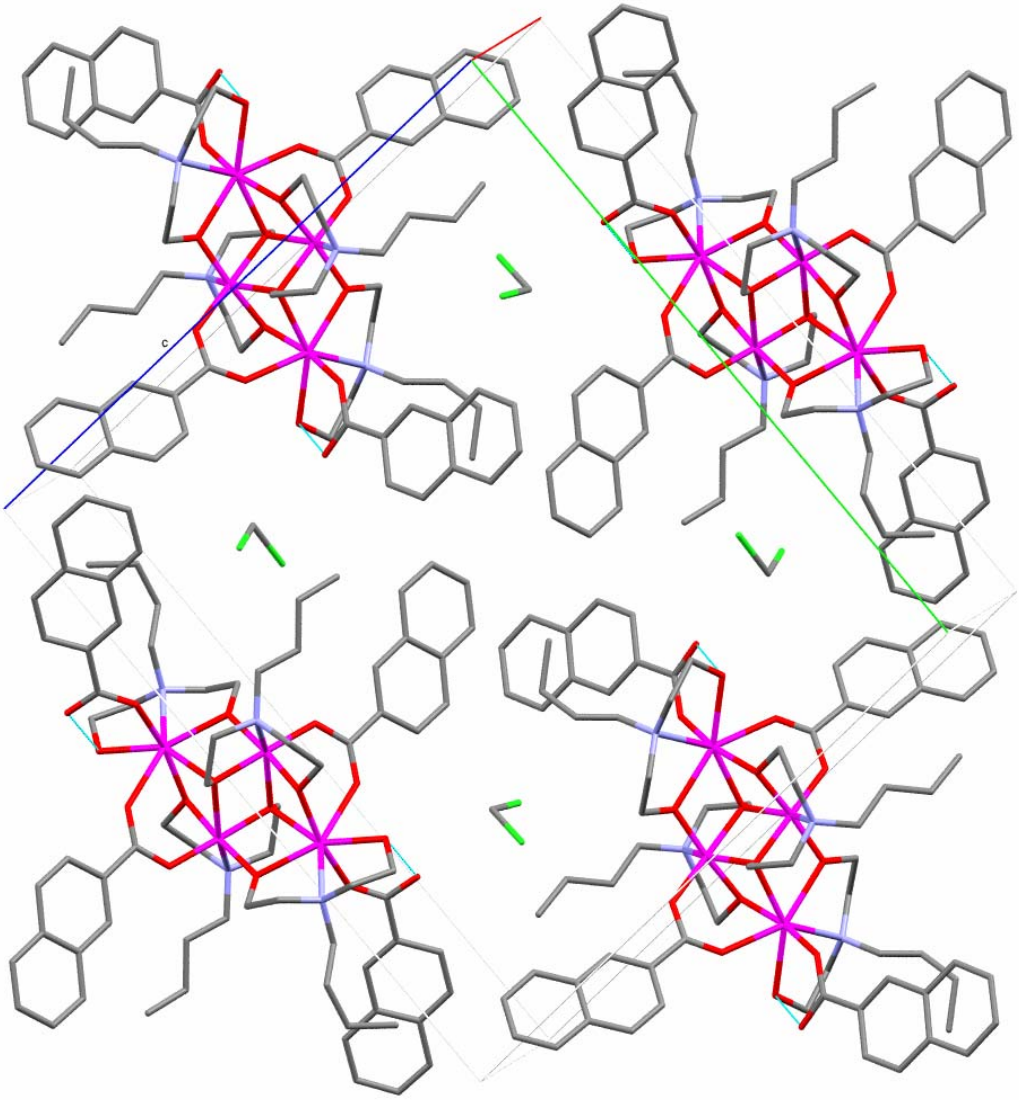

Figure 4.11. **$[Mn_4(\beta\text{-naphth})_4(Hn\text{-bdea})_2(n\text{-bdea})_2]\cdot 2CH_2Cl_2$ (4G)** crystal packing diagram showing the two independent molecular orientations.

space group. This complex co-crystallizes with one ordered methylene chloride solvate molecule per asymmetric unit (two per molecule) which exhibits a weak hydrogen-bonding interaction with the unbound oxygen atom of the β-naphth$^-$ ligand. The slightly different crystal packing in complex **4G** also decreases the overlap of neighboring naphthalene rings, minimizing intermolecular π–π stacking (Figure 4.11).

4.3.3 DC Magnetic Susceptibility Studies

Figures 4.12-4.18 illustrate variable temperature dc magnetization data for complexes **4A-4G** measured between 300-1.8K, with applied magnetic fields of 0.01-5T for complex **4A** and 0.01-1T for complexes **4B-4G**. The plots of $\chi_m T$ versus T (Figures 4.12-18, Top) exhibit pronounced temperature and field dependence, as evident in the non-superimposibility of $\chi_m T$ versus T data with different applied magnetic fields. This suggests that Zeeman effects and zero-field splitting effects become more pronounced with small changes in applied fields due to closely spaced energy levels (see fitting data Table 4.7) as documented[63] for many Mn based dicubane complexes as well as other Mn based topologies**.** Figures 4.12-4.18 (bottom) illustrate $\chi_m T$ versus T magnetization data collected between 300-1.8K, with an applied magnetic field of 0.1T, for complexes **4A-4G**. As the temperature is decreased from 300K, there is a nearly linear rise in molar magnetic susceptibility down to ~75K. Below 75K there is a sharp rise in $\chi_m T$, with maximum molar susceptibility values of 24.1-37.3 $cm^3 \cdot K \cdot mol^{-1}$. A rise in $\chi_m T$ with decreasing temperature indicates the population of larger M_s states and is indicative of dominant ferromagnetic exchange interactions. $\chi_m T$ values at 300K for complexes **4A-4G** are less than the spin-only value

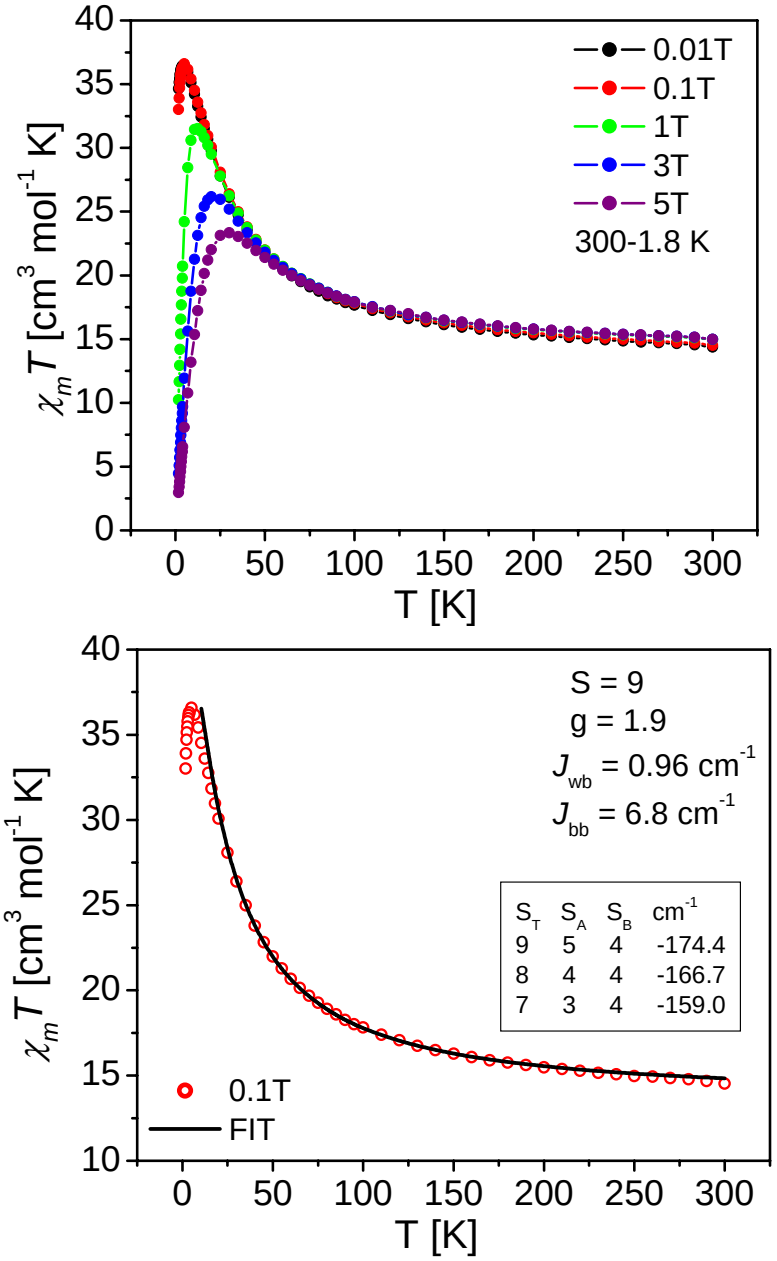

Figure 4.12. Variable temperature DC magnetic susceptibility for complex **$[Mn_4(anca)_4(mdea)_2(Hmdea)_2]\cdot 2CHCl_3$ (4A)** collected from 300K to 1.8K. (Top) Field and temperature dependence of variable temperature magnetic susceptibility with applied fields of 0.01-5T. (Bottom) Least squares fit of 0.1 Tesla data (○ observed, ─ theoretical fit). Inset box indicates eigen energy and spin state distributions (S_T, S_A, S_B and eigen energy in cm^{-1}) from theoretical fit of experimental data.

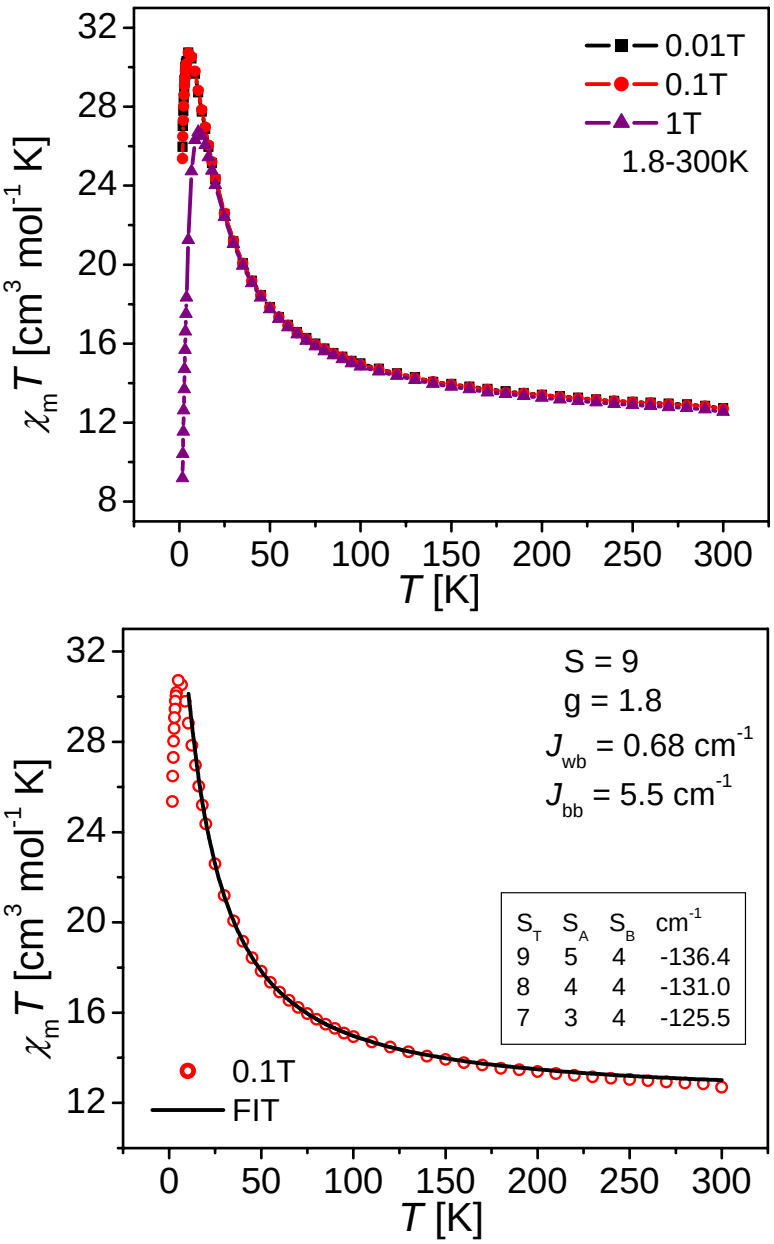

Figure 4.13. Variable temperature DC magnetic susceptibility for complex **[Mn$_4$(anca)$_4$(Hedea)$_2$(edea)$_2$]·2CHCl$_3$,2EtOH (4B)** collected from 300K to 1.8K. (Top) Field and temperature dependence of variable temperature magnetic susceptibility with applied fields of 0.01-1T. (Bottom) Least squares fit of 0.1 Tesla data (○ observed, — theoretical fit). Inset box indicates eigen energy and spin state distributions (S_T, S_A, S_B and eigen energy in cm^{-1}) from fit of experimental data.

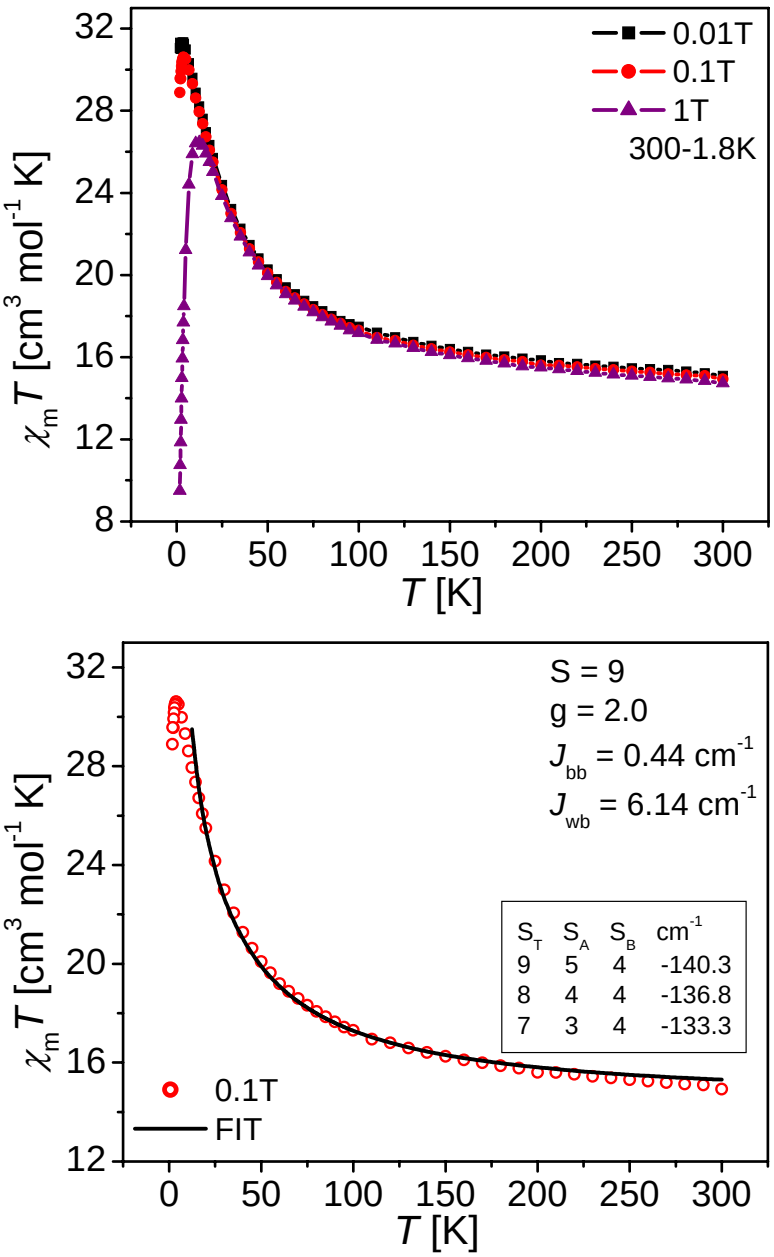

Figure 4.14. Variable temperature DC magnetic susceptibility for complex **$[Mn_4(anca)_4(Hn\text{-}bdea)_2(n\text{-}bdea)_2]\cdot 1MeCN,0.5CHCl_3$ (4C)** collected from 300K to 1.8K. (Top) Field and temperature dependence of variable temperature magnetic susceptibility with applied fields of 0.01-1T. (Bottom) Least squares fit of 0.1 Tesla data (○ observed, — theoretical fit). Inset box indicates eigen energy and spin state distributions (S_T, S_A, S_B and eigen energy in cm^{-1}) from fit of experimental data.

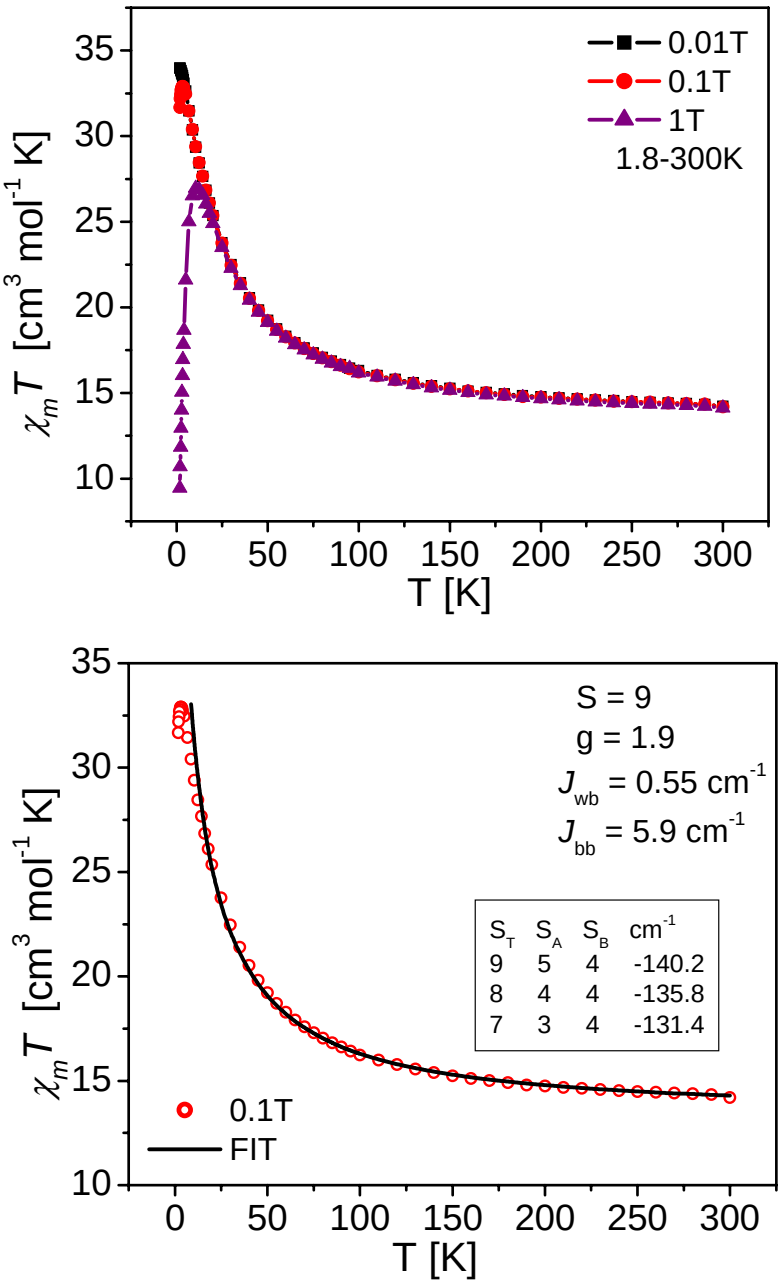

Figure 4.15. Variable temperature DC magnetic susceptibility with best fit for complex **[Mn$_4$(anca)$_4$(Hbzdea)$_2$(bzdea)$_2$]·MeCN (4D)** collected from 300K to 1.8K at an applied field of 0.1 Tesla. (○ observed, ─ theoretical fit). Inset box indicates eigen energy and spin state distributions (S_T, S_A, S_B and eigen energy in cm^{-1}) from fit of experimental data.

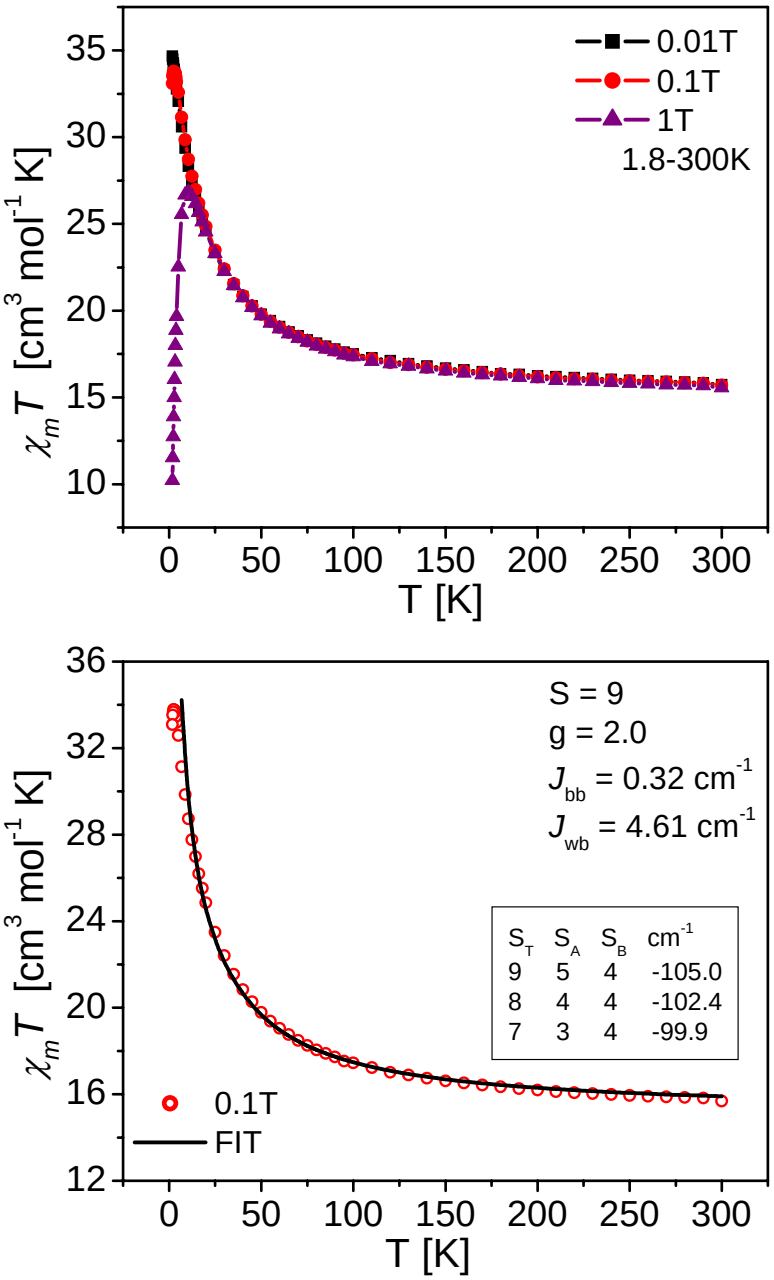

Figure 4.16. Variable temperature DC magnetic susceptibility with best fit for complex **[Mn$_4$(β-naphth)$_4$(Hmdea)$_2$(mdea)$_2$]·Et$_2$O (4E)** collected from 300K to 1.8K at an applied field of 0.1 Tesla. (○ observed, ─ theoretical fit). Inset box indicates eigen energy and spin state distributions (S_T, S_A, S_B and eigen energy in cm^{-1}) from fit of experimental data.

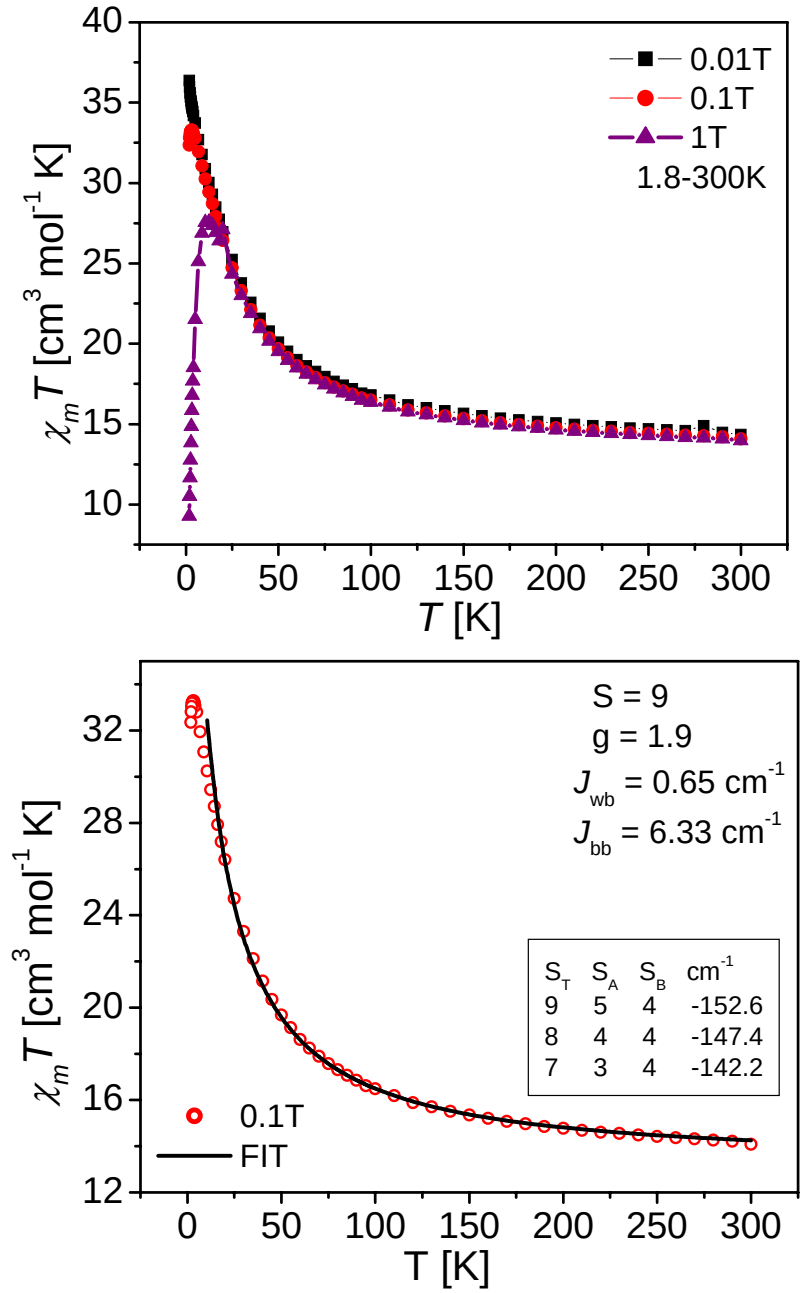

Figure 4.17. Variable temperature DC magnetic susceptibility with best fit for complex **[Mn$_4$(β-naphth)$_4$(Hedea)$_2$(edea)$_2$]·MeCN,EtOH (4F)** collected from 300K to 1.8K at an applied field of 0.1 Tesla. (○ observed, ─ theoretical fit). Inset box indicates eigen energy and spin state distributions (S_T, S_A, S_B and eigen energy in cm^{-1}) from fit of experimental data.

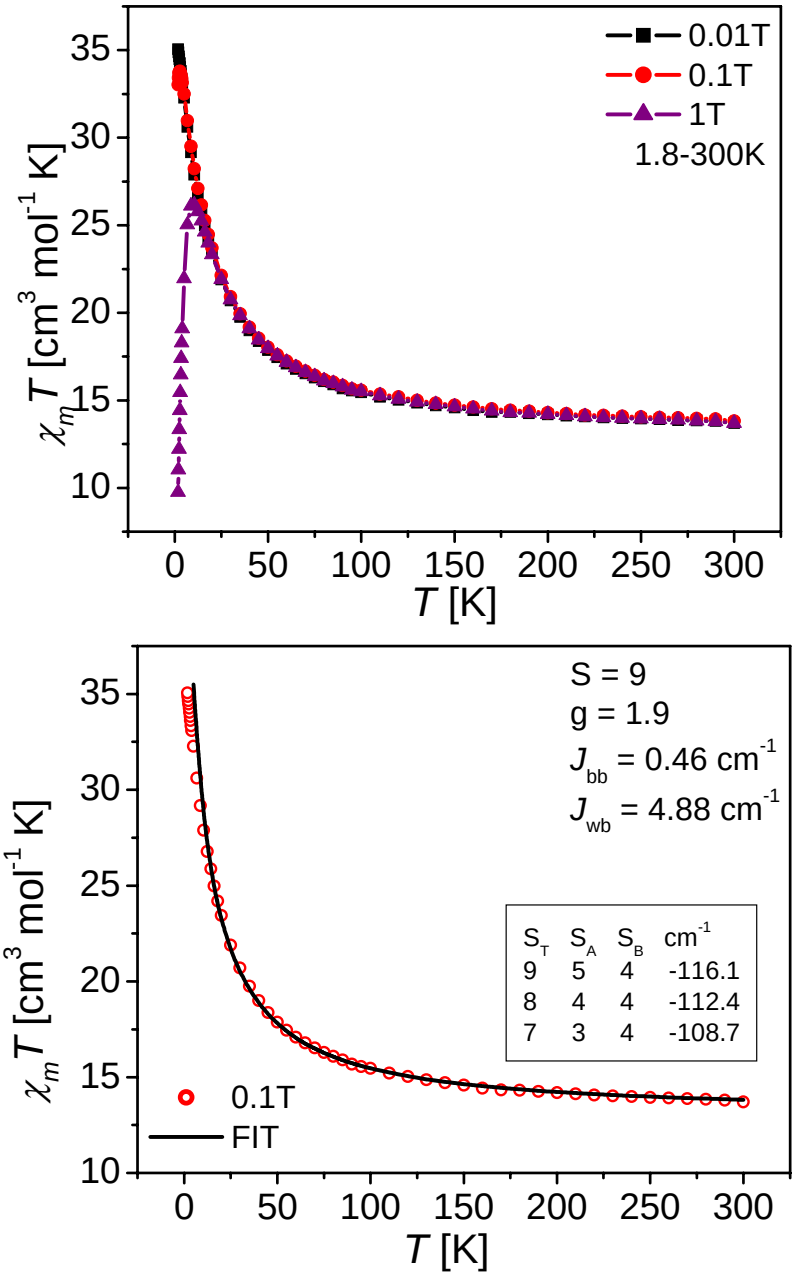

Figure 4.18. Variable temperature DC magnetic susceptibility with best fit for complex **$[Mn_4(\beta\text{-naphth})_4(Hn\text{-bdea})_2(n\text{-bdea})_2]\cdot 2CH_2Cl_2$ (4G)** collected from 300K to 1.8K at an applied field of 0.1 Tesla. (○ observed, ─ theoretical fit). Inset box indicates eigen energy and spin state distributions (S_T, S_A, S_B and eigen energy in cm^{-1}) from fit of experimental data.

of 14.75 $cm^3 \cdot K \cdot mol^{-1}$ for two Mn^{II} and two Mn^{III} non-interacting metal centers.

$$\hat{H} = -2\sum_{ij} J_{ij}\hat{S}_i \cdot \hat{S}_j \quad \textbf{(4.1)}$$

$$\hat{H} = -2[J_{12}(\hat{S}_1 \cdot \hat{S}_2) + J_{23}(\hat{S}_2 \cdot \hat{S}_3) + J_{24}(\hat{S}_2 \cdot \hat{S}_4) + J_{34}(\hat{S}_3 \cdot \hat{S}_4) + J_{41}(\hat{S}_4 \cdot \hat{S}_1)] \quad \textbf{(4.2)}$$

$$J_{12} = J_{14} = J_{23} = J_{34} = J_{wb}; \quad J_{24} = J_{bb} \quad \textbf{(4.3)}$$

$$S_A = S_1 + S_3; \quad S_B = S_2 + S_4; \quad S_T = S_A + S_B \quad \textbf{(4.4)}$$

$$E(S_T) = -J_{wb}[S_T(S_T+1) - S_A(S_A+1) - S_B(S_B+1)] - J_{bb}[S_B(S_B+1)] \quad \textbf{(4.5)}$$

$$\chi_M = \left(\frac{Ng^2\mu_B^2}{3kT}\right)\frac{\sum[S_T(S_T+1)(2S_T+1)e^{\frac{-E(S_T)}{k_BT}}}{\sum(2S_T+1)e^{\frac{-E(S_T)}{k_BT}}} \quad \textbf{(4.6)}$$

To ascertain the spin ground state (S), g and the Heisenberg isotropic intramolecular coupling constants (*J*) for complexes **4A-4G**, least-squares analysis was performed. A Kambe model [91] was employed, with exchange coupled pathways shown in Scheme 4.3. The Kambe model was used in conjunction with the Heisenberg spin Hamiltonian (Equation 4.1), where J_{ij} represents the magnetic exchange parameter between the *i*-th and *j*-th magnetic centers with spin *S*. Expansion of Equation 4.1 with appropriate exchange pathways yields Equation 4.2. Complexes **4A-G** have a mixed valent $Mn_2^{II}Mn_2^{III}$ core, thus, S_1 and S_3 in Equation 4.2 and 4.4 are Mn^{II} ions and S_2 and S_4 are Mn^{III} ions. The resultant Eigenvalue equation (Equation 4.5) was evaluated employing the Van Vleck equation (Equation 4.6) using least-squares methods. The

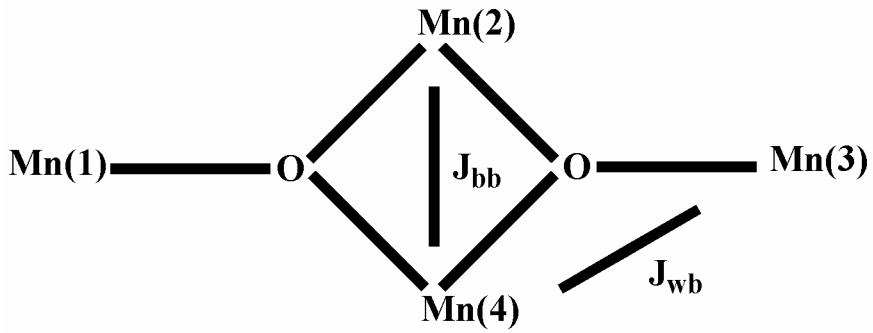

Scheme 4.3. The Kambe coupling model illustrating magnetic exchange pathways J_{wb} and J_{bb} for complexes **2-9**, where S_1, S_2, S_3 and S_4 are Mn^{III} ions for complex **2**, and S_1 and S_3 are Mn^{II} ions and S_2 and S_4 are Mn^{III} ions for complexes **4A-G.**

best fit of experimental data are presented as solid lines in Figures **3.17-3.23 (**bottom). The fitting parameters S, g, J_{wb} and J_{bb} for complexes **4A-G** are presented in Table 4.7.

Except for one S = 8,[80] all reported mixed-valent tetranuclear manganese complexes with dicubane topology have exhibited spin ground states of S = 9, and in all cases the coupling constants J_{wb} and J_{bb} have been positive.[63](and references therein). Interestingly, complexes **4A-G** do not wholly follow this trend. A good fit of magnetization data can be obtained for complexes **4A-G** with J_{wb} positive or negative, with a positive J_{wb} parameter yielding a S = 9 ground state, and negative J_{wb} resulting in a S = 8 ground state. Figure 4.19 presents fits of magnetization data (solid lines) for complexes **4B** and **4F** with fit parameters of S = 8, g = 1.8, J_{wb} = -2.35 cm^{-1}, J_{bb} = 2.76 cm^{-1} for complex **4B**, and S = 8, g =1.9, J_{wb} = -3.70 cm^{-1}, J_{bb} = 2.70 cm^{-1} for complex **4F**. The distribution of eigen-states are given in Figures 4.20 and 4.21 for complexes **4B** and **4F**, respectively, with the eigen-energies of the 110 states plotted verses spin value (S = 0, 1, 2….9). The calculated J_{wb} and J_{bb} values are commensurate with previously reported dicubanes when both coupling constants are positive.[63] However, analysis of the error surface plots given in Figures 4.22 and 4.23 for complexes **4B** and

4F, respectively, reveal that the fit error is significantly minimized when the wing-body interaction is negative. Though more pronounced for complex **4B**, Figure 4.22 (top) and Figure 4.23 (top) show that as the magnitude of the wing-body (J_{wb}) interaction goes from positive to negative the fitting error is reduced. Figures 4.22 and 4.23 show that the magnitude of the body-body interaction (J_{bb}) is relatively invariant to changes in the wing-body interaction until it reaches -1.5 cm^{-1}, at which time, the magnitude of the body-body interaction increases (more positive) with decreasing value (more negative) of the wing-body interaction. Thus, the error surface plots support the fits of $\chi_m T$ versus T data for the S = 8 ground states with negative wing-body interactions. Furthermore, the error surface plots suggest that there is not a well defined energy minimum for these complexes. This is most likely due to mixing of low-lying excited states.

Table 4.7. Comparison of $\chi_m T$ versus T fit parameters S, g, J_{wb} and J_{bb} through least squares analysis for complexes **4A-4G,** and the energy associated with the first excited state and the energy gap to the calculated spin ground state in parenthesis.

Complex	S	g	J_{bb} (cm^{-1})	J_{wb} (cm^{-1})	Excited State (S, cm^{-1})
A	9	1.9	0.96	6.8	S = 8 (7.7)
B	9	1.8	0.68	5.5	S = 8 (5.4)
C	9	2.0	0.44	6.1	S = 8 (3.5)
D	9	1.9	0.55	5.9	S = 8 (4.4)
E	9	2.0	0.32	4.6	S = 8 (2.6)
F	9	1.9	0.65	6.3	S = 8 (5.2)
G	9	1.9	0.46	4.9	S = 8 (3.7)

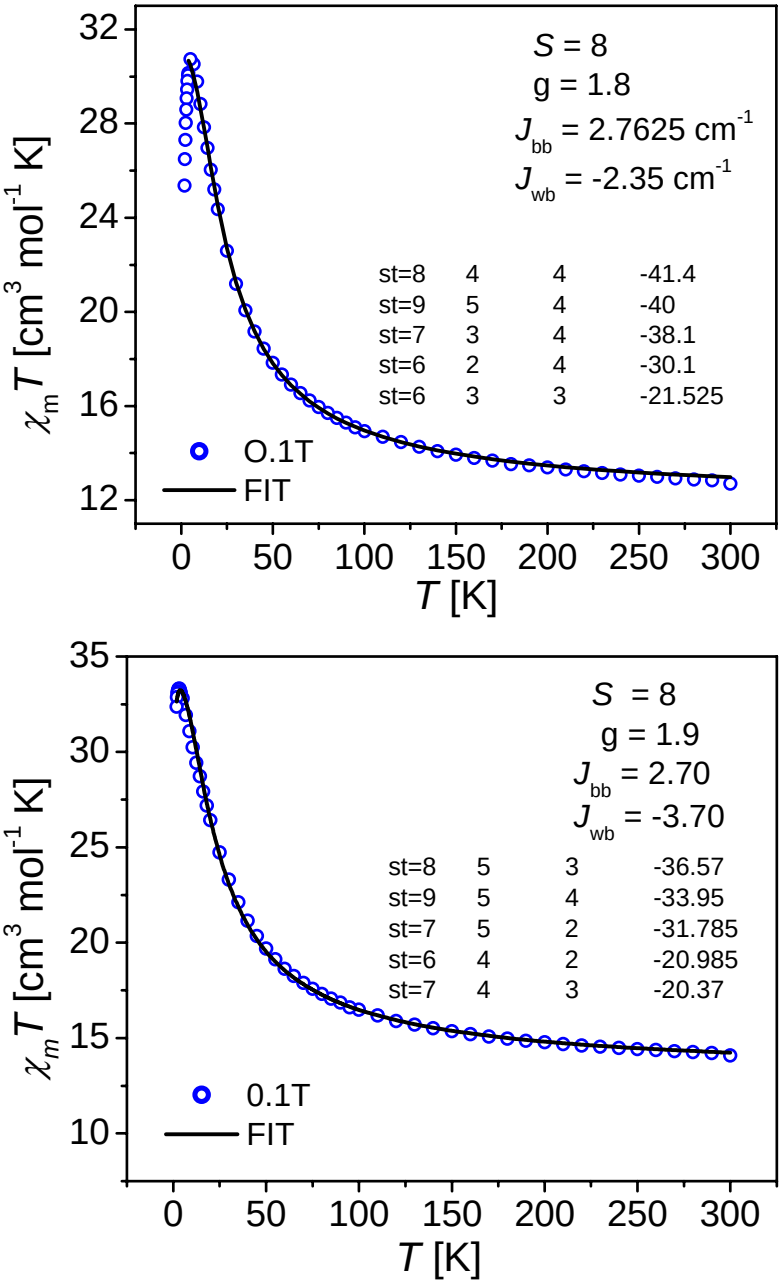

Figure 4.19. Variable temperature DC magnetic susceptibility with best fit for complexes **$Mn_4(anca)_4(Hedea)_2(edea)_2]\cdot 2CHCl_3$,2EtOH (4B)** (top) and **[Mn_4(β-naphth)$_4$(Hedea)$_2$(edea)$_2$]·MeCN,EtOH (4F)** (bottom), collected from 300K to 1.8K at an applied field of 0.1 Tesla. (○ = observed, ─ theoretical fit). Inset box indicates eigen energy and spin state distributions (S_T, S_A, S_B and eigen energy in cm^{-1}) from least-squares fitting of experimental data.

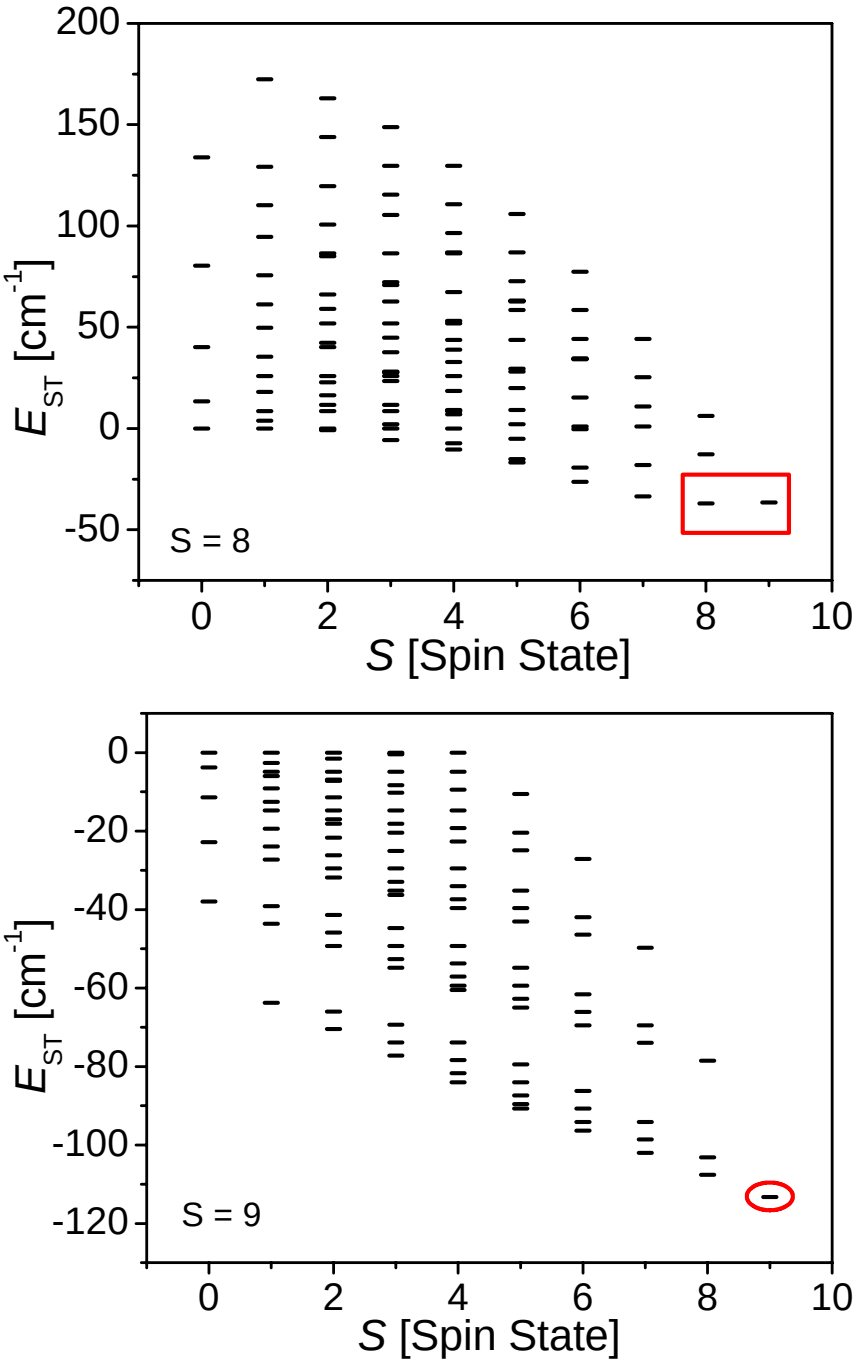

Figure 4.20. Distribution of calculated eigen-energies [$E(S_T)$] verses spin total [S_T] of the 110 states (S_T, S_B, S_A) of complex **[Mn$_4$(anca)$_4$(Hedea)$_2$(edea)$_2$]·2CHCl$_3$,2EtOH (4B)** indicating the S = 8 spin ground state lies at lowest energy when J_{wb} is negative and J_{bb} is positive (top) and S = 9 state is at lowest energy when J_{wb} and J_{bb} are both positive.

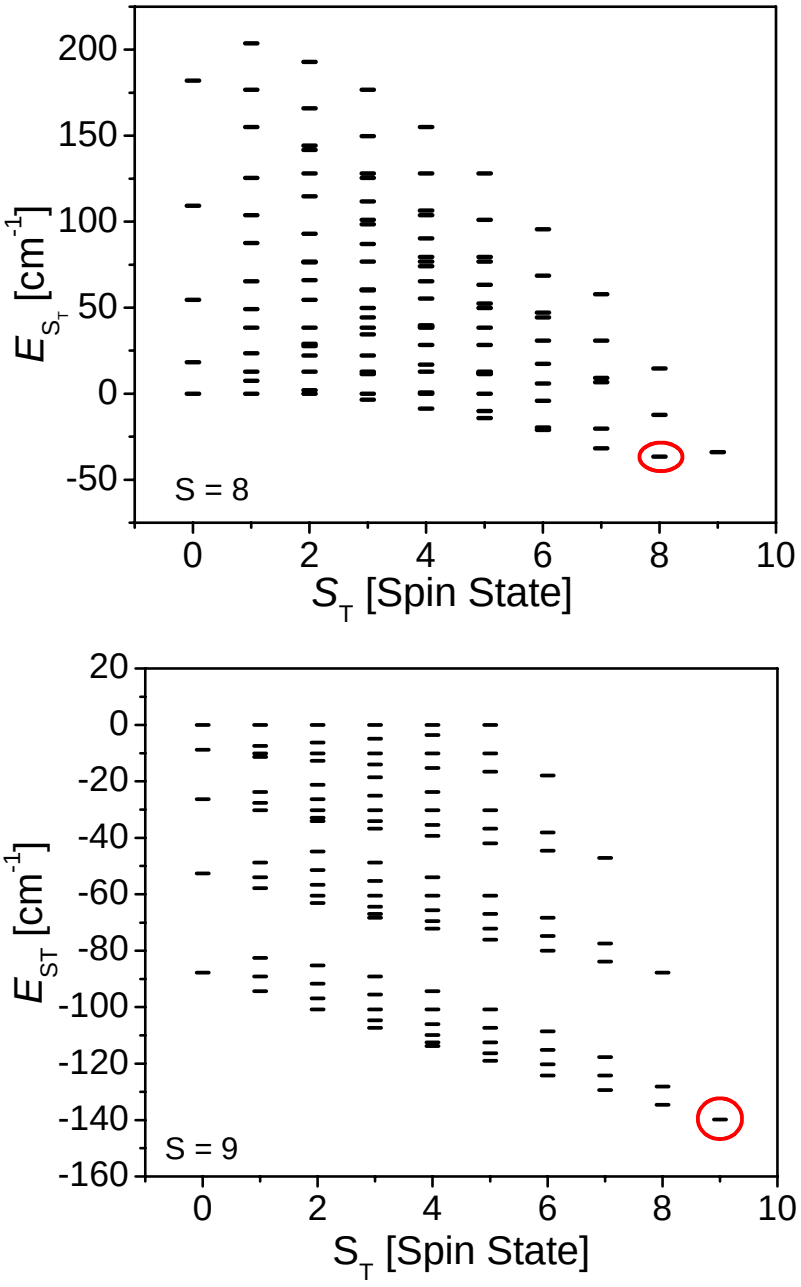

Figure 4.21. Distribution of calculated eigen-energies [$E(S_T)$] verses spin total [S_T] of the 110 states (S_T, S_B, S_A) of complex **[Mn$_4$(β-naphth)$_4$(Hedea)$_2$(edea)$_2$]·MeCN,EtOH (4F)** indicating the S = 8 spin ground state lies at lowest energy when J_{wb} is negative and J_{bb} is positive (top) and when J_{wb} and J_{bb} are both positive (bottom) yielding a S = 9 spin ground state.

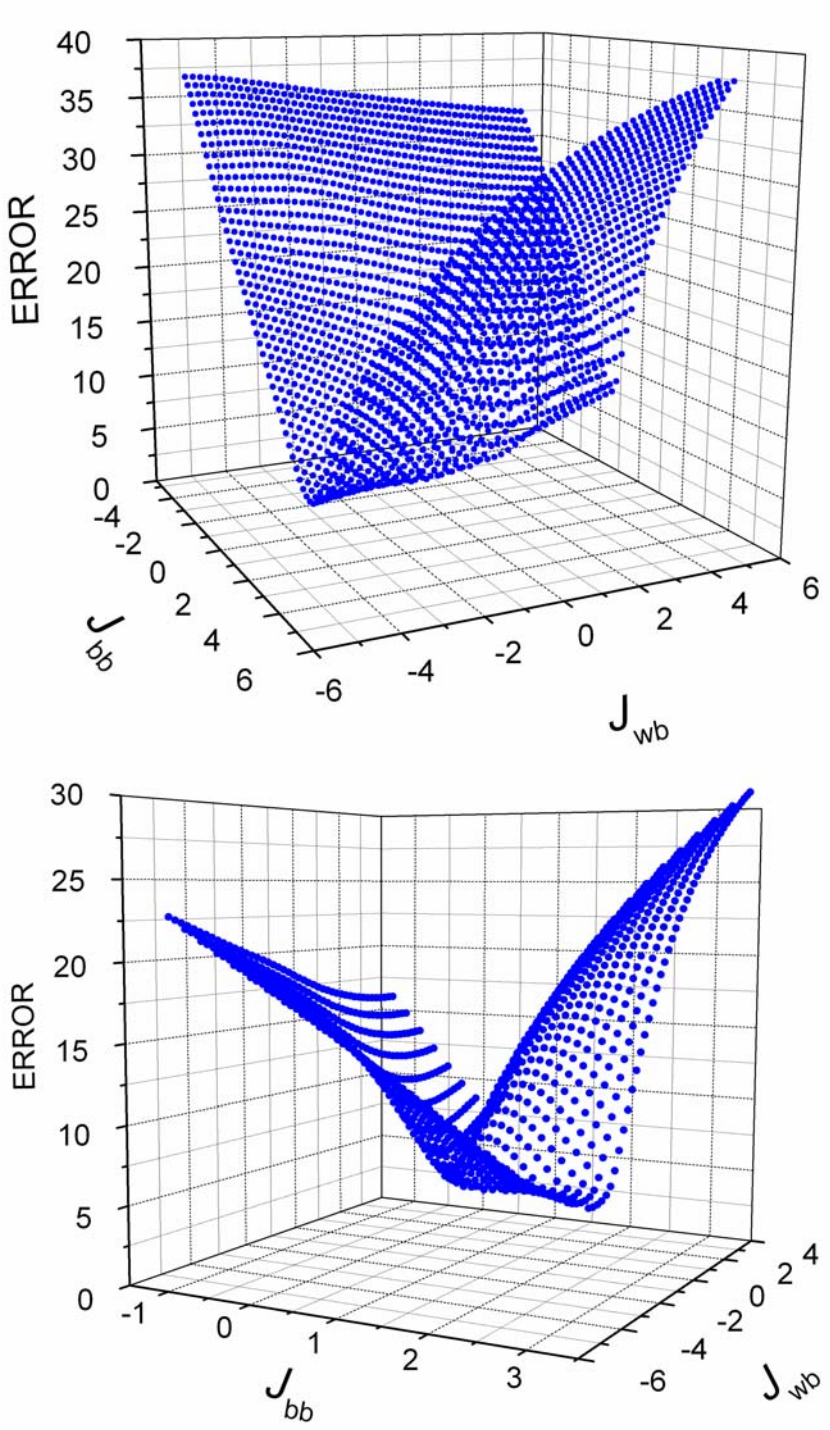

Figure 4.22. J_{bb} verses J_{wb} error surface plots for complex **$[Mn_4(anca)_4(Hedea)_2(edea)_2]\cdot 2CHCl_3$,2EtOH** (**4B**) derived from fit of variable temperature magnetic susceptibility data. (Top) Error improves as J_{wb} becomes more negative. (Bottom) The error associated with J_{bb} is invariant to changes in J_{wb}. However, the magnitude of J_{bb} increases with decreasing J_{wb}.

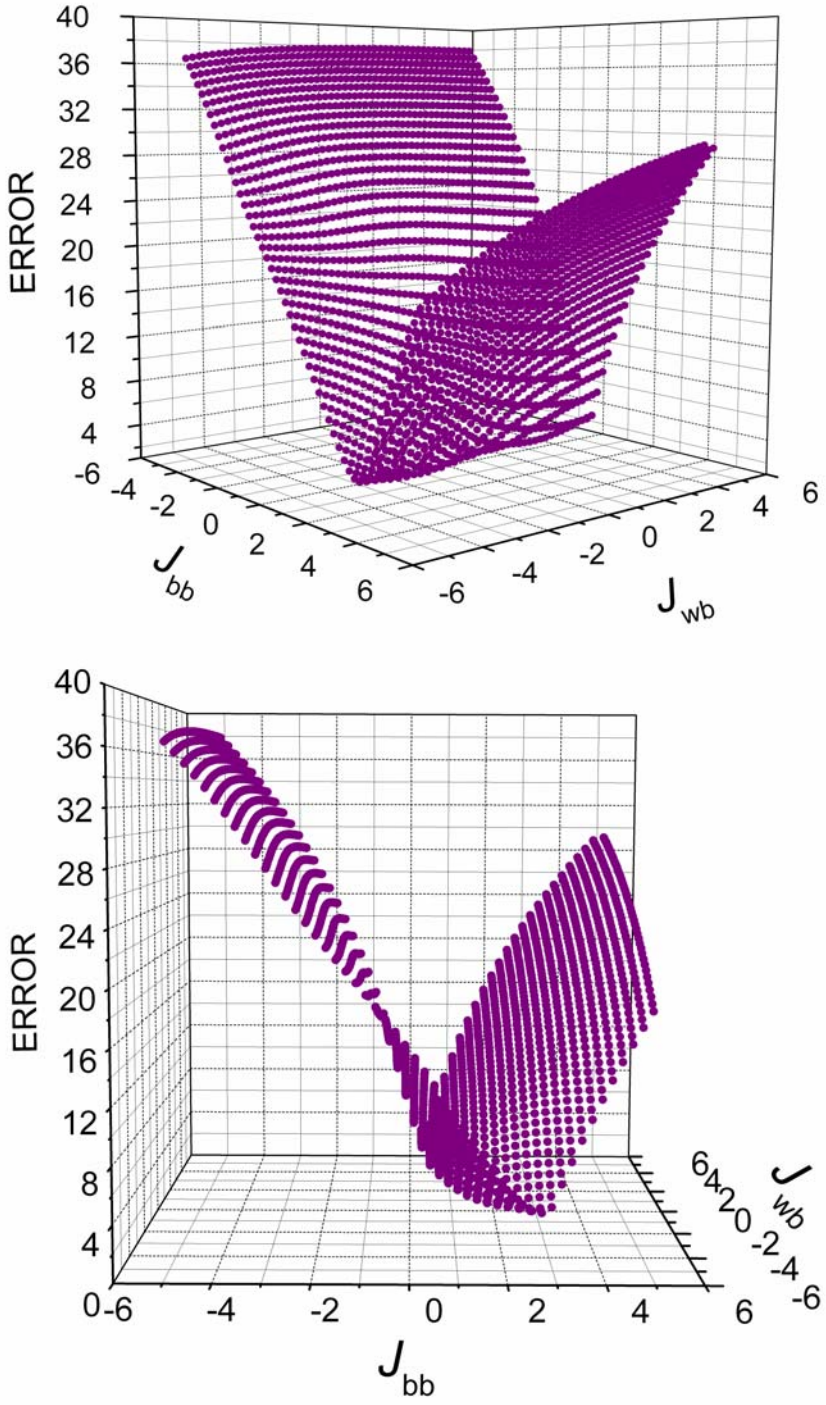

Figure 4.23. J_{bb} verses J_{wb} error surface plots for complex **[Mn$_4$(β-naphth)$_4$(Hedea)$_2$(edea)$_2$]·MeCN,EtOH** (**4F**) derived from fit of variable temperature magnetic susceptibility data. (Top) Error improves as J_{wb} becomes more negative. (Bottom) The error associated with J_{bb} is invariant to changes in J_{wb}. However, the magnitude of J_{bb} increases with decreasing J_{wb}.

Reduced Magnetization Complexes 4A-4G

To further establish the spin ground state and the magnitude of the zero-field splitting parameter *D*, variable-field magnetization data (reduced magnetization) were collected for complexes **4A-G** between 1.8K and 4K, with applied fields of 0.1-5 Tesla. At the lowest temperatures and in high applied magnetic fields it is possible to experience only the susceptibility from the lowest-energy spin state. Figures 4.24-4.30 present reduced magnetization data plotted as $M/N\beta$ vs. H/T for complexes **4A-G**, where M is the molar magnetization, N is Avogadro's number, β is the Bohr magneton and H/T is the applied magnetic field over the absolute temperature. The saturation values between ~13-15 (Figures 4.24-4.30) suggest that complexes **4A-G** exhibit significant spin ground states, and non-superimposibility of the iso-fields indicate that complexes **4A-G** exhibit appreciable ground state zero-field splitting. Theoretical fits to the magnetization data, solid lines in Figures 4.24-4.30**,** were calculated by full-matrix diagonalization employing energy Hamiltonian given in Equation 4.7, where $\mu_B g H \cdot S$ is the Zeeman term, where μ is the Bohr magneton, g is the Landé g-factor, H is the applied magnetic field, S is the total spin, D is the second–order zero-field splitting parameter and E is the second-order rhombic term. Least-squares treatment of the magnetization data (solid lines in Figures 4.24-4.30) yielded the fitting parameters given in Table 4.8. The fits of reduced magnetization for complexes **4A-G** are commensurate with previously reported

$$\mathcal{H} = \mu_B g H \cdot S + D[S_Z^2 - \frac{1}{3}S(S+1)] \qquad \textbf{(4.7)}$$

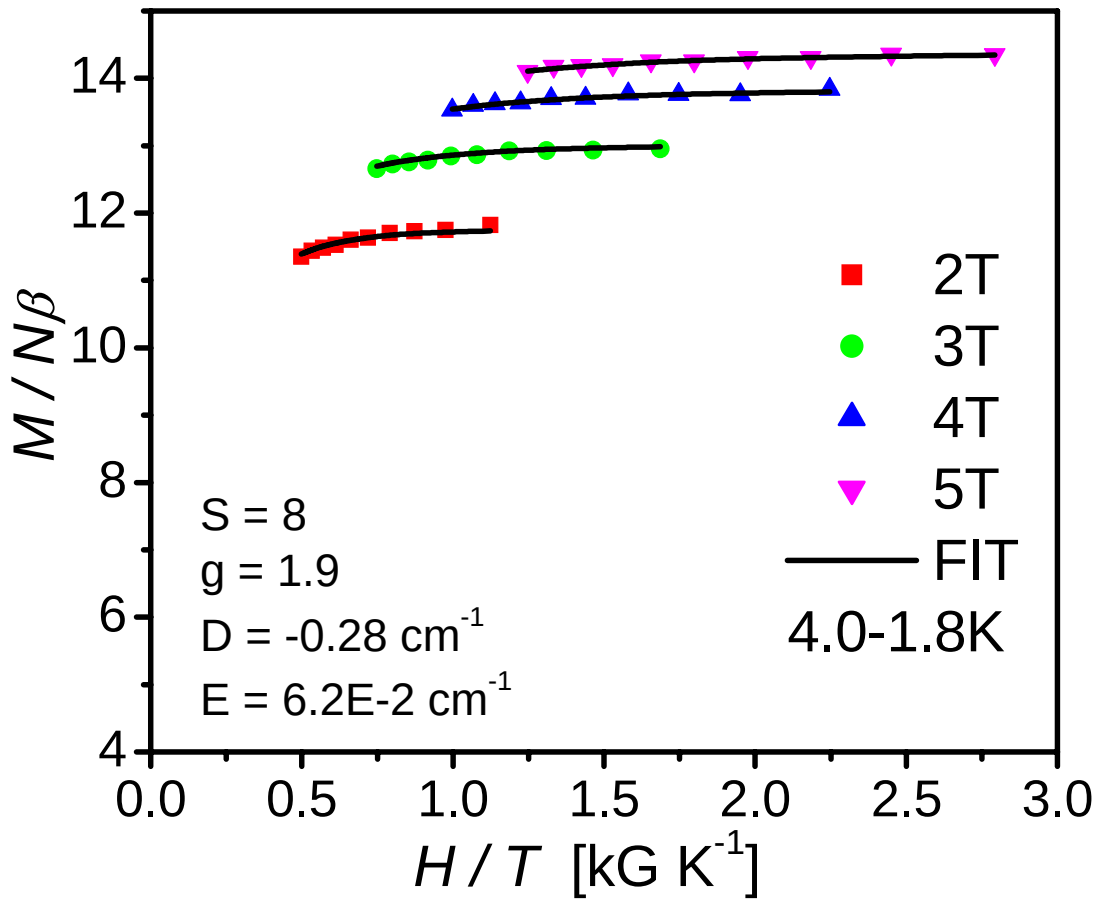

Figure 4.24. Reduced magnetization *M/Nβ* vs. *H/T* plot for **$[Mn_4(anca)_4(mdea)_2(Hmdea)_2]\cdot 2CHCl_3$ (4A)** from 1.8-4K, with applied fields of 2-5 Tesla. Calculated parameters: $S = 8$, $g = 1.9$, $D = 0.28$ cm^{-1} and $E = 6.2$E-2 cm^{-1}.

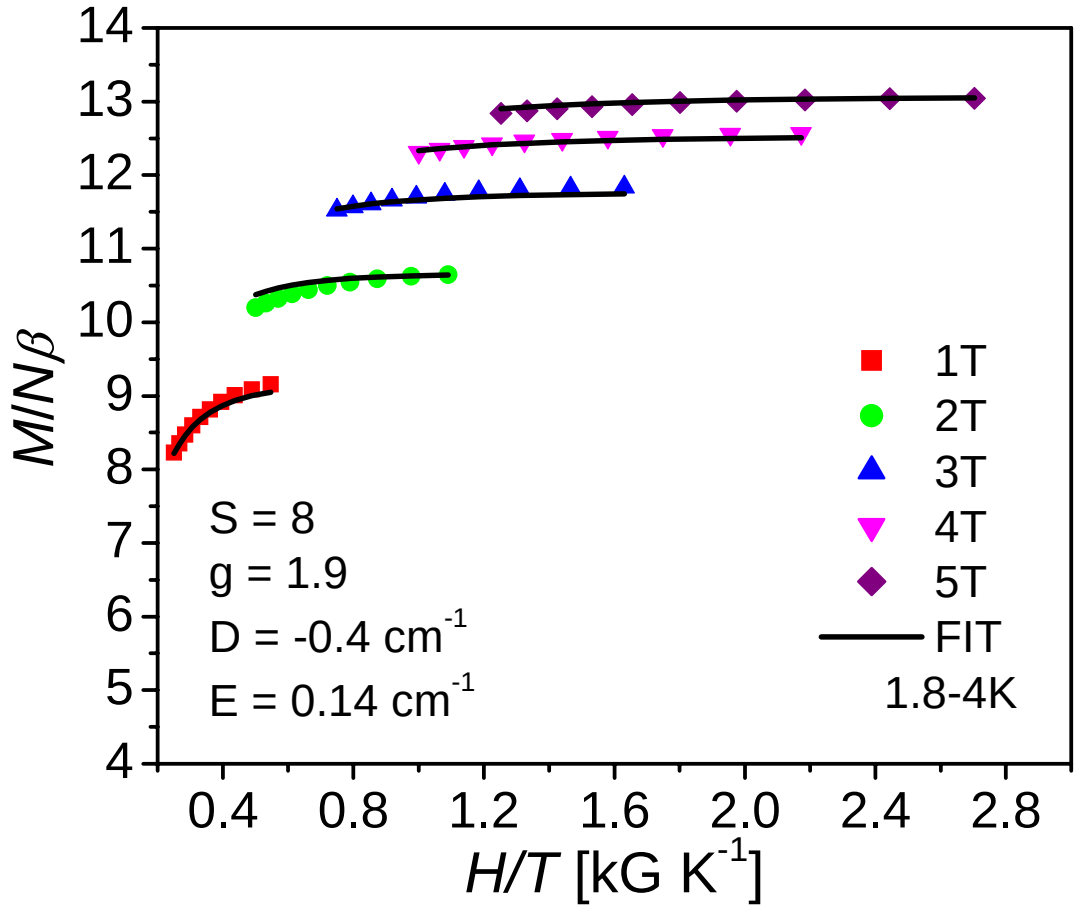

Figure 4.25. Reduced magnetization $M/N\beta$ vs. H/T plot for **$[Mn_4(anca)_4(Hedea)_2(edea)_2]\cdot 2CHCl_3,2EtOH$ (4B)** from 1.8-4K, with applied fields of 1-5 Tesla. Calculated parameters: $S = 8$, $g = 1.9$, $D = 0.40$ cm^{-1} and $E = 0.14$ cm^{-1}.

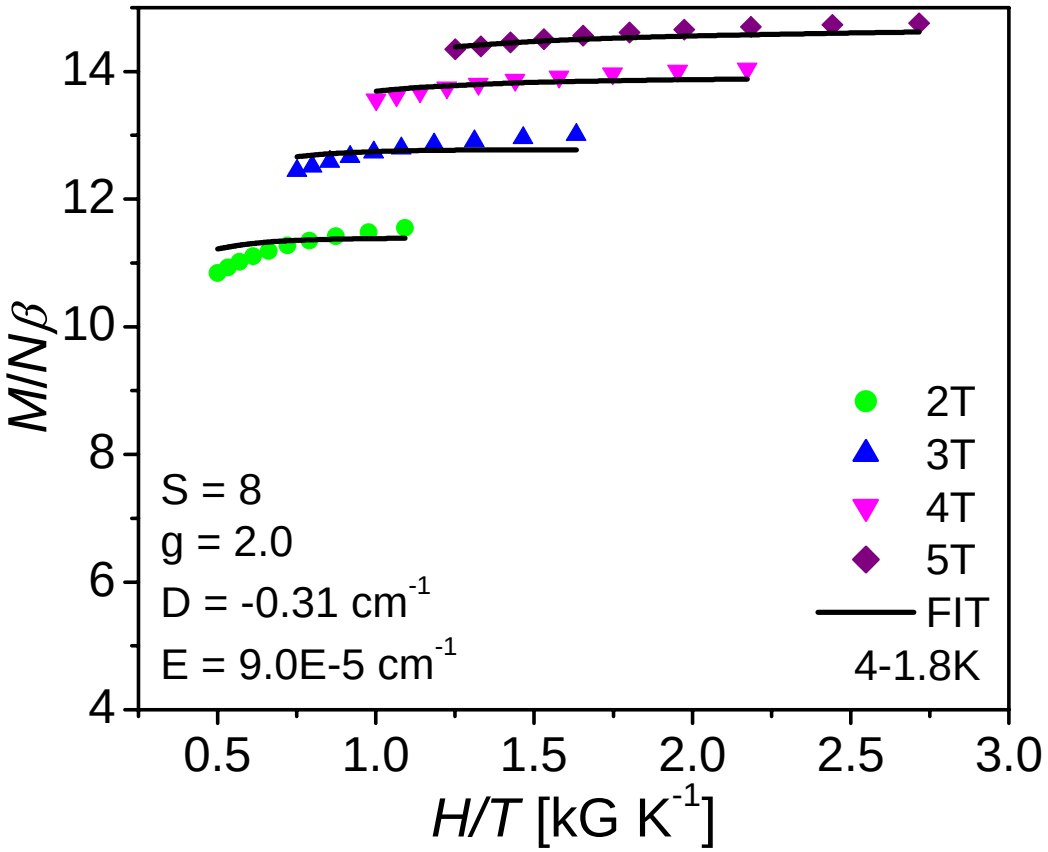

Figure 4.26. Reduced magnetization *M/Nβ* vs. *H/T* plot for **$Mn_4(anca)_4(Hn\text{-}bdea)_2(n\text{-}bdea)_2]\cdot 1MeCN,0.5CHCl_3$ (4C)** from 1.8-4K, with applied fields of 1-5 Tesla. Calculated parameters: $S =$, $g =$, $D =$ cm^{-1} and $E =$ cm^{1}.

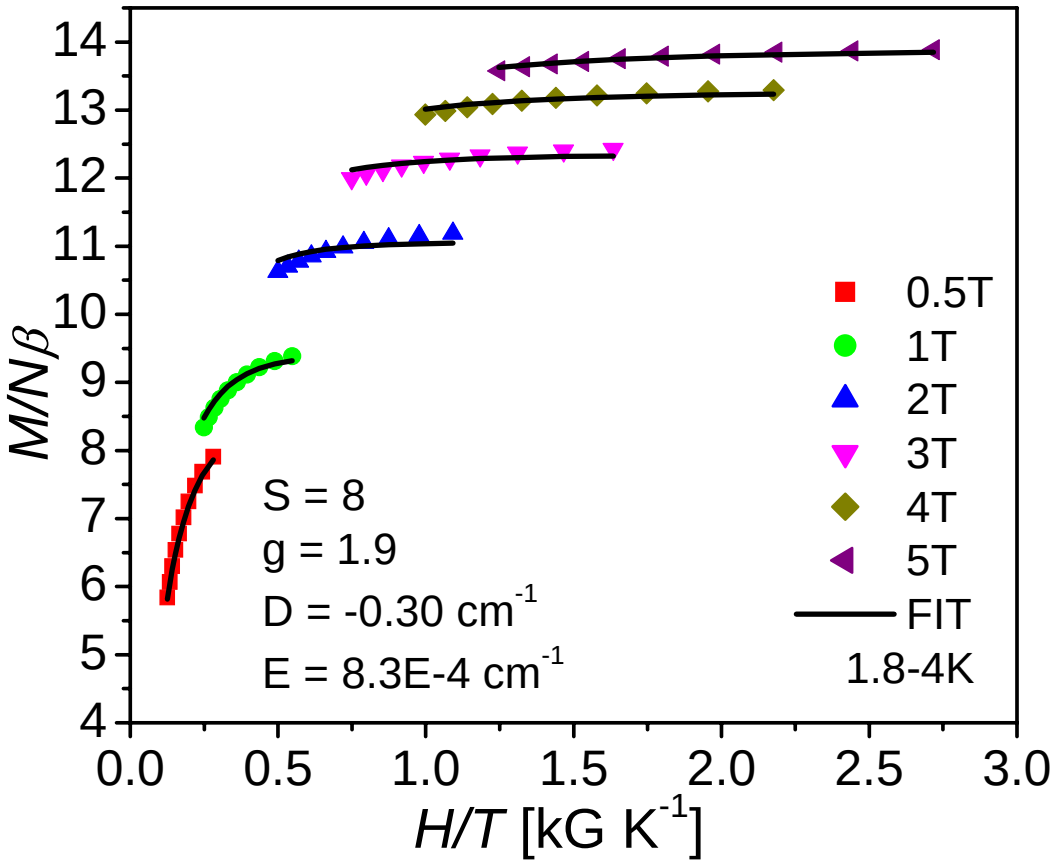

Figure 4.27. Reduced magnetization $M/N\beta$ vs.H/T plot for **$[Mn_4(anca)_4(Hbzdea)_2(bzdea)_2]\cdot MeCN$ (4D)** from 1.8-4K, with applied fields of 0.5-5 Tesla. Calculated parameters: $S = 8$, $g = 1.9$, $D = 0.30$ cm^{-1} and $E = 8.3$E-4 cm^{-1}.

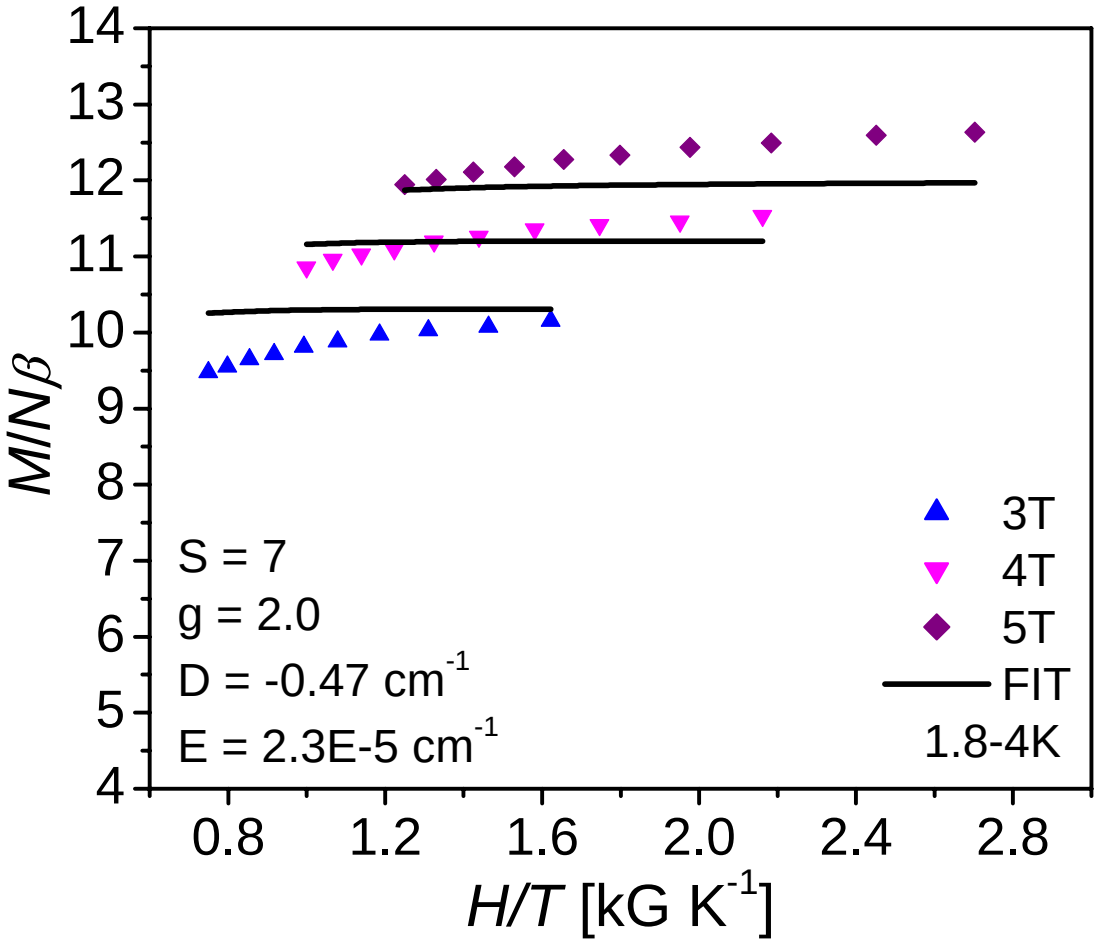

Figure 4.28. Reduced magnetization *M/Nβ* vs. *H/T* plot for **[Mn_4(β-naphth)$_4$(Hmdea)$_2$(mdea)$_2$]·Et_2O (4E)** from 1.8-4K, with applied fields of 1-5 Tesla. Calculated parameters: S =7 , g =2 , D = -0.47 cm^{-1} and E = 2.3E-5 cm^{1}.

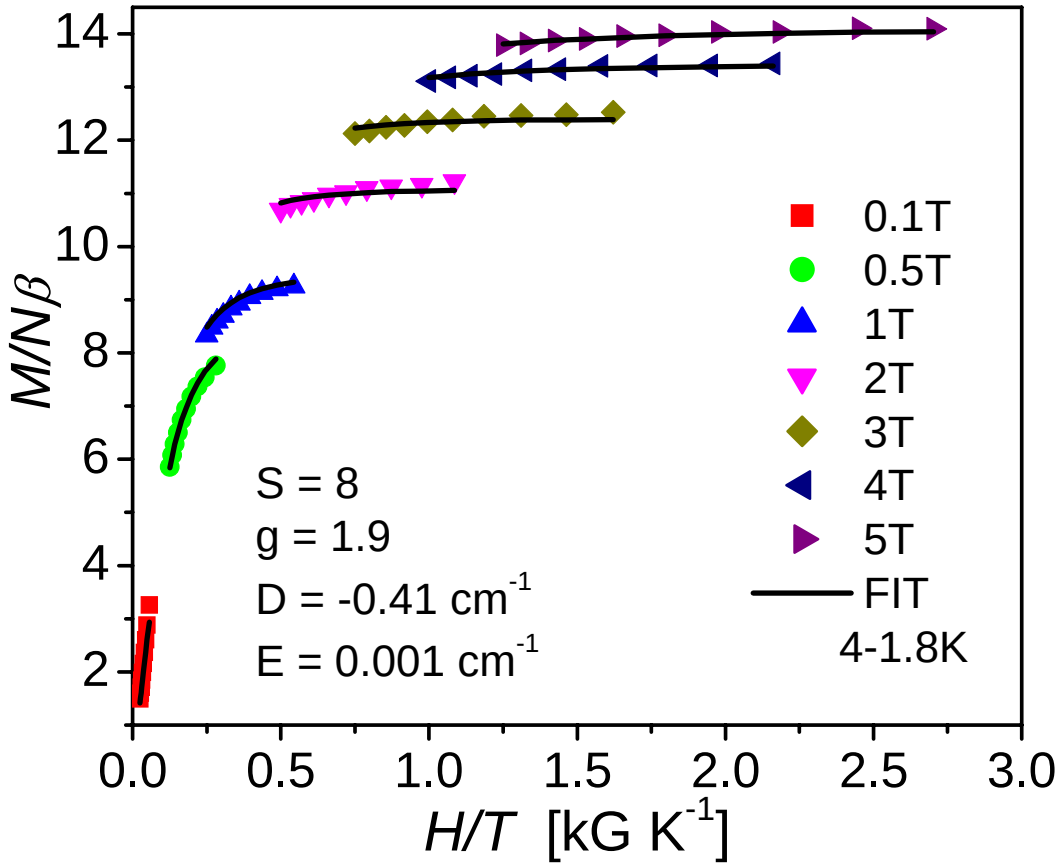

Figure 4.29. Reduced magnetization *M/Nβ* vs. *H/T* plot for **[Mn$_4$(β-naphth)$_4$(Hedea)$_2$(edea)$_2$]·MeCN,EtOH (4F)** from 1.8-4K, with applied fields of 1-5 Tesla. Calculated parameters: S = 8, g = 1.9, D = 0.41 cm^{-1} and E = 0.001 cm^{1}.

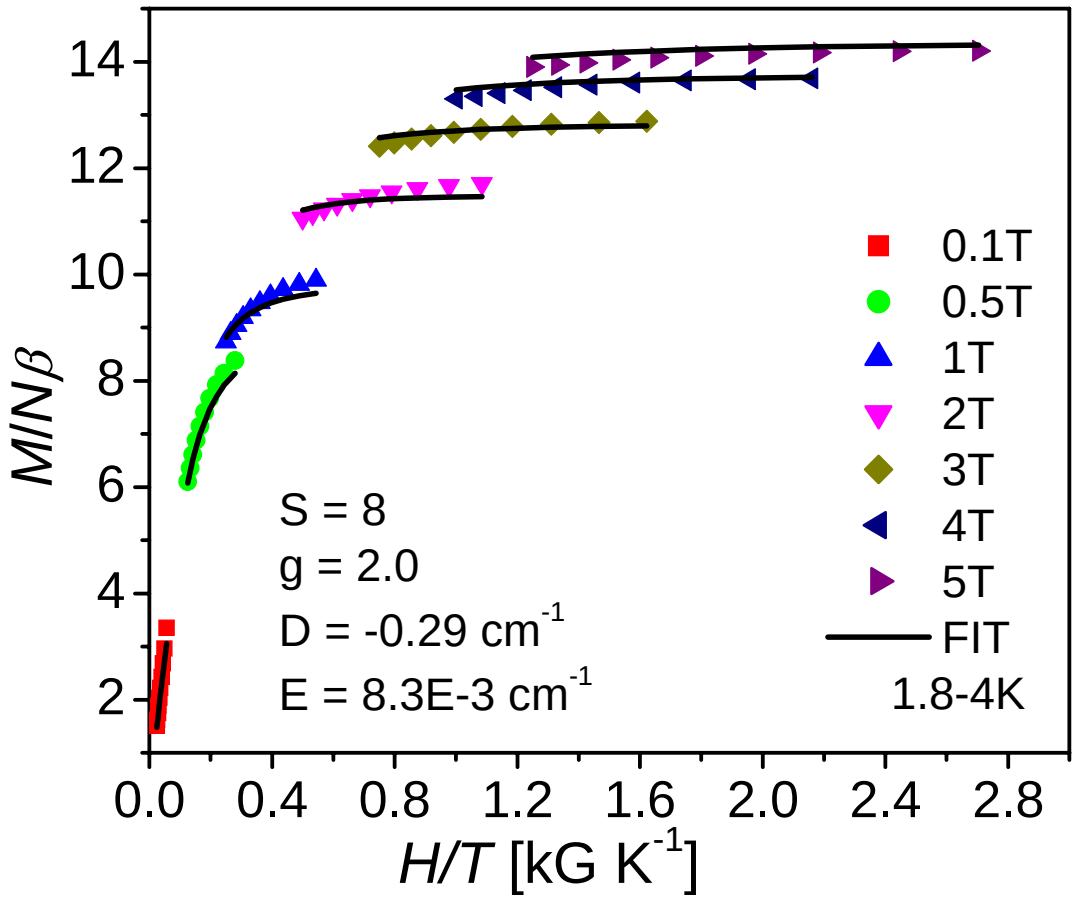

Figure 4.30. Reduced magnetization *M/Nβ* vs. *H/T* plot for **[Mn_4(β-naphth)$_4$(Hn-bdea)$_2$(n-bdea)$_2$]·2CH_2Cl_2 (4G)** from 1.8-4K, with applied fields of 1-5 Tesla. Calculated parameters: $S = 8$, $g = 2.0$, $D = 0.29$ cm^{-1} and $E = 8.3E\text{-}3$ cm^{1}.

Table 4.8. Comparison of fit parameters *for M/Nβ* verses *H/T* data for complexes **4A-4G**.

Conplex	S	g	*D*(cm^{-1})	*E*(cm^{-1})
A	8	1.9	-0.28	6.2E-2
B	8	1.9	-0.41	0.14
C	8	2.0	-0.31	9.0E-5
D	8	1.9	-0.30	8.3E-4
E	7	2.0	-0.47	2.3E-5
F	8	1.9	-0.41	1.0E-3
G	8	2.0	-0.29	8.3E-3

Mn_4 dicubane complexes.[63] Reasonable theoretical fits were obtained for complexes **4A-G** yielding $S = 8$ ground states, except for complex **4E**, which yielded a relatively poor fit with an $S = 7$ ground state. In each case, a good fit to the theoretical model could not be obtained employing all the experimental data. Satisfactory fits could only be obtained employing high-field data. The theoretical model dictates that there is a well defined, well isolated ground state. It is evident from fitting of variable temperature ($\chi_m T$) data that there are numerous energy states in close proximity to the ground state. Thus, the model cannot fully explain the electronic structure of these series of complexes. In chapter 5, full-matrix diagonalization in an uncoupled basis set will be presented along with oriented single crystal high-frequency electron paramagnetic resonance and magnetization hysteresis experiments to elucidate the ground state of these interesting complexes.

4.3.4 AC Magnetic Susceptibility Studies

AC magnetic susceptibility data for complexes **4A-G** are presented in Figures 4.31-4.37 with in-phase (top) and out-of-phase susceptibility (bottom) plotted as χ_m vs. T. The data were collected between 5K and 1.8K and frequencies of 10Hz to 1000Hz with zero applied DC field, and an oscillating AC field of 3 Gauss. Complexes **4A-G** all show both temperature and frequency dependent out-of-phase signals. Temperature and frequency dependence is indicative of slow magnetization relaxation processes that arise due to the inability of the magnetic moment of the SMM to stay in phase with the oscillating magnetic field.

Figures 4.38-4.44 present 10Hz in-phase ac magnetic susceptibility data plotted as $\chi_m T$ vs. T. The data were extrapolated to 0K to gauge the spin of the ground state in zero-field. Spin state calculations for complexes **4A-G** in Table 4.9. The experimental values of S = ~6-8 are further suggestion that these complexes exhibit low-lying excited states that these complexes also lack a well-defined global energy minimum, *i.e.* significant changes in the magnitude of the "wing-body" and body-body" magnetic exchange interactions does not seem to affect eigen-energy distributions and the spin of the ground state. Deviations between spin ground states calculated form extrapolation of in-phase ac susceptibility data and those calculated through fitting of M vs. H/T and $\chi_m T$ vs. T may in part be due to field generated Zeeman mixing.

In order to gauge magnetization relaxation rates for complexes **4A-G,** data from each of the measured frequencies were fit to a Lorentzian function and the peak position was fit to the Arrhenius equation (Equation 4.8), where τ_o is the pre-exponential value, U_{eff} is the effective barrier toward the reversal of magnetization, R is the gas constant and T is the absolute temperature in Kelvin. Ahrrenius plots for complexes 4A-G are given in Figures 4.45-4.50. The solid lines in Figures 4.45-4.50 represent the best linear fits of the peak positions, with the slope of the line equal to U_{eff} /R, and τ_o (pre-exponential term) is the y-intercept. Calculated values of τ_o and U_{eff} are summarized in Table 4.9. The effective barrier (U_{eff}) toward magnetization reversal is appreciably lower than the theoretical thermodynamic barriers calculated from DS_z^2 for each complex, strongly suggesting that the thermodynamic barrier is being circumvented via quantum tunneling of the magnetization.

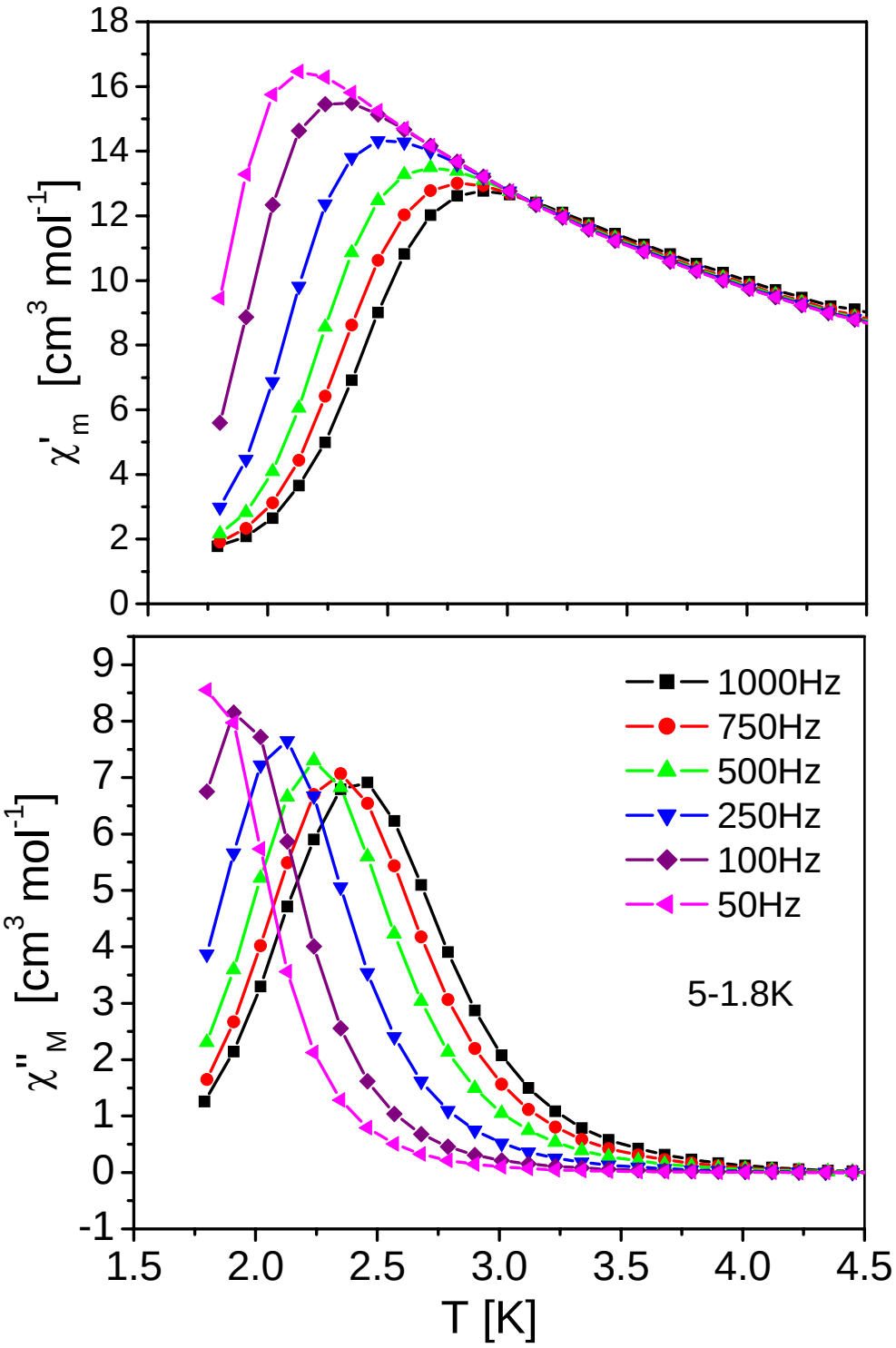

Figure 4.31. In-phase (top) and out-of-phase AC susceptibility for complex **[Mn_4(anca)$_4$(mdea)$_2$(Hmdea)$_2$]· 2$CHCl_3$ (4A)**. Data were collected from 5-1.8K with frequencies of 50-1000 Hz in a 3G field.

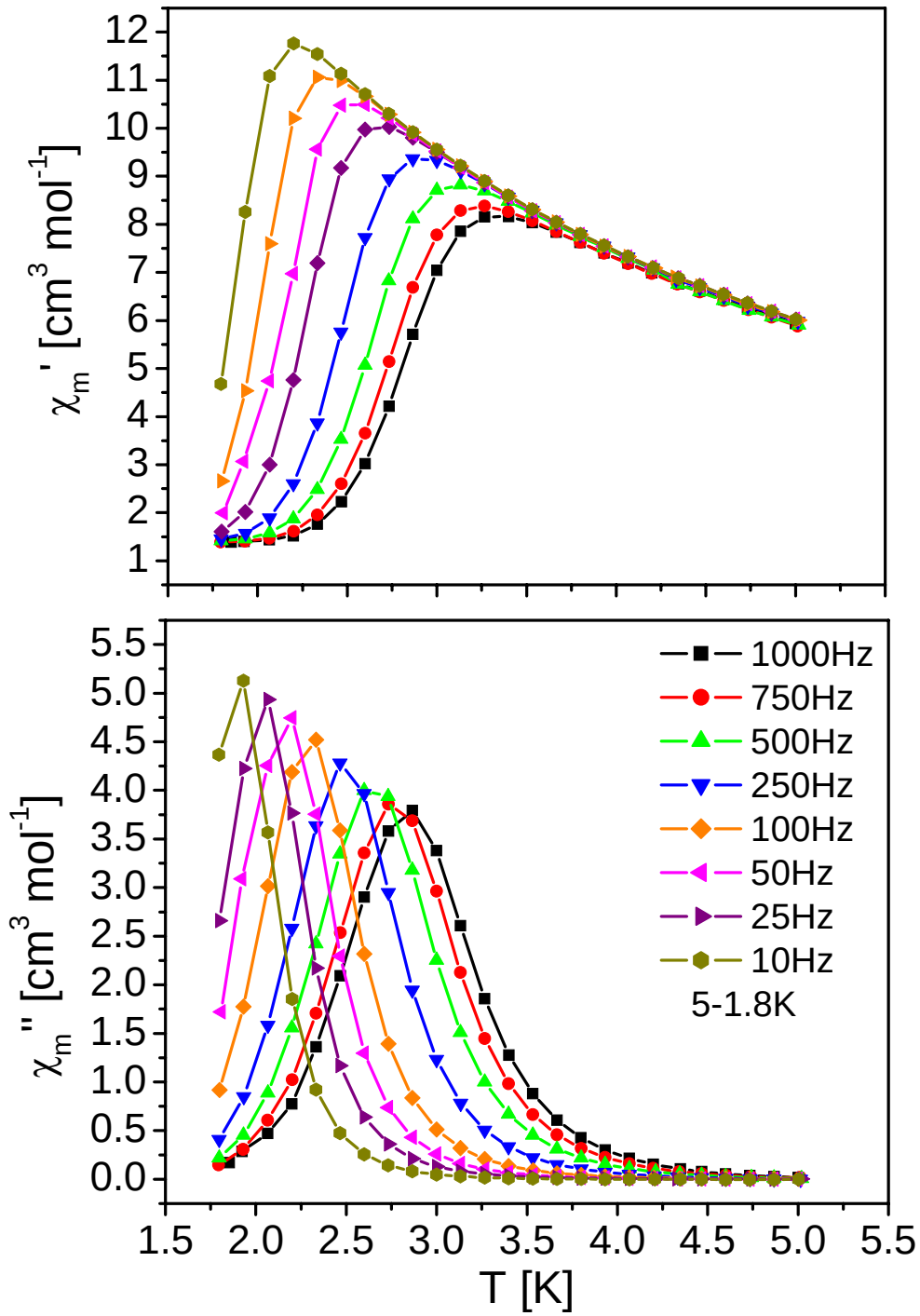

Figure 4.32. In-phase (top) and out-of-phase AC susceptibility for complex **$[Mn_4(anca)_4(Hedea)_2(edea)_2]\cdot 2CHCl_3,2EtOH$ (4B).** Data were collected from 5-1.8K with frequencies of 50-1000 Hz in a 3G field.

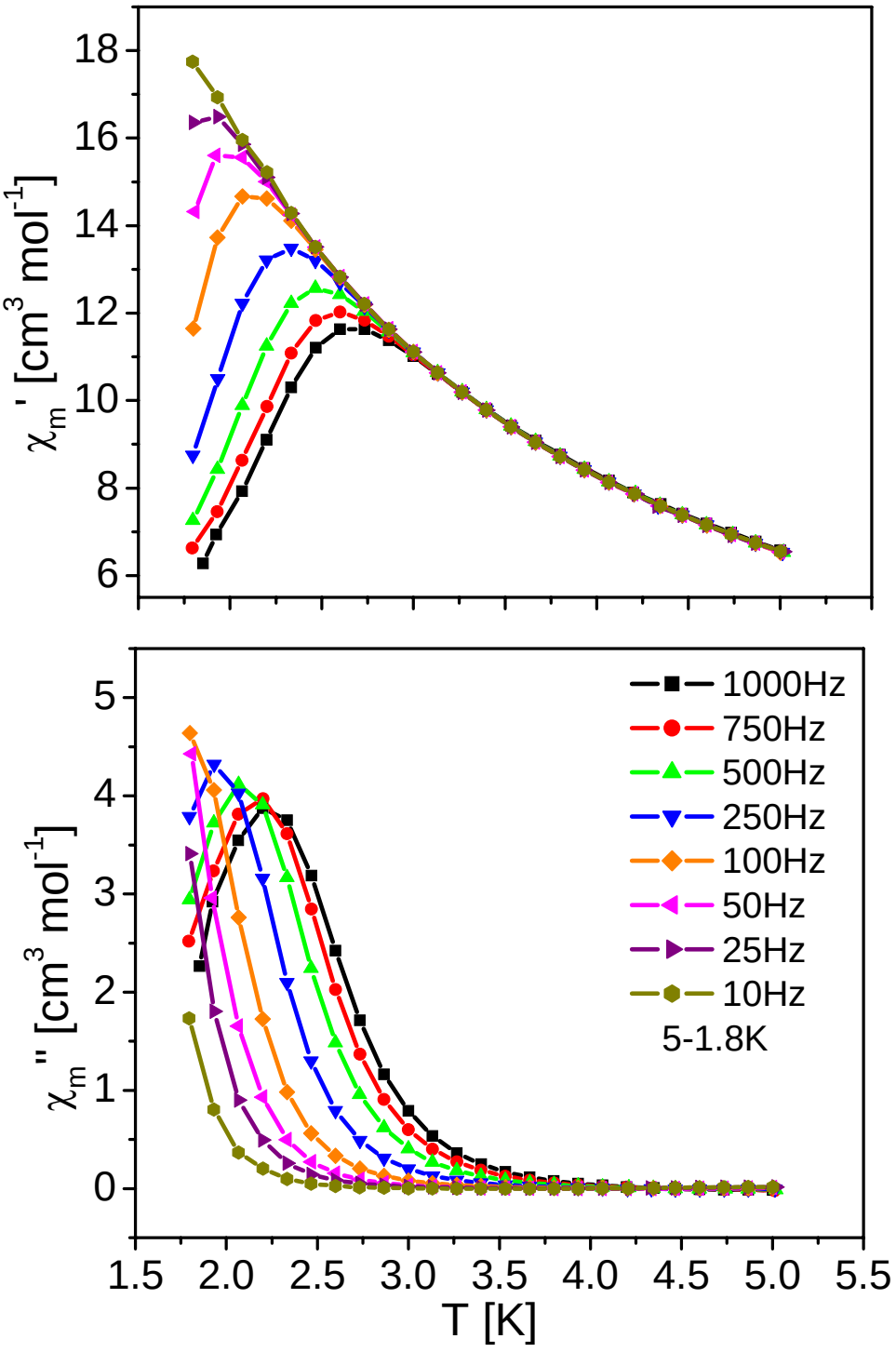

Figure 4.33. In-phase (top) and out-of-phase AC susceptibility for complex **$Mn_4(anca)_4(Hn\text{-}bdea)_2(n\text{-}bdea)_2]\cdot 1MeCN,0.5CHCl_3$ (4C).** Data were collected from 5-1.8K with frequencies of 50-1000 Hz in a 3G field.

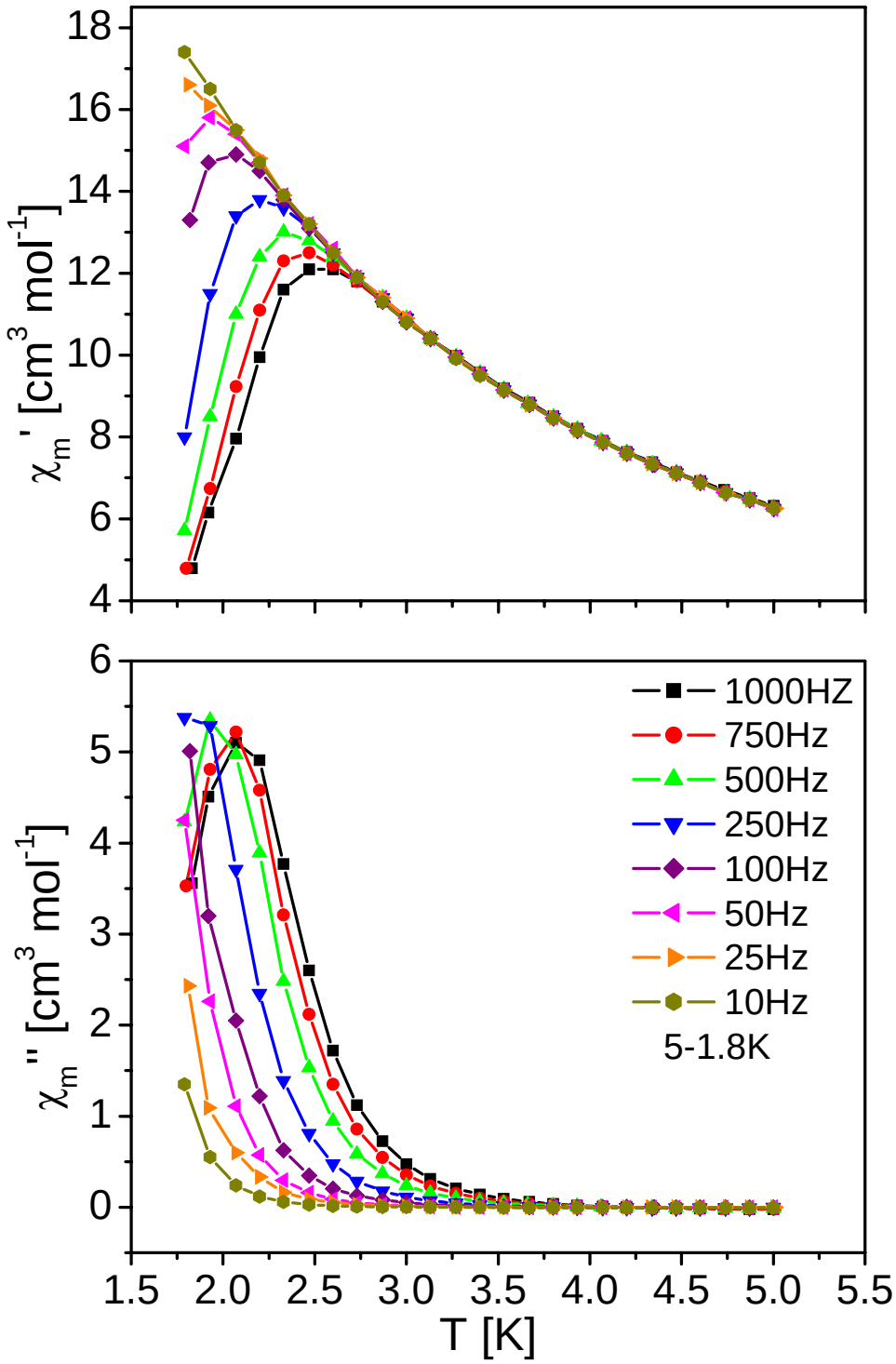

Figure 4.34. In-phase (top) and out-of-phase AC susceptibility for complex **[Mn_4(anca)$_4$(Hbzdea)$_2$(bzdea)$_2$]·MeCN (4D).** Data were collected from 5-1.8K with frequencies of 10-1000 Hz in a 3G field.

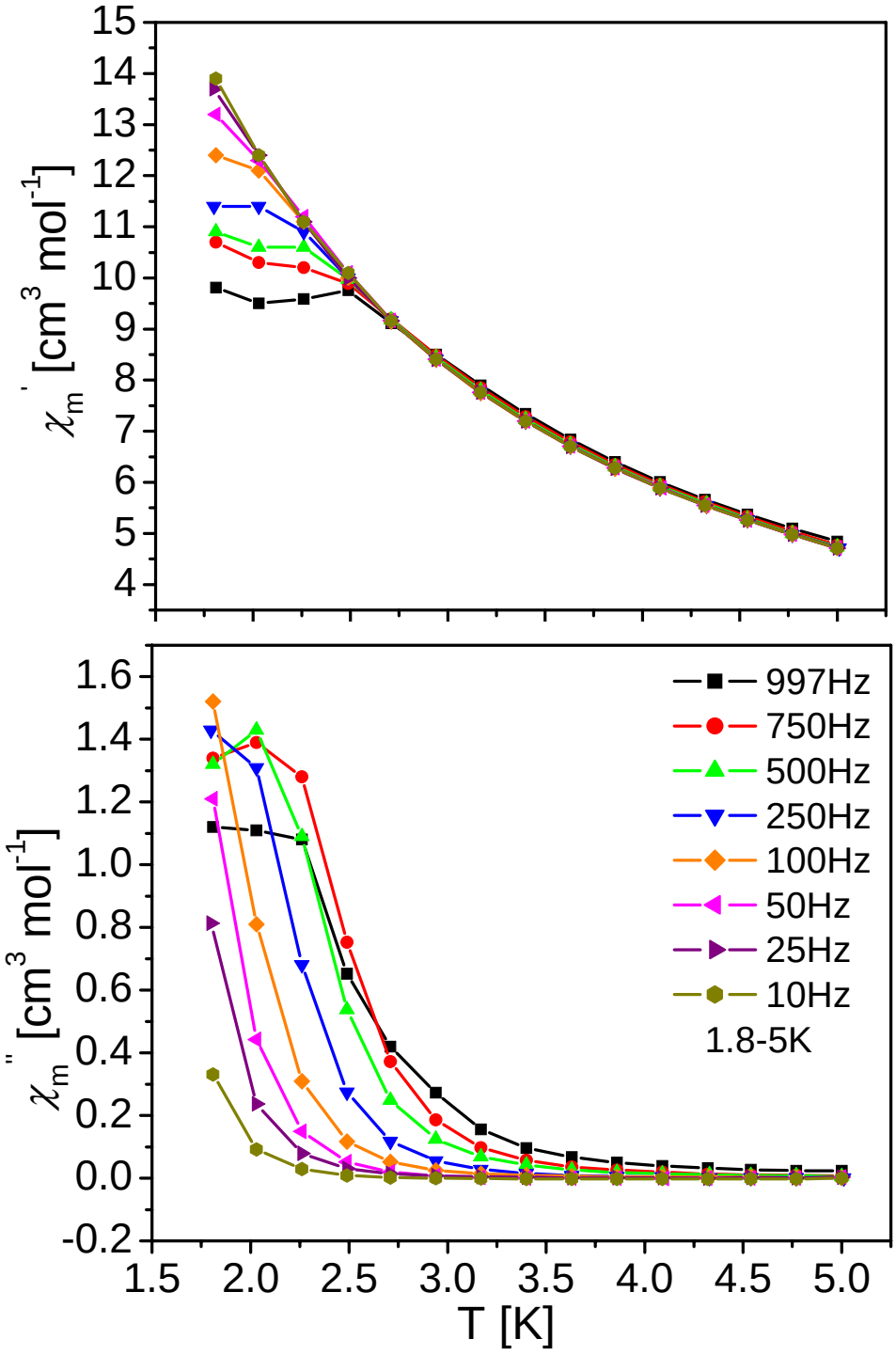

Figure 4.35. In-phase (top) and out-of-phase AC susceptibility for complex **[Mn_4(β-naphth)$_4$(Hmdea)$_2$(mdea)$_2$]·Et_2O (4E).** Data were collected from 5-1.8K with frequencies of 10-1000 Hz in a 3G field.

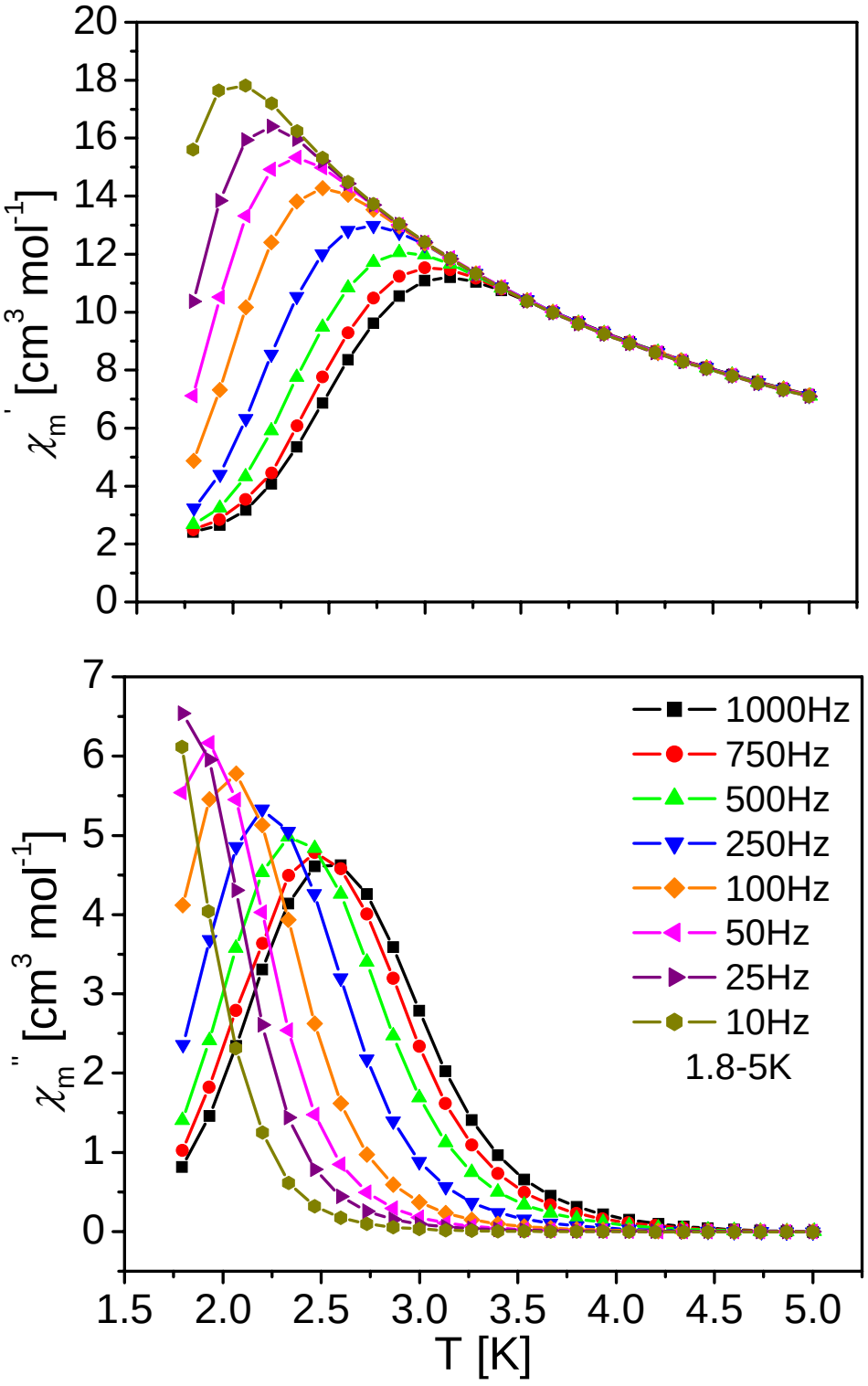

Figure 4.36. In-phase (top) and out-of-phase AC susceptibility for complex **[Mn_4(β-naphth)$_4$(Hedea)$_2$(edea)$_2$]·MeCN,EtOH (4F).** Data were collected from 5-1.8K with frequencies of 10-1000 Hz in a 3G field.

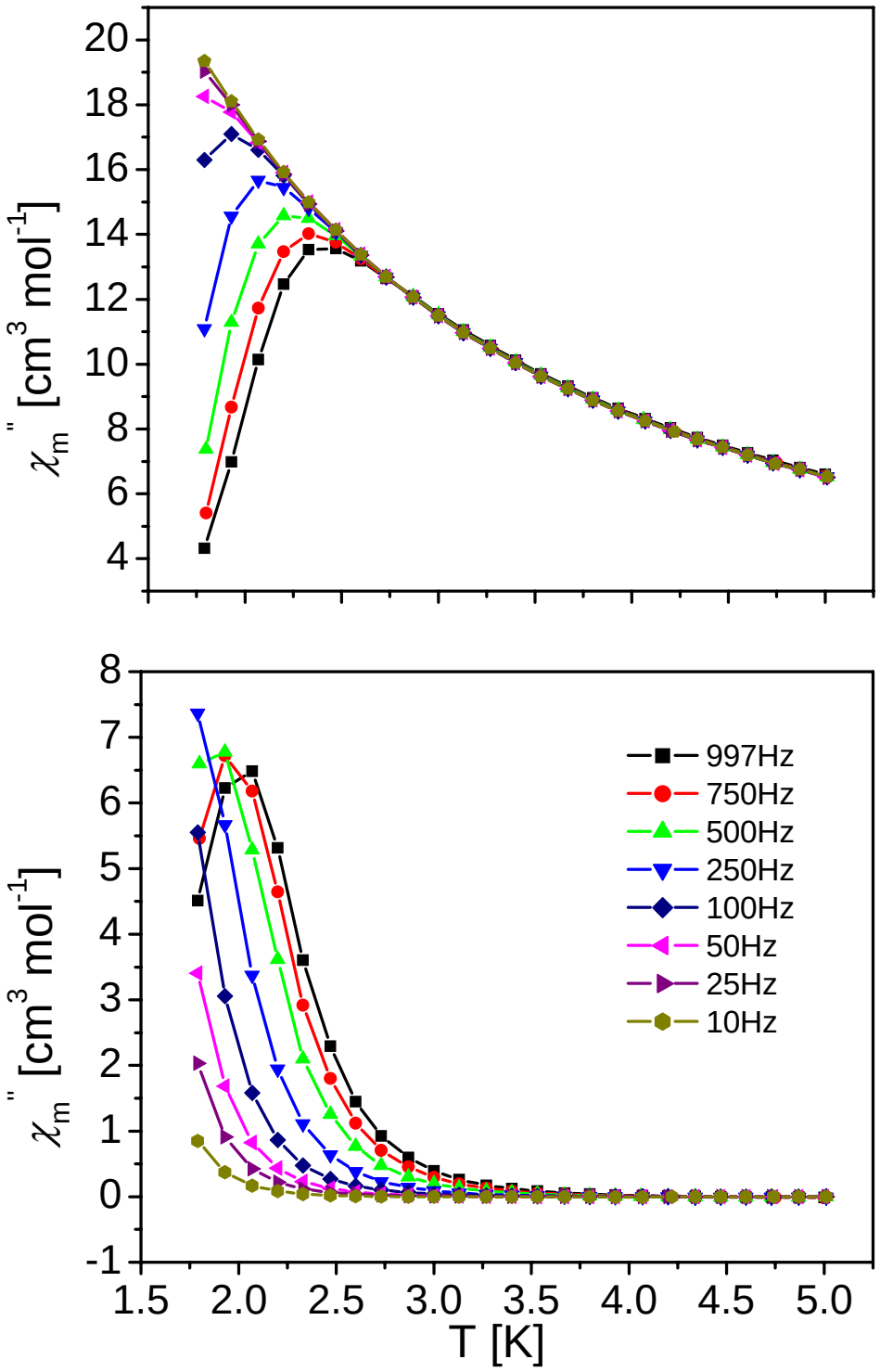

Figure 4.37. In-phase (top) and out-of-phase AC susceptibility for complex **[Mn_4(β-naphth)$_4$(Hn-bdea)$_2$(n-bdea)$_2$]·2CH_2Cl_2 (4G).** Data were collected from 5-1.8K with frequencies of 10-1000 Hz in a 3G field.

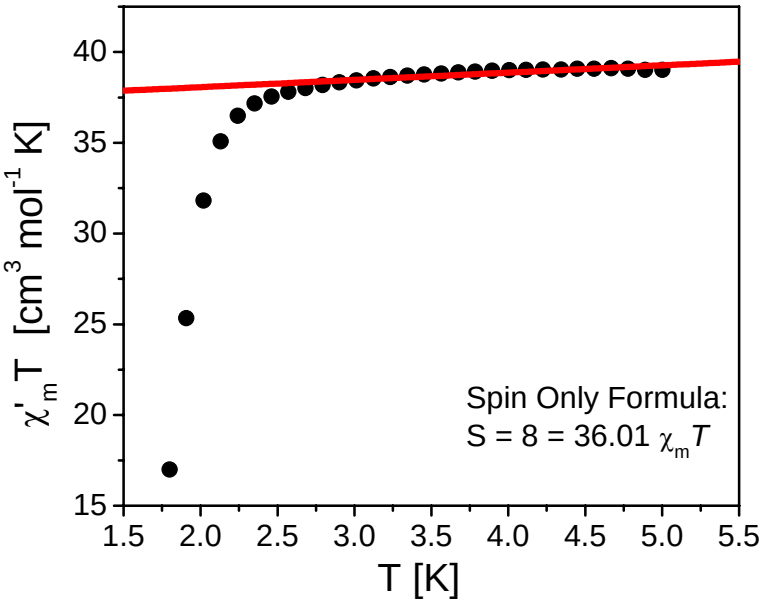

Figure 4.38. Extrapolation to zero Kelvin of 10Hz in-phase ac magnetic susceptibility for complex **$[Mn_4(anca)_4(mdea)_2(Hmdea)_2]\cdot 2CHCl_3$ (4A)**. Spin-only values for S = 9, 8, 7 and 6 are 45, 36, 28 and 21 $cm^3\cdot mol^{-1}\cdot$ K, respectively.

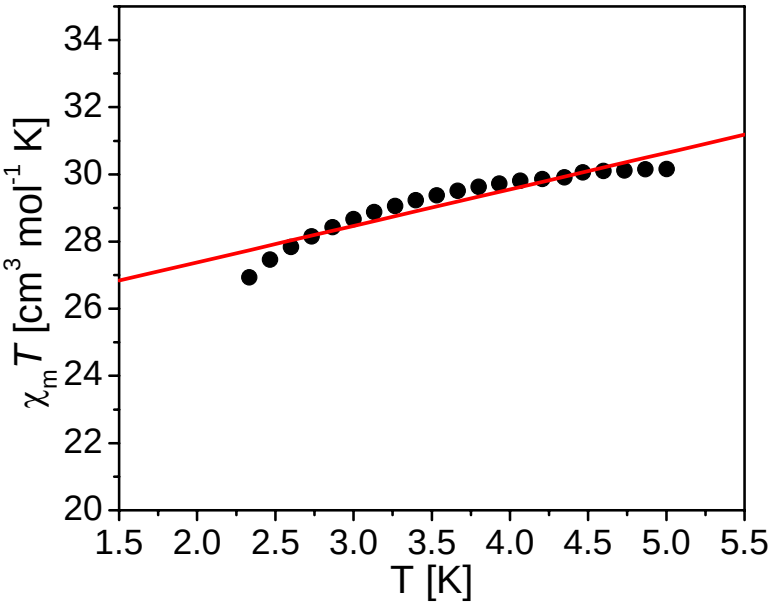

Figure 4.39. Extrapolation to zero Kelvin of 10Hz in-phase ac magnetic susceptibility for complex **$[Mn_4(anca)_4(Hedea)_2(edea)_2]\cdot 2CHCl_3$,2EtOH (4B).** Spin-only values for S = 9, 8, 7 and 6 are 45, 36, 28 and 21 $cm^3\cdot mol^{-1}\cdot$ K, respectively.

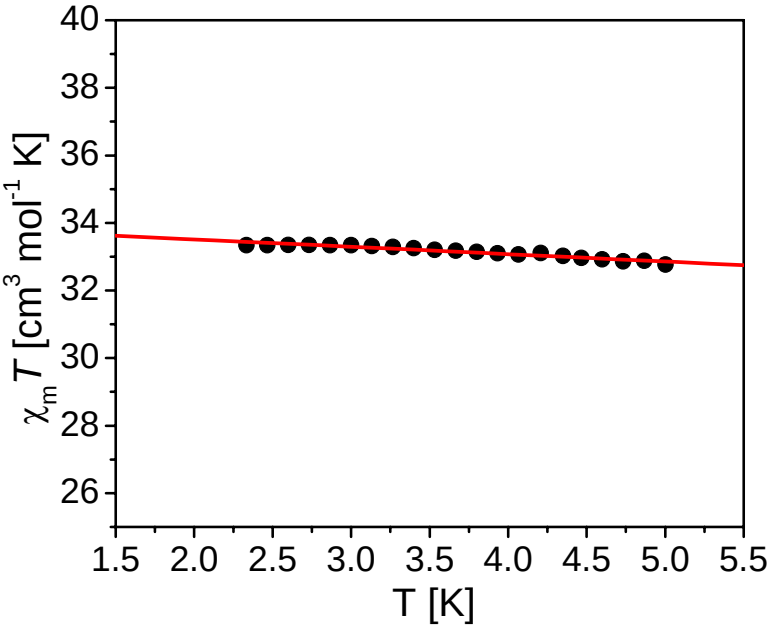

Figure 4.40. Extrapolation to zero Kelvin of 10Hz in-phase ac magnetic susceptibility for complex **[Mn$_4$(anca)$_4$(Hn-bdea)$_2$(n-bdea)$_2$]•1MeCN,0.5CHCl$_3$ (4C).** Spin-only values for S = 9, 8, 7 and 6 are 45, 36, 28 and 21 cm^3·mol^{-1}· K, respectively.

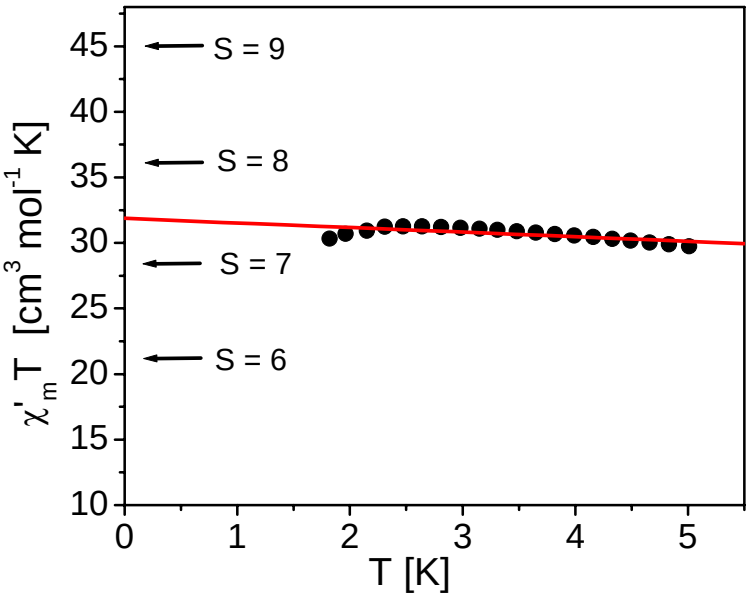

Figure 4.41. Extrapolation to zero Kelvin of 10Hz in-phase ac magnetic susceptibility for complex **[Mn$_4$(anca)$_4$(Hbzdea)$_2$(bzdea)$_2$]·MeCN (4D).** Spin-only values for S = 9, 8, 7 and 6 are 45, 36, 28 and 21 cm^3·mol^{-1}· K, respectively.

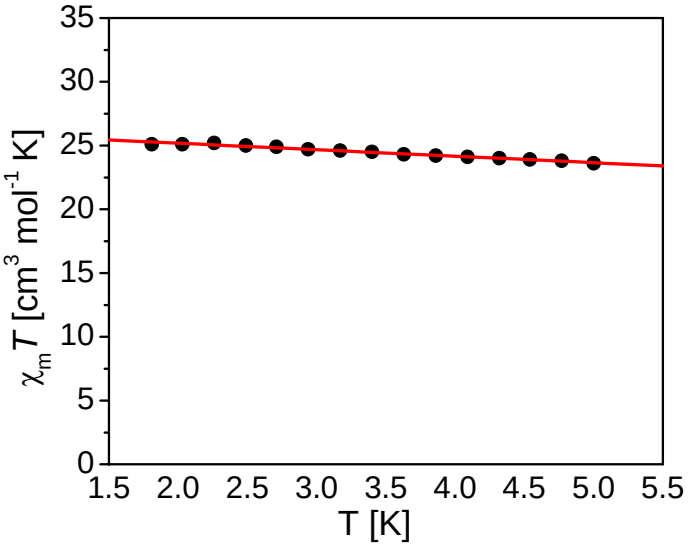

Figure 4.42. Extrapolation to zero Kelvin of 10Hz in-phase ac magnetic susceptibility for complex **[Mn_4(β-naphth)$_4$(Hmdea)$_2$(mdea)$_2$]·Et_2O (4E).** Spin-only values for S = 9, 8, 7 and 6 are 45, 36, 28 and 21 $cm^3 \cdot mol^{-1} \cdot$ K, respectively.

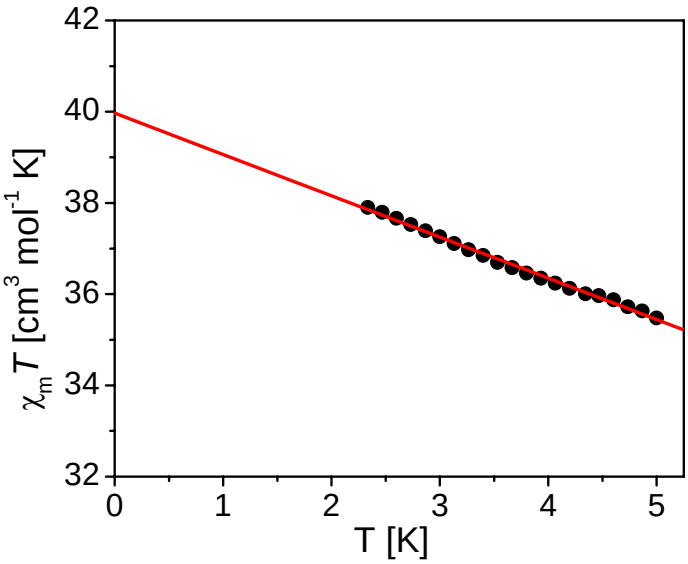

Figure 4.43. Extrapolation to zero Kelvin of 10Hz in-phase ac magnetic susceptibility for complex **[Mn_4(β-naphth)$_4$(Hedea)$_2$(edea)$_2$]·MeCN,EtOH (4F).** Spin-only values for S = 9, 8, 7 and 6 are 45, 36, 28 and 21 $cm^3 \cdot mol^{-1} \cdot$ K, respectively.

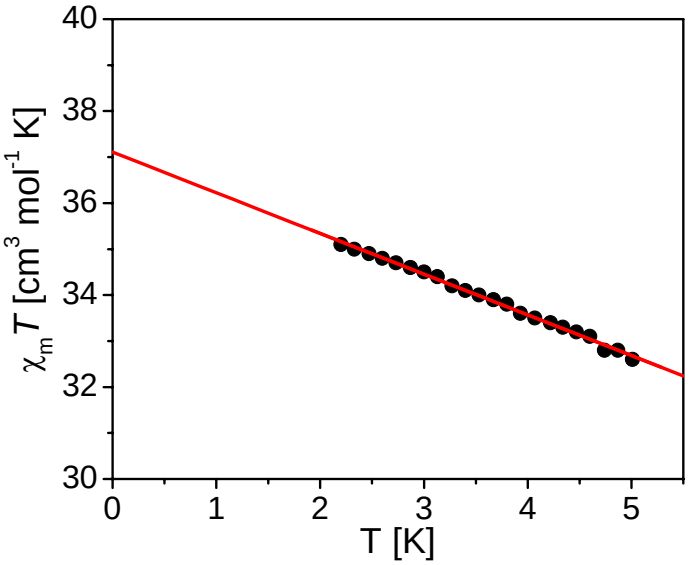

Figure 4.44. Extrapolation to zero Kelvin of 10Hz in-phase ac magnetic susceptibility for complex **[Mn$_4$(β-naphth)$_4$(Hn-bdea)$_2$(n-bdea)$_2$]·2CH$_2$Cl$_2$ (4G).** Spin-only values for S = 9, 8, 7 and 6 are 45, 36, 28 and 21 cm^3·mol^{-1}· K, respectively.

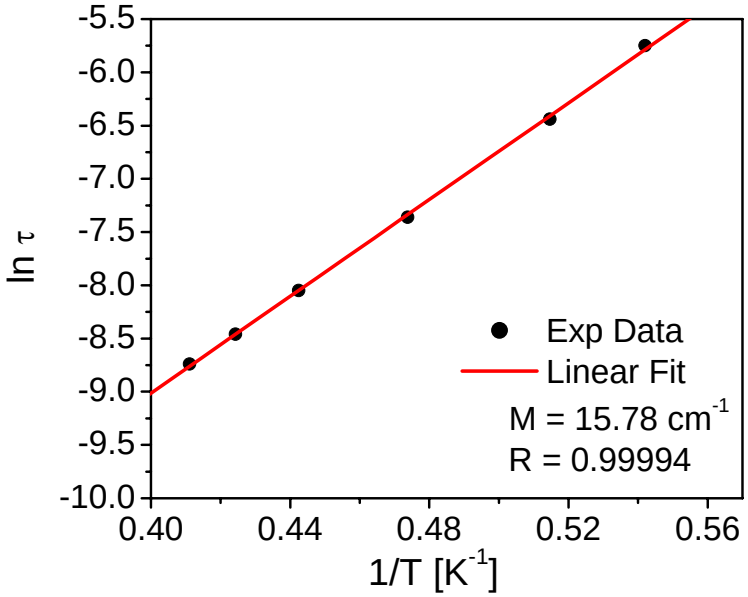

Figure 4.45. Arrhenius plot for **[Mn$_4$(anca)$_4$(mdea)$_2$(Hmdea)$_2$]·2CHCl$_3$ (4A)** given as the natural logarithm of ln τ verses the inverse absolute temperature (1/T). Best linear fit yielded a magnetization reversal barrier of 15.78 cm^{-1}.

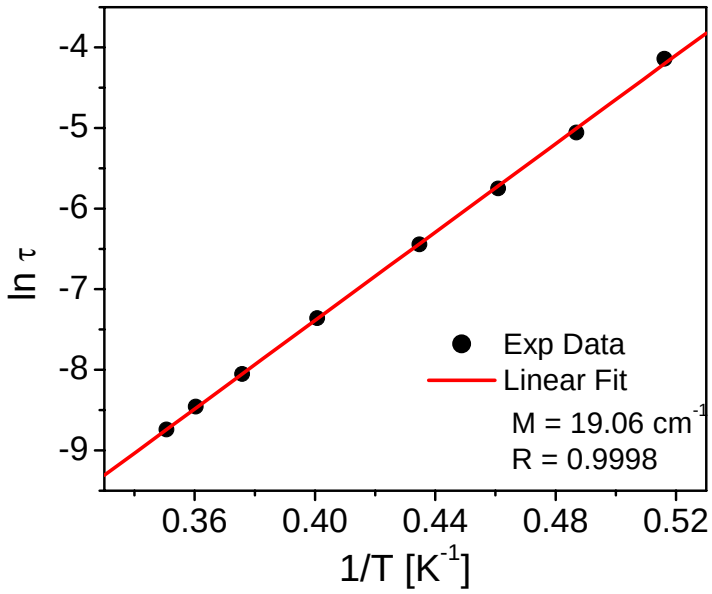

Figure 4.46. Arrhenius plot for **[Mn_4(anca)$_4$(Hedea)$_2$(edea)$_2$]·2$CHCl_3$,2EtOH** (**4B**) given as the natural logarithm of ln τ verses the inverse absolute temperature (1/T). Best linear fit yielded a barrier toward magnetization reversal of 19.06 cm^{-1}.

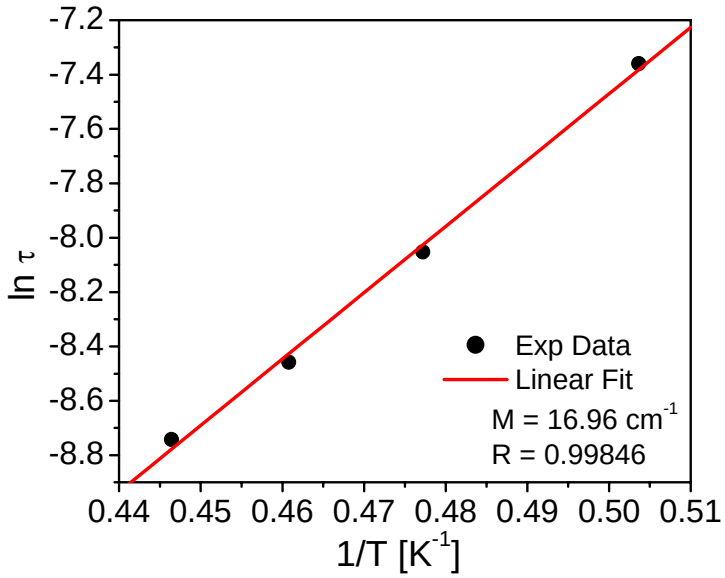

Figure 4.47. Arrhenius plot for **[Mn_4(anca)$_4$(Hn-bdea)$_2$(n-bdea)$_2$]•1MeCN,0.5$CHCl_3$** (**4C**) given as the natural logarithm of ln τ verses the inverse absolute temperature (1/T). Best linear fit yielded a barrier toward magnetization reversal of 16.96 cm^{-1}.

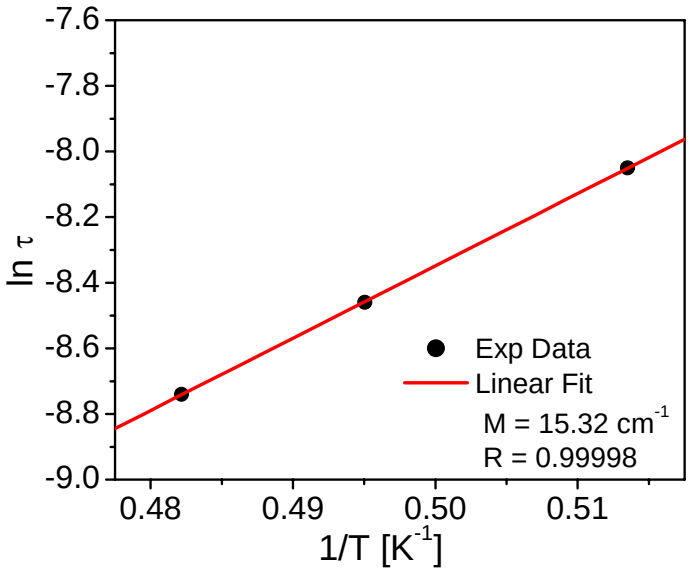

Figure 4.48. Arrhenius plot for **[Mn_4(anca)$_4$(Hbzdea)$_2$(bzdea)$_2$]·MeCN** (**4D**) given as the natural logarithm of ln τ verses the inverse absolute temperature (1/T). Best linear fit yielded a barrier toward magnetization reversal of 15.32 cm^{-1}.

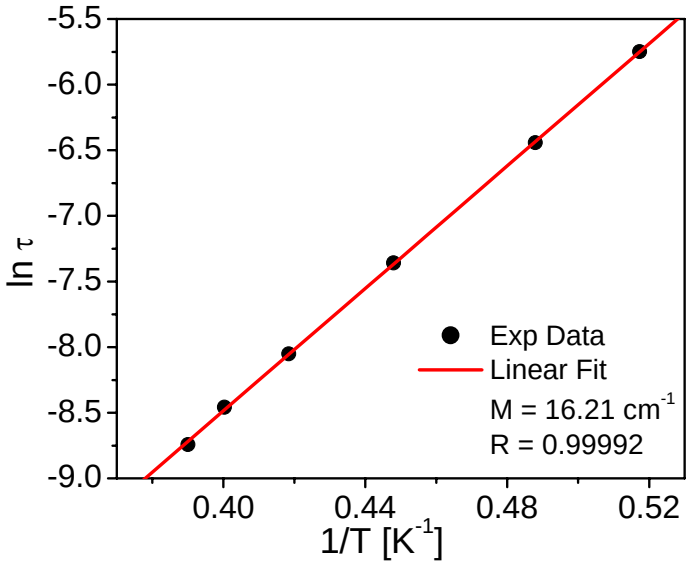

Figure 4.49. Arrhenius plot for **[Mn_4(β-naphth)$_4$(Hedea)$_2$(edea)$_2$]·MeCN,EtOH** (**4F**) given as the natural logarithm of ln τ verses the inverse absolute temperature (1/T). Best linear fit yielded a barrier toward magnetization reversal of 16.21 cm^{-1}.

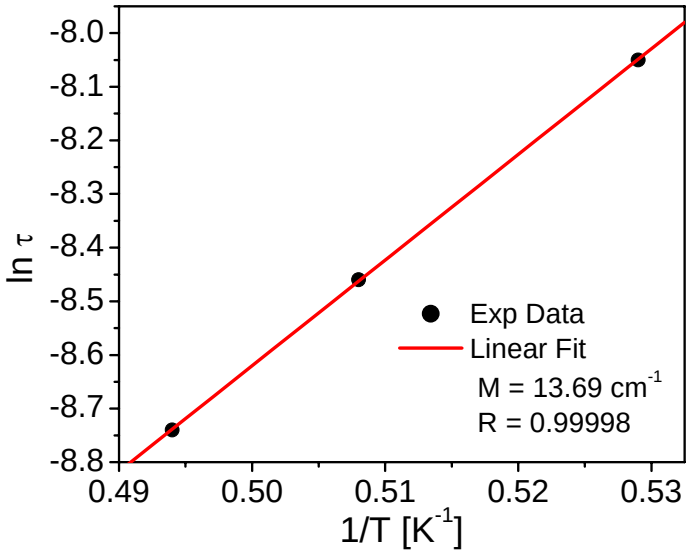

Figure 4.50. Arrhenius plot for **[Mn_4(β-naphth)$_4$(Hn-bdea)$_2$(n-bdea)$_2$]·2CH_2Cl_2 (4G)** given as the natural logarithm of ln τ verses the inverse absolute temperature (1/T). Best linear fit yielded a barrier toward magnetization reversal of 13.69 cm^{-1}.

Table 4.9. Parameters for complexes **4A-4G** calculated through AC susceptibility and variable field magnetization data. Parameters include: complex, temperature at which a peak is seen in the out-of-phase ac susceptibility at 1000Hz in Kelvin, spin ground state as calculated from extrapolation of in-phase ac magnetic susceptibility to zero Kelvin, calculated barrier toward the reversal of magnetization from ac susceptibility, barrier toward reversal of magnetization calculated from fit of reduced magnetization, and percent of out-of-phase portion of the ac susceptibility signal.

Complex	1000Hz (K)	Spin From Extrapolation of AC	U_{eff} (cm^{-1})	DS_z^2 (cm^{-1})	% Out-Of-Phase
A	2.5	8	15.8	17.9	58
B	2.9	7	19.1	25.6	46
C	2.2	8	17.0	19.8	33
D	2.1	7-8	15.3	19.2	42
E	2.2	6-7	-	23.0	11
F	2.5	8	16.2	25.6	40
G	2.1	8	13.7	18.6	56

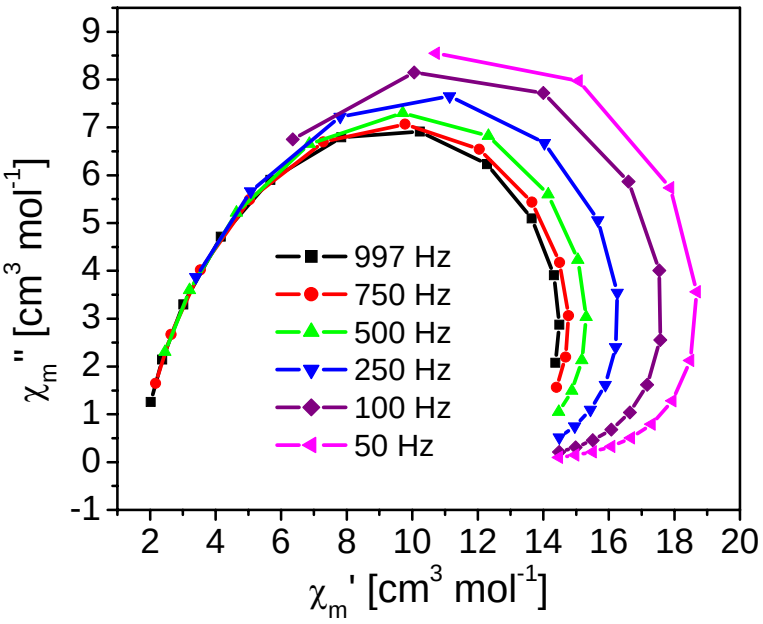

Figure 4.51. Cole-Cole plot for complex **[$Mn_4(anca)_4(mdea)_2(Hmdea)_2$]·2$CHCl_3$** (**4A**) for frequencies of 997Hz to 50Hz.

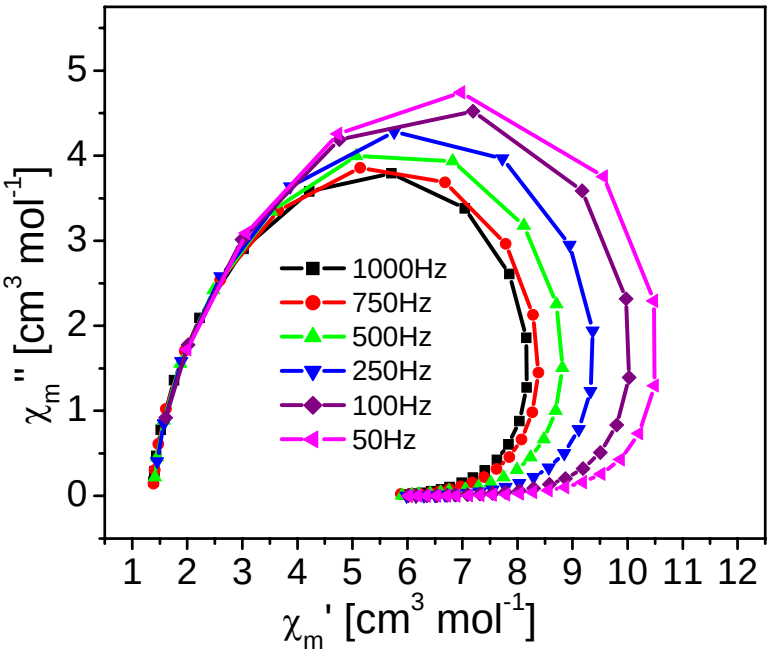

Figure 4.52. Cole-Cole plot of AC magnetic susceptibility for frequencies between 50-1000Hz for complex **[$Mn_4(anca)_4(Hedea)_2(edea)_2$]·2$CHCl_3$,2EtOH** (**4B**).

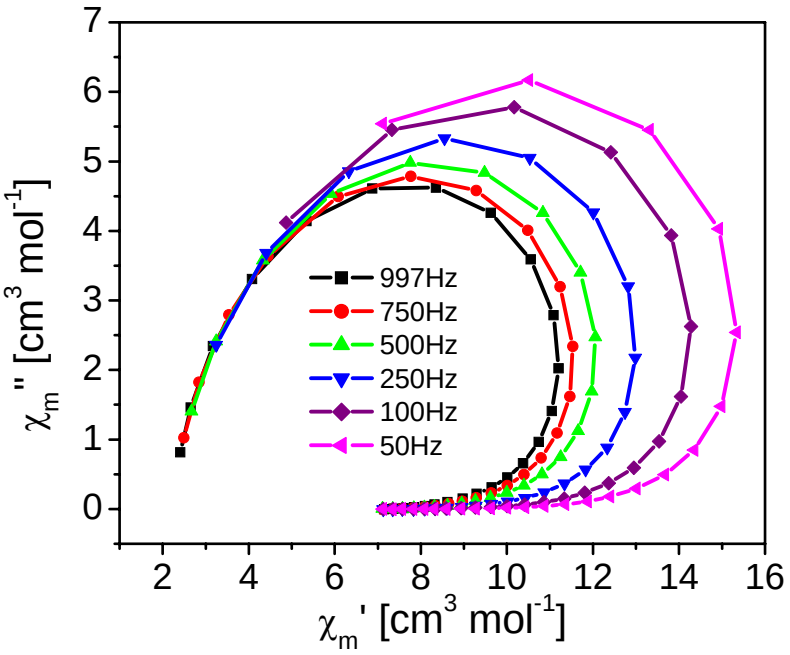

Figure 4.53. Cole-Cole plot of AC magnetic susceptibility for frequencies between 50-1000Hz for complex **[Mn_4(β-naphth)$_4$(Hedea)$_2$(edea)$_2$]·MeCN,EtOH** (**4F**).

Cole-Cole analysis for complexes **4A, B** and **F**, plotted as χ" vs. χ', are presented in Figures 4.51-4.53. If magnetization relaxation is governed by one process χ" plotted vs. χ' will yield a semi-circle that can be theoretically fit to determine the relaxation rate and relaxation distribution times. The plots of χ" vs. χ' for complexes **4A, B** and **F** reveal that magnetization relaxation processes for these complexes are highly complex, since a simple semi-circle is not observed. All iso-fields of the 10-1000Hz data are double valued, suggesting complex relaxation mechanisms are at work. Magnetization relaxation in SMMs arises due to a number of factors including: spin-phonon interactions, spin-spin interactions, dipolar coupling, intermolecular interactions, excited state mixing, nuclear hyperfine interactions and quantum tunneling processes. Thus, no simple relaxation analysis is possible with this system.

4.3.5 Fluorimetry and UV-Vis Spectroscopy

$[Mn_4(anca)_4(mdea)_2(Hmdea)_2]\cdot 2CHCl_3$ (4A). Room temperature fluorescence emission spectra for Hanca, NH_4-anca and complex **4A** are given in Figure 4.54. Fluorescence data were collected in CD_2Cl_2 with fluorophore concentrations of 10^{-6} M. The emission spectrum of complex **4A** exhibits the same line shape and peak position (460nm) as Hanca and NH_4-anca, as previously documented. Comparison of the three spectra in Figure 4.54 reveals significant quenching of the emission intensity for complex **4A** due to paramagnetic effects. Figure 4.55 illustrates room temperature UV-Vis data for Hanca, NH_4- anca and complex **4A** in CD_2Cl_2 with fluorophore concentrations of 10^{-5} M. Discernible peak position shifts (4 nm) to lower energy are clearly evident for absorption bands II through V, and band I is only evident in the

absorption spectrum of complex **4A**. Furthermore, the peak line-shapes (bands III, IV and V) for complex **4A** are sharper than the corresponding absorption bands for Hanca and NH_4-anca. Comparison of calculated molar extinction coefficients for Hanca, NH_4-anca and complex **4A** from UV-Vis molar absorbance data reveals a two-fold extinction coefficient increase in complex **4A** relative to Hanca and NH_4-anca, indicating that the electronic environment of the anthacene carboxylates is significantly modulated when coordinated to Mn ions. However, it is important to ascertain whether spectral changes can be interpreted as arising from energy shifts in π to π^* transitions originating from bound $anca^-$ ligands, or whether spectral peak shifts are a result of free $anca^-$ anions or exchanging $anca^-$ anions interacting with paramagnetic Mn ions in solution. In order to address whether complex **4A** is intact in solution detailed UV-Vis and NMR experiments were performed. UV-Vis spectral data from the addition of 0.25 mL aliquots of 10^{-5} M NH_4-anca in CD_2Cl_2 to a 10^{-5} M (by fluorophore) solution of complex **4A** are presented in Figure 4.56. It is evident from Figure 4.56 that sequential additions of $anca^-$ and subsequent decrease in complex **4A** concentration leads to a shift in corresponding peak positions II-V, and broadening of spectral line-shapes. Furthermore, the systematic disappearance of peak I is in agreement with the UV-Vis spectra in Figure 4.55 of complex **4A** and NH_4-anca, respectively. This strongly indicates that the line-shape and intensity of the UV-Vis spectrum of complex **4A** (Figure 4.55) is not due to free anions in solution.

In order to ascertain whether complex **4A** is intact in solution, proton NMR experiments were carried out. Peak broadening in NMR experiments arise from a number factors including ligand exchange and paramagnetic effects. The NMR if

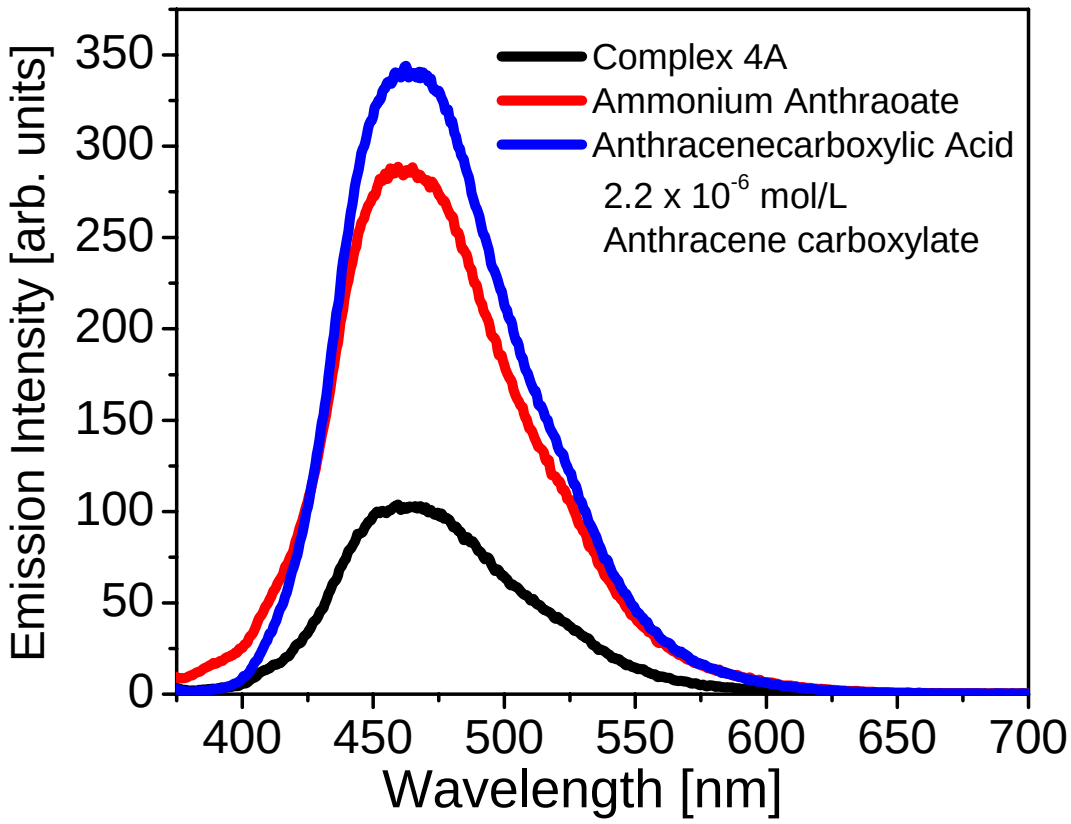

Figure 4.54. Room temperature fluorescence emission spectra for 9-anthracenecarboxylic acid (A, blue), complex **4A** (black) and ammonium-9-anthraoate (B, red) collected at 10^{-6} M in dichloromethane.

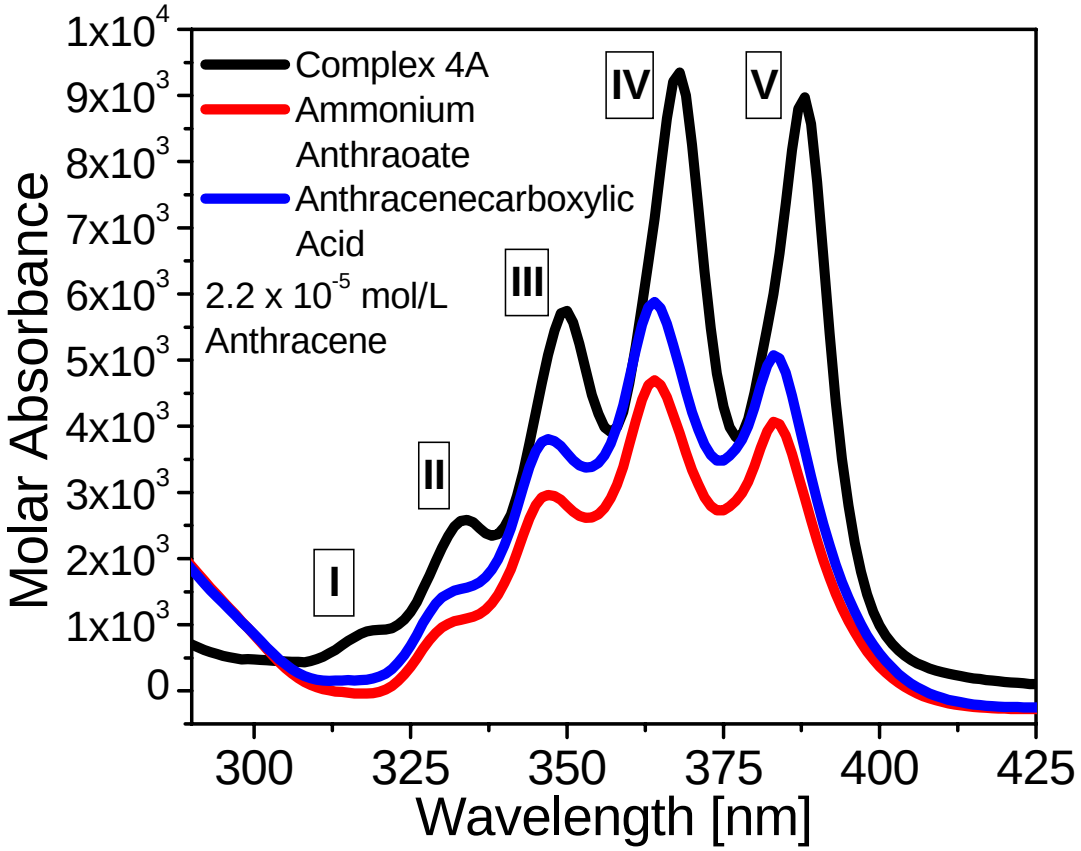

Figure 4.55. Room temperature UV-Vis spectra for 9-anthracenecarboxylic acid (A, blue), complex **4A** (black) and ammonium-9-anthraoate (B, red) collected at 10^{-5} M in dichloromethane**,** plotted as molar absorbance versus wavelength.

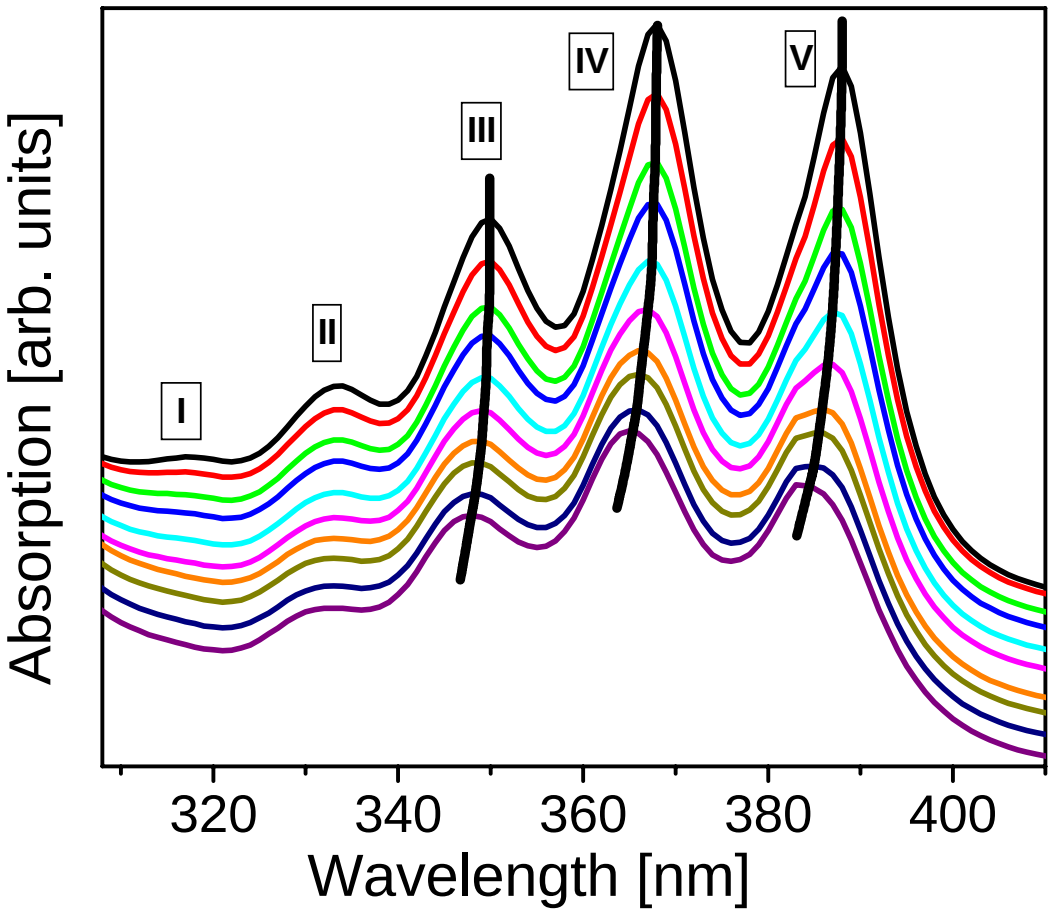

Figure 4.56. UV-Vis absorption spectra. Complex **4A**, black trace (top), in dichloromethane at 10^{-5} M. Subsequent spectra are 0.25 mL additions of 10^{-5} M ammonium-9-anthraoate in dichloromethane.

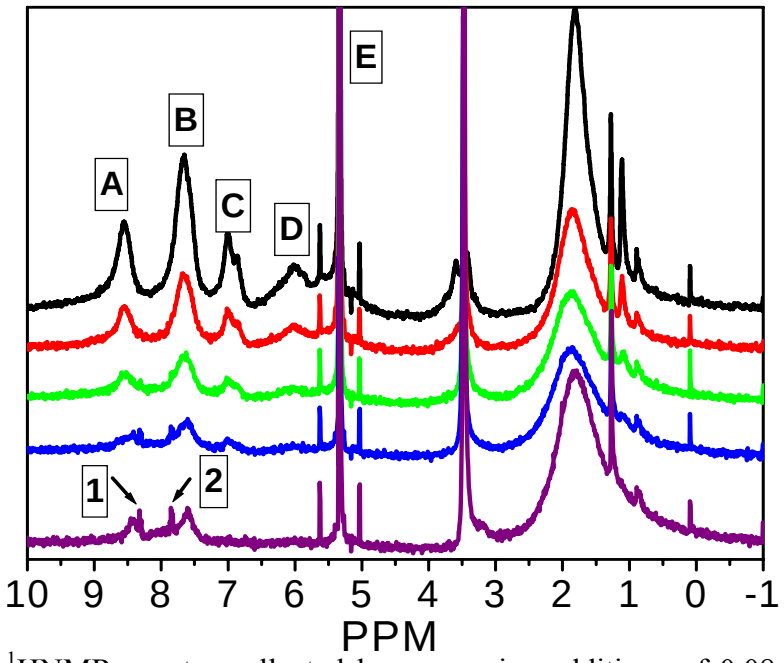

Figure 4.57. [1]HNMR spectra collected by successive additions of 0.08 mL of NH4-anca in CD2Cl2 into complex **4A** (top, black trace). Peak E is the solvent reference peak.

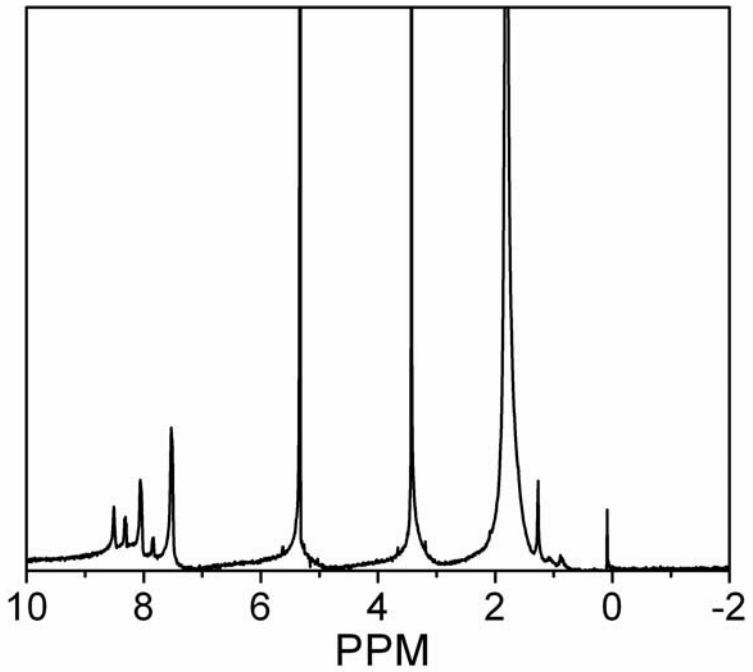

Figure 4.58. [1]HNMR in CD_2Cl_2 for NH_4-anca.

spectrum of complex **4A** in CD_2Cl_2 (top trace, black) is presented in Figure 4.57. To determine complex **4A** is intact in solution, NH_4-anca in CD_2Cl_2 was sequentially added in 0.08 mL aliquots (red, green, blue and purple traces, Figure 4.57) and the evolution of proton signals was monitored. As the concentration of anion was increased, proton signals A-D systematically disappeared (peaks A, B and C are the proton signals assigned to the conjugated anthacene ring protons). At concentrations approaching 90% anion (bottom trace, purple, Figure 4.57) the peaks labeled 1 and 2 begin to emerge and are consistent with proton signals seen in the NMR of pure NH_4-anca in CD_2Cl_2 (Figure 4.58). Thus, the spectral data in Figure 4.57 clearly support that the free anion is not a significant species in solution. Rather, NMR spectral features for complex **4A** are dominated by $anca^-$ ligands bound to the Mn_4 complex. This is further substantiated by the fact that if complex **4A** in CD_2Cl_2 is allowed to evaporate, the only product recovered is the original complex. Additionally, there is little stabilization in dichloromethane (aprotic) for the free anion.

4.4 Conclusion

In conclusion, a new series of $[Mn_2^{II}Mn_2^{III}]$ dicubane SMMs with photoluminescent properties have been synthesized, that differ in their peripheral photoluminescent ligands and R group of their tripodal diethanolamine ligands (H_2Rdea). In this family of SMMs, subtle changes in luminescent lifetimes and steric considerations may have a dramatic effect on their magnetic properties. The complexes possess significant axial magnetoanisotropy and large spin ground states. It is clear however from fitting of variable temperature dc magnetic susceptibility and fitting of

reduced magnetization data that these complexes exhibit significant mixing of low-lying states into the effective ground state, thus, S and M_s are not good quantum numbers. In chapter 5, detailed HFEPR, magnetization hysteresis and full-matrix diagonalization in an uncoupled basis set are presented to further elucidate the ground state electronces of these complexes. Future studies will include simultaneous fluorescence and magnetization hysteresis measurements below their blocking temperatures (T_B = 0.9 K for τ = 100s for **1**) to study if photo-excited states can be employed in monitoring and possible modulating quantum tunneling processes.

Chapter 4, in part, is a reprint of a published communication: Beedle, C. C., Stephenson, C. J.; Heroux, K. J., Wernsdorfer, W., Hendrickson, D. N., Photoluminescent Mn-4 Single-Molecule Magnet. *Inorganic Chemistry* **2008,** 47, (23), 10798-10800.

4.5 References

(1) Aubin, S. M. J.; Wemple, M. W.; Adams, D. M.; Tsai, H. L.; Christou, G.; Hendrickson, D. N. *Journal of the American Chemical Society* **1996**, *118*, 7746-7754.

(2) Hill, S.; Edwards, R. S.; Aliaga-Alcalde, N.; Christou, G. *Science* **2003**, *302*, 1015-1018.

(3) Sessoli, R.; Gatteschi, D.; Caneschi, A.; Novak, M. A. *Nature* **1993**, *365*, 141-143.

(4) Sessoli, R.; Tsai, H. L.; Schake, A. R.; Wang, S. Y.; Vincent, J. B.; Folting, K.; Gatteschi, D.; Christou, G.; Hendrickson, D. N. *Journal of the American Chemical Society* **1993**, *115*, 1804-1816.

(5) Christou, G.; Gatteschi, D.; Hendrickson, D. N.; Sessoli, R. *Mrs Bulletin* **2000**, *25*, 66-71.

(6) Wernsdorfer, W.; Bhaduri, S.; Boskovic, C.; Christou, G.; Hendrickson, D. N. *Physical Review B* **2002**, *65*, 180403.

(7) Wernsdorfer, W.; Bhaduri, S.; Tiron, R.; Hendrickson, D. N.; Christou, G. *Physical Review Letters* **2002**, *89*, 197201.

(8) Burkard, G.; Engel, H. A.; Loss, D. *Fortschritte Der Physik-Progress of Physics* **2000**, *48*, 965-986.

(9) Burkard, G.; Loss, D. *Acta Physica Polonica A* **2001**, *100*, 109-127.

(10) DiVincenzo, D. P.; Loss, D. *Journal of Magnetism and Magnetic Materials* **1999**, *200*, 202-218.

(11) Leuenberger, M. N.; Loss, D. *Physica E* **2001**, *10*, 452-457.

(12) Loss, D.; DiVincenzo, D. P. *Physical Review A* **1998**, *57*, 120-126.

(13) Meier, F.; Levy, J.; Loss, D. *Physical Review Letters* **2003**, *90*, -.

(14) Tejada, J.; Chudnovsky, E. M.; del Barco, E.; Hernandez, J. M.; Spiller, T. P. *Nanotechnology* **2001**, *12*, 181-186.

(15) Gatteschi, D. *Current Opinion in Solid State & Materials Science* **1996**, *1*, 192-198.

(16) Gatteschi, D. *Journal of Alloys and Compounds* **2001**, *317*, 8-12.

(17) Barra, A. L.; Caneschi, A.; Cornia, A.; de Biani, F. F.; Gatteschi, D.; Sangregorio, C.; Sessoli, R.; Sorace, L. *Journal of the American Chemical Society* **1999**, *121*, 5302-5310.

(18) Gatteschi, D.; Sessoli, R.; Cornia, A. *Chemical Communications* **2000**, 725-732.

(19) Goodwin, J. C.; Sessoli, R.; Gatteschi, D.; Wernsdorfer, W.; Powell, A. K.; Heath, S. L. *Journal of the Chemical Society-Dalton Transactions* **2000**, 1835-1840.

(20) Wernsdorfer, W.; Caneschi, A.; Sessoli, R.; Gatteschi, D.; Cornia, A.; Villar, V.; Paulsen, C. *Physical Review Letters* **2000**, *84*, 2965-2968.

(21) Andres, H.; Basler, R.; Blake, A. J.; Cadiou, C.; Chaboussant, G.; Grant, C. M.; Gudel, H. U.; Murrie, M.; Parsons, S.; Paulsen, C.; Semadini, F.; Villar, V.; Wernsdorfer, W.; Winpenny, R. E. P. *Chemistry-a European Journal* **2002**, *8*, 4867-4876.

(22) Cadiou, C.; Murrie, M.; Paulsen, C.; Villar, V.; Wernsdorfer, W.; Winpenny, R. E. P. *Chemical Communications* **2001**, 2666-2667.

(23) Kirman, C.; Lawrence, J.; Hill, S.; Yang, E. C.; Hendrickson, D. N. *Journal of Applied Physics* **2005**, *97*.

(24) Ochsenbein, S. T.; Murrie, M.; Rusanov, E.; Stoeckli-Evans, H.; Sekine, C.; Gudel, H. U. *Inorganic Chemistry* **2002**, *41*, 5133-5140.

(25) Yang, E. C.; Wernsdorfer, W.; Zakharov, L. N.; Karaki, Y.; Yamaguchi, A.; Isidro, R. M.; Lu, G. D.; Wilson, S. A.; Rheingold, A. L.; Ishimoto, H.; Hendrickson, D. N. *Inorganic Chemistry* **2006**, *45*, 529-546.

(26) Castro, S. L.; Sun, Z. M.; Grant, C. M.; Bollinger, J. C.; Hendrickson, D. N.; Christou, G. *Journal of the American Chemical Society* **1998**, *120*, 2365-2375.

(27) Oshio, H.; Hoshino, N.; Ito, T.; Nakano, M. *J. Am. Chem. Soc.* **2004**, *126*, 8805-8812.

(28) Yang, E. C.; Hendrickson, D. N.; Wernsdorfer, W.; Nakano, M.; Zakharov, L. N.; Sommer, R. D.; Rheingold, A. L.; Ledezma-Gairaud, M.; Christou, G. *Journal of Applied Physics* **2002**, *91*, 7382-7384.

(29) Osa, S.; Kido, T.; Matsumoto, N.; Re, N.; Pochaba, A.; Mrozinski, J. *Journal of the American Chemical Society* **2004**, *126*, 420-421.

(30) Aronica, C.; Pilet, G.; Chastanet, G.; Wernsdorfer, W.; Jacquot, J. F.; Luneau, D. *Angewandte Chemie (International Edition in English)* **2006**, 4659.

(31) Zaleski, C. M.; Depperman, E. C.; Kampf, J. W.; Kirk, M. L.; Pecoraro, V. L. *Angewandte Chemie International Edition* **2004**, *43*, 3912-3914.

(32) Costes, J. P.; Dahan, F.; Wernsdorfer, W. *Inorganic Chemistry* **2006**, *45*, 5-7.

(33) Zaleski, C. M.; Kampf, J. W.; Mallah, T.; Kirk, M. L.; Pecoraro, V. L. *Inorganic Chemistry* **2007**, *46*, 1954-1956.

(34) Ferbinteanu, M.; Kajiwara, T.; Choi, K. Y.; Nojiri, H.; Nakamoto, A.; Kojima, N.; Cimpoesu, F.; Fujimura, Y.; Takaishi, S.; Yamashita, M. *J. Am. Chem. Soc.* **2006**, *128*, 9008-9009.

(35) He, F.; Tong, M. L.; Chen, X. M. *Inorganic Chemistry* **2005**, *44*, 8285-8292.

(36) Wernsdorfer, W.; Allaga-Alcalde, N.; Hendrickson, D. N.; Christou, G. *Nature* **2002**, *416*, 406-409.

(37) Feng, P. L.; Beedle, C. C.; Koo, C.; Wernsdorfer, W.; Nakano, M.; Hill, S.; Hendrickson, D. N. *Inorganic Chemistry* **2008**, *47*, 3188-3204.

(38) Feng, P. L.; Beedle, C. C.; Wernsdorfer, W.; Koo, C.; Nakano, M.; Hill, S.; Hendrickson, D. N. *Inorganic Chemistry* **2007**, *46*, 8126-8128.

(39) Anastasios, J. T.; Alina, V.; Wolfgang, W.; Khalil, A. A.; George, C. *Angewandte Chemie International Edition* **2004**, *43*, 2117-2121.

(40) Cadiou, C.; Murrie, M.; Paulsen, C.; Villar, V.; Wernsdorfer, W.; Winpenny, R. E. P. *Chemical Communications* **2001**, 2666-2667.

(41) Manoli, M.; Prescimone, A.; Mishra, A.; Parsons, S.; Christou, G.; Brechin, E. K. *Dalton Transactions* **2007**, 532-534.

(42) Muralee, M.; Wolfgang, W.; Khalil, A. A.; George, C. *Angewandte Chemie International Edition* **2005**, *44*, 892-896.

(43) Murugesu, M.; Raftery, J.; Wernsdorfer, W.; Christou, G.; Brechin, E. K. *Inorganic Chemistry* **2004**, *43*, 4203-4209.

(44) Rumberger, E. M.; Shah, S. J.; Beedle, C. C.; Zakharov, L. N.; Rheingold, A. L.; Hendrickson, D. N. *Inorganic Chemistry* **2005**, *44*, 2742-2752.

(45) Rumberger, E. M.; Zakharov, L. N.; Rheingold, A. L.; Hendrickson, D. N. *Inorganic Chemistry* **2004**, *43*, 6531-6533.

(46) Shah, S. J.; Ramsey, C. M.; Heroux, K. J.; DiPasquale, A. G.; Dalal, N. S.; Rheingold, A. L.; del Barco, E.; Hendrickson, D. N. *Inorganic Chemistry* **2008**, *47*, 9569-9582.

(47) Shah, S. J.; Ramsey, C. M.; Heroux, K. J.; O'Brien, J. R.; DiPasquale, A. G.; Rheingold, A. L.; del Barco, E.; Hendrickson, D. N. *Inorganic Chemistry* **2008**, *47*, 6245-6253.

(48) Ako, A. M.; Mereacre, V.; Hewitt, I. J.; Clerac, R.; Lecren, L.; Anson, C. E.; Powell, A. K. *Journal of Materials Chemistry* **2006**, *16*, 2579-2586.

(49) Aromí, G.; Bhaduri, S.; Artús, P.; Huffman, J. C.; Hendrickson, D. N.; Christou, G. *Polyhedron* **2002**, *21*, 1779-1786.

(50) Bhattacharjee, A.; Miyazaki, Y.; Nakano, M.; Yoo, J.; Christou, G.; Hendrickson, D. N.; Sorai, M. *Polyhedron* **2001**, *20*, 1607-1613.

(51) Lecren, L.; Roubeau, O.; Li, Y. G.; Le Goff, X. F.; Miyasaka, H.; Richard, F.; Wernsdorfer, W.; Coulon, C.; Clerac, R. *Dalton Transactions* **2008**, 755-766.

(52) Miyasaka, H.; Nakata, K.; Lecren, L.; Coulon, C.; Nakazawa, Y.; Fujisaki, T.; Sugiura, K.; Yamashita, M.; Clerac, R. *Journal of the American Chemical Society* **2006**, *128*, 3770-3783.

(53) Olivier, R.; Rodolphe, C. *European Journal of Inorganic Chemistry* **2008**, *2008*, 4325-4342.

(54) Price, D. J.; Batten, S. R.; Berry, K. J.; Moubaraki, B.; Murray, K. S. *Polyhedron* **2003**, *22*, 165-176.

(55) Sañudo, E. C.; Grillo, V. A.; Yoo, J.; Huffman, J. C.; Bollinger, J. C.; Hendrickson*, D. N.; Christou*, G. *Polyhedron* **2001**, *20*, 1269-1272.

(56) Taguchi, T.; Daniels, M. R.; Abboud, K. A.; Christou, G. *Inorganic Chemistry* **2009**, *48*, 9325-9335.

(57) Aromi, G.; Bhaduri, S.; Artus, P.; Folting, K.; Christou, G. *Inorganic Chemistry* **2002**, *41*, 805-817.

(58) Beedle, C. C.; Heroux, K. J.; Nakano, M.; DiPasquale, A. G.; Rheingold, A. L.; Hendrickson, D. N. *Polyhedron* **2007**, *26*, 2200-2206.

(59) Heroux, K., J. ; Rheingold, A., L.; Hendrickson, D., N. *European Journal of Inorganic Chemistry* **2009**, *2009*, 3541-3544.

(60) Nihei, M.; Hoshino, N.; Ito, T.; Oshio, H. *Polyhedron* **2003**, *22*, 2359-2362.

(61) Yang, C. I.; Lee, G. H.; Wur, C. S.; Lin, J. G.; Tsai, H. L. *Polyhedron* **2005**, *24*, 2215-2221.

(62) Yang, E. C.; Wernsdorfer, W.; Hill, S.; Edwards, R. S.; Nakano, M.; Maccagnano, S.; Zakharov, L. N.; Rheingold, A. L.; Christou, G.; Hendrickson, D. N. *Polyhedron* **2003**, *22*, 1727-1733.

(63) Roubeau, O.; Clérac, R. *European Journal of Inorganic Chemistry* **2008**, *2008*, 4325-4342.

(64) Affronte, M.; Caneschi, A.; Cucci, C.; Gatteschi, D.; Lasjaunias, J. C.; Paulsen, C.; Pini, M. G.; Rettori, A.; Sessoli, R. *Physical Review B* **1999**, *59*, 6282-6293.

(65) Bhattacharjee, A.; Miyazaki, Y.; Nakano, M.; Yoo, J.; Christou, G.; Hendrickson, D. N.; Sorai, M. *Polyhedron* **2001**, *20*, 1607-1613.

(66) Caneschi, A.; Gatteschi, D.; Lalioti, N.; Sangregorio, C.; Sessoli, R.; Venturi, G.; Vindigni, A.; Rettori, A.; Pini, M. G.; Novak, M. A. *Europhysics Letters* **2002**, *58*, 771-777.

(67) Caneschi, A.; Gatteschi, D.; Lelirzin, A. *Journal of Materials Chemistry* **1994**, *4*, 319-326.

(68) Caneschi, A.; Gatteschi, D.; Renard, J. P.; Rey, P.; Sessoli, R. *Journal De Physique* **1988**, *49*, 859-860.

(69) Miyasaka, H.; Clerac, R. *Bulletin of the Chemical Society of Japan* **2005**, *78*, 1725-1748.

(70) Miyasaka, H.; Madanbashi, T.; Sugimoto, K.; Nakazawa, Y.; Wernsdorfer, W.; Sugiura, K.; Yamashita, M.; Coulon, C.; Clerac, R. *Chemistry-a European Journal* **2006**, *12*, 7029-7040.

(71) Miyasaka, H.; Nezu, T.; Sugimoto, K.; Sugiura, K.; Yamashita, M.; Clerac, R. *Chemistry-a European Journal* **2005**, *11*, 1592-1602.

(72) Yoo, J.; Wernsdorfer, W.; Yang, E. C.; Nakano, M.; Rheingold, A. L.; Hendrickson, D. N. *Inorganic Chemistry* **2005**, *44*, 3377-3379.

(73) Foguet-Albiol, D.; O'Brien, T. A.; Wernsdorfer, W.; Moulton, B.; Zaworotko, M. J.; Abboud, K. A.; Christou, G. *Angewandte Chemie-International Edition* **2005**, *44*, 897-901.

(74) Beedle, C. C.; Stephenson, C. J.; Heroux, K. J.; Wernsdorfer, W.; Hendrickson, D. N. *Inorganic Chemistry* **2008**, *47*, 10798-10800.

(75) Shah, S. J.; Ramsey, C. M.; Heroux, K. J.; DiPasquale, A. G.; Dalal, N. S.; Rheingold, A. L.; del Barco, E.; Hendrickson, D. N. *Inorganic Chemistry* **2008**, *47*, 9569-9582.

(76) Shah, S. J.; Ramsey, C. M.; Heroux, K. J.; O'Brien, J. R.; DiPasquale, A. G.; Rheingold, A. L.; del Barco, E.; Hendrickson, D. N. *Inorganic Chemistry* **2008**, *47*, 6245-6253.

(77) Wang, W. G.; Zhou, A. J.; Zhang, W. X.; Tong, M. L.; Chen, X. M.; Nakano, M.; Beedle, C. C.; Hendrickson, D. N. *Journal of the American Chemical Society* **2007**, *129*, 1014-1015.

(78) Zhou, A. J.; Qin, L. J.; Beedle, C. C.; Ding, S.; Nakano, M.; Leng, J. D.; Tong, M. L.; Hendrickson, D. N. *Inorganic Chemistry* **2007**, *46*, 8111-8113.

(79) Wittick, L. M.; Jones, L. F.; Jensen, P.; Moubaraki, B.; Spiccia, L.; Berry, K. J.; Murray, K. S. *Dalton Transactions* **2006**, 1534-1543.

(80) Wittick, L. M.; Murray, K. S.; Moubaraki, B.; Batten, S. R.; Spiccia, L.; Berry, K. J. *Dalton Transactions* **2004**, 1003-1011.

(81) Wernsdorfer, W.; Bhaduri, S.; Tiron, R.; Hendrickson, D. N.; Christou, G. *Journal of Magnetism and Magnetic Materials* **2004**, *272-76*, 1109-1110.

(82) Wernsdorfer, W. *Advances in Chemical Physics, Vol 118* **2001**, *118*, 99-190.

(83) Coronado, E.; Martí-Gastaldo, C.; Tatay, S. *Applied Surface Science* **2007**, *254*, 225-235.

(84) Kulzer, F.; Orrit, M. *Annual Review of Physical Chemistry* **2004**, *55*, 585-611.

(85) Moerner, W. E.; Kador, L. *Physical Review Letters* **1989**, *62*, 2535.

(86) Bogani, L.; Wernsdorfer, W. *Nature Materials* **2008**, *7*, 179-186.

(87) Jo, M.-H.; Baheti, K.; Deshmukh, M. M.; Sokol, J. J.; Rumberger, E. M.; Hendrickson, D. N.; Long, J. R.; Park, H.; Ralph, D. C. *lanl.arXiv.org/cond-mat/0603276* **2006**.

(88) Ni, C.; Shah, S.; Hendrickson, D. N.; Bandaru, P. R. *Applied Physics Letters* **2006**, *89*, 212104.

(89) Beedle, C. C.; Stephenson, C. J.; Heroux, K. J.; Wernsdorfer, W.; Hendrickson, D. N. *Inorganic Chemistry* **2008**, *47*, 10798-10800.

(90) Zhou, A. J.; Qin, L. J.; Beedle, C. C.; Ding, S.; Nakano, M.; Leng, J. D.; Tong, M. L.; Hendrickson, D. N. *Inorganic Chemistry* **2007**, *46*, 8111-8113.

(91) Kambe, K. *Journal of the Physical Society of Japan* **1950**, *5*, 48.

Chapter 5

Oriented Single-Crystal Magnetization Hysteresis and High-Frequency Electron Paramagnetic Resonance Studies of Tetranuclear Manganese Dicubanes

5.1 Introduction

Chapter 4 introduced two series of tetranuclear manganese complexes that exhibit relatively large spin ground states and appreciable axial magnetoanisotropy. These interesting complexes exhibit out-of-phase signals in their plots of molar ac magnetic susceptibility versus temperature that signify the presence of slow magnetization relaxation processes, a hallmark of single-molecule magnets (SMMs),[1-3] but not definitive proof that quantum tunneling processes are at work. Fitting of variable-field and variable-temperature dc magnetic susceptibility data in chapter 4 employed simplified theoretical models. For variable temperature data an equivalent operator method was applied. This method can be used where molecular topologies allow simplification of the magnetic exchange pathways.[4] The variable temperature data can then be fit to a spin Hamiltonian (Equation 5.1), where J is the magnetic exchange coupling constant between magnetic centers, and $\hat{S}_{ij}$ is a spin operator. Least-squares fitting yields a theoretical fit of the experimental data employing Equation 5.2, where χ_{m} is the molar magnetic susceptibility, k is the Boltzman constant and $E(S_T)$ are the eigen energies of the individual states. This method is acceptable if the system exhibits a well isolated spin ground state. However, if this requirement is not met, *i.e.* there are low-lying states or spin state mixing, S and M_{s} become invalid magnetic quantum numbers and the simplified equivalent operator method is not adequate to describe the electronic structure of the system. Furthermore, the simple spin Hamiltonian completely ignores Zeeman and zero-field interactions and other magnetic degrees of freedom. The model used for fitting variable field data is also a simplification, in that it also requires a well isolated rigid spin. Full-matrix

diagonalization to a rigid spin (Equation 5.3) yields fitting parameters which include second-order axial and transverse anisotropies, and Zeeman effects. The magnetization (*M*) can then be calculated employing the van Vleck equation given in Equation 5.4, where E_i represent the eigen-values. Even if the system exhibits a well isolated spin ground state, the sign of the zero-field splitting parameter *D* is ambiguous. In cases where a well isolated spin state is not demonstrated, full-matrix diagonalization in full Hilbert space is required to probe the electronic structure.

$$\hat{H} = -2\sum_{ij} J_{ij}\hat{S}_i \cdot \hat{S}_j \qquad \textbf{(5.1)}$$

$$\chi_M = \left(\frac{Ng^2\mu_B^2}{3kT}\right)\frac{\sum[S_T(S_T+1)(2S_T+1)e^{\frac{-E(S_T)}{k_BT}}}{\sum(2S_T+1)e^{\frac{-E(S_T)}{k_BT}}} \qquad \textbf{(5.2)}$$

$$\hat{H} = D\hat{S}_z^{\,2} + E\,(\hat{S}_x^{\,2} - \hat{S}_y^{\,2}) + g\mu_B\hat{S}B \qquad \textbf{(5.3)}$$

$$M = N\sum_i \left(\delta E_i/\delta B\right)\exp\left(-E_i/kT\right)\Big/\sum_i \exp\left(-E_i/kT\right) \qquad \textbf{(5.4)}$$

High-frequency electron paramagnetic resonance (HFEPR) is an extremely powerful tool for studying magnetic systems. The large spin ground states and appreciable axial anisotropy of SMMs often require large magnetic field strengths and high frequencies to resolve spin state transitions. Application of a magnetic field splits the 2*S* multiplet into 2*S* + 1 spin levels and evenly spaced magnetic dipole transitions

are observed that vary in M_s = ± 1 (M_s = 9 to 8, M_s = 8 to 7, M_s = 7 to 6...) in temperature and frequency dependent EPR spectra. Frequency dependent spectra can be fit employing Equation 5.5 yielding the fitting parameters for second-order and higher zero-field terms. EPR will also allow unambiguous designation of the magnitude and sign of *D*, and anisotropy in *g*, the Landé g-factor. Temperature and frequency dependent data also clearly reveal inhomogeneity as a result of solvate disorder, ligand disorder and intermolecular interactions that manifest themselves as line-broadening and asymmetry in transition peaks.[5-12]

$$\hat{H} = \mu_B \hat{S} \cdot \vec{g} \cdot \vec{B} + D\hat{S}_z^2 + E(\hat{S}_x^2 - \hat{S}_y^2) + B_4^0 \hat{O}_4^0 + \hat{O}_{4,6..}^T + \hat{H}' \qquad \textbf{(5.5)}$$

Finally, magnetization versus field hysteresis experiments can be employed to study quantum dynamics in SMMs. Quantum tunneling events will manifest themselves as steps in magnetization versus field hysteresis loops. SMMs will exhibit coercivity in hysteresis loops below their blocking temperature, as a consequence of the magnetic moments having a memory to their direction of magnetization. Thus, following saturation of the magnetization, if the external field is turned off, the sample magnetization will persist until an opposing field of adequate strength is applied, or unless thermal energy is high enough to allow molecules to relax classically. Analysis of hysteresis data provides important information regarding Hamiltonian parameters, as well as the magnitude of tunnel splittings[13-15] and experimental evidence of benchmark

observation such as spin-spin cross relaxation, ground-state excited-state transitions and spin-lattice interactions.[12,16-20]

In this chapter oriented single-crystal magnetization hysteresis, oriented single-crystal HFEPR and full matrix diagonalization data are presented for complexes **$[Mn_4(anca)_4(mdea)_2(Hmdea)_2]\cdot 2CHCl_3$ (4A)** and **$[Mn_4(anca)_4(edea)_2(Hedea)_2]$ (4B)** from chapter 4 to determine if they exhibit quantum dynamics.

5.2 Experimental Section

5.2.1 Compound Preparation

The details of compound preparation are presented in chapter 4.

5.2.2 Physical Methods

Single crystal magnetization versus field hysteresis and magnetization relaxation data for complex **4A** were carried out employing a micro-squid array technique[21] with the applied magnetic field co-linear with the crystal easy-axis.

A single crystal of complex **4B** was placed on top of a high-sensitivity micro-Hall effect magnetometer.[22] The sample magnetization was recorded at temperatures between 230 and 1400mK in an Oxford Instruments $^3He/^4He$ dilution cryostat.

High-frequency (40 – 160 GHz) electron paramagnetic resonance (HFEPR) measurements were carried out on a single crystal of $Cu_{17}Mn_{28}$ using a millimeter-wave vector network analyzer (MVNA) and a sensitive cavity technique.[23] The split-pair magnet with a 7 T horizontal field was used to apply a DC magnetic field to the sample which was aligned in a cylindrical cavity. The angle dependence of EPR data was investigated rotating the sample relative to the DC magnetic field to change the angle

between the orientation of the crystal and magnetic field by a room temperature stepper motor. The temperature was stabilized relative to a calibrated Cernox™ thermometer using a combination of heaters and cold helium gas flow in the range of 1.7 – 25 K.

5.3 Results and Discussion

5.3.1 Oriented Single Crystal Magnetization Verses Field Hysteresis

$[Mn_4(anca)_4(mdea)_2(Hmdea)_2]\cdot 2CHCl_3$ (4A). To definitively determine if complex **4A** exhibits quantum effects, oriented single-crystal magnetization versus field hysteresis experiments were performed employing a micro-squid array.[24] Since the projections of the easy-axes of the four symmetry independent molecules are not collinear, the angle of the applied field relative to the easy-axis of each molecule was calculated to be 45 degrees from crystallographic data and by systematically energizing micro-squids within the array to find the easy-axis of the individual molecular orientations. Temperature dependent magnetization verses field hysteresis loops, plotted as magnetization in terms of magnetization saturation versus applied field (M/M_s vs. H) are presented in Figure 5.1. The data were collected with a field sweep rate of 0.07T/s at 0.04 K with the magnetic field applied between the easy-axis of the four independent molecules in the crystal (Figure 5.2). Coercivity is obtained below ~1.2K, and at 1.1K, one step is seen in the hysteresis loop near zero-field. However, with decreasing temperature, multiple quantized steps appear below 0.5K, attributable to quantum tunneling of the magnetization (QTM), and signify that complex **4A** is a SMM.

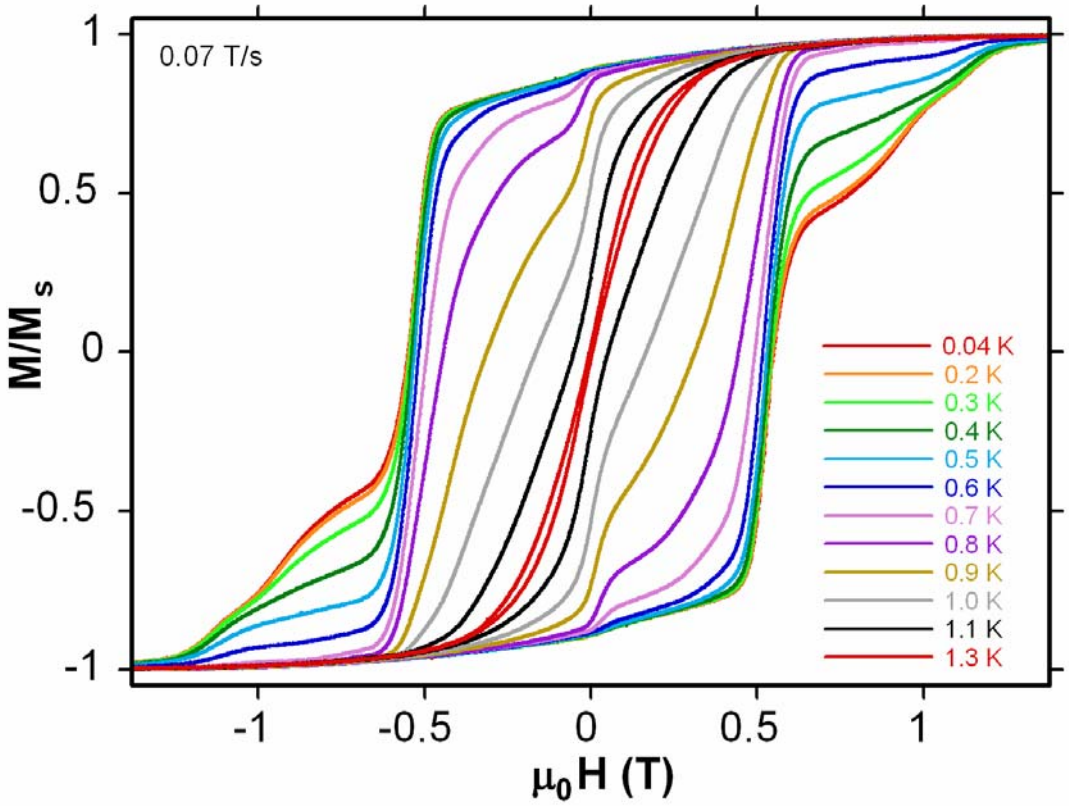

Figure 5.1. Temperature dependent magnetization verses field hysteresis loops for complex **$[Mn_4(anca)_4(mdea)_2(Hmdea)_2]\cdot 2CHCl_3$ (4A)** collected between 0.04K to 1.1K with a scan rate of 0.07 Tesla/second.

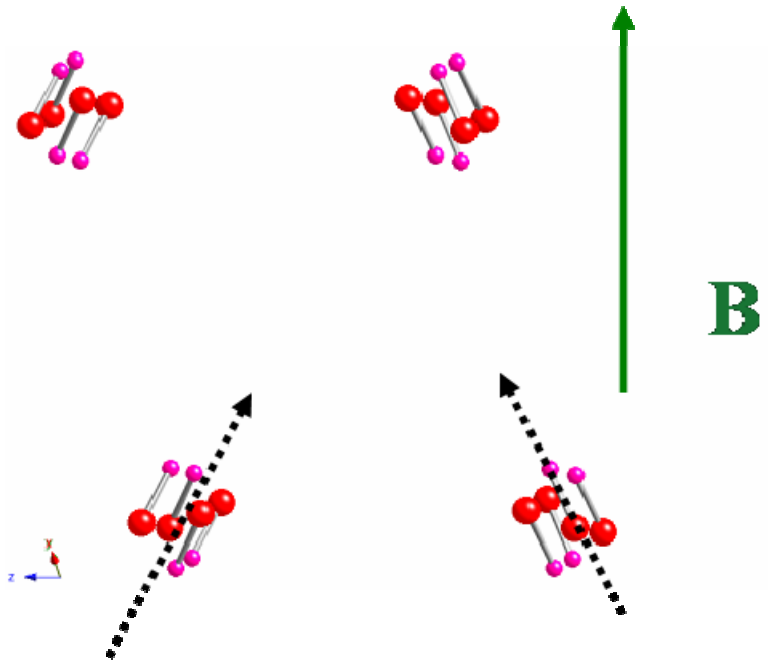

Figure 5.2. Alignment of the field relative to the four molecular orientations for complex **4A**. Arrows represent the orientations of the Jahn-Teller axes of the molecules.

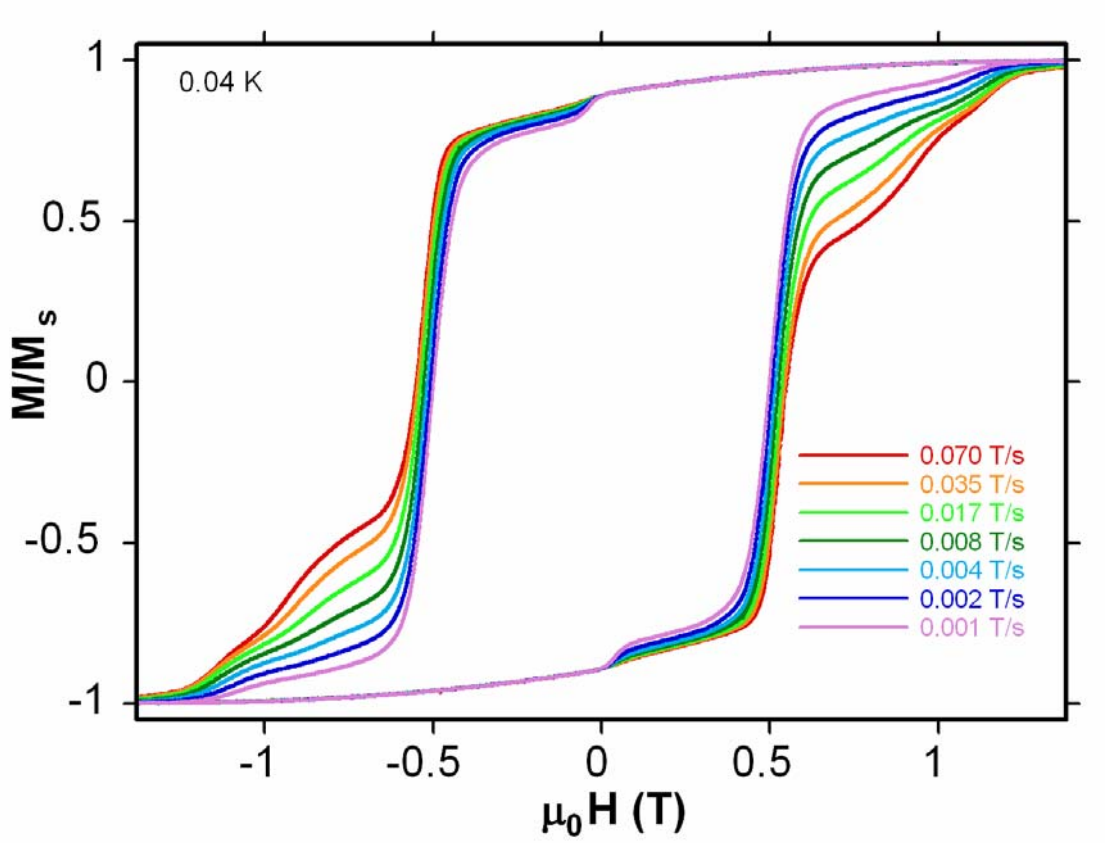

Figure 5.3. Sweep-rate dependent magnetization verses field hysteresis loops for complex **$[Mn_4(anca)_4(mdea)_2(Hmdea)_2]\cdot 2CHCl_3$ (4A)** collected at 0.04K with with sweep-rates between 0.070 and 0.001 T/s.

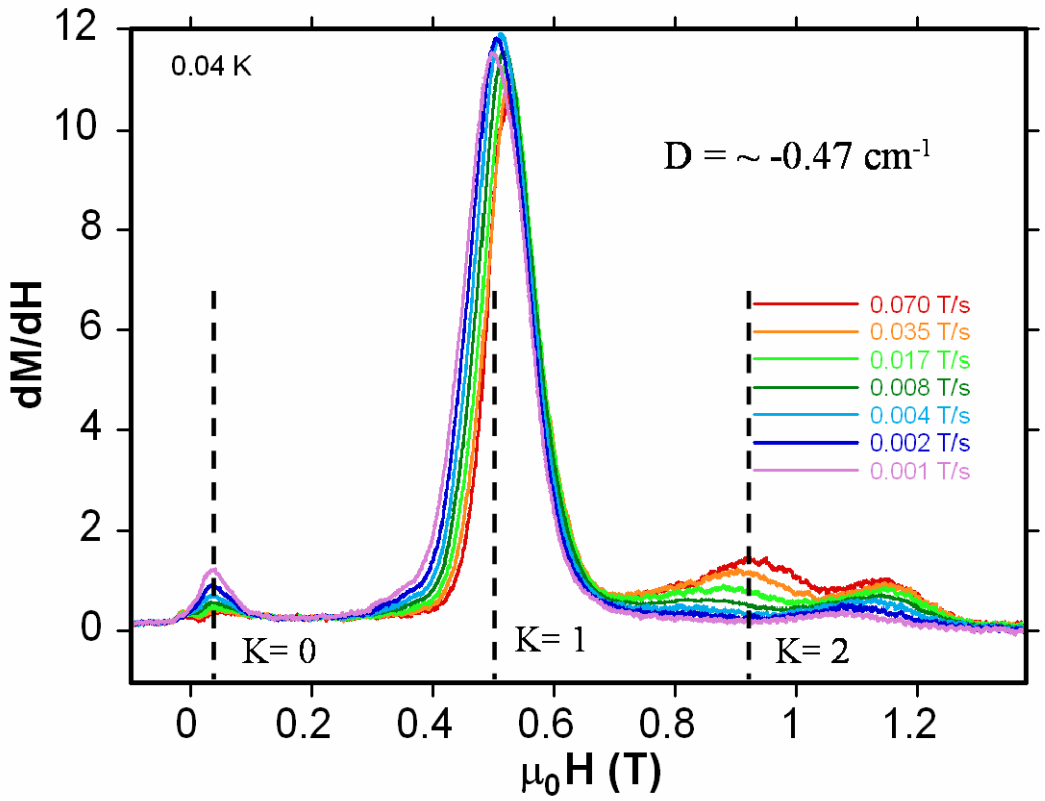

Figure 5.4. **(**Top**)** Magnetization verses field hysteresis loops for complex **$[Mn_4(anca)_4(mdea)_2(Hmdea)_2]\cdot 2CHCl_3$ (4A)** collected at 0.04K with a scan rates of 0.07 to 0.001 Tesla/second. (Bottom) First derivative dM/dH verses field (*H*) of the scan rate dependent magnetization verses field hysteresis loops for complex **4A.** Quantized resonances (*k* = 0, 1 and 2) for quantum tunneling of the magnetization are marked by vertical dashed lines.

Figure 5.3 presents sweep rate dependent magnetization hysteresis loops collected at 0.04K with sweep rates of 0.001-0.070 T/s. Figure 5.4 displays the first derivative of the sweep rate dependent magnetization data plotted as *dM/dH* verses field. There is only a small change in the total magnetization (~5%) seen in the first step ($k = 0$), attributed to tunneling between the ground $m_s = \pm 9$ states. Furthermore, the step at $H = 0$ exhibits a very small positive exchange bias of ~0.03T. Approximately 75% of the total magnetization is lost in the $k = 1$ resonance at ~0.49T indicating a faster rate of magnetization tunneling in comparison to the $k = 0$ resonance. Application of the Zeeman energy equation $E = g\beta H$, assuming g = 2.0, $H = 0.46$T, yields a value of -0.43 cm^{-1} which is significantly larger than the zero-field splitting value of $D = -0.28$ cm^{-1} calculated through fitting *M vs H/T* data for complex **4A**. The $k = 1$ peak in the *dM/dH* verses field plot (Figure 5.4) exhibits considerable sweep rate dependence. At slow sweep rates (0.001 T/s) the peak height is at a maximum. As the sweep rate is increased, the peak decreases in magnitude and shifts to larger applied fields. With faster sweep rates the tunneling window is much narrower and fewer molecules meet the resonance conditions for tunneling.

The peak in the *dM/dH* verses field plot in Figure 5.4 at 0.92T is consistent with peak spacing of 0.46T and is assigned as the $k = 2$ resonance. Interestingly however, though the peak shifts to higher applied fields with increasing sweep rates, at a sweep rate of 0.001 T/s there is no visible $k = 2$ resonance, in complete contrast to the $k = 0$ and $k = 1$ resonances. As the sweep rate is increased, a broad weak step/peak occurs at a sweep rate of 0.008 T/s that becomes more pronounced and broader as the sweep rate is increased to 0.070 T/s. The sweep rate dependence of the $k = 2$ resonance suggests that

at the slowest sweep rates measured there are large distributions of energy levels within the tunneling window. Thus, tunneling is occurring between many different m_s states simultaneously resulting in the peak being completely smoothed out. The systematic broadening of the k = 2 resonance could be due to a number of factors including, microenvironments within the crystal due to solvate disorder and distributions in molecular environments resulting from the four symmetry independent molecules within the crystal lattice. As the sweep rate is increased, the time that the magnetic field remains at a tunneling resonance is decreased. Thus, the weak resonance (k = 2) seen for faster sweep rates encompasses only those molecules that satisfy resonance conditions to tunnel.

It is not entirely clear what the origin of the fourth peak (~1.18T) is in the plot of *dM/dH*. It does not correspond to a field at which a quantized step would result (D = -0.36 cm^{-1} which is not consistent with D = -0.43 cm^{-1} calculated from the k = 1 and k = 2 resonances). The magnetization relaxation processes at work in the peak at 1.18T could be due to excited state coupling between molecules, spin-spin cross-relaxation or a phonon bottleneck as documented for other SMMs. [25-27] As the Cole-Cole plot for complex **4A** implies (chapter 4, Figure 4.51), the relaxation processes in complex **4A** are extremely complicated and cannot be attributed to a single relaxation mechanism.

Exchange bias in magnetization hysteresis loops, a shift in the k = 0 tunneling resonance from zero field, has been reported for a few SMMs. Most notably, exchange bias in the $[Mn_4O_3Cl_4(O_2CEt)_3(py)_3]_2$ molecular dimer, where py is pyridine.[28] Each Mn_4 cubane unit has a spin ground state of S =9/2 and are connect via hydrogen bonding through six C-H····Cl sites and one Cl·····Cl interaction. The resulting weak

antiferromagnetic intermolecular interaction (J = -0.05K) leads to the first step appearing at -0.33T instead of zero field. Exchange bias has also been reported for the S = 4 cubane $[Ni(hmp)(ROH)Cl]_4$ series of complexes, where hmp is hydroxymethylpyridine and ROH is methanol, ethanol and 3,3'-1-dimethylbutanol.[29,30] The observed exchange bias in the Ni_4 series of molecules is the direct result of intermolecular Cl···Cl contacts that connect each Ni_4 cube to its four nearest neighbors in the crystal lattice. However, as the insulating properties of the coordinated alcohol ligand increases, the resultant exchange bias is decreased. The Cl···Cl intermolecular contacts are closest in the methanol complex and lead to the first step in the magnetization to occur at –0.28T, whereas longer contact distances in the ethanol complex lead to the first step occurring at -0.15T. The more interesting case in the Ni_4 SMMs is the 3,3'-1-dimethylbutanol complex that exhibits a small positive exchange bias (+ 0.012T) at low temperatures which has recently been shown [27] to originate from long-range weak ferromagnetic ordering below 290 mK.

Upon inspection, there is clearly a small exchange bias in the hysteresis loops of complex **4A** which shifts the first step to 0.03T. The origin of the exhibited exchange bias is currently unknown. Heat capacity data (Figure 5.5) collected in 0, 1T from 1-10K for complex **4A** reveals no anomalies, which was collected to temperatures below which coercivity in magnetization hysteresis is exhibited. Future experiments on this system should include major and minor hysteresis loops to determine the origin of non-resonance hysteresis peaks and dilution refrigerator temperature heat capacity to determine the origin of the exhibited exchange bias.

Temperature dependent magnetization versus field hysteresis loops for complex **$[Mn_4(anca)_4(edea)_2(Hedea)_2]$ (4B)** are presented in Figure 5.6. In contrast to the hysteresis loops for complex **4A**, the magnetization data for complex **4B** are very complicated and no observable step is seen at zero-field. This is counterintuitive, since complex **4B** has only one molecular orientation in the crystal lattice. It should be noted that the magnetic field alignment was determined to be tilted 37 degrees from the easy-axis of the crystal. Misalignment of the easy-axis of the sample with respect to the external magnetic field was calculated by comparing magnetization hysteresis and HFEPR simulation data. Simulations of easy-axis and hard-plane frequency dependent data, are in relatively good agreement with bulk magnetization fitting parameters and full-matrix calculations, *vide infra.* However, initial magnetization hysteresis simulation parameters were conflicting. It was determined that rotation of the field direction by 37 degrees allowed a fit of the magnetization hysteresis data that is in good agreement with HFEPR simulations. The hysteresis loops exhibit coercivity at <1200mK that increases with decreasing temperature, indicative of slow magnetization relaxation. Figure 5.7 shows the first derivative (dM/dH vs. H) for the hysteresis loops in Figure 5.6. As previously mentioned, the evolution of the peaks is not typical of most SMMs. First there is no step at zero-field that would be associated with a tunneling transition between the $\pm m_s$ projections of the $S = 9$ spin ground state. Furthermore, there are no evenly spaced transitions as seen in the derivative plot for complex **4A**.

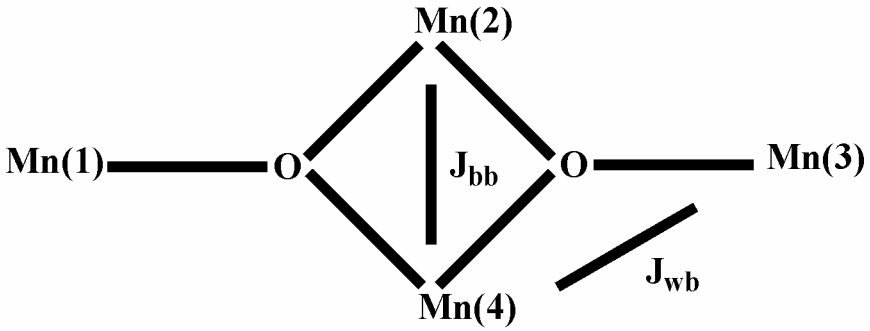

Scheme 5.1. Coupling model illustrating magnetic exchange pathways J_{wb} and J_{bb} for complexes **4A-B**, where S_1 and S_3 are Mn^{II} ions and S_2 and S_4 are Mn^{III} ions.

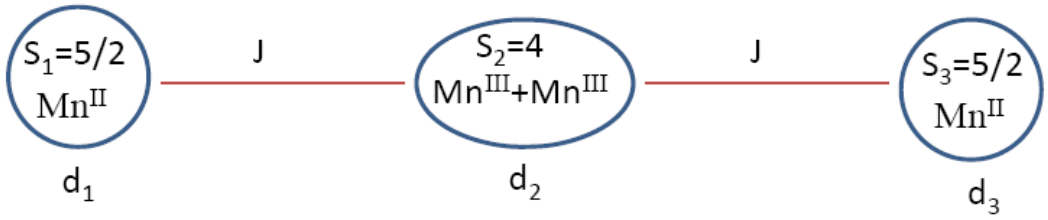

Scheme 5.2. Trimer model for the two Mn^{III} and two Mn^{II} ions in complex **4B**.

Figure 5.8 shows a Zeeman level crossing diagram for complex **4B**. The arrows represent level crossings between m_s states. The Zeeman diagram was constructed by fitting peak positions in the plot of *dM/dH* vs. *H* employing the spin-Hamiltonian in Equation 5.6, where H_{d1} and H_{d3} are S = 5/2 Mn^{II} ions and H_{d3} represents coupling of the body-centered S = 2 Mn^{III} ions (Schemes 5.1 and 5.2), and g is the Landé g-factor, *B* is the magnetic field, *S* is the spin number, *d* is the second-order zero-field splitting term, *e* is the second-order transverse zero-field splitting term and *J* represents the magnetic coupling between ions. Scheme 5.2 simplifies the four-body problem by assuming that the coupling between Mn^{III} ions is the dominant exchange pathway and that Jahn-Teller axes on the Mn^{III} ions are co-linear, so J_{wb} in Scheme 5.1 is equal to *J* in Equation 5.6.

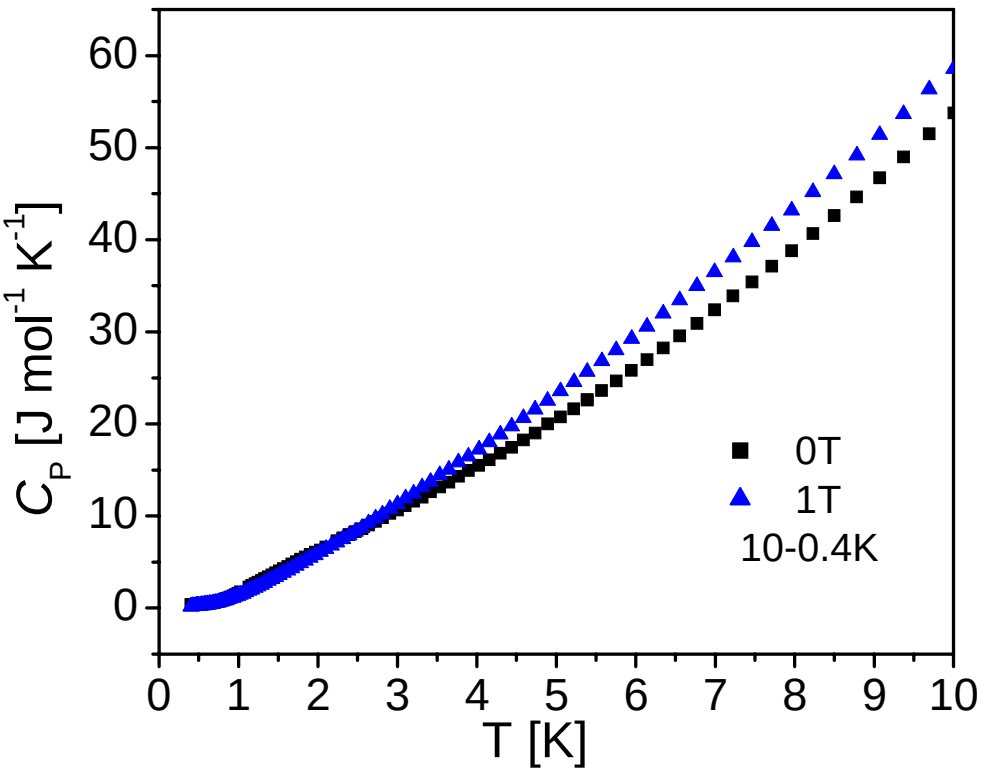

Figure 5.5. Heat capacity plotted as Cp versus T collected between 10 and 0.4K in applied fields of 0T and 1T.

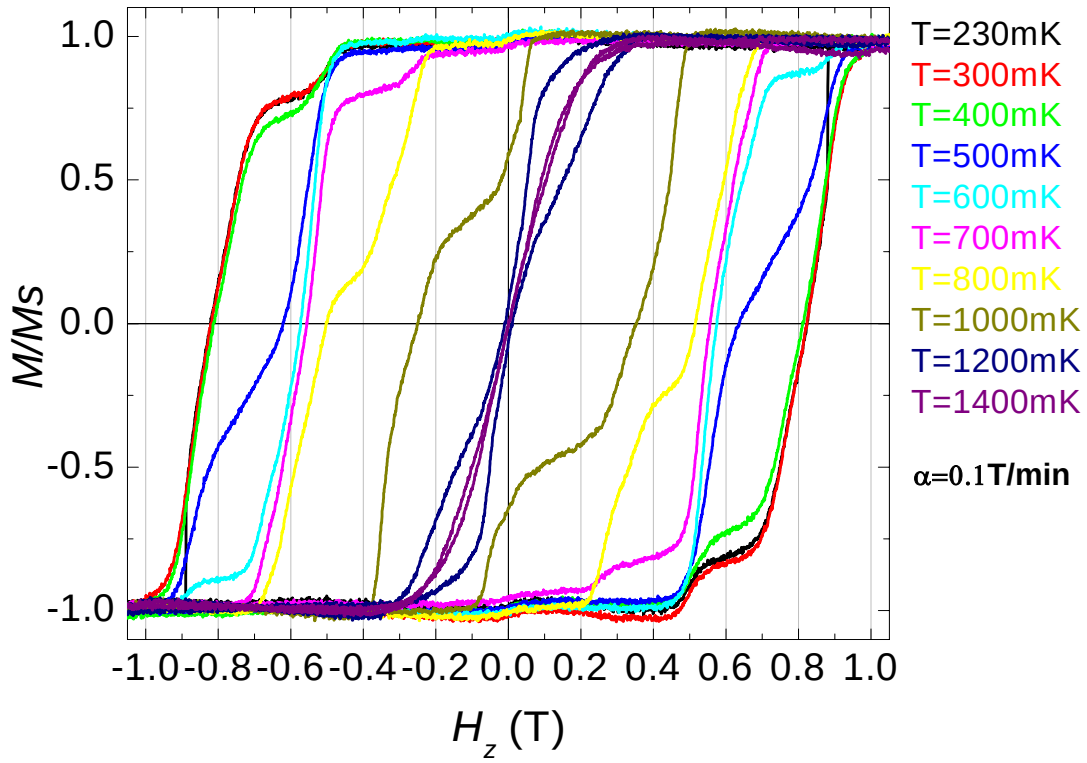

Figure 5.6. Magnetization hysteresis loops for **[$Mn_4(anca)_4(edea)_2(Hedea)_2$] (4B)** collected with a sweep-rate of 0.1T/s with temperatures between 230 and 1400mK.

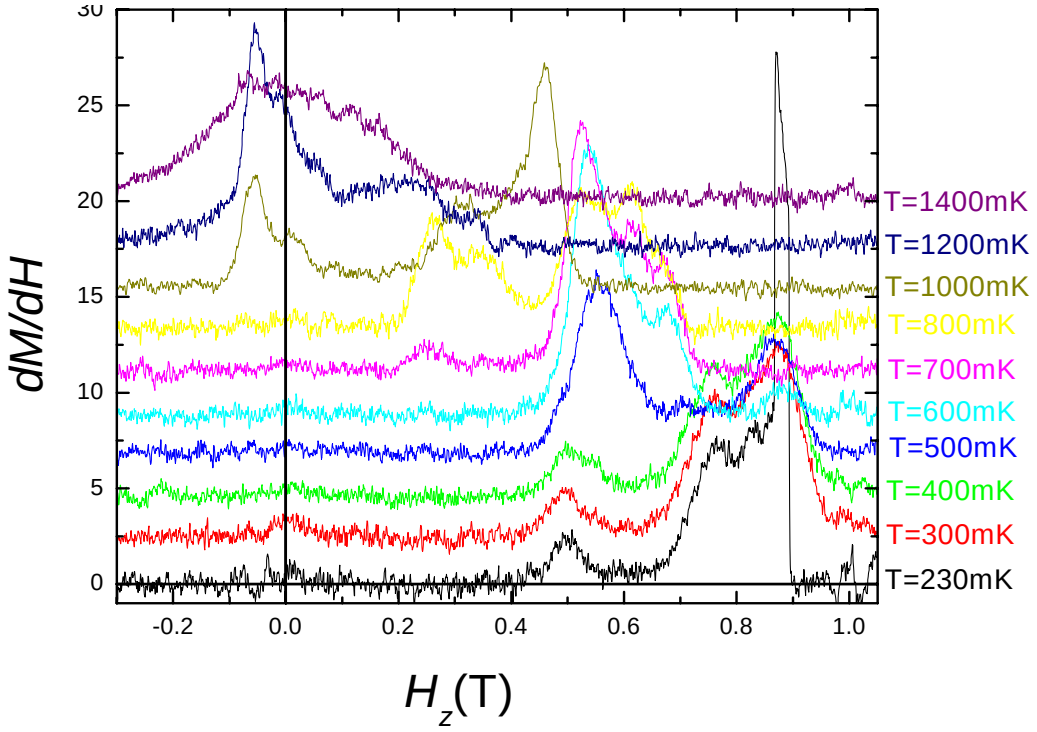

Figure 5.7. First derivative (*dM/dH* vs. *H*) of the hysteresis loops in Figure 5.6 for **[Mn_4(anca)$_4$(edea)$_2$(Hedea)$_2$] (4B)**.

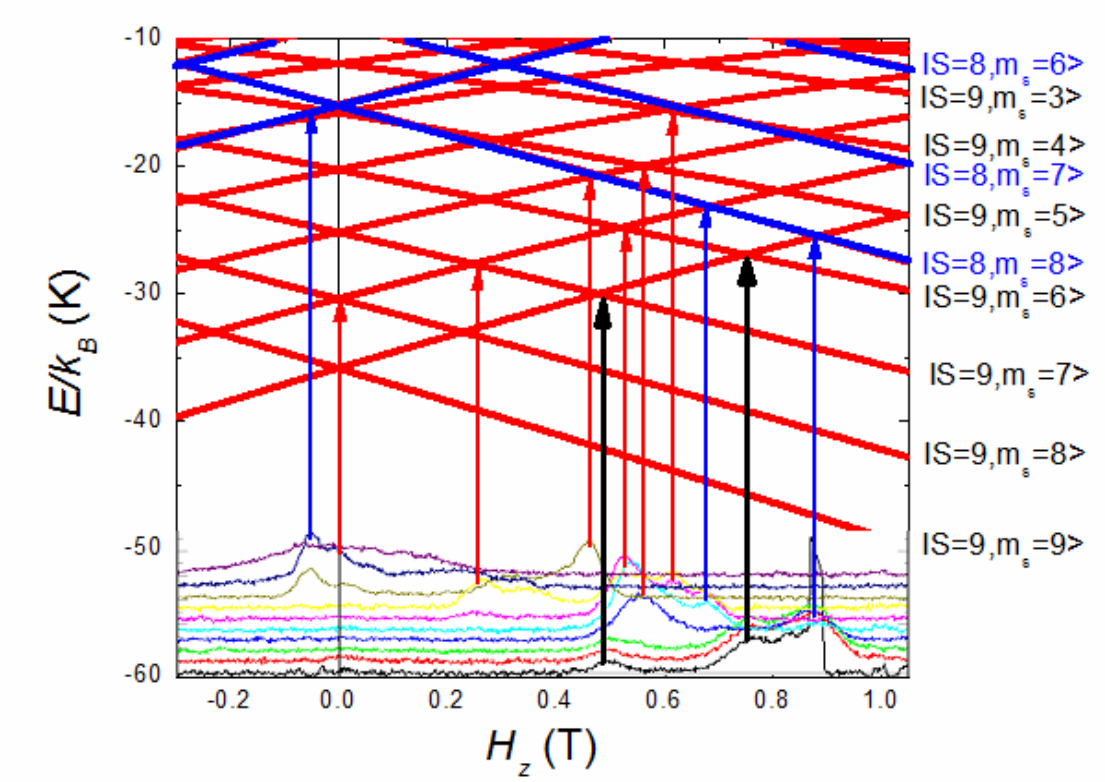

Figure 5.8. First derivative (*dM/dH* vs. *H*) of the hysteresis loops in Figure 5.6 for **[Mn_4(anca)$_4$(edea)$_2$(Hedea)$_2$] (4B)** with a Zeeman diagram depicting level crossings of the different m_s states.

$$H_{d_1} = g\vec{B}\cdot\vec{S}_{d_1}$$
$$H_{d_2} = d_2 S_{z_2}^2 + e\left(S_{x_2}^2 - S_{y_2}^2\right) + g_x B_x S_{x_2} + g_y B_y S_{y_2} + g_z B_z S_{z_2}$$
$$H_{d_3} = g\vec{B}\cdot\vec{S}_{d_3}$$

$$H = H_{d_1} + H_{d_2} + H_{d_3} + J(\vec{S}_1\cdot\vec{S}_2 + \vec{S}_2\cdot\vec{S}_3) \quad \textbf{(5.6)}$$

This is a valid assumption because the C_i site symmetry molecules possess inversion symmetry. Thus the two Mn^{III} ions are treated as a single $S = 4$ particle with single D and E zero-field splitting terms. Furthermore, since Mn^{II} ions generally exhibit orders of magnitude smaller zero-field splitting than Mn^{III}, the d and e values for each Mn^{II} ion are assumed to be zero in this model. Diagonalization of the data yielded fitting parameters of $S = 9$, $d = -1.54$ cm^{-1}, $J = 3.6$ cm^{-1}, $e = 0.14$ cm^{-1}, $g_X = g_Y = 1.95$ and $g_Z = 2$. The J-value of 3.6 cm^{-1} is smaller than the value calculated from variable temperature magnetic susceptibility fitting (5.5 cm^{-1}, see chapter 4, Figure 4.13). The D-value is three times the value determined through fitting variable field cm^{-1}, magnetic susceptibility data (0.41 cm^{-1}, see Table 4.8 in chapter 4). The e-value, 0.41 is exactly the same as the value determined through fitting variable field magnetic susceptibility (see Table 4.8 in chapter 4). It is interesting to mote that a number of the allowed tunneling transitions occur between m_s states from different spin manifolds (blue arrows in Figure 5.8), *i.e.* transitions from $S = 9$ m_s states to $S = 8$ m_s states. Mixing of states between spin multiplets has been shown to give rise to quantum phase interference of

Berry-phase[15,31-37] which could possibly be employed in quantum computation and quantum information storage.[38-42]

5.3.2 Single Crystal High-Frequency Electron Paramagnetic Resonance

Temperature dependent easy-axis high-frequency electron paramagnetic resonance (HFEPR) for complex **4B** is presented in Figure 5.9, collected between 1.7K and 25K at 165GHz on an oriented single-crystal. At higher temperatures numerous magnetic dipole transitions are seen as thermal considerations lead to Boltzman populations of higher lying energy states, so multiple spin state transitions are observed within the S = 9 multiplet and the S = 8 multiplet that are superimposed on the same spectrum.. As the temperature is lowered higher lying states are thermally depopulated until the only transition observed is the M_s = -9 to M_s = -8 transition at 1.7K. Hard-plane temperature dependent EPR data is given in Figure 5.10, collected between 1.7 and 25K and 50.5GHz. As with the easy-axis spectra, decreasing temperature leads to successive depopulation of higher energy states. And the ground state transition is shifted to higher magnetic field strengths. However, the hard-axis spectra shows better resolution of the magnetic dipole transitions. If a decrease in temperature shifts the observed transitions to lower field strength in temperature dependent spectra where the field is applied along the easy-axis of magnetization, and to higher magnetic fields with the field applied in the hard-plane, it indicates that the sign of the zero-field splitting parameter (D) is negative. The evolution of peaks in the easy-axis spectra (Figure 5.9) is not easily resolved. Significant asymmetry is observed and peak splitting is evident. Asymmetry and line-broadening in EPR spectra can arise from ligand and solvate

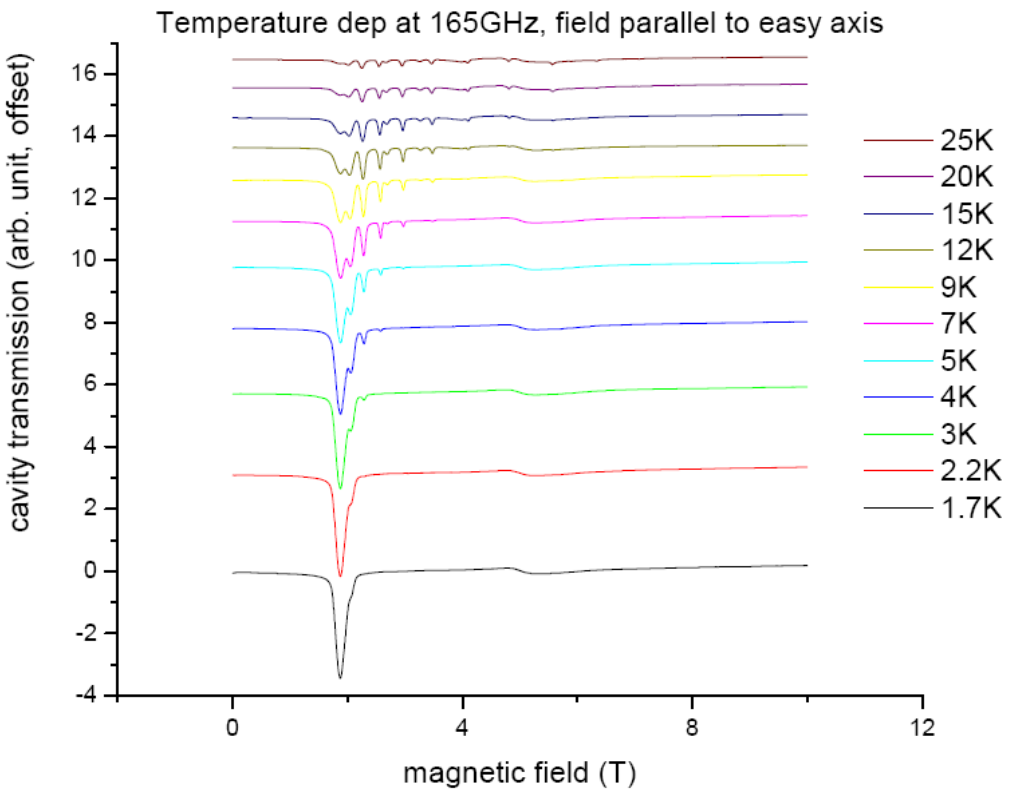

Figure 5.9. Temperature dependent HFEPR data for **[Mn_4(anca)$_4$(edea)$_2$(Hedea)$_2$] (4B)**, with the magnetic field aligned parallel to the easy-axis of magnetization.

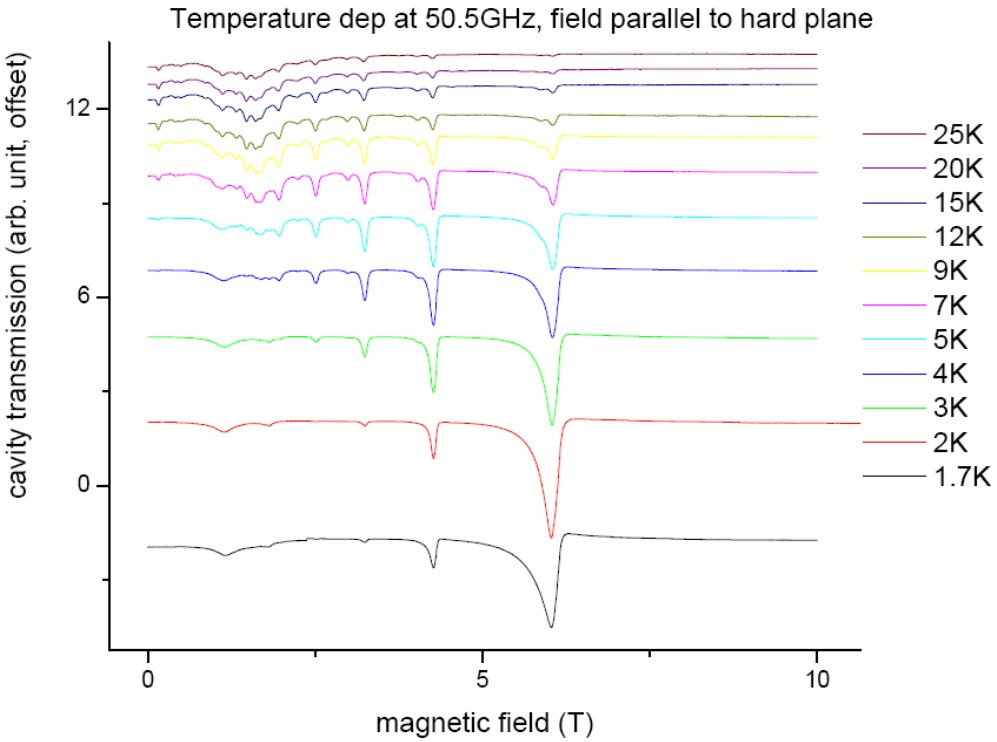

Figure 5.10. Temperature dependent HFEPR data for **$[Mn_4(anca)_4(edea)_2(Hedea)_2]$ (4B)**, with the magnetic field aligned parallel to the hard-plane of magnetization.

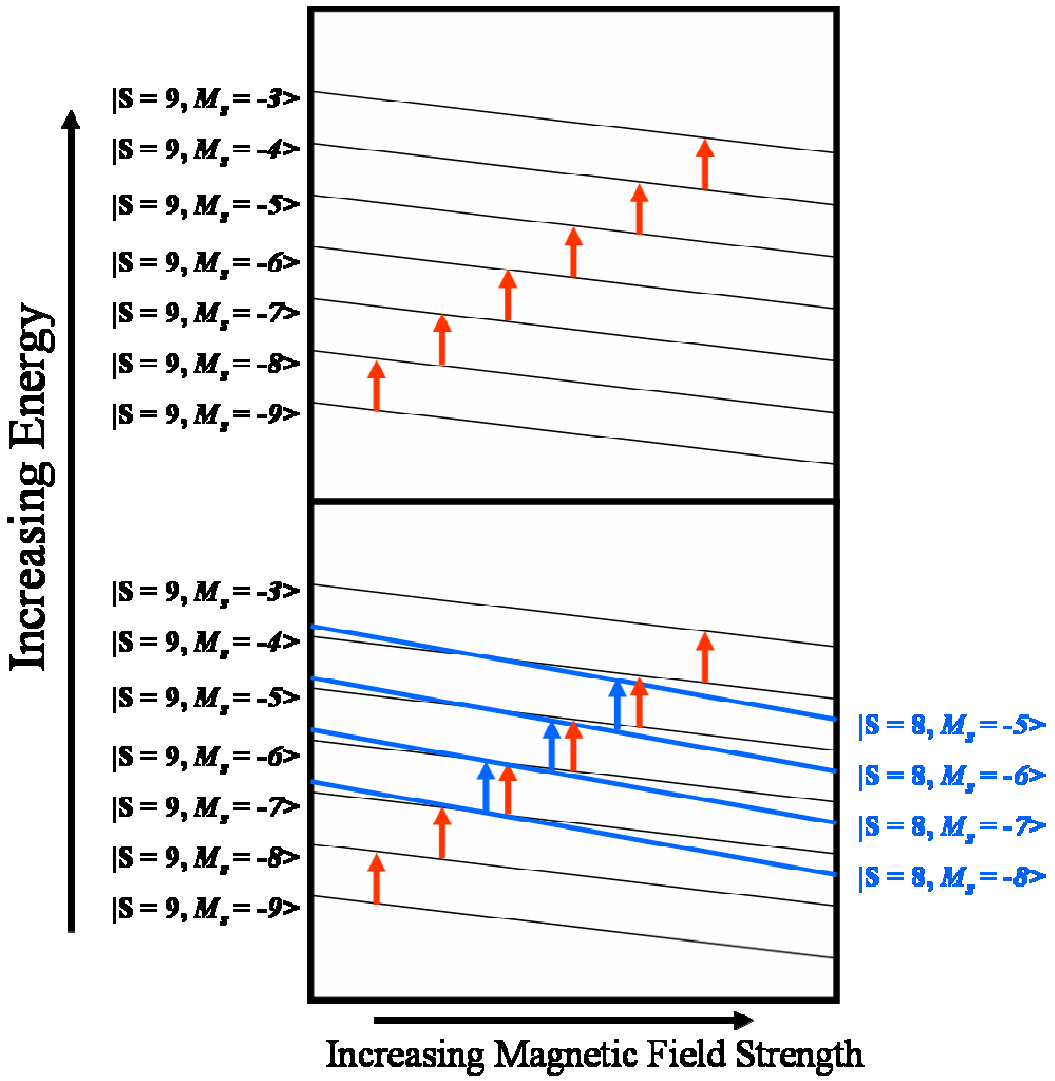

Figure 5.11. Simplified Zeeman diagram depicting magnetic dipole transitions within the $S = 9$ spin multiplet (top), and Transitions within the $S = 9$ spin multiplet and $S = 8$ spin multiplet (bottom). Note that the transitions are not between spin multiplets, *i.e.* between $S = 9$ to $S = 8$.

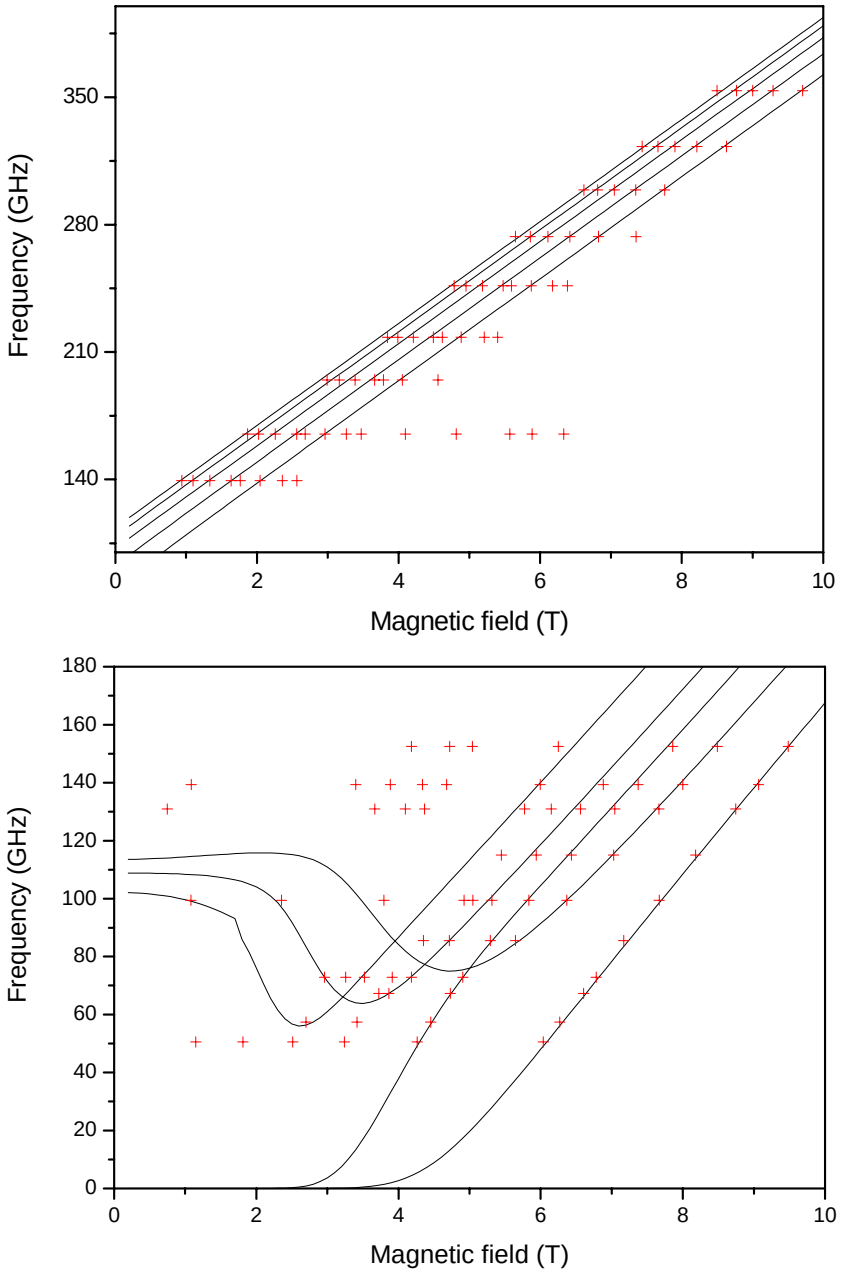

Figure 5.12. Frequency dependent HFEPR data for **[Mn_4(anca)$_4$(edea)$_2$(Hedea)$_2$] (4B)**. (red crosses) fit to the Hamiltonian (equation 5.1)(solid lines), easy-axis data (top) and hard-plane data (bottom).

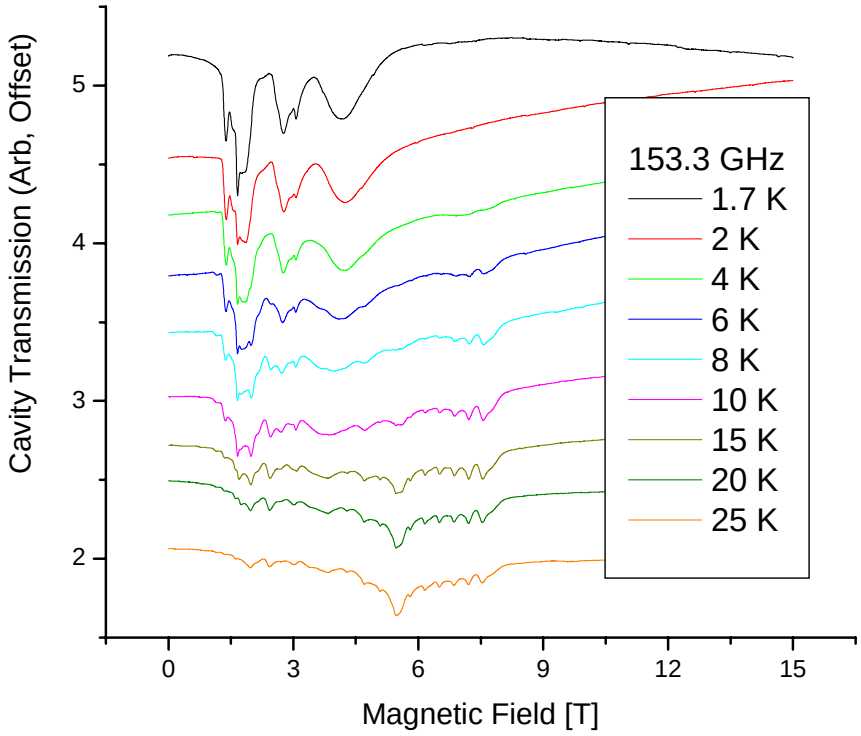

Figure 5.13. Temperature dependent HFEPR data for complex **4A**, with the magnetic field aligned parallel to the easy-axis of magnetization.

disorder, as well as, intermolecular interactions.[6,8,10,12,43] The peak splitting observed in Figure 5.9 is due to transitions within excited states that are depopulated with decreasing temperature. In contrast, the 4K spectrum in Figure 5.10 displays evenly spaced transitions that represent transitions within the ground state multiplet: S = 9 to 8, S = 8 to 7, S = 7 to 6 from right to left, respectively. However, with small applied field strengths the transitions are not well resolved due to line-broadening.

If the S = 9 (M_s = -9, -8, -7…0, 1, 2…9) ground state spin multiplet is well isolated, and can be resolved in the EPR experiment, sequential dipole transitions will be observed (chapter1, Figure 1.15, top) resulting from $M_s = \pm 1$ transitions. Figure 5.11, top shows a simplified Zeeman diagram. With increasing field, sequential transitions differing in $M_s = \pm 1$ will be observed (red arrows) at regular field intervals within a well isolated S = 9 ground state multiplet. If no lattice disorder or appreciable intermolecular interactions exist, symmetric sharp peaks will be evident in EPR spectra. Note: Figure 5.11 was not constructed from experimental data, and is purely included as a diagram to help explain the data given in Figures 5.9-10. However, if higher-lying multiplets are thermally populated or Zeeman induced, transitions from other multiplets can be resolved in EPR spectra. For instance, if the S = 9 and S = 8 multiplets are very close in energy, components of the S = 8 multiplet can cross over the S = 9 multiplet (Figure 5.11, bottom) and transitions can be observed from both multiplets at approximately the same field strength (S = 9, red arrows and S = 8, blue arrows) as the ground state transitions. Thus, peaks from excited state multiplets may resolve themselves as partially or fully superimposed in the line-width of ground state transitions, or observed as discrete peaks. It should be pointed out that these transitions

due not stem from entangled states (transitions between multiplets, *e.g.* $|S = 9, M_s = -9, S = 8, M_s = 8\rangle$ etc.). Rather, the transitions are between M_s states within either the $S = 9$ of $S = 8$ multiplets.

Easy-axis (top) and hard-plane (bottom) frequency dependent EPR data for complex **4B** are presented in Figure 5.12, at frequencies of 140 to 350GHz and 50 to 155GHz for the easy-axis and hard-plane, respectively (red data points). The solid lines represent simulations of the experimental data employing the Hamiltonian in Equation 5.6 using the exact same fitting parameters that were used to fit magnetization versus field hysteresis data ($S = 9$, $d = -1.54$ cm^{-1}, $J = 3.6$ cm^{-1}, $e = 0.14$ cm^{-1}, $g_X = g_Y = 1.95$ and $g_Z = 2$. The molecular anisotropy is dominant along the easy-axis, so with small applied transverse fields, the easy-axis components are of a greater magnitude than the Zeeman energy and mixing of easy-axis and hard-plane components occurs, and is the origin of the non-linear character of the fit lines in Figure 5.12, bottom.

Preliminary easy-axis temperature dependent EPR spectra for complex **4A** collected at 153.3GHz from 1.7 to 25K is presented in Figure 5.13. Shifting of the peaks to lower magnetic field strength with decreasing temperature indicates that the sign of the zero-field splitting parameter D is negative for complex **4A**. However, the spectra are very complex, owing to the four symmetry independent molecules in the crystal lattice. Further study of this complex will be presented in a future publication.

5.3.3 Full Matrix Diagonalization Analysis

Figure 5.14 gives a fit of variable temperature and variable field bulk magnetic susceptibility data collected from 300 to 1.8K in applied magnetic fields of 0.01 to 5T.

The data were fit employing full matrix diagonalization in full Hilbert space of the 900 x 900 matrix for complex **4A**, employing the coupling scheme presented in Scheme 5.1, with two body-centered $S = 2$ Mn^{III} ions and two wing $S = 5/2$ Mn^{II} ions. The 900 x 900 matrix arises from consideration of the possible degeneracies ($2S + 1$) associated with the four paramagnetic manganese ions: Mn^{III} ($2S + 1$) = 2(2)+1 = 5 and for Mn^{II} ($2S + 1$) = 2(5/2)+1 = 6, so the full matrix cosists of 6^2 x 5^2 or 900 elements. The data were fit employing Equation 5.7, where J_{ij} is the exchange coupling constant between magnetic nuclei, $\hat{s}_i$ and $\hat{s}_j$ are spin operators, d_i is the single ion zero-field splitting parameter and $\mu_B \vec{B} \cdot \tilde{g}_i \cdot \hat{s}_i$ is the Zeeman energy term. It is assumed that the Jahn-Teller elongation axes of the Mn^{III} ions are co-linear. The parameters g, *d*, S and *J* were allowed to vary during fitting iterations, yielding fit parameters of $S = 9$, $g = 1.8$, $d = -4.2$ cm^{-1}, $J_{wb} = 1.2$ cm^{-1} and $J_{bb} = 10.1$ cm^{-1}. The single ion *d*-value of -4.2 cm^{-1} is in line with published values for Jahn-Teller elongated octahedrally coordinated Mn^{III} ions ($d = -2$ to -5.5 cm^{-1}).[44] The calculated J_{wb} value of 1.2 cm^{-1} is quite a bit lower than the *J*-value of 3.6 cm^{-1} calculated from HFEPR and magnetization hysteresis data, and $J_{wb} = 6.8$ cm^{-1} calculated through fitting variable temperature susceptibility data in chapter 4 (Table 4.7). However, the theoretical model employed in chapter 4 does not take into account zero-field and Zeman interactions, and it employs a simple equivalent operator coupling model that assumes a rigid spin ground state, in contrast to the full-matrix approach employed here. The J_{bb} value of 10.1 cm^{-1} is much larger than the value calculated in chapter 4 of 0.96 cm^{-1}, but is quite reasonable when compared to vales for reported complexes of the same topology.[45]

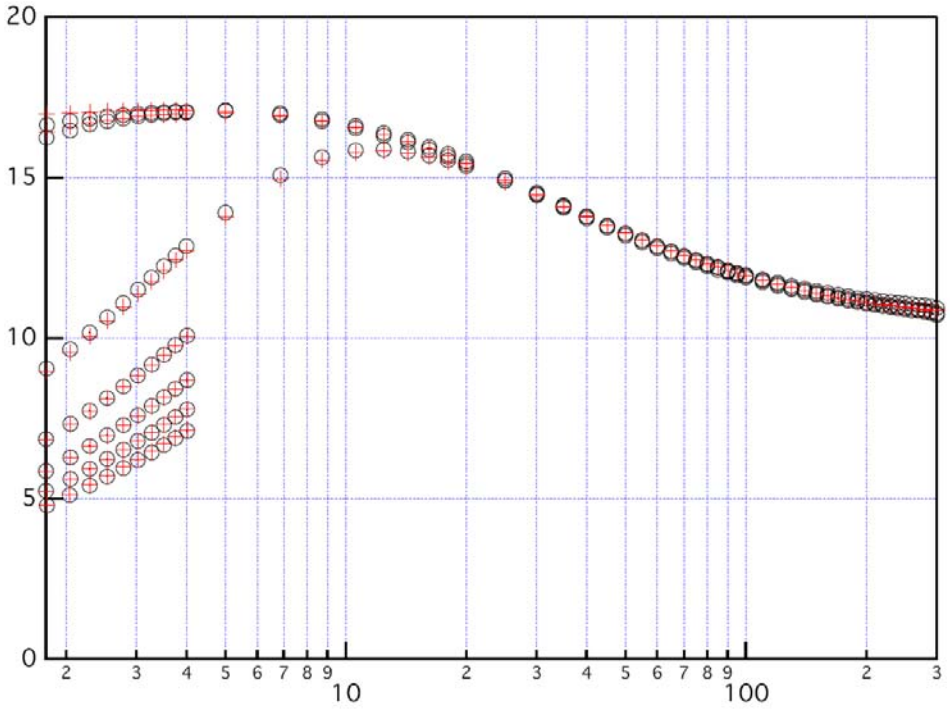

Figure 5.14. Fit of variable temperature magnetic susceptibility data in conjunction with reduced magnetization data for **$[Mn_4(anca)_4(mdea)_2(Hmdea)_2]\cdot 2CHCl_3$ (4A)** in magnetic fields of 0.001T to 5T.

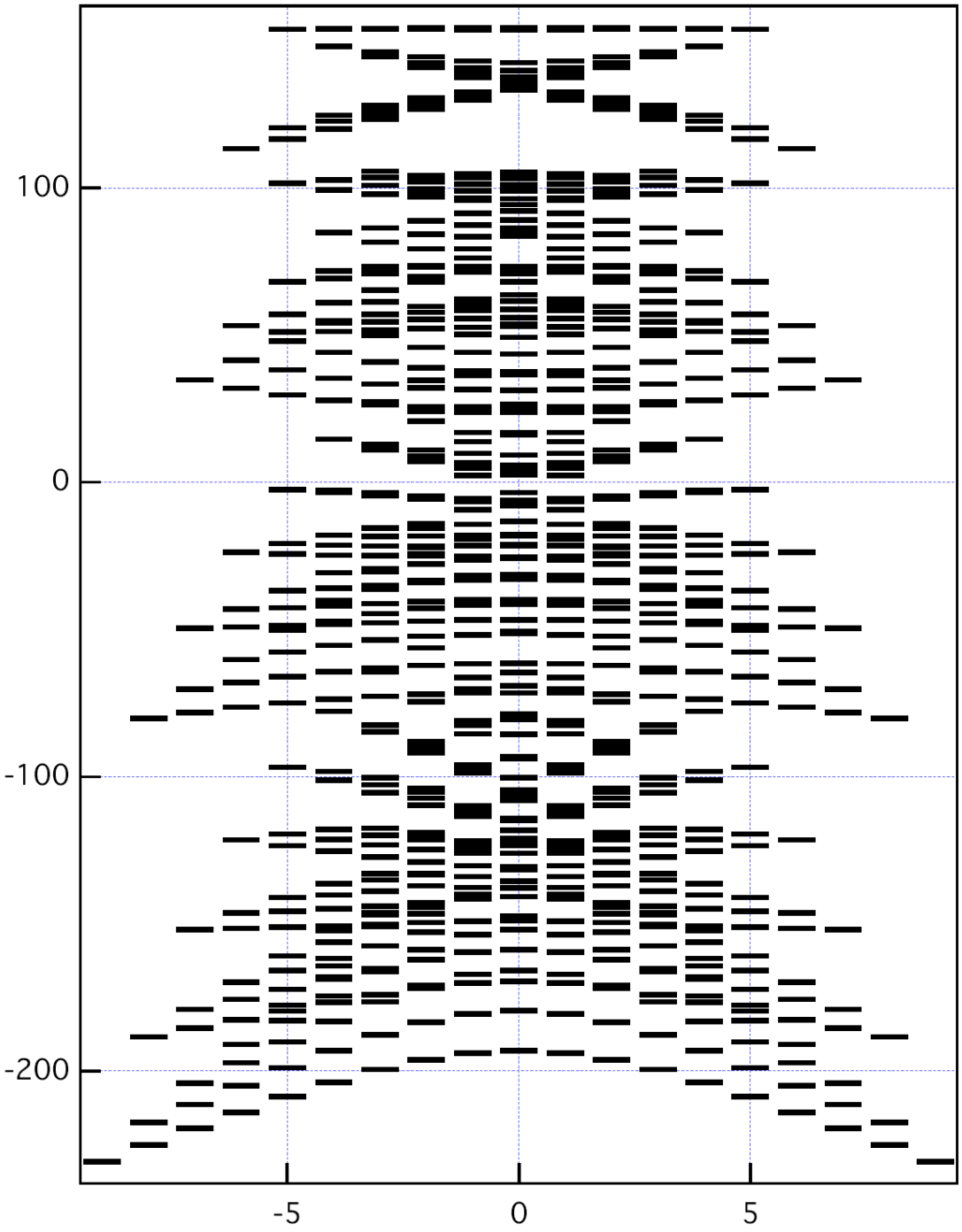

Figure 5.15. Plot of the eigen-energies versus m_s states for the S = 0 through S = 9 spin multiplets for **$[Mn_4(anca)_4(mdea)_2(Hmdea)_2]\cdot 2CHCl_3$ (4A).**

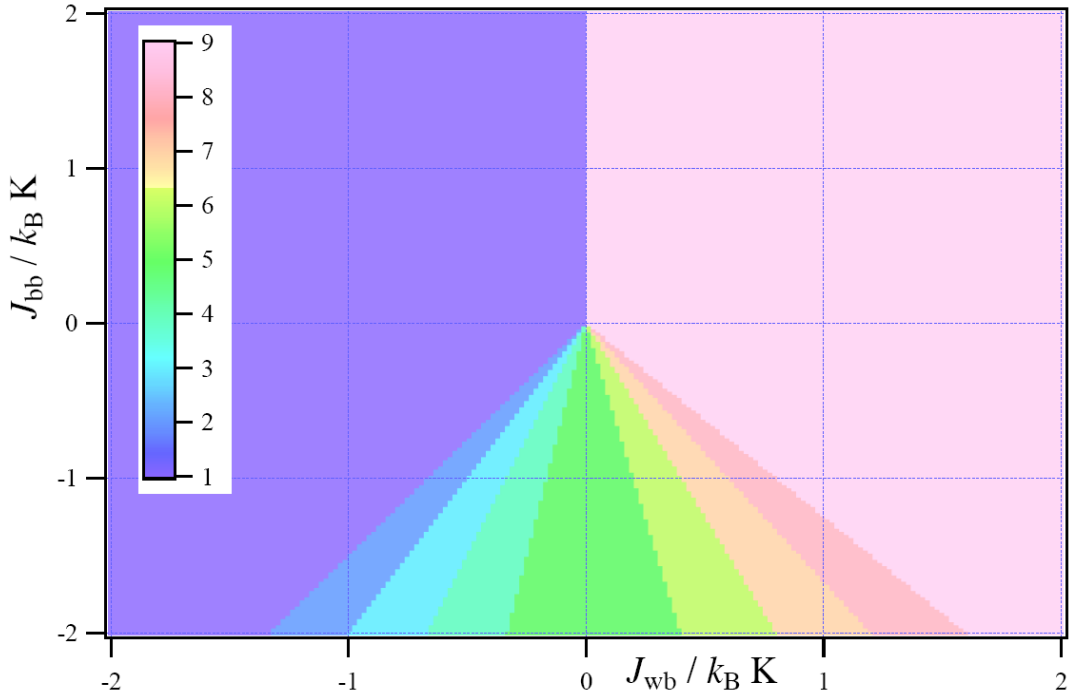

Figure 5.16. Plot of J_{bb} versus J_{wb} depicting the possible spin ground states for differing values of the exchange coupling constants for the spin arrangement presented in Scheme 5.1.

$$\hat{H} = \sum_i \sum_{j>i} J_{ij} \hat{s}_i \hat{s}_j + \sum_i \left[d_i \hat{s}_{zi}^2 + \mu_B \vec{B} \cdot \vec{\vec{g}}_i \cdot \hat{s}_i \right] \quad \textbf{(5.7)}$$

The eigen energies of the S = 0 through S = 9 possible spin multiplets are plotted in Figure 5.15 as energy in wavenumbers versus m_s. The lowest lying spin multiplet arises from S = 9, however, several spin multiplets (S = 8, S = 7 and S = 6 etc.) are nested with the S = 9 multiplet. Thus, the ground state is not well isolated and S and M_s may not be good magnetic quantum numbers. This is in good agreement with analysis of bulk magnetic susceptibility data in chapter 4, as well as, temperature dependent HFEPR data shown in Figure 5.13, that suggest the presence of low lying excited states. Though there is nesting of S-multiplets, there is no direct evidence for spin state mixing

Figure 5.16**,** plotted as J_{bb} versus J_{wb}, shows the possible spin ground states as a function of the magnitude and sign of the exchange coupling constants for the spin arrangement presented in Scheme 5.1. It was discussed in chapter 4 that reasonable fits of magnetic susceptibility data could be achieved with a positive or negative J_{wb} exchange coupling constant yielding spin states of S = 9 and S = 8, respectively. Figure 5.15 clearly shows that for negative values of J_{wb} with positive values of J_{bb} the system will have a S = 8 ground state, and with positive values of J_{wb} the S = 9 ground state predominates. This is in complete agreement with fits of variable temperature magnetic susceptibility data presented in Figure 4.19 for complexes **4B** and **4E**.

5.4 Conclusion

Oriented single-crystal magnetization hysteresis, oriented single-crystal HFEPR and full matrix diagonalization data were presented for two tetranuclear manganese complexes, **$[Mn_4(anca)_4(mdea)_2(Hmdea)_2]\cdot 2CHCl_3$ (4A)** and **$[Mn_4(anca)_4(edea)_2(Hedea)_2]$ (4B)**. The data confirm that these complexes exhibit slow magnetization dynamics and quantum tunneling of their magnetization and are SMMs. However, the preliminary data suggest that the electronic structure of these complexes is quite complex. Both complexes exhibit accessible low lying energy states as noted in Zeeman crossings in Figure 5.8, and peak splitting and asymmetry in temperature dependent EPR spectra. Complete analysis of these complexes will be published at a later date,

5.5 References

(1) Barra, A. L.; Debrunner, P.; Gatteschi, D.; Schulz, C. E.; Sessoli, R. *Europhysics Letters* **1996**, *35*, 133-138.

(2) Eppley, H. J.; Aubin, S. M. J.; Wemple, M. W.; Adams, D. M.; Tsai, H. L.; Grillo, V. A.; Castro, S. L.; Sun, Z. M.; Folting, K.; Huffman, J. C.; Hendrickson, D. N.; Christou, G. *Molecular Crystals and Liquid Crystals Science and Technology Section a-Molecular Crystals and Liquid Crystals* **1997**, *305*, 167-179.

(3) Sessoli, R.; Tsai, H. L.; Schake, A. R.; Wang, S. Y.; Vincent, J. B.; Folting, K.; Gatteschi, D.; Christou, G.; Hendrickson, D. N. *Journal of the American Chemical Society* **1993**, *115*, 1804-1816.

(4) Kambe, K. *Journal of the Physical Society of Japan* **1950**, *5*, 48.

(5) Bukalov, S. S.; Leites, L. A.; Lu, V.; Tilley, T. D. *Macromolecules* **2002**, *35*, 1757-1761.

(6) Cornia, A.; Fabretti, A. C.; Sessoli, R.; Sorace, L.; Gatteschi, D.; Barra, A. L.; Daiguebonne, C.; Roisnel, T. *Acta Crystallographica Section C-Crystal Structure Communications* **2002**, *58*, m371-m373.

(7) del Barco, E.; Kent, A. D.; Rumberger, E. M.; Hendrickson, D. N.; Christou, G. *Condensed Matter* **2002**, *cond-mat/0209167*.

(8) Hill, S.; Edwards, R. S.; North, J. M.; Park, K.; Dalal, N. S. *Polyhedron* **2003**, *22*, 1889-1896.

(9) Kadam, R. M.; Sastry, M. D.; Bhide, M. K.; Chavan, S. A.; Yakhmi, J. V.; Kahn, O. *Chemical Physics Letters* **1997**, *281*, 292-296.

(10) Lawrence, J.; Yang, E.-C.; Edwards, R.; Olmstead, M. M.; Ramsey, C.; Dalal, N. S.; Gantzel, P. K.; Hill, S.; Hendrickson, D. N. *Inorganic Chemistry* **2008**, *47*, 1965-1974.

(11) Long, S. M.; Zhou, P.; Miller, J. S.; Epstein, A. J. *Molecular Crystals and Liquid Crystals Science and Technology Section a-Molecular Crystals and Liquid Crystals* **1995**, *271*, A207-A215.

(12) Parks, B.; Loomis, J.; Rumberger, E.; Yang, E. C.; Hendrickson, D. N.; Christou, G. *Journal of Applied Physics* **2002**, *91*, 7170-7172.

(13) del Barco, E.; Kent, A. D.; Rumberger, E. M.; Hendrickson, D. N.; Christou, G. *Europhysics Letters* **2002**, *60*, 768-774.

(14) Loss, D.; Divincenzo, D. P.; Grinstein, G.; Awschalom, D. D.; Smyth, J. F. *Physica B* **1993**, *189*, 189-203.

(15) Wernsdorfer, W.; Sessoli, R. *Science* **1999**, *284*, 133-135.

(16) Kim, G. H. *Physical Review B* **2003**, *68*, -.

(17) Wernsdorfer, W.; Bhaduri, S.; Tiron, R.; Hendrickson, D. N.; Christou, G. *Physical Review Letters* **2002**, *89*, 197201.

(18) McInnes, E. J. L.; Mabbs, F. E.; Grant, C. M.; Milne, P. E. Y.; Winpenny, R. E. P. *Journal of the Chemical Society-Faraday Transactions* **1996**, *92*, 4251-4256.

(19) Petukhov, K.; Hill, S.; Chakov, N. E.; Abboud, K. A.; Christou, G. *Physical Review B* **2004**, *70*.

(20) Takahashi, S.; van Tol, J.; Beedle, C. C.; Hendrickson, D. N.; Brunel, L. C.; Sherwin, M. S. *Physical Review Letters* **2009**, *102*.

(21) Wernsdorfer, W. *Advances in Chemical Physics, Vol 118* **2001**, *118*, 99-190.

(22) Kent, A. D.; von Molnar, S.; Gider, S.; Awschalom, D. D. *Journal of Applied Physics* **1994**, *76*, 6656-6660.

(23) Monty, M.; Stephen, H.; Philippe, G.; Michel, G. *Review of Scientific Instruments* **2000**, *71*, 186-200.

(24) Wernsdorfer, W. *Superconductor Science & Technology* **2009**, *22*, 13.

25) Schenker, R.; Leuenberger, M. N.; Chaboussant, G.; Loss, D.; Gudel, H. U. *Physical Review B* **2005**, *72*.

(26) Bal, M.; Friedman, J. R.; Chen, W.; Tuominen, M. T.; Beedle, C. C.; Rumberger, E. M.; Hendrickson, D. N. *Epl* **2008**, *82*.

(27) Beedle, C. C.; Henderson, J. J.; Ho, P.-C.; Sayles, T.; Nakano, M.; O'Brien, J. R.; Heroux, K. J.; del Barco, E.; Maple, M. B.; Hendrickson, D. N. *Inorganic Chemistry* **2010**, *49*, 5780-5782.

(28) Wernsdorfer, W.; Allaga-Alcalde, N.; Hendrickson, D. N.; Christou, G. *Nature* **2002**, *416*, 406-409.

(29) Yang, E. C.; Wernsdorfer, W.; Hill, S.; Edwards, R. S.; Nakano, M.; Maccagnano, S.; Zakharov, L. N.; Rheingold, A. L.; Christou, G.; Hendrickson, D. N. *Polyhedron* **2003**, *22*, 1727-1733.

(30) Yang, E. C.; Wernsdorfer, W.; Zakharov, L. N.; Karaki, Y.; Yamaguchi, A.; Isidro, R. M.; Lu, G. D.; Wilson, S. A.; Rheingold, A. L.; Ishimoto, H.; Hendrickson, D. N. *Inorganic Chemistry* **2006**, *45*, 529-546.

(31) Ramsey, C. M.; Del Barco, E.; Hill, S.; Shah, S. J.; Beedle, C. C.; Hendrickson, D. N. *Nature Physics* **2008**, *4*, 277-281.

(32) Braun, H. B.; Loss, D. *Physical Review B* **1996**, *53*, 3237-3255.

(33) del Barco, E.; Kent, A. D.; Rumberger, E. M.; Hendrickson, D. N.; Christou, G. *Physical Review Letters* **2003**, *91*, 047203.

(34) Gatteschi, D. *Philosophical Transactions of the Royal Society of London Series a-Mathematical Physical and Engineering Sciences* **1999**, *357*, 3079-3097.

(35) Leuenberger, M. N.; Meier, F.; Loss, D. *Monatshefte Fur Chemie* **2003**, *134*, 217-233.

(36) Loss, D.; Goldbart, P. M. *Physical Review B* **1992**, *45*, 13544-13561.

(37) Wernsdorfer, W.; Soler, M.; Christou, G.; Hendrickson, D. N. *Journal of Applied Physics* **2002**, *91*, 7164-7166.

(38) Engel, H. A.; Recher, P.; Loss, D. *Solid State Communications* **2001**, *119*, 229-236.

(39) Gywat, O.; Burkard, G.; Loss, D. *Superlattices & Microstructures* **2002**, *31*, 127-140.

(40) Leuenberger, M. N.; Loss, D. *Physica E* **2001**, *10*, 452-457.

(41) Zhou, B.; Tao, R. B.; Shen, S. Q.; Liang, J. Q. *Physical Review A* **2002**, *66*, -.

(42) Tejada, J.; Chudnovsky, E. M.; del Barco, E.; Hernandez, J. M.; Spiller, T. P. *Nanotechnology* **2001**, *12*, 181-186.

(43) del Barco, E.; Kent, A. D.; Hill, S.; North, J. M.; Dalal, N.; Rumberger, E. M.; Hendrickson, D. N.; Chakov, N. E.; Christou, G. *Condensed Matter* **2004**, *cond-mat/0404390*.

(44) Krzystek, J.; Ozarowski, A.; Telser, J. *Coordination Chemistry Reviews* **2006**, *250*, 2308-2324.

(45) Roubeau, O.; Clérac, R. *European Journal of Inorganic Chemistry* **2008**, *2008*, 4325-4342.

Chapter 6

Ligand induced Spin-Tuning in Tetranuclear Manganese Dicubanes

6.1 Introduction

An ongoing goal of magnetochemists has been to develop molecules with large spin ground states (S) and appreciable magnetoanisotropy (D) to maximize the barrier toward the reversal of magnetization ($U = DS_z^2$) and enhance exhibited quantum effects.[1,2] The result is a myriad of high spin and high nuclearity complexes; however, controlling the spin of the ground state and the magnitude of the anisotropy barrier is very difficult and synthesis of large molecules enhances the difficulty in studying the electronic structure of polynuclear magnetic molecules and single-molecule magnets (SMMs). An inherent problem with large molecules is disorder in the ligand and solvate structure.[3-9] As the nuclearity of the complex increases, the number of coordinated ligands also increases leading to more molecular degrees of freedom. The magnitude of S results from maximizing ferromagnetic interactions within the molecular core. As nuclearity increases it becomes increasingly more difficult to mediate the nature of the magnetic exchange interactions and control the tensorial anisotropy projections of single ions. Often, competing magnetic exchange interactions and tilting of single-ion zero-field splitting projections leads to intermediate spin ground states and no appreciable increase in the anisotropy barrier. Recent work indicates that as the spin of the ground state increases, D decreases or remains unchanged. Experimental work on Mn_6 complexes indicates that U actually scales as S^1 not as S^2.[10] This will have a major impact on future designs for synthesizing and maximizing the physical properties of SMMs.

In the rush to larger and larger molecules with maximum spin, important fundamental studies have been somewhat overlooked that could pave the way to

producing SMMs with enhanced physical properties. It is very important to understand how environmental factors such as solvate disorder, nuclear hyperfine interactions phonon normal modes, dipolar exchange and anisotropy in magnetic exchange interactions affect the electronic structure and exhibited quantum dynamics.[3-9,11-18] Thus, chemists and physicists are turning to relatively simple low nuclearity systems. Fundamental advances in small systems can then be applied to large complicated systems.

As discussed in chapters 1, 3 and 5, manganese is well suited to fundamental studies. The d^4 Mn^{III} ions tend to undergo axial Jahn-Teller elongation as a result of crystal-field effects, and tensorial projections of Jahn-Teller distortions are usually easily detected through analysis of crystallographic data in conjunction with bond-valence sum analysis.[2,19-21] Manganese ions can also be found in a number of stable oxidation states (II, III and IV), and are fairly labile leading to ease of exchange of coordinated peripheral ligands. The preponderance of magnetic clusters and SMMs are manganese based, and include: $[Mn_2]$, $[Mn_3]$, $[Mn_4]$, $[Mn_6]$… $[Mn_{84}]$.[22-56] In many instances di-, tri- and tetranuclear manganese complexes have been employed as building-blocks for higher nuclearity systems.[22-24,27,57-59]

A definitive measure of whether a molecule exhibits quantum dynamics is the presence of evenly spaced steps in magnetization vs. field hysteresis loops. However, as the number of magnetic ions and subsequent spin increases, distributions of molecular environments and distributions of electronic excited states leads to averaging resulting in featureless hysteresis loops. The largest SMM to show steps in its hysteresis loops is a $S = 11$ $[Mn_{16}]$ wheel-shaped complex.[29] The appearance of

regularly spaced steps (tunneling resonances, *k*) in magnetization hysteresis loops, and which *k*-resonances should be resolved, is dictated by molecular and crystal symmetry. Where previous studies on SMMs reveal that sequential *k*-resonances are observed (*k* = 0, 1, 2…) regardless of symmetry, oriented single-crystal magnetization hysteresis and high-frequency electron paramagnetic resonance (HFEPR) based on [$Mn_3^{III}O$] triangles revealed quantum selection rules, for the first time.[4,60] Also, recent work by *Heroux et al.* employing betaine-carboxylate ligands on [Mn_4] SMMs conclusively showed that the addition of bulky alkyl substituents to coordinated ligands can actually lead to tighter crystal packing and increased intermolecular interactions. However, modulation of environmental factors through large bulky counter-ions led to greater molecular isolation and enhanced quantum dynamics.

In addition to fundamental studies on individual molecules, it is important to be able to study series of molecules that differ not only in their coordinated ligands and cocrystallized solvate molecules, but also employ topologies that can have their molecular anisotropy and ground state spin tuned. Only a few systems with nearly identical topologies have been studied with these attributes.[1,35,45,61,62] This chapter presents structural and magnetic data on a series of [Mn_4] dicubane structures that have the exact same topology as the high-spin complexes presented in chapters 4 and 5, however, manipulation of oxidation state arrangements yield antiferromanetically coupled low-spin molecules.

6.2 Experimental Section

6.2.1 Compound Preparation

All reactions were performed under aerobic conditions. The ligands 9-Anthracenecarboxylic acid (Hanca), dibenzoylmethane (Hdbm), triethylamine (Et_3N), triethanolamine (H_3tea), *N*-ethyldiethanolamine (H_2edea), *N*-butyldiethanolamine and *N-tert*-butyldiethanolamine were purchased from Sigma Aldrich and used without further purification. Microcrystalline $[Mn_4O_3(O_2CCH_3)_4(dbm)_3]$ was prepared by a previously reported method.[63]

$[Mn_4O_2(anca)_6(dbm)_2]\cdot 3CH_2Cl_2$ (6A). To a solution of $[Mn_4O_3(O_2CCH_3)_4(dbm)_3]$ (0.5g, 0.425 mmol) in CH_2Cl_2 (250 mL) was added solid Hanca (9.0g, 40.3 mmol). The brown-yellow solution was allowed to stir overnight. The unreacted carboxylate was subsequently removed by gravity filtration. The resulting solution was concentrated under vacuum until dry, yielding a brown microcrystalline powder $[Mn_4O_2(anca)_6(dbm)_2]\cdot 3CH_2Cl_2$ (complex **6A**). Analytically pure crystals were obtained by dissolving (0.5g, 0.246 mmol) of complex **6A** in CH_2Cl_2 (100 mL) with stirring. Gravity filtration was used to remove any undisolved product. The filtrate was then layered with diethyl ether which yielded red-brown crystals suitable for X-ray diffraction studies. Analysis of complex **6A,** C124 H84 Mn4 O18: calcd, C 71.15, H 3.78; expl, C 70.17, H 4.12. Yield 74% by manganese. Selected FT-IR Data (KBr, cm^{-1}): 3431(m,b), 3151(m,b), 1578(m), 1521(s), 1478(m), 1394(s), 1340(m), 1321(s), 1276(m), 1223(w), 1123(w), 1012(w), 727(m), 676(m), 620(m), 596(w), 501(w), 453(w).

$[Mn_4(anca)_4(Htea)_2(dbm)_2]\cdot 2MeCN$ (6B). Solid complex **6A** (0.25g, 0.124 mmol) was added to CH_2Cl_2 (30 mL) and allowed to stir until it completely dissolved. To the light brown solution was added H_3tea (0.11g, 0.740 mmol) dropwise and was

stirred for 5 minutes followed by the dropwise addition of Et_3N (0.075g, 0.740 mmol). The resulting red/brown solution was stirred for 10 minutes and then gravity filtered. The filtrate was concentrated under vacuum yielding a brown oil which was subsequently dissolved in MeCN (30 mL) and layered with diethyl ether (30 mL) yielding red/brown X-ray diffraction quality crystals after 45 days. Analysis of complex **6B**, C106 H90 Mn4 N4 O18: calcd, C 66.03, H 4.71, N 2.91; expl, C 66.75, H 5.02, N 3.15. Yield: 4% based on manganese. Selected FT-IR Data (KBr, cm^{-1}): 3434(m,b), 3052(w), 2923(w), 1567(s), 1524(s), 1479(m), 1440(m), 1391(m), 1348(m), 1320(s), 1277(m), 1227(w), 1068(m), 1025(m), 885(w), 864(w), 761(m), 734(m), 686(w), 648(w), 559(w), 418(w).

$[Mn_4(anca)_4(Htea)_2(dbm)_2]\cdot 2.5\ Et_2O$ (6C). Solid complex **6A** (0.25g, 0.124 mmol) was added to a solution of Et_3N (0.075g, 0.740 mmol) in methanol (30 mL) was allowed to stir for 30 minutes. H_3tea (0.11g, 0.740 mmol) was added to the resulting opaque, brown solution dropwise over 5 minutes. The solution was allowed to stir for 1 hour followed by gravity filtration to remove unreacted starting material. Layering of the filtrate with 50 mL of a 1:1 mixture of diethyl ether and hexanes produced red-brown analytically pure crystals (complex **6C**) suitable for X-ray diffraction studies after 30 days. Analysis of complex **6C,** C102 H84 Mn4 N2 O18: calcd, C 66.36, H 4.59, N 1.51; expl, C 66.64, H 4.21, N 1.69. Yield: 5% based on manganese. Selected FT-IR Data (KBr, cm^{-1}): 3418(m,b), 2923(s), 2825(m), 1574(s), 1524(s), 1479(m), 1440(m), 1384(s), 1348(m), 1320(s), 1277(w), 1068(m), 1025(w), 885(w), 761(w), 733(m), 686(w), 649(w), 559(w), 474(w,b), 421(w).

$[Mn_4(anca)_4(edea)_2(dbm)_2]\cdot CH_2Cl_2$ (6D). 0.5g (0.248 mmol) of solid $[Mn_4O_2(anca)_6(dbm)_2]\cdot 3CH_2Cl_2$ **(6A)** was added to 100mL CH_2Cl_2 with stirring, yielding a dark brown solution. After all solids were dissolved, 0.05mL (3.8 mmol) of H_3tea was added dropwise producing a red-brown solution that was allowed stir for one hour and then gravity filtered. The filtrate was then layered with hexanes, producing X-ray quality red-brown rectangular crystals after one week. Analysis of complex **6D,** C104 H88 Cl4 Mn4 N2 O16: calcd, C 67.55, H 4.67, N 1.54; expl, C 66.52, H 5.10, N 1.78. Yield: 30% based by manganese.

$[Mn_4(anca)_4(n\text{-}bdea)_2(dbm)_2]\cdot CH_3CN$ (6E). 0.25g (0.124 mmol) $[Mn_4O_2(anca)_6(dbm)_2]\cdot 3CH_2Cl_2$ (5) was added to 50mL dichloromethane (CH_2Cl_2) and allowed to stir for 30 minutes. To the resulting dark brown solution was added 0.1mL (0.661 mmol) H_2n-bdea dropwise, producing a deep red-brown solution. After stirring for one hour the solution was gravity filtered and reduced under vacuum to an oil. The oil was then dissolved in 20mL CH_3CN, yielding diffraction quality brown rectangular crystals after one week. Analysis of complex **6E,** C110 H98 Mn4 N2 O16: calcd, C 68.10, H 4.96, N 1.50; expl, C 67.87, H 5.00, N 1.84. Yield: 67% based by manganese.

$[Mn_4(anca)_4(t\text{-}bdea)_2(dbm)_2]\cdot Et_2O\cdot CH_3OH$ (6F). 0.25g (0.124 mmol) $[Mn_4O_2(anca)_6(dbm)_2]\cdot 3CH_2Cl_2$ **(6A)** and 0.16g (0.988 mmol) H_2t-bdea were added to 50mL MeOH with stirring. The resulting dark brown solution was allowed to stir overnight, yielding a dark red-brown solution. Following gravity filtration, diethylether diffusions were set up. Diffraction quality brown rectangular crystals were collected after two weeks. Analysis of complex **6F,** C116 H120 Mn4 N2 O16: calcd, C 67.48, H 5.41, N 1.42; expl, C 66.41, H 5.55, N 1.41. Yield: 45% based by manganese.

Table 6.1. Crystallographic data for complexes **6A.**

	6A
formula	$C_{124}\ H_{84}\ Mn_4\ O_{18}$
formula weight	2365.27
temp [K]	100(2)
wavelength [Å]	0.71073
crystal system	monoclinic
space group	C2/c
a [Å]	24.327(2)
b [Å]	16.9650(16)
c [Å]	25.508(2)
α [deg]	90
β [deg]	93.214(2)
γ [deg]	90
V [Å^3]	10510.9(17)
Z, Z′	4, 0.5
cryst color, habit	brown, plate
D_{calc} (mg m^{-3})	1.495
abs. coefficient	0.745[mm^{-1}]
F(000)	4832
theta range	1.46 to 24.00°
reflns measured	34419
reflns independent	8236 [R(int) = 0.0731]
comp. to theta [25.00°]	100.0 %
abs. correction	Semi-empirical from equivalents
Refinement method	Full-matrix least-squares on F^2
Data / restraints / param.	8236 / 0 / 641
Goodness-of-fit on F2	1.391
$R(F)$,[a] $R(\omega F^2)$[b]	R1 = 0.0774
($I > 2\sigma(I)$)	R1 = 0.0970
Largest diff. peak / hole	0.546 and -0.869 e.Å^{-3}

[a] $R = \Sigma||F_o| - |F_c||/\Sigma|F_o|$. [b] $R(\omega F^2) = \{\Sigma[\omega(F_o^2 - F_c^2)^2]/\Sigma[\omega(F_o^2)^2]\}^{1/2}$; $\omega = 1/[\sigma^2(F_o^2) + (aP)^2 + bP]$, $P = [2F_c^2 + \max(F_o, 0)]/3$.

Table 6.2. Crystallographic data for complexes **6B, 6C.**

	6B	**6C**
formula	C106 H90 Mn4 N4 O18	C102 H84 Mn4 N2 O18
formula weight	2081.74	1845.47
temp [K]	100(2)	100(2)
wavelength [Å]	0.71073	0.71073
crystal system	monoclinic	Triclinic
space group	P 21/c	P-1
a [Å]	11.8765(18)	12.8242(17)
b [Å]	25.025(4)	13.2663(17)
c [Å]	15.824(2)	14.3325(19)
α [deg]	90	80.355(2)
β [deg]	93.165(2)	82.983(2)
γ [deg]	90	85.730(2)
V [Å^3]	4695.8(12)	2382.3(5)
Z, Z′	2, 0.5	1, 0.5
cryst color, habit	brown/red, plate	red, plate
D_{calc} (mg m^{-3})	1.421	1.286
abs. coefficient [mm^{-1}]	0.601	0.585
F(000)	2084	954
cryst size [mm]	0.40 x 0.35 x 0.20	0.30 x 0.20 x 0.08
theta range	2.99 to 25.03°	1.45 to 27.54°
index range	-14<=h<=14, -29<=k<=29, -18<=l<=18	-16<=h<=16, -17<=k<=17, -18<=l<=18
reflns measured	33881	20310
reflns independent	8257 [R(int) = 0.0893]	10365 [R(int) = 0.0313]
comp. to theta [25.00°]	99.7 %	94.2 %
abs. correction	Semi-empirical from equivalents	
Max. / min. trans.	0.8893 and 0.7951	0.9547 and 0.8441
Refinement method	Full-matrix least-squares on F^2	
Data / restraints / param.	8257 / 0 / 634	10365 / 0 / 572
Goodness-of-fit on F2	1.152	1.003
$R(F)$,[a] $R(\omega F^2)$[b]	0.0463	0.0522
($I > 2\sigma(I)$)	0.0517	0.0883
Largest diff. peak / hole	0.575 and -0.705 e. Å^{-3}	0.667 and -0.403 e.Å^{-3}

[a] $R = \Sigma||F_o| - |F_c||/\Sigma|F_o|$. [b] $R(\omega F^2) = \{\Sigma[\omega(F_o^2 - F_c^2)^2]/\Sigma[\omega(F_o^2)^2]\}^{1/2}$;
$\Omega = 1/[\sigma^2(F_o^2) + (aP)^2 + bP]$, $P = [2F_c^2 + \max(F_o, 0)]/3$.

Table 6.3. Crystallographic data for complexes **6D-F.**

	6D	**6E**	**6F**
formula	C104 H88 Cl4 Mn4 N2 O16	C110 H98 Mn4 N4 O16	C116 H120 Mn4 N2 O16
formula weight	1983.32	975.84	2081.90
temp [K]	100(2)	100(2)	100(2)
wavelength [Å]	0.71073	0.71073	0.71073
crystal system	triclinic	Triclinic	triclinic
space group	P-1	P-1	P-1
a [Å]	11.8589(6)	13.0279(15)	12.8887(18)
b [Å]	13.8016(7)	14.1902(17)	13.5792(19)
c [Å]	14.8812(8)	15.6696(18)	14.322(2)
α [deg]	68.2970(10)	65.795(2)	85.660(2)
β [deg]	84.7060(10)	67.912(2)	80.991(2)
γ [deg]	89.2740(10)	81.029(2)	87.968(2)
V [Å^3]	2252.7(2)	2448.2(5)	2467.9(6)
Z, Z′	1, 0.5	1, 0.5	1, 0.5
cryst color, habit	brown, plate	brown/red, plate	red, plate
D_{calc} (mg m^{-3})	1.462	1.324	1.401
abs. coefficient	0.737 [mm^{-1}]	0.572	0.574
F(000)	1022	1014	1090
theta range	1.48 to 27.52°.	1.69 to 28.17°	1.44 to 27.54°
reflns measured	19045	18731	18590
reflns independent	9736 [R(int) = 0.0167]	11036 [R(int) = 0.0270]	10468 [R(int) = 0.0432]
comp. to theta [25.00°]	93.9 %	91.7 %	97.4 %
abs. correction	Semi-empirical from equivalents		
Refinement method	Full-matrix least-squares on F^2		
Data / restraints / param.	9736 / 0 / 754	11036 / 0 / 605	10468 / 0 / 643
Goodness-of-fit on F2	1.056	1.030	1.011
$R(F)$,[a] $R(\omega F^2)$[b]	R1 = 0.0455	R1 = 0.0527	R1 = 0.0636
($I > 2\sigma(I)$)	R1 = 0.0501	R1 = 0.0705	R1 = 0.1066
Largest diff. peak / hole	1.408 and -1.830 e.Å^{-3}	1.565 and -0.532 e Å^{-3}	0.977 and -0.853 e.Å^{-3}

[a] $R = \Sigma||F_o| - |F_c||/\Sigma|F_o|$. [b] $R(\omega F^2) = \{\Sigma[\omega(F_o^2 - F_c^2)^2]/\Sigma[\omega(F_o^2)^2]\}^{1/2}$;
$\omega = 1/[\sigma^2(F_o^2) + (aP)^2 + bP]$, $P = [2F_c^2 + \max(F_o, 0)]/3$.

Table 6.4. Selected Interatomic Distances [Å] for complex **6A**.

Mn(1)-O(1)	1.899(3)	Mn(2)-Mn(2)#1	2.8612(15)
Mn(1)-O(3)	1.901(3)	O(1)-Mn(2)#1	1.890(3)
Mn(1)-O(2)	1.920(3)	O(2)-C(3)	1.274(6)
Mn(1)-O(6)	1.968(3)	O(3)-C(1)	1.277(7)
Mn(1)-O(4)	2.136(4)	O(4)-C(16)	1.234(6)
Mn(1)-O(9)#1	2.157(3)	O(5)-C(16)	1.291(6)
Mn(2)-O(1)	1.863(3)	O(6)-C(31)	1.275(6)
Mn(2)-O(1)#1	1.890(3)	O(7)-C(31)	1.252(6)
Mn(2)-O(8)	1.934(3)	O(8)-C(46)	1.295(6)
Mn(2)-O(5)	1.952(3)	O(9)-C(46)	1.232(6)
Mn(2)-O(7)	2.114(3)	O(9)-Mn(1)#1	2.157(3)

Table 6.5. Selected Bond Angles [°] for complexe **6A**.

O(1)-Mn(1)-O(3)	178.03(16)	O(1)#1-Mn(2)-O(8)	96.83(15)
O(1)-Mn(1)-O(2)	87.42(14)	O(1)-Mn(2)-O(5)	96.81(15)
O(3)-Mn(1)-O(2)	91.06(15)	O(1)#1-Mn(2)-O(5)	159.43(15)
O(1)-Mn(1)-O(6)	95.78(14)	O(8)-Mn(2)-O(5)	84.50(15)
O(3)-Mn(1)-O(6)	85.82(15)	O(1)-Mn(2)-O(7)	94.33(14)
O(2)-Mn(1)-O(6)	174.72(15)	O(1)#1-Mn(2)-O(7)	108.51(14)
O(1)-Mn(1)-O(4)	92.41(14)	O(8)-Mn(2)-O(7)	89.41(14)
O(3)-Mn(1)-O(4)	88.84(15)	O(5)-Mn(2)-O(7)	92.01(14)
O(2)-Mn(1)-O(4)	89.61(14)	O(1)-Mn(2)-Mn(2)#1	40.68(10)
O(6)-Mn(1)-O(4)	86.07(14)	O(1)#1-Mn(2)-Mn(2)#1	39.97(10)
O(1)-Mn(1)-O(9)#1	90.87(14)	O(8)-Mn(2)-Mn(2)#1	136.80(12)
O(3)-Mn(1)-O(9)#1	87.91(15)	O(5)-Mn(2)-Mn(2)#1	134.71(11)
O(2)-Mn(1)-O(9)#1	91.52(14)	O(7)-Mn(2)-Mn(2)#1	103.66(10)
O(6)-Mn(1)-O(9)#1	92.63(14)	Mn(2)-O(1)-Mn(2)#1	99.35(15)
O(4)-Mn(1)-O(9)#1	176.57(14)	Mn(2)-O(1)-Mn(1)	122.18(18)
O(1)-Mn(2)-O(1)#1	80.61(15)	Mn(2)#1-O(1)-Mn(1)	127.00(18)
O(1)-Mn(2)-O(8)	175.99(15)		

6.2.2 X-ray Crystallography

Diffraction intensity data were collected for **6A and 6D-F** at -173 °C with a Bruker Smart Apex CCD diffractometer, integrated using Bruker SAINT software program, and corrected for absorption using the Bruker SADABS program. Crystal data, data collection, and refinement parameters were solved by direct methods (SHELXS-97), developed by successive difference Fourier syntheses, and refined by full matrix least squares on all F^2 data. All non-hydrogen atoms were refined as being anisotropic and hydrogen atoms were placed in calculated positions with temperature factors fixed at 1.2 or 1.5 times the equivalent isotropic U of the C atoms to which they were bonded. Unresolved solvent was accounted for by using the PLATON program SQUEEZE which found 654 electrons/unit cell or 4 molecules of methylene chloride (42 electrons/molecule) per molecular unit. Solvent electron density included in the molecular formula as 4 (CH_2Cl_2).

Complex **6B** was solved by direct methods (SHELXS-97) while complex **6C** was solved by a Patterson method. Both were developed by successive difference Fourier syntheses and refined by full matrix least squares on all F^2 data. All non-hydrogen atoms were refined anisotropically by full-matrix least-squares (SHELXL-97). In complex **6B**, the aminohydroxyl oxygen O9 is disordered equally over two different positions (O9 and O9a). The hydrogen atom associated with the aminohydroxyl oxygen was allowed to refine. Also, two molecules of acetonitrile co-crystallized with complex **6B**.

In complex **6C**, electron density associated with a hydrogen atom H9B attached

to oxygen O9 (distance 1.288 Å) was allowed to refine. Unresolved solvent accounted for by using the PLATON program SQUEEZE which found 106 electrons or 2.5 molecules of diethyl ether (42 electrons/molecule). Solvent electron density included in the molecular formula as 2.5 (C4 H10 O). All other hydrogen atoms in complexes **6B-6F** were placed using a riding model and their positions constrained relative to their parent atom using the appropriate HFIX command in SHELXL-97.

6.2.3 Physical Methods

FT-IR spectra were collected using a Thermo-Nicolet Avatar series spectrometer. Elemental analyses were performed by NuMega Resonance Labs (San Diego, CA) for Complexes **6A-6F**. The DC magnetic susceptibility data were collected on a Quantum Design MPMS-2 magnetometer with a 5.5 Tesla magnet. Microcrystalline samples were restrained with eicosane to prevent torquing. Diamagnetic corrections of magnetic susceptibility data were made employing Pascal's constants.

6.3 Results and Discussion

6.3.1 Synthesis

A number of synthetic strategies have been used in creating polyoxometallate complexes with interesting topologies. This has included starting with simple Mn^{II} and Mn^{III} salts of halides, carboxylates and perchlorates, as well as base starting materials such as homo-valent and mixed-valent " triangle" [Mn_3O] and " butterfly" [Mn_4O_2] clusters, in the presence of chelating ligands such as derivatives of hydroxymethylpyridine (Hhmp), diethanolamines (H_2Rdea, R = alkyl substituent) and

triethanolamine (H_3tea). The procedure of using simple metal salts usually requires the use of oxidizing agents such as tetrabutylammonium permanganate or potassium permanganate to achieve mixed-valent complexes; however, the ability to control the ratio of metal oxidation states, in attempting achieve desired products, is to a great extent serendipitous. In this study a $[Mn^{III}O_2]^{8+}$ "butterfly" complex (**6A**) was reacted with a 1:1 molar ratio of Et_3N and the tetradentate ligand H_3tea yielding the solvent dependent, mixed-valent wheels, complexes **6B** and **6C**. In the absence of a base to deprotonate the H_3tea ligand, reaction conditions favored formation of the mono-nuclear species $[Mn(dbm)_3]$. Conversely, if an excess of base is used, no product was obtained. Solubility issues with complex **6A** precluded the use of many solvent systems, and the acidity of H_3tea required the use of deprotonating agents. Even in optimum conditions for the solvents used in this study, yields for complexes **6B and 6C** were still very low. However, yields for complexes **6D-6F** were reasonably high lending yielding higher solubility of the R-diethanolamine ligands.

6.3.2 Description of Structures

Crystallographic data for complexes **6A-C** are listed in Tables 6.1 and 6.2, respectively**.** Crystallographic data for complexes **6D-F** are listed in Table 6.3**.** Complexes **6B** and **6C** are interesting in that they exhibit a pseudo wheel topology with only four Mn atoms, making them the smallest manganese based wheel-shaped complex to date.

$[Mn_4O_2(anca)_6(dbm)_2]\cdot 3CH_2Cl_2$ (6A). Selected bond distances and bond angles for complex **6A** are presented Tables 6.4 and 6.5, respectively. Figure 6.1 shows

an ORTEP of $[Mn_4O_2(anca)_6(dbm)_2]\cdot 3CH_2Cl_2$ (**6A**) which crystallizes in the monoclinic C2/c space group. The asymmetric unit contains one-half of the target molecule with the other half generated by the -x, y, -z+1/2 symmetry transformations. The molecule consists of four manganese atoms bridged by two μ_3-oxide atoms, six $anca^-$ ligands, and is capped by two dbm^- ligands. The core of the complex contains a $[Mn^{III}_4(\mu_3\text{-}O)_2]^{8+}$ rhombus which is comprised of two 5-coordinate, distorted square pyramidal Mn^{III} atoms (body position) and two 6-coordinate, near-octahedral Mn^{III} atoms (wing position).

The valency of each Mn atom was determined by the presence of Jahn-Teller distortion along the O(4)-Mn(1)-O(9) axis of the octahedral Mn^{III} atoms (wing positions) and the apical bond length (Mn(2)-O(7)) of the square pyramidal Mn^{III} atoms (body positions). The Jahn-Teller axis of the wing Mn^{III} atom is nearly coplanar with the Mn_4 core and perpendicular to the plane of the dbm^- ligand. Conversely, the elongated axis of the body Mn^{III} atom is orthogonal to the plane of the Mn_4 core atoms. Furthermore, four of the bridging carboxylates are also coplanar with the rhombus core, while the remaining two are perpendicular to the Mn_4 plane. Essentially, all six of the $anca^-$ ligands occupy the same face of the Mn_4 core which causes the molecule to adopt the "butterfly" topology.

Other known Mn_4 butterfly structures include $[Mn_4O_2(O_2CPh)_6(py)(dbm)_2]$ and $[Mn_4O_2(O_2CEt)_6(NO_3)(bpy)_2](ClO_4)$ whose cores are compared to that of complex **6A** in Figure 6.2. As observed in complex **6A**, these two butterflies also have all six μ-O_2CR groups occupying one face of the non-planar Mn_4 core. All of the Mn atoms are in the +3 oxidation state and exhibit significant Jahn-Teller distortion analogous to the

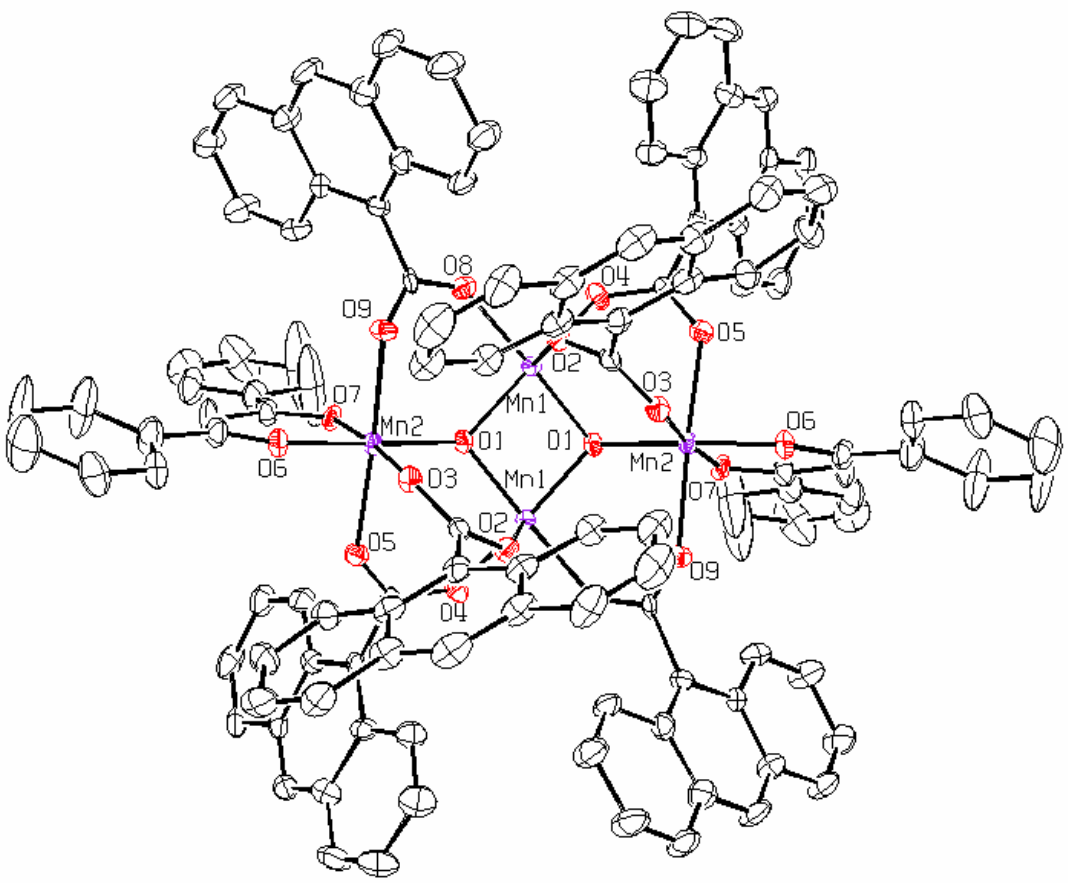

Figure 6.1. ORTEP of The $[Mn_4O_2(anca)_6(dbm)_2]\cdot 3CH_2Cl_2$ **(6A)** with thermal ellipsoids at 50%. Hydrogen atoms and solvate molecules have been removed for clarity.

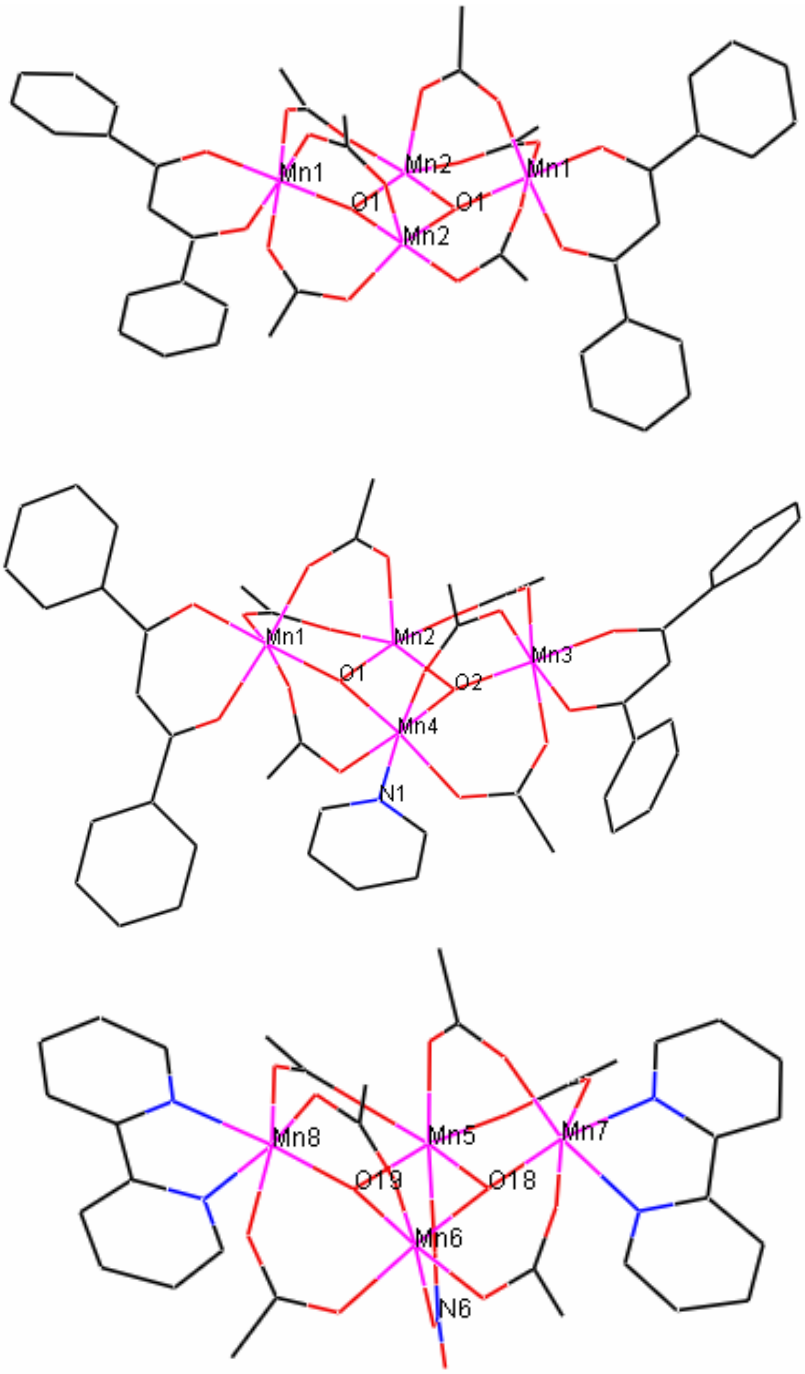

Figure 6.2. Comparison of Mn_4 cores of complex **$[Mn_4O_2(anca)_6(dbm)_2]\cdot 3CH_2Cl_2$ (6A)** (top), $[Mn_4O_2(O_2CPh)_6(py)(dbm)_2]$ (middle), and $[Mn_4O_2(O_2CEt)_6(NO_3)(bpy)_2](ClO_4)$ (bottom). Anthracene, benzoate, and ethyl groups omitted for clarity.

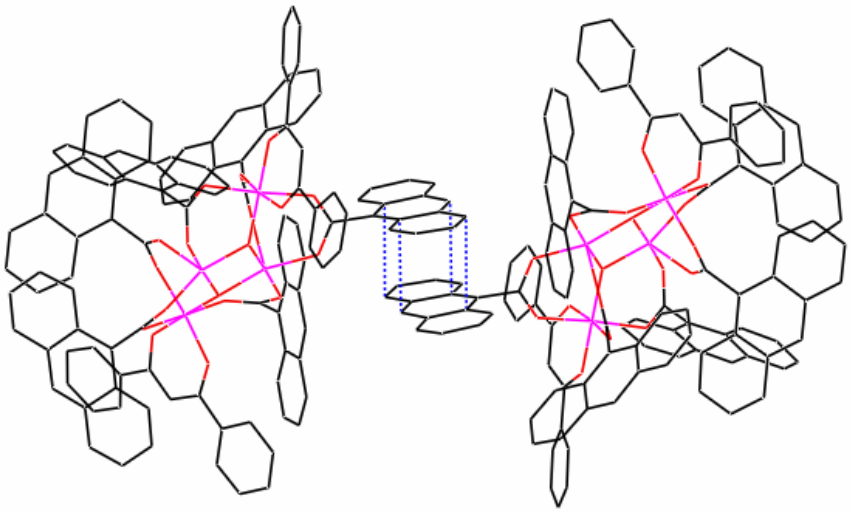

Figure 6.3. π–π stacking in complex **$[Mn_4O_2(anca)_6(dbm)_2]\cdot 3CH_2Cl_2$ (6A).**

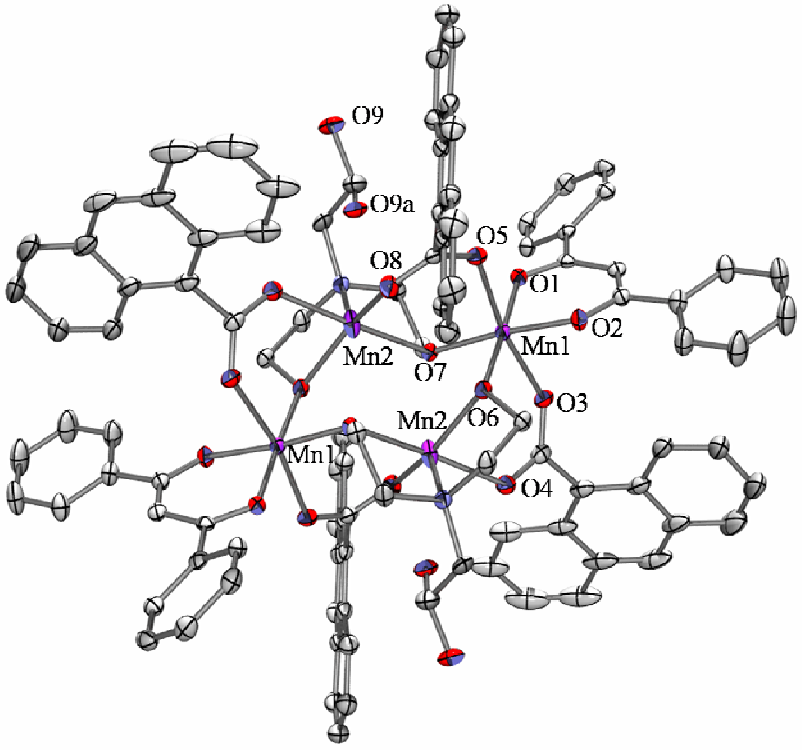

Figure 6.4. ORTEP of The **$[Mn_4(anca)_4(Htea)_2(dbm)_2]\cdot 2MeCN$ (6B)** with thermal ellipsoids at 50%. Hydrogen atoms and solvate molecules have been removed for clarity.

Table 6.6. Selected Interatomic Distances [Å] for (**6B**) and (**6C**). (Jahn-Teller axes and through-wheel Mn-O distances highlighted)

	Complex**6B**	Complex **6C**
Mn(1)-O(1)	1.9223(18)	1.9375(19)
Mn(1)-O(2)	1.9359(18)	1.9226(19)
Mn(1)-O(3)	2.2568(19)	2.1591(18)
Mn(1)-O(5)	2.2063(19)	2.2255(18)
Mn(1)-O(6)	1.8688(19)	1.8742(18)
Mn(1)-O(7)	1.9492(17)	1.9228(18)
Mn(2)-O(4)	2.1243(19)	2.1104(18)
Mn(2)-O(6)	2.1972(18)	2.1659(17)
Mn(2)-O(7)#1	2.1820(18)	2.2030(18)
Mn(2)-O(8)	2.1281(19)	2.1852(18)
Mn(2)-O(9)	-----	2.474(3)
Mn(2)-N(1)	2.366(2)	2.389(3)
Mn(2)-O(7)	~2.455	~2.703

Table 6.7. Selected Bond Angles [°] for complexes **6B** and **6C.**

	Complex **6B**	Complex **6C**
O(7)-Mn(1)-O(6)	83.22(7)	84.24(8)
O6-Mn(2)-O(7)#1	93.65(7)	92.91(6)
Mn(1)-O(6)-Mn(2)	104.57(8)	110.01(8)
Mn(1)-O(7)-Mn(2)	120.32(8)	122.00(8)
Mn(2)-O(7)-Mn(2)#1	~94.95	~97.24

elongation axes found in complex **6A**. However, in the previously reported butterflies, both the wing Mn atoms and one of the body Mn atoms have 6-coordinate, near-octahedral geometry whereas the fourth Mn atom is only 5-coordinate. The Jahn-Teller axes of these pseudo-square pyramidal metal centers is therefore observed in the apical bond between Mn and the pyridine ligand or the nitrate ion in either case.[64,65] Complex **6A** is different geometrically in that both of the Mn atoms occupying the body positions are 5-coordinate and possess Jahn-Teller distortion along their apical Mn-O bond.

In the crystal packing diagram of complex **6A**, an appreciable amount of π–π interactions between the anthracene rings of adjacent molecules is shown (Figure 6.3). The perfectly eclipsed anthracene rings have an interplanar distance of ~3.38 Å which is comparable to the interlayer C-C distance of ~3.35 Å found in graphite. Also, the curved shape of the molecule leaves a solvent accessible void in which the disordered dichloromethane solvate molecules are also involved in some hydrogen-bonding interactions.

$[Mn_4(anca)_4(Htea)_2(dbm)_2]$•2MeCN (6B). Selected bond distances for complexes **6B** and **6C** are given in Table 6.6 and the wheel bond angles are given in Table 6.7. Complex **6B** crystallizes in the monoclinic $P2_1/c$ space group as shown in the ORTEP representation in Figure 6.4. The structure is made up of a Mn_4O_4 core which lies on a 2-fold symmetry axis. Consequently, the asymmetric unit contains half of the molecule while the symmetry-equivalent atoms are generated by the –x, y+1, -z transformations. The unit cell also consists of two molecules of acetonitrile cocrystallized with the complex.

Interestingly, one of the ethanol arms of the triethanolamine ligand is not coordinated to a Mn atom. This aminohydroxyl oxygen O(9) is equally disordered over two different positions due to the free rotation of the bonds in space. The disorder is represented in the ORTEP by the oxygen atoms O(9) and O(9a) where there is 50% probability of finding that oxygen at either position at any given time. The proton associated with this oxygen is therefore also disordered over these two positions which results in numerous hydrogen-bonding pathways between neighboring molecules.

The Mn_4 core (Figure 6.5) consists of two 6-coordinate Mn^{III} atoms in the wing positions and two 5-coordinate Mn^{II} atoms in the body positions, all of which are nearly coplanar. Each Mn^{II} atom is bound to a Mn^{III} atom through a μ_2-alkoxide group from the deprotonated triethanolamine ligand and a bridging $anca^-$ ligand. The structure is capped by two dbm^- ligands, filling the remaining two coordination sites of the Mn^{III} atoms. The valency of the Mn atoms was confirmed by the presence of Jahn-Teller distortion around the Mn(1) atom. The Mn(1)-O(3) and Mn(1)-O(5) bonds (2.2568(19) Å and 2.2063(19) Å respectively) are significantly longer than the Mn(1)-O bonds making up the square planar portion of the distorted octahedron (1.87-1.95Å). The Jahn-Teller axes are oriented orthogonal to the plane of the dbm^- ligands which deviate slightly from planarity. Mn(2) is a distorted square pyramid with N(1) of the triethanolamine ligand being the apex of the pyramid.

The crystallographic data for complex **6B** strongly suggests that the molecule is a Mn_4 wheel as opposed to the more commonly encountered pseudo-dicubane structure. The Mn(2)-O(7) (body-body interaction) distance is 2.4554(18) Å which is greater than the sum of the ionic radii of a 4-coordinate O^{2-} ion and a high-spin 6-coordinate Mn^{2+}

ion (~2.2 Å).[66] Furthermore, the Mn(2)-O(7) bond is about 0.2-0.6 Å longer than the equivalent bond in previously reported mixed-valence Mn_4 dicubane complexes. The recently reported $[Mn_4(H_2L)_2(HL)_2(H_2O)_x(RCO_2)_2]^{2+}$ clusters (where L = triethanolamine and R = Me, x = 2; R = Et, x = 0; and R = Ph, x = 0) by Murray *et al.*[67] have similar topology to complex **6B** in that they form a pseudo-dicubane Mn_4 core with one of the ethanol arms of the triethanolamine uncoordinated. In these structures, the bond in question has lengths of 2.201(1) Å for Me, 2.269(3) Å for Et, and 2.255(4) Å for Ph.[66] The through-wheel, or body-body pathway, distances of several known dicubanes are compared with complexes **6B** and **6C** as summarized in Table 6.8.[56,67-70] the Mn-O distances for complexes **6B-C** are significantly longer than distances reported for other complexes and are most likely the result of torsion in induced by the triethanolamine ligands.

Complex **6B** exhibits both intra- and intermolecular hydrogen-bonding (Figure 6.6). The protonated aminohydroxyl oxygen (O(9)) is involved in intramolecular hydrogen-bonding with one of the oxygen atoms on each of the neighboring dbm^- ligands (~2.7-2.8 Å). Expansion of the contacts from O(9a) leads to one-dimensional chains down the a-axis of the unit cell due to intermolecular hydrogen-bonding between protonated ethanol arms of adjacent molecules (~2.4-2.9 Å). This hydrogen-bonding network provides multiple exchange pathways between the molecules due to the aforementioned dual occupancy of the protonated ethanol arm. The Mn_4 core bond angles compare closely with that of previously reported dicubanes except for the Mn(2)-O(7)-Mn(2)#1 angle of 94.95° which is slightly smaller than the typically observed body-body angle of 97-100°.

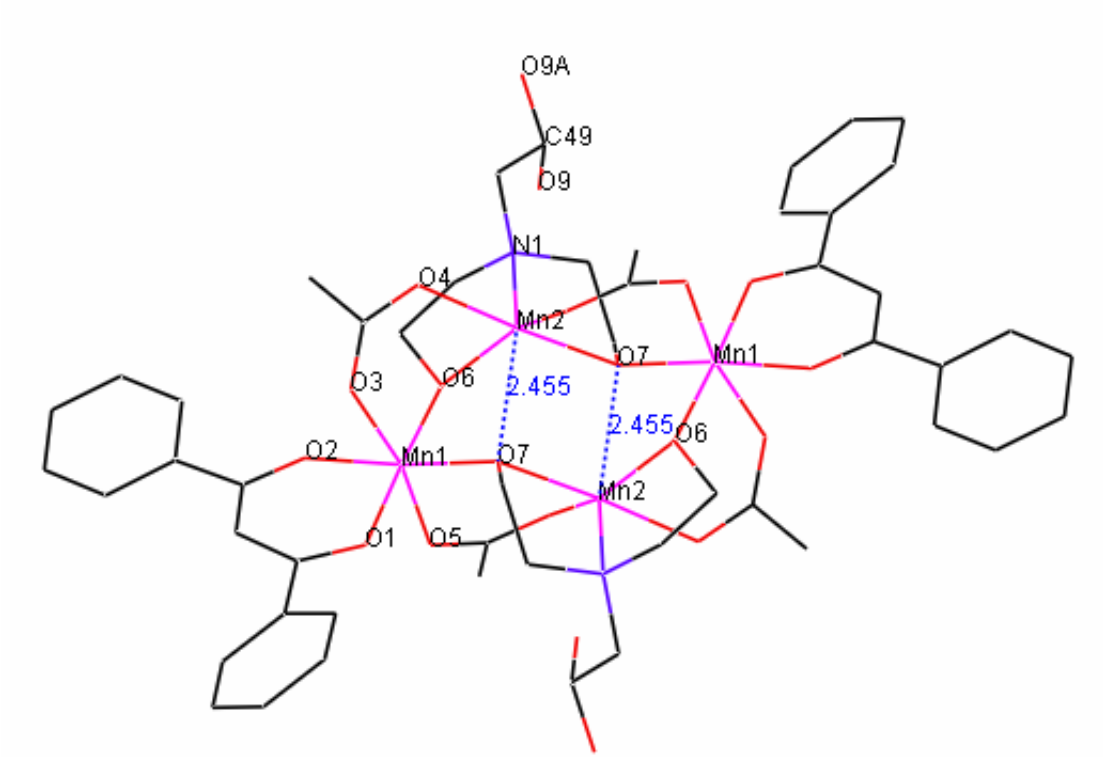

Figure 6.5. Mn_4 core of complex **6B** (anthracene rings omitted for clarity).

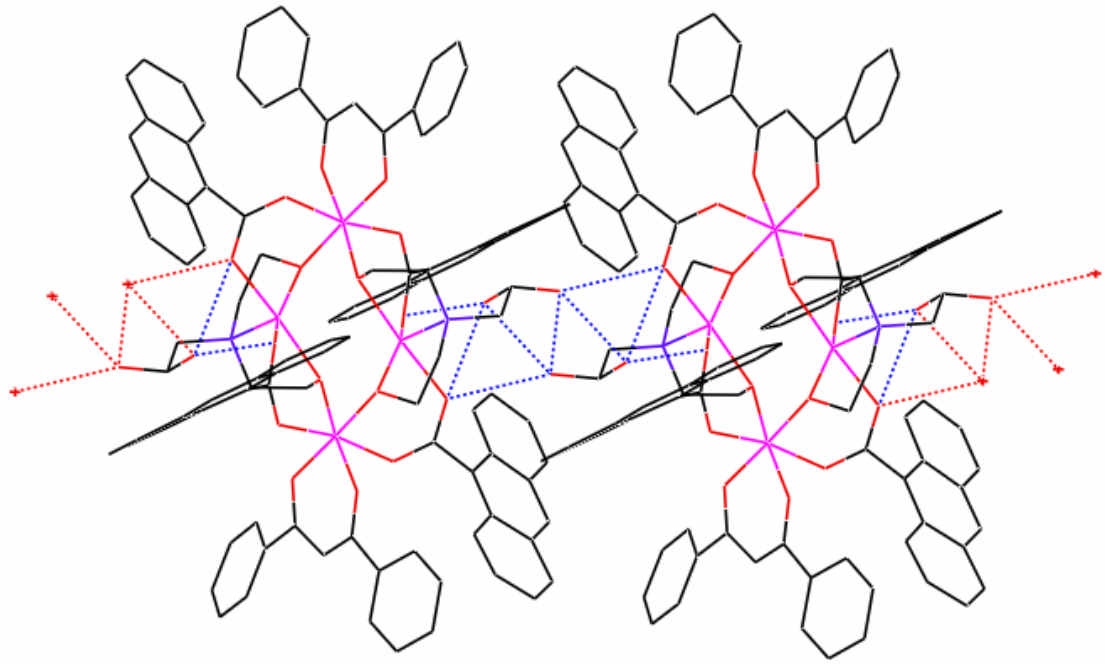

Figure 6.6. Hydrogen bonding network in complex **6B**.

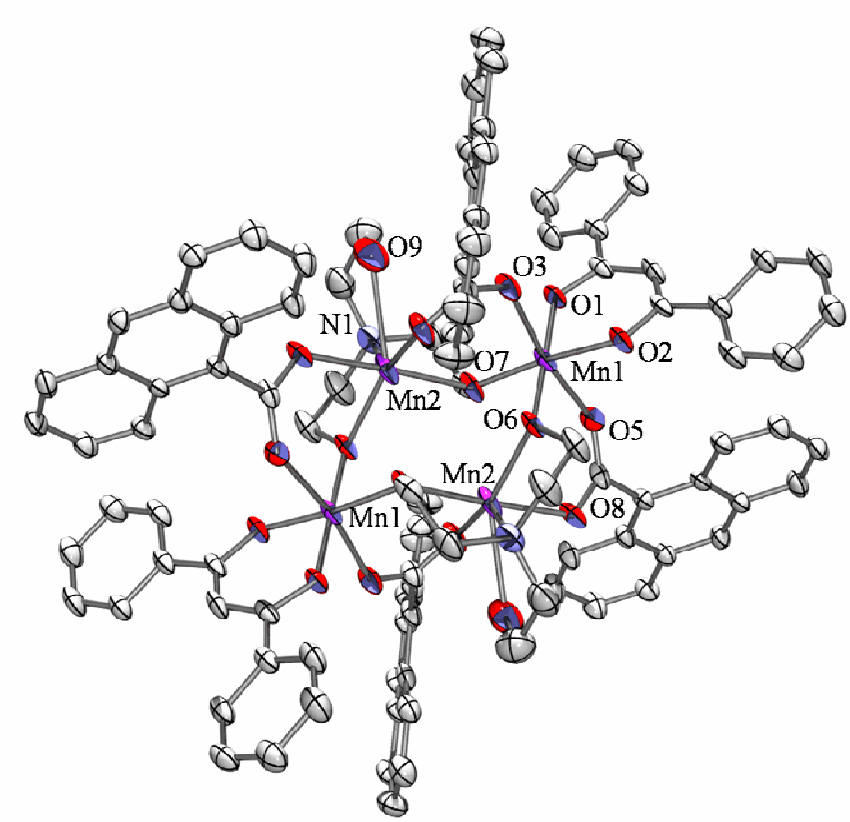

Figure 6.7. ORTEP of **$[Mn_4(anca)_4(Htea)_2(dbm)_2]\cdot 2.5Et_2O$ (6C)** with thermal ellipsoids at 50%. Hydrogen atoms and solvate molecules have been removed for clarity.

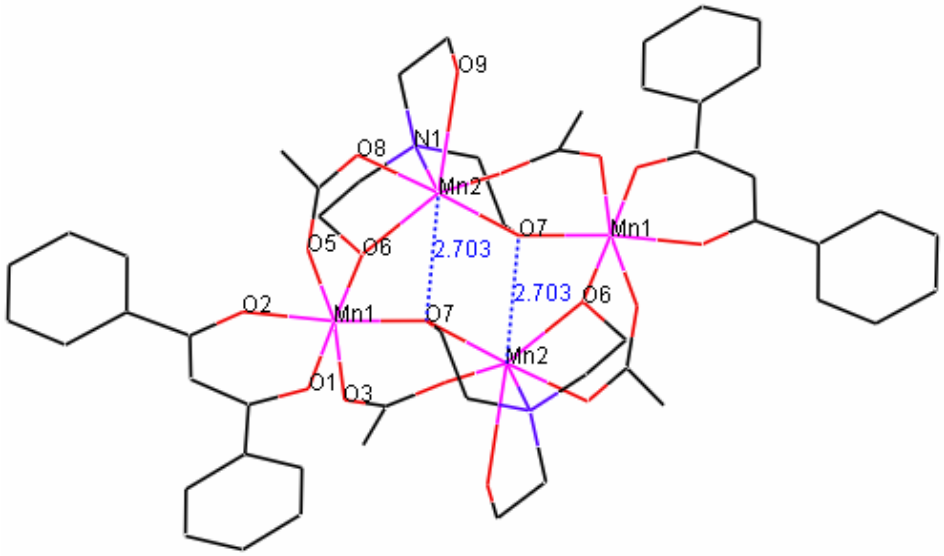

Figure 6.8. Mn_4 core of complex **6C** (anthracene rings omitted for clarity).

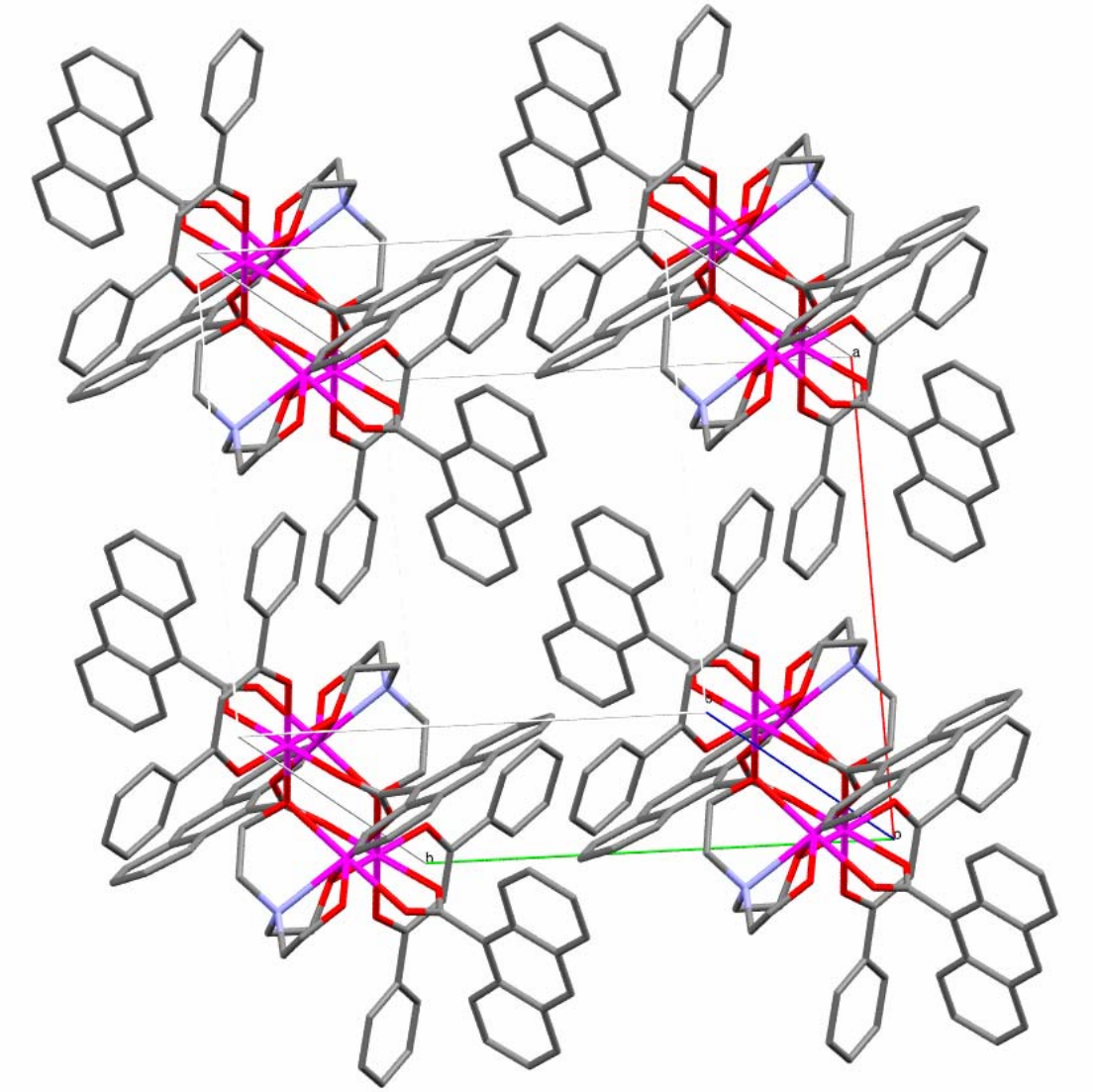

Figure 6.9. Packing diagram for **$[Mn_4(anca)_4(Htea)_2(dbm)_2]\cdot 2.5Et_2O$ (6C)** with hydrogens rempved for clarity.

Table 6.8. Comparison of Mn-O bond distances in complexes **6B**, **6C**, and selected dicubanes.

Mn_4 Complex	**Mn-O** (body-body pathway) distance [Å]
$[Mn_4(anca)_4(Htea)_2(dbm)_2]\cdot 2MeCN$ **(6B)**	**~2.455**
$[Mn_4(anca)_4(Htea)_2(dbm)_2]$ **(6C)**	**~2.703**
$[Mn_4(H_2tea)_2(Htea)_2(H_2O)_2(MeCO_2)_2]^{2+}$	2.201(1) [4]
$[Mn_4(H_2tea)_2(Htea)_2(PhCO_2)_2]^{2+}$	2.269(3) [4]
$[Mn_4(H_2tea)_2(Htea)_2(EtCO_2)_2]^{2+}$	2.255(4) [4]
$[Mn_4(O_2CMe)_2(pdmH)_6]^{2+}$	2.264(4) [6]
$[Mn_4O_2(O_2CMe)_6(py)_2(dbm)_2]$	1.894(2) [7]
$[Mn_4(hmp)_6(NO_3)_2(MeCN)_2]^{2+}$	~2.249 [8]
$[Mn_4(hmp)_6(NO_3)_4]$	~2.248 [8]
$[Mn_4(hmp)_4(acac)_2(OMe)_2]^{2+}$	~2.108 [8]
$[Mn_4(O_2CPh)4(mda)_2(Hmda)_2]$	~2.239 [5]

Table 6.9. Selected bond lengths [Å] for complex **6D.**

Mn(1)-O(8)#1	2.0985(15)	Mn(2)-O(1)	1.8708(15)
Mn(1)-O(3)	2.1439(15)	Mn(2)-O(6)	1.9203(15)
Mn(1)-O(1)	2.1746(15)	Mn(2)-O(5)	1.9268(16)
Mn(1)-O(2)	2.2369(14)	Mn(2)-O(2)#1	1.9725(15)
Mn(1)-O(2)#1	2.3307(15)	Mn(2)-O(7)	2.1804(15)
Mn(1)-N(1)	2.3310(18)	Mn(2)-O(4)	2.2272(15)

Table 6.10. Selected bond lengths [Å] for complex **6E.**

Mn(1)-O(6)#1	2.0852(19)	Mn(2)-O(7)	1.8642(17)
Mn(1)-O(1)	2.1454(17)	Mn(2)-O(3)	1.9215(17)
Mn(1)-O(7)	2.1795(17)	Mn(2)-O(4)	1.9229(17)
Mn(1)-O(8)	2.2447(16)	Mn(2)-O(8)#1	1.9731(16)
Mn(1)-O(8)#1	2.3251(16)	Mn(2)-O(5)	2.1736(19)
Mn(1)-N(1)	2.338(2)	Mn(2)-O(2)	2.1982(19)

$[Mn_4(anca)_4(Htea)_2(dbm)_2]\cdot 2.5Et_2O$ (6C). Complex **6C** has the same chemical formula as complex **6B** with the exception of solvent molecules (ORTEP shown in Figure 6.7). Despite the similar composition, complexes **6B** and **6C** have some very distinct differences. Complex **6C** has an analogous Mn_4O_4 core (Figure 6.8) but crystallizes in the triclinic P-1 space group. Since the molecule sits on an inversion center, the symmetry transformations of -x+2,-y+2, and -z+1 were used in order to generate theequivalent atoms in the target complex. Another noticeable difference is that all three arms of the triethanolamine ligands are bound to the Mn(2) atoms in complex **6C**.

Bond distances and Jahn-Teller distortions confirm that the valency of the Mn atoms in complex **6C** is the same as in complex **6B** (two Mn^{II} atoms in the body and two Mn^{III} atoms at the wing positions). The Jahn-Teller elongation is once again found along the O(3)-Mn(1)-O(5) axis which is orthogonal to the plane of the dbm^- ligand. Though all three arms of the triethanolamine ligands are coordinated, O(9) is still protonated in complex **6B** as in complex **6C**. However, there is no apparent hydrogen-bonding and very little interaction between overlapping dbm^- ligands of neighboring molecules.

The crystal data for complex **6C** shows convincing evidence for the presence of a wheel-shaped molecule as opposed to a pseudo-dicubane structure. The Mn(2)-O(7) body-body distance of 2.703 Å is ~0.2 Å longer than that in complex **6B** and ~0.4-0.8 Å longer than other known dicubanes found in Table 6.8. Again, this distance is also considerably longer than the sum of the ionic radii of the two ions (~2.2 Å).[66] Since the molecule is a wheel, the interaction between the two Mn atoms in the body positions

(body-body coupling constant, J_{bb}) does not exist and the complex can be assumed to have only one exchange pathway between the Mn atoms (wing-body, J_{wb}). This premise will be further discussed in terms of the Kambe vector approach and theoretical fitting of the magnetic susceptibility data using both single-*J* and two-*J* models for complexes **6B** and **6C**.

The Mn(2)-O(7)-Mn(2)#1 angle of the inner core of complex **6C** (97.24°) compares closely with that of previously reported dicubanes. The equivalent bond angle in other known dicubanes is typically 97-100°. In the $[Mn_4(H_2tea)_2(Htea)_2(PhCO_2)_2]^{2+}$ cluster, the Mn-O-Mn (body-body) angle is 97.03(1)°.[71] Other dicubanes such as $[Mn_4(O_2CMe)_2(pdmH)_6]^{2+}$ and $[Mn_4O_2(O_2CMe)_6(py)_2(dbm)_2]$ have smimlar body-body angles of 100.27(17)° and 99.07(9)° respectively.[69,70] The near-orthogonality of these angles predicts that there will be appreciable coupling between the two body Mn atoms (large J_{bb}) which has been shown to exist in many of these dicubane structures. However, in the case of complexes **6B** and **6C**, this large body-body interaction is not observed despite the structural similarities to known dicubanes. The presence and magnitude of the body-body and wing-body magnetic exchange pathways in will be addressed in the magnetic susceptibilty discussion.

$[Mn_4(anca)_4(edea)_2(dbm)_2]\cdot CH_2Cl_2$ (6D), $[Mn_4(anca)_4(n\text{-}bdea)_2(dbm)_2]\cdot CH_3CN$ (6E) and **$[Mn_4(anca)_4(t\text{-}bdea)_2(dbm)_2]\cdot Et_2O\cdot CH_3OH$ (6F).** Crystal data for complexes **6D-F** are presented in Table 6.3. Selected bond distances for complexes **6D-F** are given in Tables 6.9-11**,** respectively. Selected bond angles for complexes **6D-F** are found in Tables 6.12-14, respectively. Complexes **6D-F** crystallize

Table 6.11. Selected bond lengths [Å] for complex **6F.**

Mn(2)-O(1C)	1.885(2)	Mn(1)-0(8)	2.105(2)
Mn(2)-O(6)	1.908(2)	Mn(1)-O(3)	2.143(3)
Mn(2)-O(5)	1.933(2)	Mn(1)-O(1C)	2.159(2)
Mn(2)-O(2C)#1	1.964(2)	Mn(1)-O(2C)	2.216(3)
Mn(2)-0(7)#1	2.172(3)	Mn(1)-O(2C)#1	2.344(3)
Mn(2)-O(4)	2.221(3)	Mn(1)-N(1)	2.389(3)

Table 6.12. Selected bond angles [°] for complex **6D.**

O(8)#1-Mn(1)-O(3)	84.82(6)	O(1)-Mn(1)-O(2)#1	68.22(5)
O(8)#1-Mn(1)-O(1)	162.62(6)	O(2)-Mn(1)-O(2)#1	86.59(5)
O(3)-Mn(1)-O(1)	88.64(6)	O(8)#1-Mn(1)-N(1)	120.82(6)
O(8)#1-Mn(1)-O(2)	94.68(6)	O(3)-Mn(1)-N(1)	92.34(6)
O(3)-Mn(1)-O(2)	169.79(6)	O(1)-Mn(1)-N(1)	75.46(6)
O(1)-Mn(1)-O(2)	94.56(5)	O(2)-Mn(1)-N(1)	79.13(6)
O(8)#1-Mn(1)-O(2)#1	97.68(6)	O(2)#1-Mn(1)-N(1)	139.62(6)
O(3)-Mn(1)-O(2)#1	103.59(6)		

Table 6.13. Selected bond angles [°] for complex **6E.**

O(6)#1-Mn(1)-O(1)	83.77(7)	O(7)-Mn(1)-O(8)#1	67.60(6)
O(6)#1-Mn(1)-O(7)	166.08(8)	O(8)-Mn(1)-O(8)#1	86.93(6)
O(1)-Mn(1)-O(7)	88.83(7)	O(6)#1-Mn(1)-N(1)	116.84(9)
O(6)#1-Mn(1)-O(8)	94.75(7)	O(1)-Mn(1)-N(1)	94.19(7)
O(1)-Mn(1)-O(8)	171.50(6)	O(7)-Mn(1)-N(1)	75.37(7)
O(7)-Mn(1)-O(8)	94.25(6)	O(8)-Mn(1)-N(1)	78.97(7)
O(6)#1-Mn(1)-O(8)# 1	102.31(8)	O(8)#1-Mn(1)-N(1)	139.13(7)
O(1)-Mn(1)-O(8)#1	101.57(6)		

Table 6.14. Selected bond angles [°] for complex **6F.**

O(1C)-Mn(2)-O(6)	91.50(11)	O(6)-Mn(2)-0(7)#1	88.42(11)
O(1C)-Mn(2)-O(5)	177.03(11)	O(5)-Mn(2)-0(7)#1	84.78(10)
O(6)-Mn(2)-O(5)	91.30(10)	O(2C)#1-Mn(2)-0(7)#1	97.25(10)
O(1C)-Mn(2)-O(2C)#1	81.57(10)	O(1C)-Mn(2)-O(4)	97.27(10)
O(6)-Mn(2)-O(2C)#1	171.33(11)	O(6)-Mn(2)-O(4)	86.84(10)
O(5)-Mn(2)-O(2C)#1	95.73(10)	O(5)-Mn(2)-O(4)	83.88(10)
O(1C)-Mn(2)-0(7)#1	94.31(10)	O(2C)#1-Mn(2)-O(4)	88.86(10)

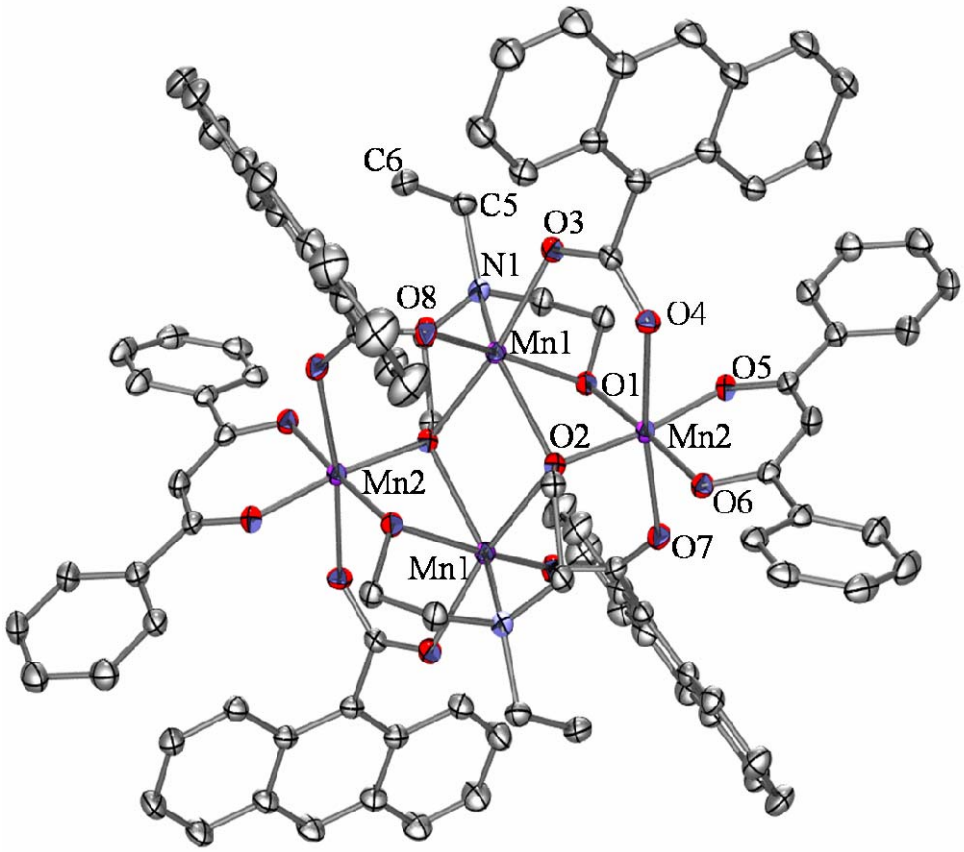

Figure 6.10. Ortep drawing of **$[Mn_4(anca)_4(edea)_2(dbm)_2]\cdot CH_2Cl_2$ (6D)** with thermal ellipsoids at 50%. Hydrogen atoms and solvate molecules have been removed for clarity.

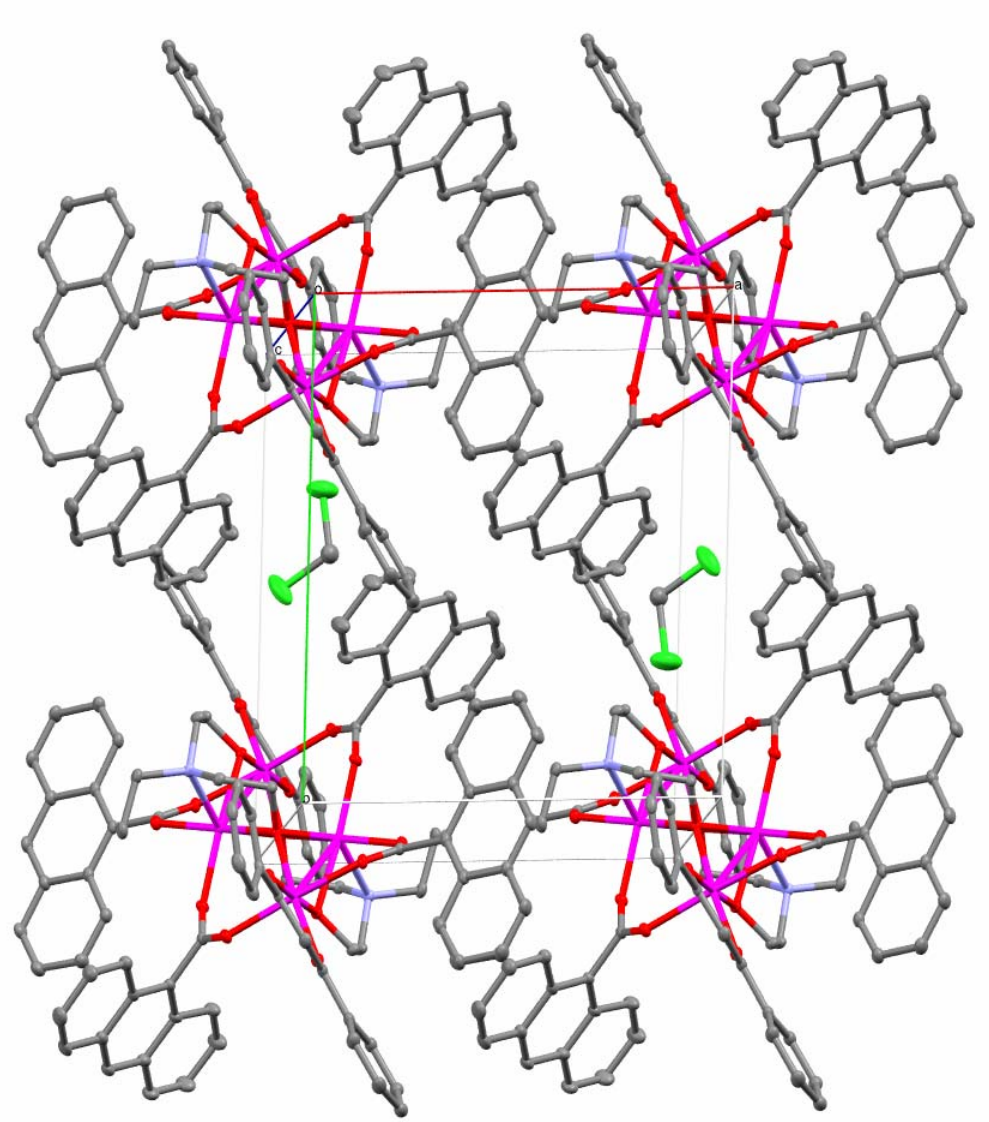

Figure 6.11. Packing diagram of **$[Mn_4(anca)_4(edea)_2(dbm)_2]\cdot CH_2Cl_2$ (6D)**. Hydrogen atoms have been removed for clarity.

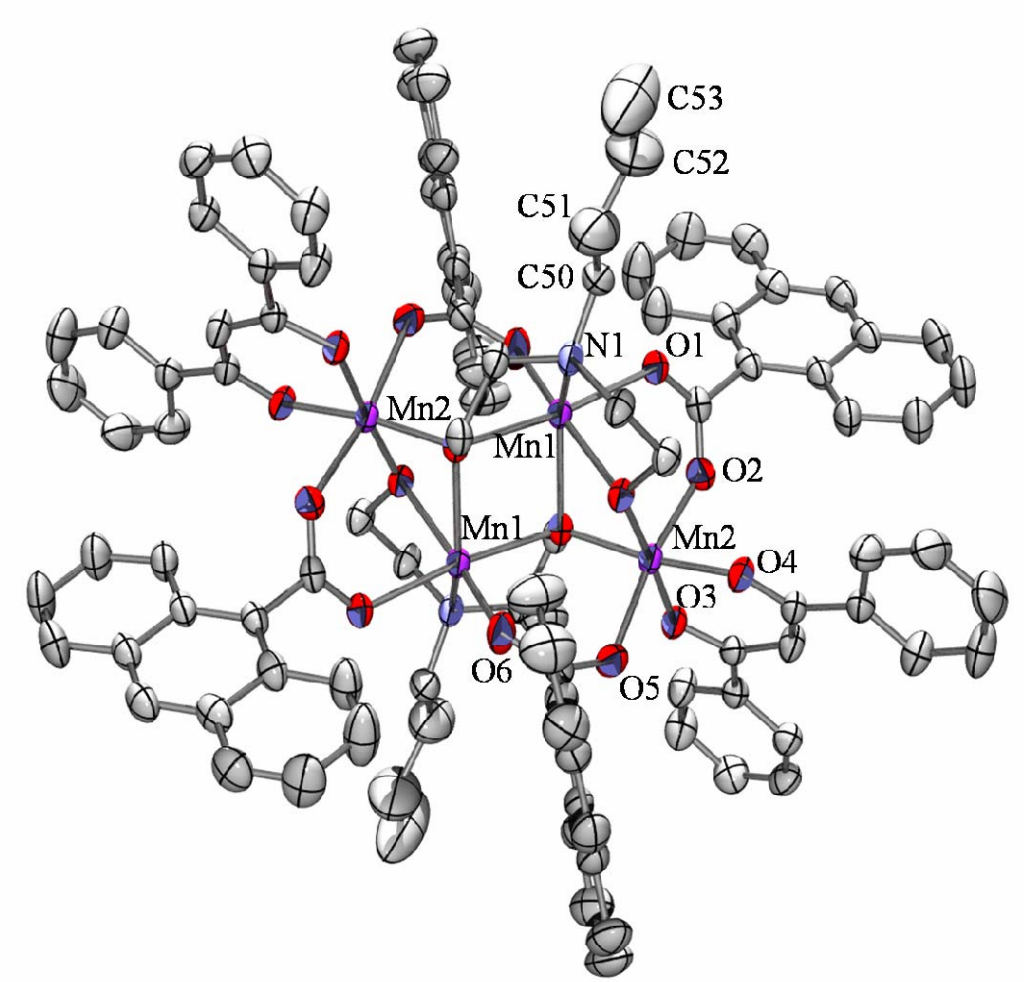

Figure 6.12. Ortep drawing of **$[Mn_4(anca)_4(n\text{-}bdea)_2(dbm)_2]\cdot CH_3CN$ (6E)** with thermal ellipsoids at 50%. Hydrogen atoms and solvate molecules have been removed for clarity.

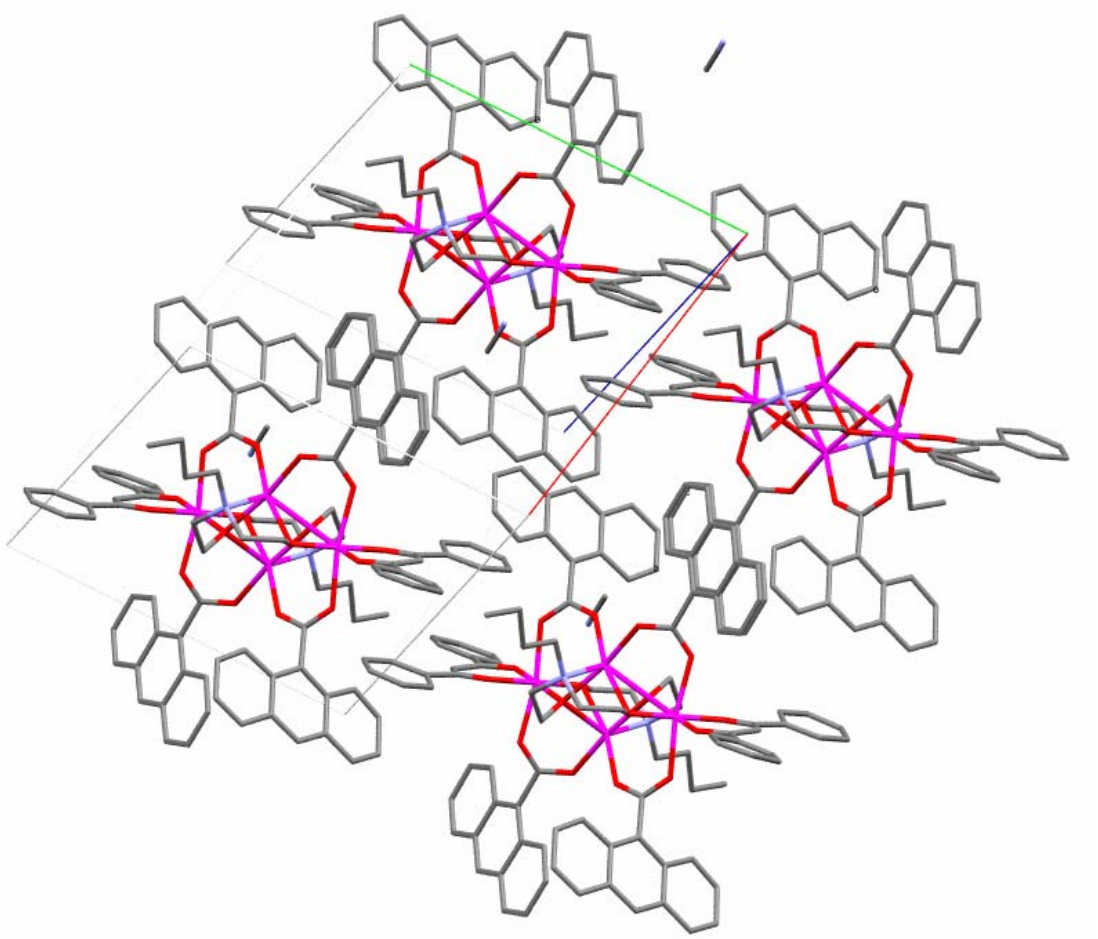

Figure 6.13. Packing diagram of **$[Mn_4(anca)_4(n\text{-}bdea)_2(dbm)_2]\cdot CH_3CN$ (6E).** Hydrogens have been removed for clarity.

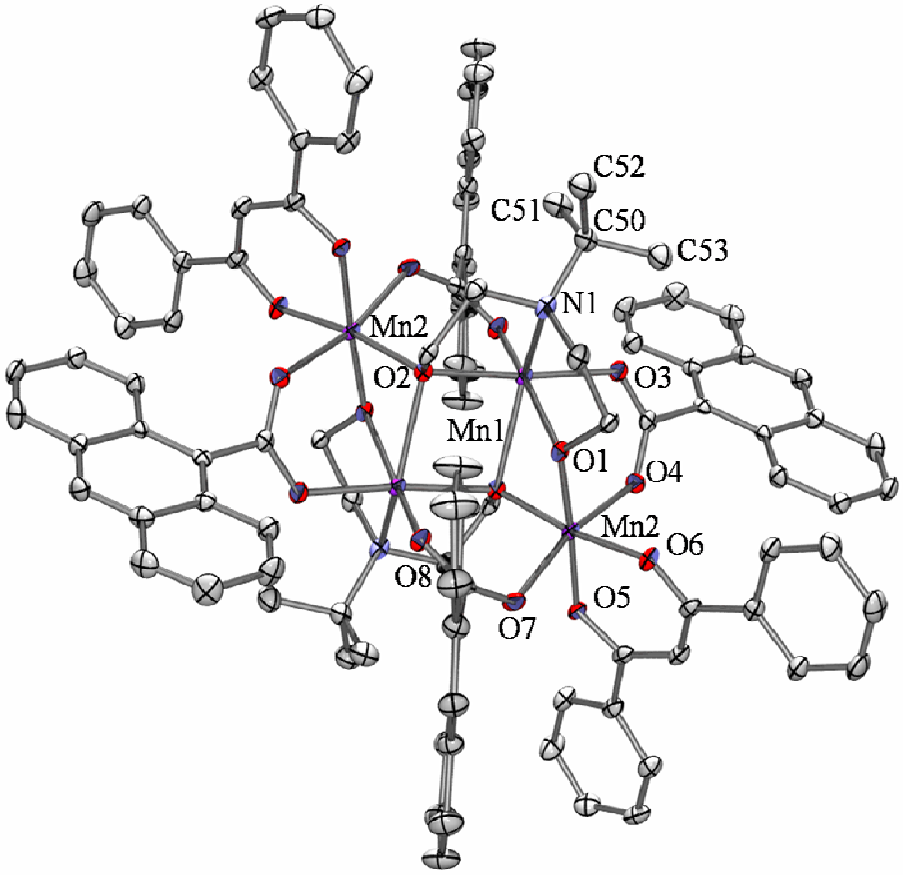

Figure 6.14. Ortep drawing of **[Mn_4(anca)$_4$(t-bdea)$_2$(dbm)$_2$]·Et_2O·CH_3OH (6F)** with thermal ellipsoids at 50%. Hydrogen atoms and solvate molecules have been removed for clarity.

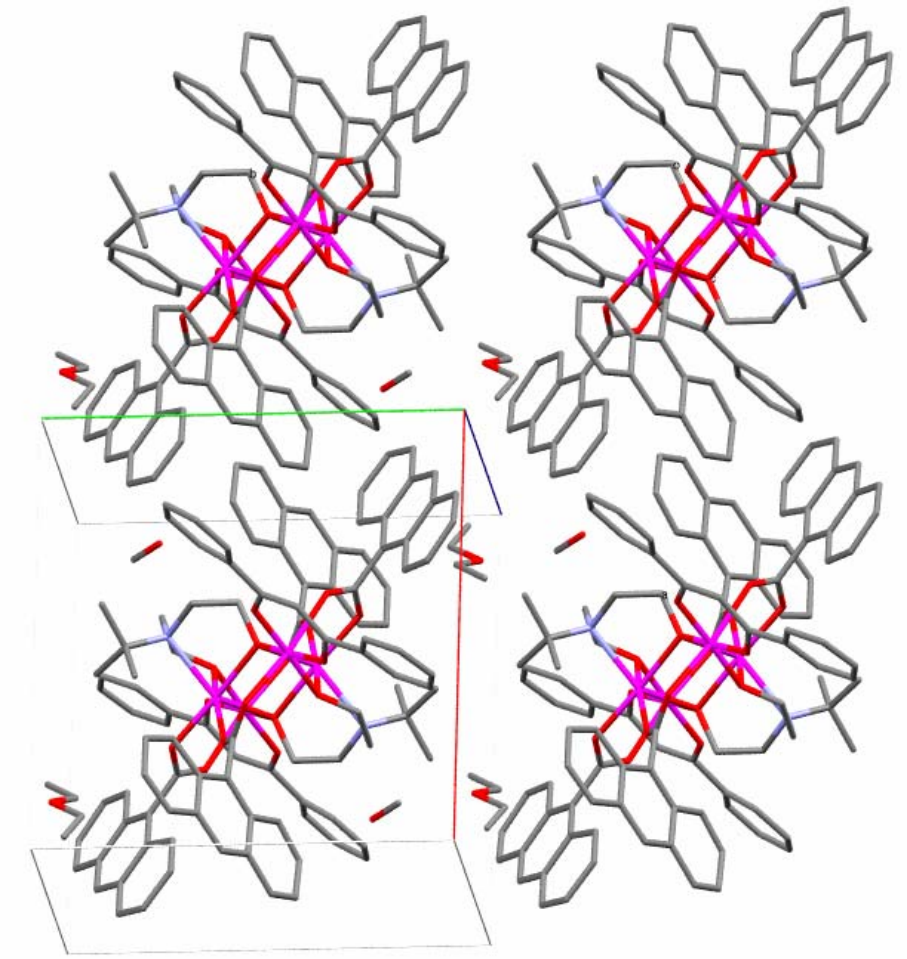

Figure 6.15. Packing diagram of **$[Mn_4(anca)_4(t\text{-}bdea)_2(dbm)_2]\cdot Et_2O\cdot CH_3OH$ (6F)**. Hydrogens have been removed for clarity.

in the triclinic P-1 space group. As with complexes **6B** and **6C**, the structure is made up of a Mn_4O_4 core which lies on a 2-fold symmetry axis and the asymmetric unit contains half of the molecule while the symmetry-equivalent atoms are generated by the symmetry transformations of -x+2,-y+2, and -z+1. ORTEP representations and crystal packing diagrams for complexes **6D-F** are presented in Figures 6.10-6.15.The Mn_4 cores of complexes **6D-F** are nearly identical, and consist of two 6-coordinate Mn^{III} atoms in the wing positions and two 6-coordinate Mn^{II} atoms in the body positions forming a planar core. Each Mn^{II} atom is bound to a Mn^{III} atom through two μ_3-alkoxide moieties from the R-diethanolamine ligands and a bridging $anca^-$ ligand, and the body centered Mn^{II} ions are bonded through μ_3-alkoxides from arms of the R-diethanolamine ligands. As was found with complexes **6B** and **6C**, the Mn^{III} atoms at the wing positions are capped by two dbm^- ligands, with the Jahn-Teller axes oriented orthogonal to the plane of the dbm ligands which are nearly orthogonal to the plane made by the Mn_4 core. The valency of the Mn atoms was confirmed by the presence of Jahn-Teller distortion around the Mn(1) atoms and valence bond sum analysis. The Mn(1)-O(2) bonds of 2.331Å and 2.334Å in **6D** and **6F**, and Mn(1)-O(8) bond of 2.334Å in **6E** are ~0.1Å shorter than those found in **6B** and **6C**, suggesting a greater degree of interaction between the central Mn^{II} atoms in complexes **6D-F** (see section 5.3.4). Furthermore, Mn^{II}- Mn^{II} distances in complexes **6D-F** (3.325Å, 3.114Å and 3.362Å) are significantly shorter than those in complexes **6B** and **6C**, 3.423Å and 3.697Å, respectively.

6.3.3 Origin of Manganese Oxidation-State Reversal with a Dicubane Core

An interesting difference between complexes **6B-F** in comparison to previously reported mixed-valence tetranuclear Mn complexes is that the valency of the Mn atoms is reversed. In complexes **6B-F**, the Mn^{III} atoms are located at the wing positions as opposed to the body of the molecule. The one common factor of the complexes showing this reversal is the use of the dbm^- ligand. In complexes **6B-F**, the Mn^{III} atoms are both capped by a dbm^- ligand. Based on the crystallographic data for these complexes, as well as several published Mn-dbm structures of various topologies (butterfly, cubane, dicubane, trigonal pyramid, etc.), the dbm^- ligand is always bound to Mn^{III} atoms. The position of the Jahn-Teller axes of the Mn^{III} atoms is consistent over a wide range of both homo- and hetero-valent Mn complexes.

The previously published structure of the $[Mn_4O_2(O_2CMe)_6(py)_3(dbm)_2]$ butterfly[63] consists of four coplanar Mn^{III} atoms bridged by two μ_3-oxo groups and six acetate ligands. Each of the two Mn atoms in the wing positions are chelated by a dbm^- ligand as in complexes **6B-F**. These two Mn^{III} atoms exhibit Jahn-Teller elongation along the O(4)-Mn(1)-O(12), O(3)-Mn(1)-O(5), O(4)-Mn(2)-O(7), O(2)-Mn(2)-O(5), and O(4)-Mn(2)-O(7) axis of complexes **6B-F**, respectively. The orientation of the distortion in this dicubane is also similar to complexes **6B-F** in that it is nearly coplanar with the Mn_4 core.[67] Related to the dicubane topology is the non-planar Mn_4 butterfly as discussed earlier. Butterfly complexes of the formula $[Mn_4O_2(O_2CR)_6(py)_2(dbm)_2]$ (where R = Me, Et, Ph, etc.) also show the same trends in Jahn-Teller elongation associated with the Mn^{III} atoms bound to dbm^- ligands.[64,65] Furthermore, the Jahn-Teller

Mn-O, Mn-N, and Mn-X bond distances of the Mn complexes discussed here are all within their expected ranges and comparable to those found in complexes **6B-F**.

A series of distorted Mn_4 cubane structures (also referred to as trigonal pyramids) has also been shown to have the same Mn^{III}-dbm interaction. These complexes are comprised of a $Mn^{III}_3Mn^{IV}$ core with the formula $[Mn_4O_3X(O_2CR)_3(dbm)_3]$ (where R = Me, Ph and X = Cl, Br, F, N_3, OCN, OMe, O_2CMe, and OH). Each Mn^{III} atom is again bound to a dbm^- ligand and shows significant Jahn-Teller elongation along the O-Mn-X axis which is orthogonal to the plane of the dbm^- ligand. The Mn^{IV} atom serves as the apex of the pyramid and does not exhibit any significant distortion as would be expected of a d^3, near-octahedral metal center. A schematic representation of the dicubane and butterfly core, $[Mn^{III}_4(\mu_3\text{-}O)_2]^{8+}$, as well as the trigonal pyramidal core, $[Mn^{III}_3Mn^{IV}(\mu_3\text{-}O)_3(\mu_3\text{-}X)]^{6+}$, is shown in Scheme 6.1.[64,65,72,73]

Lastly, the Mn_6 cluster of $[Mn_6O_4X_4(Me_2dbm)_6]$ (where X = Cl or Br) shows the same predictability in the oxidation states of the Mn atoms. This cluster consists of six Mn^{III} atoms arranged in a pseudo-octahedron with four nonadjacent faces bridged by μ_3-O^{2-} ions and the remaining four faces bridged by μ_3-X^- ions. Each Mn atom is also bound to a dbm^- ligand and possesses 6-coordinate, near-octahedral geometry. As expected, the two trans Mn-X bonds of each Mn^{III} atom are involved in Jahn-Teller elongation (2.618(3)-2.692(3) Å).[72]

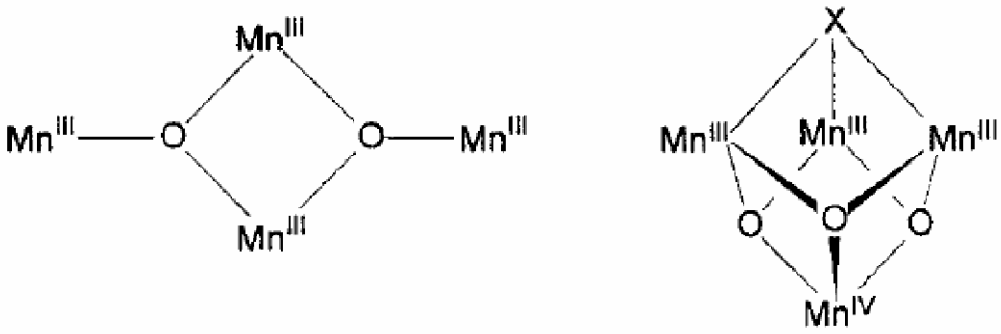

I II

Scheme 6.1. (I) Mn_4 core for dicubane (planar Mn_4) and butterfly (non-planar Mn_4); **(II)** Mn_4 core for trigonal pyramid (distorted cubane).

The consistency of these observations leads to the conclusion that the reversal of oxidation states in complexes **6B-F** compared to other known Mn_4 complexes is due to the chelating effects of the dbm^- ligand. The Jahn-Teller elongation axes of the Mn^{III} atoms tend to be oriented in such a way as to avoid the Mn-O^{2-} bonds (Mn-dbm bonds). The Mn-O^{2-} bonds are typically the shortest and the strongest bonds in these molecules (<1.9 Å) which explains the resulting distortion seen around the Mn^{III}-dbm centers.[65] Furthermore, it is plausible to conclude that the Mn oxidation states of a mixed-valence system could easily be reversed by replacing the dbm^- ligands with a chelator that forms less robust bonds with Mn. This would lend to more flexibility in the orientation of Jahn-Teller distorted axes, and thus lead to other possible oxidation states.

6.3.4 Magnetic Susceptibility Studies

$[Mn_4O_2(anca)_6(dbm)_2]\cdot 3CH_2Cl_2$ (6A). Figure 6.16 (Top) illustrates the variable temperature dc magnetization data for complex **6A** measured between 300 K

and 5 K at an applied field of 0.01Tesla. The plot of $\chi_m T$ versus T exhibits a maximum molar susceptibility of ~ 8.24 $cm^3 \cdot K \cdot mol^{-1}$ at 300 K that decreases nearly linearly to around 30 K and then decreases more rapidly as the temperature is further decreased to 5 K, which is indicative of antiferromagnetic exchange interactions. The $\chi_m T$ value of ~8.24 $cm^3 \cdot mol^{-1} \cdot K$ at 300 K is less than the theoretical spin-only value of 12.0 $cm^3 \cdot K \cdot mol^{-1}$ for four non-interacting Mn^{III} ions.

A small inflection can be seen in the observed molar susceptibility data in Figure 6.16 (Top) at 190 K. This is likely the result of thermal ordering of solvent molecules within the crystal lattice. As discussed in terms of structural characteristics, each molecule in complex **6A** co-crystallizes with three highly-disordered dichloromethane molecules: two lie between molecules in the crystal lattice, and one occupies a void adjacent to one face of the Mn_4 rhombus. Inspection of van der Waals radii associated with the dichloromethane molecule adjacent to the Mn4 rhombus reveals close contacts between the dichloromethane Cl atoms and C(12) dbm^- phenyl ring-carbons of 3.35 Å. These interactions likely influence the planarity of the $[Mn_4O_2]^{8+}$ core thus influencing the magnetic superexchange.

In order to determine the spin ground-state of complex **6A**, the $\chi_m T$ vs temperature data were fit employing least squares methods and the Kambe vector model.[74] Symmetry considerations warrant the use of a model employing two coupling constants, J_{wb} and J_{bb}, to describe the isotropic magnetic exchange pathways associated with the Mn_4 "butterfly" topology as presented in Scheme 6.2. The Kambe vector model was applied to the Heisenberg spin Hamiltonian (Equation 6.1, where $\hat{S}_i$ is the spin-operator of Mn_i). Expansion of Equation 6.1, taking into account all spin-coupling

possibilities, leads to Equation 6.2. The $J_{13}(\hat{S}_1 \cdot \hat{S}_3)$ term has been neglected in Equation 6.2 because it is assumed that there is no direct exchange pathway between Mn(1) and Mn(3) as viewed in Scheme 6.2.[75] Substitution of equivalent terms, as previously reported for $[Mn^{III}_4]$ and mixed valent $[Mn^{II}_2Mn^{III}_2]$ "butterfly" complexes leads to the resultant eigen-value equation (Equation 6.5) which was used in conjunction with the Van Vleck equation (Equation 6.6)[76] to give the theoretical fitting values of J_{wb}, J_{bb}, and g as -10.5 cm^{-1}, -22.7 cm^{-1}, and 2.0 respectively. It should be noted that $\chi_m T$ data below approximately 25 K were omitted in the fitting procedure due to appreciable zero-field splitting at low temperatures. Coupling constants J_{wb} and J_{bb} reported for

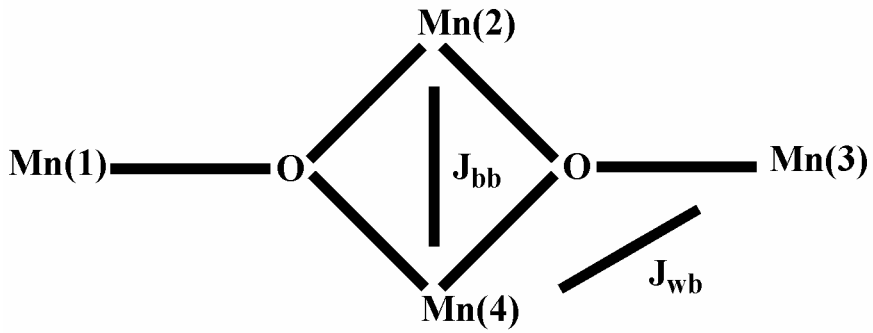

Scheme 6.2. The Kambe coupling model illustrating magnetic exchange pathways J_{wb} and J_{bb}, where S_1, S_2, S_3 and S_4 are Mn^{III} ions for complex **6A**, and S_1 and S_3 are Mn^{III} ions and S_2 and S_4 are Mn^{II} ions for complexes **6B-F.**

$$\hat{H} = -2\sum_{ij} J_{ij}\hat{S}_i \cdot \hat{S}_j \qquad \textbf{(6.1)}$$

$$\hat{H} = -2[J_{12}(\hat{S}_1 \cdot \hat{S}_2) + J_{23}(\hat{S}_2 \cdot \hat{S}_3) + J_{24}(\hat{S}_2 \cdot \hat{S}_4) + J_{34}(\hat{S}_3 \cdot \hat{S}_4) + J_{41}(\hat{S}_4 \cdot \hat{S}_1)] \qquad \textbf{(6.2)}$$

$$J_{12} = J_{14} = J_{23} = J_{34} = J_{wb}; \quad J_{24} = J_{bb} \qquad \textbf{(6.3)}$$

$$\hat{S}_A = \hat{S}_1 + \hat{S}_3; \quad \hat{S}_B = \hat{S}_2 + \hat{S}_4; \quad \hat{S}_T = \hat{S}_A + \hat{S}_B \qquad \textbf{(6.4)}$$

$$E(S_T) = -J_{wb}[S_T(S_T+1) - S_A(S_A+1) - S_B(S_B+1)] - J_{bb}[S_A(S_A+1)] \quad \textbf{(6.5)}$$

$$\chi_M = \left(\frac{Ng^2\mu_B^2}{3kT}\right)\frac{\sum[S_T(S_T+1)(2S_T+1)e^{\frac{-E(S_T)}{k_BT}}}{\sum(2S_T+1)e^{\frac{-E(S_T)}{k_BT}}} \quad \textbf{(6.6)}$$

similar complexes range between -4.9 cm^{-1} to -5.6 cm^{-1} for J_{wb} and -21.9 cm^{-1} to -23.9 cm^{-1} for J_{bb}. The two-fold increase in the calculated wing-body interaction (J_{wb}) for complex **6A** as compared to similar complexes could be due to the same solvent effects responsible for the observed $\chi_m T$ inflection in Figure 6.16 (Top) This is a reasonable conclusion because weighting of data leading to the calculation of coupling parameters is mainly from susceptibility values in the high temperature region.

A plot of eigen-energies [$E(S_T)$] versus spin total [S_T] (Figure 6.16, Bottom) indicates an overall calculated spin ground-state of $S = 2$ with the first excited state, $S = 3$, lying 14 cm^{-1} above the ground state. The calculated spin ground state of $S = 2$ is consistent with other complexes of the same topology ($S = 0$ to $S = 3$).[49,64,77,78]

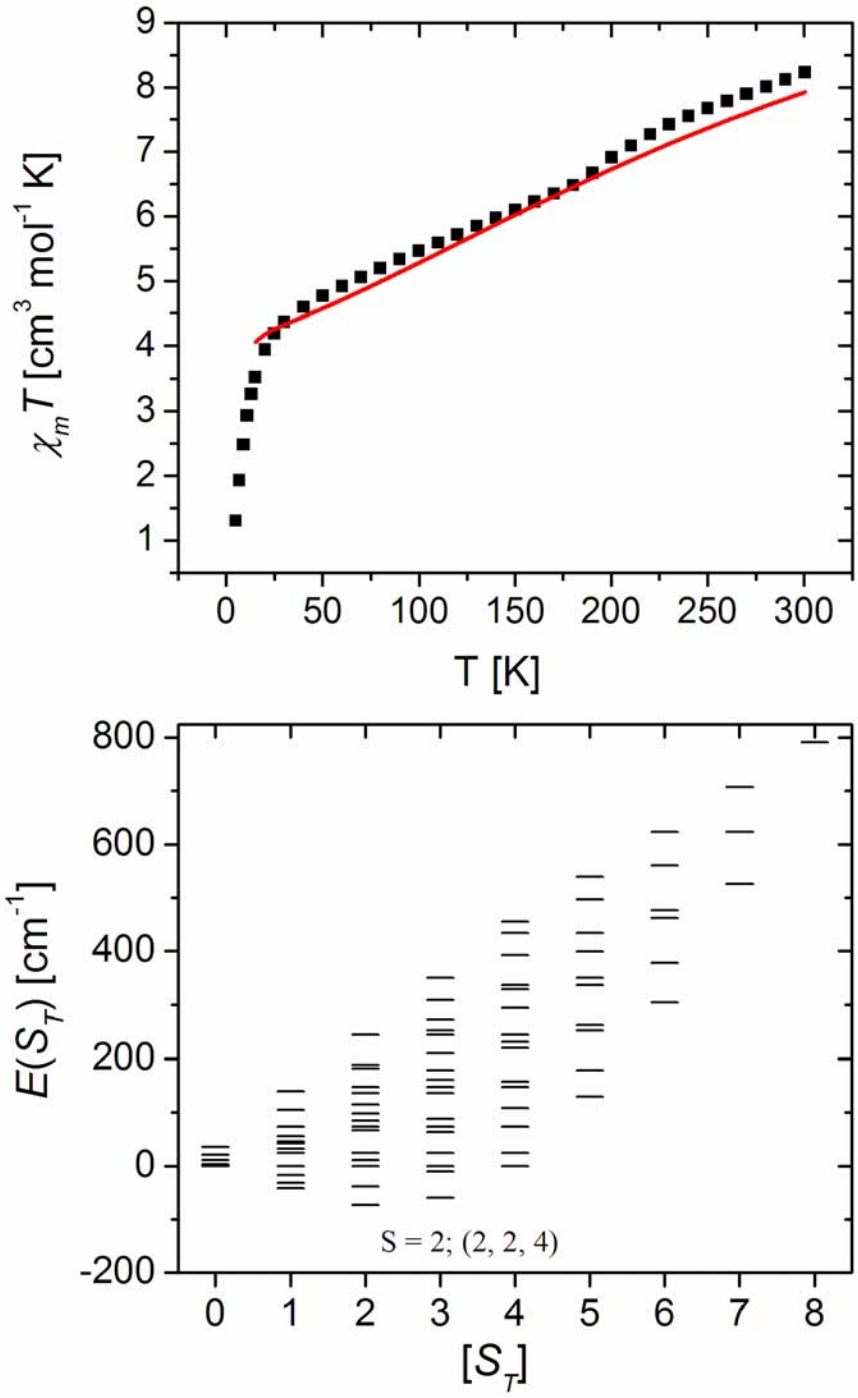

Figure 6.16. (Top) Plot of dc magnetic susceptibility and fit for **[Mn_4O_2(anca)$_6$(dbm)$_2$]** **(6A)** from 300K to 1.8 K at an applied field of 0.01 Tesla (■ observed, ─ theoretical fit). (Bottom) Illustrates the distribution of calculated eigen-energies [$E(S_T)$] versus spin total [S_T] of the 110 microstates (S_T, S_B, S_A).

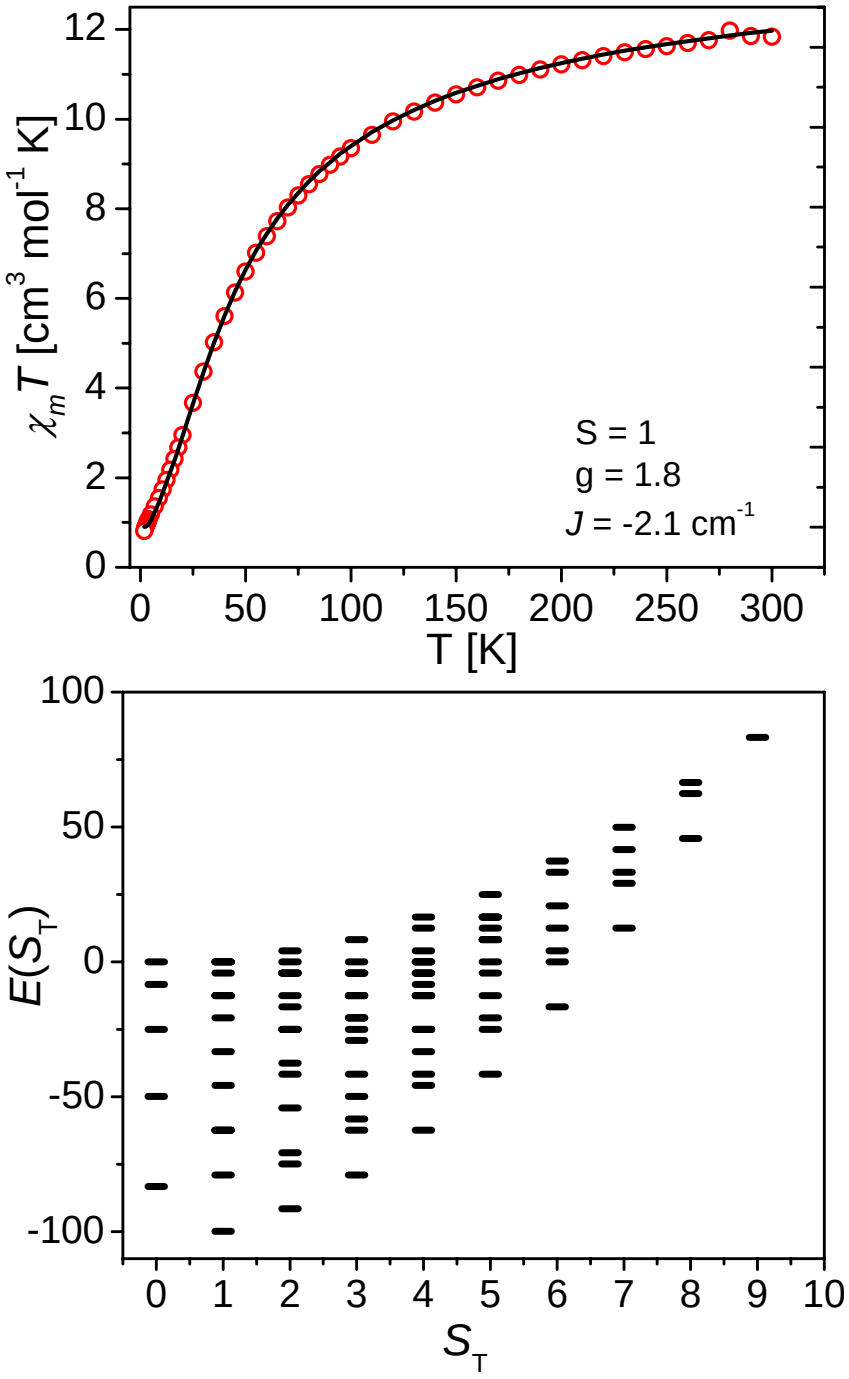

Figure 6.17. (Top) DC magnetic susceptibility taken from 300K to 1.8K with best fit line obtained from least squares analysis for **[Mn_4(anca)$_4$(Htea)$_2$(dbm)$_2$]·2MeCN (6B)** at an applied field of 0.1 Tesla. (○ observed, ─ theoretical fit). (Bottom) Illustrates the distribution of calculated eigen-energies [$E(S_T)$] versus spin total [S_T] of the 110 microstates (S_T, S_B, S_A).

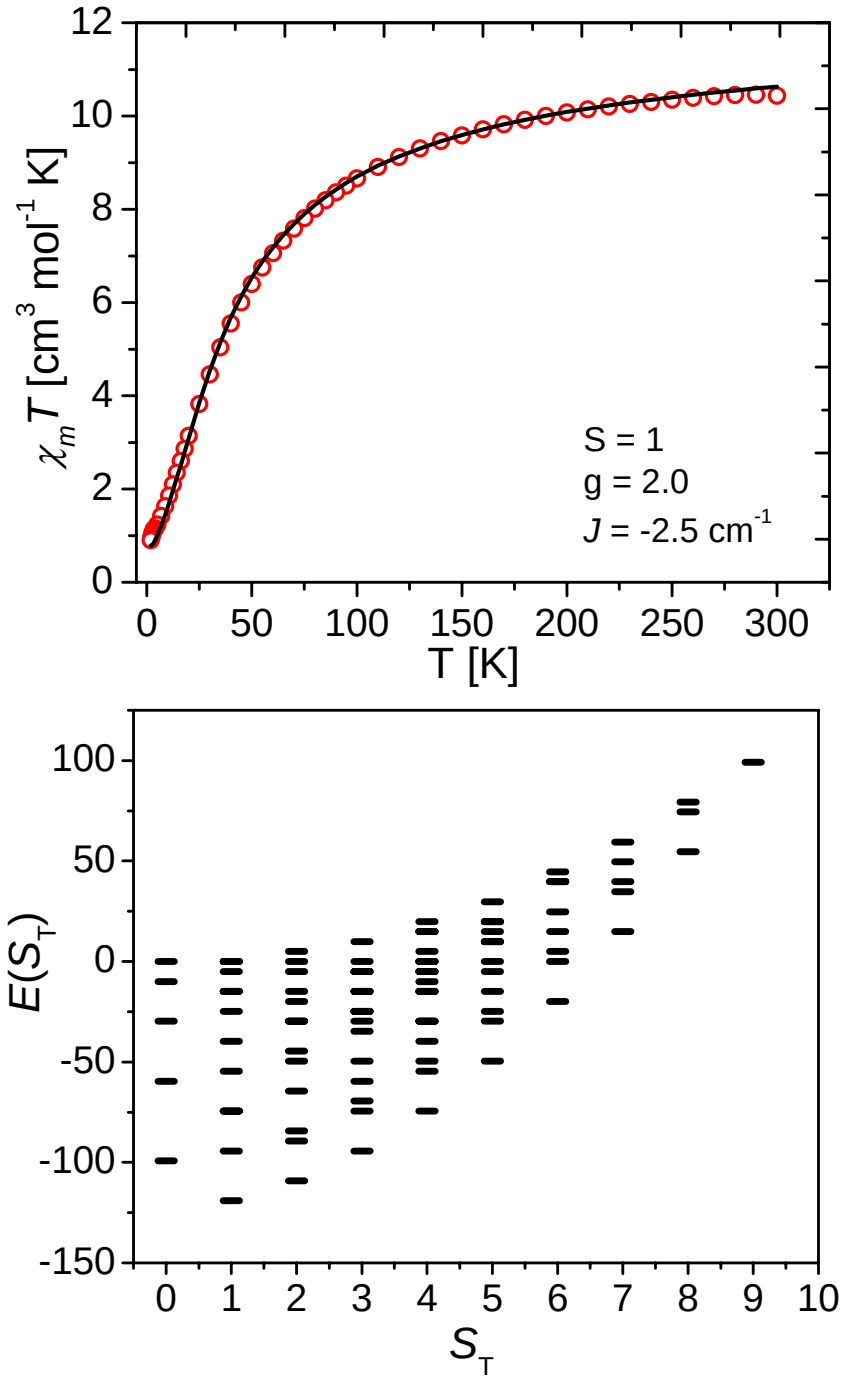

Figure 6.18. (Top) DC magnetic susceptibility with best fit for **[Mn_4(anca)$_4$(Htea)$_2$(dbm)$_2$] (6C)** from300K to 1.8K at an applied field of 0.1 Tesla. (○ observed, ─ theoretical fit). (Bottom) Illustrates the distribution of calculated eigen-energies [$E(S_T)$] versus spin total [S_T] of the 110 microstates (S_T, S_B, S_A).

$[Mn_4(anca)_4(Htea)_2(dbm)_2]\cdot 2MeCN$ (6B) and $[Mn_4(anca)_4(Htea)_2(dbm)_2]$ (6C). Variable temperature dc magnetization data taken at 0.1 T, from 300 K to 1.8 K, for complexes **6B** and **6C** are given in Figures 6.17 (Top) and 6.18 (Top) respectively. Maximum molar susceptibilities for complexes **6B** and **6C** at 300 K were found to be ~11.9 $cm^3\cdot mol^{-1}\cdot K$ for complex **6B** and ~10.6 $cm^3\cdot mol^{-1}\cdot K$ for complex **6C**. These observed $\chi_m T$ values are smaller than the theoretical spin-only value of 14.8 $cm^3\cdot K\cdot mol^{-1}$ calculated for two Mn^{II} and two Mn^{III} non-interacting ions. The gradual decrease in $\chi_m T$ with decreasing temperature from 300 K to 50 K in complex **6B,** Figure 6.17 (Top) and complex **6C,** Figure 6.18 (Top), is indicative of weak antiferromagnetic exchange interactions. The steep decline in molar magnetic susceptibility at low temperatures is due to zero-field splitting and Zeeman interactions. Below 5 K the value of $\chi_m T$ does not tend toward zero, but rather tails off to a plateau at approximately 0.8 $cm^3\cdot K\cdot mol^{-1}$. Theoretical fitting of the dc molar magnetic susceptibility for complexes **6B** and **6C** were carried out using a model instituting a single coupling constant *J* (Scheme 6.3) representing the super-exchange between Mn^{II} (body) and Mn^{III} (wing) atoms, where Mn(1,3) are Mn^{III} atoms and Mn(2,4) are Mn^{II} atoms. This approach was employed due to the long Mn(2)-O(7) distances found in complexes **6B** and **6C**, 2.5Å and 2.7Å respectively. These distances are considerably longer than those found in reported dicubane complexes (2.2 Å to 2.3 Å) and suggest that the body-body (Mn^{II}-Mn^{II}) magnetic exchange pathways found in most reported dicubanes do not exist in complexes **6B** and **6C**. This implies that magnetic exchange interactions occur only around the periphery of each molecule (Mn^{II}-Mn^{III}) which is consistent with a wheel topology.

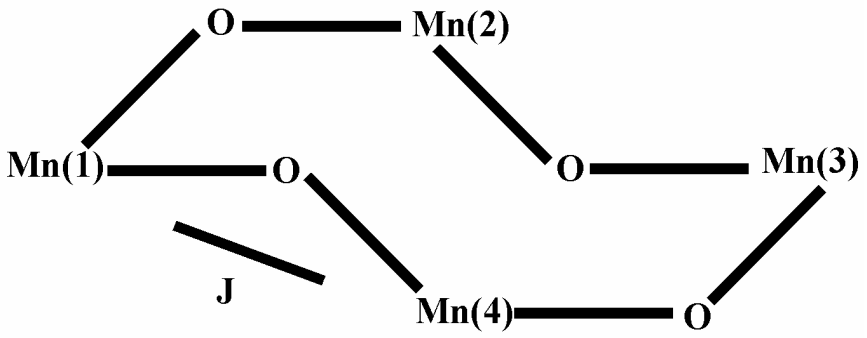

6.3A

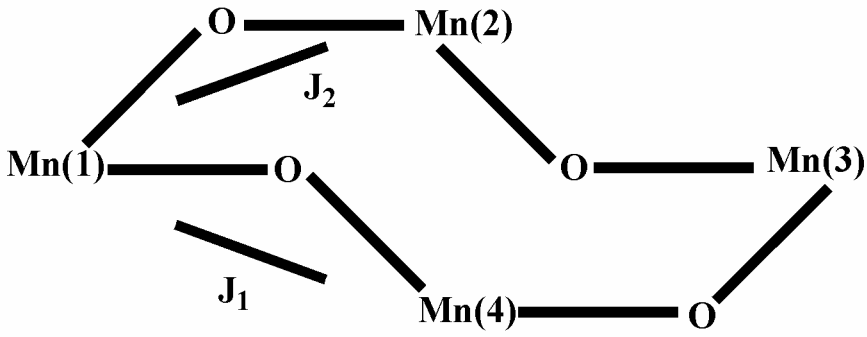

6.3B

Scheme 6.3. Kambe exchange model showing exchange pathways for complexes **6B** and **6C.** Mn(1) and Mn(2) represent Mn^{III} atoms and Mn(2) and Mn(4) represent Mn^{II} atoms.

The Heisenberg spin Hamiltonian (Equation 6.1) for complexes **6B** and **6C** is given in Equation 5.2. It is assumed in this model that the Mn(1)-Mn(2), Mn(2)-Mn(3), Mn(3)-Mn(4) and Mn(4)-Mn(1) symmetry imposed exchange pathways shown in Scheme 6.3 are all equivalent. Use of a single coupling constant *J* simplifies the spin-Hamiltonian in Equation 6.2 to yield Equation 6.8, where $S_1 = S_3 = 2$ for Mn(1) and Mn(3) and $S_2 = S_4 = 5/2$ for Mn(2) and Mn(4) in Scheme 6.3. Application of the

Kambe vector coupling scheme (Equation 6.4),[74] where S_T represents the total spin of the molecule, allows for the calculation of the energies of the individual spin states (Equations 6.8 and 6.9) because they are eigen-functions of the overall spin-Hamiltonian. Spin total for complexes **6B** and **6C** can vary between S_T =0 for complete antiferromagnetic coupling to S_T = 9 for complete ferromagnetic coupling which gives an overall spin degeneracy of 900, consisting of 110 non-degenerate states.

$$H = -J[\hat{S}_T^2 - \hat{S}_A^2 - \hat{S}_B^2] \quad \textbf{(6.8)}$$

$$E(S_T) = -J[S_T(S_T+1) - S_A(S_A+1) - S_B(S_B+1)] \quad \textbf{(6.9)}$$

Least squares analysis of the observed molar magnetic susceptibility gave good theoretical fits as noted by the solid lines in Figures 6.17 (Top) and 6.18 (Top). Theoretical fits were calculated using data encompassing the entire measured temperature range (300 K to 1.8 K) and were found to be g =1.9 and J =-2.6 cm^{-1} for complex **6B** and g = 1.8 and J = -2.1cm^{-1} for complex **6C.** where both complexes were calculated to have a S = 1 spin ground state. The calculated coupling constants (J) for complexes **6B** and **6C** are lower in the case of complex **6C**, and equal to the smallest reported exchange parameters for complex **6B**, with reported values of -2.6 to -24.6 cm^{-1} for Mn^{II}-O-Mn^{III} exchange pathways in reported dicubane complexes. The weak Mn^{II}-Mn^{III} coupling between manganese atoms in complexes **6B** and **6C** is a product of "spin-frustrated" exchange pathways which have been extensively studied for the types

of exchange pathways found in complexes **6B** and **6C**.[49,79] Plots of distribution of eigen-energies [$E(S_T)$] versus spin total [S_T] for complexes **6B** and **6C** are given in Figure 6.17 (Bottom) and Figure 6.18 (Bottom) showing the lowest energy state associated with a S = 1 spin ground-state.

In an attempt to discern if in fact magnetic exchange interactions occur across the Mn(2)-O-Mn(4) position in the ring, theoretical fits of magnetic susceptibility data for complexes **6B** and **6C** were also carried out employing the same Kambe strategy (Scheme 6.2) as that used for complex **6A** with two coupling constants (J_{wb} and J_{bb}). Theoretical fits of the $\chi_m T$ verses T data for complexes **6B** and **6C** yielded values for g, J_{wb} and J_{bb} of 1.9, -2.5 cm^{-1} and -0.3 cm^{-1} for complex **6B** and 1.8, -2.2 cm^{-1} and -0.7 cm^{-1} for complex **6C**. Only the J and J_{wb} were compared because these represent Mn^{II}-O-Mn^{III} exchange pathways which are equivalent in the two models. Comparison of g and coupling constants J with J_{wb} obtained from the two fitting models, Scheme 6.2 and Scheme 6.3, (Table 6.15) reveal distinct similarities. It should be further noted that the susceptibility fits in both cases superimpose the fits obtained using just a single coupling constant J. Since the two models produce nearly identical results, it follows that the simpler model should be taken to represent the exchange coupling in the system.

Though good fits were obtained for complexes **6A** and **6B** utilizing the Kambe equivalent operator method, these complexes exhibit a number of accessible low lying excited states as illustrated in Figure 6.17 (Bottom) and Figure 6.18 (Bottom) for complexes **6B** and **6C,** respectively. The calculated spin ground state of both complexes is represented by the S = 1 state (1(S_T), 5(S_B), 4(S_A)) which is -122.88 cm^{-1}

Table 6.15. Comparison of fitting parameters for complexes **6B** and **6C.**

	g	***J***	J_{wb}
Complex **6B**			
Scheme 2	1.9	-2.6 cm^{-1}	-
Scheme 3	1.9	-	-2.5 cm^{-1}
Complex **6C**			
Scheme 2	1.8	-2.1 cm^{-1}	-
Scheme 3	1.8	-	-2.2 cm^{-1}

Table 6.16. Fitting parameters for complexes **6D-F** from least-squares fitting of variable temperature molar magnetic susceptibility data (χ_mT vs. T).

Complex	***S***	**g**	J_{wb} **(cm^{-1})**	J_{bb} **(cm^{-1})**
6D	1	1.9	-1.6	-3.0
6E	1	1.9	-1.9	-2.7
6F	1	1.8	-0.3	-2.4

Table 6.17. Fitting parameters for complexes **6C-F** from theoretical fits of *M/Nβ vs. H/T* variable field magnetic susceptibility data.

Complex	***S***	***g***	***D*** **(cm^{-1})**	***E*** **(cm^{-1})**
6C	1	2.2	-9.2	-
6D	1	2.0	-2.7	0.03
6E	1	2.0	-5.5	0.6
6F	1	2.0	-6.0	0.02

for complex **6B** and -99.84 cm^{-1} for complex **6C**. Complexes **6B** and **6C** each have at least ten microstates which fall within 50 cm^{-1} of the calculated ground spin state, with the (2, 5, 4) microstate lying 10.24 cm^{-1} and 8.32 cm^{-1} above the ground state for complexes **6B** and **6C,** respectively.

Figures 6.19-21 (Top) illustrate variable temperature molar magnetic susceptibility data for **$[Mn_4(anca)_4(edea)_2(dbm)_2]\cdot CH_2Cl_2$ (6D), $[Mn_4(anca)_4(n\text{-}bdea)_2(dbm)_2]\cdot CH_3CN$ (6E)** and **$[Mn_4(anca)_4(t\text{-}bdea)_2(dbm)_2]\cdot Et_2O\cdot CH_3OH$ (6F)**, respectively. The maximum molar susceptibility for complexes **6D-F** at 300K are between 9 and 11 $cm^3\cdot mol^{-1}\cdot K$, and slowly decrease with decreasing temperature, reaching minimums of 2.5, 0.8 and 0.8 $cm^3\cdot mol^{-1}\cdot K$ at the lowest temperature measured (1.8K). Least-squares analysis were carried out for complexes **6D-F** employing the same coupling scheme (Scheme 6.2) and Kambe[74] model as that used for complex **6A**, where S_1 and S_3 are Mn^{II} ions and S_2 and S_4 are Mn^{III} ions. The best theoretical fit of experimental data for complexes **6D-F** (solid lines in Figures 6.19-21 (Top)) yielded spin ground states of $S = 1$, and antiferromagnetic (negative J-values), which is what one would expect given the topology and positions of the Mn^{II} and Mn^{III} ions. Parameters from the best fit of variable temperature magnetic susceptibility data for complexes **6D-F** are presented in Table 6.16. The dominant exchange pathway in these complexes is the "body-body" pathway (J_{bb}) between the Mn^{II} ions, and is expected to be dominated by antiferromagnetic interactions.[20] Figures 6.19-21 (Bottom) show the eigen-energy distributions (plotted as $E(S_T)$ vs. S_T) for complexes **6D-F**. All three complexes are characterized by the same $S = 1$ ($1(S_T)$, $5(S_B)$, $4(S_A)$) energy state, with first excited states lying between 4 cm^{-1} and 10 cm^{-1} above the $S = 1$ ground state.

Figure 6.22 illustrates an error surface plot for the fit of variable temperature magnetic susceptibility data for complex **6D**, plotted as a function of J_{wb} and J_{bb} calculated with a *g*-value of 1.9 and a *D*-value of -2.7 cm^{-1}. The plot of J_{wb} vs. J_{bb} vs. error clearly indicates a well defined minimum associated with the calculated fit parameters. It is interesting to note that the magnitude of J_{bb} is invariant to large changes in J_{wb}, suggesting that the "body-body" interaction is the dominant exchange pathway. If the magnitude of J_{wb} is allowed to vary larger or smaller than ±4 cm^{-1} the associated error becomes exceedingly large, confirming that the minimum shown in Figure 6.22 is not merely a local minimum of the error surface, but rather, the system's global minimum.

Complexes **6D-F** can exhibit spin ground states between $S = 0$ and $S = 9$ represented by combinations of values of S_A (4, 3, 2, 1 and 0) and S_B (5, 4, 3, 2, 1 and 0) yielding 110 total non-degenerate states. The population of these states relies heavily on the nature or the exchange pathways (ferromagnetic or antiferromagnetic), the magnitude of the exchange pathways, and the relative ratio of the pathways J_{wb} and J_{bb}. In the case where the magnitude of J_{wb} and J_{bb} is $J < 0$, the total spin will be represented by smaller total spin values, where the total spin is denoted as $S_T = | S_B - S_A|$. However, for the lowest allowable value ($S = 0$) to be the ground state, the spin vectors must all be anti-parallel. It is evident from Scheme 6.2 that this case is impossible to achieve for the exchange pathways intrinsic to the dicubane topology. If Mn(2) and Mn(4) are antiparallel, it is not possible for Mn(1) and Mn(3) to be simultaneously anti-parallel to Mn(2) and Mn(4). This results in a "spin-frustrated" system, where the magnitude of

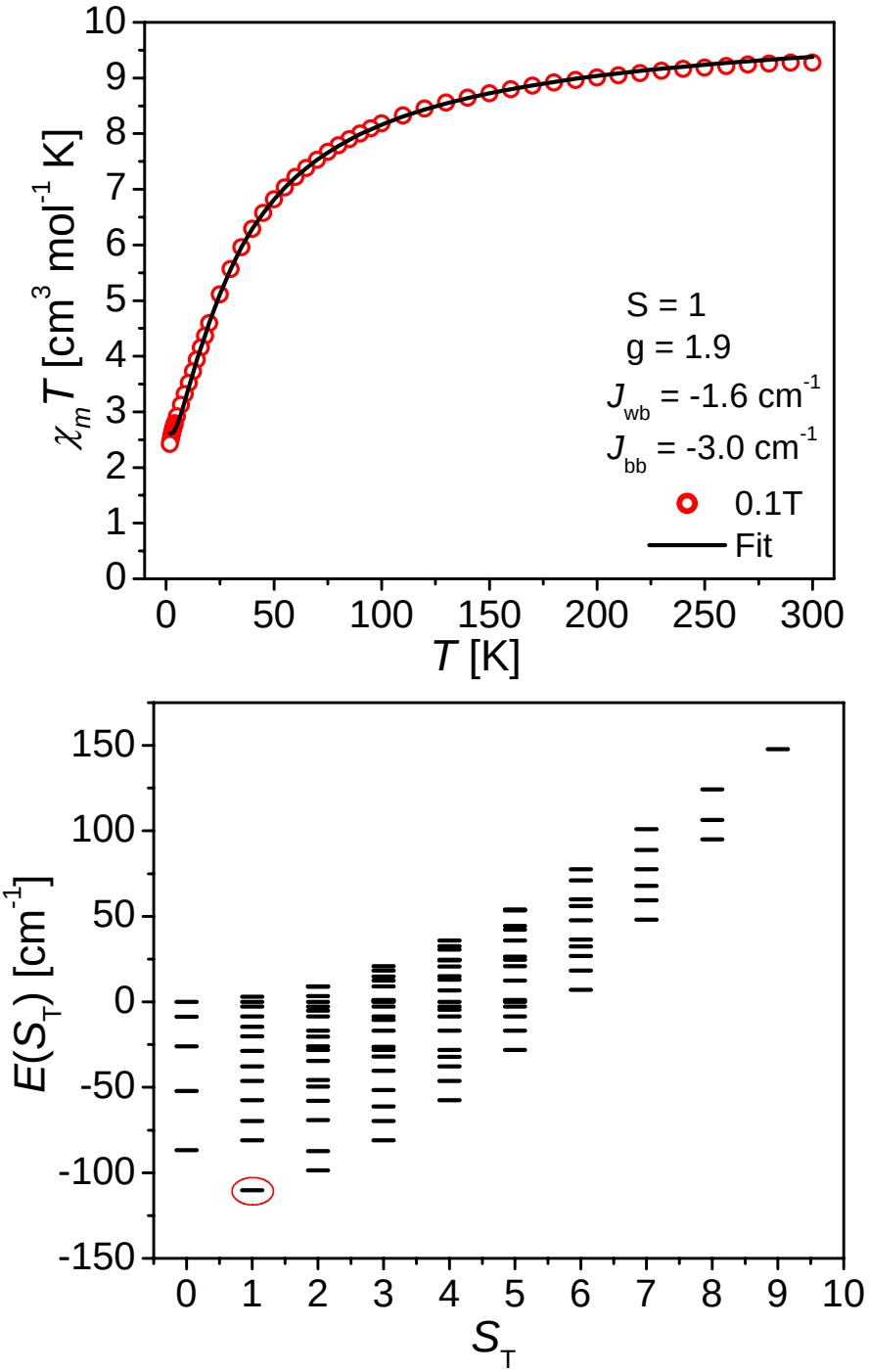

Figure 6.19. (Top) DC magnetic susceptibility with best fit for **[Mn_4(anca)$_4$(edea)$_2$(dbm)$_2$]·CH_2Cl_2 (6D)** from 300K to 1.8K at an applied field of 0.1 Tesla. (○ observed, ─ theoretical fit). (Bottom) Illustrates the distribution of calculated eigen-energies [$E(S_T)$] versus spin total [S_T] of the 110 microstates (S_T, S_B, S_A).

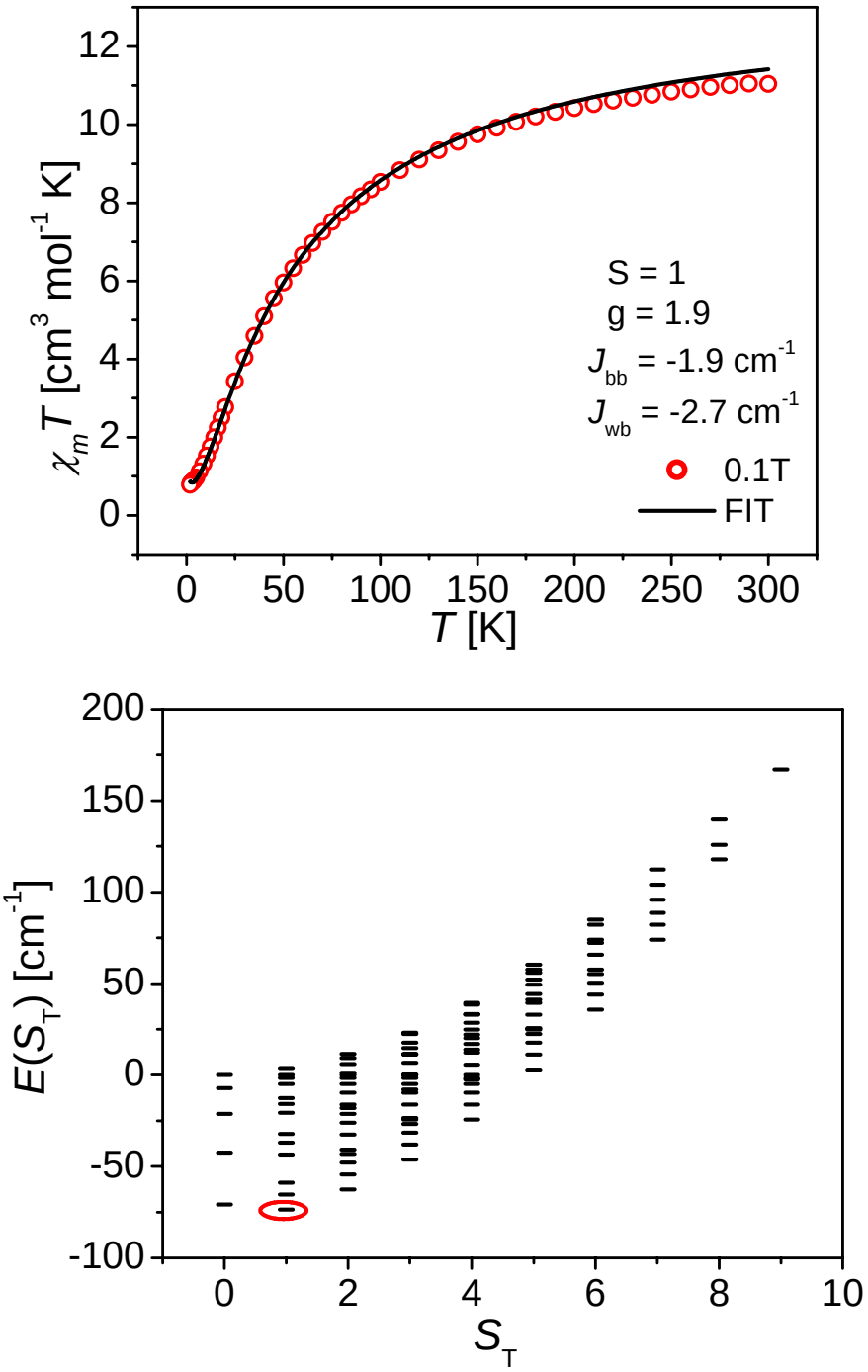

Figure 6.20. (Top) DC magnetic susceptibility with best fit for **[Mn_4(anca)$_4$(n-bdea)$_2$(dbm)$_2$]·CH_3CN (6E)** from 300K to 1.8K at an applied field of 0.1 Tesla. (○ observed, ─ theoretical fit). (Bottom) Illustrates the distribution of calculated eigen-energies [$E(S_T)$] versus spin total [S_T] of the 110 microstates (S_T, S_B, S_A).

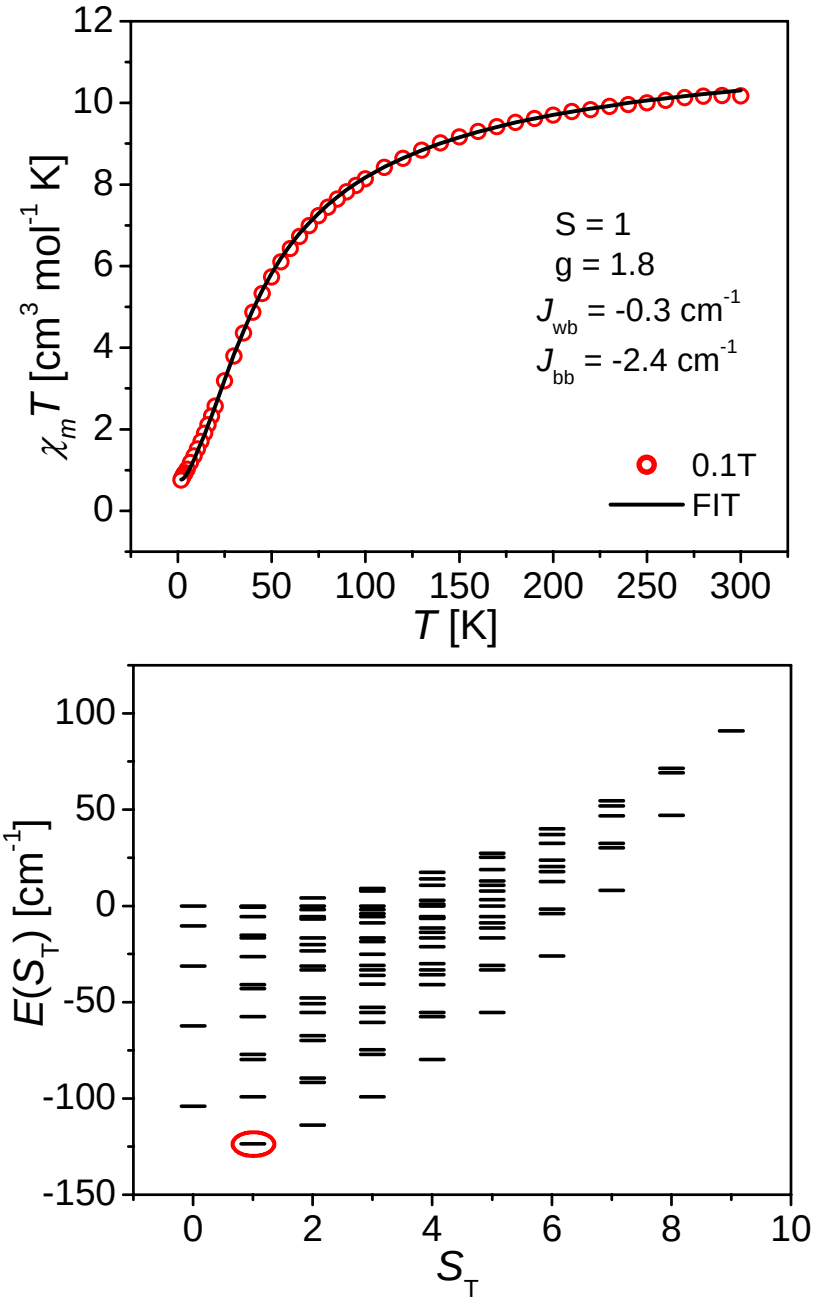

Figure 6.21. (Top) DC magnetic susceptibility with best fit for **[Mn_4(anca)$_4$(t-bdea)$_2$(dbm)$_2$]·Et_2O·CH_3OH (6F)** from 300K to 1.8K at an applied field of 0.1 Tesla. (○ observed, ─ theoretical fit). (Bottom) Illustrates the distribution of calculated eigen-energies [$E(S_T)$] versus spin total [S_T] of the 110 microstates (S_T, S_B, S_A).

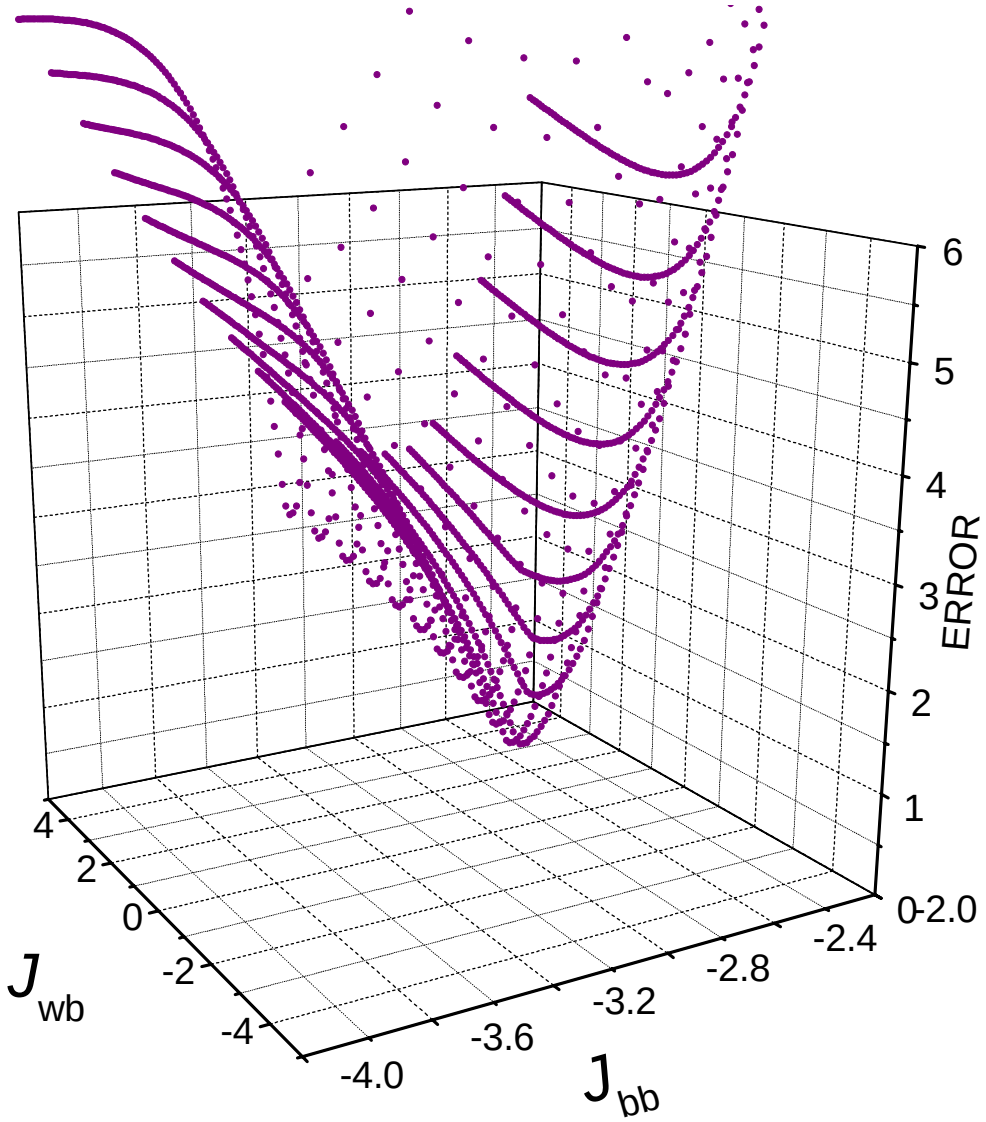

Figure 6.22. Error surface plot for **[Mn_4(anca)$_4$(edea)$_2$(dbm)$_2$]·CH_2Cl_2 (6D)**, with the magnetic exchange pathways J_{bb} and J_{wb} given as a function of the fitting error.

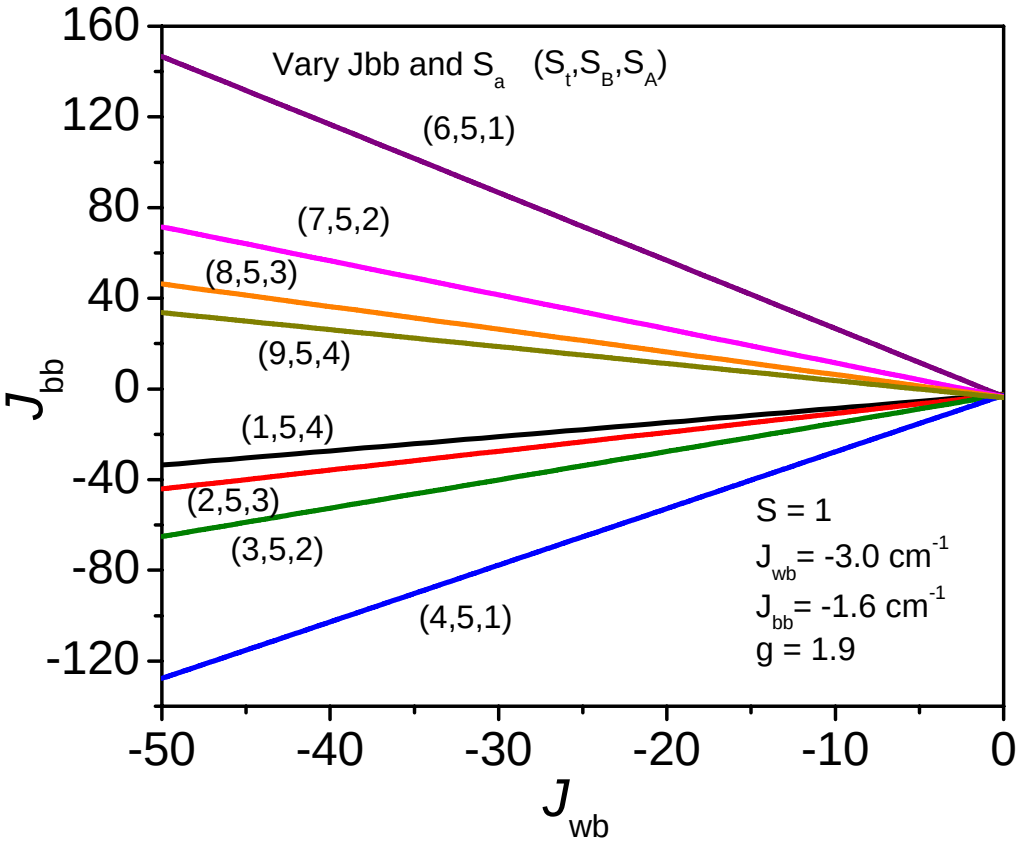

Figure 6.23. Energy diagram for **[Mn_4(anca)$_4$(edea)$_2$(dbm)$_2$]·CH_2Cl_2 (6D)** plotted as J_{bb} vs. J_{wb}. The diagram shows changes in the total spin (S_T) as a function of J_{wb} and S_A.

the frustration, and thus the value of the intermediate spin, is governed by the magnitude of the competing magnetic exchange pathways. The frustrated pathways lead to canting of one or more of the spin-vectors from anti-parallel yielding a non-zero, intermediate, ground state as previously demonstrated by Libby *et al* for Mn_4 "butterfly" complexes.[77]

Figure 6.23 shows the effect that the magnitudes of J_{wb} and J_{bb} have on the overall spin ground state for complex **6D**. Though, this method is applicable to all of the complexes herein. As documented in the error surface map in Figure 6.22, the spin ground state for complex **6D** is invariant to quite large changes in the magnitude of the "wing-body" interaction. However, small changes in J_{bb} with values of J_{wb} (J = 0 to -4 cm^{-1}) incrementally step through all of the possible spin ground states, assuming that S_B is constant and relies only on changes in S_A, J_{bb} and J_{wb}, as seen in Figure 6.23.

There are notable differences between complexes **6D-F** and complexes reported by Wittick *et al.* [67] that have a similar dicubane topology with reversed oxidation states. The Mn^{II}-O-Mn^{II} ('body-body") interaction is the dominant pathway in the present case as well as the complexes reported by Wittick.[67] However, in the previously reported complexes the J_{bb} interaction was reported to be weakly ferromagnetic, with calculated values of 0.7 cm^{-1} and 2.1 cm^{-1}, with bond angles Mn^{II}-O-Mn^{II} of 99.09Å and 97.48Å, respectively. Interestingly, the Mn^{II}-O-Mn^{II} bond angles in complexes **6D-F** are significantly smaller, ranging between 93.07Å and 94.95Å, but are all negative and weakly antiferromagnetic. One might expect that the smaller bond angles in complexes **6D-F** would exhibit similar behavior (positive coupling constants) due to greater orthogonality. However, reasonable fits of magnetic susceptibility data for complexes

6D-F could not be achieved with a positive "body-body" coupling constant, suggesting that the "body-body" exchange parameter is greatly influenced by the magnitude of other exchange pathways within the oxo-bridged tetranuclear core leading to greater orbital mixing and dominant antiferromagnetic exchange interactions.

Reduced Magnetization

To further ascertain the spin ground state and magnitude of the zero-field splitting parameter *D*, magnetization data were collected for complexes **$[Mn_4(anca)_4(edea)_2(dbm)_2]\cdot CH_2Cl_2$ (6D), $[Mn_4(anca)_4(n\text{-}bdea)_2(dbm)_2]\cdot CH_3CN$ (6E)** and **$[Mn_4(anca)_4(t\text{-}bdea)_2(dbm)_2]\cdot Et_2O\cdot CH_3OH$ (6F)** between 4K and 1.9K with applied fields of 2-5T and are plotted in Figures 6.24-26 as *M/Nβ vs. H/T*, where *M* is the molar magnetization, *N* is Avogadro's number, β is the Bohr magneton, *H* is the applied magnetic field and *T* is the absolute temperature in Kelvin. The saturation values between ~1.9-1.8 in Figures 6.24-4.26 suggest that complexes **6D-F** exhibit approximately S = 1

$$\mathcal{H} = \mu_B gH \cdot S + D[S_Z^2 - \frac{1}{3}S(S+1)] \qquad \textbf{(6.10)}$$

spin ground states, and a small degree of zero-field splitting, due to the presence of non-superimposibility of the iso-fields. Theoretical fits to the magnetization data, solid lines in Figures 6.24-6.26 were calculated by full-matrix diagonalization employing energy Hamiltonian given in Equation 6.10, where $\mu_B gH\cdot S$ is the Zeeman term, where μ is the

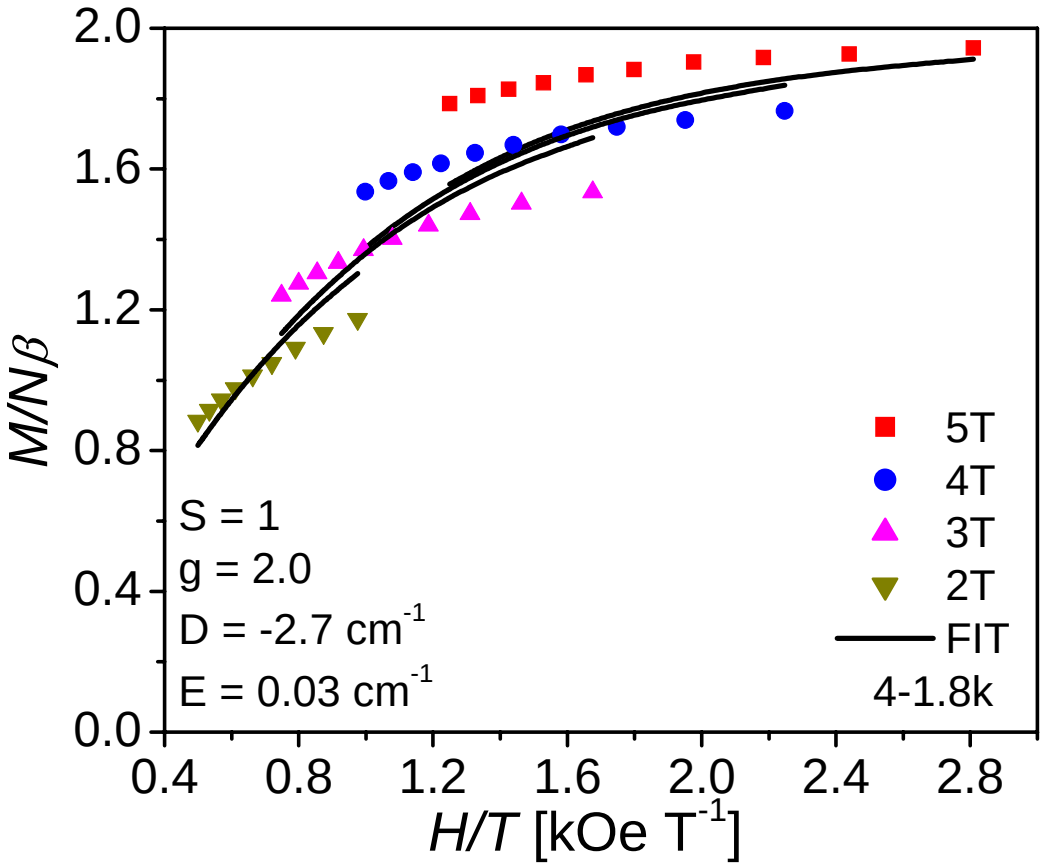

Figure 6.24. Plot of reduced magnetization ($M/N\beta$) versus H/T data for complex **[Mn_4(anca)$_4$(edea)$_2$(dbm)$_2$]·CH_2Cl_2 (6D)**, where M is the molar magnetization, N is Avogadro's number, and β is the Bohr magneton. Data were collected at 5 (■), 4 (●), 3 (▲) and 2 (▼) in the temperature range of 4-1.8 K. The solid lines represent a theoretical fit of the data yielding fitting parameters of S = 1, g = 2.0, D = -2.7 cm^{-1}, and E = 0.03 cm^{-1}.

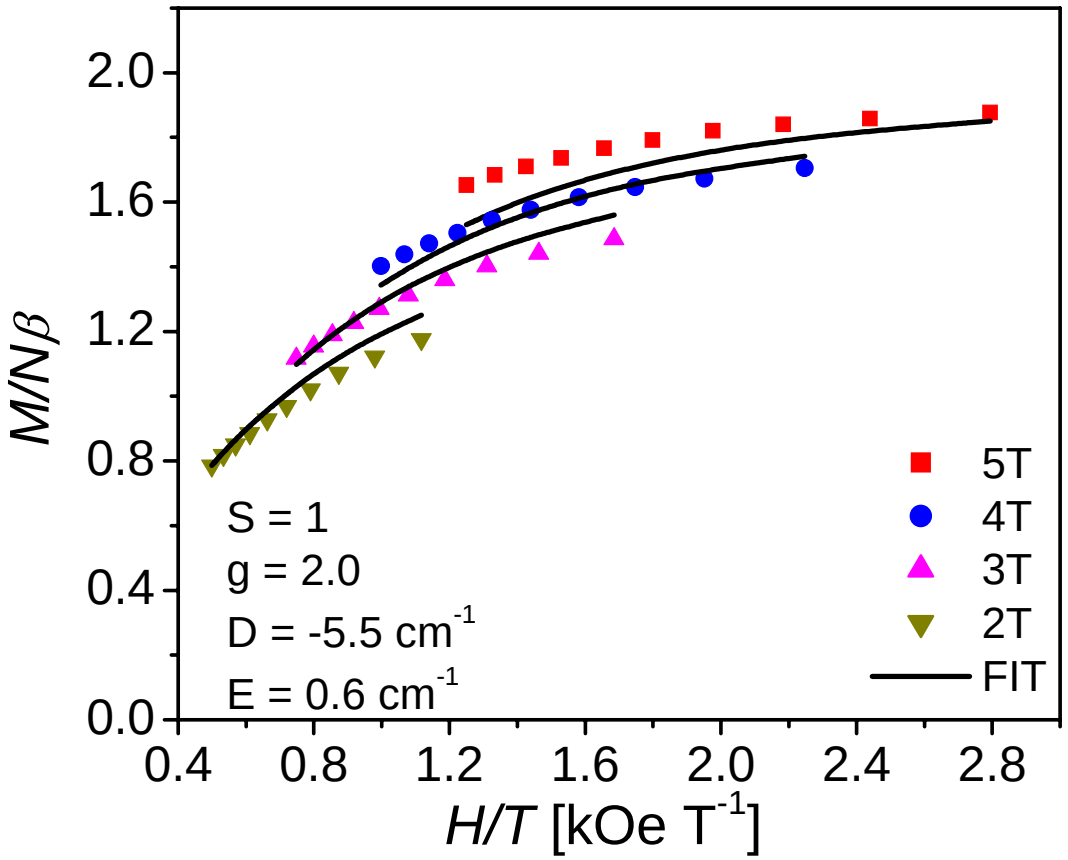

Figure 6.25. Plot of reduced magnetization ($M/N\beta$) versus H/T data for complex **$[Mn_4(anca)_4(n\text{-}bdea)_2(dbm)_2]\cdot CH_3CN$ (6E)**, where M is the molar magnetization, N is Avogadro's number, and β is the Bohr magneton. Data were collected at 5 (■), 4 (●), 3 (▲) and 2 (▼) in the temperature range of 4-1.8 K. The solid lines represent a theoretical fit of the data yielding fitting parameters of S = 1, g = 2.0, D = -5.5 cm^{-1}, and E = 0.6 cm^{-1}.

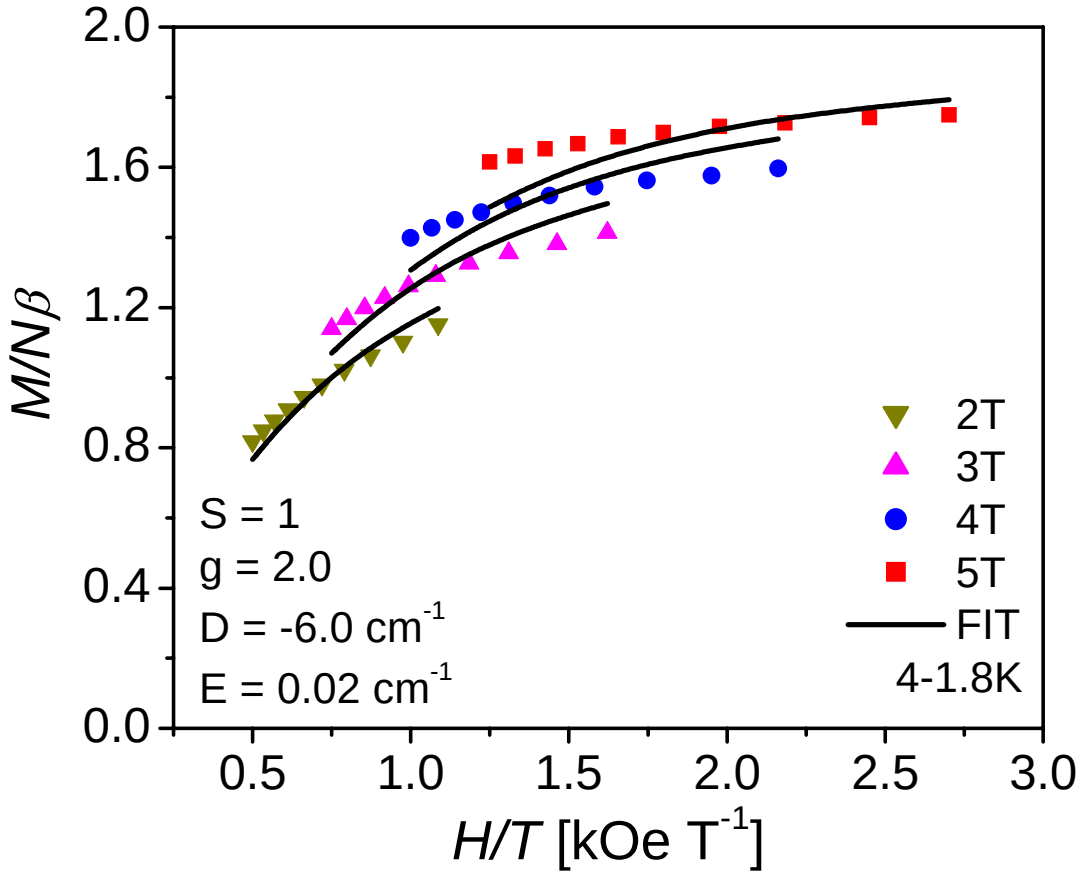

Figure 6.26. Plot of reduced magnetization (*M/Nβ*) versus H/T data for complex **[Mn_4(anca)$_4$(t-bdea)$_2$(dbm)$_2$]·Et_2O·CH_3OH (6F),** where *M* is the molar magnetization, *N* is Avogadro's number, and *β* is the Bohr magneton. Data were collected at 5 (■), 4 (●), 3 (▲) and 2 (▼) Tesla in the temperature range of 4-1.8 K. The solid lines represent a theoretical fit of the data yielding fitting parameters of S = 1, *g* = 2.0, *D* = -6.0 cm^{-1}, and *E* = 0.02 cm^{-1}.

Bohr magneton, g is the Landé g-factor, H is the applied magnetic field, S is the total spin, D is the second–order zero-field splitting parameter and E is the second-order rhombic term. Least-squares treatment of the magnetization data gave a best fit, indicated by the solid lines in Figures 6.24-6.26, and the calculated fitting parameters presented in Table 6.17.

The model used to fit the *M/Nβ vs. H/T* data for complexes **6D-F** assumes that there exists only a well-isolated ground state experiencing zero-field splitting. However, the relatively poor fits to *M/Nβ vs. H/T*, as seen by the solid lines in Figures 6.24-6.26**,** further corroborate the presence of excited states that lie very close in energy to the calculated $S = 1$ ground state, suggesting that S and M_s are not good quantum number, and thus, cannot be used to properly describe the electronic interactions in these complexes.

$[Mn_4(anca)_4(Htea)_2(dbm)_2]$ (6C). It has been shown that the equivalent operator method is only truly valid where there exists a well-behaved, or well-isolated spin ground state such as in the $Mn^{III}_3Mn^{IV}$, $S = 9/2$ cubane complexes. Thus, a more complete basis set must be employed in order to fully describe the ground state $S = 1$ spin-manifold. To account for mixing of all the populated low lying excited states into the ground state, an uncoupled basis set was used for complex **6C** employing full matrix diagonalization. In addition to the HDVV type (isotropic) super-exchange discussed in section *vide supra*, the Dzialoshinsky-Moriya type antisymmetric exchange interactions, zero-field splitting, and Zeeman interactions were also factored in order to fully model the spin Hamiltonian of the system (Equation 6.11):

$$\hat{H} = \hat{H}_{\text{ex}} + \hat{H}_{\text{DM}} + \hat{H}_{\text{zfs}} + \hat{H}_{\text{Zeeman}} \quad \textbf{(6.11)}$$

$$\hat{H}_{ex} = -2J_{wb}(\hat{S}_1 + \hat{S}_3) \bullet (\hat{S}_2 + \hat{S}_4) - 2J_{bb}\hat{S}_2\hat{S}_4 = J_{wb}(\hat{S}_{13}^2 + \hat{S}_{24}^2 - \hat{S}_T^2) + J_{bb}(\hat{S}_2^2 + \hat{S}_4^2 - \hat{S}_{24}^2) \quad \textbf{(6.12)}$$

$$\hat{H}_{\text{DM}} = \boldsymbol{d}_{12} \bullet \hat{S}_1 \times \hat{S}_2 + \boldsymbol{d}_{23} \bullet \hat{S}_2 \times \hat{S}_3 + \boldsymbol{d}_{34} \bullet \hat{S}_3 \times \hat{S}_4 + \boldsymbol{d}_{41} \bullet \hat{S}_4 \times \hat{S}_1 \quad \textbf{(6.13)}$$

$$\hat{H}_{zfs} = \sum_{j=1,3} D(\hat{S}_{j\zeta}^2 - \frac{1}{3}\hat{S}_j^2) = \sum_{j=1,3} D\left[(\hat{S}_j^x \cos\phi_j \sin\theta_j + \hat{S}_j^y \sin\phi_j \sin\theta_j + \hat{S}_j^z \cos\theta_j)^2 - \frac{1}{3}\hat{S}_j^2 \right]$$

$$= \sum_{j=1,3} D\left[(\frac{\sin\theta_j}{2} e^{-i\phi_j} \hat{S}_j^+ + \frac{\sin\theta_j}{2} e^{+i\phi_j} \hat{S}_j^- + \hat{S}_j^z \cos\theta_j)^2 - \frac{1}{3} S_j(S_j+1) \right], \quad \textbf{(6.14)}$$

$$\hat{H}_{\text{Zeeman}} = -g\beta \sum_{j=1}^{4} (H_x \hat{S}_j^x + H_y \hat{S}_j^y + H_z \hat{S}_j^z), \quad \textbf{(6.15)}$$

where $\hat{S}_j$ stands for the spin operator of *j*-th spin (S = 5/2 for Mn^{II} and S = 2 for Mn^{III}), $\hat{S}_{13} \equiv \hat{S}_1 + \hat{S}_3$, $\hat{S}_{24} \equiv \hat{S}_2 + \hat{S}_4$ and $\hat{S}_{\text{T}} \equiv \hat{S}_{13} + \hat{S}_{24}$ are the partial-sum and the resultant spin operators, respectively, J_{wb} and J_{bb} are defined as in Equation 6.12 , $\boldsymbol{d}_{ij}$ is the Dzialoshinsky-Moriya vector for the interaction between *i*-th and *j*-th ions (Equation. 6.13), D is the uniaxial zero-field splitting parameter for each ion, (ϕ_j, θ_j) are the azimuthal and polar angles of single-ion anisotropy axis ζ for *j*-th ion (Equation. **6.14**), g is the Landé g factor, β is the Bohr magneton, and H_α is α-component of external magnetic field H (Equation. **6.15**).

Due to the symmetry of the $Mn^{III}_2Mn^{II}_2$ cluster, the quantization axes in the anisotropy term $\hat{H}_{\text{zfs}}$ are aligned in the same direction, and were taken as parallel, *i.e.* (ϕ_1, θ_1) = (ϕ_3, θ_3) = (0°, 0°). The Jahn-Teller elongation axes for the two Mn^{III} ions in complex **6C** are parallel. In order to avoid over-parameterization, the Dzialoshinsky-

Moriya vectors for the Mn-O-Mn interaction pathways were taken to be identical, and perpendicular to the molecular plane,[64] *i.e.* $\boldsymbol{d}_{12} = \boldsymbol{d}_{23} = \boldsymbol{d}_{34} = \boldsymbol{d}_{41} = (0, 0, d)$. Other interactions, such as biquadratic exchange interaction, were omitted in the present treatment since their contribution to thermodynamic quantities is not dominant.

Based on this spin Hamiltonian, magnetization values $M(H, T)$ are evaluated by the conventional way as given in equation Equation 6.16:

$$M(H,T) = \frac{Ng\mu_{\mathrm{B}}}{4\pi} \int \mathrm{d}\cos\theta \int \mathrm{d}\phi \frac{\langle \boldsymbol{S}_{\mathrm{T}} \rangle \bullet \boldsymbol{H}}{H} \tag{6.16}$$

$$\text{where, } \langle \boldsymbol{S}_{\mathrm{T}} \rangle = \mathrm{Tr}\left[\hat{S}_{\mathrm{T}} \exp\left(-\hat{H}(\boldsymbol{H})/k_{\mathrm{B}}T\right)\right] / Z(\boldsymbol{H}) \tag{6.17}$$

$$\text{and, } Z(\boldsymbol{H}) \equiv \mathrm{Tr}\left[\exp\left(-\hat{H}(\boldsymbol{H})/k_{\mathrm{B}}T\right)\right] \tag{6.18}$$

where N is Avogadro's number, and (θ, ϕ) are polar and azimuthal angles of the external field $\boldsymbol{H}$, k_{B} is the Boltzmann constant, T is the temperature, and the trace is evaluated using a set of energy eigenvectors $|E_i\rangle$, *i.e.* $\mathrm{Tr}[A] = \sum_i \langle E_i | A | E_i \rangle$, following the full-matrix diagonalization of the spin Hamiltonian by an LAPACK subroutine ZHEEV.[80] The powder average procedure over (θ, ϕ) was approximated by spherical gaussian quadrature using 43-point Lebedev grid on a hemisphere.[81] The temperature-independent contribution from the Van Vleck paramagnetism χ_{TIP}, was also considered.

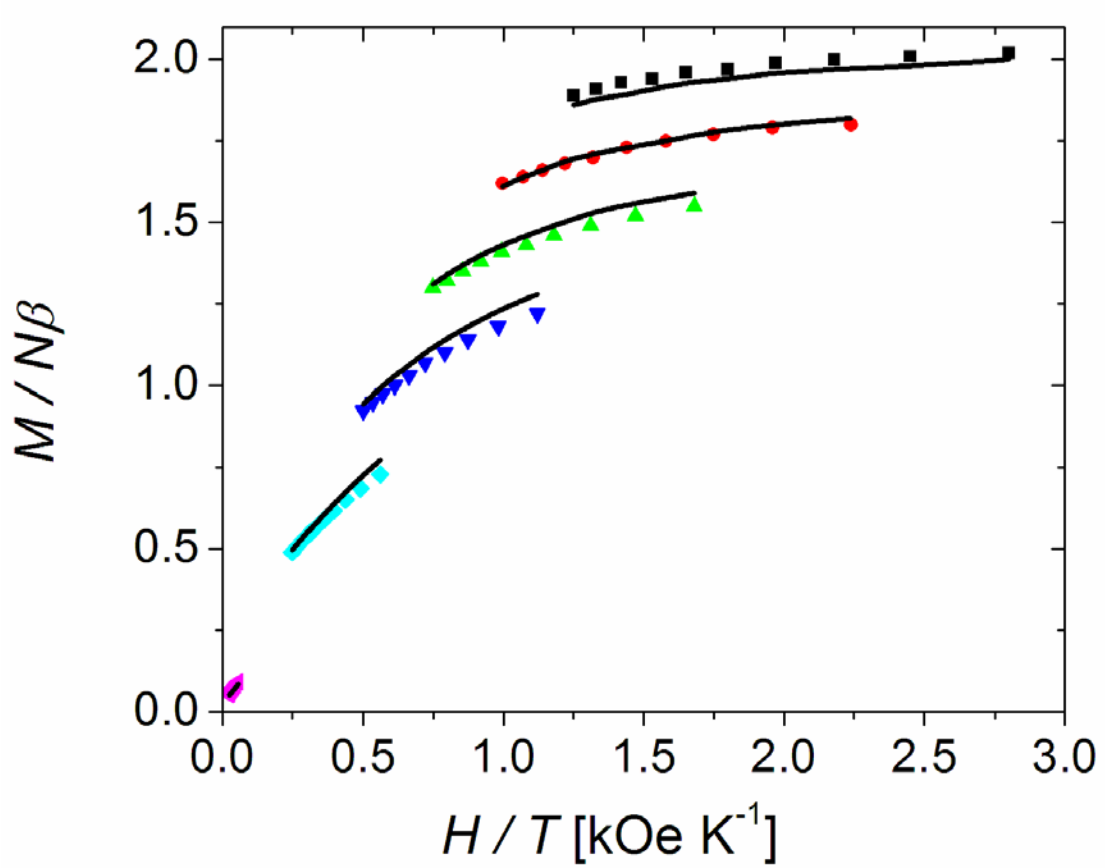

Figure 6.27. Plot of reduced magnetization ($M/N\beta$) versus H/T data for complex **6C**, where M is the molar magnetization, N is Avogadro's number, and β is the Bohr magneton. Data were collected at 5 (■), 4 (●), 3 (▲), 2 (▼), 1 (♦) and 0.1T (◀) in the temperature range of 1.8-4 K. The solid lines represent a theoretical fit of the data employing the full (900 x 900) Hamiltonian matrix diagonalization on each iteration. This gave fitting values of S = 1, g = 2.2, D = -9.2 cm^{-1}, and J = -2.8 cm^{-1}.

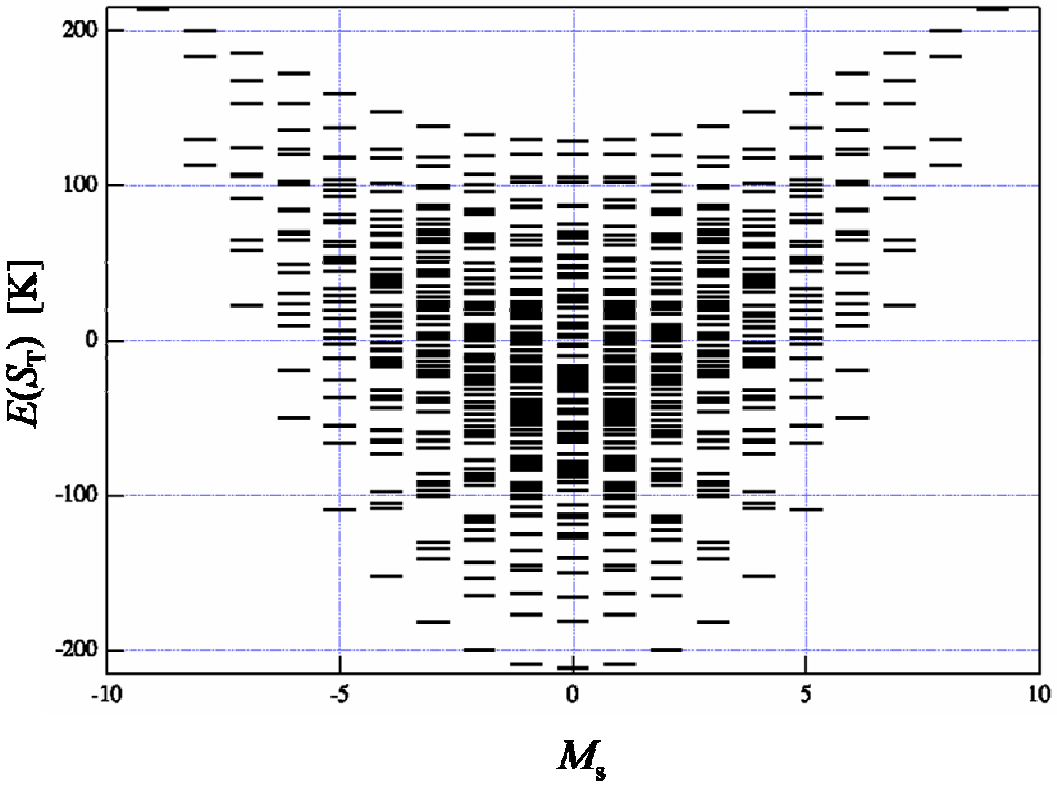

Figure 6.28. Plot of the eigen-energies ($E(S_T)$) of the M_s states of the S = 0, 1, 2 ….9 spin multiplets versus M_s, depicting nesting of the individual spin multiplets.

The optimized parameter set (g, J_{wb}, J_{bb}, d, D, χ_{TIP}) for complex **6C** is obtained by minimizing a square deviation sum of effective magnetic moment, $\sum[\mu_{eff}(obs)-\mu_{eff}(calc)]^2$ ($\mu_{eff}=\sqrt{3Mk_BT/NH}$), using a downhill simplex algorithm.[82-85]

Figure 6.27 illustrates a plot of the reduced magnetization ($M/N\beta$) versus H/T data for complex **6C** employing the full-matrix diagonalization approach. Data were collected at 5, 4, 3, 2, 1 and 0.1T in the temperature range of 1.8-4 K. The solid lines represent a theoretical fit that gave fitting values of S = 1, g = 2.2, D = -9.2 cm^{-1}, and J = -2.8 cm^{-1}. It should be noted that the theoretical fit depicted in Figure 6.27 (solid lines) is based on a model employing a single J-value (Scheme 6.3A), however, it can be seen in Figure 6.27 that the fit is quite good. It is not possible to fit these magnetization data assuming only an isolated S = 1 ground state. Figure 6.28 presents a plot of the eigen-energy ($E(S_T)$) as a function of the M_s spin manifolds, and there is clearly a high degree of nesting of the S multiplets suggesting that S and M_s are not good magnetic quantum numbers.

6.4 Conclusion

A series of new [Mn_4] dicubane complexes have been prepared that exhibit S =1 ground states that are heavily influenced by low-lying excited states. Two of the complexes (**6A** and **6B**) appear to be have a wheel topology, supported by the relatively long Mn-O contact distances across the wheel and by the success of fitting the susceptibility data with only one J-value. Since there are low-lying excited states, the

Kambe approach is a simplified method. The full Hilbert space (900 x 900) Hamiltonian matrix (set up in the uncoupled basis set and incorporating single-ion zero-field and Zeeman interactions) has to be diagonalized on fitting iterations. Results from the full-matrix diagonalization approach show that the reduced magnetization data for both complexes can be fit employing only one *J*-value. Additional full-matrix diagonalization calculations are in progress for both variable temperature dc susceptibility data and reduced magnetization data employing a two *J*-value model (Scheme **2**) and a symmetry dictated two *J*-value model (Scheme **3**) where there are alternating coupling constants around the periphery of the wheel. These calculations will be fully described in a later paper.

Chapter 6, in part, is a reprint: Beedle, C. C., Heroux, K. J., Nakano, M.; DiPasquale, A. G., Rheingold, A. L., Hendrickson, D. N., Antiferromagnetic Tetranuclear Manganese Complex: Wheel or Dicubane? *Polyhedron* **2007,** 26, (9-11), 2200-2206. The dissertation author is the primary investigator and author of this material.

6.5 References

(1) Sessoli, R.; Tsai, H. L.; Schake, A. R.; Wang, S. Y.; Vincent, J. B.; Folting, K.; Gatteschi, D.; Christou, G.; Hendrickson, D. N. *Journal of the American Chemical Society* **1993**, *115*, 1804-1816.

(2) Christou, G.; Gatteschi, D.; Hendrickson, D. N.; Sessoli, R. *Mrs Bulletin* **2000**, *25*, 66-71.

(3) Cornia, A.; Fabretti, A. C.; Sessoli, R.; Sorace, L.; Gatteschi, D.; Barra, A. L.; Daiguebonne, C.; Roisnel, T. *Acta Crystallographica Section C-Crystal Structure Communications* **2002**, *58*, m371-m373.

(4) Hill, S.; Datta, S.; Liu, J.; Inglis, R.; Milios, C. J.; Feng, P. L.; Henderson, J. J.; del Barco, E.; Brechin, E. K.; Hendrickson, D. N. *Dalton Transactions*, *39*, 4693-4707.

(5) Hill, S.; Edwards, R. S.; North, J. M.; Park, K.; Dalal, N. S. *Polyhedron* **2003**, *22*, 1889-1896.

(6) Kadam, R. M.; Sastry, M. D.; Bhide, M. K.; Chavan, S. A.; Yakhmi, J. V.; Kahn, O. *Chemical Physics Letters* **1997**, *281*, 292-296.

(7) Lawrence, J.; Yang, E.-C.; Edwards, R.; Olmstead, M. M.; Ramsey, C.; Dalal, N. S.; Gantzel, P. K.; Hill, S.; Hendrickson, D. N. *Inorganic Chemistry* **2008**, *47*, 1965-1974.

(8) Oshio, H.; Toriumi, K.; Maeda, Y.; Takashima, Y. *Inorganic Chemistry* **1991**, *30*, 4252-4260.

(9) Parks, B.; Loomis, J.; Rumberger, E.; Yang, E. C.; Hendrickson, D. N.; Christou, G. *Journal of Applied Physics* **2002**, *91*, 7170-7172.

(10) Datta, S.; Bolin, E.; Inglis, R.; Milios, C. J.; Brechin, E. K.; Hill, S. *Polyhedron* **2009**, *28*, 1788-1791.

(11) Bencini, A.; Gatteschi, D. *Journal of Magnetic Resonance* **1979**, *34*, 653-656.

(12) Friedman, J. R.; Sarachik, M. P.; Ziolo, R. *Physical Review B* **1998**, *58*, R14729-R14732.

(13) Parks, B.; Loomis, J.; Rumberger, E.; Hendrickson, D. N.; Christou, G. *Physical Review B* **2001**, *64*, 184426.

(14) Sessoli, R.; Caneschi, A.; Gatteschi, D.; Sorace, L.; Cornia, A.; Wernsdorfer, W. *Journal of Magnetism and Magnetic Materials* **2001**, *226*, 1954-1960.

(15) Wernsdorfer, W.; Caneschi, A.; Sessoli, R.; Gatteschi, D.; Cornia, A.; Villar, V.; Paulsen, C. *Physical Review Letters* **2000**, *84*, 2965-2968.

(16) Wernsdorfer, W.; Mailly, D.; Timco, G. A.; Winpenny, R. E. P. *Physical Review B (Condensed Matter and Materials Physics)* **2005**, *72*, 060409.

(17) Wernsdorfer, W.; Ohm, T.; Sangregorio, C.; Sessoli, R.; Gatteschi, D.; Paulsen, C. *Physica B* **2000**, *284*, 1229-1230.

(18) Zeng, Z.; Guenzburger, D.; Ellis, D. E. *Physical Review B* **1999**, *59*, 6927-6937.

(19) Gatteschi, D.; Sessoli, R.; Villian, J. *Molecular Nanomagnets*; Oxford University Press: Oxford, 2006.

(20) Kahn, O. *Molecular magnetism*; VCH: New York, NY, 1993.

(21) Carlin, R. L.; van Duyneveldt, A. J. *Magnetic Properties of Transition Metal Complexes*; Springer-Verlag: New York, NY, 1977.

(22) Anastasios, J. T.; Alina, V.; Wolfgang, W.; Khalil, A. A.; George, C. *Angewandte Chemie International Edition* **2004**, *43*, 2117-2121.

(23) Manoli, M.; Prescimone, A.; Mishra, A.; Parsons, S.; Christou, G.; Brechin, E. K. *Dalton Transactions* **2007**, 532-534.

(24) Murugesu, M.; Raftery, J.; Wernsdorfer, W.; Christou, G.; Brechin, E. K. *Inorganic Chemistry* **2004**, *43*, 4203-4209.

(25) Rumberger, E. M.; Shah, S. J.; Beedle, C. C.; Zakharov, L. N.; Rheingold, A. L.; Hendrickson, D. N. *Inorganic Chemistry* **2005**, *44*, 2742-2752.

(26) Rumberger, E. M.; Zakharov, L. N.; Rheingold, A. L.; Hendrickson, D. N. *Inorganic Chemistry* **2004**, *43*, 6531-6533.

(27) Scott, R. T. W.; Milios, C. J.; Vinslava, A.; Lifford, D.; Parsons, S.; Wernsdorfer, W.; Christou, G.; Brechin, E. K. *Dalton Transactions* **2006**, 3161-3163.

(28) Shah, S. J.; Ramsey, C. M.; Heroux, K. J.; DiPasquale, A. G.; Dalal, N. S.; Rheingold, A. L.; del Barco, E.; Hendrickson, D. N. *Inorganic Chemistry* **2008**, *47*, 9569-9582.

(29) Shah, S. J.; Ramsey, C. M.; Heroux, K. J.; O'Brien, J. R.; DiPasquale, A. G.; Rheingold, A. L.; del Barco, E.; Hendrickson, D. N. *Inorganic Chemistry* **2008**, *47*, 6245-6253.

(30) Theocharis , C. S.; Khalil , A. A.; Wolfgang, W.; George, C. *Angewandte Chemie International Edition* **2008**, *47*, 6694-6698.

(31) Abbati, G. L.; Cornia, A.; Fabretti, A. C.; Caneschi, A.; Gatteschi, D. *Inorganic Chemistry* **1998**, *37*, 1430-+.

(32) Alexiou, M.; Zaleski, C. M.; Dendrinou-Samara, C.; Kampf, J.; Kessissoglou, D. P.; Pecoraro, V. L. *Zeitschrift Fur Anorganische Und Allgemeine Chemie* **2003**, *629*, 2348-2355.

(33) Aromi, G.; Claude, J. P.; Knapp, M. J.; Huffman, J. C.; Hendrickson, D. N.; Christou, G. *Journal of the American Chemical Society* **1998**, *120*, 2977-2978.

(34) Aromi, G.; Claude, J. P.; Knapp, M. J.; Huffman, J. C.; Hendrickson, D. N.; Christou, G. *Journal of the American Chemical Society* **1998**, *120*, 2977-2978.

(35) Aubin, S. M. J.; Wemple, M. W.; Adams, D. M.; Tsai, H. L.; Christou, G.; Hendrickson, D. N. *Journal of the American Chemical Society* **1996**, *118*, 7746-7754.

(36) Bolcar, M. A.; Aubin, S. M. J.; Folting, K.; Hendrickson, D. N.; Christou, G. *Chemical Communications* **1997**, 1485-1486.

(37) Brechin, E. K.; Boskovic, C.; Wernsdorfer, W.; Yoo, J.; Yamaguchi, A.; Sanudo, E. C.; Concolino, T. R.; Rheingold, A. L.; Ishimoto, H.; Hendrickson, D. N.; Christou, G. *Journal of the American Chemical Society* **2002**, *124*, 9710-9711.

(38) Brechin, E. K.; Sanudo, E. C.; Wernsdorfer, W.; Boskovic, C.; Yoo, J.; Hendrickson, D. N.; Yamaguchi, A.; Ishimoto, H.; Concolino, T. E.; Rheingold, A. L.; Christou, G. *Inorganic Chemistry* **2005**, *44*, 502-511.

(39) Brechin, E. K.; Soler, M.; Christou, G.; Davidson, J.; Hendrickson, D. N.; Parsons, S.; Wernsdorfer, W. *Polyhedron* **2003**, *22*, 1771-1775.

(40) Brechin, E. K.; Soler, M.; Christou, G.; Helliwell, M.; Teat, S. J.; Wernsdorfer, W. *Chemical Communications* **2003**, 1276-1277.

(41) Christmas, C.; Vincent, J. B.; Chang, H. R.; Huffman, J. C.; Christou, G.; Hendrickson, D. N. *Journal of the American Chemical Society* **1988**, *110*, 823-830.

(42) Eppley, H. J.; Aubin, S. M. J.; Streib, W. E.; Bollinger, J. C.; Hendrickson, D. N.; Christou, G. *Inorganic Chemistry* **1997**, *36*, 109-115.

(43) Eppley, H. J.; deVries, N.; Wang, S. Y.; Aubin, S. M.; Tsai, H. L.; Folting, K.; Hendrickson, D. N.; Christou, G. *Inorganica Chimica Acta* **1997**, *263*, 323-340.

(44) Eppley, H. J.; Wang, S. Y.; Tsai, H. L.; Aubin, S. M.; Folting, K.; Streib, W. E.; Hendrickson, D. N.; Christou, G. *Molecular Crystals & Liquid Crystals Science & Technology Section A-Molecular Crystals & Liquid Crystals* **1995**, *273*, A 159-A 166.

(45) Feng, P. L.; Beedle, C. C.; Koo, C.; Wernsdorfer, W.; Nakano, M.; Hill, S.; Hendrickson, D. N. *Inorganic Chemistry* **2008**, *47*, 3188-3204.

(46) Feng, P. L.; Stephenson, C. J.; Amjad, A.; Ogawa, G.; del Barco, E.; Hendrickson, D. N. *Inorganic Chemistry*, *49*, 1304-1306.

(47) Hendrickson, D. N.; Christou, G.; Schmitt, E. A.; Libby, E.; Bashkin, J. S.; Wang, S. Y.; Tsai, H. L.; Vincent, J. B.; Boyd, P. D. W.; Huffman, J. C.; Folting, K.; Li, Q. Y.; Streib, W. E. *Journal of the American Chemical Society* **1992**, *114*, 2455-2471.

(48) Libby, E.; Webb, R. J.; Streib, W. E.; Folting, K.; Huffman, J. C.; Hendrickson, D. N.; Christou, G. *Inorganic Chemistry* **1989**, *28*, 4037-4040.

(49) McCusker, J. K.; Jang, H. G.; Wang, S.; Christou, G.; Hendrickson, D. N. *Inorganic Chemistry* **1992**, *31*, 1874-1880.

(50) Miyasaka, H.; Nezu, T.; Iwahori, F.; Furukawa, S.; Sugimoto, K.; Clerac, R.; Sugiura, K.; Yamashita, M. *Inorganic Chemistry* **2003**, *42*, 4501-4503.

(51) Miyasaka, H.; Nezu, T.; Sugimoto, K.; Sugiura, K.; Yamashita, M.; Clerac, R. *Chemistry-a European Journal* **2005**, *11*, 1592-1602.

(52) Murugesu, M.; Takahashi, S.; Wilson, A.; Abboud, K. A.; Wernsdorfer, W.; Hill, S.; Christou, G. *Inorganic Chemistry* **2008**, *47*, 9459-9470.

(53) Murugesu, M.; Wernsdorfer, W.; Abboud, K. A.; Christou, G. *Polyhedron* **2005**, *24*, 2894-2899.

(54) Oshio, H.; Nihei, M.; Yoshida, A.; Nojiri, H.; Nakano, M.; Yamaguchi, A.; Karaki, Y.; Ishimoto, H. *Chemistry-a European Journal* **2005**, *11*, 843-848.

(55) Sessoli, R.; Gatteschi, D.; Caneschi, A.; Novak, M. A. *Nature* **1993**, *365*, 141-143.

(56) Yang, E. C.; Harden, N.; Wernsdorfer, W.; Zakharov, L.; Brechin, E. K.; Rheingold, A. L.; Christou, G.; Hendrickson, D. N. *Polyhedron* **2003**, *22*, 1857-1863.

(57) Libby, E.; Folting, K.; Huffman, C. J.; Huffman, J. C.; Christou, G. *Inorganic Chemistry* **1993**, *32*, 2549-2556.

(58) Liu, F. Q.; Tilley, T. D. *Inorganic Chemistry* **1997**, *36*, 5090-5096.

(59) Miyasaka, H.; Clerac, R.; Mizushima, K.; Sugiura, K.; Yamashita, M.; Wernsdorfer, W.; Coulon, C. *Inorganic Chemistry* **2003**, *42*, 8203-8213.

(60) Henderson, J. J.; Koo, C.; Feng, P. L.; del Barco, E.; Hill, S.; Tupitsyn, I. S.; Stamp, P. C. E.; Hendrickson, D. N. *Physical Review Letters* **2009**, *103*, 4.

(61) Aubin, S. M. J.; Sun, Z. M.; Pardi, L.; Krzystek, J.; Folting, K.; Brunel, L. C.; Rheingold, A. L.; Christou, G.; Hendrickson, D. N. *Inorganic Chemistry* **1999**, *38*, 5329-5340.

(62) Feng, P. L.; Beedle, C. C.; Wernsdorfer, W.; Koo, C.; Nakano, M.; Hill, S.; Hendrickson, D. N. *Inorganic Chemistry* **2007**, *46*, 8126-8128.

(63) Vincent, J. B.; Christmas, C.; Huffman, J. C.; Christou, G.; Chang, H. R.; Hendrickson, D. N. *Journal of the Chemical Society-Chemical Communications* **1987**, 236-238.

(64) Aromi, G.; Bhaduri, S.; Artus, P.; Folting, K.; Christou, G. *Inorganic Chemistry* **2002**, *41*, 805-817.

(65) Wang, S. Y.; Wemple, M. S.; Yoo, J.; Folting, K.; Huffman, J. C.; Hagen, K. S.; Hendrickson, D. N.; Christou, G. *Inorganic Chemistry* **2000**, *39*, 1501-1513.

(66) Miessler, G. L.; Tarr, D. A. *Inorganic Chemistry*; 3rd ed.; Pearson Education: New Jersey, 2004.

(67) Wittick, L. M.; Jones, L. F.; Jensen, P.; Moubaraki, B.; Spiccia, L.; Berry, K. J.; Murray, K. S. *Dalton Transactions* **2006**, 1534-1543.

(68) Foguet-Albiol, D.; O'Brien, T. A.; Wernsdorfer, W.; Moulton, B.; Zaworotko, M. J.; Abboud, K. A.; Christou, G. *Angewandte Chemie-International Edition* **2005**, *44*, 897-901.

(69) Yoo, J.; Brechin, E. K.; Yamaguchi, A.; Nakano, M.; Huffman, J. C.; Maniero, A. L.; Brunel, L. C.; Awaga, K.; Ishimoto, H.; Christou, G.; Hendrickson, D. N. *Inorganic Chemistry* **2000**, *39*, 3615-3623.

(70) Wang, S. Y.; Folting, K.; Streib, W. E.; Schmitt, E. A.; Mccusker, J. K.; Hendrickson, D. N.; Christou, G. *Angewandte Chemie-International Edition in English* **1991**, *30*, 305-306.

(71) Wittick, L. M.; Murray, K. S.; Moubaraki, B.; Batten, S. R.; Spiccia, L.; Berry, K. J. *Dalton Transactions* **2004**, 1003-1011.

(72) Wemple, M. W.; Adams, D. M.; Hagen, K. S.; Folting, K.; Hendrickson, D. N.; Christou, G. *Journal of the Chemical Society-Chemical Communications* **1995**, 1591-1593.

(73) Yoo, J.; Yamaguchi, A.; Nakano, M.; Krzystek, J.; Streib, W. E.; Brunel, L. C.; Ishimoto, H.; Christou, G.; Hendrickson, D. N. *Inorganic Chemistry* **2001**, *40*, 4604-4616.

(74) Kambe, K. *Journal of the Physical Society of Japan* **1950**, *5*, 48.

(75) Vincent, J. B.; Christmas, C.; Chang, H. R.; Li, Q. Y.; Boyd, P. D. W.; Huffman, J. C.; Hendrickson, D. N.; Christou, G. *Journal of the American Chemical Society* **1989**, *111*, 2086-2097.

(76) Van Vleck, J. H. *Physical Review* **1941**, *59*, 724.

(77) Libby, E.; Mccusker, J. K.; Schmitt, E. A.; Folting, K.; Hendrickson, D. N.; Christou, G. *Inorganic Chemistry* **1991**, *30*, 3486-3495.

(78) Wang, S.; Tsai, H. L.; Folting, K.; Martin, J. D.; Hendrickson, D. N.; Christou, G. *Journal of the Chemical Society-Chemical Communications* **1994**, 671-673.

(79) Mccusker, J. K.; Vincent, J. B.; Schmitt, E. A.; Mino, M. L.; Shin, K.; Coggin, D. K.; Hagen, P. M.; Huffman, J. C.; Christou, G.; Hendrickson, D. N. *Journal of the American Chemical Society* **1991**, *113*, 3012-3021.

(80) Anderson, E.; Bai, Z.; Bischof, C.; Blackford, S.; Demmel, J.; Dongarra, J.; Croz, J. D.; Greenbaum, A.; Hammarling, S.; McKenney, A.; Sorrensen, D. *LAPACK Users' Guide* **1999**.

(81) Eden, M.; Levitt, M. H. *J. Magnetic Resonance* **1998**, *132*, 220.

(82) Nelder, J. A.; Mead, R. *Computer Journal* **1965**, *7*, 308-313.

(83) Parkinson, J. M.; Huchinson, D. *Numerical Methods for Non-Linear Optimization*; London Achademic Press, 1972.

(84) Press, W. H.; Teukolsky, A.; Vetterling, W. T.; Flannery, B. P. *Numerical Recipies*; Cambridge University Press, 1986.

(85) Kelly, C. T. *J. Optim* **1999**, *10*, 43-55.

Chapter 7

Single-Stranded [Mn_{12}] Wheel-Shaped Single-Molecule Magnets

7.1 Introduction

There is currently much interest in the preparation and physical properties of polynuclear transition metal complexes that exhibit interesting magnetic behavior. A number of these complexes have been shown to exhibit quantum effects such as quantum tunneling of magnetization (QTM) and slow magnetization relaxation dynamics at low temperatures.[1-5] Coined single-molecule magnets (SMMs)[6] these molecules have spurred great interest in their possible application as molecule-based electronic devices such as magnetic storage units and molecular switches.[7-13] Exploration in this area has yielded an increasing number of new topologies which have in turn offered new insights relating to how molecular construction influences magnetic exchange and associated quantum dynamics.

Recently, ring, or wheel-shaped, molecules have drawn considerable interest. Molecular wheels represent an important frontier in the study of molecular magnetic materials and present interesting magnetic exchange interaction situations due to their inherent topology. Furthermore, theoretical studies have suggested that wheel-shaped complexes based on transition metals could be used for quantum computation.[14-17] A number of hetero-metallic and homo-metallic wheel-shaped complexes have been reported that contain Dy,[18] Fe,[19-29] Cr,[30-34] Co,[35] Ni,[29,33,36-38] Cu[39] and Mn[40-49] of varying nuclearity, with spin ground states ranging from S=0 in the $Fe(III)_6$[21] and $Fe(III)_8$[33] complexes to S=12 in a $Ni(II)_{12}$[37] wheel complex.

Antiferromagnetically coupled S = 0 wheels represent an area of intense interest since they can be used to model the magnetic properties found in one-dimensional paramagnetic materials.[50] It is also believed that these complexes are ideal for studying

quantum coherence.[14,15] This phenomenon is not seen in SMMs because the magnetic moment of the ferromagnetically coupled spins can interact with the magnetic moments of neighboring molecules or external magnetic fields leading to tunneling decoherence. The magnitude of the interaction or coupling a system has with its environment determines its metastability. Strong environmental coupling imparts preferred energy population orientations in SMMs due to spin-lattice interactions, long-range magnetic ordering and intermolecular magnetic exchange. However, if there is no coupling between molecules and their environment, tunneling can take place in a coherent manner; that is, tunneling will occur between two metastable states, spin-up to spin-down, without dissipating or absorbing energy from the environment.

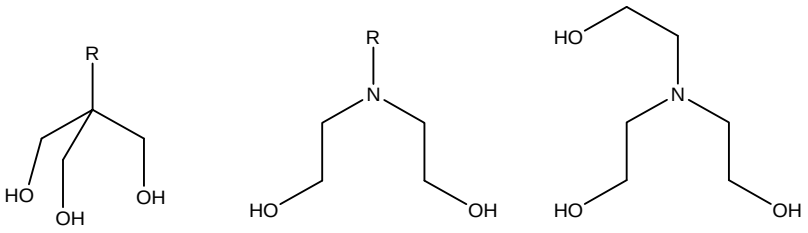

1a (R = Me, Et, CH_2OH) **1b** (R = Me, Et, n-butyl) **1c**

Scheme 7.1. Illustrations depicting the construction of the carbon based **1a**, and amine based, **1b** and **1c** dipodal and tripodal ligand systems.

Wheel-shaped complexes based on manganese have been synthesized consisting of Mn^{II}, Mn^{III} and Mn^{IV} atoms in a variety of spatial arrangements. Examples of homo-valent wheel complexes include the S = 12 [Mn^{II}_6] complex reported by Caneschi *et al.*,[26] and [Mn_6],[51] [Mn_{10}][19] and [Mn_{84}][52] assemblies containing all Mn^{III} atoms. The most common motif found in molecular wheel complexes contains Mn-O-Mn moieties where the bridging oxygen is part of a carboxylate or alkoxy ligand. The

aforementioned [Mn_{10}],[19] [Mn_{84}],[52] and [Mn_{24}][53] complexes and a [Mn_{22}] complex reported by Murugesu *et al*.[44] are exceptions to this trend. The exchange pathways between manganese atoms in the metallocrown [Mn_{10}] complex consist of conjugated, complex pentadentate ligands between metal ions. The [Mn_{84}] complex is made up of alternating [Mn_3O_4] and [$Mn_4O_2(O_2Me)_2$] clusters and the [Mn_{22}] complex contains two pseudo-[Mn_3O_4] clusters which break the linear Mn-O-Mn arrangement found in the rest of the complex. All three of these cases yield intermediate-spin S = 2, S = 6 and S = 10 spin ground states, respectively, with complicated multiple exchange pathways, making the study of their magnetic properties difficult.

A large sub-class of manganese-based wheel complexes have been synthesized using dipodal and tripodal ligand systems such as the [Mn_{22}][44] SMM complex employing a carbon based 1,1,1-tris(hydroxymethyl)alkyl ligand (H_3thmR, R= Me, Et, MeOH, Scheme **7.1a**). More widely used are the dipodal and tripodal amine-based diethanolamine (H_2Rdea, R = Me, Et, n-Butyl, Scheme **7.1b**) and triethanolamine (H_3tea, Scheme **1c**) ligands.[43,45-48,52] These polydentate ligands have proven to be very versatile due to their ability to coordinate in various binding modes and as well impart structural flexibility.

Many aspects must be taken into account in order to thoroughly study and understand the intricacies related to the magnetic properties of this topology. In order to decipher complicated systems such as the [Mn_{10}] and [Mn_{84}] systems, wheel complexes with more basic geometry and exchange pathways should first be studied. In this chapter, the synthesis, structure and magnetic properties of two [Mn_{12}] single-stranded wheel shaped SMM's are presented.

7.2 Experimental Section

7.2.1 Compound Preparation

All manipulations were performed under aerobic conditions. The ligands *N*-ethyldiethanol amine (H_2edea) and *N*-methyldiethanol amine (H_2mdea) were purchased from Aldrich and used without further purification. Crystals of the compound $[Mn_{12}O_{12}(O_2CCH_3)_{16}(H_2O)_4] \cdot 4H_2O \cdot 2CH_3COOH$ (Mn_{12}Ac) were prepared by standard methods.[54]

$[Mn_{12}(mdea)_8(O_2CCH_3)_{14}]\cdot CH_3CN$ (complex 7A) and $[Mn_{12}(mdea)_8(O_2CCH_3)_{14}]$ (complex 7B). CH_2Cl_2 (100 mL) slurry of Mn_{12}Ac (2.0g, 0.971 mmol) was added drop wise a CH_2Cl_2 (25 mL) solution of H_2mdea (0.462 g, 3.88 mmol). The slurry was allowed to stir for overnight, during which the Mn_{12}Ac slowly dissolved forming a black/brown solution. The undissolved Mn_{12}Ac was removed by filtration. The filtrate was evaporated by vacuum distillation yielding a brown oil. This oil was washed with 30 mL of diethyl ether to remove the excess ligand. This oil was then dissolved in 30 mL of acetonitrile and left undisturbed. After 30 minutes, crystals of complex **7A** started to precipitate. Yield 0.160 g (7 %, based on Mn). Anal. Calcd (found) for $C_{68}H_{130}Mn_{12}N_8O_{44}$: C, 33.70 (33.96); H, 5.40 (5.00); N, 4.62 (4.64). Selected IR data (KBr): 3440 (m,br), 3143 (m,br), 2848 (m), 1581 (s), 1400 (s), 1334 (m), 1079 (m), 663 (w), 522 cm^{-1} (w). Crystals of the formulation $[Mn_{12}(mdea)_8(O_2CCH_3)_{14}] \cdot CH_3CN$ were grown by allowing diethyl ether vapors to slowly diffuse into an acetonitrile solution of **7A**. Two different crystallographic forms of III.1 have been isolated. Red rod shaped crystals of the second form, complex

$[Mn_{12}(mdea)_8(O_2CCH_3)_{14}]$ (complex **7B**), are grown by very slowly adding 30 mL of acetonitrile to the oil collected from the vacuum distillation step.

Method (b). Solid $[Mn_4O_2(O_2CCH_3)_7(bpy)_2](ClO_4)$ (0.5 g, 0.442 mmol) was added to CH_2Cl_2 (30 mL). After being stirred for 1 h, the brown/red solution was filtered to remove undissolved $[Mn_4O_2(O_2\text{-}CMe)_7(bpy)_2](ClO_4)$. H_2mdea (0.239 g, 1.77 mmol) dissolved in CH_2Cl_2 (10 mL) was added dropwise over a 5 min period to the filtrate. The resulting red solution was stirred for 30 min. The solution was allowed to stand undisturbed for 3 days, after which a brown/red precipitate formed (complex **7A**). Complex **7A** was collected via vacuum filtration and washed with three successive 30 mL treatments of diethyl ether. Crystals of **7A** were grown by layering a 50 mL CH_3CN solution with a 50 mL 1:1 mixture of diethyl ether and hexanes. Elemental analysis and FT-IR spectral data agree with the data collected for crystals prepared via method (a) for complex **7A**. Crystals prepared by method (b) have the same X-ray structure as complex **7A**. Yield: 0.0384 g (3% based on Mn).

$[Mn_{12}(edea)_8(O_2CCH_3)_{14}]$. (**Complex 7C**) was prepared in an analogous fashion as III.1, except H_2edea (0.516g, 3.88 mmol) was used. Yield 0.202 g (8 %, based on Mn). Anal. Calcd (found) for $C_{76}H_{146}Mn_{12}N_8O_{44}$: C, 36.00 (36.65); H, 5.80 (5.35); N, 4.41 (4.35). Selected IR data (KBr): 3421(s,br), 1560 (s), 1403 (s), 1342 (w), 1078 (m), 661 (w), 458 cm^{-1} (w).

Method (b). Complex **7C** was prepared in a procedure analogous to that used to prepare complex **7A** (method (b)) except that the precipitation of **7C** immediately followed the addition of H_2edea (0.233 g, 1.77 mmol) to the CH_2Cl_2 solution (30 mL). The FT-IR spectra of crystals prepared by method (b) agree with the data collected for

crystals prepared using method (a) for complex **7C**. The yield of complex **7C** formed by method (b) was very small.

7.2.2 X-ray Crystallography

Diffraction intensity data were collected with a Bruker Smart Apex CCD diffractometer for complexes $[Mn_{12}(mdea)_8(O_2CCH_3)_{14}] \cdot CH_3CN$ (**7A**) and $[Mn_{12}(mdea)_8(O_2CCH_3)_{14}]$ (**7B**). Crystal, data collection, and refinement parameters are given in Table **7.1.** The space groups were chosen based on intensity statistics for complexes **7A** and by systematic absences in **7B**. The structures were solved employing direct methods, completed by subsequent difference Fourier syntheses, and refined by full matrix least-squares procedures on F^2. SADABS[55] absorption corrections were applied to all data (T_{min}/T_{max}= 0.774). In addition to the Mn_{12} wheel complexes in the crystal structure there is one CH_3CN molecule in **7A**. All non-hydrogen atoms in the structures were refined with anisotropic displacement coefficients except the Me-groups belonging to the amine ligand coordinated to the divalent Mn3 atom in complex **7B**. These groups were disordered over two positions and were refined with isotropic thermal parameters. The hydrogen atoms in **7A** and **7B** were treated as idealized contributions. All software and sources of scattering factors are contained in the SHELXTL (5.10) program package (G. Sheldrick, Bruker XRD, Madison, WI).

Table 7.1. Crystallographic Data for $[Mn_{12}(mdea)_8(O_2CCH_3)_{14}] \cdot CH_3CN$ (**7A**), $[Mn_{12}(mdea)_8(O_2CCH_3)_{14}]$ (**7B**).

Compound	**7A**	**7B**
Formula	$C_{72}H_{136}N_{10}O_{44}Mn_{12}$	$C_{68}H_{130}N_8O_{44}Mn_{12}$
Formula weight	2505.18	2423.08
Space group	*P-1*	$P2_1/n$
a, Å	13.1038(17)	10.1919(5)
b, Å	13.2726(18)	15.8827(8)
c, Å	17.265(2)	31.3229(16)
α, deg	107.290(2)	--
β, deg	109.195(2)	98.096(1)
γ, deg	99.309(2)	--
V, Å^3	2593.1(6)	5019.9(4)
Z,Z'	1,0.5	2,0.5
Crystal color, habit	Red, Block	Red, Block
Crystal sizes (mm)	0.32x0.20x0.15	0.19x0.18x0.15
D(calc), g cm^{-3}	1.604	1.603
μ(MoKα), cm^{-1}	14.95	15.41
Temp, K	100(2)	100(2)
Diffractometer	Bruker Smart Apex CCD	Bruker Smart Apex CCD
Radiation	MoKα (λ=0.71073 Å)	
Reflections measured	21928	32841
Reflections independent	11460[R_{int}=0.0228]	7890[0.0251]
R(F)[a], R(wF^2)[b]	0.0365, 0.0908	0.0547, 0.1213
S	1.009	1.268

[a] $R=\sum||F_o|-|F_c||/\sum|F_o|$,

[b] $R(\omega F^2;\ \omega=1/[\sigma^2(F_o^2)+(aP)^2+bP], P=[2F_c^2+\max(F_o,0)]/3$

7.2.3 Physical Methods

FT-IR spectra were collected using a Thermo-Nicolet Avatar series spectrometer. Elemental analyses were performed by Prevalere Life Sciences (Whitesboro, NY). AC and DC magnetic susceptibility data were collected with Quantum Design MPMS magnetometers equipped with 1.0 T and 5.5 T magnets, respectively. Microcrystalline samples were restrained with eicosane to prevent torquing of the crystallites. Pascal's constants were employed to adjust observed magnetic susceptibilities with a diamagnetic correction. All NMR spectra were recorded at room temperature (20 °C) in d^3-chloroform solutions on Varian spectrometers operating at 300 MHz (1H NMR) and referenced to residual solvent peaks unless otherwise noted.

7.3 Results and Discussion

7.3.1 Synthesis

The use of amine based poly-dentate poly-alcohols has yielded a wonderfully diverse family or families of molecules with varying nuclearity and topology, such as butterflies,[56] dicubanes,[49,56-58] extended structures,[59] and heteronuclear complexes.[60] The amine based poly-alcohols are quite versatile and are found as bridging ligands between two metal centers or as bridging ligands between three metal centers, where the alkoxy oxygen of a ethoxy arm is in a μ_3 or μ_4 coordination mode. It can also be found as a capping ligand in both small and extended structures.

In most cases no deprotonating agent is required during synthesis, whether one begins from simple halide or carboxylate salts of Mn^{II} or Mn^{III}. Often, the addition of

R-diethanolamine or triethanol amine quickly promotes oxidation of Mn^{II} salts yielding dark brown to brown/red solutions without the presence of an oxidizing agent such as tetrabutylammonium permanganate or potassium permanganate, though the exact mechanism is not clearly understood. Interestingly, the length of the R group does not seem to be the limiting factor when it pertains to the formation of wheel or dicubane topologies, which seem to be the toplogical molecular sinks in these types of reactions, as noted from the variety of starting materials that can be employed to synthesize these complexes. Rather, it appears that it is the nature of the R group on the carboxylates that seems to govern whether synthesis leads to a wheel or dicubane. This is evident in the work published by Foguet-Albiol *et al.*[49] where the product of the reaction between *N*-methyldiethanolamine and $Mn(O_2CPh)_2$ or $Mn(O_2CCH_3)_2$ leads to the formation of a dicubane and a wheel, respectively. This idea is further supported by complexes reported in this dissertation in chapters 4, 5, where large bulky carboxylate lead to the formation of dicubanes.

7.3.2 Description of Structure

Figure **7.1** shows an ORTEP illustration and asymmetric unit for $[Mn_{12}(mdea)_8(O_2CCH_3)_{14}] \cdot CH_3CN$ (**7A**), with hydrogens removed for clarity. The asymmetric unit contains three Mn^{II} and three Mn^{III} ions, with the complete wheel-shaped structure being generated by inversion symmetry equivalents (x, y, z to -x, -y, -z). A stereo packing diagram is given in Figure **7.2** for complex **7A**. Selected bond distances and angles are given in Tables **7.2** and **7.3** for complex **7A**. Complex **7A** crystallizes in the *P-1* space group with one molecular orientation in the crystal lattice.

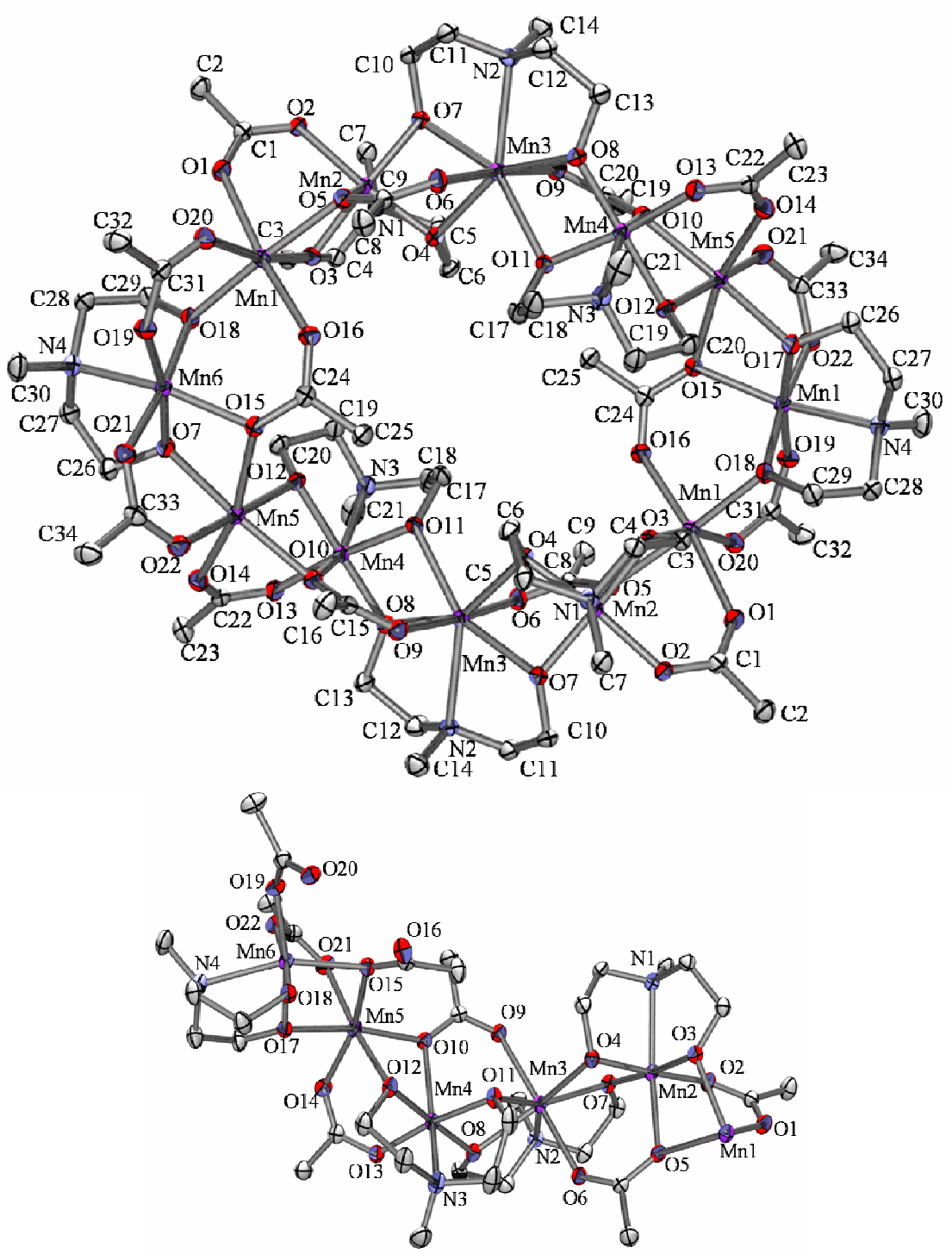

Figure 7.1. ORTEP of $Mn_{12}(mdea)_8(O_2CCH_3)_{14}] \cdot CH_3CN$ (**7A**) (upper), displayed at the 50% probability level. Hydrogen atoms have been omitted for clarity. The lower plot displays the asymmetric unit of complex **7A**.

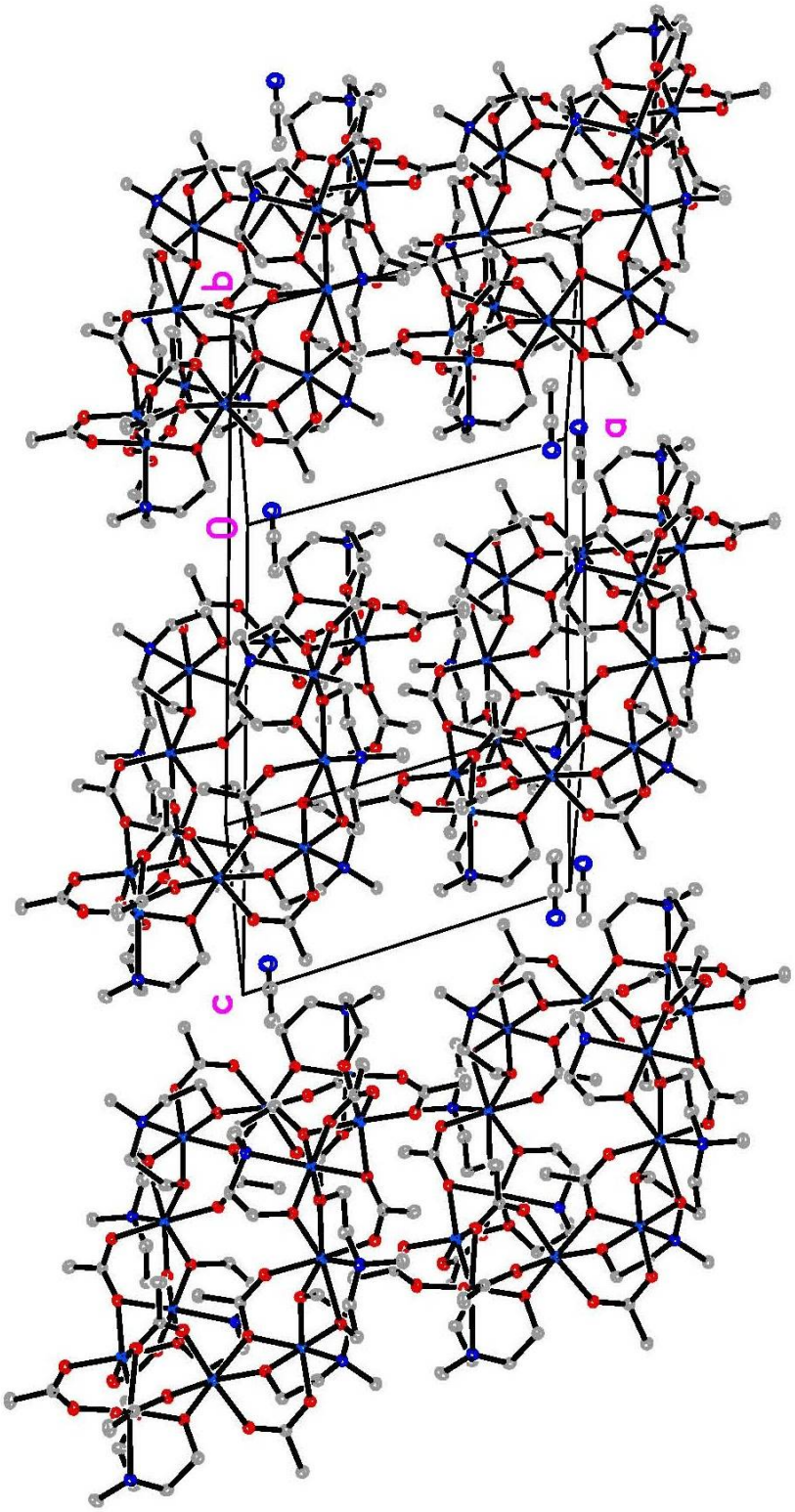

Figure 7.2. Packing diagram of $Mn_{12}(mdea)_8(O_2CCH_3)_{14}] \cdot CH_3CN$ (**7A**) viewed approximately along the *b* direction.

Table 7.2. Selected interatomic distances (Å) for $[Mn_{12}(mdea)_8(O_2CCH_3)_{14}] \cdot CH_3CN$ (**7A**)

Mn(1)-O(16)#1	2.1107(18)	Mn(3)-Mn(4)	3.1695(7)
Mn(1)-O(18)#1	2.1430(18)	Mn(4)-O(8)	1.8819(17)
Mn(1)-O(3)	2.1719(18)	Mn(4)-O(11)	1.9066(17)
Mn(1)-O(20)#1	2.1990(18)	Mn(4)-O(12)	1.9170(17)
Mn(1)-O(1)	2.2008(18)	Mn(4)-O(13)	1.9498(18)
Mn(1)-O(5)	2.2225(17)	Mn(4)-O(10)	2.2545(18)
Mn(1)-Mn(2)	3.1980(7)	Mn(4)-N(3)	2.302(2)
Mn(2)-O(7)	1.8890(17)	Mn(4)-Mn(5)	3.1499(6)
Mn(2)-O(4)	1.9015(17)	Mn(5)-O(12)	2.0972(18)
Mn(2)-O(3)	1.9290(17)	Mn(5)-O(21)	2.1199(19)
Mn(2)-O(2)	1.9848(17)	Mn(5)-O(14)	2.1593(18)
Mn(2)-O(5)	2.1989(17)	Mn(5)-O(17)	2.1827(17)
Mn(2)-N(1)	2.311(2)	Mn(5)-O(10)	2.1942(17)
Mn(2)-Mn(3)	3.1824(6)	Mn(5)-O(15)	2.2502(18)
Mn(3)-O(4)	2.2040(18)	Mn(5)-Mn(6)	3.2065(6)
Mn(3)-O(8)	2.2106(18)	Mn(6)-O(17)	1.9006(18)
Mn(3)-O(6)	2.2335(18)	Mn(6)-O(18)	1.9137(18)
Mn(3)-O(11)	2.2346(17)	Mn(6)-O(19)	1.9389(18)
Mn(3)-O(9)	2.2459(18)	Mn(6)-O(22)	1.9761(18)
Mn(3)-O(7)	2.2878(17)	Mn(6)-O(15)	2.1768(17)
Mn(3)-N(2)	2.419(2)	Mn(6)-N(4)	2.334(2)

Table 7.3. Selected interatomic angles (º) for $[Mn_{12}(mdea)_8(O_2CCH_3)_{14}] \cdot CH_3CN$ (**7A**)

O(16)#1-Mn(1)-O(18)#1	92.96(7)	O(13)-Mn(4)-Mn(3)	129.70(5)
O(16)#1-Mn(1)-O(3)	97.25(7)	O(10)-Mn(4)-Mn(3)	80.19(4)
O(18)#1-Mn(1)-O(3)	96.90(7)	N(3)-Mn(4)-Mn(3)	107.24(6)
O(16)#1-Mn(1)-O(20)#1	93.87(7)	Mn(5)-Mn(4)-Mn(3)	122.558(16)
O(18)#1-Mn(1)-O(20)#1	87.58(7)	O(12)-Mn(5)-O(21)	173.86(7)
O(3)-Mn(1)-O(20)#1	167.77(7)	O(12)-Mn(5)-O(14)	91.50(7)
O(16)#1-Mn(1)-O(1)	172.41(7)	O(21)-Mn(5)-O(14)	94.23(7)
O(18)#1-Mn(1)-O(1)	94.54(7)	O(12)-Mn(5)-O(17)	94.01(7)
O(3)-Mn(1)-O(1)	83.02(6)	O(21)-Mn(5)-O(17)	88.31(7)
O(20)#1-Mn(1)-O(1)	85.29(7)	O(14)-Mn(5)-O(17)	88.83(7)
O(16)#1-Mn(1)-O(5)	86.13(7)	O(12)-Mn(5)-O(10)	76.80(6)
O(18)#1-Mn(1)-O(5)	173.86(7)	O(21)-Mn(5)-O(10)	101.19(7)
O(3)-Mn(1)-O(5)	77.21(6)	O(14)-Mn(5)-O(10)	87.85(7)
O(20)#1-Mn(1)-O(5)	98.54(7)	O(17)-Mn(5)-O(10)	170.14(7)
O(1)-Mn(1)-O(5)	86.54(6)	O(12)-Mn(5)-O(15)	89.21(7)
O(16)#1-Mn(1)-Mn(2)	102.84(5)	O(21)-Mn(5)-O(15)	85.89(7)
O(18)#1-Mn(1)-Mn(2)	131.31(5)	O(14)-Mn(5)-O(15)	163.89(7)
O(3)-Mn(1)-Mn(2)	36.11(4)	O(17)-Mn(5)-O(15)	75.07(6)
O(20)#1-Mn(1)-Mn(2)	135.65(5)	O(10)-Mn(5)-O(15)	107.96(6)
O(1)-Mn(1)-Mn(2)	72.93(5)	O(12)-Mn(5)-Mn(4)	36.32(5)
O(5)-Mn(1)-Mn(2)	43.38(4)	O(21)-Mn(5)-Mn(4)	144.14(5)
O(7)-Mn(2)-O(4)	82.67(7)	O(14)-Mn(5)-Mn(4)	74.35(5)
O(7)-Mn(2)-O(3)	175.29(8)	O(17)-Mn(5)-Mn(4)	124.44(5)
O(4)-Mn(2)-O(3)	94.60(7)	O(10)-Mn(5)-Mn(4)	45.70(5)
O(7)-Mn(2)-O(2)	91.58(7)	O(15)-Mn(5)-Mn(4)	114.30(5)
O(4)-Mn(2)-O(2)	172.75(7)	O(12)-Mn(5)-Mn(6)	103.52(5)
O(3)-Mn(2)-O(2)	90.82(7)	O(21)-Mn(5)-Mn(6)	75.25(5)
O(7)-Mn(2)-O(5)	100.93(7)	O(14)-Mn(5)-Mn(6)	121.85(5)
O(4)-Mn(2)-O(5)	92.53(7)	O(17)-Mn(5)-Mn(6)	35.23(5)
O(3)-Mn(2)-O(5)	82.99(7)	O(10)-Mn(5)-Mn(6)	150.10(5)
O(2)-Mn(2)-O(5)	92.90(7)	O(15)-Mn(5)-Mn(6)	42.69(4)
O(7)-Mn(2)-N(1)	96.26(8)	Mn(4)-Mn(5)-Mn(6)	139.722(16)
O(4)-Mn(2)-N(1)	81.89(7)	O(17)-Mn(6)-O(18)	94.24(8)
O(3)-Mn(2)-N(1)	79.52(7)	O(17)-Mn(6)-O(19)	169.69(8)
O(2)-Mn(2)-N(1)	94.40(7)	O(18)-Mn(6)-O(19)	91.38(8)
O(5)-Mn(2)-N(1)	161.11(7)	O(17)-Mn(6)-O(22)	90.02(8)
O(7)-Mn(2)-Mn(3)	45.27(5)	O(18)-Mn(6)-O(22)	172.14(7)
O(4)-Mn(2)-Mn(3)	42.76(5)	O(19)-Mn(6)-O(22)	83.45(7)
O(3)-Mn(2)-Mn(3)	133.64(5)	O(17)-Mn(6)-O(15)	82.68(7)
O(2)-Mn(2)-Mn(3)	133.56(5)	O(18)-Mn(6)-O(15)	96.22(7)
O(5)-Mn(2)-Mn(3)	82.22(5)	O(19)-Mn(6)-O(15)	105.31(7)
N(1)-Mn(2)-Mn(3)	104.90(5)	O(22)-Mn(6)-O(15)	90.87(7)
O(7)-Mn(2)-Mn(1)	142.94(6)	O(17)-Mn(6)-N(4)	78.93(7)
O(4)-Mn(2)-Mn(1)	106.24(5)	O(18)-Mn(6)-N(4)	81.45(7)
O(3)-Mn(2)-Mn(1)	41.57(5)	O(19)-Mn(6)-N(4)	93.40(8)
O(2)-Mn(2)-Mn(1)	81.01(5)	O(22)-Mn(6)-N(4)	92.92(8)
O(5)-Mn(2)-Mn(1)	43.97(5)	O(15)-Mn(6)-N(4)	161.22(7)
N(1)-Mn(2)-Mn(1)	120.39(5)	O(17)-Mn(6)-Mn(5)	41.49(5)

Table 7.3. Continued.

Mn(3)-Mn(2)-Mn(1)	120.861(15)	O(18)-Mn(6)-Mn(5)	109.96(5)
O(4)-Mn(3)-O(8)	148.68(6)	O(19)-Mn(6)-Mn(5)	143.02(6)
O(4)-Mn(3)-O(6)	85.27(7)	O(22)-Mn(6)-Mn(5)	77.54(5)
O(8)-Mn(3)-O(6)	88.16(6)	O(15)-Mn(6)-Mn(5)	44.50(5)
O(4)-Mn(3)-O(11)	80.90(6)	N(4)-Mn(6)-Mn(5)	118.75(6)
O(8)-Mn(3)-O(11)	68.77(6)	C(1)-O(1)-Mn(1)	130.15(16)
O(6)-Mn(3)-O(11)	92.21(7)	C(1)-O(2)-Mn(2)	128.70(16)
O(4)-Mn(3)-O(9)	93.17(7)	C(3)-O(3)-Mn(2)	113.49(14)
O(8)-Mn(3)-O(9)	91.18(6)	C(3)-O(3)-Mn(1)	126.54(14)
O(6)-Mn(3)-O(9)	175.79(7)	Mn(2)-O(3)-Mn(1)	102.33(8)
O(11)-Mn(3)-O(9)	83.69(6)	C(6)-O(4)-Mn(2)	115.86(15)
O(4)-Mn(3)-O(7)	67.72(6)	C(6)-O(4)-Mn(3)	121.08(15)
O(8)-Mn(3)-O(7)	142.55(6)	Mn(2)-O(4)-Mn(3)	101.38(7)
O(6)-Mn(3)-O(7)	87.41(6)	C(8)-O(5)-Mn(2)	123.44(15)
O(11)-Mn(3)-O(7)	148.55(6)	C(8)-O(5)-Mn(1)	134.07(15)
O(9)-Mn(3)-O(7)	95.62(6)	Mn(2)-O(5)-Mn(1)	92.65(7)
O(4)-Mn(3)-N(2)	138.36(7)	C(8)-O(6)-Mn(3)	134.85(17)
O(8)-Mn(3)-N(2)	72.38(7)	C(10)-O(7)-Mn(2)	128.89(15)
O(6)-Mn(3)-N(2)	92.06(7)	C(10)-O(7)-Mn(3)	119.97(15)
O(11)-Mn(3)-N(2)	140.73(7)	Mn(2)-O(7)-Mn(3)	98.82(7)
O(9)-Mn(3)-N(2)	91.70(7)	C(13)-O(8)-Mn(4)	127.15(15)
O(7)-Mn(3)-N(2)	70.65(7)	C(13)-O(8)-Mn(3)	120.58(15)
O(4)-Mn(3)-Mn(4)	116.53(4)	Mn(4)-O(8)-Mn(3)	101.21(8)
O(8)-Mn(3)-Mn(4)	35.62(4)	C(15)-O(9)-Mn(3)	132.49(16)
O(6)-Mn(3)-Mn(4)	101.56(5)	C(15)-O(10)-Mn(5)	139.76(16)
O(11)-Mn(3)-Mn(4)	36.38(4)	C(15)-O(10)-Mn(4)	125.43(15)
O(9)-Mn(3)-Mn(4)	75.63(4)	Mn(5)-O(10)-Mn(4)	90.14(6)
O(7)-Mn(3)-Mn(4)	170.20(5)	C(17)-O(11)-Mn(4)	116.58(16)
N(2)-Mn(3)-Mn(4)	104.73(5)	C(17)-O(11)-Mn(3)	121.47(15)
O(4)-Mn(3)-Mn(2)	35.86(4)	Mn(4)-O(11)-Mn(3)	99.57(7)
O(8)-Mn(3)-Mn(2)	160.74(5)	C(20)-O(12)-Mn(4)	114.68(16)
O(6)-Mn(3)-Mn(2)	72.94(5)	C(20)-O(12)-Mn(5)	123.79(15)
O(11)-Mn(3)-Mn(2)	114.57(5)	Mn(4)-O(12)-Mn(5)	103.29(8)
O(9)-Mn(3)-Mn(2)	107.95(5)	C(22)-O(13)-Mn(4)	130.71(17)
O(7)-Mn(3)-Mn(2)	35.91(4)	C(22)-O(14)-Mn(5)	127.77(17)
N(2)-Mn(3)-Mn(2)	103.97(5)	C(24)-O(15)-Mn(6)	128.33(16)
Mn(4)-Mn(3)-Mn(2)	150.943(16)	C(24)-O(15)-Mn(5)	128.46(16)
O(8)-Mn(4)-O(11)	83.01(7)	Mn(6)-O(15)-Mn(5)	92.81(7)
O(8)-Mn(4)-O(12)	178.39(8)	C(24)-O(16)-Mn(1)#1	137.71(17)
O(11)-Mn(4)-O(12)	95.80(8)	C(26)-O(17)-Mn(6)	114.68(15)
O(8)-Mn(4)-O(13)	89.26(8)	C(26)-O(17)-Mn(5)	120.76(15)
O(11)-Mn(4)-O(13)	171.61(8)	Mn(6)-O(17)-Mn(5)	103.27(8)
O(12)-Mn(4)-O(13)	91.99(7)	C(29)-O(18)-Mn(6)	116.12(15)
O(8)-Mn(4)-O(10)	99.81(7)	C(29)-O(18)-Mn(1)#1	122.68(15)
O(11)-Mn(4)-O(10)	87.27(7)	Mn(6)-O(18)-Mn(1)#1	117.63(8)
O(12)-Mn(4)-O(10)	79.02(7)	C(31)-O(19)-Mn(6)	138.15(17)
O(13)-Mn(4)-O(10)	97.29(7)	C(31)-O(20)-Mn(1)#1	128.87(17)
O(8)-Mn(4)-N(3)	102.29(8)	C(33)-O(21)-Mn(5)	128.04(17)

Table 7.3. Continued.

O(11)-Mn(4)-N(3)	82.08(8)	C(33)-O(22)-Mn(6)	131.54(17)
O(12)-Mn(4)-N(3)	78.59(8)	C(7)-N(1)-Mn(2)	111.84(16)
O(13)-Mn(4)-N(3)	96.47(8)	C(5)-N(1)-Mn(2)	100.53(15)
O(10)-Mn(4)-N(3)	154.03(8)	C(4)-N(1)-Mn(2)	105.37(15)
O(8)-Mn(4)-Mn(5)	139.02(6)	C(11)-N(2)-Mn(3)	104.68(15)
O(11)-Mn(4)-Mn(5)	108.53(6)	C(12)-N(2)-Mn(3)	106.30(15)
O(12)-Mn(4)-Mn(5)	40.39(5)	C(14)-N(2)-Mn(3)	111.99(16)
O(13)-Mn(4)-Mn(5)	79.49(5)	C(21)-N(3)-Mn(4)	113.34(18)
O(10)-Mn(4)-Mn(5)	44.15(4)	C(18)-N(3)-Mn(4)	100.20(15)
N(3)-Mn(4)-Mn(5)	117.98(6)	C(19)-N(3)-Mn(4)	105.80(16)
O(8)-Mn(4)-Mn(3)	43.17(5)	C(30)-N(4)-Mn(6)	113.50(17)
O(11)-Mn(4)-Mn(3)	44.05(5)	C(28)-N(4)-Mn(6)	100.43(15)
O(12)-Mn(4)-Mn(3)	135.32(6)	C(27)-N(4)-Mn(6)	104.80(15)

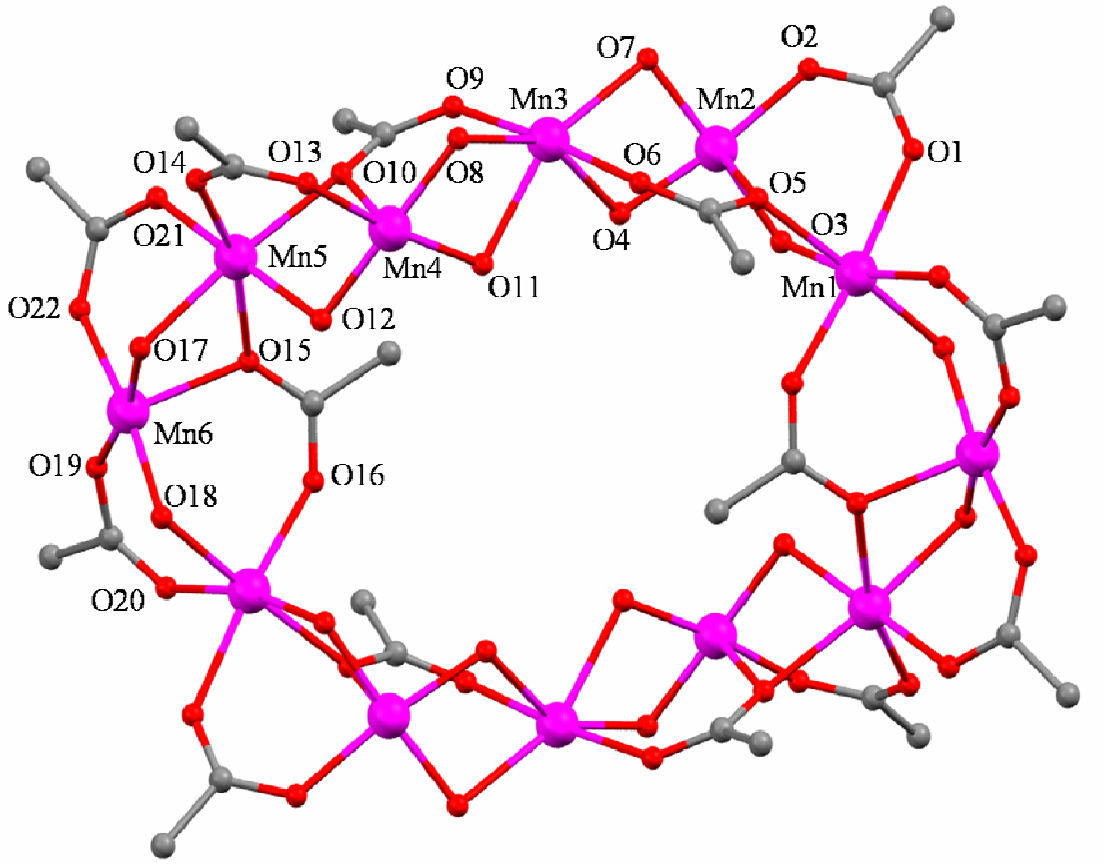

Figure 7.3. ORTEP diagram of complex $[Mn_{12}(mdea)_8(O_2CCH_3)_{14}] \cdot CH_3CN$ (**7A**) emphasizing the Mn-O-Mn connectivity and magnetic exchange pathways. For clarity, all hydrogens amine ligands have been omitted.

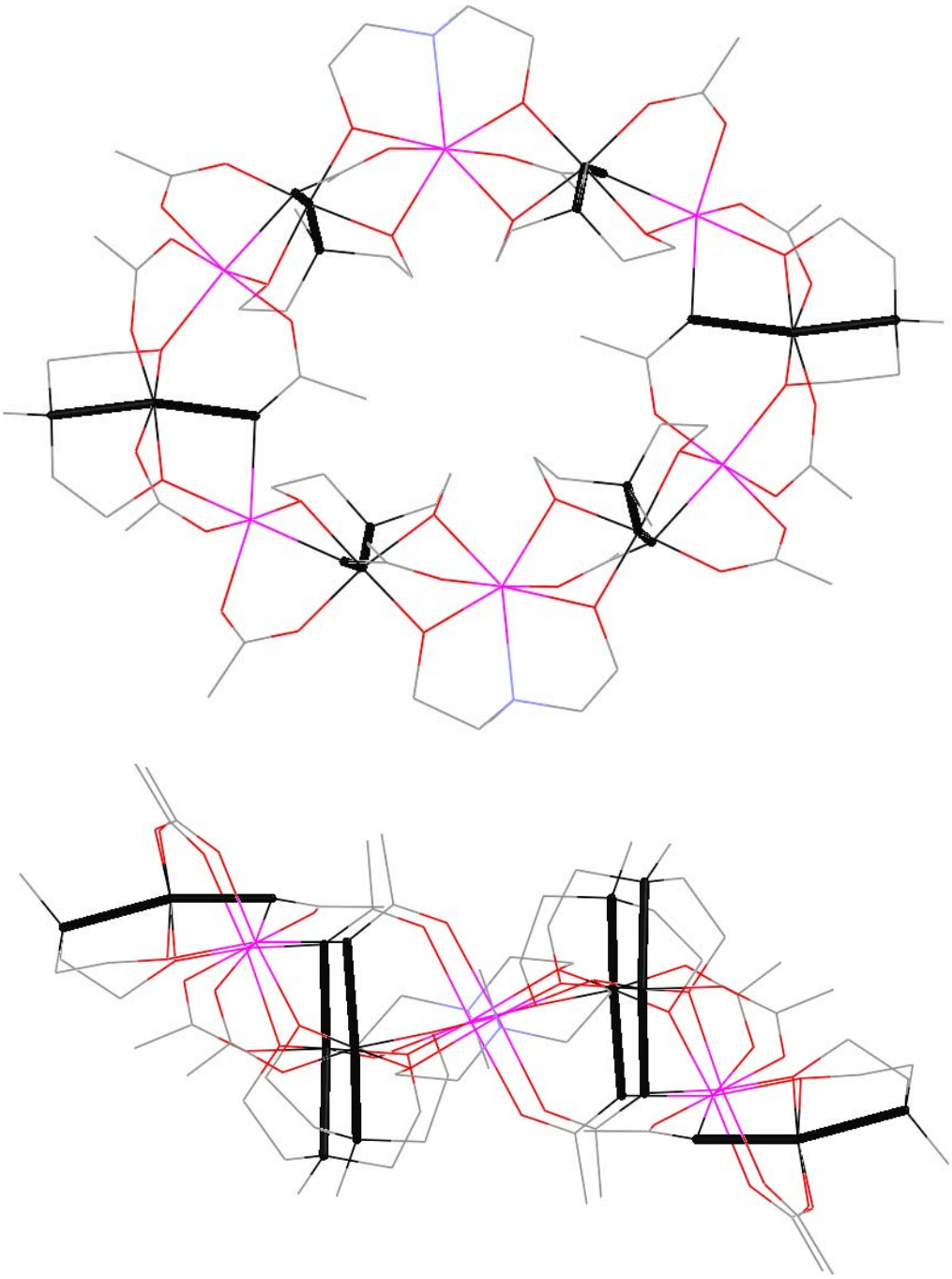

Figure 7.4. Illustration of complex $[Mn_{12}(mdea)_8(O_2CCH_3)_{14}] \cdot CH_3CN$ (**7A**) viewed orthogonal to the plane of the ring (upper plot) and a side view of the ring (lower plot). The directions of the Jahn-Teller elongation axes at Mn^{III} sites are colored in black.

Table 7.4. Selected interatomic distances (Å) for $[Mn_{12}(mdea)_8(O_2CCH_3)_{14}]$ (**7B**)

Mn(1)-O(16)#1	2.1107(18)	Mn(3)-Mn(4)	3.1695(7)
Mn(1)-O(18)#1	2.1430(18)	Mn(4)-O(8)	1.8819(17)
Mn(1)-O(3)	2.1719(18)	Mn(4)-O(11)	1.9066(17)
Mn(1)-O(20)#1	2.1990(18)	Mn(4)-O(12)	1.9170(17)
Mn(1)-O(1)	2.2008(18)	Mn(4)-O(13)	1.9498(18)
Mn(1)-O(5)	2.2225(17)	Mn(4)-O(10)	2.2545(18)
Mn(1)-Mn(2)	3.1980(7)	Mn(4)-N(3)	2.302(2)
Mn(2)-O(7)	1.8890(17)	Mn(4)-Mn(5)	3.1499(6)
Mn(2)-O(4)	1.9015(17)	Mn(5)-O(12)	2.0972(18)
Mn(2)-O(3)	1.9290(17)	Mn(5)-O(21)	2.1199(19)
Mn(2)-O(2)	1.9848(17)	Mn(5)-O(14)	2.1593(18)
Mn(2)-O(5)	2.1989(17)	Mn(5)-O(17)	2.1827(17)
Mn(2)-N(1)	2.311(2)	Mn(5)-O(10)	2.1942(17)
Mn(2)-Mn(3)	3.1824(6)	Mn(5)-O(15)	2.2502(18)
Mn(3)-O(4)	2.2040(18)	Mn(5)-Mn(6)	3.2065(6)
Mn(3)-O(8)	2.2106(18)	Mn(6)-O(17)	1.9006(18)
Mn(3)-O(6)	2.2335(18)	Mn(6)-O(18)	1.9137(18)
Mn(3)-O(11)	2.2346(17)	Mn(6)-O(19)	1.9389(18)
Mn(3)-O(9)	2.2459(18)	Mn(6)-O(22)	1.9761(18)
Mn(3)-O(7)	2.2878(17)	Mn(6)-O(15)	2.1768(17)
Mn(3)-N(2)	2.419(2)	Mn(6)-N(4)	2.334(2)

Table 7.5. Selected interatomic angles (º) for $[Mn_{12}(mdea)_8(O_2CCH_3)_{14}]$ (**7B**)

O(3)-Mn(1)-O(20)#1	175.04(13)	O(8)-Mn(4)-Mn(5)	142.44(11)
O(3)-Mn(1)-O(18)#1	94.46(13)	O(11)-Mn(4)-Mn(5)	107.69(10)
O(20)#1-Mn(1)-O(18)#1	88.83(13)	O(12)-Mn(4)-Mn(5)	40.85(9)
O(3)-Mn(1)-O(16)#1	91.59(13)	O(13)-Mn(4)-Mn(5)	79.28(10)
O(20)#1-Mn(1)-O(16)#1	92.09(14)	O(10)-Mn(4)-Mn(5)	43.56(8)
O(18)#1-Mn(1)-O(16)#1	90.61(14)	N(3)-Mn(4)-Mn(5)	119.45(10)
O(3)-Mn(1)-O(1)	84.49(12)	Mn(3)-Mn(4)-Mn(5)	122.26(3)
O(20)#1-Mn(1)-O(1)	91.67(13)	O(12)-Mn(5)-O(17)	97.61(12)
O(18)#1-Mn(1)-O(1)	92.35(13)	O(12)-Mn(5)-O(14)	88.56(12)
O(16)#1-Mn(1)-O(1)	175.25(13)	O(17)-Mn(5)-O(14)	91.15(13)
O(3)-Mn(1)-O(5)	77.56(12)	O(12)-Mn(5)-O(21)	176.04(12)
O(20)#1-Mn(1)-O(5)	99.23(12)	O(17)-Mn(5)-O(21)	86.20(12)
O(18)#1-Mn(1)-O(5)	171.86(12)	O(14)-Mn(5)-O(21)	90.28(13)
O(16)#1-Mn(1)-O(5)	88.02(13)	O(12)-Mn(5)-O(15)	97.13(12)
O(1)-Mn(1)-O(5)	88.53(12)	O(17)-Mn(5)-O(15)	74.58(13)
O(3)-Mn(1)-Mn(2)	36.19(9)	O(14)-Mn(5)-O(15)	165.19(13)
O(20)#1-Mn(1)-Mn(2)	139.43(9)	O(21)-Mn(5)-O(15)	84.90(13)
O(18)#1-Mn(1)-Mn(2)	128.26(9)	O(12)-Mn(5)-O(10)	76.75(12)
O(16)#1-Mn(1)-Mn(2)	102.00(10)	O(17)-Mn(5)-O(10)	174.36(12)
O(1)-Mn(1)-Mn(2)	73.26(9)	O(14)-Mn(5)-O(10)	88.55(12)
O(5)-Mn(1)-Mn(2)	44.51(8)	O(21)-Mn(5)-O(10)	99.44(12)
O(7)-Mn(2)-O(4)	84.12(14)	O(15)-Mn(5)-O(10)	106.04(12)
O(7)-Mn(2)-O(3)	177.14(14)	O(12)-Mn(5)-Mn(4)	36.09(8)
O(4)-Mn(2)-O(3)	93.77(14)	O(17)-Mn(5)-Mn(4)	129.84(9)
O(7)-Mn(2)-O(2)	90.83(14)	O(14)-Mn(5)-Mn(4)	74.45(9)
O(4)-Mn(2)-O(2)	173.62(14)	O(21)-Mn(5)-Mn(4)	139.99(9)
O(3)-Mn(2)-O(2)	91.15(14)	O(15)-Mn(5)-Mn(4)	117.72(9)
O(7)-Mn(2)-O(5)	99.63(13)	O(10)-Mn(5)-Mn(4)	44.77(8)
O(4)-Mn(2)-O(5)	88.73(13)	O(18)-Mn(6)-O(17)	94.02(15)
O(3)-Mn(2)-O(5)	82.21(13)	O(18)-Mn(6)-O(22)	174.51(15)
O(2)-Mn(2)-O(5)	95.97(13)	O(17)-Mn(6)-O(22)	90.47(14)
O(7)-Mn(2)-N(1)	98.06(15)	O(18)-Mn(6)-O(19)	92.02(14)
O(4)-Mn(2)-N(1)	80.57(14)	O(17)-Mn(6)-O(19)	169.26(14)
O(3)-Mn(2)-N(1)	79.67(15)	O(22)-Mn(6)-O(19)	83.07(14)
O(2)-Mn(2)-N(1)	96.35(15)	O(18)-Mn(6)-O(15)	93.53(14)
O(5)-Mn(2)-N(1)	158.24(14)	O(17)-Mn(6)-O(15)	78.36(13)
O(7)-Mn(2)-Mn(3)	44.38(10)	O(22)-Mn(6)-O(15)	90.47(13)
O(4)-Mn(2)-Mn(3)	42.86(10)	O(19)-Mn(6)-O(15)	110.13(14)
O(3)-Mn(2)-Mn(3)	134.17(10)	O(18)-Mn(6)-N(4)	81.94(14)

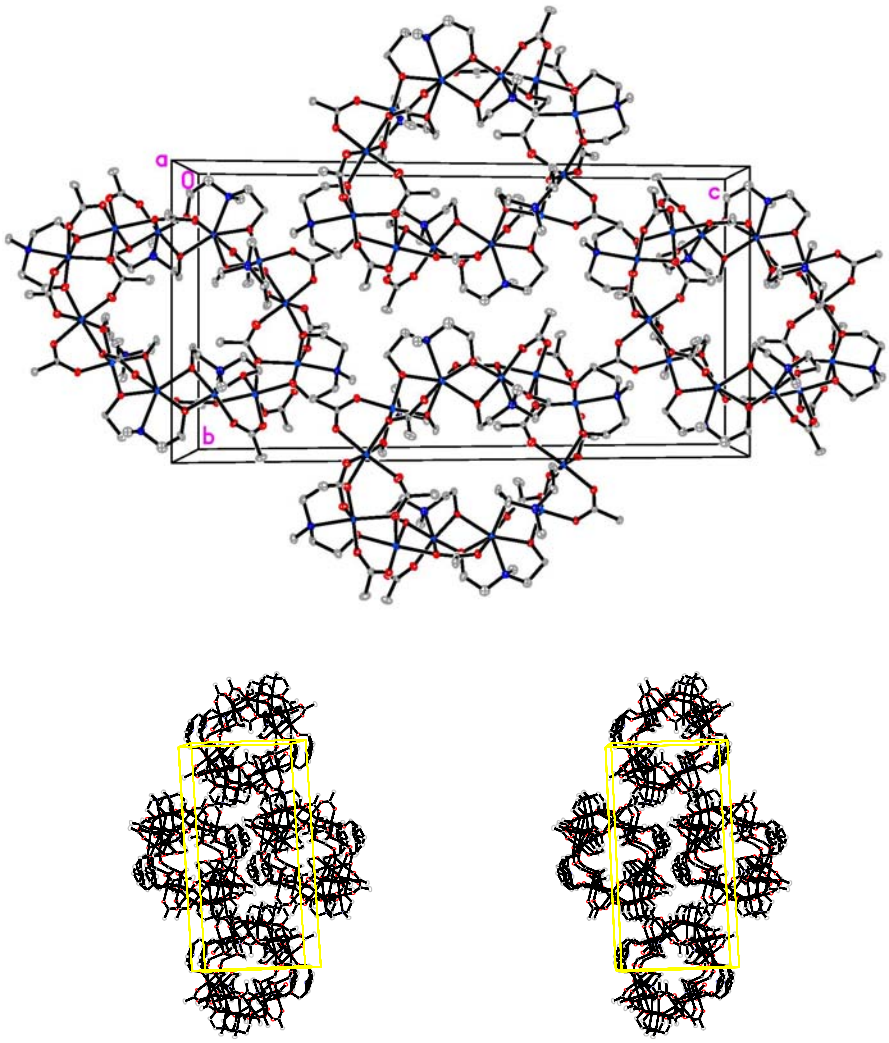

Figure 7.5. Packing (top) and Stereo packing (bottom) diagram of $[Mn_{12}(mdea)_8(O_2CCH_3)_{14}]$ (**7B**). Hydrogen atoms, have been omitted for clarity.

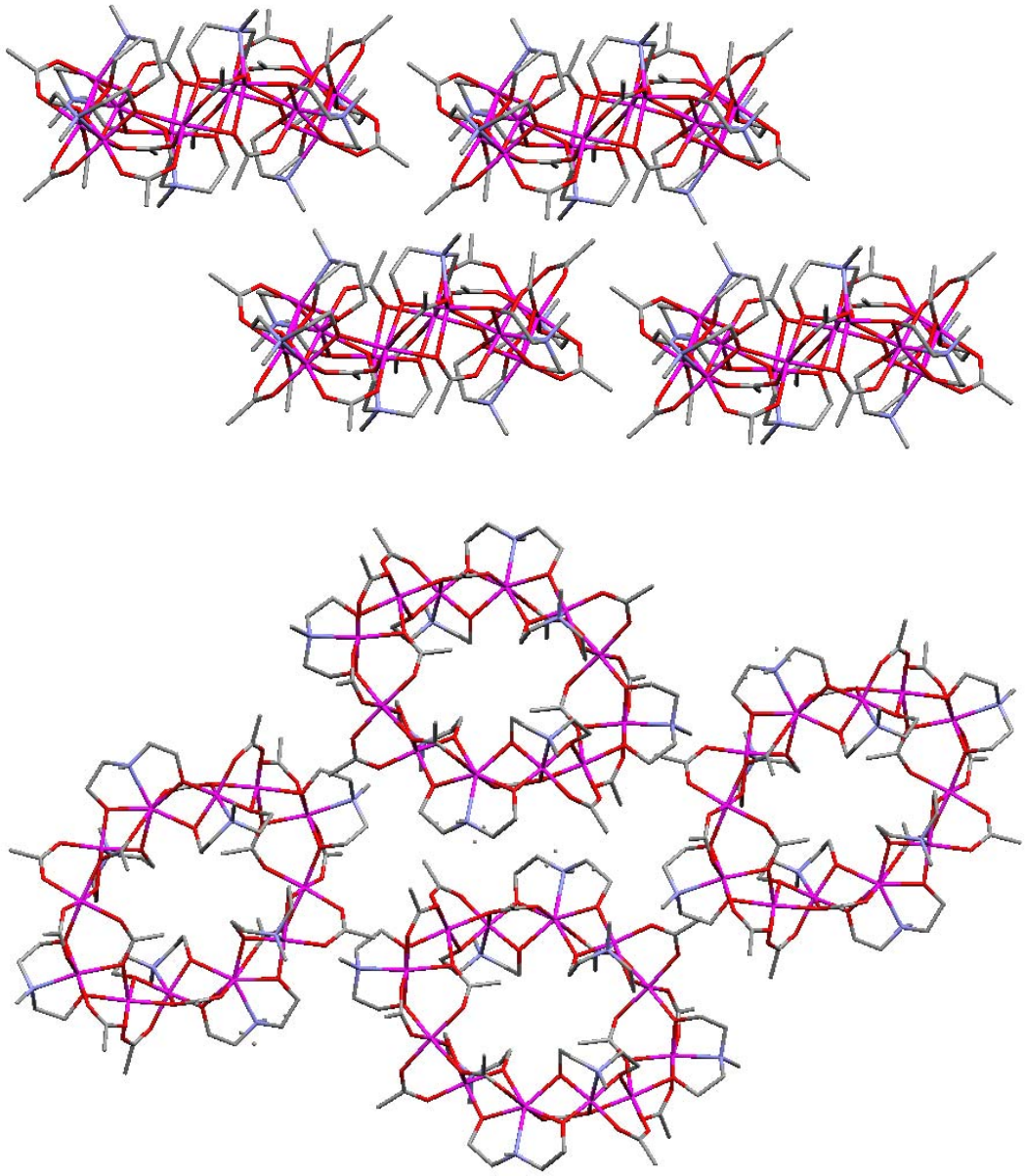

Figure 7.6. Packing diagrams for complex $[Mn_{12}(mdea)_8(O_2CCH_3)_{14}] \cdot CH_3CN$ (**7A**) (top) and complex $[Mn_{12}(mdea)_8(O_2CCH_3)_{14}]$ (**7B**) (bottom).

Figure **7.3** shows a simplified view of the wheel Mn-O-Mn connectivity and magnetic exchange pathways. The alternating Mn^{II} and Mn^{III} ions are coordinated to the acetate and the deprotonated alcohol amine ligand $mdea^{2-}$. The acetate and alkoxide arms of the amine ligands act as bridges between each Mn atom and are the backbone of the wheel. The acetate ligands exhibit two different bridging modes: Eight of the fourteen acetate ligands bridge in a η^1:η^1:μ_2 mode that does not act as a dominant exchange pathway, while the other six acetate ligand bridge in a η^1: η^2: μ_2 mode where O5, O10, O15 and their symmetry equivalents act as principal super-exchange pathways. All of the oxo atoms of the amine ethoxy arms act as principal exchange pathways between alternating M^{II} and Mn^{III} centers. The atoms Mn2, Mn4, Mn6 (and the symmetry related Mn2a, Mn4a, and Mn6a) have been determined to be trivalent by noting their Jahn-Teller distorted geometries and through bond valence sum analysis. These atoms exhibit Jahn-Teller elongation axes with two bond lengths that are significantly longer (e.g. 2.1989(17) - 2.3111(2) Å for Mn2) than the other four bonds (1.8890(17) and 1.9015(17) Å for Mn2). As shown in Figure **7.4**, four of these Jahn-Teller elongation axes (Mn2, Mn2a, Mn4, Mn4a) orient virtually parallel to one another and orthogonal to plane of the ring, while the other two Jahn-Teller axes are nearly in the plane of the ring. The atoms Mn1, Mn3, Mn5, and the symmetry equivalent Mn1a, Mn3a, and Mn5a are divalent, having bond lengths spanning a much more restricted range (e.g. 2.0972(18) to 2.2502(18) Å for Mn5). The divalent atoms Mn3 and Mn3A are seven coordinate. Selected bond distances and bond angles for complex **7B** are given in Tables **7.4** and **7.5** for complex **7B**.

Complex **[$Mn_{12}(mdea)_8(O_2CCH_3)_{14}$] (7B)** is chemically equivalent to complex 7A with the exception of how it crystallizes within the lattice. Complex **7B** crystallizes in the P21/n space group with two molecular orientations and contains no solvate molecules in the crystal lattice. Figure **7.5** illustrates a packing diagram (top) and a stereo packing diagram (bottom) for complex **7B**. Figure **7.6** illustrates packing diagrams for complex **7A** (top) and complex **7B** (bottom). Complex **7A** packs with each of its [Mn_{12}] molecules oriented in the same direction, and complex **7B** crystallizes with two molecular orientations that are rotated approximately 30º apart from each other. The [Mn_{12}] molecules propagate in the crystallographic *a* direction for complex **7B**. Each [Mn_{12}] unit is close in proximity to nearest neighbor [Mn_{12}] molecules with a intermolecular distance of 3.38 Å is between the methyl group of one $mdea^{2-}$ and the methyl of the carboxylate of the second [Mn_{12}] molecule. Each [Mn_{12}] molecule in complex **7A** is more isolated than the molecules in **7B**, with a nearest neighbor intermolecular distance of 3.79 Å for an analogous pathway.

7.3.3 Nuclear Magnetic Resonance Studies

^1H NMR data were collected for complexes [$Mn_{12}(mdea)_8(O_2CCH_3)_{14}$] (**7A**) and [$Mn_{12}(edea)_8(O_2CCH_3)_{14}$] (**7C**) on a Varian 300MHz spectrometer to verify the structure of complex **7C,** and to determine if both complexes are stable in solution. Figure **7.7** gives the spectra collected for complexes **7A** and **7C** collected in $CDCl_3$ at room temperature. As evident in Figure **7.7**, both complexes have very similar NMR spectra. Peak assignments were made based on peak integration (Table **7.6**). Strong broad peaks associated with the methylene- and methyl- groups of the *N*-

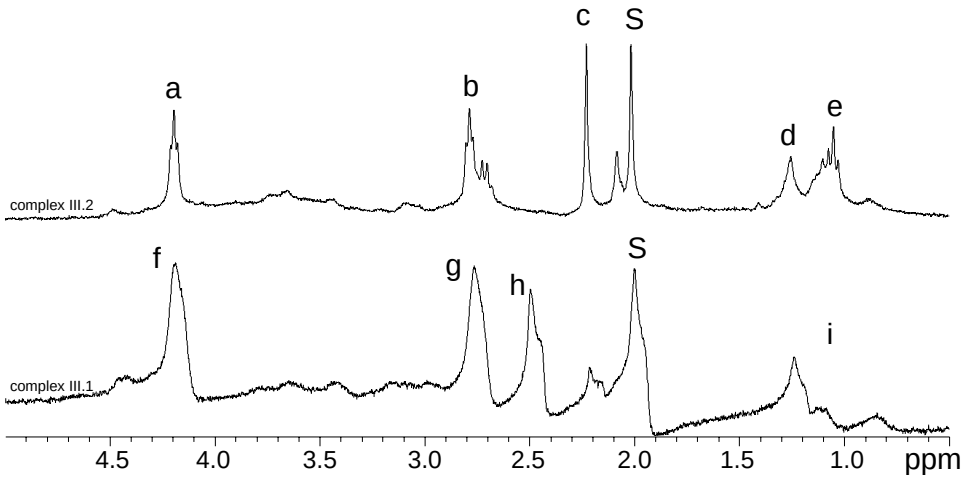

Figure 7.7. Solution ($CDCl_3$) ^1H NMR (300 MHz) spectra of complexes $[Mn_{12}(edea)_8(O_2CCH_3)_{14}]$ (**7C**, top trace) and $[Mn_{12}(mdea)_8(O_2CCH_3)_{14}] \cdot CH_3CN$ (**7A**, bottom trace).

Table 7.6. Solution ^1H NMR spectral data for complexes $[Mn_{12}(mdea)_8(O_2CCH_3)_{14}] \cdot CH_3CN$ (**7A**) and $[Mn_{12}(edea)_8(O_2CCH_3)_{14}]$ (**7C**)

Complex	Peak (δ)	Integration	Assignment	Label
7A	4.18	4.0	CH_2	f
	2.74	4.0	CH_2	g
	2.43	3.0	CH_3	h
	1.17-0.82	5.2	CH_3 acetate	i
	1.94		CH_3CN	S
7C	4.12	4.0	CH_2	a
	2.71	3.9	CH_2	b
	2.16	2.0	CH_2	c
	1.18	3.0	CH_3	d
	0.98	5.3	CH_3 acetate	e
	1.94		CH_3CN	S

methyldiethoxide (**7A**) or *N*-ethyldiethoxide (**7C**) amine ligands are observed. The strong peak at 1.94 ppm is from the acetonitrile that complexes **7A** and **7C** cocrystallize with. The X-ray structure of complex **7A** reveals a C_2 axis orthogonal to the plane of the wheel. There are three pairs of equivalent Mn^{III} ions and three pairs of equivalent Mn^{II} atoms. Four of the diethoxide amine ligands are coordinated to Mn^{II} atoms, while the other two are coordinated to Mn^{III} atoms. There are three magnetic environments for the diethoxide amine ligands if the solid state C_2 axis is preserved in solution. However, only one grouping of resonances belonging to the diethoxide amine ligand is observed, suggesting equivalency as a consequence of fast interchange in solution. Peak broadening due to the presence of paramagnetic manganese ions precludes resolution and detailed analysis of peak groupings. However, the similarity in spectra for complexes **7A** and **7C** suggest that they have very similar molecular structure.

7.3.4 DC Magnetic Susceptibility Studies

Variable temperature magnetic susceptibility data were collected for complexes **7A** and **7C** between 300-1.8K with an applied field of 1T, and are plotted as molar susceptibility ($\chi_m T$) verses the absolute temperature (T) in Figures **7.8** and **7.9**, respectively. The $\chi_m T$ maximum for complexes **7A** and **7C** at 300K are 39.7 $cm^3 \cdot mol^{-1} \cdot K$ and 39.0 $cm^3 \cdot mol^{-1} \cdot K$, respectively, and are less than the spin-only value of 44.26 $cm^3 \cdot mol^{-1} \cdot K$ expected for six Mn^{III} and six Mn^{II} non-interacting metal centers. With decreasing temperature, the molar susceptibility slowly decreases to about ~50K and then decreases more rapidly to approximately ~23K. Below 23K the dramatic drop in

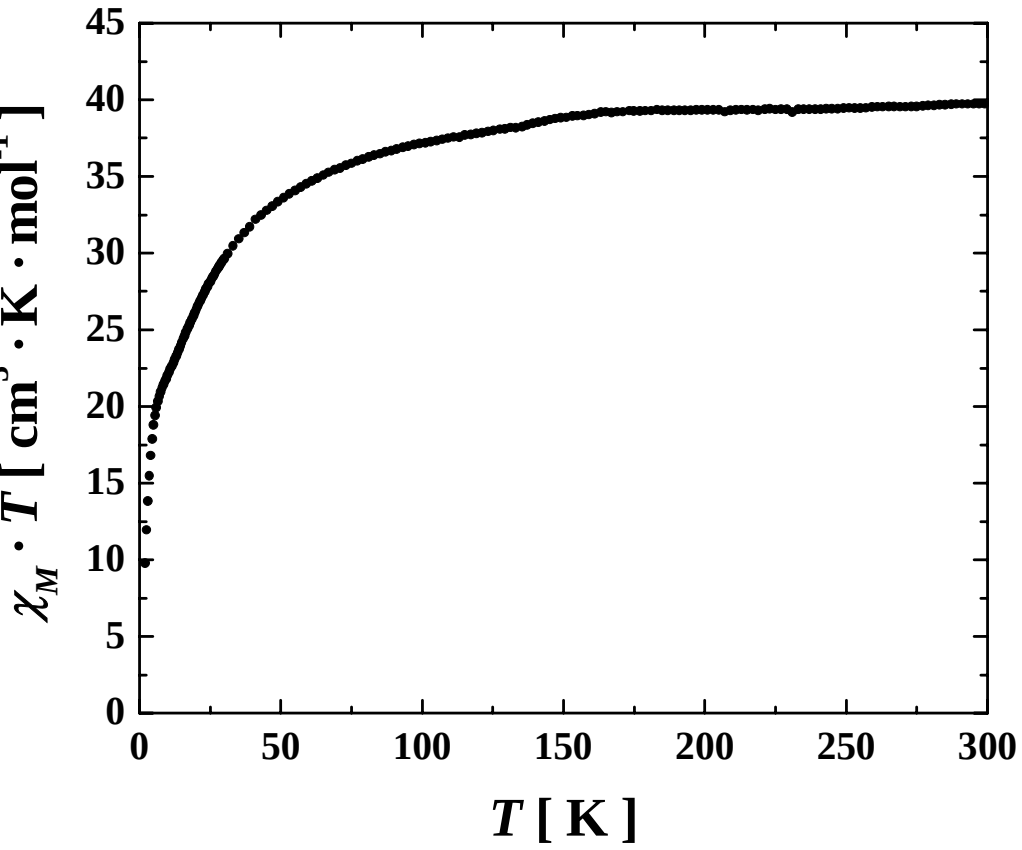

Figure 7.8. Plot of $\chi_M T$ *versus* temperature where χ_M is the molar susceptibility for complex $[Mn_{12}(mdea)_8(O_2CCH_3)_{14}] \cdot CH_3CN$ (**7A**). The data were collected with an applied field of 1 Tesla.

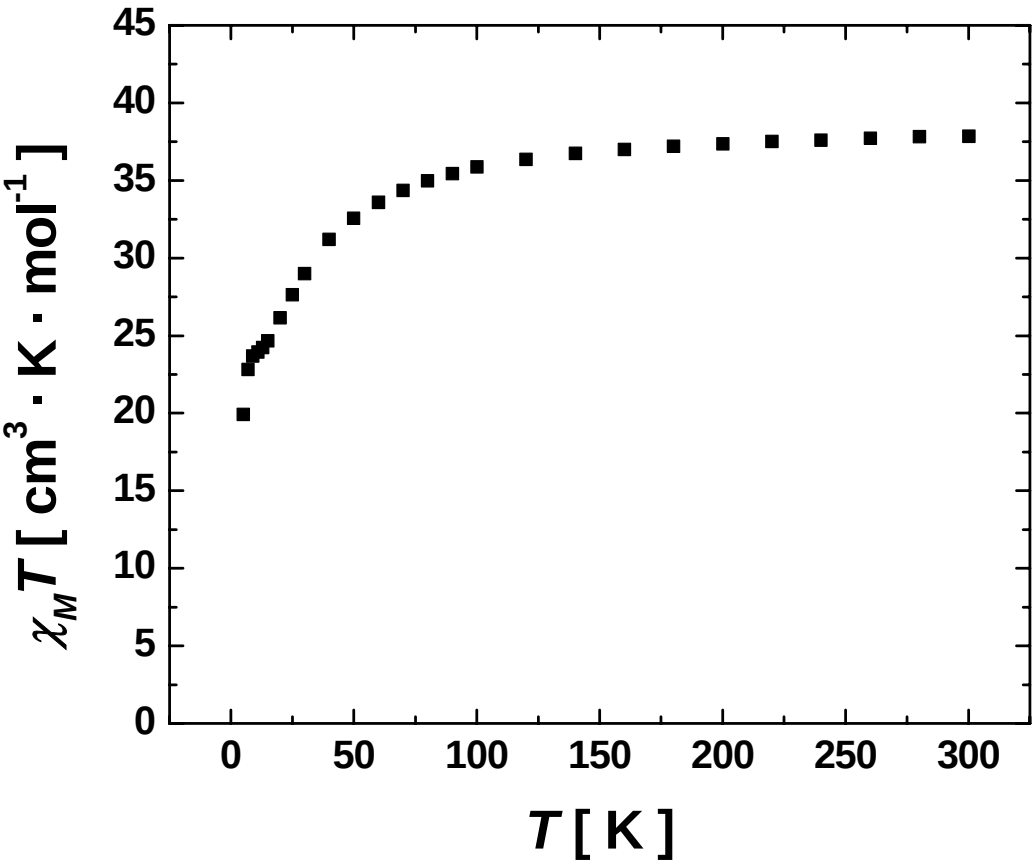

Figure 7.9. Plot of $\chi_M T$ *versus* temperature where χ_M is the molar susceptibility for complex $[Mn_{12}(edea)_8(O_2CCH_3)_{14}]$ (**7C**). The data were collected with an applied field of 1 Tesla.

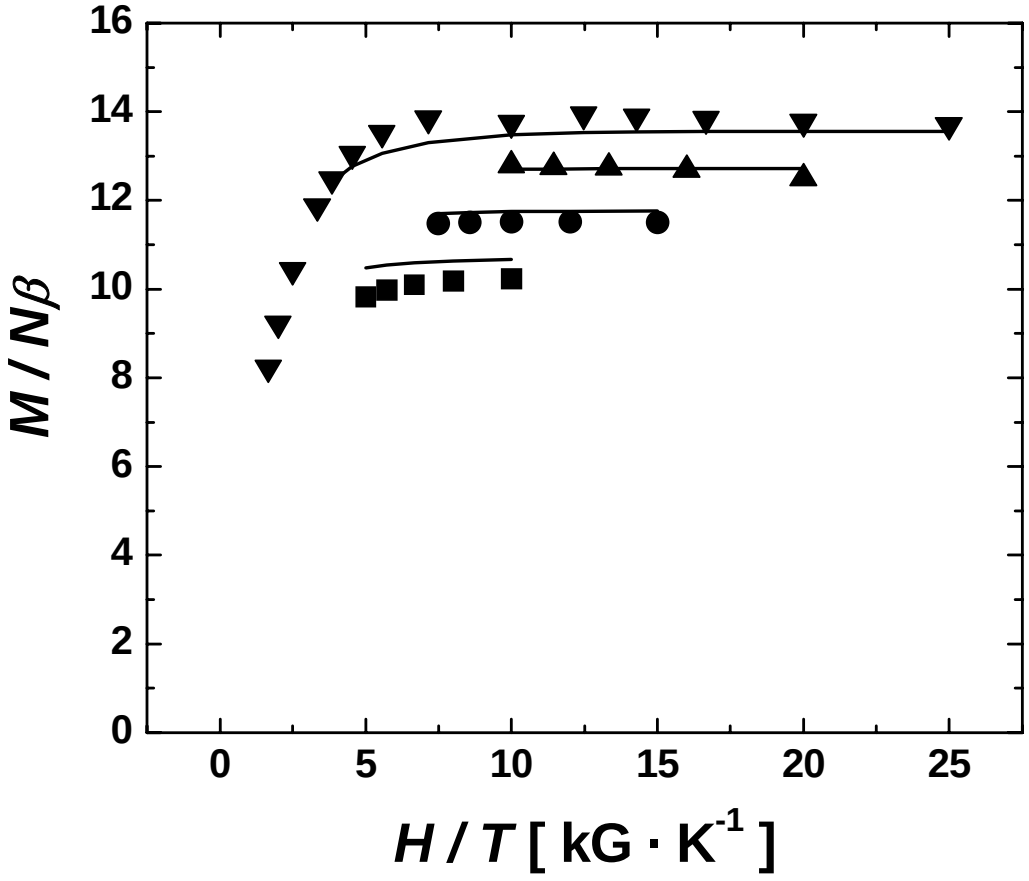

Figure 7.10. Plot of the reduced magnetization (M/Nβ) where M is the molar magnetization, N is Avogadro's number, and β is the Bohr magneton, plotted *versus* H/T for complex $[Mn_{12}(mdea)_8(O_2CCH_3)_{14}] \cdot CH_3CN$ (**7A**). Data were collected at 5 T (▼), 4 T (▲), 3 T (ℓ), and 2 T (□) in the temperature range of 2.0 – 30.0 K. The solid line represents the least squares fit of the data with the parameters S = 8, g = 2.0, D = -0.47 cm^{-1} for the temperature rage 2-13 K.

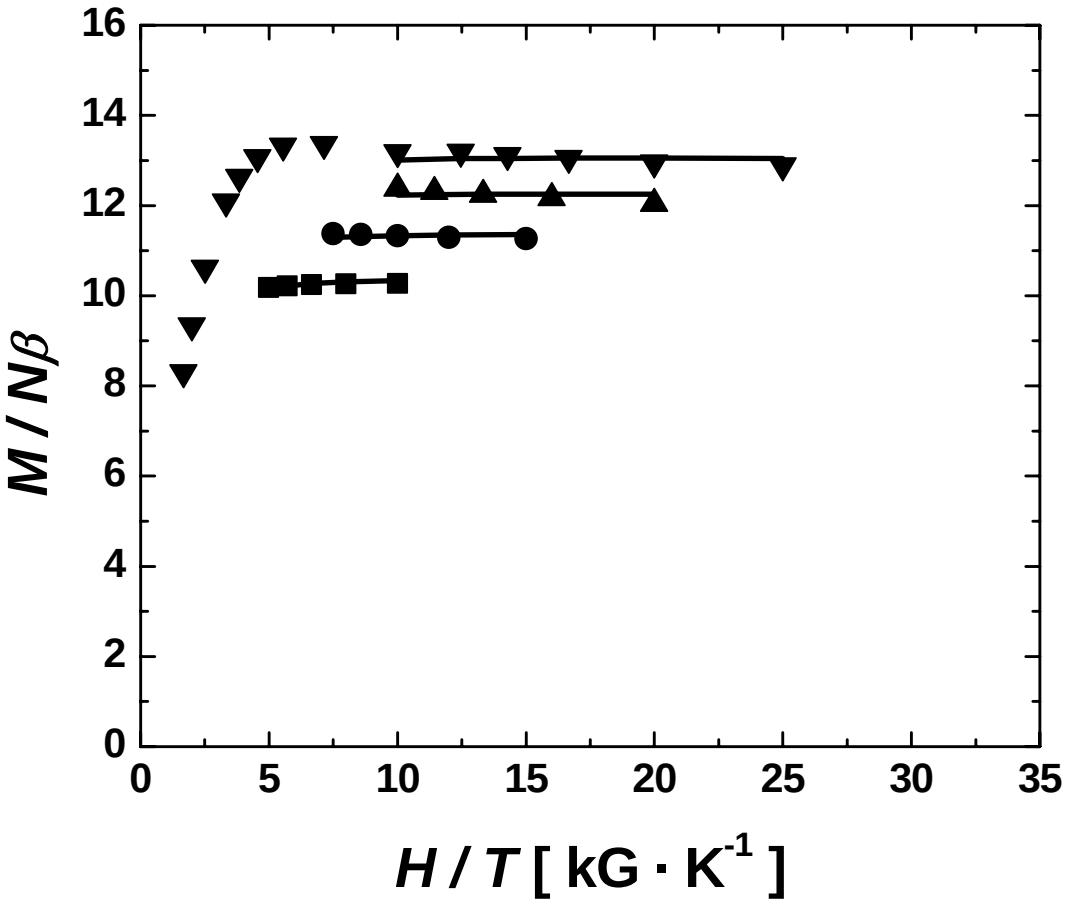

Figure 7.11. Plot of the reduced magnetization (M/Nβ) where M is the molar magnetization, N is Avogadro's number, and β is the Bohr magneton, plotted *versus* H/T for complex $[Mn_{12}(edea)_8(O_2CCH_3)_{14}]$ (**7C**). Data were collected at 5 T (▼), 4 T (▲), 3 T (ℓ), and 2 T (◆) in the temperature range of 2.0 – 30.0 K. The solid line represents the least squares fit of the data with the parameters S = 8, g = 2.0, D = -0.49 cm^{-1} for the temperature rage 2-5 K.

$$\mathcal{H} = \mu_B gH \cdot S + D[S_Z^2 - \frac{1}{3}S(S+1)] \quad \textbf{(7.1)}$$

susceptibility is due to zero-field interactions and Zeeman interactions, with $\chi_m T$ minimum occurring at ~10 $cm^3 \cdot mol^{-1} \cdot K$ and ~19.2 $cm^3 \cdot mol^{-1} \cdot K$ for complexes **7A** and **7C**, respectively, at the lowest temperature measured (1.8K). A small plateau or inflection can be seen in Figures **7.8** and **7.9.** Recent heat capacity work on similar [Mn_{12}] single-stranded wheels[47] revealed that the origin of this peak is attributed to Schottky effects (changes in Boltzman populations of M_s states) giving rise to a broad peak in the plot of *Cp* vs *T* and is not due to a magnetic or crystallographic phase transition. This phenomenon has been previously reported for [Mn_4] dicubane complexes.[61]To ascertain the spin ground state and the magnitude of the zero-field splitting parameter *D*, variable-field magnetization data (reduced magnetization) were collected for complexes **7A** and **7C** between 1.8K and 13K, with applied fields of 2-5 Tesla. Figures **7.10** and **7.11** present reduced magnetization data plotted as $M/N\beta$ *vs* H/T for complexes **7A** and **7C**, where *M* is the molar magnetization, *N* is Avagadro's number, β is the Bohr magneton and H/T is the applied magnetic field over the absolute temperature. The saturation values between ~13-14 (Figures **7.10** and **7.11**) suggest that complexes **7A** and **7C** exhibit significant spin ground states, and non-superimposibility of the iso-fields indicate that complexes **7A** and **7C** exhibit appreciable ground state zero-field splitting. Theoretical fits to the magnetization data, solid lines in Figures **7.10** and **7.11,** were calculated by full-matrix diagonalization employing energy Hamiltonian given in Equation **7.1**, where $\mu_B gH \cdot S$ is the Zeeman term (μ is the Bohr

magneton, g is the Landé g-factor, *H* is the applied magnetic field and *S* is the spin) and *D* is the second –order zero-field splitting parameter. Least-squares treatment of the magnetization data (solid lines in Figures **7.10** and **7.11**) yielded fitting parameters of *S* = 8, g = 2 and *D* = -0.47 cm^{-1} for complex **7A** and *S* = 8, g = 2 and *D* = -0.49 cm^{-1} for complex **7C**.

7.3.5 AC Magnetic Susceptibility Studies

In-phase and out-of-phase AC magnetic susceptibility data for complexes **7A** and **7C** are presented in Figures **7.12** and **7.13**, respectively and are plotted as $\chi_m'T$ vs *T* for the in-phase portion and χ_m'' vs *T* for the out-of phase portion, top and bottom, respectively, in Figures **7.12** and **7.13.** The data were collected between 5-1.8K in a 3 Gauss AC field in frequencies of 1000Hz to 50Hz in zero applied DC magnetic fields.

An out-of phase component is clearly evident for complexes **7A** and **7C** (Figures **7.12** and **7.13**, bottom) and is indicative of kinetically driven slow magnetization relaxation dynamics, and is both temperature and frequency dependent. The out-of phase component arises due to the inability of the magnetic moment of the [Mn_{12}] molecules to stay in phase with the oscillating AC magnetic field, which is more prominent at higher frequencies. Though an out-of-phase AC signal is not proof that these [Mn_{12}] wheel complexes are single-molecule magnets, they are one of the components along with steps in the hysteresis loops of magnetization verses field (*M* vs. *H*) data that signify SMM behavior. Since only the onset of an out-of –phase component is seen in Figures **7.12** and **7.13** (bottom) for complexes **7A** and **7C** (no peaks are seen) no meaningful information can be extracted regarding the energy

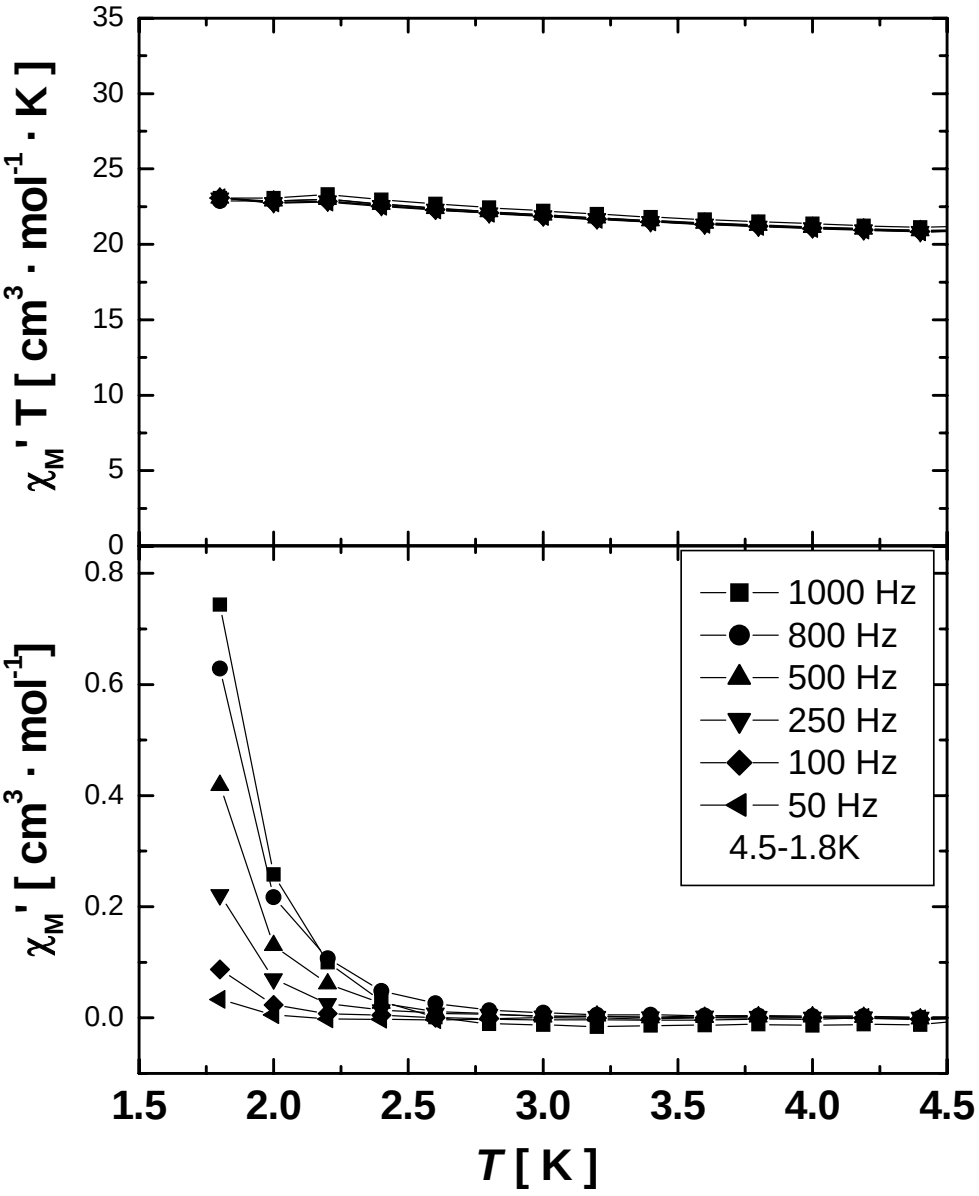

Figure 7.12. Plot (upper) of $\chi'_M T$ *versus* temperature where χ'_M is the molar in-phase *ac* susceptibility for complex $[Mn_{12}(mdea)_8(O_2CCH_3)_{14}] \cdot CH_3CN$ (**7A**). Plot (upper) of χ''_M *versus* temperature where χ''_M is the molar out-of-phase *ac* susceptibility for complex $[Mn_{12}(mdea)_8(O_2CCH_3)_{14}] \cdot CH_3CN$ (**17**). The data were collected with a 3 G *ac* field oscillating at the frequencies of 1000(◆), 800(ℓ), 500(▲), 250(▼), 100(◆) and 50(◄) Hz.

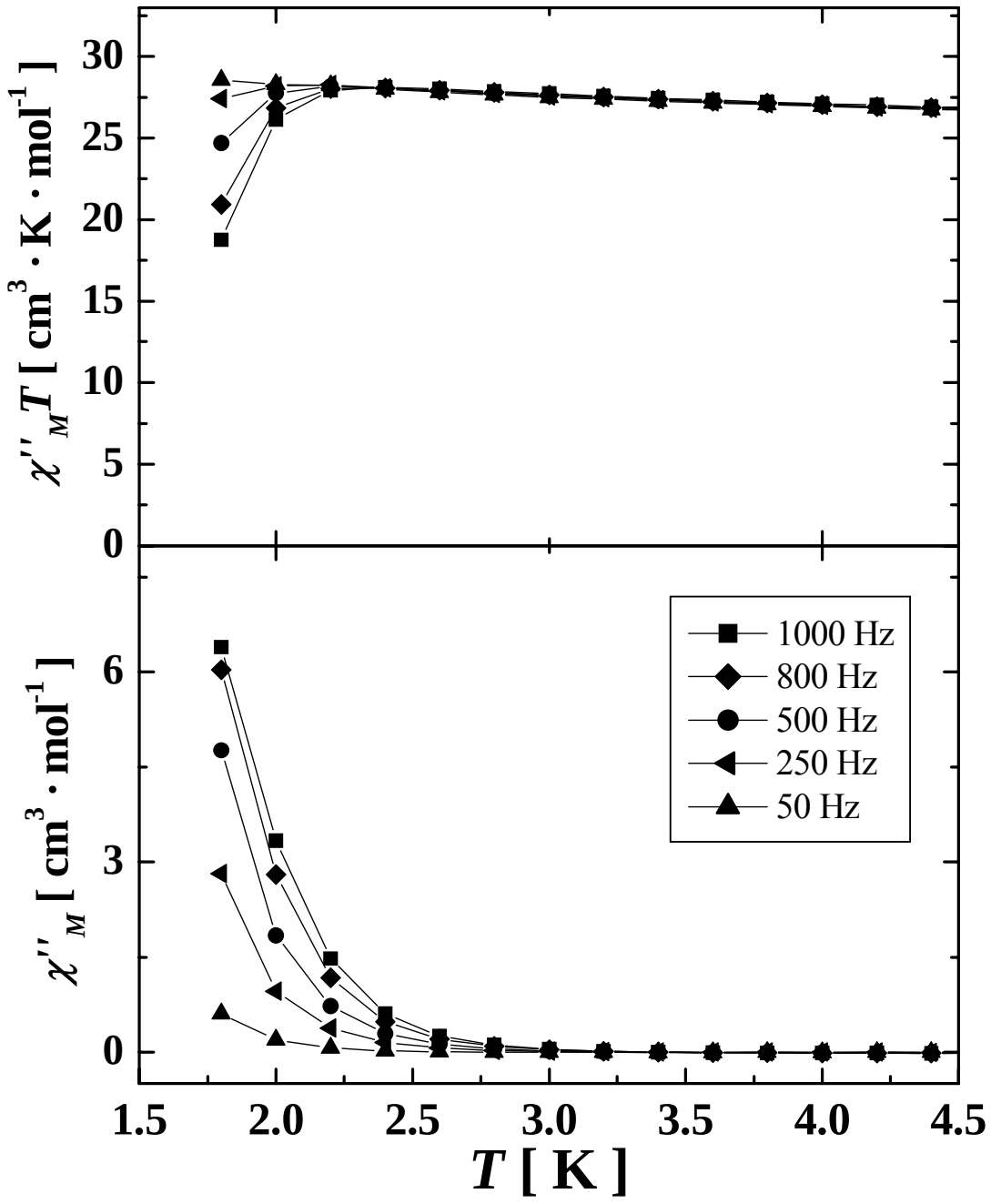

Figure 7.13. Plot (upper) of $\chi'_M T$ *versus* temperature where χ'_M is the molar in-phase *ac* susceptibility for complex **7C**. Plot (upper) of χ''_M *versus* temperature where χ''_M is the molar out-of-phase *ac* susceptibility for complex **7C**. The data were collected with a 3 G *ac* field oscillating at the indicated frequencies.

associated with the barrier toward the reversal of magnetization, and whether the barrier is less than the theoretical value of DS_z^2 due to tunneling of the magnetization.

Extrapolation of the 50Hz in-phase susceptibility data for complexes **7A** and **7C** to zero Kelvin yielded molar magnetic susceptibility values ($\chi_m T$) of 20.71 $cm^3 \cdot mol^{-1} \cdot K$ for complex **7A** and 26.57 $cm^3 \cdot mol^{-1} \cdot K$ for complex **7C**, which is significantly lower than the theoretical value of 38 $cm^3 \cdot mol^{-1} \cdot K$ expected for a well isolated $S = 8$ spin system.

7.4 Conclusion

Though crystals suitable for X-ray diffraction could not be obtained for complex **7C**, the AC and DC magnetization, NMR and hysteresis data collected on analogous [Mn_{12}] wheel complexes confirms that complex **7C** is structurally analogous to complexes **7A** and **7B**.

It is evident from extrapolation of AC in-phase magnetic susceptibility data that the zero temperature data are more consistent with a ground state spin of $S = 7$ (28 $cm^3 \cdot mol^{-1} \cdot K$ from the spin-only formula). The $S = 8$ spin ground state calculated through least-squares fitting of magnetization data are most likely significantly affected by Zeeman interactions and low-lying excited states. Furthermore, there is no simple model, such as having the moments of all of the Mn^{III} ions projected as "spin-up" and the moments of the Mn^{II} ion projected as "spin-down" that could explain the spin ground state calculated through least squares fitting of *M vs H/T* data ($S = 8$) or extrapolation of AC susceptibility data at zero temperature ($S = 7$). This is most likely a consequence of the topology and magnetic exchange pathways within the [Mn_{12}]

complexes. Firstly, rather than being truly circular, complexes **7A**, **7B** and **7C** are ellipses. Thus, oxo-mediated Mn^{III}-O-Mn^{II} super-exchange pathways within the wheel complexes are not equivalent. Furthermore, there are multiple exchange pathways between neighboring trivalent and divalent manganese ions suggesting that complicated competing ferromagnetic and antiferromagnetic exchange interactions lead to closely spaced energy levels and an intermediate spin ground state.

Subsequent work by Ramsey *et al.*[62] have revealed that the single-stranded [Mn_{12}] family of molecular wheels indeed have a complex molecular structure that is still not fully understood. Members of this family of wheel complexes have been shown to exhibit Berry-phase oscillations. The [Mn_{12}] family of wheels has in general yielded incredibly interesting physics in terms of whether energy terms associated with antisymmetric interactions can arise in molecular systems with inversion symmetry.

One area for further study may be to synthesize single stranded manganese based wheels with smaller nuclearity, and perhaps, with fewer exchange pathways. The information extracted from simple systems may then be applied to better understand larger, more complicated systems.

Chapter 7, figures are a reprint: Rumberger, E. M., Shah, S. J., Beedle, C. C.; Zakharov, L. N., Rheingold, A. L., Hendrickson, D. N., Wheel-shaped [Mn-12] Single-Molecule Magnets. *Inorganic Chemistry* **2005,** 44, (8), 2742-2752. The author of the dissertation was a highly contributing investigator of the material.

7.5 References

(1) Christou, G.; Gatteschi, D.; Hendrickson, D. N.; Sessoli, R. *Mrs Bulletin* **2000**, *25*, 66-71.

(2) Sessoli, R.; Gatteschi, D.; Caneschi, A.; Novak, M. A. *Nature* **1993**, *365*, 141-143.

(3) Wernsdorfer, W.; Allaga-Alcalde, N.; Hendrickson, D. N.; Christou, G. *Nature* **2002**, *416*, 406-409.

(4) Wernsdorfer, W.; Bhaduri, S.; Boskovic, C.; Christou, G.; Hendrickson, D. N. *Physical Review B* **2002**, *65*, 180403.

(5) Wernsdorfer, W.; Bhaduri, S.; Tiron, R.; Hendrickson, D. N.; Christou, G. *Physical Review Letters* **2002**, *89*, 197201.

(6) Sessoli, R.; Tsai, H. L.; Schake, A. R.; Wang, S. Y.; Vincent, J. B.; Folting, K.; Gatteschi, D.; Christou, G.; Hendrickson, D. N. *Journal of the American Chemical Society* **1993**, *115*, 1804-1816.

(7) Varret, F.; Bleuzen, A.; Boukheddaden, K.; Bousseksou, A.; Codjovi, E.; Enachescu, C.; Goujon, A.; Linares, J.; Menendez, N.; Verdaguer, M. *Pure and Applied Chemistry* **2002**, *74*, 2159-2168.

(8) Bogani, L.; Wernsdorfer, W. *Nature Materials* **2008**, *7*, 179-186.

(9) Cuniberti, G.; Grossman, F.; Gutierrez, R. *arXiv:cond-mat/0209138* **2002**.

(10) Gutlich, P.; Garcia, Y.; Woike, T. *Coord. Chem. Rev.* **2001**, *219-221*, 839.

(11) Gutlich, P.; Hauser, A.; Spiering, H. *Angewandte Chemie Int. Edn.* **1994**, *33*, 2024.

(12) Heath, J. R.; Ratner, M. A. *Physics Today* **2003**, 43-49.

(13) Bogani, L.; Wernsdorfer, W. *Nature Materials* **2008**, *7*, 179-186.

(14) Meier, F.; Loss, D. *Physica B-Condensed Matter* **2003**, *329*, 1140-1141.

(15) Meier, F.; Levy, J.; Loss, D. *Physical Review B* **2003**, *68*, (13).

(16) Honecker, A.; Meier, F.; Loss, D.; Normand, B. *European Physical Journal B* **2002**, *27*, 487-495.

(17) Chiolero, A.; Loss, D. *Physica E* **1997**, *1*, 292-296.

(18) Westin, L. G.; Kritikos, M.; Caneschi, A. *Chemical Communications* **2003**, 1012-1013.

(19) Liu, S. X.; Lin, S.; Lin, B. Z.; Lin, C. C.; Huang, J. Q. *Angewandte Chemie-International Edition* **2001**, *40*, 1084-+.

(20) Rumberger, E. M.; Zakharov, L. N.; Rheingold, A. L.; Hendrickson, D. N. *Inorganic Chemistry* **2004**, *43*, 6531-6533.

(21) Saalfrank, R. W.; Bernt, I.; Uller, E.; Hampel, F. *Angewandte Chemie-International Edition* **1997**, *36*, 2482-2485.

(22) Taft, K. L.; Delfs, C. D.; Papaefthymiou, G. C.; Foner, S.; Gatteschi, D.; Lippard, S. J. *Journal of the American Chemical Society* **1994**, *116*, 823-832.

(23) Taft, K. L.; Lippard, S. J. *Journal of the American Chemical Society* **1990**, *112*, 9629-9630.

(24) Abbati, G. L.; Cornia, A.; Fabretti, A. C.; Malavasi, W.; Schenetti, L.; Caneschi, A.; Gatteschi, D. *Inorganic Chemistry* **1997**, *36*, 6443-6446.

(25) Waldmann, O.; Koch, R.; Schromm, S.; Schulein, J.; Muller, P.; Bernt, I.; Saalfrank, R. W.; Hampel, F.; Balthes, E. *Inorganic Chemistry* **2001**, *40*, 2986-2995.

(26) Caneschi, A.; Cornia, A.; Fabretti, A. C.; Gatteschi, D. *Angewandte Chemie-International Edition* **1999**, *38*, 1295-1297.

(27) Lascialfari, A.; Gatteschi, D.; Borsa, F.; Shastri, A.; Jang, Z. H.; Carretta, P. *Physical Review B* **1998**, *57*, 514-520.

(28) Watton, S. P.; Fuhrmann, P.; Pence, L. E.; Caneschi, A.; Cornia, A.; Abbati, G. L.; Lippard, S. J. *Angewandte Chemie-International Edition* **1997**, *36*, 2774-2776.

(29) Oshio, H.; Hoshino, N.; Ito, T.; Nakano, M.; Renz, F.; Gutlich, P. *Angewandte Chemie-International Edition* **2003**, *42*, 223-+.

(30) van Slageren, J.; Sessoli, R.; Gatteschi, D.; Smith, A. A.; Helliwell, M.; Winpenny, R. E. P.; Cornia, A.; Barra, A. L.; Jansen, A. G. M.; Rentschler, E.; Timco, G. A. *Chemistry-a European Journal* **2002**, *8*, 277-285.

(31) Atkinson, I. M.; Benelli, C.; Murrie, M.; Parsons, S.; Winpenny, R. E. P. *Chemical Communications* **1999**, 285-286.

(32) Eshel, M.; Bino, A.; Felner, I.; Johnston, D. C.; Luban, M.; Miller, L. L. *Inorganic Chemistry* **2000**, *39*, 1376-1380.

(33) Helliwell, M.; Smith, A. A.; Teat, S. J.; Winpenny, R. E. P. *Inorganica Chimica Acta* **2003**, *354*, 49-53.

(34) McInnes, E. J. L.; Anson, C.; Powell, A. K.; Thomson, A. J.; Poussereau, S.; Sessoli, R. *Chemical Communications* **2001**, 89-90.

(35) Brechin, E. K.; Cador, O.; Caneschi, A.; Cadiou, C.; Harris, S. G.; Parsons, S.; Vonci, M.; Winpenny, R. E. P. *Chemical Communications* **2002**, 1860-1861.

(36) Andres, H.; Basler, R.; Blake, A. J.; Cadiou, C.; Chaboussant, G.; Grant, C. M.; Gudel, H. U.; Murrie, M.; Parsons, S.; Paulsen, C.; Semadini, F.; Villar, V.; Wernsdorfer, W.; Winpenny, R. E. P. *Chemistry-a European Journal* **2002**, *8*, 4867-4876.

(37) Cadiou, C.; Murrie, M.; Paulsen, C.; Villar, V.; Wernsdorfer, W.; Winpenny, R. E. P. *Chemical Communications* **2001**, 2666-2667.

(38) Hanspeter, A.; Reto, B.; Alexander, J. B.; Cyril, C.; Gregory, C.; Craig, M. G.; Hans-Ulrich, G.; Mark, M.; Simon, P.; Carley, P.; Fabrizzio, S.; Vincent, V.; Wolfgang, W.; Richard, E. P. W. *Chemistry - A European Journal* **2002**, *8*, 4867-4876.

(39) Lascialfari, A.; Gatteschi, D.; Cornia, A.; Balucani, U.; Pini, M. G.; Rettori, A. *Physical Review B* **1998**, *57*, 1115-1123.

(40) Laye, R. H.; Larsen, F. K.; Overgaard, J.; Muryn, C. A.; McInnes, E. J. L.; Rentschler, E.; Sanchez, V.; Teat, S. J.; Gudel, H. U.; Waldmann, O.; Timco, G. A.; Winpenny, R. E. P. *Chemical Communications* **2005**, 1125-1127.

(41) Manoli, M.; Prescimone, A.; Mishra, A.; Parsons, S.; Christou, G.; Brechin, E. K. *Dalton Transactions* **2007**, 532-534.

(42) Moushi, E. E.; Lampropoulos, C.; Wernsdorfer, W.; Nastopoulos, V.; Christou, G.; Tasiopoulos, A. J. *Inorganic Chemistry* **2007**, *46*, 3795-3797.

(43) Muralee, M.; Wolfgang, W.; Khalil, A. A.; George, C. *Angewandte Chemie International Edition* **2005**, *44*, 892-896.

(44) Murugesu, M.; Raftery, J.; Wernsdorfer, W.; Christou, G.; Brechin, E. K. *Inorganic Chemistry* **2004**, *43*, 4203-4209.

(45) Rumberger, E. M.; Shah, S. J.; Beedle, C. C.; Zakharov, L. N.; Rheingold, A. L.; Hendrickson, D. N. *Inorganic Chemistry* **2005**, *44*, 2742-2752.

(46) Rumberger, E. M.; Zakharov, L. N.; Rheingold, A. L.; Hendrickson, D. N. *Inorganic Chemistry* **2004**, *43*, 6531-6533.

(47) Shah, S. J.; Ramsey, C. M.; Heroux, K. J.; DiPasquale, A. G.; Dalal, N. S.; Rheingold, A. L.; del Barco, E.; Hendrickson, D. N. *Inorganic Chemistry* **2008**, *47*, 9569-9582.

(48) Shah, S. J.; Ramsey, C. M.; Heroux, K. J.; O'Brien, J. R.; DiPasquale, A. G.; Rheingold, A. L.; del Barco, E.; Hendrickson, D. N. *Inorganic Chemistry* **2008**, *47*, 6245-6253.

(49) Foguet-Albiol, D.; O'Brien, T. A.; Wernsdorfer, W.; Moulton, B.; Zaworotko, M. J.; Abboud, K. A.; Christou, G. *Angewandte Chemie-International Edition* **2005**, *44*, 897-901.

(50) Meier, F.; Loss, D. *Physical Review Letters* **2001**, *86*, 5373-5376.

(51) Abbati, G. L.; Cornia, A.; Fabretti, A. C.; Caneschi, A.; Gatteschi, D. *Inorganic Chemistry* **1998**, *37*, 1430-+.

(52) Anastasios, J. T.; Alina, V.; Wolfgang, W.; Khalil, A. A.; George, C. *Angewandte Chemie International Edition* **2004**, *43*, 2117-2121.

(53) Theocharis , C. S.; Khalil , A. A.; Wolfgang, W.; George, C. *Angewandte Chemie International Edition* **2008**, *47*, 6694-6698.

(54) Lis, T. *Acta Crystallographica Section B-Structural Science* **1980**, *36*, 2042-2046.

(55) Sheldrick, G. M.; 2.01 ed.; Bruker AXS: Madison, 1998.

(56) Beedle, C. C.; Heroux, K. J.; Nakano, M.; DiPasquale, A. G.; Rheingold, A. L.; Hendrickson, D. N. *Polyhedron* **2007**, *26*, 2200-2206.

(57) Beedle, C. C.; Stephenson, C. J.; Heroux, K. J.; Wernsdorfer, W.; Hendrickson, D. N. *Inorganic Chemistry* **2008**, *47*, 10798-10800.

(58) Wittick, L. M.; Jones, L. F.; Jensen, P.; Moubaraki, B.; Spiccia, L.; Berry, K. J.; Murray, K. S. *Dalton Transactions* **2006**, 1534-1543.

(59) Zhou, A. J.; Qin, L. J.; Beedle, C. C.; Ding, S.; Nakano, M.; Leng, J. D.; Tong, M. L.; Hendrickson, D. N. *Inorganic Chemistry* **2007**, *46*, 8111-8113.

(60) Wang, W. G.; Zhou, A. J.; Zhang, W. X.; Tong, M. L.; Chen, X. M.; Nakano, M.; Beedle, C. C.; Hendrickson, D. N. *Journal of the American Chemical Society* **2007**, *129*, 1014-1015.

(61) Bhattacharjee, A.; Miyazaki, Y.; Nakano, M.; Yoo, J.; Christou, G.; Hendrickson, D. N.; Sorai, M. *Polyhedron* **2001**, *20*, 1607-1613.

(62) Ramsey, C. M.; del Barco, E.; Hill, S.; Shah, S. J.; Beedle, C. C.; Hendrickson, D. N. *Nat Phys* **2008**, *4*, 277-281.

Chapter 8

High-Frequency Electron Paramagnetic Resonance Studies of Anisotropic Exchange in a Tetranuclear Co^{II} Complex

8.1 Introduction

A number of first-row transitions metals, including Ni^{II}, [1-4] Mn^{II-IV}[5-7] and Fe^{III}[8-11] exhibit anisotropy as a result of crystal field effects and spin-orbit interactions. The single-ion anisotropy exhibited by these paramagnetic metals, in conjunction with appreciable spin, leads to a thermodynamic barrier between m_s states of opposite spin projection. Complexes formed from these transition metals, called single-molecule magnets (SMMs),[5,12] have yielded interesting low-temperature magnetization and quantum dynamics and continue to draw considerable interest as they show evidence of both classical and quantum properties.

As discussed in chapters 1 and 3, the Ni_4^{II} series of complexes, and most importantly $[Ni(hmp)(dmb)Cl]_4$[13,14] and the diamagnetic analogue $[Zn(hmp)(dmb)Cl]_4$[15] complex doped with small amounts of Ni^{II} ions, have yielded essential information regarding how the special orientation and projection of single-ion anisotropies, the interplay of local anisotropies and the magnitude of nearest neighbor pairwise magnetic exchange interactions affect magnetization and quantum dynamics.[13-16] Furthermore, this system clearly illustrates break-downs in methods currently employed by physicists and chemists to quantitatively understand the complex electronic structure of these amazing systems.[17,18]

Very few examples exist where Co^{II}[19-23] ions have been employed in the construction of SMMs, in part, because they exhibit exceptionally strong spin-orbit interactions which complicates [24] detailed electronic analysis. This is particularly true in cases where there are magnetic exchange interactions, and multiple exchange pathways between Co^{II} ions. In many instances the chemistry involving Co^{II} and Ni^{II}

ions is very similar. Thus, analogues of $[Ni(hmp)(dmb)Cl]_4$ and the doped $[Zn(hmp)(dmb)Cl]_4$ complexes have been synthesized employing paramagnetic Co^{II} metal centers.[15] The $[Co(hmp)(dmb)Cl]_4$ complex exhibits weak out-of-phase signals in its ac magnetic susceptiblility and extremely weak magnetization versus field hysteresis loops, typical of slow magnetization relaxation behavior as exhibited by SMMs.[25] In addition, this complex exhibits non-superimposable iso-fields in plots of magnetization versus field and inverse temperature (*M* vs. *H/T*, reduced magnetization), and is usually a direct result of axial zero-field splitting and a thermodynamic barrier for magnetization reversal. In this chapter oriented single-crystal high-frequency electron paramagnetic resonance (HFEPR) is employed to study the origin of anisotropy and exhibited SMM behavior of the $[Co(hmp)(dmb)Cl]_4$ by studying the analogous $[Zn(hmp)(dmb)Cl]_4$ complex doped with Co^{II} ions. The metal content in the doped complex**,** $[Zn_{0.995}Co_{0.005}(hmp)(dmb)Cl]_4$, was determined employing induced-coupled plasma optical emission spectroscopy (OCP-OES).

8.2 Experimental Section

8.2.1 Compound Preparation

All reactions were performed under aerobic conditions. The ligands 3,3-dimethylbutanol (dmb), 2-pyridylcarbinol (Hhmp) were purchased from Sigma Aldrich and used without further purification.

$[Zn_{0.995}Co_{0.005}(hmp)(dmb)Cl]_4$ (8A). To 80 mL of methanol was added solid $CoCl_2 \cdot 6H_2O$, 0.48g (2 mmol) and solid $ZnCl_2 \cdot 2H_2O$, 2.45g (18 mmol) with stirring until totally dissolved. To the resultant pale pink solution was added dropwise, 2.18g (20

mmol) Hhmp and refluxed for 30 minutes, at which time, 1.08g (20 mmol) of NaOMe dissolved in hot methanol (20 mL) was added dropwise over 3 minutes. The red/brown solution was gravity filtered while still hot, covered with aluminum foil, and allowed to stand undisturbed overnight yielding light pink prism-shaped crystals. 2.0g of the collected crystals were dissolved in CH_2Cl_2 (80 mL) and 25.0g (0.24 mol) 3,3-dimethylbutanol. The light pink solution was stirred for 10 minutes and then gravity filtered. Pale pink, prismatic crystals suitable for study by X-ray crystallography were collected by slow evaporation after 1 week. Yield: 73 % by zinc and cobalt. Anal. Calcd for complex **8A**, $C_{48}H_{80}Cl_4N_4O_8Zn_{3.98}Co_{0.02}$: C, 46.32; N, 4.50; H, 6.48. Found: C, 46.13; N, 4.60; H, 5.98. Selected FT-IR data (KBr, cm^{-1}): 3304 (b,s), 2955 (s), 2903 (s), 1605 (s), 1572 (s), 1481 (s), 1440 (s), 1397 (s), 1364 (s), 1288 (s), 1247 (m), 1219 (m), 1203 (w), 1220 (m), 1156 (s), 1080 (s), 1047 (s), 1024 (s), 997 (s), 973 (m), 818 (m), 754 (s), 730 (s), 642 (s), 496 (s), 463 (m), 412 (m).

$[Co(hmp)(dmb)Cl]_4$ (8B).[25] The systhesis of complex **8B** is analogous to the systhesis for complex **3C** presented in chapter 3. A mixture of $CoCl_2 \cdot 4H2O$ (4.75 g, 20 mmol), 2-hydroxymethylpyridine (hmpH) (2.18 g, 20 mmol), and NaOMe (1.08 g, 20 mmol) in 100 mL of MeOH was refluxed for 30 min. The resulting solution was filtered when it was still hot, producing green prismatic crystals upon cooling (**$[Co(hmp)(MeOH)Cl]_4$**).[26] 3.9g of the collected green crystals was dissolved in a solution of 50g of 3,3-dimethyl-1-butanol (dmb) and 60 mL of methylenechloride. After filtration, the solution was allowed to evaporate slowly. Green-colored crystals suitable for X-ray diffraction were collected after 1 week.

8.2.2 X-ray Crystallography

A pale pink prism 0.29 x 0.17 x 0.15 mm in size was mounted on a cryoloop with Paratone® oil. Data was collected in a nitrogen gas stream at -173 ° C. Crystal-to-detector distance was 60 mm and exposure time was 10 seconds per frame using a scan width of 0.3°. Data collection was 99.8% complete to 25° in θ. A total of 10,226 reflections were collected covering the indices, -6<=h<=16, -16<=k<=13, -24<=l<=46. 3,307 reflections were found to be symmetry independent with an [Rint] of 0.0256 indicating that the data was of good quality (0.07). Indexing and unit cell refinement indicated a body-centered, orthorhombic lattice setting. The space group was found to be $I4_1/a$. The data was integrated using the Bruker SAINT software program and scaled using the Bruker SADABS software program. Solution by direct methods (SHELXS-97) produced a complete heavy atom phasing model consistent with the proposed structure. All non-hydrogen atoms were refined anisotropically by full-matrix least-squares methods (SHELXL-97). All hydrogen atoms were placed using a riding model and their positions constrained relative to their parent atom using the appropriate HFIX command in SHELXL-97.

8.2.3 Physical Methods

Experiments were performed in a 9 T superconducting magnet, and temperature control achieved using a 4He flow cryostat equipped with a calibrated temperature sensor. As a spectrometer, we utilized a Millimeter-wave Vector Network Analyzer (MVNA, described elsewhere,[27] enabling measurements from 8 to 715 GHz at the University of Florida. At the higher frequencies (>200 GHz), a pair of external Gunn

diodes were associated with the MVNA on both source and detection sides, enabling phase sensitive measurements up to 715 GHz. A quasioptical spectrometer was used for frequencies above 200 GHz. This spectrometer, which has been described previously, employs a tapered corrugated HE_{11} waveguide tube, enabling single-pass reflectivity measurements with good coupling to relatively small crystals (<1 mm3). For frequencies below 200 GHz, a cavity perturbation technique was employed.

8.3 Results and Discussion

8.3.1 Description of Structure

Complex **8A** crystallizes in the tetragonal $I4_1/a$ space group with Z = 8 (4 molecules) and void of any solvent molecules, which is identical to complex **8B**. Crystallographic data are given in Table 8.1. All crystallographic refinement was completed treating all metal atoms as zinc. Figure 8.1 illustrates the ORTEP drawing at 50% probability of complex **8A.** The $[M_4O_4]$ core of complex **8A** (M = Zn or Co) is analogous to $[Co(hmp)(dmb)Cl]_4$ complex **8B**, forming a distorted cube with pseudo S_4 site symmetry along the crystallographic *c*-axis with metal atoms and oxo-atoms, from the alkoxy-arm of the deprotonated Hhmp ligand, occupying alternate vertices. Each of the four metal centers is additionally coordinated to an hmp nitrogen atom, a chloride ion and a dmb ligand in a distorted 6-coordinate octahedral geometry. The oxygens of the dmb ligands are still protonated. Comparison of bond angles and bond distances for complexes **8A** and **8B** is presented in Table 8.2, and reveals only slight variations in distances (0.01-0.06 Å) in the $[M_4O_4]$ core associated with magnetic exchange

Table 8.1. Crystallographic data for $[Zn_{3.98}Co_{0.02}(hmp)_4(dmb)_4Cl_4]$ (Complex **8A**)

Formula[a]	C48 H81 Cl4 N4 O8 M4
Formula weight	1245.55
Temperature	100(2) K
Wavelength	0.71073 Å
Crystal system	Tetragonal
Space group	I41/a
Unit cell dimensions	a = 12.9141(7) Å
	b = 12.9141 Å
	c = 35.001(2) Å
Volume	5837.3(5) $Å^3$
Z, Z'	4, 0.25
Density (calculated)	1.411 Mg/m^3
Absorption coefficient	1.856 mm^{-1}
F(000)	2576
Crystal size	0.29 x 0.17 x 0.15 mm^3
Theta range for data collection	1.68 to 28.16°.
Index ranges	-6<=h<=16, -16<=k<=13, -24<=l<=46
Reflections collected	10226
Independent reflections	3307 [R(int) = 0.0256]
Completeness to theta = 25.00°	99.8 %
Absorption correction	Semi-empirical from equivalents
Max. and min. transmission	0.7681 and 0.6151
Refinement method	Full-matrix least-squares on F^2
Data / restraints / parameters	3307 / 1 / 157
Goodness-of-fit on F^2	1.059
Final R indices [I>2sigma(I)]	R1 = 0.0349, wR2 = 0.0874
R indices (all data)	R1 = 0.0403, wR2 = 0.0902
Largest diff. peak and hole	0.975 and -0.461 $e.Å^{-3}$

[a] M represents Zn or Co

Table 8.2. Comparison of selected bond lengths (Å) and bond angles (deg) for **[$Zn_{3.98}Co_{0.02}(hmp)_4(dmb)_4Cl_4$]** (**8A**) and **[$Co(hmp)(dmb)Cl]_4$** (**8B**)[a]

	Complex **8A**	Complex **8B**
M(1)-O(1)	2.0683(15)	2.0751(10)
M(1)-N(1)	2.1241(19)	2.1221(12)
M(1)-O(1)#1	2.1260(14)	2.0810(10)
M(1)-O(1)#2	2.1338(14)	2.1409(9)
M(1)-O(2)	2.2031(15)	2.1462(11)
M(1)-Cl(1)	2.3386(5)	2.3689(4)
O(1)#1-M(1)-O(1)#2	79.91(6)	78.20(4)
O(1)-M(1)-N(1)	156.38(6)	159.25(4)
O(1)-M(1)-O(1)#1	80.98(6)	82.27(4)
N(1)-M(1)-O(1)#1	103.41(6)	102.40(4)
O(1)-M(1)-O(1)#2	80.79(6)	80.70(4)
O(1)-M(1)-O(2)	82.91(6)	85.05(4)
N(1)-M(1)-O(2)	88.75(6)	89.10(5)
O(1)#1-M(1)-O(2)	162.47(6)	164.79(4)
O(1)-M(1)-Cl(1)	103.69(4)	101.92(3)
N(1)-M(1)-Cl(1)	98.78(5)	98.19(3)
O(1)#1-M(1)-Cl(1)	97.71(4)	95.73(3)
O(1)#2-M(1)-Cl(1)	174.61(4)	173.32(3)
O(2)-M(1)-Cl(1)	92.75(4)	92.39(3)

[a] M represents Zn or Co for complex **8A** and Co for complex **8B**

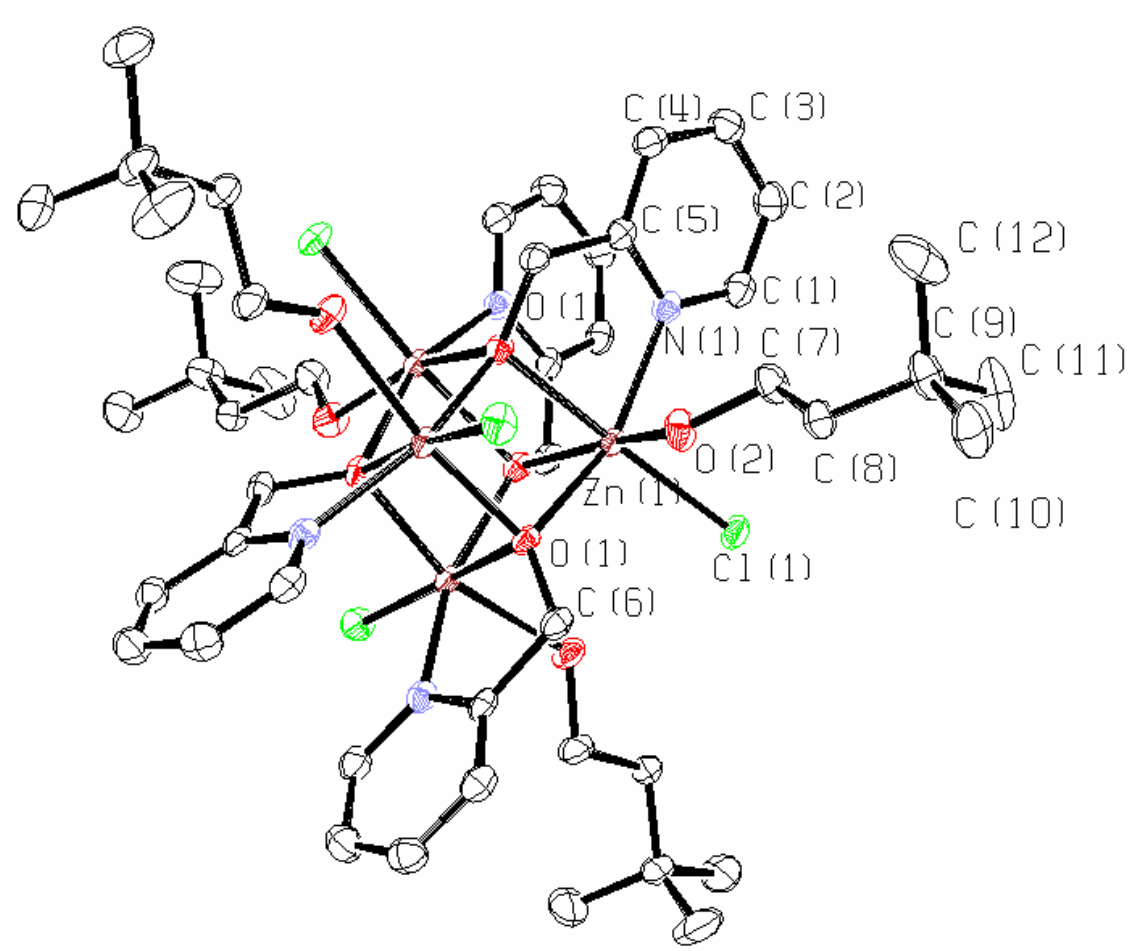

Figure 8.1. ORTEP illustration of complex **8B [$Zn_{3.98}Co_{0.02}(hmp)_4(dmb)_4Cl_4$]** at the 50% probability level. The asymmetric unit is labeled for simplicity.

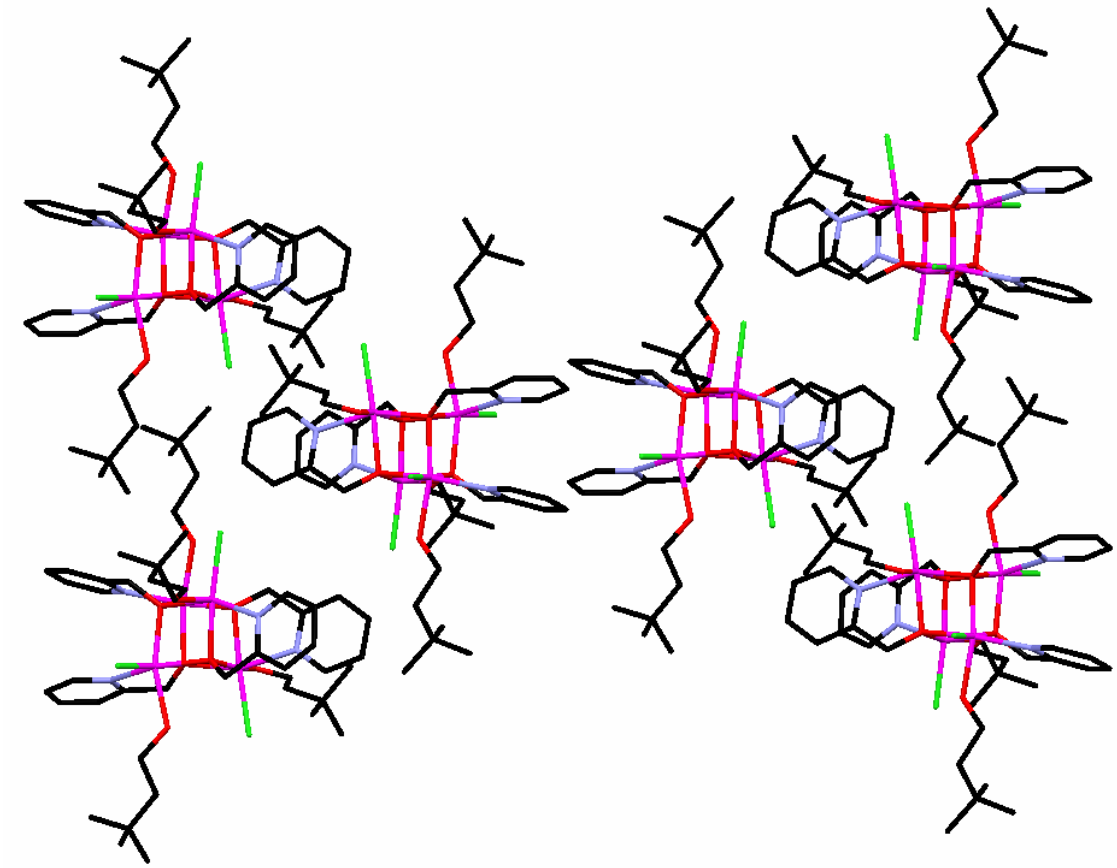

Figure 8.2. Crystal packing diagram of Complex **8B [$Zn_{3.98}Co_{0.02}(hmp)_4(dmb)_4Cl_4$]**.

pathways. The M-Cl distance is 0.03 Å longer in complex **8B** than in complex **8A** and ~0.08 Å longer than the Co-Cl bonds found in literature for a distorted octahedral field. A packing diagram for complex **8A** is given in Figure 8.2 with two of the molecules fully occupying the unit cell and four others half occupy the cell giving a Z of 4, and the asymmetric unit, Z'= 0.25, represents one quarter of a molecule. The largest distribution of molecules in complex **8A** should contain $[Zn_4O_4]$ cores with a non-systematic distribution of $[Zn_{3.98}Co_{0.002}]$ cores. Complexes **8A** and **8B** have comparable bond angles and bond distances, and they crystallize in the same space group with the same packing arrangement void of solvent molecules. The similarities between these complexes suggest that treatment of these complexes regarding exchange parameters should be equivalent.

8.3.2 Induced-Coupled Plasma Optical Emission

The ICP-OES system used was a Perkin-Elmer Optima 3000 DV with axially viewed plasmas. System processes were followed as previously reported.[28] Seven standards were prepared of $CoCl_2 \cdot 6H_2O$ and $ZnCl_2 \cdot 2H_2O$ respectively. Concentrations for standards were between 0 and 30,000 ppb at 5000 ppb increments yielding a best fit calibration line (0.9997 sdev). 0.0378g of complex **8A** was dissolved and diluted 118.5 times in 1% HNO_3 solution and then further diluted 160 times to ensure Co and Zn concentrations were within the specified range of the calibration curve. The maximum calculated dilution factors for cobalt and zinc were 37 ppb and 8000 ppb respectively, yielding a molar ratio of Zn/Co of 99.94/0.06.

8.3.3 Single-Crystal High-Frequency Paramagnetic Resonance

As previously discussed, complex **8A** is effectively a diamagnetic lattice of Zn_4 cubane molecules with a very small amount of Co^{II} ions doped in. Thus the sites at which we find Co^{II} ions are random. Statistically, only a minute number of molecules will contain more than one Co^{II} ion, so the spectra are dominated by single-ion signals for the Zn_3Co complexes diluted in a matrix of diamagnetic Zn_4 complexes, in the absence of antiferromagnetic of ferromagnetic exchange coupling to neighboring magnetic centers. This isolation allows very precise measurements to be performed regarding the environment of the individual Co^{II} sites in the lattice.

HFEPR data were collected on an oriented single crystal at an angle (32°, see insets in Figure 8.5) from the crystallographic *c*-axis and S_4 molecular principal axis, in the 100 plane of the crystal. If the magnetic field were aligned along the molecular easy-axis, only one peak, consisting of an average of the four Co^{II} sites, would be observed. Thus an arbitrary angle was chosen to probe the individual Co^{II} sites. It should be noted, due to symmetry considerations, certain rotational orientations may lead to degeneracy between one or more Co^{II} sites.

Figure 8.3 presents frequency dependent HFEPR data for complex **8A**, plotted as frequency versus magnetic field strength. The data were collected at 2K to ensure that only the ground state multiplet is populated, and in frequencies between ~50-100GHz. The inset in Figure 8.3 shows the EPR spectrum collected at 51.8GHz. The spectrum is composed of three well separated peaks that exhibit fine structure due to disorder and g-strain. In fact, the *g*-values were calculated from the slope of the line fitting. As will be further discussed, the peak at ~1T in the 51.8GHz inset and $g = 4.2$

in Figure 8.3 are assigned as a degenerate branch containing signals from two Co^{II} ions from analysis of line spacing in the temperature dependent and frequency dependent data. One can see that linear fits of frequency dependent data exactly go through the origin and are not parallel to one another, indicating the signal is not due to successive $m_s \pm 1$ magnetic dipole transitions, but rather are signals from individual Co^{II} ions in their ground state. Also, the straight line fit indicates that each of the ions possesses a well isolated spin ground state.

$$\hat{H} = \mu_B \hat{S} \bullet \vec{\vec{g}} \bullet \vec{B} \qquad \textbf{(8.1)}$$

Temperature dependent EPR spectra collected for complex **8A** in the same special orientation and frequency (51.8GHz) as Figure 8.3 are shown in Figure 8.4. As the temperature is lowered, the spectral peaks gain in intensity, but do not exhibit m_s transitions. This, in conjunction with frequency dependent data allow assignment of an effective $S = 1/2$ Kramer's doublet ground state for the $S = 3/2$ Co^{II} ions, employing the Zeeman Hamiltonian (Equation 8.1), where μ_B is the Bohr magneton, S is the spin, g is the Landé factor and B is the applied magnetic field. Reduction to an effective spin 1/2 greatly simplifies the problem of analysis. Boltzman populations of excited states lead to line broadening at higher temperatures which are systematically removed as the temperature is decreased, leading to sharper, well defined peaks at low temperatures when only the ground state is populated.

A 360° rotation around any plane will produce a spectrum that in low symmetry positions will yield four distinct signals associated with the four independent Co^{II} ions. However, as a rotation passes through a high symmetry position, *e.g.* directly along the crystallographic *c*-axis or z-axis of the molecules, the peaks will coalesce into a single peak, or average of the four Co^{II} ion positions. If rotation is done exactly in the hard-axis (xy plane) of the molecules two symmetry independent signals will be observed that will decoalesce into four peaks if there is deviation from the hard-plane orientation, because the symmetry dictated degeneracy is lifted.

Figure 8.5 presents angle-dependent EPR spectra, collected at 2K at 51.6GHz, plotted as applied magnetic field versus rotation angle. In this experiment the rotation angle is oriented in the 110 crystal plane. From left to right in Figure 8.5a three signals are seen that represent two individual Co^{II} sites and a degenerate branch which is shown in solid round circles. At theta = 0 the magnetic field must be oriented along the *c*-axis direction because the signals coalesce into one minimum, and thus, the four sites are equivalent. At theta = 90 the signal consists of two peaks that represent positions near the hard-plane of two sites and near the easy-axis of the other two sites. Since all of the molecules in the crystal are oriented along the same axis (*c*-axis) and the fact that the system has a preferred orientation in a magnetic field, we assume the octahedrally coordinated Co^{II} ions each contribute to the overall anisotropy of the system, and thus exhibit easy-axis type anisotropy. Close examination of the spectra in Figure 8.5a reveals that the magnetic axes of the four Co^{II} ions are not collinear, rather, they are tilted with respect to the easy-axis of the molecules and with respect to each other. One

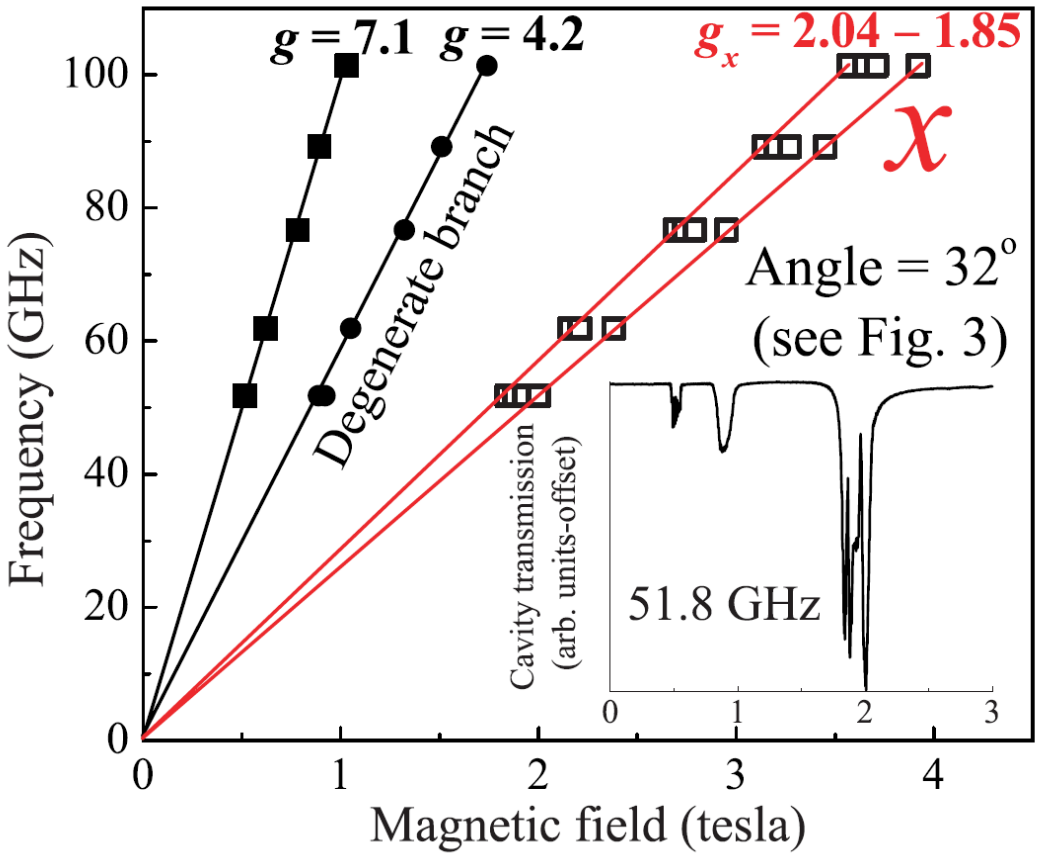

Figure 8.3. Frequency-dependent data for complex 1 obtained at 2 K, with the field tilted _32_ away from the c-axis (see also Figure 5). The inset shows a typical spectrum obtained at a frequency of 51.8 GHz. The positions of each of the three main peaks are plotted versus frequency in the main part of the figure. Lande´ g-factors have been assigned to each of the peaks based on the slope of the straight line through each set of data points; the field is oriented such that the highest field peak corresponds approximately to the x-component of the g-tensor.

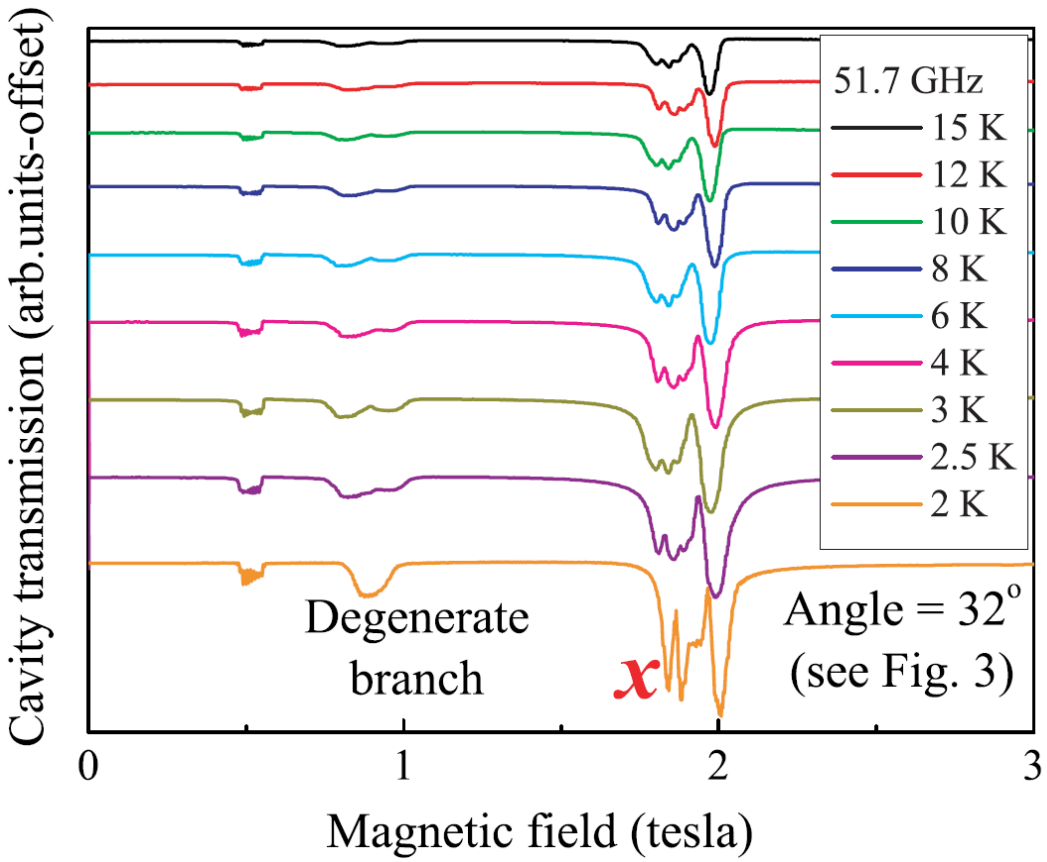

Figure 8.4. Temperature dependence of the HFEPR spectra for approximately the same frequency and field orientation as the data in Figure 8.3.

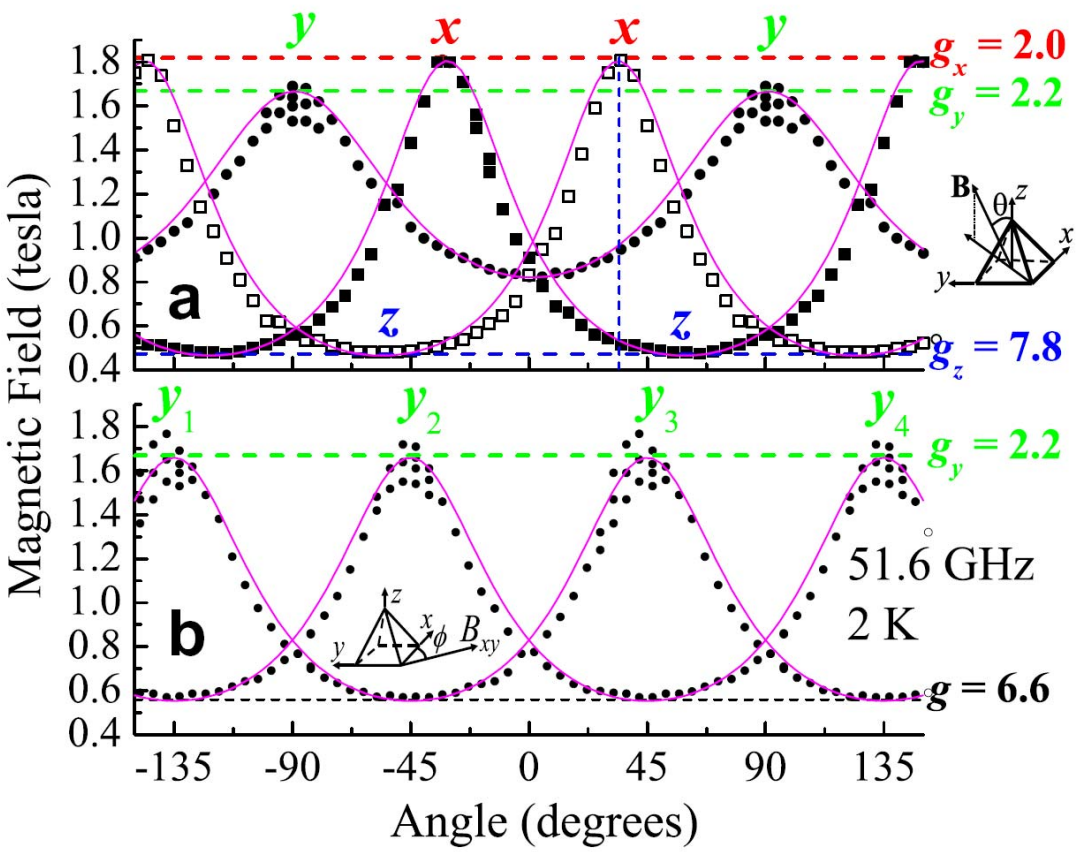

Figure 8.5. Angle dependence of the HFEPR peak positions observed for a frequency of 51.6 GHz and a temperature of 3 K, for field rotation in (a) the (110) plane, and (b) the ab-plane. In (a), the angle is referenced to the crystallographic c-axis while, in (b), the angle is referenced to either the a or b axes. In (a), the degenerate branch is indicated by the solid circles, while the squares denote rotations along a plane intersecting two of the easy-axes (labeled z). The schematic insets illustrate the two field rotation planes relative to the pyramid shaped single crystal. The g-values associated with the extreme positions in the angle-dependence are indicated on the right. The magenta curves are simulations based on the obtained extreme g-values for each plane of rotation. The directions of the local magnetic axes (x, y, z) are indicated in the figure.

can rationalize this by analysis of the spectral data. As the rotational angle deviates from theta = 0, the signal from three sites (single and degenerate signals) shift to higher magnetic field strength, and the fourth moves to lower field strength. This suggests that if the field strength increases the rotation is moving into the hard-plane of three of the sites and toward the easy axis of the fourth. This would not be the case if the individual Co^{II} sites were 1) collinear, and 2) not of easy-axis type anisotropy.

Rotation in a 180 degree plane cycles through the hard-planes of the individual Co^{II} sites, as dictated by the maxima observed in Figure 8.5a. The maxima occur at ± 90° and ± 32° for Figure 8.5a. Figure 8.5b represents angle dependent data collected in a plane that exhibits two signals, and thus, each signal is representative of two ion sites that are degenerate, with maxima at ± 45°. From Figure 8.5a we can see that the degenerate branch exactly coincides with signals from two ion sites, and the other two sites are totally symmetric to one another throughout the rotation. This signifies that the easy axes of these sites are found exactly corresponding to *Z* in Figure 8.5a. Employing the Zeeman Hamiltonian, with an effective S =1/2 Kramer's doublet ground state, a value of g_z = 7.80 can be assigned (blue dashed line). And from the orientations of the observed maxima and minima it is determined the *g*–tensors for the individual sites are tilted 58° away from the crystallographic *c*-axis. Values for the x and y directions were calculated in a similar manner. Interestingly, g_x and g_y are not equivalent and suggest xy-plane anisotropy (g_x = 2.20 and g_y = 2.20), most likely as a result of orthorhombic distortion of the octahedrally coordinated Co^{II} sites. The magenta curves depicted in Figure 8.5 (a and b) are fits to experimental data. With a well isolated ground state and ions that experience only spin-orbit interaction in the absence of magnetic exchange

interactions, the relationship between the applied frequency and the magnetic field strength at resonance can be fit to Equation 8.2, where h is Plank's constant, g is the Landé g-factor, f is the frequency, μ_B is the Bohr magneton and B_{res} is the applied magnetic field strength at resonance. So the fit (magenta lines) represent the angle dependence of the g-tensors, and is analyzed employing Equation 8.3.

$$hf = g(\theta)\mu_B B_{res} \quad \textbf{(8.2)}$$

$$g(\theta) = g_{\min} + \delta g \cos^2(\theta - \theta_0) \quad \textbf{(8.3)}$$

The question becomes, how does the observed anisotropy of complex **8B** arise? In the absence of an applied magnetic field the single ion $S = 1/2$ ions exhibit no zero-field spitting component, and thus, cannot be responsible for observed magnetization dynamics. In contrast to complex **8B** which exhibits substantial magnetic exchange between Co^{II} ions, the diamagnetic lattice of complex **8A** allows analysis of individual paramagnetic Co^{II} ions. Anisotropy in spin-spin interactions can then be modeled by adding an exchange parameter to the Zeeman Hamiltonian (Equation 8.1), where S_i and S_j represent the spin on nearest-neighbor magnetic centers, and J_{ij} gauges the magnitude of the exchange coupling between magnetic centers. Analysis is simplified by the fact that the Co^{II} ions can be modeled as an effective $S = 1/2$ system, and yields a 16 x 16 Hamiltonian matrix that is easily diagonalized.

Figure 8.6 presents oriented single-crystal frequency dependent data for complex **8B** collected at 2K in frequencies between 50 and 715GHz. Where frequency

dependent spectra for complex **8A** all intersect the origin in Figure 8.3, and arises completely due to anisotropy in *g*, the frequency dependent spectra in Figure 8.6 represent m_s magnetic dipole transitions within the exchange coupled Co_4 magnetic core. There are four very important observations that should be made regarding Figure 8.6: 1) non-linearity is exhibited by some of the transitions, 2) the transitions deviate from parallel relative to one another, 3) the branches intersect the frequency axis at different points, and 4) more transitions are observed than would be expected for an exchange coupled tetranuclear core of effective $S = 1/2$ Kramer's ions (solid lines are not fits of frequency dependent data, and are only included to group related transitions). The data clearly show that complex **8B** is highly anisotropic, and there exists both a wide distribution in *g* and values of zero-field interactions. A qualitative look at the slope of the lines of the different resonance branches yields *g*-tensor values of 2.0 to 7.4, which is commensurate with single ion values assigned in analysis of complex **8A**, and are near the maximum of what is expected for octahedrally coordinated Co^{II} ions. At lower frequencies transitions are predominantly due to excited state transitions (red squares). Evidence for this can be seen in the temperature dependent spectra for complex **8B** (Figure 8.7). At 99GHz several of the transitions at higher field strength decrease with decreasing temperature. If a transition emanates from ground state transitions within the ground state multiplet, transitions will become sharper and exhibit greater intensity with decreasing temperature due to depopulation of Boltzman energy states. Thus, the transitions observed at higher fields in the 99GHz spectra can only originate from populated excited states. At higher frequencies (288 and 501 GHz) the transition intensity increases with decreasing temperature, and are assigned as magnetic

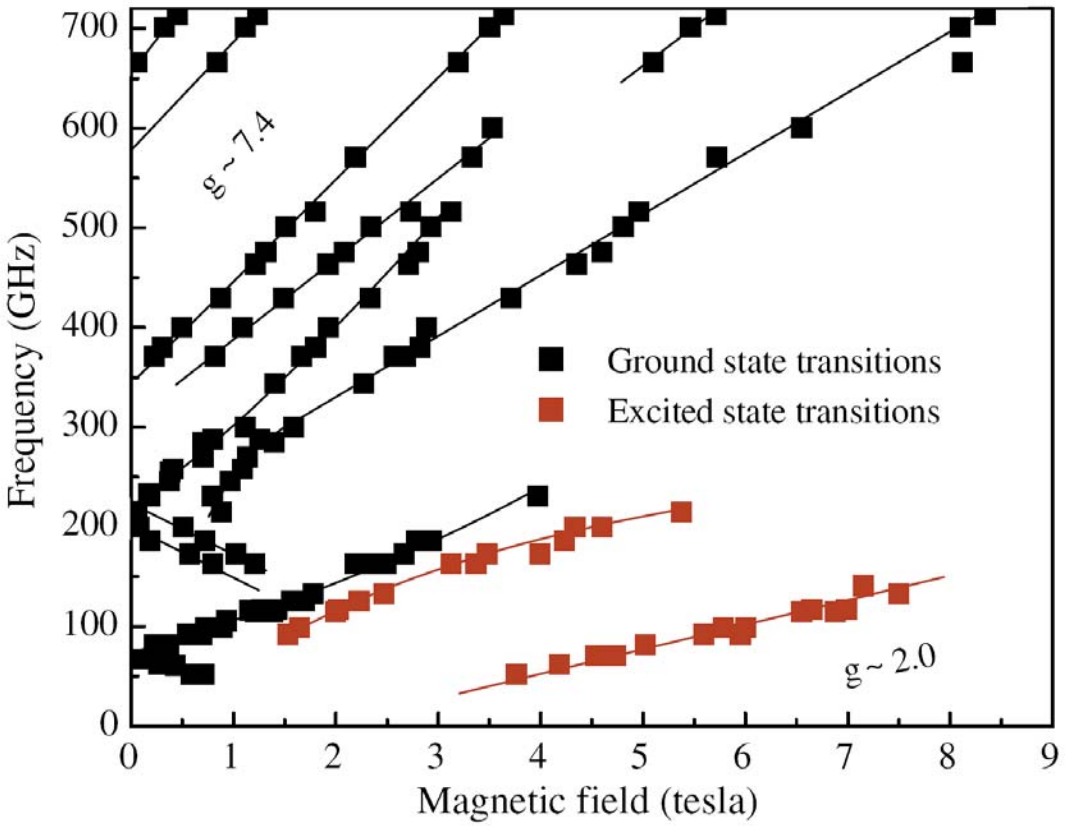

Figure 8.6. A 2D frequency verses field plot representing the positions of the stronger resonances observed from the frequency dependence measurements with the field parallel to the c-axis. The solid curves are purely guides to the eye.

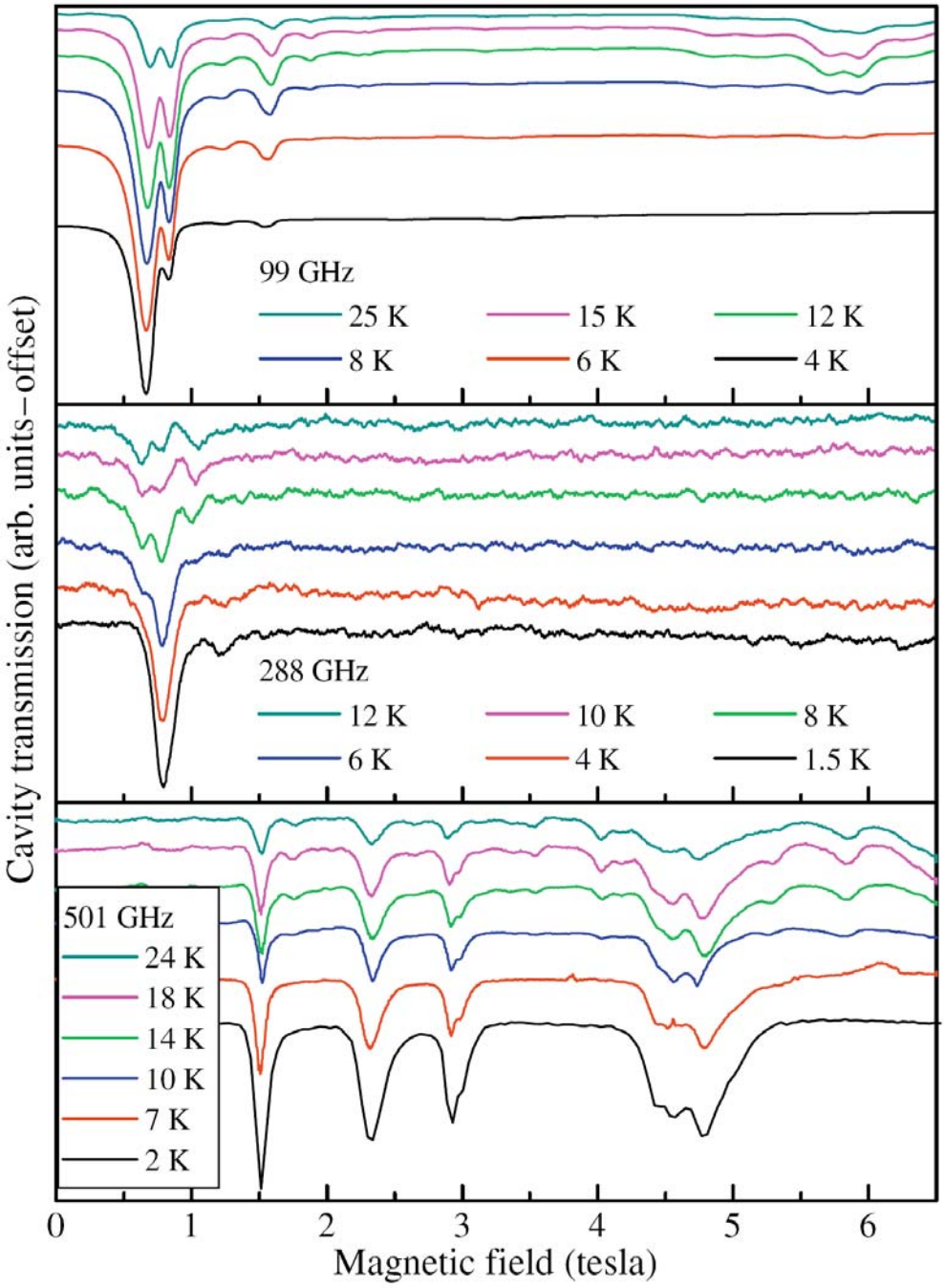

Figure 8.7. Temperature dependence measurements (B//c) for three different frequencies; the temperatures and frequencies are given in the figures.

transitions within the ground state multiplet. Comparison of frequency and temperature dependent data are consistent, and in complete agreement regarding the origin of observed transitions.

Inhomogeneity in values of *g* and zero-field splitting values make analysis of the frequency dependent transitions extremely difficult. The temperature and frequency dependent data strongly suggest that there is considerable mixing of states within the *S*-multiplets, and thus *S* and m_s are not good quantum numbers, leading to a break-down of EPR selection rules ($m_s = \pm 1$). In a well isolated ground state multiplet frequency dependent spectra would exhibit well-spaced near parallel resonance branches as a result of successive Δm_s transitions, *i.e.* -2 to -1…-1 to 0…0 to 1 etc, which is not evident in experimental data. At frequencies below 300GHz there are resonance branches that run perpendicular to the other resonance branches and are an indication of strong repulsion between energy levels. This suggests that mixing is occurring between the ground state multiplet and excited state multiplets and may also be occurring purely between excited multiplets.

$$H = J\sum_{i<j}[\hat{S}_{iz}\hat{S}_{jz} + \alpha(\hat{S}_{ix}\hat{S}_{jx} + \hat{S}_{iy}\hat{S}_{jy})] + \sum_i \mu_B \vec{B}\bullet\vec{g}\bullet\hat{S}_i \qquad \textbf{(8.4)}$$

A qualitative/semi-quantitative approach can be applied for analysis of complex **8B** through theoretical simulations. If the magnetic exchange between Co^{II} ions is strictly isotropic and the projections of the four *g*-tensors are parallel with respect to the easy-axis of the molecule and to each other, application of an external

magnetic field lifts the degeneracy of the spin multiplets, and transitions resonances will depend linearly on the magnetic field strength (transitions between m_s states will occur at the same magnetic field strength). Figure 8.8a shows the splitting of the $S_T = 0$, 1 and 2 spin multiplets derived from diagonalization of the energy Hamiltonian Equation 8.1, with J = -200GHz and g = 6.0. Since the system is isotropic, no zero-field interactions are present, and a plot of frequency dependence data would be very similar to the data in Figure 8.3, *i.e.* each branch would pass exactly through the origin.

If we include axial anisotropy in the magnetic exchange interactions in conjunction with the first model (Equation 8.4), where J represents isotropic exchange and α is the measure of anisotropy (when α = 1 the system is isotropic), diagonalization of the Hamiltonian with $\alpha = 2^{-1/2}$ and J = -200GHz results in Figure 8.8b. The anisotropy lifts the degeneracy of the $2S + 1$ spin multiplets, but in contrast to Figure 8.8a, the transitions are field dependent with successive $m_s \pm 1$ transitions occurring at regularly spaced intervals of B (the applied magnetic field). Though the resonance pattern depicted in Figure 8.8b mimics quite well the spectra exhibited by known SMMs, it falls short of explaining the HFEPR data for complex **8B**.

HFEPR analysis of complex **8A** revealed that the tensorial projections of the single ions are tilted 58° from the molecular easy-axis. Furthermore, symmetry considerations dictate that two J values are required in the analysis of a cubane molecule with S_4 molecular site symmetry. Frequency versus magnetic field data from diagonalization of the Hamiltonian including single ion tilt angles is presented in Figure 8.8c. A number of interesting observations can be made from this data. First, the line

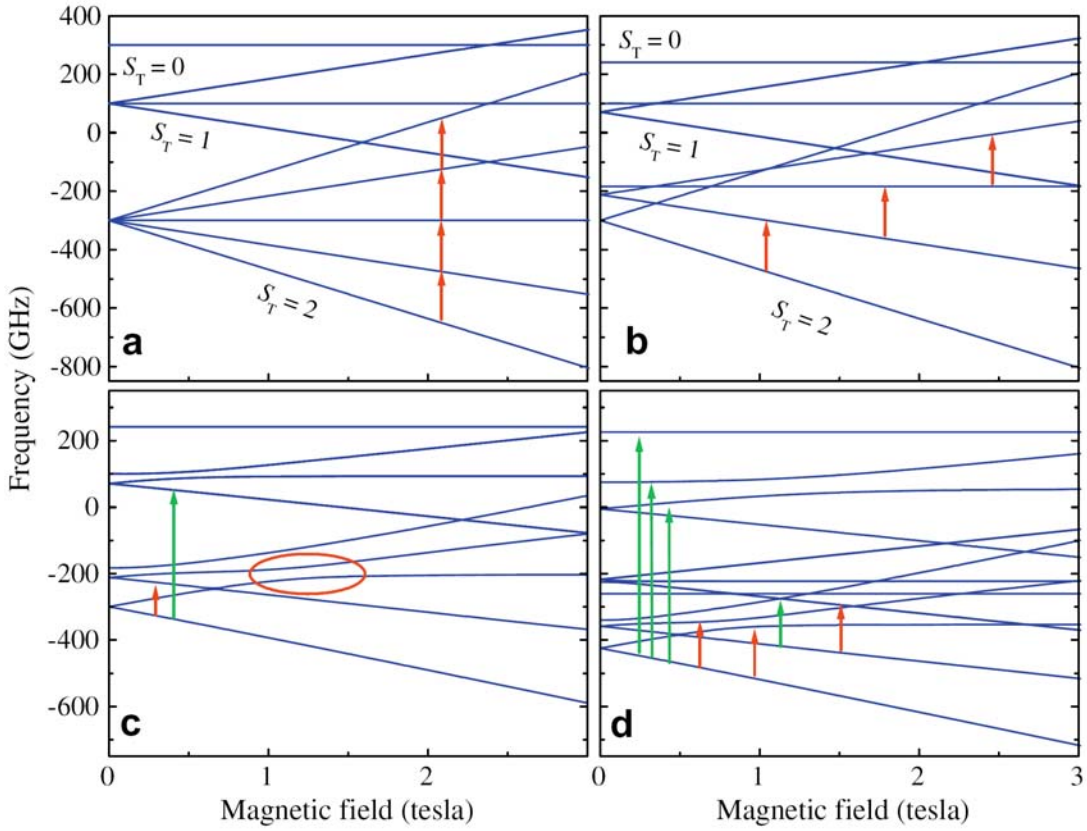

Figure 8.8. Simulated Zeeman diagrams obtained for complex 1 on the basis of Equation 8.4 using various different parameter sets: (a) represents the isotropic case; (b) adds an axial exchange anisotropy; (c) includes the effect of a tilting (58°) of the single-ion g-tensors away from the axial direction; and (d) considers two inequivalent exchange parameters within the cluster.

slope of the data suggests strongly that *g* is significantly reduced. This makes intuitive sense because the molecular *g*-tensor is a product of the projection of the individual ions, and the magnitude is significantly reduced as the tensorial projections deviate from the z-axis. Second, tilting of tensorial projections and exchange anisotropy induces level repulsions between *S*-multiplets (red circle in Figure 8.8c), as are evident in the frequency dependent data for complex **8B**. And third, multiple ground state transitions between multiplets differing in *S* are evident as indicated by the green and red arrows. In Figures 8.8a and b it is apparent that no spin mixing is evident and the ground state is relatively isolated, thus, *S* and m_s are good magnetic quantum numbers. This is not the case in regards to Figures 8.8c and d. In these figures the tilting of ion projections, anisotropy in exchange, and competing exchange significantly mix spin-multiplets leading to a break-down of EPR transition selection rules. The addition of a second magnetic exchange parameter J_2 significantly intensifies spin mixing and transitions between spin-multiplets that differ in *S*. A plot of frequency dependence versus field for such a system would begin to take on characteristics very similar to experimental data for complex **8**B**.**

8.4 Conclusion

Though the experimental HFEPR data for complex **8B** can not be analyzed in great detail due to extreme complexity, we have shown that application of HFEPR data collected on an analogous diamagnetic complex doped with small amounts of Co^{II} ions we can begin to rationalize the magnetization dynamics and exhibited magnetization hysteresis behavior of this interesting tetranuclear cobalt complex. We have shown the

S = 3/2 cobalt ions can be modeled effectively as S = 1/2 Kramer's doublets. The Kramer's ions exhibit no zero-field anisotropy individually, but strong exchange anisotropy leads significant easy-axis molecular anisotropy.

Chapter 8, figures and captions are reprints from: Lawrence, J., Beedle, C. C.; Yang, E. C., Ma, J.; Hill, S., Hendrickson, D. N., High Frequency Electron Paramagnetic Resonance (HF-EPR) Study of a High Spin Co(II) Complex. *Polyhedron* **2007,** 26, (9-11), 2299-2303, and, Liu, J.; Datta, S.; Bolin, E.; Lawrence, J.; Beedle, C. C.; Yang, E.-C.; Goy, P.; Hendrickson, D. N.; Hill, S., Anisotropic Exchange in a Tetranuclear Co^{II} Complex. *Polyhedron* **2009**, 28, (9) 1922-1926. The dissertation author was a highly contributing investigator on the material.

8.5 References

(1) Barra, A. L.; Caneschi, A.; Cornia, A.; de Biani, F. F.; Gatteschi, D.; Sangregorio, C.; Sessoli, R.; Sorace, L. *Journal of the American Chemical Society* **1999**, *121*, 5302-5310.

(2) Gatteschi, D.; Sessoli, R.; Cornia, A. *Chemical Communications* **2000**, 725-732.

(3) Goodwin, J. C.; Sessoli, R.; Gatteschi, D.; Wernsdorfer, W.; Powell, A. K.; Heath, S. L. *Journal of the Chemical Society-Dalton Transactions* **2000**, 1835-1840.

(4) Wernsdorfer, W.; Caneschi, A.; Sessoli, R.; Gatteschi, D.; Cornia, A.; Villar, V.; Paulsen, C. *Physical Review Letters* **2000**, *84*, 2965-2968.

(5) Christou, G.; Gatteschi, D.; Hendrickson, D. N.; Sessoli, R. *Mrs Bulletin* **2000**, *25*, 66-71.

(6) Gatteschi, D. *Current Opinion in Solid State & Materials Science* **1996**, *1*, 192-198.

(7) Gatteschi, D. *Journal of Alloys and Compounds* **2001**, *317*, 8-12.

(8) Oshio, H.; Hoshino, N.; Ito, T.; Nakano, M. *J. Am. Chem. Soc.* **2004**, *126*, 8805-8812.

(9) Rumberger, E. M.; Hill, S.; Edwards, R. S.; Wernsdorfer, W.; Zakharov, L. N.; Rheingold, A. L.; Christou, G.; Hendrickson, D. N. *Polyhedron* **2003**, *22*, 1865-1870.

(10) Barra, A. L.; Gatteschi, D.; Sessoli, R. *Chemistry-a European Journal* **2000**, *6*, 1608-1614.

(11) Brechin, E. K.; Knapp, M. J.; Huffman, J. C.; Hendrickson, D. N.; Christou, G. *Inorganica Chimica Acta* **2000**, *297*, 389-399.

(12) Sessoli, R.; Tsai, H. L.; Schake, A. R.; Wang, S. Y.; Vincent, J. B.; Folting, K.; Gatteschi, D.; Christou, G.; Hendrickson, D. N. *Journal of the American Chemical Society* **1993**, *115*, 1804-1816.

(13) Yang, E. C.; Wernsdorfer, W.; Hill, S.; Edwards, R. S.; Nakano, M.; Maccagnano, S.; Zakharov, L. N.; Rheingold, A. L.; Christou, G.; Hendrickson, D. N. *Polyhedron* **2003**, *22*, 1727-1733.

(14) Yang, E. C.; Wernsdorfer, W.; Zakharov, L. N.; Karaki, Y.; Yamaguchi, A.; Isidro, R. M.; Lu, G. D.; Wilson, S. A.; Rheingold, A. L.; Ishimoto, H.; Hendrickson, D. N. *Inorganic Chemistry* **2006**, *45*, 529-546.

(15) Yang, E. C.; Kirman, C.; Lawrence, J.; Zakharov, L. N.; Rheingoid, A. L.; Hill, S.; Hendrickson, D. N. *Inorganic Chemistry* **2005**, *44*, 3827-3836.

(16) Lawrence, J.; Yang, E.-C.; Edwards, R.; Olmstead, M. M.; Ramsey, C.; Dalal, N. S.; Gantzel, P. K.; Hill, S.; Hendrickson, D. N. *Inorganic Chemistry* **2008**, *47*, 1965-1974.

(17) Wilson, A.; Lawrence, J.; Yang, E. C.; Nakano, M.; Hendrickson, D. N.; Hill, S. *Physical Review B (Condensed Matter and Materials Physics)* **2006**, *74*, 140403.

(18) Wilson, A.; Yang, E. C.; Hendrickson, D. N.; Hill, S. *Polyhedron* **2007**, *26*, 2065-2068.

(19) Aromi, G.; Batsanov, A. S.; Christian, P.; Helliwell, M.; Parkin, A.; Parsons, S.; Smith, A. A.; Timco, G. A.; Winpenny, R. E. P. *Chemistry-a European Journal* **2003**, *9*, 5142-5161.

(20) Brechin, E. K.; Coxall, R. A.; Parkin, A.; Parsons, S.; Tasker, P. A.; Winpenny, R. E. P. *Angewandte Chemie-International Edition* **2001**, *40*, 2700-2703.

(21) Brechin, E. K.; Graham, A.; Parkin, A.; Parsons, S.; Seddon, A. M.; Winpenny, R. E. P. *Journal of the Chemical Society-Dalton Transactions* **2000**, 3242-3252.

(22) Cadiou, C.; Coxall, R. A.; Graham, A.; Harrison, A.; Helliwell, M.; Parsons, S.; Winpenny, R. E. P. *Chemical Communications* **2002**, 1106-1107.

(23) Zarembowitch, J.; Kahn, O. *Inorganic Chemistry* **1984**, *23*, 589-593.

(24) Kahn, O. *Molecular magnetism*; VCH: New York, NY, 1993.

(25) Yang, E. C. *Ph.D. Dissertation, University of California, San Diego, La Jolla, CA*. **2004**.

(26) Yang, E. C.; Hendrickson, D. N.; Wernsdorfer, W.; Nakano, M.; Zakharov, L. N.; Sommer, R. D.; Rheingold, A. L.; Ledezma-Gairaud, M.; Christou, G. *Journal of Applied Physics* **2002**, *91*, 7382-7384.

(27) Mola, M.; Hill, S.; Goy, P.; Gross, M. *Review of Scientific Instruments* **2000**, *71*, 186-200.

(28) Fujita, Y.; Mori, I.; Yamaguchi, T.; Hoshino, M.; Shigemura, Y.; Shimano, M. *Analytical Sciences* **2001**, *17*, 853-857.